

**Bis(tridentate) Polypyridine Ruthenium(II)  
Complexes with *Push-Pull* Character**

Synthesis, Understanding and Application

**Dissertation**

Zur Erlangung des Grades

„Doktor der Naturwissenschaften“

Im Promotionsfach Chemie

am Fachbereich Chemie, Pharmazie und Geowissenschaften  
der Johannes Gutenberg-Universität Mainz

**Christoph Kreitner**

geboren in Wiesbaden

Mainz, 2016





Die vorliegende Arbeit wurde in der Zeit von Januar 2013 bis Juni 2016 am Institut für Anorganische Chemie und Analytische Chemie der Johannes Gutenberg-Universität Mainz unter Anleitung von [REDACTED] angefertigt.

Mainz, Juni 2016

Dekan:

[REDACTED]

1. Berichterstatter:

[REDACTED]

2. Berichterstatter:

[REDACTED]

Tag der mündlichen Prüfung: 11. Juli 2016

## Zusammenfassung

Die genaue Kenntnis der elektronischen Eigenschaften einer Klasse von Übergangsmetallkomplexen ist für Chemiker und Materialwissenschaften von großem Interesse, da es das Einstellen der Eigenschaften ermöglicht und die Entwicklung passender Anwendungen erleichtert. In der hier vorgestellten Arbeit wird die Synthese und Charakterisierung neuer *push-pull*-substituierter bis(tridentater) Rutheniumkomplexe diskutiert.

Im ersten Abschnitt wird ein zweikerniger amid-verbrückter Bis(terpyridin)ruthenium-Komplex mit einer hohen elektronischen Symmetrie trotz der intrinsischen strukturellen Asymmetrie diskutiert. Im gemischtvalenten Zustand wird keine Metall-Metall-Wechselwirkung beobachtet. Das ungepaarte Elektron ist vollständig auf einem der beiden Rutheniumatome lokalisiert, weil die spintragenden Orbitale und die Grenzorbitale des die elektronische Kopplung vermittelnden Brückenliganden energetisch zu weit auseinanderliegen. Im photoangeregten Zustand jedoch ist der Brückenligand einfach reduziert. Dies ermöglicht eine elektronische Wechselwirkung zwischen den Metallzentren, sodass bei Raumtemperatur zwei Valenztautomere anhand ihrer dualen Emission gleichzeitig beobachtet werden können.

Weiterhin wurden cyclometallierte  $\text{Ru}(\text{N}^{\wedge}\text{N}^{\wedge}\text{N})(\text{N}^{\wedge}\text{C}^{\wedge}\text{N})^+$ -Komplexe mit Substituenten entweder nur am cyclometallisierenden oder an beiden Liganden synthetisiert und untersucht. Ihre Absorptionseigenschaften wurden durch eine Kombination von spektroskopischen und theoretischen Methoden studiert, die gezeigt haben, dass die niederenergetischen Absorptionsbanden aus  $\text{Ru} \rightarrow (\text{N}^{\wedge}\text{N}^{\wedge}\text{N})$  und  $\text{Ru} \rightarrow (\text{N}^{\wedge}\text{C}^{\wedge}\text{N})$ -Übergängen in ähnlichen Anteilen zusammengesetzt sind. Alle untersuchten Komplexe sind bei Raumtemperatur schwach emissiv ausgehend von einem  $^3\text{MLCT}$ -Zustand (Metal-zu-Ligand-Charge-Transfer), der allerdings durch einen wohlbekannten metallzentrierten und einen zuvor unerkannten Ligand-zu-Ligand-Charge-Transfer-Zustand effizient depopuliert wird. Dies wurde durch temperaturabhängige Messung der Quantenausbeute sowie unterstützende dichtefunktionaltheoretische Rechnungen weiter untermauert. Darüber hinaus wurden cyclometallierte Komplexe mit  $[\text{Ru}(\text{N}^{\wedge}\text{N})_2(\text{N}^{\wedge}\text{C})]^+$ - und  $[\text{Ru}(\text{N}^{\wedge}\text{N}^{\wedge}\text{N})(\text{N}^{\wedge}\text{N}^{\wedge}\text{C})]^+$ -Koordinationsumgebung auf theoretischer Ebene untersucht und Gemeinsamkeiten und Unterschiede in den Mechanismen der Depopulation der angeregten Zustände herausgestellt.

In Analogie zum zweikernigen Bis(terpyridin)ruthenium-Komplex wurde ein strukturell ähnlicher Komplex mit einem zweifach cyclometallisierenden amidverknüpften Brückenliganden hergestellt und untersucht. Die veränderten Energien der Grenzorbitale des Brückenliganden ermöglichen hier eine elektronische Wechselwirkung zwischen den Metallzentren, sodass im gemischtvalenten Zustand eine intensive Intervallenz-Charge-Transfer-Bande im Nahinfrarot-Bereich des elektromagnetischen Spektrums beobachtet werden kann. Im photoangeregten Zustand wird darüber hinaus duale Emission beobachtet. Diese resultiert aus zwei elektronisch ungekoppelten  $^3\text{MLCT}$ -Zuständen, die auf den äußeren Terpyridinliganden lokalisiert sind. Die Distanz zwischen diesen beiden angeregten Zuständen ist zu groß, um die Einstellung eines thermischen Gleichgewichts via Energietransfer zu erlauben. Erst durch Abkühlen und Einfrieren der Lösung werden die strahlungslosen Zerfallsprozesse ausreichend verlangsamt, dass eine Equilibrierung stattfindet.

Unter Berücksichtigung dieser Erkenntnisse wurden cyclometallierte Polypyridinruthenium-Komplexe mit Triarylamin-Substituenten entwickelt und ihre Eignung als Sensibilisatoren in Farbstoffsolarzellen untersucht. Diese Komplexe sind im gemischtvalenten Zustand valenzdelokalisiert, was nach der Ladungsinjektion einen mesomeren Ladungstransport weg von der Halbleiteroberfläche ermöglicht. Allerdings resultiert aus der Delokalisation auch eine messbare Resonanzstabilisierung des gemischtvalenten Zustands. Dies führte zu einer erschwerten Regeneration des Farbstoffs in mehreren der gewählten Farbstoff/Elektrolyt-Kombinationen. Als Folge davon wird die Effizienz der Solarzellen mit dem Referenzfarbstoff **N719** in Gegenwart von Iodid/Triiodid als Elektrolyt von keinem der entwickelten cyclometallierten Farbstoffe erreicht. Bei der Verwendung kationischer Polypyridinocobalt-Elektrolyte hingegen zeigen **N719** und die cyclometallierten Farbstoffe eine ähnliche Performance, aber die Effizienzen sind insgesamt deutlich geringer als mit Iodid/Triiodid.

## Abstract

The profound understanding of the electronic properties of a class of transition metal complexes is of interest to chemists and material scientists as it allows the tuning of their properties and the development of suitable applications. In the work presented herein, the synthesis and characterization of novel *push-pull* substituted bis(tridentate) ruthenium complexes is presented.

In the first section, a dinuclear amide-bridged bis(terpyridine) ruthenium complex with a high electronic symmetry despite the intrinsic structural asymmetry is studied. No metal-metal-interaction is detected in the mixed valent state with the odd electron being entirely localized at one of the two ruthenium centers. This is because the spin carrying orbitals and the mediating orbitals of the bridging ligand are energetically fairly separated. In the photo-excited state, on the other hand, the bridging ligand is formally reduced by one electron. This enables electronic coupling between the two metal centers, so that two valence tautomers are detected simultaneously at room temperature by their dual emission.

Further, cyclometalated  $\text{Ru}(\text{N}^{\wedge}\text{N}^{\wedge}\text{N})(\text{N}^{\wedge}\text{C}^{\wedge}\text{N})]^+$  complexes with substituents on either the cyclometalating ligand or both ligands have been synthesized and investigated. Their absorption properties were studied using a combination of spectroscopic and theoretical methods showing that the low-energy absorption bands are composed of  $\text{Ru} \rightarrow (\text{N}^{\wedge}\text{N}^{\wedge}\text{N})$  and  $\text{Ru} \rightarrow (\text{N}^{\wedge}\text{C}^{\wedge}\text{N})$  transitions to a similar extent in all cases. All complexes are very weakly emissive at room temperature from a  $^3\text{MLCT}$  (metal-to-ligand charge transfer) state, that is efficiently depopulated *via* a well-known metal-centered excited state and a previously unrecognized ligand-to-ligand charge transfer state. This was evidenced by temperature-dependent quantum yield measurements and supplementary density functional theory calculations. Additionally,  $[\text{Ru}(\text{N}^{\wedge}\text{N})_2(\text{N}^{\wedge}\text{C})]^+$  and  $[\text{Ru}(\text{N}^{\wedge}\text{N}^{\wedge}\text{N})(\text{N}^{\wedge}\text{N}^{\wedge}\text{C})]^+$  complexes were studied on a theoretical basis highlighting common features and differences in the excited state depopulation mechanics of the different classes of complexes.

In analogy to the dinuclear bis(terpyridine) ruthenium complex, a structurally related complex with an amide-linked biscyclometalating bridging ligand was synthesized and studied. The altered bridge's frontier orbitals result in electronic coupling between the metal centers in the mixed-valent state as evidenced from an intense intervalence charge transfer band in near infrared region of the electromagnetic spectrum. In the photo-excited state, dual emission is observed at room temperature from two electronically uncoupled  $^3\text{MLCT}$  states localized at peripheral terpyridine ligands. The distance between the emissive states is too large to allow for a thermally equilibrating energy transfer to occur. Only upon freezing the solution, the non-radiative decay processes are retarded sufficiently to allow for equilibration.

Considering these findings, cyclometalated polypyridine ruthenium complexes bearing triarylamine substituents were devised for use as sensitizers in dye-sensitized solar cells. These complexes are substantially valence-delocalized in the mixed-valent state allowing for mesomeric charge delocalization away from the semiconductor surface after charge injection. However, this delocalization results in a measurable resonance stabilization of the mixed-valent state that hampers dye regeneration by the electrolyte in several of the employed dye/electrolyte combinations. As a consequence, the efficiency of solar cells employing benchmark sensitizer **N719** are unmatched by the developed cyclometalated polypyridine ruthenium dyes when combined with iodide/triiodide as electrolyte. Using cationic polypyridine cobalt electrolytes, **N719** and the cyclometalated dyes exhibit similar performances, but the overall efficiencies are lower than with iodide/triiodide.



# TABLE OF CONTENTS

<b>1</b>	<b>Introduction</b>	<b>1</b>
1.1	Redox and Photochemistry of Bis(terpyridine) Ruthenium(II) Amino Acids and Their Amide Conjugates – from Understanding to Applications	3
1.2	Excited State Decay Mechanisms in Polypyridine Ruthenium Complexes	29
1.2.1	<i>Phosphorescence</i>	29
1.2.2	<i>Non-radiative Decay</i>	30
1.2.3	<i>Other Excited State Decay Channels</i>	33
1.3	Mixed Valence and Optical Electron Transfer	36
1.4	Cyclometalation	39
1.5	Dye-Sensitized Solar Cell	42
<b>2</b>	<b>Aim of the Work</b>	<b>47</b>
<b>3</b>	<b>Results and Discussion</b>	<b>49</b>
3.1	Dual Emission and Excited-State Mixed-Valence in a Quasi-Symmetric Dinuclear Ru–Ru Complex	53
3.2	Understanding the Excited State Behavior of Cyclometalated Bis(tridentate)ruthenium(II) Complexes: A Combined Experimental and Theoretical Study	69
3.3	The Photochemistry of Mono- and Dinuclear Cyclometalated Bis(tridentate)ruthenium(II) Complexes: Dual Excited State Deactivation and Dual Emission	89
3.4	Strongly Coupled Cyclometalated Ruthenium Triarylamine Chromophores as Sensitizers for DSSCs	109
3.5	Excited State Decay of Cyclometalated Polypyridine Ruthenium Complexes: Insight from Theory and Experiment	125
3.6	[Cr(ddpd) <sub>2</sub> ] <sup>3+</sup> : A Molecular, Water-Soluble, Highly NIR-Emissive Ruby Analogue	155
<b>4</b>	<b>Summary and Outlook</b>	<b>161</b>
<b>5</b>	<b>References</b>	<b>165</b>
<b>6</b>	<b>Appendix</b>	<b>171</b>
6.1	Supporting Information To 1.1: Redox and Photochemistry of Bis(terpyridine) Ruthenium(II) Amino Acids and Their Amide Conjugates – from Understanding to Applications	171
6.2	Supporting Information To 3.1: Dual Emission and Excited-State Mixed-Valence in a Quasi-Symmetric Dinuclear Ru–Ru Complex	175

6.3	Supporting Information to 3.2: Understanding the Excited State Behavior of Cyclometalated Bis(tridentate)ruthenium(II) Complexes: A Combined Experimental and Theoretical Study	184
6.4	Supporting Information to 3.3: The Photochemistry of Mono- and Dinuclear Cyclometalated Bis(tridentate)ruthenium(II) Complexes: Dual Excited State Deactivation and Dual Emission	209
6.5	Supporting Information to 3.4: Strongly Coupled Cyclometalated Ruthenium Triarylamine Chromophores as Sensitizers for DSSCs	240
6.6	Supporting Information to 3.5: Excited State Decay of Cyclometalated Polypyridine Ruthenium Complexes: Insight from Theory and Experiment	259
6.7	Supporting Information to 3.6: $[\text{Cr}(\text{ddpd})_2]^{3+}$ : A Molecular, Water-Soluble, Highly NIR-Emissive Ruby Analogue	281
<b>7</b>	<b>Acknowledgments</b>	<b>311</b>
<b>8</b>	<b>Curriculum Vitae</b>	<b>313</b>
8.1	List of Publications	315
8.2	Conference Contributions	316

## ABBREVIATIONS AND PHYSICAL QUANTITIES

<b>bpy</b>	2,2'-bipyridine
$\beta_{EnT}$	attenuation factor for energy transfer
$c$	speed of light
<b>CS</b>	charge-separated
<b>dcbpy</b>	4,4'-dicarboxy-2,2'-bipyridine
<b>ddpd</b>	<i>N,N'</i> -dimethyl- <i>N,N'</i> -dipyridine-2-ylpyridine-2,6-diamine
$\Delta E$	energy difference
$\Delta E_a$	activation energy
$\Delta G^\ddagger$	Gibbs free energy of activation
<b>DFT</b>	density functional theory
<b>DSSC</b>	Dye-sensitized solar cell
$E$	energy/potential
$E_M$	Stokes shift
$E_{ox}$	oxidation potential
$E_{red}$	reduction potential
$E_{00}$	energy gap between ground and first excited state
$e$	elementary charge
$\epsilon_{max}$	extinction coefficient
<b>ES</b>	excited state
$F$	Faraday constant
$\phi$	quantum yield
$ff$	fill factor
<b>FTO</b>	fluorine-doped tin oxide
$\Gamma$	measure of electronic delocalization in mixed-valent systems
$\eta$	solvent's refractive index
$\eta$	quantum efficiency
$\hbar$	reduced Planck constant $\hbar = \frac{h}{2\pi}$
$H_{ab}$	electronic coupling matrix element
$\hat{H}_{SOC}$	spin-orbit coupling Hamiltonian
$I$	current / current density
<b>IPCE</b>	incident-photon-to-current conversion efficiency
<b>IR</b>	infrared

<b>ISC</b>	intersystem crossing
<b>IVCT</b>	intervalence charge transfer
$J_D$	Dexter overlap integral
$J_F$	Förster resonance integral
$k$	rate constant
$\kappa$	orientational factor
$k_B$	Boltzmann constant
$K_c$	comproportionation constant
$\kappa_{el}$	electronic transmission factor
$k_{ET}$	electron transfer rate
$k_{ENT}$	energy transfer rate
$k_{nr}$	non-radiative decay constant
$k_q$	quenching rate
$k_r$	radiative decay constant
$K_{SV}$	Stern-Volmer constant
$\lambda$	reorganization energy
$\lambda_s$	solvent's reorganizational energy
<b>LL'CT</b>	ligand-to-ligand charge transfer
<b>LUMO</b>	lowest unoccupied molecular orbital
<b>MC</b>	metal centered
<b>MLCT</b>	metal-to-ligand charge transfer
<b>NIR</b>	near infrared
$\tilde{\nu}$	frequency in wavenumbers
$\nu_N$	average nuclear frequency factor
$\tilde{\nu}_{1/2}$	full width at half maximum
$O_h$	octahedral point group
<b>pbpyH</b>	6-phenyl-2,2'-bipyridine
<b>P</b>	power
<b>PES</b>	potential energy surface
<b>ppyH</b>	2-phenylpyridine
$Q$	reaction coordinate
$[Q]$	concentration of quencher
$r$	distance
<b>R</b>	ideal gas constant
<b>S</b>	sensitizer



$S_M$	Huang-Rhys factor
$\tau$	lifetime
$t_{2g}$	symmetry label
<b>tctpy</b>	4,4',4''-tricarboxy-2,2';6',2''-terpyridine
<b>tpy</b>	2,2';6',2''-terpyridine
$U$	voltage
<b>UV</b>	ultra violett
<b>VIS</b>	visible
$\chi$	nuclear wavefunction
$\omega$	frequency



# 1 INTRODUCTION

Polypyridine complexes of ruthenium have fascinated inorganic chemists for the past 60 years. With the discovery of their luminescent properties in the late 1950s<sup>1</sup> a lot of effort has been put into understanding the origin of the emission and the underlying mechanisms controlling its efficiency.<sup>2-8</sup> Furthermore, a variety of other photophysical phenomena such as energy transfer,<sup>9</sup> photoinduced electron transfer<sup>10-12</sup> and mixed-valency<sup>13-15</sup> have been studied using oligonuclear polypyridine ruthenium complexes.<sup>16</sup>

Soon thereafter, the potential of this class of complexes for interesting applications was discovered. The long excited state lifetimes and high excited state reduction potentials allowed for usage in the field of photocatalysis, particularly as light-harvesting sensitizer in water and carbon dioxide reduction.<sup>17-20</sup> Additionally, the typically intense color and emission of polypyridine complexes allows for colorimetric and luminescent sensing applications, respectively.<sup>21</sup> However, most of this research was essentially academic with little economic driving force.

This changed in the early 1990s, with the ground-breaking discovery of the dye-sensitized solar cell (DSSC),<sup>22</sup> when a materials science oriented community turned their attention to polypyridine ruthenium complexes. With an increasing need for renewable energy resources, the DSSC was considered a sustainable and cheap alternative to the conventional silicon-based solar cell.<sup>23-25</sup> Ruthenium-based dyes are easily accessible from a synthetic point of view and their electronic properties are tunable in a wide range based on the ligand properties which made them a prime target for researchers all over the world.<sup>26,27</sup> In the following, a still on-going hunt for more and more efficient dyes began, particularly focused around ruthenium, although other transition metals proved suitable in this context as well.<sup>28-31</sup> In the periphery of this research, not only the light-harvesting properties of polypyridine ruthenium complexes were exploited, but also their luminescence, leading to the development of ruthenium-based light-emitting electrochemical cells as well.<sup>32,33</sup>

Among the studied systems, ruthenium complexes bearing tridentate ligands provide a particularly interesting class.<sup>11,34-36</sup> Their meridional coordination sphere suppresses the occurrence of stereoisomers even in the presence of several differing functional groups or in oligonuclear systems. Additionally, the facile introduction of functional groups allows for an individual tailoring of the molecular frontier orbitals. This was taken advantage of by several research groups installing electron-donating and -accepting functionalities in the same complex on opposing ligands.<sup>11,37</sup> Such *push-pull* substituted systems are nowadays well-understood and provide sophisticated insight into the molecular electronics.

However, an electronic *push-pull* environment cannot only be introduced by peripheral substituents but also by altering the nature of the ligands themselves. A prominent example is the class of cyclometalated polypyridine ruthenium complexes, which, despite known since the late 1980s, has received more interest just in the past decade.<sup>38-40</sup> This was mainly due to the discovery of their astonishingly good performance as sensitizers in DSSCs in 2007.<sup>41,42</sup> In a cyclometalated polypyridine complex, one of the nitrogen atoms of the metal's coordination sphere is replaced

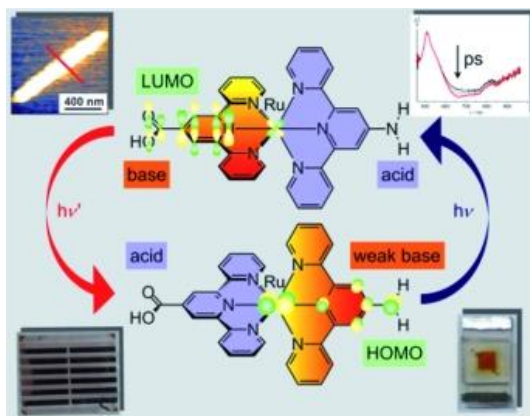
by an isoelectronic carbon anion. This leads to an interesting electronic situation: Since polypyridine ligands are good  $\pi$ -acceptors and cyclometalation typically yields a strong  $\sigma$ - and  $\pi$ -donating ligand, cyclometalated polypyridine complexes are inherently strong *push-pull* systems.<sup>43,44</sup> This intrinsic electronic directionality has made them a high-priority research target for DSSC sensitizers.<sup>45,46</sup> However, the luminescence of these systems is generally less intensively studied and thus, the understanding of their photophysical properties is not as elaborate as for conventional polypyridine ruthenium complexes. Hence, one of the major purposes of this dissertation is the elucidation of the electronic properties of cyclometalated polypyridine ruthenium complexes.

In the following introduction, the current state of research on bis(tridentate) polypyridine ruthenium complexes with *push-pull* substitution will be summarized in section 1.1 in terms of a *Microreview* article written by Aaron Breivogel, Christoph Kreitner and Katja Heinze, which was published in the *European Journal of Inorganic Chemistry* in 2014. This article already covers to some extent the general photophysical properties of polypyridine ruthenium complexes governing their excited state deactivation. However, the excited state decay mechanisms in polypyridine ruthenium complexes will be further elaborated in section 1.2 as those are a key component of this dissertation. This will be followed by an introduction of the concept of mixed valence and optical electron transfer in section 1.3. Cyclometalation reactions in general and cyclometalated polypyridine complexes in particular will be discussed in section 1.4. The introduction will be rounded off by a description of the working principle of the dye-sensitized solar cell and an illustrative selection of current state-of-the-art sensitizers in section 1.5.

## 1.1 REDOX AND PHOTOCHEMISTRY OF BIS(TERPYRIDINE) RUTHENIUM(II) AMINO ACIDS AND THEIR AMIDE CONJUGATES – FROM UNDERSTANDING TO APPLICATIONS

Aaron Breivogel, Christoph Kreitner and Katja Heinze

*Eur. J. Inorg. Chem.* **2014**, 2014, 5468–5490.



Ruthenium(II) amino acid  $[\text{Ru}(4'\text{-tpy-COOH})(4'\text{-tpy-NH}_2)]^{2+}$  interacts with photons, electrons, and/or protons, to lead to phosphorescence, oxidative and reductive chemistry, acid/base chemistry, proton-coupled electron transfer, photoinduced reductive and oxidative electron transfer, excited-state proton transfer, and energy transfer. Applications include light-emitting electrochemical and dye-sensitized solar cells.

### Author contributions

The ruthenium complexes were synthesized and characterized by Aaron Breivogel. The manuscript for this invited microreview was written by Aaron Breivogel (40 %), Christoph Kreitner (40 %) and Katja Heinze (20 %). Aaron Breivogel used parts of it for the introduction of his dissertation.

### Supporting Information

for this article is found at pp. 171. For full Supporting Information, refer to [http://onlinelibrary.wiley.com/store/10.1002/ejic.201402466/asset/supinfo/ejic\\_201402466\\_sm\\_miscellaneous\\_information.pdf?v=1&s=d36c160e970e957a0a90f0bedd7c19747c8b4daa](http://onlinelibrary.wiley.com/store/10.1002/ejic.201402466/asset/supinfo/ejic_201402466_sm_miscellaneous_information.pdf?v=1&s=d36c160e970e957a0a90f0bedd7c19747c8b4daa).

„Reprinted with permission from Breivogel, A.; Kreitner, C.; Heinze, K. *Chem. Eur. J.* **2014**, 2014, 5468–5490. Copyright 2016 Jon Wiley and Sons.”

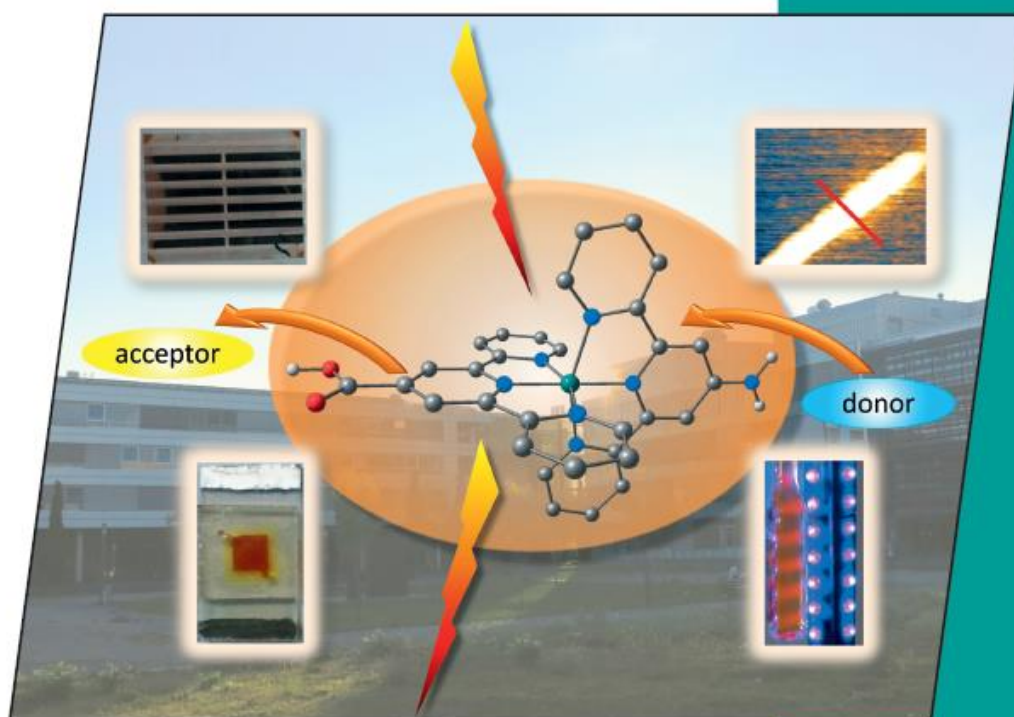


# EurJIC

European Journal of  
Inorganic Chemistry

Fully Electronic  
& Printed on Demand

32/2014  
2nd November Issue



Cover Picture / Microreview

Katja Heinze et al.

*Bis(terpyridine)ruthenium(II) Amino Acids and Their Amide Conjugates*

WILEY-VCH

www.eurjic.org

EJICFK (32) 5453–5624 (2014) · ISSN 1099-0682 · No. 32/2014

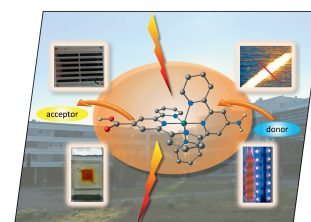
A Journal of



ChemPubSoc  
Europe

DOI:10.1002/ejic.201402466

## Redox and Photochemistry of Bis(terpyridine) ruthenium(II) Amino Acids and Their Amide Conjugates – from Understanding to Applications

 Aaron Breivogel,<sup>[a]</sup> Christoph Kreitner,<sup>[a,b]</sup> and Katja Heinze\*<sup>[a]</sup>


COVER PICTURE

**Keywords:** Electron transfer / Energy transfer / Luminescence / Photochemistry / Redox chemistry / Ruthenium / Tridentate ligands

The push-pull-substituted bis(terpyridine)ruthenium(II) amino acid  $[\text{Ru}(4'\text{-tpy-COOH})(4'\text{-tpy-NH}_2)]^{2+}$  ( $[\mathbf{5}]^{2+}$ ; tpy = 2,2',6',2''-terpyridine) with carboxylic acid and amino substituents features exceptional chemical and photophysical properties. Its interaction with photons, electrons, and/or protons results in room-temperature phosphorescence, reversible oxidative and reductive redox chemistry, reversible acid/base chemistry, proton-coupled electron transfer, photoinduced reductive and oxidative electron transfer, excited-state proton transfer and energy transfer reactions. These properties can be fine-tuned by variations of the bis(terpyridine) amino acid motif, namely extension of the  $\pi$  system and ex-

pansion of the chelate ring. Furthermore, the chemically orthogonal functional groups enable the incorporation of this metallo amino acid into peptide architectures in a highly selective manner, even by solid-phase peptide synthesis protocols. Amide-linked conjugates with other metal complexes [(terpyridine)ruthenium(II), ferrocene, (bipyridine)rhenium(I), (bipyridine)platinum(II)], organic chromophores, or ZnO nanoparticles underscore the versatile synthetic, redox, and photochemistry of this building block. First real-world applications of  $[\mathbf{5}]^{2+}$  and its derivatives include light-emitting electrochemical cells (LECs) and dye-sensitized solar cells (DSSCs).

### 1. Introduction and Scope of the Review

Polypyridine complexes of ruthenium(II) are a unique class of complexes with unprecedented photophysical, chemical, and electrochemical properties.<sup>[1]</sup> There is a plethora of applications of polypyridine complexes of ruthenium(II) such as dye-sensitized solar cells (DSSCs),<sup>[2–4]</sup> light-emitting devices,<sup>[5–8]</sup> anticancer and photodynamic therapy,<sup>[9–11]</sup> sensing of ions<sup>[12–14]</sup> and small neutral molecules,<sup>[15–17]</sup> energy transfer,<sup>[18,19]</sup> electron transfer and mixed valency,<sup>[20–25]</sup> triplet–triplet annihilation upconversion,<sup>[26–29]</sup> and molecular data storage.<sup>[30–32]</sup> Catalytic applications comprise important photocatalytic reactions such as water oxidation,<sup>[33,34]</sup> generation of  $\text{H}_2$ ,<sup>[35–39]</sup> reduction of  $\text{CO}_2$ ,<sup>[37–39]</sup> and photocatalysis of organic redox reactions.<sup>[38,40–44]</sup> Tris(2,2'-bipyridine)ruthenium(II),  $[\text{Ru}(\text{bpy})_3]^{2+}$ , is one of the most prominent ruthenium(II) complexes. The absorption of a 450 nm photon by  $[\text{Ru}(\text{bpy})_3]^{2+}$  populates an excited  $^1\text{MLCT}$  state (MLCT = metal-to-li-

gand charge transfer; Figure 1a). From this state quantitative intersystem crossing (ISC) into the  $^3\text{MLCT}$  state oc-

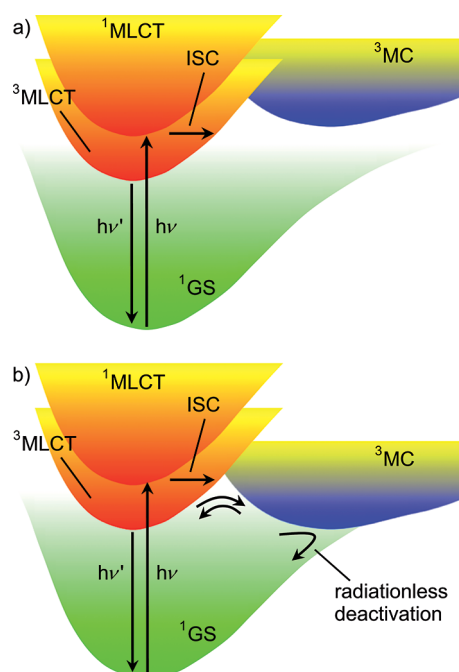


Figure 1. Qualitative state diagrams of (a)  $[\text{Ru}(\text{bpy})_3]^{2+}$  and (b)  $[\text{Ru}(\text{tpy})_2]^{2+}$   $[\mathbf{1}]^{2+}$  (MLCT = metal-to-ligand charge transfer, ISC = intersystem crossing, MC = metal-centered, GS = ground state, bpy = 2,2'-bipyridine, tpy = 2,2',6',2''-terpyridine).

[a] Institute of Inorganic Chemistry and Analytical Chemistry, Johannes Gutenberg University of Mainz, Duesbergweg 10-14, 55128 Mainz, Germany  
E-mail: katja.heinze@uni-mainz.de  
<http://www.ak-heinze.chemie.uni-mainz.de/>

[b] Graduate School "Materials Science in Mainz", Staudinger Weg 19, 55128 Mainz, Germany

Supporting information for this article is available on the WWW under <http://dx.doi.org/10.1002/ejic.201402466>.



curs.<sup>[1]</sup> The long excited-state lifetime ( $\tau \approx 1 \mu\text{s}$ ) of the  $^3\text{MLCT}$  state at room temperature in solution renders  $[\text{Ru}(\text{bpy})_3]^{2+}$  exceptionally suitable as a photoredox catalyst (Table 1).<sup>[38,45,46]</sup> The  $^3\text{MLCT}$  state is emissive with a high phosphorescence quantum yield ( $\Phi \approx 10\%$ ), which favors applications in light-emitting devices as luminescent sensors or as imaging agents.<sup>[46]</sup>

The properties of  $[\text{Ru}(\text{bpy})_3]^{2+}$  can easily be tailored by modifications of the bpy ligand. However, the intrinsic  $\Delta$ ,  $\Delta$  chirality of  $[\text{Ru}(\text{bpy})_3]^{2+}$  is a serious drawback when more than one bpy ligand is substituted or when more than one  $[\text{Ru}(\text{bpy})_3]^{2+}$ -type complexes are combined to form di- or oligonuclear complexes, because diastereomeric complexes (e.g. *rac*- $\Delta$ , $\Delta$ / $\Delta$ , $\Delta$  and *meso*- $\Delta$ , $\Delta$ ) have to be separated or avoided by complicated synthetic procedures.<sup>[47–49]</sup> It is obvious that interaction with chiral molecules, such as DNA or proteins, will even modify the individual properties of  $\Delta$ ,  $\Delta$  enantiomers, and any interaction with chiral biomolecules is complicated when using racemates, for example as anticancer drugs.<sup>[48d]</sup>

Bis(tridentate) *meridional* coordination as in  $[\text{Ru}(\text{tpy})_2]^{2+}$  ( $[\mathbf{1}]^{2+}$ , Figure 2) avoids the formation of diastereomers even in the case of heteroleptic  $[\text{Ru}(\text{tpy-R}^1)(\text{tpy-R}^2)]^{2+}$ <sup>[50]</sup> and dinuclear complexes ( $\text{tpy-R}^1$ ,  $\text{tpy-R}^2 = 4'$ -substituted 2,2';6',2''-terpyridine).<sup>[25,51,52]</sup> Furthermore, the stronger

chelate effect of tridentate ligands as compared with that of bidentate ligands is favorable in terms of complex stability.<sup>[53]</sup> However, despite the similar absorption characteristics and redox potentials of  $[\text{Ru}(\text{bpy})_3]^{2+}$  and  $[\mathbf{1}]^{2+}$ , the excited state properties differ significantly (Table 1). Unfortunately,  $[\mathbf{1}]^{2+}$  has a dramatically reduced lifetime of the lowest excited  $^3\text{MLCT}$  state ( $\tau \approx 0.1\text{--}0.2 \text{ ns}$ ) and emission quantum yield ( $\Phi \leq 0.0007\%$ ; Table 1). The underlying reason for the poor excited-state photophysical properties is an effective radiationless deactivation process via  $^3\text{MC}$  states [from the electron configuration  $(t_{2g})^5(e_g^*)^1$ ], which are thermally populated from  $^3\text{MLCT}$  states ( $\text{MC} = \text{metal-centered}$ ; Figure 1b).<sup>[54]</sup>

The three bpy ligands in  $[\text{Ru}(\text{bpy})_3]^{2+}$  create a coordination sphere that enables better metal–ligand orbital overlap than that in  $[\text{Ru}(\text{tpy})_2]^{2+}$  with two constrained tpy ligands. As the overlap between the nitrogen lone pairs of pyridine and the  $e_g^*$  orbitals of Ru is higher in  $[\text{Ru}(\text{bpy})_3]^{2+}$ , the ligand-field splitting is stronger in  $[\text{Ru}(\text{bpy})_3]^{2+}$ , which induces less accessible  $^3\text{MC}$  states with a larger  $^3\text{MLCT}$ – $^3\text{MC}$  energy gap compared with that of  $[\text{Ru}(\text{tpy})_2]^{2+}$  (Figure 1).<sup>[54]</sup> In order to improve ground-state and especially excited-state photophysical properties of bis(terpyridine)-ruthenium(II) complexes, extensive efforts have been made in the last two decades.<sup>[55]</sup> Long-lived and highly emissive



Aaron Breivogel received his diploma in chemistry at the Johannes Gutenberg University of Mainz, Germany, in 2009, and he is currently finishing his Ph.D. Thesis in the research group of Prof. Dr. Katja Heinze in inorganic chemistry. During his studies he spent one semester (2007/2008) at the University of Valencia, Spain, in the Department of Analytical Chemistry in the group of Prof. Dr. Miguel de la Guardia working on the quantitative determination of glycolic acid in cosmetics by online liquid chromatography and Fourier transform infrared spectroscopy. Currently he is working on the synthesis of bis(tridentate) complexes of ruthenium(II) and their applications in dye-sensitized solar cells and light-emitting electrochemical cells. He received a grant from the “International Research Training Group (IRTG) 1404 – Self-organized Materials for Optoelectronics” funded by the Deutsche Forschungsgemeinschaft (2011–2013) and served as IRTG student speaker for 18 months. During his Ph.D. Thesis he went for a six-month research stay to the group of Prof. Dr. Kookheon Char at the Seoul National University in Seoul, Republic of Korea. His research interests focus on the application of novel ruthenium complexes in dye-sensitized solar cells and light-emitting electrochemical cells. He has co-authored nine refereed papers.



Christoph Kreitner received his diploma in chemistry at the Johannes Gutenberg University of Mainz, Germany, in 2012, and he is currently doing his Ph.D. Thesis in the research group of Prof. Dr. Katja Heinze at the Johannes Gutenberg University of Mainz, Germany. His research focuses on the design and synthesis of new cyclometalated ruthenium complexes and their applications in dye-sensitized solar cells and photocatalytic systems. During his studies he spent one semester at the University of Toronto, Toronto, Canada (2010/2011), working in the Department of Inorganic Chemistry in the group of Prof. Dr. Douglas W. Stephan on frustrated Lewis pairs and their reactions with lactones and lactide. For his Ph.D. Thesis he received a scholarship from the Graduate School of Excellence “Materials Science in Mainz” (2013). Recently he was elected a junior member of the Gutenberg Academy of the Johannes Gutenberg University of Mainz, Germany (2014). His research interests aim at the understanding of electron transfer and optical excitation mechanisms in molecular systems and the possibility of utilizing sunlight in chemical syntheses.



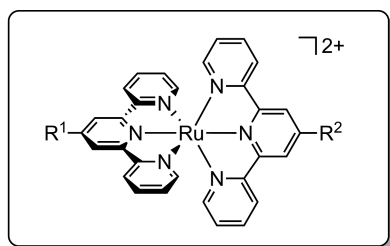
Katja Heinze is professor of organometallic and bioinorganic chemistry at the Johannes Gutenberg University of Mainz, Germany. After receiving a diploma degree (1995) and a Ph.D. degree (1998) from the Ruprecht Karls University of Heidelberg, Germany (G. Huttner), she went for a postdoctoral stay to the University of Zurich, Zurich, Switzerland (1999). She was appointed Privatdozent in 2004 at the University of Heidelberg, Germany, and Full Professor in 2008 at the Johannes Gutenberg University of Mainz, Germany. She received the Lieseberg award of the Faculty of Chemistry and Earth Sciences, University of Heidelberg (2002), a Heisenberg fellowship from the Deutsche Forschungsgemeinschaft (2004), and a Hengstberger Award of the University of Heidelberg (2007). Currently she serves as vice spokesperson of the International Research Training Group 1404 – Self-organized Materials for Optoelectronics and as vice chair of the Institute of Inorganic and Analytical Chemistry, University of Mainz. Since 2011 she has been serving as a member of the International Advisory Board of Organometallics. Her key research interests comprise functional complex systems based on coordination and organometallic compounds with special emphasis on molecular wires, light-harvesting systems, bistable systems, switches, and sensors as well as on (biomimetic) catalysts. She has authored more than 100 international refereed papers.



Table 1. Photophysical and electrochemical properties of ruthenium(II) polypyridine complexes in CH<sub>3</sub>CN at 295 K. See Figures 2, 11, 12, 13, 15, 17, and 18 for compound numbering.

Complex	Absorption	Emission			Electrochemistry	
	$\lambda_{\max}$ [nm] ( $\epsilon$ [M <sup>-1</sup> cm <sup>-1</sup> ])	$\lambda_{\max}$ [nm]	$\Phi$ [%]	$\tau$ [ns]	$E_{1/2}$ (Ru <sup>II</sup> /Ru <sup>III</sup> ) [V] <sup>[a]</sup>	$E_{1/2}^{\text{red}}$ [a] [V]
[Ru(bpy) <sub>3</sub> ] <sup>2+</sup> [46,57]	452 (13000)	615	9.4	1100	+0.89	-1.73
[1] <sup>2+</sup> [50,54b]	474 (10400)	629	≤ 0.0007 <sup>[b]</sup>	0.1–0.2 <sup>[c]</sup>	+0.92	-1.67
[2] <sup>2+</sup> [8]	485 (18100)	667	0.041 <sup>[d]</sup>	32	+0.96 <sup>[e]</sup>	-1.27 <sup>[e]</sup>
[3] <sup>2+</sup> [58]	479 (19500)	637 <sup>[f]</sup>	0.02 <sup>[f]</sup>	–	+0.91	-1.69
[4] <sup>2+</sup> [59,60]	502 (19100)	734	0.27 <sup>[d]</sup>	34	+0.68	-1.54
[5] <sup>2+</sup> [59,60]	501 (20700)	739	0.18 <sup>[d]</sup>	26 (92%), 4 (8%)	+0.66	-1.60
[6] <sup>2+</sup> [61,62]	492 (22100)	677	0.059	22	+0.90	-1.46
[7] <sup>2+</sup> [50]	490 (16800)	706	0.07 <sup>[b]</sup>	50	+0.92	-1.53
[8] <sup>2+</sup> [63]	490 (24000)	660	–	–	+0.87	-1.58
[9] <sup>2+</sup> [64]	493 (29300) <sup>[g]</sup>	660	0.029 <sup>[h]</sup>	1.1	+0.63	-1.43
[10] <sup>2+</sup> [50]	487 (26200)	715	0.006 <sup>[b]</sup>	1.0	+0.90	-1.66
[11] <sup>2+</sup> [60]	502 (35600)	707	0.053 <sup>[d]</sup>	23	–	–
[12] <sup>2+</sup> [60]	501 (24700)	659	0.053 <sup>[d]</sup>	21 (3%), 3 (97%)	–	–
[13] <sup>2+</sup> [60]	498 (26600)	664	0.030 <sup>[d]</sup>	23 (96%), 2 (4%)	–	–
[14a] <sup>2+</sup> [65]	495 (31300)	713	0.13 <sup>[b]</sup>	200	+0.95	-1.32
[14b] <sup>2+</sup> [65]	506 (42000)	705	0.17 <sup>[b]</sup>	231	+0.99	-1.29
[15a] <sup>2+</sup> [66]	511 (44800)	698	0.76 <sup>[d]</sup>	580	–	–
[15b] <sup>2+</sup> [66]	500 (25000)	710	0.45 <sup>[d,i]</sup>	2500	+0.94	-1.49
[16] <sup>2+</sup> [67]	463 (10000)	643 <sup>[j]</sup>	17.3 <sup>[d,j]</sup>	385 <sup>[j]</sup>	+0.60	-1.95
[17] <sup>2+</sup> [67]	473 (10000)	694 <sup>[j]</sup>	2.6 <sup>[d,j]</sup>	7900 <sup>[j]</sup>	+0.58	-1.88
[18] <sup>2+</sup> [68,69]	491 (14000)	700 <sup>[j]</sup>	3.2 <sup>[i,h]</sup>	3000 <sup>[j]</sup>	+0.71	-1.73
[19] <sup>2+</sup> [70]	553 (10000)	693 <sup>[j]</sup>	11.2 <sup>[i,h]</sup>	5500 <sup>[j]</sup>	+0.82	-1.52
[20] <sup>2+</sup> [71]	522 (6425)	608	30 <sup>[k]</sup>	3300	+1.11	-1.36
[21] <sup>2+</sup> [56]	517 (7500)	729	0.45 <sup>[d]</sup>	722 <sup>[i]</sup>	+0.81	-1.47
[22] <sup>2+</sup> [56]	539 (6360)	744	1.1 <sup>[d]</sup>	841 <sup>[i]</sup>	+0.92	-1.25
[23] <sup>2+</sup> [56]	525 (8230)	762	0.042 <sup>[d]</sup>	149 <sup>[i]</sup>	+0.64	-1.50
[24] <sup>2+</sup> [56]	546 (7810)	788	0.052 <sup>[d]</sup>	136 <sup>[i]</sup>	+0.73	-1.32
[25] <sup>2+</sup> [72]	517 (8110)	732	0.068 <sup>[d]</sup>	–	+0.81	-1.50 <sup>[l]</sup>
[26] <sup>2+</sup> [72]	537 (6600)	743	0.059 <sup>[d]</sup>	–	+0.87	-1.37 <sup>[l]</sup>
[27] <sup>2+</sup> [72]	544 (6690)	771	0.067 <sup>[d]</sup>	–	+0.71	-1.53 <sup>[l]</sup>
[33a] <sup>2+</sup> [18]	490 (22290)	670	0.093 <sup>[d]</sup>	19 (5%), 4 (95%)	+0.90	-1.34
[33b] <sup>2+</sup> [18]	490 (26180)	667	0.082 <sup>[d]</sup>	18 (9%), 3 (91%)	+0.90	-1.35
[33c] <sup>2+</sup> [18]	490 (25820)	665	0.13 <sup>[d]</sup>	19 (1%), 3 (10%), 0.5 (89%)	+0.92	-1.70
[33d] <sup>2+</sup> [18]	491 (25830)	666	0.16 <sup>[d]</sup>	22 (9%), 4 (91%)	+0.91	-1.45
[33e] <sup>2+</sup> [18]	490 (20590)	667	0.11 <sup>[d]</sup>	19 (13%), 4 (87%)	+0.87	-1.25
[34] <sup>2+</sup> [18]	492 (25750)	668	0.14 <sup>[d]</sup>	17 (7%), 3 (93%)	+0.92	-1.16
[35] <sup>2+</sup> [18]	490 (24950)	665	0.076 <sup>[d]</sup>	15 (2%), 4 (40%), 0.4 (57%)	+0.91	-1.23
[36] <sup>2+</sup>	490 (17100)	668	0.12 <sup>[d]</sup>	–	+0.89	-1.15
[37] <sup>2+</sup>	490 (16500)	667	0.080 <sup>[d]</sup>	–	+0.88	-1.14
[38] <sup>4+</sup> [25]	522 (50620)	750	0.24 <sup>[d]</sup>	22 (99%), 2 (1%)	+0.68, +0.91	-1.48
[39] <sup>4+</sup> [25]	496 (46550)	692	0.21 <sup>[d]</sup>	22	+0.80, +0.90	-1.49
[40] <sup>4+</sup> [62]	504 (63000)	684	0.032	24 (71%), 44 (29%)	+0.91 (2e)	-1.49 (2e)
[41] <sup>4+</sup> [73]	487 (50800)	–	–	–	+0.85 (2e)	-1.75
[42] <sup>1+</sup> [74]	494 (ca. 60000)	–	–	–	+0.86 (2e)	-1.57
[43] <sup>1+</sup> [51]	499 (63000)	–	–	–	+0.87 (2e)	-1.58
[44] <sup>2+</sup> [59]	496 (26200)	704 <sup>[m]</sup>	0.011	–	+0.65 <sup>[l,n]</sup>	-1.50
[45] <sup>2+</sup> [59]	502 (19300)	739 <sup>[m]</sup>	< 0.01	–	+0.90 <sup>[l,o]</sup>	-1.61
[46] <sup>2+</sup> [59]	496 (25300)	704 <sup>[m]</sup>	< 0.01	–	+0.90 <sup>[l,p]</sup>	-1.58
[47] <sup>0</sup> [75a,75b]	478 (15000)	–	–	–	+1.01 <sup>[l,q]</sup>	-1.60
[48] <sup>0</sup> [75a,75b]	482 (15000)	–	–	–	+0.98 <sup>[l,r]</sup>	-1.62
[47] <sup>1+</sup> [75c]	489 (28700)	699 <sup>[v]</sup>	0.040 <sup>[k,v]</sup>	260 <sup>[v]</sup>	+0.94 <sup>[s,t]</sup>	-1.55 <sup>[s]</sup>
[48] <sup>1+</sup> [75c]	505 (28000)	697 <sup>[v]</sup>	0.084 <sup>[k,v]</sup>	260 <sup>[v]</sup>	+1.00 <sup>[s,u]</sup>	-1.52 <sup>[s]</sup>
[49] <sup>2+</sup> [77]	493 (24400)	673	0.17	16	+0.92	-1.57
[50] <sup>2+</sup> [78]	502 (23000)	735	0.20	29	+0.68	-1.51
[51] <sup>2+</sup> [77]	492 (26000)	674	0.16	–	+0.90	-1.48
[52] <sup>2+</sup> [77]	500 (23500)	727	0.15	–	+0.68	-1.53
[53] <sup>2+</sup> [77]	496 (27800)	678	0.14	–	+0.92	-1.53
[54] <sup>2+</sup> [77]	494 (27700)	674	0.19	–	+0.91	-1.48
[55] <sup>2+</sup> [77]	502 (21800)	739	0.11	–	+0.69	-1.47
[57] <sup>2+</sup> [78]	494 (26600)	671	0.12	18	+0.93	-1.30, -1.47
[58] <sup>2+</sup> [78]	504 (22900)	739	0.12	22	+0.69	-1.45, -1.69

[a] Vs. ferrocene/ferrocenium. [b] Recalculated from used value  $\Phi = 0.028$ <sup>[79]</sup> for [Ru(bpy)<sub>3</sub>]Cl<sub>2</sub> in H<sub>2</sub>O to the updated [Ru(bpy)<sub>3</sub>]Cl<sub>2</sub> standard  $\Phi = 0.040$  in H<sub>2</sub>O.<sup>[57]</sup> [c] Various solvents. [d] Recalculated from used value  $\Phi = 0.062$ <sup>[79]</sup> for [Ru(bpy)<sub>3</sub>]Cl<sub>2</sub> in CH<sub>3</sub>CN to the updated [Ru(bpy)<sub>3</sub>]Cl<sub>2</sub> standard  $\Phi = 0.094$  in CH<sub>3</sub>CN.<sup>[57]</sup> [e] No solvent given. [f] In DMF vs. 9,10-diphenylanthracene as reference. [g] In MeOH. [h] Recalculated from used value  $\Phi = 0.059$  for [Ru(bpy)<sub>3</sub>]Cl<sub>2</sub> in CH<sub>3</sub>CN to the updated [Ru(bpy)<sub>3</sub>]Cl<sub>2</sub> standard  $\Phi = 0.094$  in CH<sub>3</sub>CN.<sup>[57]</sup> [i] In PrCN. [j] In EtOH/MeOH (4:1, v/v). [k] As given in the reference. [l] Irreversible. [m] In acetone. [n]  $E_{1/2}$ (Fe<sup>II</sup>/Fe<sup>III</sup>) = 0.24 V. [o]  $E_{1/2}$ (Fe<sup>II</sup>/Fe<sup>III</sup>) = -0.03 V. [p]  $E_{1/2}$ (Fe<sup>II</sup>/Fe<sup>III</sup>) = -0.03, 0.26 V. [q]  $E_{1/2}$ (Fe<sup>II</sup>/Fe<sup>III</sup>) = 0.18 V. [r]  $E_{1/2}$ (Fe<sup>II</sup>/Fe<sup>III</sup>) = 0.17 V (2 e). [s] In dichloromethane. [t]  $E_{1/2}$ (Fe<sup>II</sup>/Fe<sup>III</sup>) = 0.15 V. [u]  $E_{1/2}$ (Fe<sup>II</sup>/Fe<sup>III</sup>) = 0.24 V (2e). [v] In H<sub>2</sub>O/CH<sub>3</sub>CN (4:1, v/v).



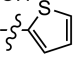
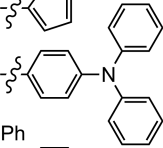
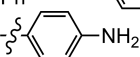
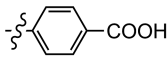
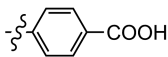
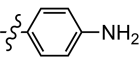
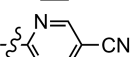
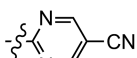
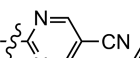
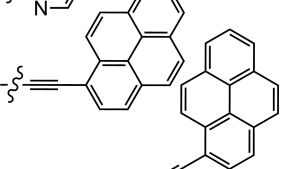
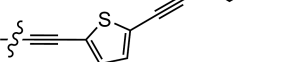
	R <sup>1</sup>	R <sup>2</sup>
[1] <sup>2+</sup>	H	H
[2] <sup>2+</sup>	COOEt	H
[3] <sup>2+</sup>	COOH	H
[4] <sup>2+</sup>	COOEt	NH <sub>2</sub>
[5] <sup>2+</sup>	COOH	NH <sub>2</sub>
[6] <sup>2+</sup>	COOEt	NHCOMe
[7] <sup>2+</sup>	SO <sub>2</sub> Me	OH
[8] <sup>2+</sup>	COOH	
[9] <sup>2+</sup>	H	
[10] <sup>2+</sup>	Ph	Ph
[11] <sup>2+</sup>	COOEt	
[12] <sup>2+</sup>		NH <sub>2</sub>
[13] <sup>2+</sup>		
[14a] <sup>2+</sup>	H	
[14b] <sup>2+</sup>		
[15a] <sup>2+</sup>	H	
[15b] <sup>2+</sup>	H	

Figure 2. Bis(terpyridine) complexes of ruthenium(II) relevant for this review.

excited states in bis(tridentate) complexes of ruthenium(II) can be obtained by the introduction of substituents in the 4'-position of the tpy ligand.<sup>[8,50]</sup> Electron-withdrawing substituents stabilize the <sup>3</sup>MLCT state with respect to the <sup>3</sup>MC state, while electron-donating substituents destabilize the <sup>3</sup>MC state. Both effects increase the <sup>3</sup>MLCT–<sup>3</sup>MC energy gap and diminish radiationless deactivation via the <sup>3</sup>MC state.<sup>[50,56]</sup> In 4'-substituted [Ru(tpy)(tpy-COOEt)]<sup>2+</sup> ([2]<sup>2+</sup>, Figure 2) prepared by Bolink, the electron-withdrawing character of the ester substituent leads to a less accessible <sup>3</sup>MC state, a significantly longer lifetime of the <sup>3</sup>MLCT state, and a higher emission quantum yield ( $\tau = 32$  ns,  $\Phi = 0.04\%$ ) compared with that of unsubstituted [1]<sup>2+</sup> (Table 1).<sup>[8]</sup> Furthermore, [2]<sup>2+</sup> has a redshifted absorption maximum ( $\lambda_{\text{max}} = 485$  nm;  $\epsilon_{\text{max}} = 18100$  M<sup>-1</sup> cm<sup>-1</sup>)

and higher extinction coefficients compared with those of [Ru(bpy)<sub>3</sub>]<sup>2+</sup> ( $\lambda_{\text{max}} = 452$  nm;  $\epsilon_{\text{max}} = 13000$  M<sup>-1</sup> cm<sup>-1</sup>) and [1]<sup>2+</sup> ( $\lambda_{\text{max}} = 474$  nm;  $\epsilon_{\text{max}} = 10400$  M<sup>-1</sup> cm<sup>-1</sup>), which is beneficial for efficient light harvesting in DSSCs, especially in the low-energy part of the electromagnetic spectrum (Table 1).<sup>[8]</sup>

In this overview we will discuss the chemical, photochemical, and redox properties of heteroleptic bis(terpyridine)ruthenium(II) complexes with two orthogonal functional groups, especially with R<sup>1</sup> = COOH and R<sup>2</sup> = NH<sub>2</sub> (ruthenium amino acid [5]<sup>2+</sup>, Figure 2),<sup>[59]</sup> and related complexes. These multifunctional complexes enable electron-transfer (Ru<sup>II/III</sup>, tpy/tpy<sup>-</sup>) and proton-transfer studies (tpy-COOH/tpy-COO<sup>-</sup>; tpy-NH<sub>3</sub><sup>+</sup>/tpy-NH<sub>2</sub>/tpy-NH<sup>-</sup>) as well as selective functionalization at the C- or at the N-terminus, or at both termini, to give amide-linked conjugates, nanocomposites, and functionalized materials with potential applications in photophysics, photochemistry, and materials science.

## 2. Physicochemical Properties of Bis(tridentate) Ruthenium(II) Polypyridine Complexes

The physicochemical properties of bis(tridentate) ruthenium(II) polypyridine complexes will be illustrated by examples of donor–acceptor-substituted bis(terpyridine) complexes [4]<sup>2+</sup> and [5]<sup>2+</sup> (Figure 2) prepared in our group.<sup>[59]</sup> Heteroleptic complexes such as [4]<sup>2+</sup> are readily synthesized by a stepwise approach.<sup>[50,80,81]</sup> RuCl<sub>3</sub> is treated with the first tpy ligand (tpy-R<sup>1</sup>, e.g. tpy-COOEt) to form the ruthenium(III) complex Ru(tpy-R<sup>1</sup>)Cl<sub>3</sub>, which is typically easily isolated by precipitation. In the second step, the chlorido ligands are replaced by the second tpy ligand (tpy-R<sup>2</sup>, e.g. tpy-NH<sub>2</sub>) under reducing conditions (e.g. *N*-ethylmorpholine), often assisted by microwave irradiation. This two-step procedure results in the desired heteroleptic complex [Ru<sup>II</sup>(tpy-R<sup>1</sup>)(tpy-R<sup>2</sup>)]<sup>2+</sup> with *meridional* coordination of the two chelate ligands without formation of homoleptic complexes [Ru(tpy-R<sup>1</sup>)<sub>2</sub>]<sup>2+</sup> and [Ru(tpy-R<sup>2</sup>)<sub>2</sub>]<sup>2+</sup>.<sup>[59]</sup> Typically, these dications are isolated as hexafluorophosphate salts. The ester group of [4]<sup>2+</sup> is straightforwardly hydrolyzed to the carboxylic acid [5]<sup>2+</sup> by refluxing [4]<sup>2+</sup> in 20% sulfuric acid. The harsh reaction conditions already underline the high thermal and chemical stability of bis(tridentate) complexes such as [4]<sup>2+</sup> and [5]<sup>2+</sup>.<sup>[59]</sup> The two functional groups of amino acid [5]<sup>2+</sup> offer the possibility of orthogonal functionalization either at the C-terminus or at the N-terminus.

Ruthenium amino acid [5]<sup>2+</sup> itself displays unique acid–base properties. The amino function of [5]<sup>2+</sup> is a poor nucleophile and a weak base {[5 + H]<sup>3+</sup>; pK<sub>a</sub> < 0 (estimated by UV/Vis spectroscopy in concentrated sulfuric acid)<sup>[59]</sup> and pK<sub>a</sub> ≈ 1.6 (estimated electrochemically in nitric acid); Ph-NH<sub>3</sub><sup>+</sup>; pK<sub>a</sub> = 4.9<sup>[82]</sup>}, because the lone pair is substantially delocalized into the aromatic ring and towards the electron-withdrawing metal cation to give an essentially planar C–NH<sub>2</sub> unit.<sup>[59,61]</sup> On the other hand, the acidity of

the COOH group ( $pK_a = 2.7^{[59]}$ ) is increased in comparison to those of organic aromatic acids (benzoic acid:  $pK_a = 4.2^{[83]}$ , isonicotinic acid:  $pK_a = 4.9^{[84]}$ ) because of the electron-withdrawing effect of the pyridine backbone and the coordinated positively charged metal ion. In contrast to aliphatic amino acids, such as natural  $\alpha$ -amino acids, no zwitterionic character is observed for  $[5]^{2+}$ , which again is based on the low basicity of the amino group.<sup>[59]</sup> Species  $[5]^{2+}$  is dominant in aqueous solutions at pH 2 and can be protonated at the amino function to afford  $[5 + H]^{3+}$  at lower pH values. Deprotonation of  $[5]^{2+}$  first leads to the amino carboxylate  $[5 - H]^+$  and then to the neutral species  $[5 - 2H]$ , where both the COOH and the  $NH_2$  group are deprotonated. During purification and precipitation of  $[5]^{2+}$  careful pH control is imperative, as otherwise mixtures of species with different degrees of protonation  $[5 + H]^{3+}/[5]^{2+}$  or  $[5 - H]^+/[5]^{2+}$  are obtained. For synthetic applications, the amine deprotonation step  $[5 - H]^+ \rightarrow [5 - 2H]$  needs to be carried out in rigorously dried, aprotic media by employing strong bases such as the phosphazene base  $P_1-tBu$  [*tert*-butylimino-tris(dimethylamino)phosphorane<sup>[85]</sup>].

In the presence of nitrate ions, dicationic amino acid  $[5]^{2+}$  is water soluble, which also enables pH-dependent electrochemical measurements. The Pourbaix diagram of  $[5]^{2+}$  compiles the redox potentials ( $E_{1/2}$ ) of the  $Ru^{II}/Ru^{III}$  couple at different pH values (Figure 3). Below pH 1.6 the potential amounts to  $E_{1/2} = 0.79$  V (vs. SCE). Between pH 1.6 and 2.7 the redox potential drops to 0.74 V, which is because of the deprotonation of the carboxylic acid group, and the potential is hence assigned to the  $[5]^{2+}/[5 - H]^{2+}$  redox couple.<sup>[59]</sup> For a typical proton-coupled electron transfer (PCET), the expected slope of the redox potential is given by  $-(m/n) \times 59$  mV per pH unit ( $m$  = number of transferred protons,  $n$  = number of transferred electrons; Nernstian behavior; 298 K).<sup>[86]</sup> The experimental slope amounts to  $46 \pm 10$  mV per pH unit suggesting that the electron transfer is indeed coupled to proton transfer in this pH region. The drop of the redox potential between pH 1.6 and 2.7 is easily rationalized, as the  $COO^-$  group is a weaker electron acceptor than the COOH group. Thus,  $[5 - H]^+$  is oxidized at lower potential than  $[5]^{2+}$ . From pH 2.7 to 9.2, the redox potential is pH-independent with  $E_{1/2} = 0.74$  V. When the pH is above 9.2, the redox potential again drops as a result of deprotonation of the amino group, which is converted into an even stronger electron donor by deprotonation.<sup>[59]</sup> At pH values below 9.2, the  $Ru^{II/III}$  oxidation process is reversible on the electrochemical timescale, while the process becomes irreversible at  $pH > 9.2$ .

The irreversibility of the  $[5 - 2H]$  oxidation has been rationalized by density functional theory (DFT) calculations. The DFT-calculated spin densities of the ruthenium(III) complexes  $[5]^{3+}$ ,  $[5 - H]^{2+}$ , and  $[5 - 2H]^+$  are depicted in Figure 4. The spin density in  $[5]^{3+}$  is located at the ruthenium center with a small contribution at the amino nitrogen atom. The Mulliken spin densities on Ru and on the amino nitrogen atom are calculated as 0.76 and 0.11,

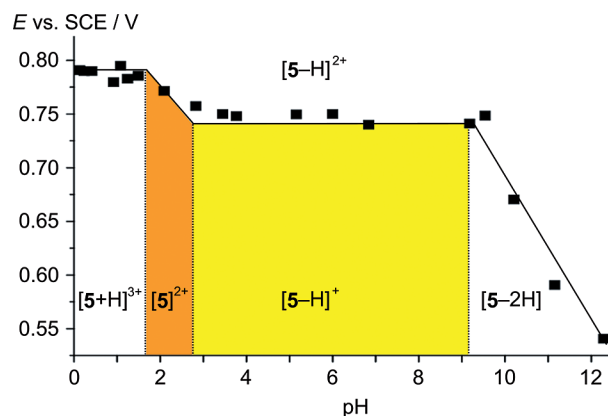


Figure 3. Pourbaix diagram of  $[5]^{2+}$  recorded in 0.5 M  $HNO_3/H_2O$  titrated with NaOH.  $E$  (vs. SCE) – 0.16 V  $\approx E$  (vs. ferrocene/ferrocenium);<sup>[87]</sup> estimated  $pK_a$  values are denoted by vertical dotted lines.

respectively. Similarly, for  $[5 - H]^{2+}$  Mulliken spin densities at Ru and N amount to 0.78 and 0.10, respectively. Thus, when  $[5]^{3+}$  is deprotonated to  $[5 - H]^{2+}$  at the carboxylic acid group, the redox process remains essentially ruthenium-centered and reversible. The second deprotonation occurs at the amino group. The resulting complex,  $[5 - 2H]^+$ , features Mulliken spin densities of 0.36 and 0.51 on Ru and the amino nitrogen atom, respectively (Figure 4). Thus, the deprotonated amino group is considerably engaged in the oxidation process, which renders the oxidation irreversible. In summary, at  $pH < 9.2$   $[5]^{2+}$  and  $[5 - H]^{2+}$  are reversibly oxidized at the ruthenium center on the electrochemical time scale, while at higher pH the (deprotonated) amino group is irreversibly oxidized.

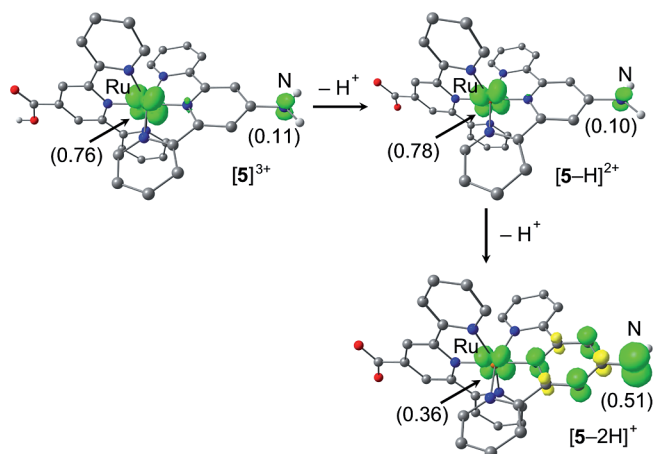


Figure 4. DFT-calculated spin densities of ruthenium(III) complexes  $[5]^{3+}$ ,  $[5 - H]^{2+}$ , and  $[5 - 2H]^+$  (B3LYP/LANL2DZ, IEFPCM,  $H_2O$ ; contour value 0.01; CH hydrogen atoms omitted; Mulliken spin densities at indicated atoms in parentheses).

In aprotic acetonitrile the fully reversible simple one-electron  $Ru^{II}/Ru^{III}$  oxidation of amino acid ester  $[4]^{2+}$  is observed at  $E_{1/2} = 0.68$  V vs. ferrocene/ferrocenium.<sup>[59]</sup> The EPR spectrum of  $[4]^{3+}$  prepared by chemical oxidation of  $[4]^{2+}$  with ceric ammonium nitrate shows a rhombic signal with  $g_{1,2,3} = 2.347, 2.178, 1.843$  in frozen solution, which

is characteristic for Ru<sup>III</sup>.<sup>[56,77]</sup> The reversible one-electron reduction of [4]<sup>2+</sup> to [4]<sup>+</sup> is located at the tpy-COOEt ligand.<sup>[56,59]</sup> The EPR spectrum of the *N*-acetylated analogue [6]<sup>+</sup> (Figure 2) after reduction of [6]<sup>2+</sup> with decamethylcobaltocene shows a rhombic signal with  $g_{1,2,3} = 2.005, 1.989, 1.955$  and small  $g$  anisotropy in frozen solution.<sup>[62]</sup> This is in full accord with a ligand-centered reduction with some ruthenium admixture.<sup>[56]</sup> The DFT-calculated spin densities of [4]<sup>3+</sup> and [4]<sup>+</sup> confirm that oxidation occurs at the ruthenium center ([4]<sup>3+</sup>: Mulliken spin density on Ru = 0.76, Figure 5a) with some admixture from the amino nitrogen atom (Mulliken spin density on N = 0.11), while reduction is essentially localized at the tpy-COOEt ligand ([4]<sup>+</sup>: Mulliken spin density on Ru = 0.10, Figure 5b). Due to the *meridional* coordination of the tpy ligands involved, these two redox processes occur in orthogonal  $\pi$  systems (Figure 5a, b).

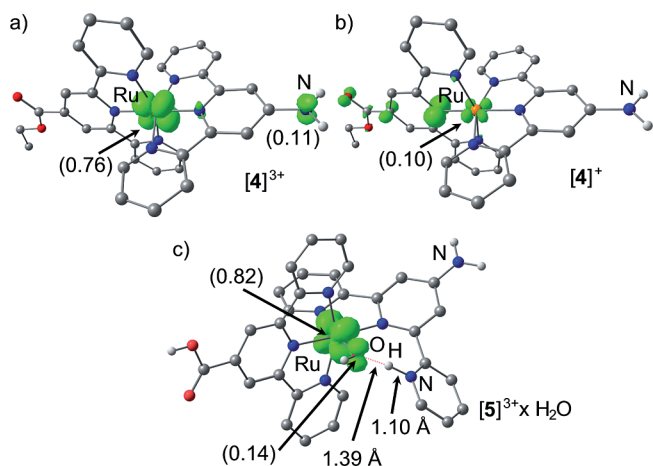


Figure 5. DFT-calculated spin densities (B3LYP/LANL2DZ, IEFPCM, CH<sub>3</sub>CN; contour value 0.01; CH hydrogen atoms omitted; Mulliken spin densities at indicated atoms in parentheses) of (a) [4]<sup>3+</sup>, (b) [4]<sup>+</sup>, and (c) [5]<sup>3+</sup> × H<sub>2</sub>O with  $\kappa^2$ -tpy-NH<sub>2</sub> (IEFPCM, H<sub>2</sub>O).

The stability of the ruthenium(III) complex [4]<sup>3+</sup> in the presence of water and potentially coordinating hydroxide ions has been probed by spectroelectrochemical measurements.<sup>[72]</sup> Indeed, ruthenium(II) complex [4]<sup>2+</sup> is reversibly oxidized to ruthenium(III) complex [4]<sup>3+</sup> by gradually increasing the potential. By reversing the potential, [4]<sup>3+</sup> is then quantitatively reduced back to [4]<sup>2+</sup> (Figure 6). Upon oxidation, the MLCT band of [4]<sup>2+</sup> at  $\lambda = 502$  nm disappears while a LMCT band of [4]<sup>3+</sup> at  $\lambda = 729$  nm rises (LMCT = ligand-to-metal charge transfer). Seven isosbestic points are observed and confirm the clean conversion of [4]<sup>2+</sup> to [4]<sup>3+</sup> (Figure 6). Back reduction fully restores the initial spectrum, and the same isosbestic points are observed, which clearly demonstrates the stability of ruthenium(II/III) complexes [4]<sup>2+</sup> and [4]<sup>3+</sup> in the presence of water and coordinating OH<sup>-</sup> ions on this time scale (hours).<sup>[72]</sup> In contrast, the famous N719 sensitizer as tetraethyl ester, *cis*-[Ru{bpy(COOEt)<sub>2</sub>]<sub>2</sub>(NCS)<sub>2</sub>, featuring bidentate 4,4'-diethylcarboxy-2,2'-bipyridine ligands and monodentate isothiocyanato ligands, is much more suscep-

tible to ligand loss and ligand degradation under these oxidative conditions than the [4]<sup>2+</sup>/[4]<sup>3+</sup> couple.<sup>[72,88]</sup> Under acidic conditions (0.5 M TFA), the re-reduction of [5]<sup>3+</sup> → [5]<sup>2+</sup> in the spectroelectrochemical experiments is only complete to approximately 90% and features different isosbestic points as compared with the oxidation [5]<sup>2+</sup> → [5]<sup>3+</sup>. We suggest that, under acidic conditions irreversible substitution of even a tpy ligand is feasible via the six-coordinate ruthenium(III) aqua complex [Ru( $\kappa^2$ -tpy-R<sup>1</sup>)( $\kappa^3$ -tpy-R<sup>2</sup>)(H<sub>2</sub>O)]<sup>3+</sup>, which tautomerizes to the six-coordinate hydroxido pyridinium complex [Ru(H- $\kappa^2$ -tpy-R<sup>1</sup>)( $\kappa^3$ -tpy-R<sup>2</sup>)(OH)]<sup>3+</sup> (Figure 5c). Finally, protonated [H<sub>3</sub>tpy-R<sup>1</sup>]<sup>3+</sup> can be irreversibly released after further protonation to di(pyridinium) and tri(pyridinium) under acidic conditions.

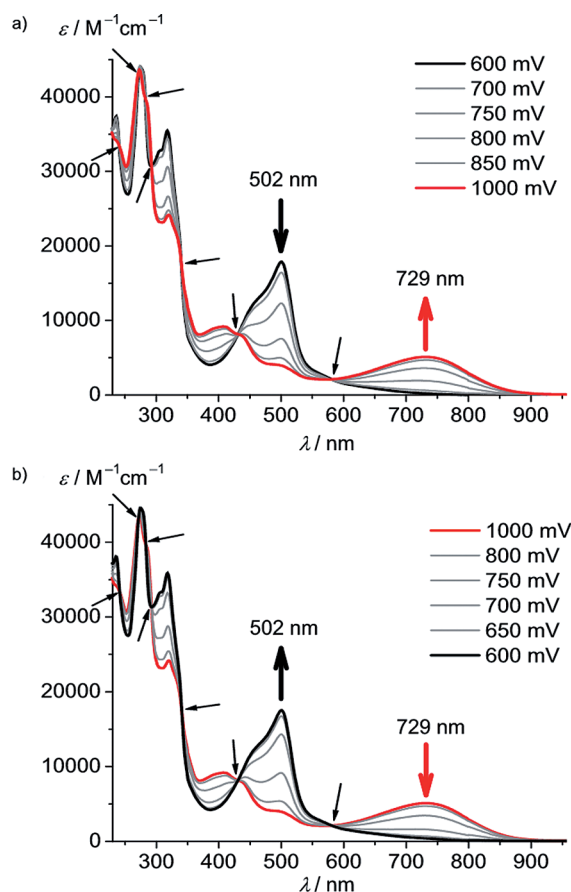


Figure 6. UV/Vis spectra during (a) electrochemical oxidation of [4]<sup>2+</sup> ( $E = 600 \rightarrow 1000$  mV) and (b) back reduction of [4]<sup>3+</sup> ( $E = 1000 \rightarrow 600$  mV) in an optically transparent thin layer electrochemical (OTTLE) cell in 10<sup>-3</sup> M NaOH and 0.1 M [*n*Bu<sub>4</sub>N](PF<sub>6</sub>) in CH<sub>3</sub>CN/H<sub>2</sub>O (98:2, v/v%). Black arrows indicate isosbestic points.<sup>[72]</sup>

The UV/Vis absorption spectrum of [4]<sup>2+</sup> features  $\pi \rightarrow \pi^*$  transitions below  $\lambda = 400$  nm and a characteristic MLCT band at  $\lambda_{\text{max}} = 502$  nm ( $\epsilon_{\text{max}} = 19100$  M<sup>-1</sup> cm<sup>-1</sup>; Figures 6 and 7).<sup>[59]</sup> Time-dependent DFT calculations (B3LYP/LANL2DZ, IEFPCM, CH<sub>3</sub>CN) confirm the ligand-centered character of the  $\pi \rightarrow \pi^*$  transitions at  $\lambda < 400$  nm and the essentially MLCT character of the transitions at  $\lambda > 400$  nm. Relevant Kohn–Sham frontier molecular or-



bitals of  $[4]^{2+}$  are depicted in Figure 8. Five frontier orbitals, HOMO-2 to LUMO+1, participate in transitions with  $\lambda > 400$  nm. HOMO to HOMO-2 correspond to the  $t_{2g}$  orbitals in  $O_h$  symmetry and are mainly ruthenium-centered with a small contribution from the amino nitrogen atom in the HOMO. The contribution of the amino group to the MLCT transition is experimentally verified by resonance Raman experiments involving excitations of the MLCT transitions ( $\lambda = 458$ – $514$  nm).<sup>[61]</sup> The LUMO and LUMO+1 are located on the acceptor-functionalized tpy ligand. Again, resonance Raman spectroscopy corroborates the participation of the respective ligand, namely the tpy-COOEt ligand by the enhancement of the characteristic  $1726\text{ cm}^{-1}$  ester stretching mode.<sup>[61]</sup> Thus, the 500 nm absorption band is best described by a mixed  $^1\text{MLCT}/^1\text{LL}'\text{CT}$  character ( $\text{LL}'\text{CT} = \text{ligand-to-ligand charge transfer}$ ). For brevity we will refer to this mixed charge transfer transition in the following as MLCT only. The high-energy orbitals LUMO+9 and LUMO+13 corresponding to the  $e_g^*$  orbitals (in  $O_h$  symmetry) do not participate in the  $^1\text{MLCT}$  absorption process (Figure 8).

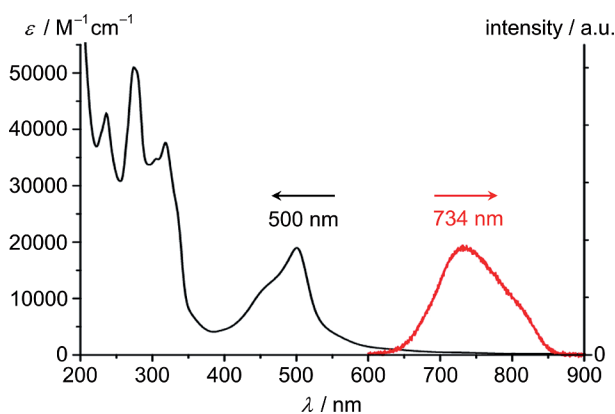


Figure 7. UV/Vis absorption spectrum (black) and emission spectrum (red) of  $[4](\text{PF}_6)_2$  in  $\text{CH}_3\text{CN}$  at 295 K.

After population of the initial  $^1\text{MLCT}$  state, ISC and vibrational relaxation occur, forming the emissive  $^3\text{MLCT}$  state (Figure 1). Excited-state dynamics on the picosecond timescale of  $[4]^{2+}$  has been experimentally probed by transient absorption measurements.<sup>[56]</sup> When  $[4]^{2+}$  is excited at  $\lambda_{\text{exc}} = 400$  nm, its transient absorption spectra show an instant ground-state bleach at  $\lambda = 509$  nm together with a photoinduced absorption at  $\lambda = 565$ – $960$  nm (Figure 9). The latter absorption nicely fits to a LMCT absorption of a  $\text{Ru}^{\text{III}}$ -based excited state (cf. Figure 6 for  $[4]^{3+}$ ).<sup>[56]</sup> The region of the photoinduced absorption reveals a fast process with a time constant of 7.2 ps at 295 K before reaching the thermalized  $^3\text{MLCT}$  state. These dynamics might be associated with localization of the excited electron on the tpy-COOEt ligand, ISC, or vibrational relaxation within  $^1/3\text{MLCT}$  states.<sup>[56]</sup> In essence, the  $^3\text{MLCT}$  state is populated and thermally equilibrated in the picosecond time scale.

At 295 K in fluid solution,  $[4]^{2+}$  shows phosphorescence from this  $^3\text{MLCT}$  state at  $\lambda_{\text{max}} = 734$  nm with a  $^3\text{MLCT}$

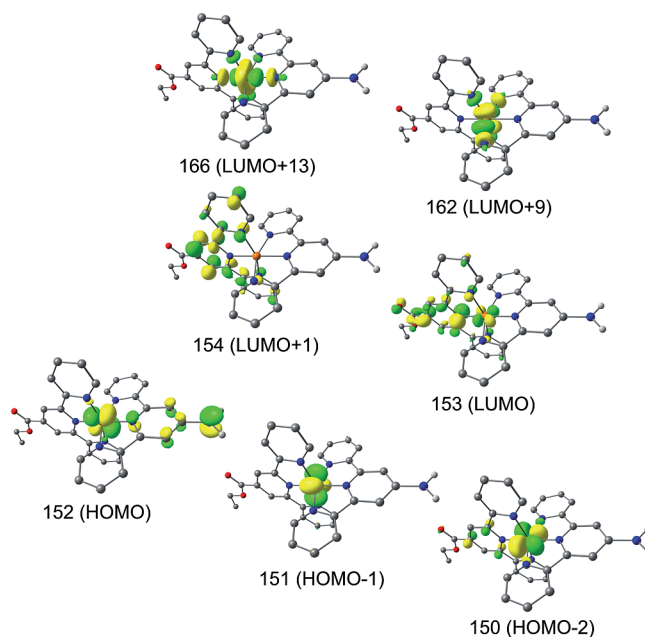


Figure 8. DFT-calculated Kohn–Sham frontier molecular orbitals (contour value 0.06 a. u.) of  $[4]^{2+}$  (B3LYP/LANL2DZ, IEFPCM,  $\text{CH}_3\text{CN}$ ; CH hydrogen atoms omitted).

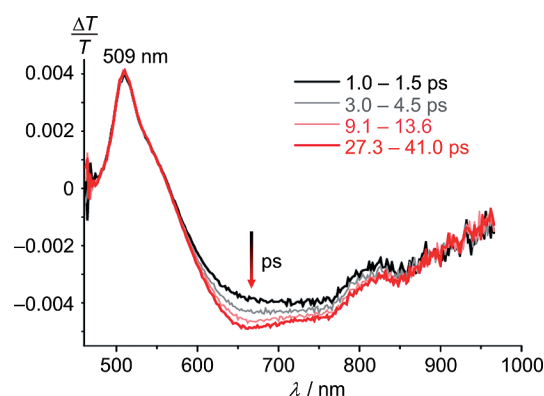


Figure 9. Transient absorption spectra of  $[4]^{2+}$  (pulse  $\lambda_{\text{exc}} = 400$  nm, 2600 nJ) in  $\text{PrCN}$  at 295 K.<sup>[56]</sup>

lifetime of  $\tau = 34$  ns and a quantum yield of  $\Phi = 0.27\%$  (Figure 7).<sup>[61]</sup> In frozen butyronitrile at 77 K, the emission energy shifts to higher values ( $\lambda = 702$  nm).<sup>[56]</sup> Notably, amino acid  $[5]^{2+}$  shows a second time constant of  $\tau = 4$  ns (8%) for the excited-state decay, which might be ascribed to proton quenching of the MLCT state by a nearby acid.<sup>[89]</sup> Indeed, ground-state aggregation of carboxylic acids is very common,<sup>[90]</sup> and in the MLCT excited state the basicity of the formally reduced tpy-COOH ligand should be increased, which suggests a proton transfer to the tpy-CO group of the excited complex from a ground-state acid (excited-state proton transfer, ESPT<sup>[89]</sup>).

The emitting  $^3\text{MLCT}$  state as well as the deactivating  $^3\text{MC}$  state were successfully modeled by DFT calculations.<sup>[56]</sup> The  $^3\text{MC}$  state of push-pull-substituted  $[4]^{2+}$  is calculated to be higher in energy by  $26.8\text{ kJ mol}^{-1}$  relative to its  $^3\text{MLCT}$  state (Figure 10). On the other hand, the corre-

sponding triplet states of the parent complex,  $[1]^{2+}$ , are found to be essentially isoenergetic.<sup>[56]</sup> While the geometry of the  $^3\text{MLCT}$  state of  $[4]^{2+}$  differs only slightly from the  $^1\text{GS}$  geometry, the  $^3\text{MC}$  geometry is significantly distorted with respect to the  $^1\text{GS}$  and  $^3\text{MLCT}$  states. For example, the bond lengths between Ru and the central N atom of tpy-COOEt are 1.99, 2.04, and 2.17 Å for the  $^1\text{GS}$ ,  $^3\text{MLCT}$ , and  $^3\text{MC}$  states, respectively. The N–C–N dihedral angles of the tpy-COOEt ligand amount to  $0^\circ$ ,  $0^\circ$ , and  $11^\circ$  for the  $^1\text{GS}$ ,  $^3\text{MLCT}$ , and  $^3\text{MC}$  states, respectively, which shows that the tpy-COOEt ligand has lost its planarity in the  $^3\text{MC}$  state. The spin density of the  $^3\text{MLCT}$  state is shared between the ruthenium center and the tpy-COOEt ligand, while for the  $^3\text{MC}$  state the spin density is confined to the ruthenium center, as expected for a ligand-field excited state based on the  $(t_{2g})^5(e_g^*)^1$  electron configuration (Figure 10). The connecting transition state ( $^3\text{TS}$ ) between the  $^3\text{MLCT}$  and the  $^3\text{MC}$  state of  $[4]^{2+}$  is calculated to have an energy 31.7 kJ mol<sup>-1</sup> higher than the  $^3\text{MLCT}$  state, while the  $^3\text{TS}$  of  $[1]^{2+}$  is only 7.2 kJ mol<sup>-1</sup> higher than its  $^3\text{MLCT}$  state, which explains its rapid radiationless excited-state decay. Regarding energy, spin density, and geometry, the  $^3\text{TS}$  transition states strongly resemble the  $^3\text{MC}$  rather than the  $^3\text{MLCT}$  states (Figure 10).<sup>[56]</sup>

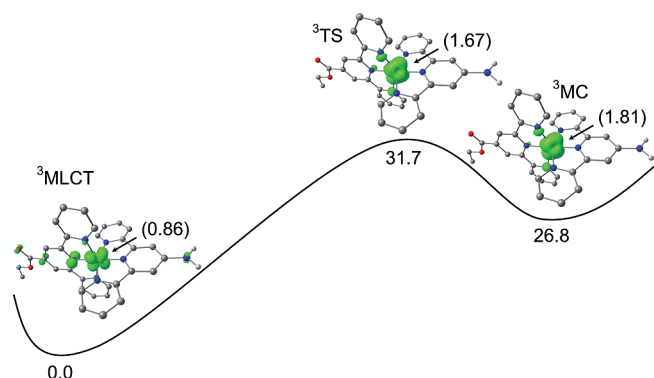


Figure 10. DFT-calculated geometries, relative energies, and spin densities of triplet minima ( $^3\text{MLCT}$  and  $^3\text{MC}$ ) and the transition state ( $^3\text{TS}$ ) of  $[4]^{2+}$  (B3LYP/LANL2DZ, IEFPCM,  $\text{CH}_3\text{CN}$ ; contour value 0.015; energies in kJ mol<sup>-1</sup>; CH hydrogen atoms omitted; Mulliken spin densities at indicated atoms in parentheses).<sup>[56]</sup>

### 3. Strategies toward Long-Lived and Highly Emissive Excited States

With respect to ester complex  $[2]^{2+}$  ( $\tau = 32$  ns;  $\Phi = 0.04\%$ ; Table 1; Figure 2),<sup>[8]</sup> the electron-donating  $\text{NH}_2$  group in the bis-4'-substituted amino acid ester  $[4]^{2+}$  destabilizes the  $^3\text{MC}$  state compared with the  $^3\text{MLCT}$  state, which leads to a further improvement of the excited-state properties ( $\tau = 34$  ns;  $\Phi = 0.27\%$ ; Table 1; Figure 2).<sup>[59]</sup> The push-pull substitution of  $[4]^{2+}$  induces an even smaller HOMO–LUMO energy gap (Figure 8), which significantly shifts the MLCT absorption maximum to lower energy ( $\lambda_{\text{max}} = 502$  nm). In addition, the  $\text{NH}_2$  group in  $[4]^{2+}$  enlarges the chromophore system and raises the extinction co-

efficient ( $\epsilon_{\text{max}} = 19100$  M<sup>-1</sup> cm<sup>-1</sup>).<sup>[59]</sup> In the electronically similar push-pull-substituted  $[\text{Ru}(\text{tpy-OH})(\text{tpy-SO}_2\text{Me})]^{2+}$  complex  $[7]^{2+}$  (Figure 2, Table 1), the combination of an OH donor with a  $\text{SO}_2\text{Me}$  acceptor group enables similar excited-state properties ( $\tau = 50$  ns;  $\Phi = 0.07\%$ ; Table 1).<sup>[50]</sup> Thiophene or triarylamine substituents, for example in  $[8]^{2+}$ <sup>[63]</sup> and  $[9]^{2+}$ ,<sup>[64]</sup> also exert an electron-donating effect as seen in the bathochromically shifted MLCT absorption maxima with respect to that of  $[1]^{2+}$  (Figure 2, Table 1).

Typically, an enlargement of the chromophore system stabilizes the  $^3\text{MLCT}$  state relative to the  $^3\text{MC}$  state. Indeed, in  $[\text{Ru}(\text{tpy-Ph})_2]^{2+}$  ( $[10]^{2+}$ , Figure 2), featuring phenyl groups appended to the 4'-positions of the tpy ligands, the  $^3\text{MLCT}$  lifetime and quantum yield ( $\tau = 1$  ns;  $\Phi = 0.006\%$ ) of  $[10]^{2+}$  are substantially enhanced as compared with those of  $[1]^{2+}$ , but they are still far from useful (Table 1).<sup>[50]</sup> The combination of donor–acceptor functionalization and an enlarged chromophore system has been realized in extended amino acid derivatives  $[11]^{2+}$ – $[13]^{2+}$  featuring *para*-phenylene spacers between the 4'-substituents and the tpy ligands (Figure 2).<sup>[60]</sup> However, this combination does not lead to a synergetic effect:  $[11]^{2+}$  features a lower  $^3\text{MLCT}$  lifetime and a lower quantum yield ( $\tau = 23$  ns;  $\Phi = 0.053\%$ ) compared with those of the phenylene-free analogue  $[4]^{2+}$  (Table 1). Compounds  $[12]^{2+}$  and  $[13]^{2+}$  also exhibit excited-state properties that are inferior to those of the phenylene-free analogue  $[5]^{2+}$  (Figure 2, Table 1).<sup>[59,60]</sup> The ring planes of the phenylene ring and the central pyridyl ring of a tpy ligand are far from co-planar. Thus, the reduced  $\pi$ -conjugation mitigates the positive effect of donor–acceptor substitution.<sup>[60]</sup> Coplanarity in extended tpy ligands has been achieved by replacing *para*-phenylene with pyrimidine spacers, for example in complexes  $[14a]^{2+}$  and  $[14b]^{2+}$  (Figure 2).<sup>[65]</sup> In these complexes the enhanced  $\pi$ -conjugation efficiently stabilizes the  $^3\text{MLCT}$  state with respect to the  $^3\text{MC}$  state, giving long excited-state lifetimes up to  $\tau = 231$  ns and quantum yields up to  $\Phi = 0.17\%$  (Table 1).<sup>[65]</sup>

Long excited-state lifetimes can also be achieved by the so-called multichromophore approach: additional appended chromophores, such as pyrene or anthracene, can possess triplet intraligand excited states ( $^3\text{IL}$ ) with energies similar to the  $^3\text{MLCT}$  state. In this case, a triplet–triplet equilibrium between these triplet states is feasible.<sup>[11]</sup> As deactivation from the triplet state of the organic chromophore is spin-forbidden and hence slow, the  $^3\text{IL}$  state of the organic chromophore acts as an excited state reservoir for the emitting  $^3\text{MLCT}$  state and such a  $^3\text{MLCT}/^3\text{IL}$  equilibrium can significantly prolong the phosphorescence.<sup>[91,92]</sup> For instance, complexes  $[15a]^{2+}$  and  $[15b]^{2+}$  (Figure 2), featuring pyrene units as organic triplet reservoirs, indeed reach lifetimes of  $\tau = 580$  and 2500 ns, respectively.<sup>[66]</sup>

A pronounced push-pull situation is also present in carbene complexes  $[16]^{2+}$  and  $[17]^{2+}$  (Figure 11) prepared by Schubert and Berlinguette.<sup>[67]</sup> The combination of an electron-accepting tpy ligand with the strongly  $\sigma$ -donating CNC bis(carbene) ligand 2',6'-bis(3-methyl-1,2,3-triazol-4-yl-5-ylene)pyridine results in exceptionally long excited-state lifetimes and quantum yields up to  $\tau = 7900$  ns and  $\Phi$

= 17.3% (Table 1).<sup>[67]</sup> Further N-heterocyclic carbene donor ligands as well as cyclometalating ligands and their ruthenium complexes will not be discussed here in more detail, and the reader is referred to recent literature.<sup>[4,93–97]</sup>

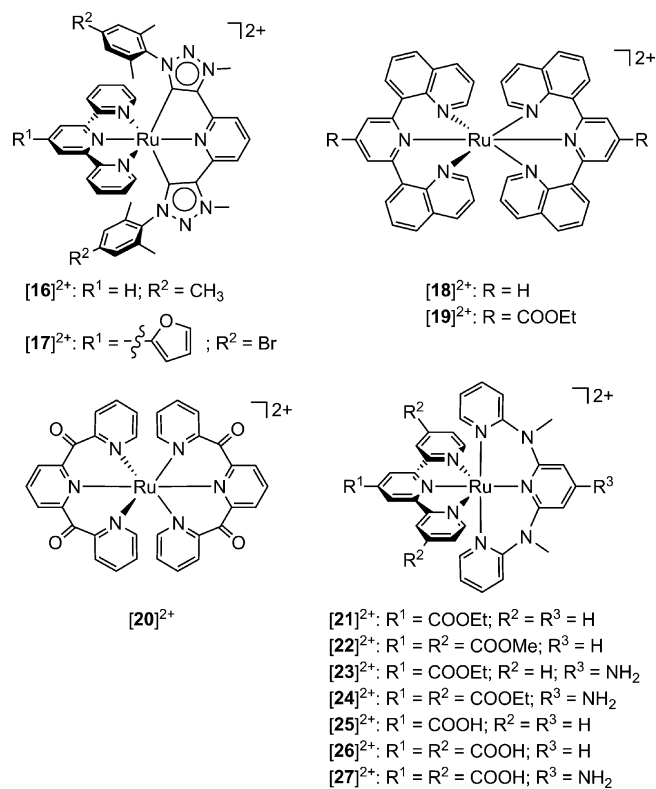


Figure 11. Bis(tridentate) complexes of ruthenium(II)  $[16]^{2+}$ – $[27]^{2+}$ .

A further successful strategy to improve the excited-state properties in bis(tridentate) ruthenium(II) complexes is the optimization of N–Ru–N bite angles. All complexes  $[1]^{2+}$ – $[17]^{2+}$  feature five-membered chelate rings and N–Ru–N bite angles of around  $79^\circ$ . The carbene chelate ligands in  $[16]^{2+}$  and  $[17]^{2+}$  have even smaller C–Ru–N bite angles of  $77^\circ$ .<sup>[54c,56,59,67]</sup> Bite angles of  $90^\circ$  maximize the orbital overlap between the pyridine nitrogen lone pairs and the d orbitals of the central metal with  $e_g$  symmetry and hence increase the antibonding character of the  $e_g^*$  orbitals and the ligand-field splitting. This stronger ligand-field splitting augments the energy difference between  $^3MLCT$  and  $^3MC$  states, which again hampers radiationless deactivation via the latter state (Figure 1).<sup>[54c]</sup> Hammarström et al. introduced bite angles of  $90^\circ$  by using six-membered chelates in  $[Ru(dqp)_2]^{2+}$  ( $[18]^{2+}$ , Figure 11), which led to high values for the room-temperature lifetime of the excited state and emission quantum yield [ $\tau = 3000$  ns,  $\Phi = 3.2\%$ ,  $dqp = 2,6$ -di(quinolin-8-yl)pyridine].<sup>[68,69,98]</sup> Homoleptic complex  $[Ru(EtOOC-dqp)_2]^{2+}$  ( $[19]^{2+}$ , Figure 11) with electron-withdrawing substituents features even higher values ( $\tau = 5500$  ns;  $\Phi = 11.2\%$ , Table 1).<sup>[70]</sup> Ruben et al. introduced  $[Ru(dcpp)_2]^{2+}$  ( $[20]^{2+}$ , Figure 11), featuring six-membered chelates and  $90^\circ$  bite angles by formal insertion of carbonyl spacers between the pyridine rings of the parent  $[Ru(tpy)_2]^{2+}$  complex [ $dcpp = 2,6$ -di(2-carboxypyridyl)pyr-

idine]. Compound  $[20]^{2+}$  has a very long-lived  $^3MLCT$  state ( $\tau = 3300$  ns) and the highest room-temperature quantum yield in fluid solution ( $\Phi = 30\%$ ) reported to date among bis(tridentate) ruthenium(II) complexes (Table 1).<sup>[71]</sup>

Although these excellent photophysical properties are highly beneficial, one drawback is associated with large chelate rings. Six-membered chelate rings such as those found in  $[18]^{2+}$  and  $[19]^{2+}$  enable highly flexible coordination, and this can lead to undesired stereoisomers, namely *mer*, *cis-fac*, and *trans-fac* isomers.<sup>[99]</sup> Mixed-ligand complex  $[Ru(tpy-COOEt)(ddpd)]^{2+}$  ( $[21]^{2+}$ , Figure 11) prepared by our group overcomes the problem of *fac/mer*-stereoisomers by using the combination of a five-membered tpy and a six-membered ddpd chelate ligand (ddpd = *N,N'*-dimethyl-*N,N'*-dipyridin-2-ylpyridine-2,6-diamine).<sup>[56,100]</sup> Complex  $[21]^{2+}$  can be prepared in a stepwise manner by first introducing the tpy ligand to obtain ruthenium(III) complex  $Ru(tpy-COOEt)Cl_3$ , which is converted into the final, pure *meridional* stereoisomer  $[21]^{2+}$  by treatment with the ddpd ligand. The tpy ligand only coordinates in a planar *meridional* fashion, thus forcing the ddpd ligand to adopt the *meridional* coordination as well. The bite angles of the ddpd ligand are  $88^\circ$ , similar to those of *dqp* and *dcpp*. Despite the presence of only a single ddpd ligand with  $88^\circ$  bite angles and a tpy ligand with only  $79^\circ$  angles, complex  $[21]^{2+}$  achieves a quantum yield of  $\Phi = 0.45\%$  and a remarkably long  $^3MLCT$  lifetime of  $\tau = 722$  ns at room temperature in solution (Table 1).<sup>[100]</sup> The synergy of the electron-accepting tpy ligand and the electron-donating ddpd ligand containing  $NCH_3$  groups ( $[21]^{2+}$ ) creates a push-pull situation and shifts the maximum absorption wavelength further to lower energy ( $\lambda_{max} = 517$  nm) relative to that of  $[2]^{2+}$  lacking the  $NCH_3$  groups ( $\lambda_{max} = 485$  nm) (Figure 2, Table 1). In push-pull complex  $[22]^{2+}$ , the two outer pyridine rings of the tpy ligand are additionally functionalized by electron-withdrawing ester groups. The maximum absorption wavelength of  $[22]^{2+}$  (Figure 11) is further red-shifted ( $\lambda_{max} = 539$  nm), and even higher values for the  $^3MLCT$  lifetime ( $\tau = 841$  ns) and the quantum yield ( $\Phi = 1.1\%$ ) are obtained (Table 1).<sup>[56]</sup>

However, the increase of  $^3MLCT$  lifetimes and quantum yields by push-pull substitution tuning has a limit. A pronounced push-pull situation not only increases the energy gap between  $^3MLCT$  and  $^3MC$  states but simultaneously lowers the gap between the  $^3MLCT$  state and the ground state  $^1GS$ . According to the energy gap law, a small  $^3MLCT$ – $^1GS$  energy difference induces fast radiationless deactivation into the ground state.<sup>[79,101–103]</sup> Such a strong push-pull situation exists in complexes  $[23]^{2+}$  and  $[24]^{2+}$  (Figure 11), which feature an additional  $NH_2$  group on the electron-donating ddpd ligand relative to their  $NH_2$ -free counterparts  $[21]^{2+}$  and  $[22]^{2+}$ , respectively. The push-pull character of  $[23]^{2+}$  and  $[24]^{2+}$  manifests itself by the red-shifted absorption maxima and by the lower  $Ru^{II}/Ru^{III}$  redox potentials (ca. 0.2 V) as compared with those of  $[21]^{2+}$  and  $[22]^{2+}$ , respectively (Table 1).<sup>[56]</sup> Indeed,  $[23]^{2+}$  and  $[24]^{2+}$  are among the best red absorbers (and red emitters) collected in Table 1. However, the  $NH_2$  group dramatically



reduces the  $^3\text{MLCT}$  lifetimes of  $[\mathbf{23}]^{2+}$  and  $[\mathbf{24}]^{2+}$  by a factor of about five to six, and quantum yields are reduced by an even higher factor compared with those of the  $\text{NH}_2$ -free analogues (Table 1). The faster excited state deactivation in  $[\mathbf{23}]^{2+}$  and  $[\mathbf{24}]^{2+}$  is induced by high-energy oscillators, in this case predominantly by the N–H modes (multiphonon deactivation). This is shown by ( $\text{NH}_2 \rightarrow \text{ND}_2$ ) deuteration experiments with deuterated complexes  $[\mathbf{23}^{\text{D}}]^{2+}$  and  $[\mathbf{24}^{\text{D}}]^{2+}$  featuring higher quantum yields than those of their parent complexes  $[\mathbf{23}]^{2+}$  and  $[\mathbf{24}]^{2+}$ , respectively.<sup>[56]</sup> In essence, the above-mentioned small  $^3\text{MLCT}^{-1}\text{GS}$  energy gap, together with high-energy oscillators, is responsible for radiationless deactivation of the  $^3\text{MLCT}$  state in  $[\mathbf{23}]^{2+}$  and  $[\mathbf{24}]^{2+}$ .

Regarding thermal and photochemical stability, bis(tridentate) complexes should outperform tris(bidentate) complexes. The benchmark complex,  $[\text{Ru}(\text{bpy})_3]^{2+}$ , has been reported to be photolabile in the presence of coordinating anions such as  $\text{Cl}^-$ ,  $\text{Br}^-$ ,  $\text{I}^-$ ,  $\text{SCN}^-$ , or  $\text{NO}_3^-$ . In its excited state,  $[\text{Ru}(\text{bpy})_3]^{2+}$  is prone to photoinduced ligand substitution, photooxygenation, and photoracemization.<sup>[104–108]</sup> In contrast, bis(tridentate) ruthenium(II) complexes such as  $[\mathbf{4}]^{2+}$ ,  $[\mathbf{18}]^{2+}$ , and  $[\mathbf{21}]^{2+}$  feature significantly higher photostabilities under constant irradiation ( $\lambda = 400\text{--}500\text{ nm}$ ) as compared with that of  $[\text{Ru}(\text{bpy})_3]^{2+}$ .<sup>[70,72]</sup> The enhanced photostability of complexes with tridentate ligands is obviously highly favorable for photo applications of all kinds, and some aspects will be discussed in the following sections.

## 4. Conjugates of the Ruthenium(II) Amino Acids

### 4.1 Amide Bond Formation and Solid-Phase Peptide Synthesis

Amide bond formation at the C-terminus of amino acid  $[\mathbf{5}]^{2+}$  is straightforward by using standard amide coupling reagents such as HOBt/DCC, PfpOH/DCC, PyBOP, or HATU/ $\text{NEt}_3$  {HOBt = 1-hydroxybenzotriazole, DCC = *N,N'*-dicyclohexylcarbodiimide, PfpOH = pentafluorophenol, PyBOP = benzotriazole-1-yl-oxy-tris-pyrrolidino-phosphonium hexafluorophosphate, HATU = 1-[bis(dimethylamino)methylene]-1*H*-1,2,3-triazolo[4,5-*b*]pyridinium 3-oxide hexafluorophosphate}.<sup>[25,77,78]</sup> The choice of coupling reagent hereby solely depends on the nucleophilicity of the chosen amine and eventual protective groups to be employed. Even under the strongest coupling conditions (HATU) no amide coupling of  $[\mathbf{5}]^{2+}$  with itself is observed, which underlines once again the extremely poor reactivity of the  $\text{NH}_2$  group.<sup>[77]</sup> The amino group can be transformed into a much better nucleophile by deprotonation with a strong base (see above), so that amide-bond formation becomes feasible. Then, even comparably mild coupling conditions, for example PfpOH/DCC, are sufficient to overcome the Coulomb repulsion between two positively charged complex fragments to yield dinuclear quadruply charged species (see below).<sup>[25,62]</sup> Coupling of organic acids to  $[\mathbf{5}]^{2+}$  is successful by using acid chlorides or anhydrides without further activation of the  $\text{NH}_2$  group of  $[\mathbf{5}]^{2+}$ .<sup>[18,25,61,77,78]</sup>

Amino acid  $[\mathbf{5}]^{2+}$  (Figure 2) has even been employed as building block in solid-phase peptide synthesis (SPPS) by our group.<sup>[18]</sup> The general synthetic strategy is depicted in Figure 12. Initially, a polymer TentaGel S resin<sup>[109,110]</sup> equipped with a Wang linker<sup>[111]</sup> (compound  $\mathbf{28}$ ) is functionalized with Cl-Gly-Fmoc (Gly = glycine, Fmoc = fluorenylmethoxycarbonyl). The Fmoc protecting group is removed by piperidine to obtain the free  $\text{NH}_2$  group (compound  $\mathbf{29}$ ). After activation of the carboxylic acid group of  $[\mathbf{5}]^{2+}$  by PyBOP, activated  $[\mathbf{5}]^{2+}$  is connected to the solid support through an amide bond to obtain the immobilized complex  $[\mathbf{30}]^{2+}$ . The weak nucleophilicity of the aromatic  $\text{NH}_2$  group of  $[\mathbf{5}]^{2+}$  renders an amino protection group unnecessary.<sup>[18,61]</sup> However, for the activation of the  $\text{NH}_2$  group of  $[\mathbf{30}]^{2+}$ , strong coupling reagents such as acid chlorides (e.g. Cl-Gly-Fmoc) are necessary in order to form an amide bond such as that in  $[\mathbf{31}]^{2+}$ . Monitoring of SPPS reactions with charged ruthenium amino acids is advantageously achieved by treating a small portion of the resin

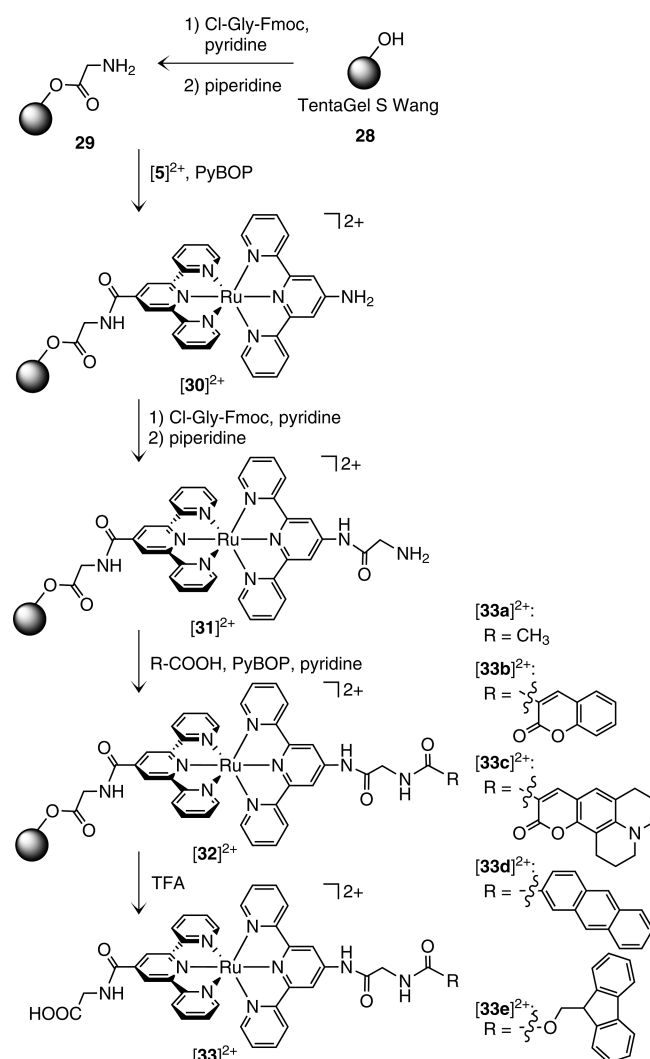


Figure 12. Solid-phase peptide synthesis including ruthenium(II) amino acid  $[\mathbf{5}]^{2+}$  (Fmoc = fluorenylmethoxycarbonyl, PyBOP = benzotriazole-1-yl-oxy-tris-pyrrolidino-phosphonium hexafluorophosphate, TFA = trifluoroacetic acid).<sup>[18]</sup>



with TFA, drying the filtered solution, re-dissolving in  $\text{CH}_3\text{CN}$  and recording ESI mass spectra of the released cationic intermediates). After deprotection by piperidine, the aliphatic  $\text{NH}_2$  group of  $[\mathbf{31}]^{2+}$  readily forms amide bonds with carboxylic acids  $\text{R}-\text{COOH}$  of all kind by PyBOP or acid chloride activation to give peptides  $[\mathbf{32}]^{2+}$ . Several (activated) acids  $\text{R}-\text{COOH}$  have been attached as terminal functional group, for example  $\text{CH}_3\text{COOH}$ , coumarin-3-carboxylic acids, anthracene-2-carboxylic acid, or 9-fluorenylmethoxycarbonyl chloride.<sup>[18]</sup> Finally, metallo peptides  $[\mathbf{33}]^{2+}$  are released from the solid phase by treatment with TFA.

#### 4.2 Energy Transfer between Organic Dyes and Bis(terpyridine)ruthenium(II)

Polypyridine complexes of ruthenium(II), especially  $[\text{Ru}(\text{bpy})_3]^{2+}$ -type complexes, are suitable compounds for directional energy transfer and can act as donors and acceptors for photoinduced energy transfer.<sup>[112]</sup> Bis(tridentate) complexes of ruthenium(II) have been incorporated into energy-transfer systems by using ethynyl spacers between a  $[\text{Ru}(\text{tpy})_2]^{2+}$  donor and thiophene units as acceptors.<sup>[113]</sup> Donor-acceptor-substituted complex  $[\mathbf{5}]^{2+}$  has been connected to organic chromophores with amide bridges by means of SPPS (Figure 12) with a different number of glycine amino acids in between (Figure 13).<sup>[18]</sup> A single glycine unit or none ( $[\mathbf{34}]^{2+}$ :  $n = 0$ ;  $[\mathbf{35}]^{2+}$ :  $n = 1$ ) enables coplanarity of the coumarin dye and the adjacent tpy ligand, which is favorable for efficient energy transfer by the Dexter mechanism.<sup>[18]</sup> With these short bridges, excitation of the coumarin ( $[\mathbf{35}]^{2+}$ ,  $n = 1$ ,  $\lambda_{\text{exc}} = 422 \text{ nm}$ ) induces energy transfer to the  $[\text{Ru}(\text{tpy})_2]^{2+}$  moiety, while the coumarin fluorescence is

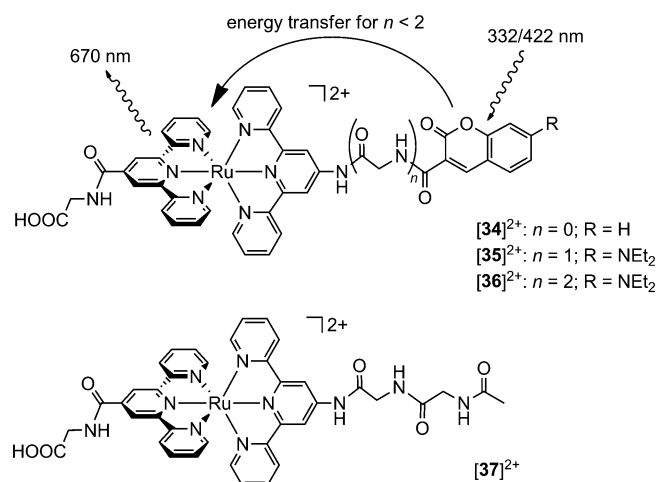


Figure 13. Energy transfer in peptides of  $[\mathbf{5}]^{2+}$ , coumarin dyes  $[\mathbf{34}]^{2+}$ – $[\mathbf{36}]^{2+}$ , and reference complex  $[\mathbf{37}]^{2+}$ .<sup>[18]</sup>

efficiently quenched (Figure 14b).<sup>[18]</sup> The excitation emission matrix of  $[\mathbf{35}]^{2+}$  shows that excitation at  $\lambda_{\text{exc}} = 470$ – $500 \text{ nm}$  results in emission at  $\lambda_{\text{em}} = 670 \text{ nm}$ , which perfectly corresponds to the phosphorescence of the coumarin-free reference  $[\mathbf{37}]^{2+}$  (Figure 14a). Furthermore irradiation of  $[\mathbf{35}]^{2+}$  at a wavelength of  $\lambda_{\text{exc}} = 390$ – $460 \text{ nm}$ , which corresponds to the coumarin excitation, leads to ruthenium-based phosphorescence (Figure 14b). For the longer bis(glycine) bridge ( $[\mathbf{36}]^{2+}$ ,  $n = 2$ , Figure 13), excitation of the coumarin at  $\lambda_{\text{exc}} = 390$ – $460 \text{ nm}$  essentially leads to fluorescence of the organic chromophore at  $\lambda_{\text{max}} = 465 \text{ nm}$ , while phosphorescence from the  $[\text{Ru}(\text{tpy})_2]^{2+}$  moiety is practically not observed (Figure 14c and Supporting Information). Hence energy transfer is inefficient in  $[\mathbf{36}]^{2+}$  ( $n = 2$ ) but efficient in  $[\mathbf{34}]^{2+}$  and  $[\mathbf{35}]^{2+}$  ( $n = 0, 1$ ). Interestingly, all peptides  $[\mathbf{33}]^{2+}$ – $[\mathbf{35}]^{2+}$  with a terminal  $\text{COOH}$  group possess an additional  $\tau = 2$ – $4 \text{ ns}$  emission component similar to that of amino acid

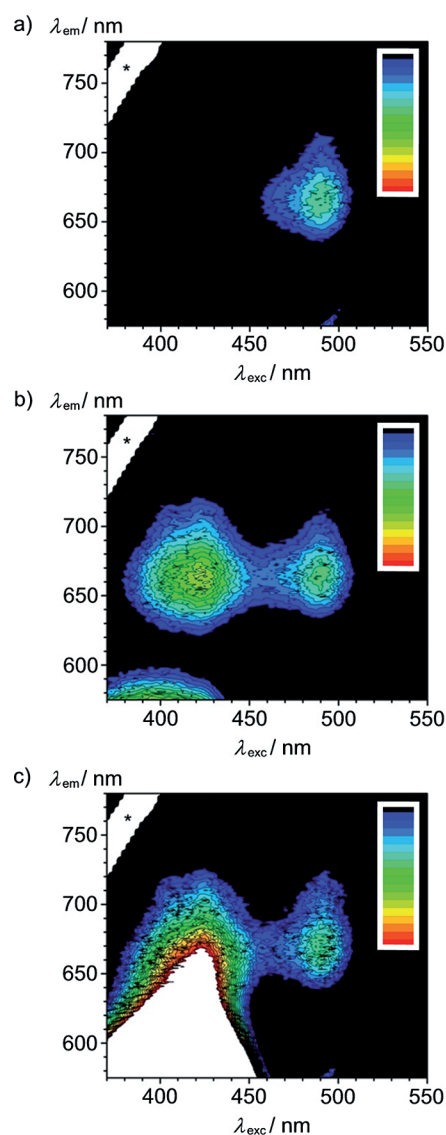


Figure 14. Excitation emission matrices of (a) reference complex  $[\mathbf{37}]^{2+}$ , (b)  $[\mathbf{35}]^{2+}$  ( $n = 1$ ), and (c)  $[\mathbf{36}]^{2+}$  ( $n = 2$ ). The color bar indicates the emission intensity (\* =  $2\lambda_{\text{exc}}$ ).

[5]<sup>2+</sup> (Table 1). Again, we ascribe this additional pathway of <sup>3</sup>MLCT decay in carboxylic acids to ESPT, namely to proton transfer from an acid to the excited complex.<sup>[18,89]</sup>

#### 4.3 Mixed-Valence and Mixed-Metal Complexes

As described in Section 4.1, amide coupling reactions with building block [5]<sup>2+</sup> can also be used to selectively build dinuclear complexes containing two ruthenium(II) centers without formation of *rac/meso* diastereomers (Figure 15, [38]<sup>4+</sup>–[40]<sup>4+</sup>).<sup>[25,62]</sup> The electrochemical properties of these systems are very similar to those of their constituent mononuclear systems. For example, dinuclear [38]<sup>4+</sup> (Figure 15) can be considered to be built up from mononuclear complexes [4]<sup>2+</sup> and [6]<sup>2+</sup> (Figure 2). The redox potentials of the Ru<sup>II</sup>/Ru<sup>III</sup> couples in [38]<sup>4+</sup> are  $E_{1/2} = 0.68$  V at the *N*-terminal ruthenium center and  $E_{1/2} = 0.91$  V at the *C*-terminus,<sup>[25]</sup> and thus they are essentially unperturbed in comparison with mononuclear species [4]<sup>2+</sup> and [6]<sup>2+</sup> ( $E_{1/2} = 0.68$  and 0.85 V, respectively; Table 1).<sup>[59,61]</sup> On the other hand, the absorption spectrum of [38]<sup>4+</sup> (Table 1) cannot be regarded as a simple superposition of the absorption spectra of [4]<sup>2+</sup> and [6]<sup>2+</sup>. A bathochromic and hyperchromic shift of the MLCT band from around  $\lambda_{\max} = 500/490$  nm ( $\epsilon_{\max} \approx 20000$  M<sup>-1</sup> cm<sup>-1</sup> for mononuclear complexes [4]<sup>2+</sup> and [6]<sup>2+</sup>) to  $\lambda_{\max} = 522$  nm ( $\epsilon_{\max} = 50600$  M<sup>-1</sup> cm<sup>-1</sup>)<sup>[25]</sup> is observed relative to the mononuclear complexes due to an extension and stronger push-pull substitution of the chromophores. Emission of [38]<sup>4+</sup> occurs from the lowest-energy <sup>3</sup>MLCT state ( $\lambda_{\max} = 750$  nm,  $\Phi = 0.24\%$ ,  $\tau = 22$  ns, Table 1), which is located on the *N*-terminal side of the dinuclear system, because of the electron-donating effect of the amino group and the strongly electron-withdrawing effect of the Ru<sup>II</sup> complex attached to the *C*-terminus. This is why the emission energy and quantum yield of [38]<sup>4+</sup> better match those of NH<sub>2</sub>-substituted [5]<sup>2+</sup> than those of NHAc-substituted [6]<sup>2+</sup> (Table 1). Obviously, the excited-state energy is efficiently transferred to the lowest emitting <sup>3</sup>MLCT state irrespective of the initial excitation locus. Similar observations are made for the phenylene-extended dinuclear amide [39]<sup>4+</sup> (Figure 15), although the bathochromic and hyperchromic effects are less pronounced because of the “phenylene dilution” (see above).<sup>[25]</sup> Similar to acids [33]<sup>2+</sup>–[35]<sup>2+</sup> and to amino acid [5]<sup>2+</sup> itself, acid [38]<sup>4+</sup> shows a second decay component with  $\tau = 2$  ns ascribed to ESPT.<sup>[18,89]</sup>

One-electron oxidation of these dinuclear complexes yields mixed-valent Ru<sup>II</sup>Ru<sup>III</sup> complexes [38]<sup>5+</sup> and [39]<sup>5+</sup>.<sup>[25]</sup> No photoinduced intervalence charge transfer (IVCT) from Ru<sup>II</sup> to Ru<sup>III</sup> is observed by UV/Vis/NIR spectroscopy. Theoretical results also indicate no electronic interaction between the metal centers in [38]<sup>5+</sup> and [39]<sup>5+</sup>. This is attributed to the substantial electronic difference of the individual complex moieties and the resulting high redox asymmetry within the complexes, the large distance between the ruthenium centers of about 13 and 18 Å for [38]<sup>5+</sup> and [39]<sup>5+</sup>, respectively, and the twisting in the bridge.

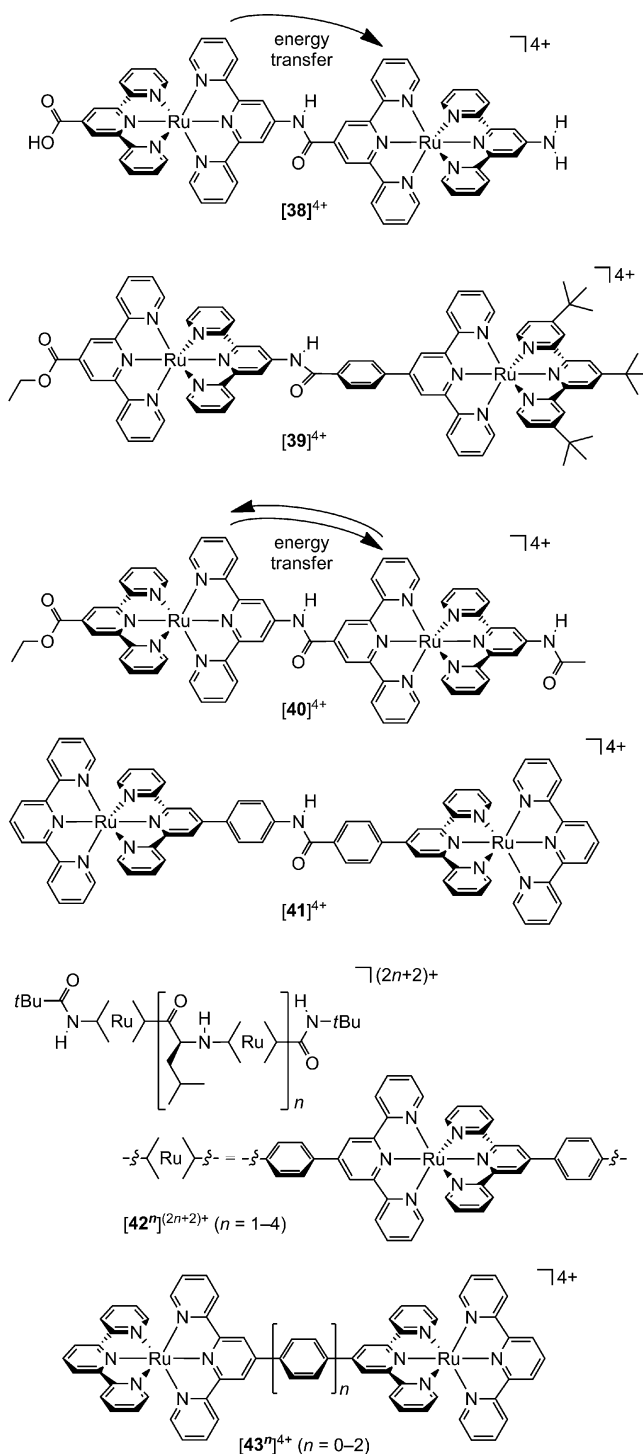


Figure 15. Dinuclear amide-linked bis(terpyridine)ruthenium(II) complexes and related complexes.<sup>[25,51,52,62,73,74]</sup>

All these facts result in valence-localized mixed-valent systems [38]<sup>5+</sup> and [39]<sup>5+</sup> of Robin–Day class I.<sup>[25,114]</sup>

In order to maximize the redox symmetry of [38]<sup>4+</sup>, the capping functionalities were adjusted to give dinuclear amide-linked complex [40]<sup>4+</sup> (Figure 15) with ethyl carboxylate and acetamido functional groups.<sup>[62]</sup> While the redox asymmetry indeed essentially vanishes in [40]<sup>4+</sup> and both ruthenium(II) ions are oxidized at  $E_{1/2} = 0.91$  V, still no

electronic communication is observed after oxidation of  $[40]^{4+}$  to mixed-valent  $Ru^{II}Ru^{III}$  cation  $[40]^{5+}$  with ceric ammonium nitrate in aqueous sulfuric acid solution. Theoretical data on  $[40]^{5+}$  again indicate an entirely valence-localized mixed-valent complex. According to paramagnetic NMR spectroscopy studies, the first oxidation yields the  $Ru^{II}Ru^{III}$  valence isomer that has the  $Ru^{III}$  center located at the N-terminus. The observation of electronically essentially uncoupled ruthenium centers in these dinuclear mixed-valence complexes with two terpyridine ligands is consistent with data on similar systems reported in the literature: dinuclear amide  $[41]^{4+}$  and its mixed-valence congener  $[41]^{5+}$  reported by Colbran et al.,<sup>[73]</sup> in which two *para*-phenylene linkers connect the chromophores with the amide bridge, contain two electronically isolated ruthenium ions with identical properties (Figure 15). This can be attributed to the even larger Ru–Ru distance compared with that in  $[39]^{4+}$ . A similar picture was obtained for the alternating leucine bis(terpyridine)ruthenium(II) peptides  $[42]^{(2n+2)+}$  ( $n = 1-4$ )<sup>[74]</sup> with two chromophores separated by two *para*-phenylene groups and a leucine spacer. Extinction coefficients of this series of compounds are proportional to the number ( $n$ ) of chromophores present per molecule with unshifted absorption maxima. The observation of a single redox wave for all  $Ru^{II}/Ru^{III}$  couples additionally underlines the electronic independence of the complex fragments. The parent dinuclear complex,  $[43]^{4+}$  ( $n = 0$ ),<sup>[51,52]</sup> with directly linked (back-to-back) terpyridine ligands also exhibits only a single redox wave for the two  $Ru^{II}/Ru^{III}$  couples. Upon oxidation to  $[43]^{5+}$  ( $n = 0$ ), however, a weak IVCT band is observed in the NIR region, which is indicative of an electronic interaction of the ruthenium centers. Extension of the bridge by one or two *para*-phenylene linkers reduces the electronic coupling parameter in the complexes  $[43]^{5+}$  ( $n = 1, 2$ ),<sup>[51]</sup> but despite the significant twisting of the *para*-phenylene linkers against each other the communication does not vanish completely. We suggest that the combination of an amide linker with terpyridine ligands in  $[38]^{4+}$ – $[42]^{4+}$  suppresses an electronic coupling of the ruthenium ions. The lack of interaction is attributed to a mismatch of the orbital energies of the bridge and the metal centers but not to unsuitable frontier orbital symmetries.<sup>[114–118]</sup>

One-electron reduction of  $[40]^{4+}$  to  $[40]^{3+}$  by cobaltocene affords a ligand mixed-valent complex in which the unpaired electron is localized on the carboxy terpyridine of the bridging ligand according to DFT calculations and paramagnetic NMR spectroscopy studies. EPR spectroscopic studies on  $[40]^{3+}$  reveal a rhombic signal pattern ( $g_{1,2,3} = 2.006, 1.989, 1.958$ ) in frozen solution, closely resembling the spectrum of the singly reduced complex  $[6]^+$  (see above) and suggesting a valence-localized radical at the bridging ligand.<sup>[62]</sup>

The optical properties of dinuclear compound  $[40]^{4+}$  are related to those of mononuclear  $[6]^{2+}$  carrying the same functional groups.<sup>[61,62]</sup> A hyperchromic effect on the MLCT absorption band stronger than that for the  $[5]^{2+}/[38]^{4+}$  pair is observed, while the bathochromic shift is less pronounced (Table 1). Compound  $[40]^{4+}$  is emissive at room

temperature in solution and has an emission band significantly broadened in comparison to that of  $[6]^{2+}$  and other mononuclear complexes. Indeed, this broad band can be perfectly approximated by two emission bands with  $\lambda_{\max} = 675$  nm (71%) and  $\lambda_{\max} = 706$  nm (29%).<sup>[62]</sup> Notably,  $[40]^{4+}$  also shows two decay components with  $\tau_1 = 24$  ns (71%) and  $\tau_2 = 44$  ns (29%). These components are observed independent of the presence of additional water, chloride, or dioxygen. Hence, this biexponential excited decay is an intrinsic property of  $[40]^{4+}$  and is assigned to the dual emissions of the two different chromophores in  $[40]^{4+}$ . As the emission band shape and position are independent of the excitation energy ( $\lambda_{\text{exc}} = 450\text{--}550$  nm), these two chromophores are involved in a rapid excited-state equilibration at room temperature (triplet–triplet energy transfer).

In addition to the rich optical and redox chemistry of the dinuclear complexes, acid–base reactivity arises from the two amide functionalities in  $[40]^{4+}$ , similar to  $[5]^{2+}$  (see above). The electron-withdrawing effects of the complex fragments strongly polarize the N–H bonds and thus these protons become substantially acidic. This is especially pronounced for the central amide unit flanked by two doubly cationic charges. The combination of two oxidation and two deprotonation steps yields eight conceivable species starting from  $[40]^{4+}$ . These are summarized in the  $3 \times 3$  square scheme in Figure 16. While the successive deprotonation steps  $[40]^{4+} \rightarrow [40 - H]^{3+} \rightarrow [40 - 2H]^{2+}$  could be thoroughly examined experimentally (horizontal reactions), preparative oxidation of deprotonated species (vertical reactions), ( $[40 - H]^{3+} \rightarrow [40 - H]^{4+} \rightarrow [40 - H]^{5+}$ ) was successful neither by chemical nor by electrochemical means because of the high  $Ru^{II}/Ru^{III}$  potential. NMR spectroscopy reveals that the bridging amide proton of  $[40]^{4+}$  is readily deprotonated in MeCN/H<sub>2</sub>O mixtures by employing NEt<sub>3</sub> as base, which leads to  $[40 - H]^{3+}$ . The less acidic terminal amide proton requires the much stronger phosphazene base P<sub>1</sub>-tBu<sup>[85]</sup> in dry acetonitrile and gives  $[40 - 2H]^{2+}$  (Figure 16).<sup>[62]</sup> For each deprotonation step, a unique set of six isosbestic points is observed in the UV/Vis spectra indicative of two successive reversible processes. The <sup>1</sup>MLCT band of  $[40]^{4+}$  is substantially shifted by 22 nm to  $\lambda_{\max} = 526$  nm during the first  $[40]^{4+} \rightarrow [40 - H]^{3+}$  deprotonation and further to  $\lambda_{\max} = 533$  nm during the second  $[40 - H]^{3+} \rightarrow [40 - 2H]^{2+}$  step. This is certainly related to the strong electron-donating character of deprotonated amide moieties that increases the push-pull character of the respective  $[Ru(\text{tpy})_2]^{2+}$  chromophores in  $[40 - H]^{3+}$  and in  $[40 - 2H]^{2+}$ .

Using ferrocene carboxylic acid or aminoferrocene and  $[5]^{2+}$  as coupling partners affords heterodinuclear  $Ru^{II}/Fe^{II}$  complexes  $[44]^{2+}$  or  $[45]^{2+}$ , respectively, which differ in the site of ferrocene attachment at the ruthenium amino acid (Figure 17).<sup>[59]</sup> Heterotrinnuclear  $Fe^{II}/Ru^{II}/Fe^{II}$  complex  $[46]^{2+}$  is obtained by treatment of  $[5]^{2+}$  (with HOBt/DCC activation) with aminoferrocene followed by reaction with an activated ferrocene carboxylic acid without using any amine protection groups (Figure 17).<sup>[59]</sup> The MLCT ab-

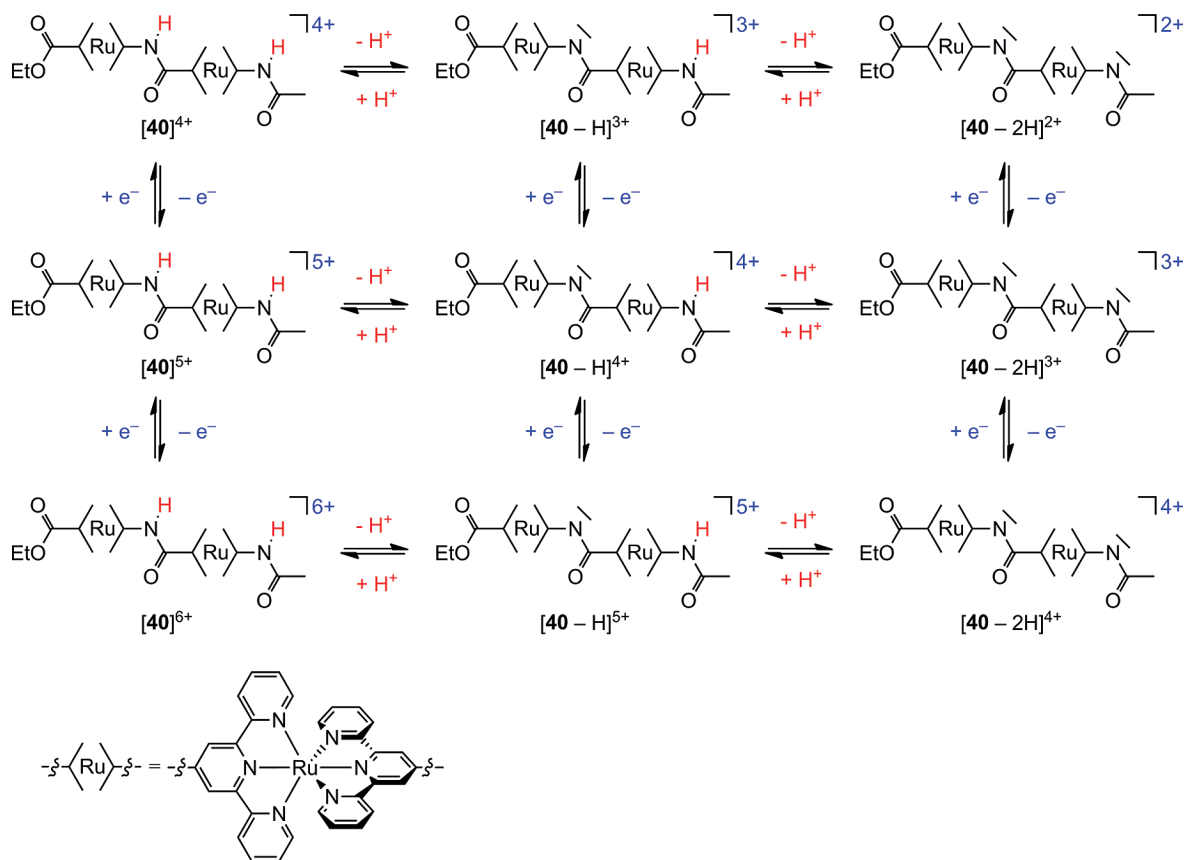


Figure 16.  $3 \times 3$  square scheme of multifunctional  $[40]^{4+}$  comprising two  $\text{Ru}^{\text{II}}/\text{Ru}^{\text{III}}$  oxidations and two NH deprotonations.<sup>[62]</sup>

sorption bands of  $[44]^{2+}$  and  $[46]^{2+}$  appear at  $\lambda_{\text{max}} = 496$  nm, somewhat shifted to lower energy as compared with that of  $[6]^{2+}$  ( $\lambda_{\text{max}} = 492$  nm), possibly because of the slightly stronger electron-donating effect of ferrocenyl compared with methyl. The MLCT band of  $[45]^{2+}$  is shifted to  $\lambda_{\text{max}} = 502$  nm, similar to that of amino acid ester  $[4]^{2+}$  (Table 1). In addition, difference spectra reveal the presence of a  $d(\text{FcCO}) \rightarrow \pi^*(\text{tpyNH})$  MLCT band at  $\lambda_{\text{max}} = 493$  nm in  $[44]^{2+}$  and in  $[46]^{2+}$ , similar to those in amide-free ferrocenyl complexes  $[\text{Ru}(\text{tpy})(\text{tpy-Fc})]^{2+}$   $[47^0]^{2+}$  and  $[\text{Ru}(\text{tpy-Fc})_2]^{2+}$   $[48^0]^{2+}$  featuring extra  $d(\text{Fe}) \rightarrow \pi^*(\text{tpy})$  CT bands at  $\lambda_{\text{max}} = 515$  and  $526$  nm, respectively.<sup>[75a,75b]</sup> The difference in the  $d(\text{Fe}) \rightarrow \pi^*(\text{tpy})$  CT energies between  $[47^0]^{2+}/[48^0]^{2+}$  on the one hand and  $[44]^{2+}/[46]^{2+}$  on the other hand is attributed to the electron-withdrawing effect of the carboxyl group at the ferrocene in the latter complexes, lowering the ferrocene HOMO energy and hence increasing the  $d(\text{FcCO}) \rightarrow \pi^*(\text{tpyNH})$  absorption band energy. A corresponding inverse  $d(\text{FcNH}) \rightarrow \pi^*(\text{tpyCO})$  MLCT band in  $[45]^{2+}$  is obviously of low intensity and not observed.<sup>[59]</sup>

Cyclic voltammograms (Table 1) of the ferrocenyl compounds reveal two (for  $[44]^{2+}$  and  $[45]^{2+}$ ) and three (for  $[46]^{2+}$ ) oxidation waves, corresponding to  $\text{Fe}^{\text{II}}/\text{Fe}^{\text{III}}$  (reversible) and  $\text{Ru}^{\text{II}}/\text{Ru}^{\text{III}}$  redox couples (irreversible as a result of the large positive charge accumulation and deposition on the electrode).<sup>[59]</sup> As expected from substituent effects, the oxidation of the  $\text{FcNH}$  moiety ( $E_{1/2} = -0.03$  V) occurs at

lower potential than that of the  $\text{Fc-CO}$  moiety ( $E_{1/2} = +0.25$  V).<sup>[119,120]</sup> The first reduction of the ferrocenyl complexes is located at the carboxy-substituted tpy ligand (see above) differing only slightly between tpy-COOEt compound  $[44]^{2+}$  and tpy-CONHFc compounds  $[45]^{2+}$  and  $[46]^{2+}$  (Table 1).

Ferrocene is known to deactivate electronically excited states either by electron transfer from ferrocene to the excited chromophore or by energy transfer from the chromophore to give the ferrocene triplet state (Figure 17).<sup>[76]</sup> All three  $\text{Ru}^{\text{II}}/\text{Fe}^{\text{II}}$  conjugates  $[44]^{2+}$ – $[46]^{2+}$  are emissive at room temperature with emission wavelength maxima of 739 nm for  $[45]^{2+}$  bearing an amino group and 704 nm for the amide-functionalized conjugates  $[44]^{2+}$  and  $[46]^{2+}$  similar to the ferrocene-free counterparts  $[4]^{2+}$  and  $[6]^{2+}$  (Table 1). While the emission quantum yield of  $[44]^{2+}$  is in the range of those of other bis(terpyridine)ruthenium(II) complexes (Table 1), the phosphorescence of complexes  $[45]^{2+}$  and  $[46]^{2+}$  is strongly quenched. Obviously, this phenomenon is related to the presence of a C-terminal easy-to-oxidize ferrocenyl substituent while an N-terminal  $\text{Fc-CO}$  substituent has only a marginal effect on the quantum yield (Table 1). With the Rehm–Weller equation,  $\Delta G_{\text{ET}} = E_{1/2}(\text{Fc}/\text{Fc}^+) - E_{1/2}(\text{tpy}^-/\text{tpy}) - e_0^2/[4\pi\epsilon_0\epsilon(\text{solvent})r] - E_{00}$ ,<sup>[121]</sup> experimental redox potentials and emission energies can be used to estimate that photoinduced electron transfer to the  $^3\text{MLCT}$  excited ruthenium moiety is more exergonic from



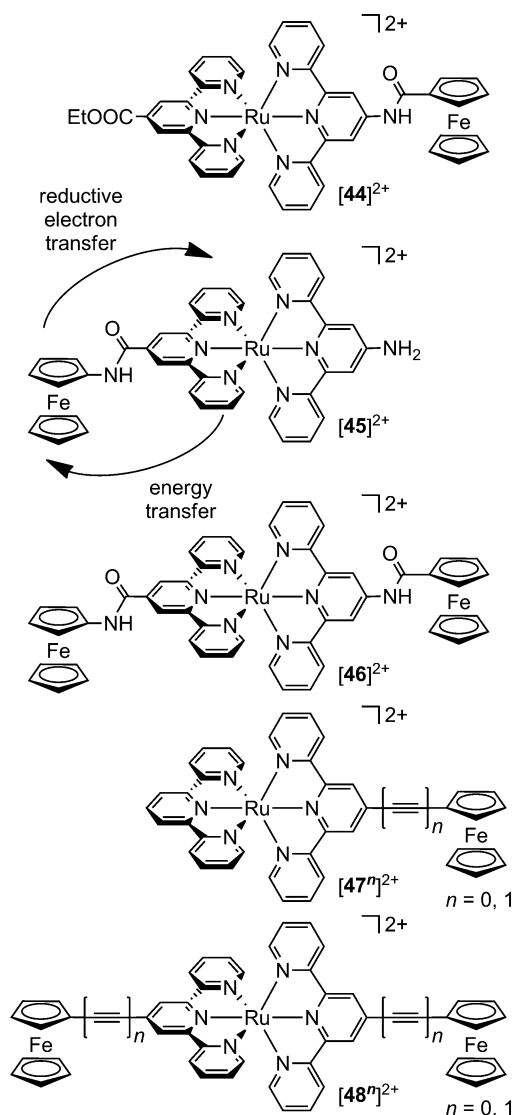


Figure 17. Ferrocene conjugates  $[44]^{2+}$ – $[46]^{2+}$  of  $[5]^{2+}$ <sup>[59]</sup> and reference compounds  $[47]^{2+}$  and  $[48]^{2+}$ .<sup>[59,75]</sup>

the NH-substituted ferrocene in  $[45]^{2+}$  and  $[46]^{2+}$  ( $\Delta G_{\text{ET}} < 0$ ) than that from the CO-substituted ferrocene in  $[44]^{2+}$  by the difference in Fc/Fc<sup>+</sup> oxidation potentials (ca. 0.27 eV, Table 1). Hence, reductive quenching seems to be a feasible deactivation pathway in  $[45]^{2+}$  and  $[46]^{2+}$  in addition to triplet–triplet energy transfer to give ferrocene triplet states similar to amide-linked porphyrin–ferrocenyl dyads<sup>[122,123]</sup> and alkyne-bridged ferrocenyl ruthenium(II) complexes  $[47]^{2+}$ / $[48]^{2+}$ .<sup>[75c]</sup> Unfortunately, a meaningful comparison with the series  $[1]^{2+}$ / $[47]^{2+}$ / $[48]^{2+}$  is impossible because of the very low quantum yields and excited-state lifetimes of  $[1]^{2+}$ / $[47]^{2+}$  and  $[48]^{2+}$  in fluid solution (as discussed above).<sup>[75b]</sup> Interestingly, excited-state mixed-valent Fe<sup>III</sup>/Ru<sup>II</sup> species seem to be accessible either from direct excitation of the d(FcCO)→ $\pi^*(\text{tpyNH})$  MLCT in  $[44]^{2+}$  and  $[46]^{2+}$  or through the ruthenium-based MLCT followed by reductive photoinduced electron transfer from FcNH in  $[45]^{2+}$  and  $[46]^{2+}$ .

Intermolecular, concentration-dependent phosphorescence quenching is also found for  $[6]^{2+}$  and ferrocene ( $E_{1/2} = 0.0$  V), ferrocenecarboxylic acid methyl ester ( $E_{1/2} = 0.27$  V<sup>[87]</sup>) and ferrocene-1,1'-dicarboxylic acid dimethyl ester ( $E_{1/2} = 0.49$  V<sup>[87]</sup>). For the first two ferrocenes reductive quenching is exergonic ( $\Delta G_{\text{ET}} < 0$ ), while it is estimated slightly endergonic for the latter ( $\Delta G_{\text{ET}} > 0$ ). The Stern–Volmer constants<sup>[124]</sup> of  $K_{\text{SV}} = 244(5)$ , 162(6), 148(2) L mol<sup>-1</sup> reflect this trend predicted by Marcus theory.<sup>[62]</sup> However, considerable quenching is even observed for ferrocene-1,1'-dicarboxylic acid dimethyl ester, and this excited state deactivation is largely attributed to triplet–triplet energy transfer to give the ferrocene triplet state. Hence, the organometallic ferrocene seems to act both as electron donor as well as energy acceptor towards excited bis(terpyridine)ruthenium(II) chromophores, in an intramolecular ( $[44]^{2+}$ – $[46]^{2+}$ ) as well as intermolecular fashion ( $[6]^{2+}$  + ferrocene).

To broaden the scope of the bis(terpyridine)ruthenium(II) chromophores in heterometallic assemblies, 2,2'-bipyridine units have been attached either at the C- or at the N-terminus by using 4- or 5-amino-2,2'-bipyridine and 2,2'-bipyridine-4- or -5-carboxylic acid chloride and  $[4]^{2+}$  or  $[5]^{2+}$  as coupling partners, respectively, to obtain metallo ligands  $[49]^{2+}$ – $[52]^{2+}$  with bipyridine coordination sites (Figure 18).<sup>[77,78]</sup> The attachment of an additional bpy unit

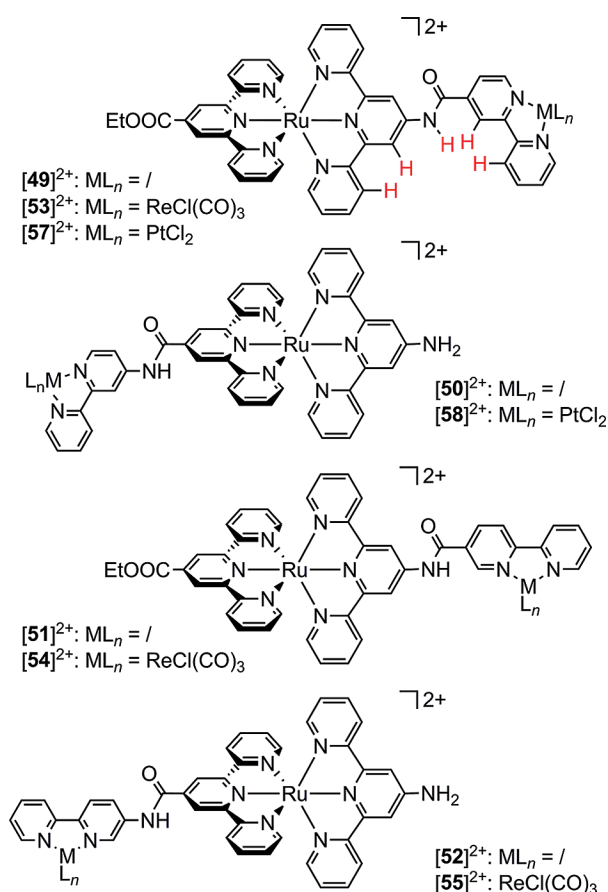


Figure 18. 2,2'-Bipyridine conjugates  $[49]^{2+}$ – $[52]^{2+}$  of  $[5]^{2+}$  and their heterometallic complexes.<sup>[77,78]</sup>

hardly affects the UV/Vis absorption properties of  $[49]^{2+}$ – $[52]^{2+}$  with respect to the parent bis(terpyridine)ruthenium(II) complexes  $[5]^{2+}$  and  $[6]^{2+}$ , only the  $\pi$ – $\pi^*$  transitions in the UV range are intensified as a result of the presence of the bpy.

Electrochemical studies reveal a reversible Ru<sup>II</sup>/Ru<sup>III</sup> redox process at  $E_{1/2} = 0.68$  V for amines  $[50]^{2+}$  and  $[52]^{2+}$  and at  $E_{1/2} = 0.90$ – $0.92$  V for esters  $[49]^{2+}$  and  $[51]^{2+}$ , matching the data of  $[4]^{2+}$ – $[6]^{2+}$  (see above, Table 1). Additionally, several reduction waves are observed between  $E_{1/2} = -1.48$  and  $E_{1/2} = -2.5$  V. The first reductions are ascribed to ligand-centered processes localized on the tpy-CO unit. This is supported by DFT-calculated spin densities and EPR spectroscopic signatures of radical species  $[49]^+$ – $[52]^+$  prepared by chemical reduction. All four metallo ligands  $[49]^{2+}$ – $[52]^{2+}$  are emissive at room temperature with emission wavelengths in typical regions (Table 1). Amino-substituted complexes  $[50]^{2+}$ /[52]<sup>2+</sup> emit at  $\lambda_{\text{max}} = 735/727$  nm, while amide-functionalized counterparts  $[49]^{2+}$ /[51]<sup>2+</sup> emit at  $\lambda_{\text{max}} = 673/674$  nm. Their emission quantum yields are very similar and in the range  $\Phi = 0.15$ – $0.20\%$ .<sup>[77,78]</sup>

The optical and redox data of bpy derivatives  $[49]^{2+}$ – $[52]^{2+}$  suggest that these complexes can be considered as chromophore- and redox-switch-functionalized metallo ligands. Hence, typical bpy coordination chemistry is possible with these phosphorescent, redox-active metallo ligands. First studies were devoted to the coordination of these metallo ligands to rhenium(I) and platinum(II) complex fragments. Treating  $[49]^{2+}$ ,  $[51]^{2+}$ , and  $[52]^{2+}$  with  $\text{Re}(\text{CO})_5\text{Cl}$  affords heterodinuclear complexes  $[53]^{2+}$ – $[55]^{2+}$  with  $\text{Re}(\text{CO})_3\text{Cl}$  fragments coordinated to the 2,2'-bpy unit.<sup>[77]</sup> These Ru–Re complexes exhibit a new shoulder in their UV/Vis absorption spectra at around  $\lambda_{\text{max}} = 350$ – $370$  nm attributed to the <sup>1</sup>MLCT transitions of the bipyridine rhenium(I) unit. A new oxidation wave is observed in the cyclic voltammograms of  $[53]^{2+}$ – $[55]^{2+}$  at  $E_{1/2} = 0.98$  V, which is assigned to the Re<sup>I</sup>/Re<sup>II</sup> couple. The reduction potentials are essentially unaffected by coordination of the additional  $\text{Re}(\text{CO})_3\text{Cl}$  fragment. Phosphorescence is observed for all three heterodinuclear complexes with wavelengths and emission band shapes very similar to those of the parent metallo ligands. As emissive <sup>3</sup>MLCT(Ru/pyridine) and <sup>3</sup>MLCT(Re/pyridine) states are typically located in a comparable energy range, a distinction based solely on energy data is arguable; however, the striking resemblance of the emission band shapes of mixed-metal complexes  $[53]^{2+}$ ,  $[54]^{2+}$ , and  $[55]^{2+}$  and the corresponding metallo ligands  $[49]^{2+}$ ,  $[51]^{2+}$ , and  $[52]^{2+}$  strongly suggests a <sup>3</sup>MLCT(Ru/tpy)-based phosphorescence. In all cases, triplet–triplet energy transfer from <sup>3</sup>MLCT(Re/bpy) states to the slightly favored bis(terpyridine)ruthenium moiety is thermodynamically feasible. Indeed, DFT studies suggest a localization of the lowest-energy <sup>3</sup>MLCT state on ruthenium and the carboxy-substituted terpyridine ligand for  $[54]^{2+}$  and  $[55]^{2+}$ . In contrast to experimental results, DFT calculations localize the lowest <sup>3</sup>MLCT state at the Re(bpy) site in  $[53]^{2+}$  (Figure 19a).<sup>[77]</sup> An explanation for this unexpected finding will be given below.

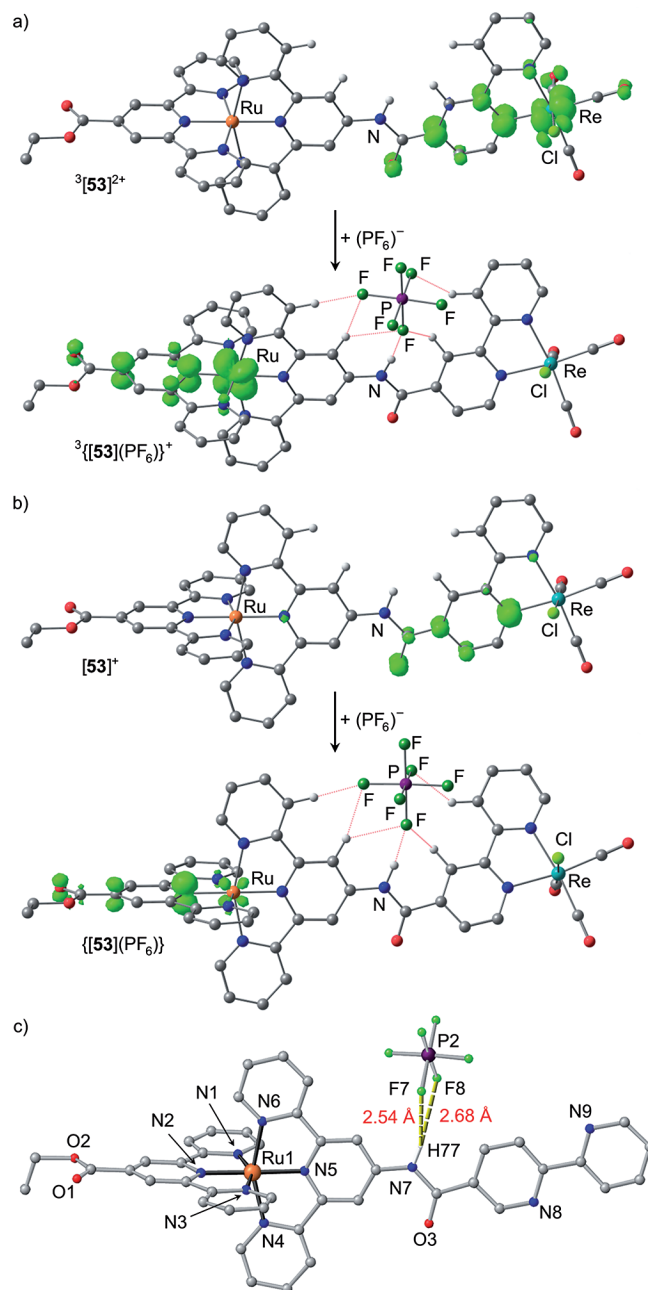


Figure 19. DFT-calculated spin densities (B3LYP/LANL2DZ, IEFPCM,  $\text{CH}_3\text{CN}$ ; contour value 0.01; irrelevant CH hydrogen atoms omitted) of the <sup>3</sup>MLCT states of  $[53]^{2+}$  and its contact ion pair  $[53](\text{PF}_6)^+$  (a), and the radical  $[53]^+$  and its contact ion pair  $[53](\text{PF}_6)$  (b). (c) The molecular structure of  $[51]^{2+}$  showing the anion-amide hydrogen bonding interaction of the contact ion pair  $[51](\text{PF}_6)^+$  in the solid state (CH hydrogen atoms omitted).<sup>[77]</sup>

While the first oxidation of  $[53]^{2+}$ – $[55]^{2+}$  to  $[53]^{3+}$ – $[55]^{3+}$  is unambiguously ruthenium-centered, the assignment of the first reduction site (tpy or bpy) is not straightforward. Hence, the  $\text{Re}(\text{bpy})(\text{CO})_3$  moiety was experimentally interrogated by means of IR spectroscopic analysis. Indeed, the CO stretching vibrations are only marginally affected by chemical reduction of  $[53]^{2+}$ – $[55]^{2+}$  to  $[53]^+$ – $[55]^+$ , in contrast to the significant shifts observed for the  $\text{Re}(\text{bpy})(\text{CO})_3\text{Cl}/[\text{Re}(\text{bpy})(\text{CO})_3\text{Cl}]^-$  redox couple resulting

from an increased Re-to-CO  $\pi$ -backbonding. This finding rules out a significant localization of the odd electron at the Re(bpy)(CO)<sub>3</sub> site in [53]<sup>2+</sup>–[55]<sup>2+</sup> and localizes the unpaired electron in the proximity of the ruthenium center, namely at the tpy-CO ligand.<sup>[77]</sup>

Interestingly, DFT calculations for radical [55]<sup>+</sup> fully agree with experimental findings, while for radical [53]<sup>+</sup> the spin density is calculated at the Re(bpy) site (Figure 19b) and for [54]<sup>+</sup> the reduction site even depends on the orientation of the bpy.<sup>[77]</sup> Hence, the [Re(bpy-CO)]<sup>+</sup> and [Ru(tpy-CO)]<sup>2+</sup> moieties feature a similar electron affinity according to the calculations, and small perturbations, such as the position of the counterions, might favor one valence isomer over the other. Indeed, the hexafluorophosphate counterions – neglected in all discussions so far – might play a decisive role. This is clearly seen already in the solid-state structures of metallo ligands [51](PF<sub>6</sub>)<sub>2</sub> and [49](PF<sub>6</sub>)<sub>2</sub>·HPF<sub>6</sub>·2H<sub>2</sub>O, featuring contact ion pairs through NH···FPF<sub>5</sub> hydrogen bonds (Figure 19c) and solvent-separated ion pairs through NH···OH<sub>2</sub>···FPF<sub>5</sub> hydrogen bonds, respectively.<sup>[77]</sup> Such hydrogen bonds of the counterions to the central amide units might be even more important in heterobimetallic complexes because of the additional polarization by the second metal center. Indeed, for the [49]–(PF<sub>6</sub>)<sub>2</sub>/[53](PF<sub>6</sub>)<sub>2</sub> pair, significant shifts of distinct proton resonances at the tpy-NH unit and the bpy-CO unit are observed (NH:  $\Delta\delta$  = 2.28 ppm; CH:  $\Delta\delta$  = 0.35–0.71 ppm; Figure 18, top; relevant hydrogen atoms highlighted in red) in addition to the expected coordination shift induced by the rhenium atom. These additional shifts are attributed to the effect of CH···FPF<sub>5</sub> and NH···FPF<sub>5</sub> hydrogen bonds persisting even in solution. In DFT geometry optimizations of the contact ion pair {[53](PF<sub>6</sub>)<sup>+</sup>}, the explicit inclusion of a (PF<sub>6</sub>)<sup>−</sup> counterion in this binding pocket confirms hydrogen bonds to these very CH and NH groups (shown in red in Figure 18). In the radical contact ion pair {[53](PF<sub>6</sub>)<sup>•</sup>} including the counterion, the spin density is now shifted from the [Re(bpy-CO)] unit to the terminal [Ru(tpy-CO)] unit according to the DFT calculations (Figure 19b). The same holds for the localization of the lowest-energy <sup>3</sup>MLCT state, which is shifted from the [Re(bpy-CO)] to the [Ru(tpy-CO)] site by including the counterion (Figure 19a). Hence, for these positively charged bimetallic complexes, the explicit inclusion of the counterion is essential to correctly reproduce the experimental data.<sup>[77]</sup> Conversely, the experimental exchange of the coordinating (PF<sub>6</sub>)<sup>−</sup> counterion by a non-coordinating (BPh<sub>4</sub>)<sup>−</sup> counterion leads to [Re(bpy-CO)]<sup>−</sup>-centered radicals as shown by the characteristic IR pattern of the [Re(bpy)(CO)<sub>3</sub>Cl]<sup>−</sup> unit in [53]<sup>+</sup> prepared by chemical reduction of [53](BPh<sub>4</sub>)<sub>2</sub>.<sup>[77]</sup> Hence, the equilibrium between the [(EtOOC-tpy)Ru(tpy-NHCO-bpy)Re(CO)<sub>3</sub>Cl]<sup>+</sup> and [(EtOOC-tpy)Ru(tpy-NHCO-bpy)Re(CO)<sub>3</sub>Cl]<sup>+</sup> valence isomers of [53]<sup>+</sup>, as well as the triplet-excited-state equilibrium between the <sup>3</sup>MLCT(Ru/tpy) and <sup>3</sup>MLCT(Re/bpy) states of [53]<sup>2+</sup>, is shifted by the coordinating properties of the counterion. Simply speaking, coordination of the counterion to the bridging amide pushes the partial negative charge and spin

density from the bridging bpy-CO to the terminal tpy-CO ligand both in radical [53]<sup>+</sup> and in the triplet excited state of [53]<sup>2+</sup>. This is an important finding, as Re(bpy)(L)<sub>3</sub>X complexes and chromophore-appended derivatives, for example [56]<sup>3+</sup> in Figure 20, have been reported to photocatalytically reduce CO<sub>2</sub> to CO via [Re(bpy)]<sup>+</sup> active sites.<sup>[125,126]</sup>

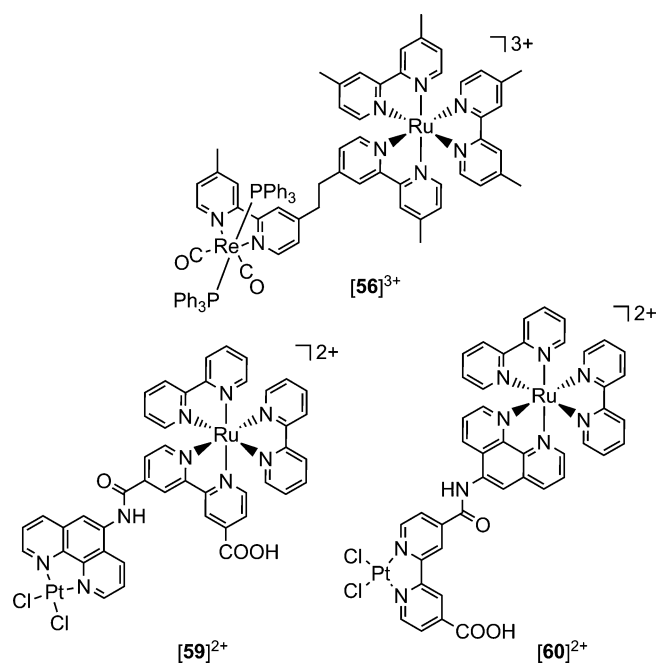


Figure 20. Heterometallic Ru/M reference compounds (M = Re, Pt).<sup>[126,127]</sup>

Metallation of metallo ligands [49]<sup>2+</sup> and [50]<sup>2+</sup> with PtCl<sub>2</sub>(dmsO)<sub>2</sub> gives heterodinuclear complexes [57]<sup>2+</sup> and [58]<sup>2+</sup> in which the Pt<sup>II</sup>(bpy)Cl<sub>2</sub> fragment is positioned either at the N- or at the C-terminus of amino acid [5]<sup>2+</sup>.<sup>[78]</sup> Upon coordination of the PtCl<sub>2</sub> fragment, new absorption bands appear at  $\lambda_{\text{max}}$  = 408 nm ([57]<sup>2+</sup>) and at  $\lambda_{\text{max}}$  = 364 nm ([58]<sup>2+</sup>), assigned to platinum to bpy-CO and platinum to bpy-NH MLCT bands [<sup>1</sup>MLCT(Pt/bpy)], respectively.<sup>[78]</sup>

In addition to the expected tpy-CO reductions at  $E_{1/2}$  = −1.47 and −1.45 V and Ru<sup>II</sup>/Ru<sup>III</sup> oxidation waves at  $E_{1/2}$  = +0.93 and +0.69 V (Table 1), the cyclic voltammograms of [57]<sup>2+</sup> and [58]<sup>2+</sup> reveal additional reduction waves at  $E_{1/2}$  = −1.30 and −1.69 V, respectively. Both EPR spectroscopic and DFT studies on radicals [57]<sup>+</sup> and [58]<sup>+</sup> confirm that the odd electron is localized on the bpy-CO unit in [57]<sup>+</sup> but on the tpy-CO unit in [58]<sup>+</sup> (Figure 21). Specifically, the EPR signal pattern of [57]<sup>+</sup> can only be explained properly by taking a significant superhyperfine coupling to the platinum nucleus (<sup>195</sup>Pt;  $I = 1/2$ ; 33.8% natural abundance) into account [ $|A_{1,2,3}({}^{195}\text{Pt})| = 68, 68, 23$  G]. Furthermore, the  $g$  values for [57]<sup>+</sup> ( $g_{1,2,3} = 2.0290, 2.0049, 1.9400$ ; Figure 21a) are close to those found for genuine [Pt(bpy)Cl<sub>2</sub>]<sup>−</sup> radicals [ $g_{1,2,3} = 2.0380, 2.0110, 1.9380$ ;  $|A_{1,2,3}({}^{195}\text{Pt})| = 61, 86, 22$  G] and distinct from those for ruthenium(II)-coordinated tpy-CO radicals (Figure 21b; and see above).<sup>[78]</sup>



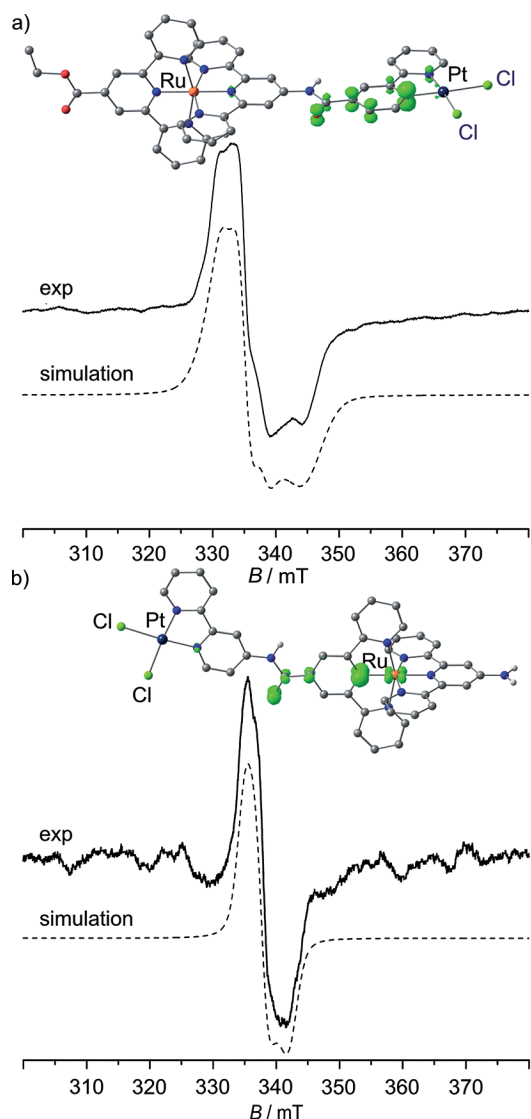


Figure 21. DFT-calculated spin densities (B3LYP/LANL2DZ, IEFPCM, CH<sub>3</sub>CN; contour value 0.01; CH hydrogen atoms omitted), X-band EPR spectra (77 K, CH<sub>3</sub>CN, 9.42 GHz), and simulations of (a) [57]<sup>2+</sup> and (b) [58]<sup>2+</sup>.<sup>[78]</sup>

In spite of the presence of platinum, phosphorescence is still observed for both Ru–Pt complexes [57]<sup>2+</sup> and [58]<sup>2+</sup> with essentially unperturbed band shapes and band maxima, albeit with lower quantum yield. Hence, the lowest-energy emissive states are best described as <sup>3</sup>MLCT(Ru/tpy), while the <sup>3</sup>MLCT(Pt/bpy) states are possibly higher in energy. However, they might be thermally accessible by triplet–triplet energy transfer, which decreases the phosphorescence quantum yield. Conversely, irradiation in the <sup>1</sup>MLCT(Pt/bpy) absorption band results in emission from the <sup>3</sup>MLCT(Ru/tpy) state, which also suggests the accessibility of an intramolecular triplet–triplet energy transfer pathway. In this respect, Ru–Pt complexes [57]<sup>2+</sup> and [58]<sup>2+</sup> behave similarly to the ferrocenyl-appended ruthenium amino acids [44]<sup>2+</sup>–[46]<sup>2+</sup>.

The lifetime of the excited states of derivatives of [5]<sup>2+</sup> is long enough to enable bimolecular reactions with external

quenchers (Table 1). Indeed, the excited states of metallo ligands [49]<sup>2+</sup>–[52]<sup>2+</sup> as well as heterobimetallic complexes [53]<sup>2+</sup>–[58]<sup>2+</sup> are quenched by triethanolamine (TEOA), which can, in principle, act as electron donor or proton acceptor { $E_{1/2}(\text{TEOA}/\text{TEOA}^+) = 0.19 \text{ V}$ ,<sup>[125,128]</sup>  $\text{p}K_{\text{a}}[\text{H}(\text{TEOA})]^+ = 7.76$ <sup>[81]/7.74</sup><sup>[129]</sup>} towards the MLCT excited states. The Stern–Volmer constants  $K_{\text{SV}}$ <sup>[124]</sup> of [49]<sup>2+</sup>–[58]<sup>2+</sup> are not strictly correlated to the driving force for photoinduced electron transfer,  $\Delta G_{\text{ET}}$ , although some reasonable relations are obvious, for example the susceptibility of the ester-substituted complexes towards quenching is always higher than that of the amino-substituted complexes ([49]<sup>2+</sup> > [50]<sup>2+</sup>, [51]<sup>2+</sup> > [52]<sup>2+</sup>, [57]<sup>2+</sup> > [58]<sup>2+</sup>, [54]<sup>2+</sup> > [55]<sup>2+</sup>), which matches the ease of reduction and hence the driving force  $\Delta G_{\text{ET}}$ .<sup>[77,78]</sup> However, proton transfer to the amine, especially when pre-coordinated to the amide unit through  $\text{NH}\cdots\text{N}(\text{CH}_2\text{CH}_2\text{OH})_3$  hydrogen bonds, might be a further feasible pathway (ESPT<sup>[89]</sup>). Indeed, excitation of the esters should yield the [(EtOOC-tpy)Ru<sup>III</sup>(tpy-NHCO-bpy)-ML<sub>*n*</sub>]<sup>2+</sup> state which should feature a polarized and more acidic NHCO group as a result of the Ru<sup>III</sup> center. In fact, the strongly polarized amide in the highly charged bis(ruthenium) complex [40]<sup>4+</sup> is already deprotonated in the ground state by triethylamine (see above). Furthermore, for the Ru–Pt complexes, non-linear Stern–Volmer plots<sup>[124]</sup> have been obtained, which suggests a pre-coordination of TEOA, possibly to the polarized amide unit (static quenching). Hence, TEOA might compete with the (PF<sub>6</sub>)<sup>−</sup> counterions for the “binding pocket” as described above (Figure 19). This pre-coordination followed by ESPT is even responsible for some photoinduced hydrolysis of [57]<sup>2+</sup> to amine [4]<sup>2+</sup> and acid Pt(bpy-COOH)Cl<sub>2</sub> in the presence of water/TEOA.<sup>[78]</sup>

Photocatalytic reduction of CO<sub>2</sub> or H<sub>2</sub>O<sup>[37–39]</sup> by Ru–Re and Ru–Pt complexes [53]<sup>2+</sup>–[58]<sup>2+</sup> to CO or H<sub>2</sub> by using TEOA as sacrificial reductant, as reported by Ishitani and Sakai for several ruthenium/bipyridine-based bimetallic complexes (Figure 20),<sup>[126,127]</sup> were unsuccessful. Even, complexes [53](BPh<sub>4</sub>)<sub>2</sub> (Figure 19b) and [57](PF<sub>6</sub>)<sub>2</sub> (Figure 21a), with a favorable bpy-centered reduction site, are catalytically incompetent. In the Ru–Re case, [53](BPh<sub>4</sub>)<sub>2</sub> this failure is ascribed to the insufficient reduction potential of the one-electron-reduced species [53]<sup>+</sup> to reduce the intermediate Re–CO<sub>2</sub> adduct.<sup>[77]</sup> For Ru–Pt-based proton reduction, for example by [59]<sup>2+</sup> or [60]<sup>2+</sup> (Figure 20), charge-separated states Ru<sup>III</sup>(bpy-CONH-phen')PtCl<sub>2</sub> or Ru<sup>III</sup>(phen-NHCO-bpy)PtCl<sub>2</sub> are believed to be responsible for photohydrogen production.<sup>[127]</sup> The corresponding Ru<sup>III</sup>(tpy-NHCO-bpy)PtCl<sub>2</sub> charge-separated state of [57]<sup>2+</sup>, however, is thermodynamically uphill because of the comparably low-energy <sup>3</sup>MLCT state of the push-pull bis(terpyridine)ruthenium chromophore {[57]<sup>2+</sup>:  $\lambda_{\text{max}} = 671 \text{ nm}$ ; [Ru(bpy)<sub>3</sub>]<sup>2+</sup>:  $\lambda_{\text{max}} = 615 \text{ nm}$ ; Table 1}. Furthermore, ESPT<sup>[89]</sup> and subsequent chemical reactions might additionally impede photocatalytic reduction of carbon dioxide or protons. Hence, the push/pull functional groups favorable for long excited-state lifetimes and phosphorescence also pave the way for undesired side reactions with sub-



strates in the excited state, especially ESPT to the reduced tpy-CO unit (see above) or ESPT from the polarized tpy-NH unit. Other photocatalytic applications circumventing coordinating and basic/acidic substrates and reductants are currently under investigation. Photoinduced electron transfer between electronically excited complexes based on  $[5]^{2+}$  and non-molecular acceptors (interfacial electron transfer) will be discussed in the next section.

#### 4.4 Photoinduced Electron Transfer at Interfaces

In order to probe light-induced interfacial charge separation on the nanoscale, bifunctional amino acid  $[5]^{2+}$  has been incorporated as chromophore in a donor–chromophore–acceptor nanocomposite.<sup>[130]</sup> A block-copolymer with triphenylamine units in one block was used as electron donor and the second block was equipped with the  $[5]^{2+}$  chromophore. ZnO nanorods were employed as electron acceptor. Experimentally,  $[5]^{2+}$  was converted into the ruthenium-containing tripeptide  $[61]^{2+}$  by SPPS (Figure 12),<sup>[18]</sup> and the amino group of  $[61]^{2+}$  was attached to the Pfp-activated carboxylic acid of block-copolymer **62** through an amide bond to give  $[63]^{2m+}$  (Figure 22). The remaining

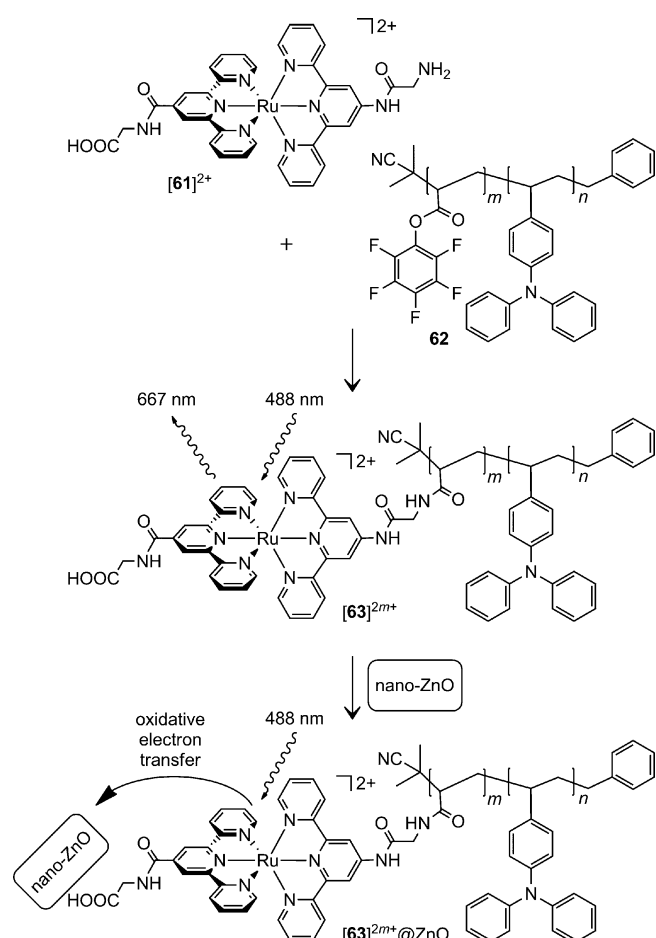


Figure 22. Assembly of donor–chromophore–acceptor nanocomposite  $[63]^{2m+}@ZnO$  by coupling of tripeptide  $[61]^{2+}$  to block-copolymer **62** ( $n \approx 50$ ,  $m \approx 10$ ) and coating of ZnO nanorods with functionalized block-copolymer  $[63]^{2m+}$ .<sup>[130]</sup>

COOH groups in  $[63]^{2m+}$  anchor block-copolymer  $[63]^{2m+}$  to ZnO nanorods in a multipoint fashion to give the stable non-aggregated nanocomposite  $[63]^{2m+}@ZnO$ .<sup>[130]</sup> In contrast to  $[63]^{2m+}$ , excitation of the  $[Ru(tpy)_2]^{2+}$  chromophore in  $[63]^{2m+}@ZnO$  by irradiation into its absorption band ( $\lambda_{max} = 498$  nm,  $\lambda_{exc} = 488$  nm) does not lead to phosphorescence. Instead, excited electrons are injected into the ZnO nanorods, and electron holes are generated in the triphenylamine-containing polymer block (Figure 22). Kelvin probe force microscopic (KPFM) studies of  $[63]^{2m+}@ZnO$  reveal a significant difference of the surface potential of the polymer-coated nanorod in the dark and under irradiation into the MLCT band, which is assigned to oxidative quenching of the excited chromophore, that is, charge injection into ZnO and hence positive charging of the polymer (Figure 23).<sup>[130]</sup> Such semiconductor/chromophore/conducting polymer architectures are of particular interest for solid-state dye-sensitized solar cells (ssDSSCs).<sup>[131]</sup>

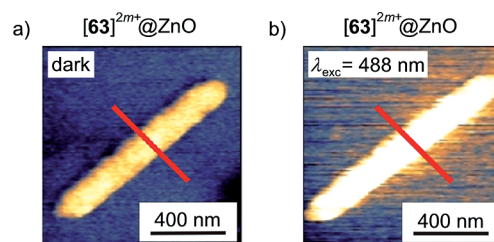


Figure 23. Surface potential maps of  $[63]^{2m+}@ZnO$  obtained by KPFM (a) in the dark and (b) under irradiation with  $\lambda_{exc} = 488$  nm.<sup>[130]</sup>

## 5. Applications

### 5.1 Dye-Sensitized Solar Cells

COOH-substituted complexes  $[5]^{2+}$ ,  $[25]^{2+}$ ,  $[26]^{2+}$ ,  $[27]^{2+}$ , as well as 2,2'-bipyridine-substituted complexes  $[49]^{2+}$  and  $[50]^{2+}$  (Figures 2, 11, 18, and 24) have been adsorbed onto nanostructured  $TiO_2$  and employed as sensitizers in standard DSSCs with an  $I^-/I_3^-$  redox electrolyte.<sup>[72]</sup> All complexes feature absorption spectra similar to that of the standard ruthenium(II) sensitizer N719 with  $[27]^{2+}$ , and they even have a somewhat stronger absorption in the NIR region. Optical inspection of the loaded FTO/ $TiO_2$  electrode already reveals that the 2,2'-bipyridine anchors in  $[49]^{2+}$  and  $[50]^{2+}$  are inferior to carboxylate linkers (Figure 24a), likely because these large functional groups require more space and hence the dye loading with  $[49]^{2+}$  and  $[50]^{2+}$  is significantly reduced ( $1.0\text{--}2.6 \times 10^{-8}$  mol  $cm^{-2}$ ) relative to those with the other sensitizers  $[5]^{2+}$ ,  $[25]^{2+}$ ,  $[26]^{2+}$ ,  $[27]^{2+}$ , and N719 ( $5.6\text{--}11 \times 10^{-8}$  mol  $cm^{-2}$ ).<sup>[72]</sup> In spite of the similar loadings, cells with  $[5]^{2+}$ ,  $[25]^{2+}$ ,  $[26]^{2+}$ , and  $[27]^{2+}$  deliver only low cell-power conversion efficiencies ( $\eta = 0.13\text{--}0.26\%$ ) relative to those with N719 ( $\eta = 5.03\%$ ). This has been traced back to the poor short-circuit current, the large dark current, and the high electron  $Ti(e^-)/I_2$  recombination rate of the cells based on  $[5]^{2+}$ ,  $[25]^{2+}$ ,  $[26]^{2+}$ , and  $[27]^{2+}$ .

This might be due to the twofold positive charge of the complexes, which increases the  $I_3^-/I_2$  concentration near the  $TiO_2$  electrode as a result of electrostatic interactions (ion pairing and hydrogen bonding, see above) favoring electron recombination.<sup>[132]</sup> In contrast, N719 is twofold negatively charged, which prevents fast recombination with the electrolyte.<sup>[72]</sup> The positive charge of bis(tridentate) complexes of ruthenium(II) such as  $[5]^{2+}$ ,  $[25]^{2+}$ ,  $[26]^{2+}$ , and  $[27]^{2+}$  might be reduced in the future by introduction of negatively charged chelating ligands. Indeed, ruthenium(II) complexes with pyrazolato or cyclometalating ligands have been reported to give DSSCs with high power conversion efficiencies up to  $\eta = 10.7\%$ .<sup>[96,133]</sup> Another approach would be to employ other electrolytes instead of the classical  $I^-/I_3^-$  couple, such as positively charged metal complexes, for example  $[Co\{4,4'-(tBu)_2bpy\}_3]^{2+/3+}$ .<sup>[63]</sup>

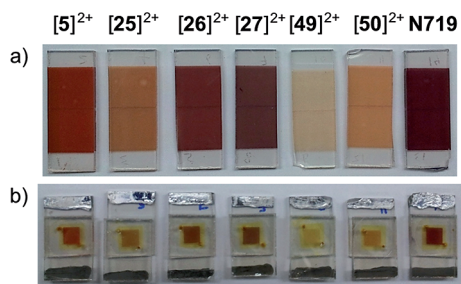


Figure 24. (a) Photographs of  $TiO_2$  on FTO impregnated with the indicated adsorbed ruthenium sensitizers and (b) photographs of the corresponding DSSCs with FTO/ $TiO_2$ /sensitizer/electrolyte/Pt/FTO structure (FTO = fluorine-doped tin oxide).<sup>[72]</sup>

## 5.2 Light-Emitting Electrochemical Cells

Charged bis(tridentate) complexes  $[4]^{2+}$ ,  $[21]^{2+}$ , and  $[22]^{2+}$  have been utilized as emitters in light-emitting electrochemical cells (LECs).<sup>[134]</sup> In comparison to organic light-emitting diodes (OLEDs), LECs feature a much simpler device structure and are hence less difficult to prepare.<sup>[5–8]</sup> A device composition of ITO/PEDOT:PSS/ruthenium(II) complex/Ag has been used [ITO = indium tin oxide, PEDOT = 3,4-ethylenedioxythiophene, PSS = poly(styrenesulfonate), Figure 25]. The thickness of the PEDOT/PSS and ruthenium complex layers were characterized by atomic force microscopy. Upon applying moderate potentials, emission up to a maximum emission wavelength of 722–755 nm is achieved. The CIE coordinates<sup>[135]</sup> of the electroluminescence of  $[22]^{2+}$  are  $x = 0.731$  and  $y = 0.269$ , which corresponds to a deep red emission. To the best of our knowledge, the observed electroluminescence features the lowest emission energy for LECs containing bis(tridentate) ruthenium(II) complexes so far.<sup>[7,8,136]</sup> In fact, most of the emission occurs in the near infrared, invisible to the human eye.<sup>[134]</sup> For such a low emission energy, the energy gap law<sup>[79,101–103]</sup> predicts enhanced radiationless deactivation of the excited state, which explains the comparatively small external quantum efficiencies. However, diluting the ruthenium(II) complexes in poly(methyl methacrylate)

somewhat enhances the external quantum efficiencies as a result of diminished excited-state deactivation by radiationless processes.<sup>[134]</sup>

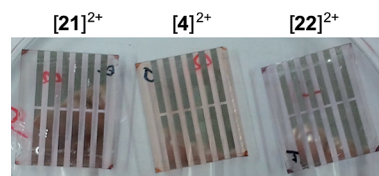


Figure 25. Photographs of LECs with ITO/PEDOT:PSS/ruthenium(II) dye/Ag structure.<sup>[134]</sup>

## Conclusions

The use of amino acids as building blocks of well-defined arrays is certainly one of the most successful ideas nature has come up with. The versatile heteroleptic, push-pull-substituted ruthenium(II) amino acid  $[5]^{2+}$  constitutes an important member of a growing class of metallo amino acids, such as 1,1'-ferrocene amino acid<sup>[119,137]</sup> or biferrocene amino acid,<sup>[138]</sup> based on ferrocenes or metallo porphyrin amino acids based on porphyrins.<sup>[122,123,139]</sup> Such metallo amino acids expand our pool of useful building blocks with specialized properties not covered by organic amino acids.

Ruthenium(II) amino acid  $[5]^{2+}$  is readily prepared from  $RuCl_3$  and the 4'-substituted terpyridine ligands 4'-tpy-COOEt and 4'-tpy-NH<sub>2</sub> in isomerically pure form (tpy = 2,2';6',2''-terpyridine).<sup>[59]</sup> Its exceptionally rich redox, acid/base, and photochemical properties are now well understood, namely metal-based oxidation, ligand-centered reduction, ground-state protonation and deprotonation, proton-coupled electron transfer, excited-state dynamics, phosphorescence, oxidative and reductive quenching, excited-state proton transfer, and triplet-triplet energy transfer.

As is characteristic for amino acids, the orthogonal reactivity at the C- and N-terminal sites of  $[5]^{2+}$  enables highly selective transformations and precise incorporation in larger peptide architectures. Even solid-phase peptide synthesis protocols are applicable with only minor modifications.<sup>[118,140]</sup>

The special electrochemical and optical properties of push-pull-substituted complex  $[5]^{2+}$  are highly useful for applications in photochemical, photophysical, and redox chemical contexts. Therefore, the versatile building block  $[5]^{2+}$  has been successfully incorporated into molecular and nanoscale energy- and electron-transfer systems<sup>[18,25,59,77,78,130]</sup> as well as in first applications of low-cost lighting devices (LECs)<sup>[134]</sup> and solar energy conversion (DSSCs).<sup>[72]</sup> Future applications will involve sensing of small molecules that can switch the phosphorescence of suitable sensors based on  $[5]^{2+}$ .

In terms of excited-state properties (emission quantum yield, excited state lifetime), a successful tpy ligand variation is the expansion of the small N–Ru–N bite angle by formally inserting a N–CH<sub>3</sub> fragment between the chelating pyridines of tpy to give ddpd-based amino acid derivatives

[23]<sup>2+</sup>, [24]<sup>2+</sup>, and [27]<sup>2+</sup> (ddpd = *N,N'*-dimethyl-*N,N'*-dipyridin-2-ylpyridine-2,6-diamine).<sup>[56,100]</sup> In photophysical respects, extension of the tpy ligands by phenylene groups at the 4'-positions ([11]<sup>2+</sup>–[13]<sup>2+</sup>) is rather ineffective [4'-(4-NH<sub>2</sub>-C<sub>6</sub>H<sub>4</sub>)-tpy, 4'-(4-ROOC-C<sub>6</sub>H<sub>4</sub>)-tpy],<sup>[60]</sup> and other ligand extensions might be envisaged in future work.

In essence, the present report summarizes the rich chemistry of the ruthenium(II) amino acid [5]<sup>2+</sup> and its derivatives, demonstrating that this research is an interdisciplinary field comprising ligand design, coordination chemistry, peptide chemistry, redox chemistry, photochemistry, and materials science. It is hoped that further variations and optimizations of the basic design concept will further expand the utility of metallo amino acids in general and upgrade the useful redox and optical properties of [5]<sup>2+</sup> in particular while maintaining its high chemical flexibility. In our opinion there is still a lot of room for improvement and development in this highly interdisciplinary field.

**Supporting Information** (see footnote on the first page of this article): Synthesis and analytical data of tetrapeptides [36](PF<sub>6</sub>)<sub>2</sub> and [37](PF<sub>6</sub>)<sub>2</sub>.

## Acknowledgments

This work was supported by the International Research Training Group “Self Organized Materials for Optoelectronics” funded by the Deutsche Forschungsgemeinschaft (DFG) (IRTG 1404). Financial support through the Excellence Initiative (DFG/GSC 266) is acknowledged by C. K.

- [1] S. Campagna, F. Puntoriero, F. Nastasi, G. Bergamini, V. Balzani, *Top. Curr. Chem.* **2007**, *280*, 117–214.
- [2] B. O'Regan, M. Grätzel, *Nature* **1991**, *353*, 737–740.
- [3] J.-F. Yin, M. Velayudham, D. Bhattacharya, H.-C. Lin, K.-L. Lu, *Coord. Chem. Rev.* **2012**, *256*, 3008–3035.
- [4] P. G. Bomben, K. C. D. Robson, B. D. Koivisto, C. P. Berlinguette, *Coord. Chem. Rev.* **2012**, *256*, 1438–1450.
- [5] R. D. Costa, E. Ortí, H. J. Bolink, F. Monti, G. Accorsi, N. Armaroli, *Angew. Chem. Int. Ed.* **2012**, *51*, 8178–8211; *Angew. Chem.* **2012**, *124*, 8300–8334.
- [6] P. Dreyse, B. Loeb, M. Soto-Arriaza, D. Tordera, E. Ortí, J. J. Serrano-Pérez, H. J. Bolink, *Dalton Trans.* **2013**, *42*, 15502–15513.
- [7] H. J. Bolink, E. Coronado, R. D. Costa, P. Gaviña, E. Ortí, S. Tatay, *Inorg. Chem.* **2009**, *48*, 3907–3909.
- [8] H. J. Bolink, L. Cappelli, E. Coronado, P. Gaviña, *Inorg. Chem.* **2005**, *44*, 5966–5968.
- [9] L. Marcéllis, J. Ghesquière, K. Garnir, A. K.-D. Mesmaeker, C. Moucheron, *Coord. Chem. Rev.* **2012**, *256*, 1569–1582.
- [10] M. R. Gill, J. A. Thomas, *Chem. Soc. Rev.* **2012**, *41*, 3179–3192.
- [11] H. Komatsu, K. Yoshihara, H. Yamada, Y. Kimura, A. Son, S.-i. Nishimoto, K. Tanabe, *Chem. Eur. J.* **2013**, *19*, 1971–1977.
- [12] D. Maity, C. Bhaumik, D. Mondal, S. Baitalik, *Dalton Trans.* **2014**, *43*, 1829–1845.
- [13] Z.-B. Zheng, Z.-M. Duan, Y.-Y. Ma, K.-Z. Wang, *Inorg. Chem.* **2013**, *52*, 2306–2316.
- [14] M. Li, Q. Liang, M. Zheng, C. Fang, S. Peng, M. Zhao, *Dalton Trans.* **2013**, *42*, 13509–13515.
- [15] S. A. Poteet, F. M. MacDonnell, *Dalton Trans.* **2013**, *42*, 13305–13307.
- [16] H. Chen, X. Li, Y. Wu, W. Gao, R. Bai, *Dalton Trans.* **2012**, *41*, 13292–13297.
- [17] R. Zhang, Z. Ye, G. Wang, W. Zhang, J. Yuan, *Chem. Eur. J.* **2010**, *16*, 6884–6891.
- [18] K. Heinze, K. Hempel, *Chem. Eur. J.* **2009**, *15*, 1346–1358.
- [19] R. Horvath, J. Lombard, J.-C. Leprêtre, M.-N. Collomb, A. Deronizer, J. Chauvin, K. C. Gordon, *Dalton Trans.* **2013**, *42*, 16527–16537.
- [20] S. Roeser, M. Z. Ertem, C. Cady, R. Lomoth, J. Benet-Buchholz, L. Hammarström, B. Sarkar, W. Kaim, C. J. Cramer, A. Llobet, *Inorg. Chem.* **2012**, *51*, 320–327.
- [21] L.-Z. Sui, W.-W. Yang, C.-J. Yao, H.-Y. Xie, Y.-W. Zhong, *Inorg. Chem.* **2012**, *51*, 1590–1598.
- [22] O. S. Wenger, *Chem. Soc. Rev.* **2012**, *41*, 3772–3779.
- [23] H.-J. Nie, X. Chen, C.-J. Yao, Y.-W. Zhong, G. R. Hutchison, J. Yao, *Chem. Eur. J.* **2012**, *18*, 14497–14509.
- [24] C.-J. Yao, Y.-W. Zhong, J. Yao, *Inorg. Chem.* **2013**, *52*, 4040–4045.
- [25] A. Breivogel, K. Hempel, K. Heinze, *Inorg. Chim. Acta* **2011**, *374*, 152–162.
- [26] P. Ceroni, *Chem. Eur. J.* **2011**, *17*, 9560–9564.
- [27] T. N. Singh-Rachford, F. N. Castellano, *Coord. Chem. Rev.* **2010**, *254*, 2560–2573.
- [28] W. Wu, S. Ji, W. Wu, J. Shao, H. Guo, T. D. James, J. Zhao, *Chem. Eur. J.* **2012**, *18*, 4953–4964.
- [29] P. Hanczyc, B. Norden, M. Samoc, *Dalton Trans.* **2012**, *41*, 3123–3125.
- [30] P. Ceroni, G. Bergamini, V. Balzani, *Angew. Chem. Int. Ed.* **2009**, *48*, 8516–8518; *Angew. Chem.* **2009**, *121*, 8668–8670.
- [31] J. Lee, H. Chang, S. Kim, G. S. Bang, H. Lee, *Angew. Chem. Int. Ed.* **2009**, *48*, 8501–8504; *Angew. Chem.* **2009**, *121*, 8653–8656.
- [32] K. Terada, K. Kanaizuka, V. M. Iyer, M. Sannodo, S. Saito, K. Kobayashi, M.-a. Haga, *Angew. Chem. Int. Ed.* **2011**, *50*, 6287–6291; *Angew. Chem.* **2011**, *123*, 6411–6415.
- [33] R. H. Crabtree, *Energy Production and Storage: Inorganic Chemical Strategies for a Warming World*, Wiley-VCH, Weinheim, **2010**.
- [34] X. Liu, F. Wang, *Coord. Chem. Rev.* **2012**, *256*, 1115–1136.
- [35] W. T. Eckenhoff, R. Eisenberg, *Dalton Trans.* **2012**, *41*, 13004–13021.
- [36] T. Stoll, M. Gennari, I. Serrano, J. Fortage, J. Chauvin, F. Odobel, M. Rebarz, O. Poizat, M. Sliwa, A. Deronizer, M.-N. Collomb, *Chem. Eur. J.* **2013**, *19*, 782–792.
- [37] M. Schulz, M. Karnahl, M. Schwalbe, J. G. Vos, *Coord. Chem. Rev.* **2012**, *256*, 1682–1705.
- [38] A. Inagaki, M. Akita, *Coord. Chem. Rev.* **2010**, *254*, 1220–1239.
- [39] Z. Chen, P. Kang, M.-T. Zhang, T. J. Meyer, *Chem. Commun.* **2014**, *50*, 335–337.
- [40] S. Ohzu, T. Ishizuka, Y. Hirai, S. Fukuzumi, T. Kojima, *Chem. Eur. J.* **2013**, *19*, 1563–1567.
- [41] H. Nitadori, T. Takahashi, A. Inagaki, M. Akita, *Inorg. Chem.* **2012**, *51*, 51–62.
- [42] P. Guillo, O. Hamelin, P. Batat, G. Jonusauskas, N. D. McClenaghan, S. Ménage, *Inorg. Chem.* **2012**, *51*, 2222–2230.
- [43] F. Li, M. Yu, Y. Jiang, F. Huang, Y. Li, B. Zhang, L. Sun, *Chem. Commun.* **2011**, *47*, 8949–8951.
- [44] D. Chao, W.-F. Fu, *Dalton Trans.* **2014**, *43*, 306–310.
- [45] C. K. Prier, D. A. Rankic, D. W. C. MacMillan, *Chem. Rev.* **2013**, *113*, 5322–5363.
- [46] A. Juris, V. Balzani, F. Barigelletti, S. Campagna, P. Belser, A. von Zelewsky, *Coord. Chem. Rev.* **1988**, *84*, 85–277.
- [47] A. Reynal, E. Palomares, *Eur. J. Inorg. Chem.* **2011**, 4509–4526.
- [48] a) C. Fu, M. Wenzel, E. Treutlein, K. Harms, E. Meggers, *Inorg. Chem.* **2012**, *51*, 10004–10011; b) E. Meggers, *Chem. Eur. J.* **2010**, *16*, 752–758; c) E. Meggers, *Eur. J. Inorg. Chem.* **2011**, 2911–2926; d) T. Joshi, V. Pierroz, C. Mari, L. Gemperle, S. Ferrari, G. Gasser, *Angew. Chem. Int. Ed.* **2014**, *53*, 2960–2963; *Angew. Chem.* **2014**, *126*, 3004–3007.
- [49] a) A. C. Lees, C. J. Kleverlaan, C. A. Bignozzi, J. G. Vos, *Inorg. Chem.* **2001**, *40*, 5343–5349; b) D. M. D'Alessandro, F. R. Keene, S. D. Bergman, M. Kol, *Dalton Trans.* **2005**, 332–337; c) S. Bodge, A. S. Torres, D. J. Maloney, D. Tate, G. R. Kinsel, A. K. Walker, F. M. MacDonnell, *J. Am. Chem. Soc.* **1997**, *119*,



- 10364–10369; d) E. Baggaley, M. R. Gill, N. H. Green, D. Turton, I. V. Sazanovich, S. W. Botchway, C. Smythe, J. W. Haycock, J. A. Weinstein, J. A. Thomas, *Angew. Chem. Int. Ed.* **2014**, *53*, 3367–3371; *Angew. Chem.* **2014**, *126*, 3435–3439.
- [50] M. Maestri, N. Armaroli, V. Balzani, E. C. Constable, A. M. W. Cargill Thompson, *Inorg. Chem.* **1995**, *34*, 2759–2767.
- [51] J.-P. Collin, P. Lainé, J.-P. Launay, J.-P. Sauvage, A. Sour, *J. Chem. Soc., Chem. Commun.* **1993**, 434–435.
- [52] E. C. Constable, M. D. Ward, *J. Chem. Soc., Dalton Trans.* **1990**, 1405–1409.
- [53] a) R. Hogg, R. G. Wilkins, *J. Chem. Soc.* **1962**, 341–350; b) R. H. Holyer, C. D. Hubbard, S. F. A. Kettle, R. G. Wilkins, *Inorg. Chem.* **1966**, *5*, 622–625.
- [54] a) J.-P. Sauvage, J.-P. Collin, J.-C. Chambron, S. Guillerez, C. Coudret, V. Balzani, F. Barigelletti, L. D. Cola, L. Flamigni, *Chem. Rev.* **1994**, *94*, 993–1019; b) Y. Liu, R. Hammitt, D. A. Lutterman, R. P. Thummel, C. Turro, *Inorg. Chem.* **2007**, *46*, 6011–6021; c) L. Hammarström, O. Johansson, *Coord. Chem. Rev.* **2010**, *254*, 2546–2559.
- [55] a) E. A. Medlycott, G. S. Hanan, *Coord. Chem. Rev.* **2006**, *250*, 1763–1782; b) E. A. Medlycott, G. S. Hanan, *Chem. Soc. Rev.* **2005**, *34*, 133–142.
- [56] A. Breivogel, M. Meister, C. Förster, F. Laquai, K. Heinze, *Chem. Eur. J.* **2013**, *19*, 13745–13760.
- [57] K. Suzuki, A. Kobayashi, S. Kaneko, K. Takehira, T. Yoshihara, H. Ishida, Y. Shiina, S. Oishi, S. Tobita, *Phys. Chem. Chem. Phys.* **2009**, *11*, 9850–9860.
- [58] a) B. D. Koivisto, K. C. D. Robson, C. P. Berlinguette, *Inorg. Chem.* **2009**, *48*, 9644–9652; b) V. Duprez, M. Biancardo, F. C. Krebs, *Sol. Energy Mater. Sol. Cells* **2007**, *91*, 230–237.
- [59] K. Heinze, K. Hempel, M. Beckmann, *Eur. J. Inorg. Chem.* **2006**, 2040–2050.
- [60] K. Heinze, K. Hempel, A. Breivogel, *Z. Anorg. Allg. Chem.* **2009**, *635*, 2541–2549.
- [61] K. Heinze, K. Hempel, S. Tschierlei, M. Schmitt, J. Popp, S. Rau, *Eur. J. Inorg. Chem.* **2009**, 3119–3126.
- [62] C. Kreitner, K. Heinze, to be submitted.
- [63] S. Caramori, J. Husson, M. Beley, C. A. Bignozzi, R. Argazzi, P. C. Gros, *Chem. Eur. J.* **2010**, *16*, 2611–2618.
- [64] K. C. D. Robson, B. D. Koivisto, T. J. Gordon, T. Baumgartner, C. P. Berlinguette, *Inorg. Chem.* **2010**, *49*, 5335–5337.
- [65] a) Y.-Q. Fang, N. J. Taylor, G. S. Hanan, F. Loiseau, R. Passalacqua, S. Campagna, H. Nierengarten, A. V. Dorsselaer, *J. Am. Chem. Soc.* **2002**, *124*, 7912–7913; b) Y.-Q. Fang, N. J. Taylor, F. Laverdière, G. S. Hanan, F. Loiseau, F. Nastasi, S. Campagna, H. Nierengarten, E. Leize-Wagner, A. V. Dorsselaer, *Inorg. Chem.* **2007**, *46*, 2854–2863.
- [66] a) A. Harriman, M. Hissler, A. Khatyr, R. Ziessel, *Chem. Commun.* **1999**, 8, 735–736; b) M. Hissler, A. Harriman, A. Khatyr, R. Ziessel, *Chem. Eur. J.* **1999**, *5*, 3366–3381; c) A. C. Benniston, A. Harriman, D. J. Lawrie, A. Mayeux, *Phys. Chem. Chem. Phys.* **2004**, *6*, 51–57.
- [67] D. G. Brown, N. Sanguantrakun, B. Schulze, U. S. Schubert, C. P. Berlinguette, *J. Am. Chem. Soc.* **2012**, *134*, 12354–12357.
- [68] M. Abrahamsson, M. Jäger, T. Österman, L. Eriksson, P. Persson, H.-C. Becker, O. Johansson, L. Hammarström, *J. Am. Chem. Soc.* **2006**, *128*, 12616–12617.
- [69] G. A. Parada, L. A. Fredin, M.-P. Santoni, M. Jäger, R. Lomoth, L. Hammarström, O. Johansson, P. Persson, S. Ott, *Inorg. Chem.* **2013**, *52*, 5128–5137.
- [70] M. Abrahamsson, M. Jäger, R. J. Kumar, T. Österman, P. Persson, H.-C. Becker, O. Johansson, L. Hammarström, *J. Am. Chem. Soc.* **2008**, *130*, 15533–15542.
- [71] F. Schramm, V. Meded, H. Fliegl, K. Fink, O. Fuhr, Z. Qu, W. Klopffer, S. Finn, T. E. Keyes, M. Ruben, *Inorg. Chem.* **2009**, *48*, 5677–5684.
- [72] A. Breivogel, S. Wooh, J. Dietrich, T. Y. Kim, Y. S. Kang, K. Char, K. Heinze, *Eur. J. Inorg. Chem.* **2014**, 2720–2734.
- [73] G. D. Storrer, S. B. Colbran, *Inorg. Chim. Acta* **1999**, *284*, 76–84.
- [74] T.-a. Okamura, T. Iwamura, S. Seno, H. Yamamoto, N. Ueyama, *J. Am. Chem. Soc.* **2004**, *126*, 15972–15973.
- [75] a) B. Farlow, T. A. Nile, J. L. Walsh, A. T. McPhail, *Polyhedron* **1993**, *12*, 2891–2894; b) K. Hutchison, J. C. Morris, T. A. Nile, J. L. Walsh, D. W. Thompson, J. D. Petersen, J. R. Schoonover, *Inorg. Chem.* **1999**, *38*, 2516–2523; c) U. Siemeling, J. Vor der Brüggen, U. Vorfeld, B. Neumann, A. Stammler, H.-G. Stammler, A. Brockhinke, R. Plessow, P. Zanello, F. Laschi, F. Fabrizi de Biani, M. Fontani, S. Steenken, M. Stapper, G. Gurzadyan, *Chem. Eur. J.* **2003**, *9*, 2819–2833.
- [76] a) A. Farmilo, F. Wilkinson, *Chem. Phys. Lett.* **1975**, *34*, 575–580; b) M. S. Wrighton, L. Pdungsap, D. L. Morse, *J. Phys. Chem.* **1975**, *79*, 66–71; c) R. Ciasson, E. J. Lee, X. Zhao, M. S. Wrighton, *J. Phys. Chem.* **1993**, *97*, 2596–2601.
- [77] J. Dietrich, U. Thorenz, C. Förster, K. Heinze, *Inorg. Chem.* **2013**, *52*, 1248–1264.
- [78] J. Dietrich, A. Wünsche von Leupoldt, M. Grabolle, U. Resch-Genger, K. Heinze, *Eur. J. Inorg. Chem.* **2013**, 3009–3019.
- [79] J. V. Caspar, T. J. Meyer, *J. Am. Chem. Soc.* **1983**, *105*, 5583–5590.
- [80] H. Hofmeier, U. S. Schubert, *Chem. Soc. Rev.* **2004**, *33*, 373–399.
- [81] U. S. Schubert, H. Hofmeier, G. R. Newkome, *Modern Terpyridine Chemistry*, Wiley-VCH, Weinheim, **2006**.
- [82] D. Xiong, Z. Li, H. Wang, J. Wang, *Green Chem.* **2013**, *15*, 1941–1948.
- [83] a) A. Habibi-Yangjeh, M. Danandeh-Jenagharad, M. Nooshyar, *Bull. Korean Chem. Soc.* **2005**, *26*, 2007–2016; b) Y. Kobayashi, T. Komatsu, M. Sumi, S. Numajiri, M. Miyamoto, D. Kobayashi, K. Sugibayashi, Y. Morimoto, *Eur. J. Pharm. Sci.* **2004**, *21*, 471–477.
- [84] B. García, S. Ibeas, J. M. Leal, *J. Phys. Org. Chem.* **1996**, *9*, 593–597.
- [85] R. Schwesinger, J. Willaredt, H. Schlemper, M. Keller, D. Schmitt, H. Fritz, *Chem. Ber.* **1994**, *127*, 2435–2454.
- [86] M. D. Kärkäs, T. Åkermark, H. Chen, J. Sun, B. Åkermark, *Angew. Chem. Int. Ed.* **2013**, *52*, 4189–4193; *Angew. Chem.* **2013**, *125*, 4283–4287.
- [87] N. G. Connelly, W. E. Geiger, *Chem. Rev.* **1996**, *96*, 877–910.
- [88] a) G. Wolfbauer, A. M. Bond, D. R. MacFarlane, *Inorg. Chem.* **1999**, *38*, 3836–3846; b) S. Kämper, A. Paretzki, J. Fiedler, S. Zális, W. Kaim, *Inorg. Chem.* **2012**, *51*, 2097–2104.
- [89] a) L. G. Arnaut, S. J. Formosinho, *J. Photochem. Photobiol. A: Chem.* **1993**, *75*, 1–20; b) C. Turro, S. H. Bossmann, Y. Jenkins, J. K. Barton, N. J. Turro, *J. Am. Chem. Soc.* **1995**, *117*, 9026–9032.
- [90] G. R. Desiraju, *Angew. Chem. Int. Ed. Engl.* **1995**, *34*, 2311–2327; *Angew. Chem.* **1995**, *107*, 2541–2558.
- [91] S. Ji, W. Wu, W. Wu, H. Guo, J. Zhao, *Angew. Chem. Int. Ed.* **2011**, *50*, 1626–1629; *Angew. Chem.* **2011**, *123*, 1664–1667.
- [92] a) J. Wang, G. S. Hanan, F. Loiseau, S. Campagna, *Chem. Commun.* **2004**, 2068–2069; b) J. Wang, Y.-Q. Fang, L. Bourget-Merle, M. I. J. Polson, G. S. Hanan, A. Juris, F. Loiseau, S. Campagna, *Chem. Eur. J.* **2006**, *12*, 8539–8548; c) E. A. Medlycott, G. S. Hanan, F. Loiseau, S. Campagna, *Chem. Eur. J.* **2007**, *13*, 2837–2846.
- [93] Y. Chi, P.-T. Chou, *Chem. Soc. Rev.* **2010**, *39*, 638–655.
- [94] V. Friese, S. Nag, J. Wang, M.-P. Santoni, A. Rodrigue-Witchel, G. S. Hanan, F. Schaper, *Eur. J. Inorg. Chem.* **2011**, 39–44.
- [95] W. Ghattas, H. Müller-Bunz, M. Albrecht, *Organometallics* **2010**, *29*, 6782–6789.
- [96] K. C. D. Robson, B. D. Koivisto, A. Yella, B. Sporinova, M. K. Nazeeruddin, T. Baumgartner, M. Grätzel, C. P. Berlinguette, *Inorg. Chem.* **2011**, *50*, 5494–5508.
- [97] a) F. Barigelletti, B. Ventura, J.-P. Collin, R. Kayhanian, P. Gaviña, J.-P. Sauvage, *Eur. J. Inorg. Chem.* **2000**, 113–119; b) S. H. Wadman, J. M. Kroon, K. Bakker, R. W. A. Havenith, G. P. M. van Klink, G. van Koten, *Organometallics* **2010**, *29*, 1569–1579;

- c) K. C. D. Robson, B. D. Koivisto, C. P. Berlinguette, *Inorg. Chem.* **2012**, *51*, 1501–1507; d) B. Schulze, D. Escudero, C. Friebel, R. Siebert, H. Görls, S. Sinn, M. Thomas, S. Mai, J. Popp, B. Dietzek, L. González, U. S. Schubert, *Chem. Eur. J.* **2012**, *18*, 4010–4025; e) S. Sinn, B. Schulze, C. Friebe, D. G. Brown, M. Jäger, E. Altuntaş, J. Kübel, O. Guntner, C. P. Berlinguette, B. Dietzek, U. S. Schubert, *Inorg. Chem.* **2014**, *53*, 2083–2095.
- [98] T. Österman, M. Abrahamsson, H.-C. Becker, L. Hammarström, P. Persson, *J. Phys. Chem. A* **2012**, *116*, 1041–1050.
- [99] M. Jäger, R. J. Kumar, H. Görls, J. Bergquist, O. Johansson, *Inorg. Chem.* **2009**, *48*, 3228–3238.
- [100] A. Breivogel, C. Förster, K. Heinze, *Inorg. Chem.* **2010**, *49*, 7052–7056.
- [101] T. J. Meyer, *Pure Appl. Chem.* **1986**, *58*, 1193–1206.
- [102] J. V. Caspar, E. M. Kober, B. P. Sullivan, T. J. Meyer, *J. Am. Chem. Soc.* **1982**, *104*, 630–632.
- [103] J. V. Caspar, T. J. Meyer, *J. Phys. Chem.* **1983**, *87*, 952–957.
- [104] R. J. Watts, *J. Chem. Educ.* **1983**, *60*, 834–842.
- [105] B. Durham, J. V. Caspar, J. K. Nagle, T. J. Meyer, *J. Am. Chem. Soc.* **1982**, *104*, 4803–4810.
- [106] Z. J. Fuller, W. D. Bare, K. A. Kneas, W.-Y. Xu, J. N. Demas, B. A. DeGraff, *Anal. Chem.* **2003**, *75*, 2670–2677.
- [107] W. M. Wallace, P. E. Hoggard, *Inorg. Chem.* **1979**, *18*, 2934–2935.
- [108] T. E. Keyes, E. Gicquel, L. Guerin, R. J. Forster, V. Hultgren, A. M. Bond, A. G. Wedd, *Inorg. Chem.* **2003**, *42*, 7897–7905.
- [109] E. Bayer, *Angew. Chem. Int. Ed. Engl.* **1991**, *30*, 113–129; *Angew. Chem.* **1991**, *103*, 117–133.
- [110] M. Grötli, C. H. Gotfredsen, J. Rademann, J. Buchardt, A. J. Clark, J. Ø. Duus, M. Meldal, *J. Comb. Chem.* **2000**, *2*, 108–119.
- [111] W. C. Chan, P. D. White (Eds.), *Fmoc Solid Phase Peptide Synthesis* Oxford University Press, Oxford, **2000**.
- [112] A. Barbieri, B. Ventura, R. Ziessel, *Coord. Chem. Rev.* **2012**, *256*, 1732–1741.
- [113] A. Barbieri, B. Ventura, F. Barigelletti, A. D. Nicola, M. Quezada, R. Ziessel, *Inorg. Chem.* **2004**, *43*, 7359–7368.
- [114] a) M. B. Robin, P. Day, *Adv. Inorg. Chem.* **1968**, *10*, 247–422; b) N. S. Hush, *Prog. Inorg. Chem.* **1967**, *8*, 391–444.
- [115] N. Hush, *Coord. Chem. Rev.* **1985**, *64*, 135–157.
- [116] J.-P. Launay, *Chem. Soc. Rev.* **2001**, *30*, 386–397.
- [117] C. Chiorboli, M. T. Indelli, F. Scandola, *Top. Curr. Chem.* **2005**, *257*, 63–102.
- [118] W. Kaim, G. K. Lahiri, *Angew. Chem. Int. Ed.* **2007**, *46*, 1778–1796; *Angew. Chem.* **2007**, *119*, 1808–1828.
- [119] K. Heinze, D. Siebler, *Z. Anorg. Allg. Chem.* **2007**, *633*, 2223–2233.
- [120] S. Lu, V. V. Strelets, M. F. Ryan, W. J. Pietro, A. B. P. Lever, *Inorg. Chem.* **1996**, *35*, 1013–1023.
- [121] A. Weller, *Z. Phys. Chem. (München Ger.)* **1982**, *133*, 93–98.
- [122] J. Melomedov, J. R. Ochsmann, M. Meister, F. Laquai, K. Heinze, *Eur. J. Inorg. Chem.* **2014**, 1984–2001.
- [123] J. Melomedov, J. R. Ochsmann, M. Meister, F. Laquai, K. Heinze, *Eur. J. Inorg. Chem.* **2014**, 2902–2915.
- [124] a) O. Stern, M. Volmer, *Phys. Z.* **1919**, *20*, 183–188; b) J. R. Lakowicz, *Principles of Fluorescence Spectroscopy*, 3rd edition, Springer Science+Business Media, LLC, New York, **2006**.
- [125] J. Hawecker, J.-M. Lehn, R. Ziessel, *J. Chem. Soc., Chem. Commun.* **1983**, 536–538.
- [126] a) H. Takeda, O. Ishitani, *Coord. Chem. Rev.* **2010**, *254*, 346–354; b) Y. Tamaki, K. Watanabe, K. Koike, H. Inoue, T. Morimoto, O. Ishitani, *Faraday Discuss.* **2012**, *155*, 115–127.
- [127] a) H. Ozawa, M.-a. Haga, K. Sakai, *J. Am. Chem. Soc.* **2006**, *128*, 4926–4927; b) H. Ozawa, K. Sakai, *Chem. Lett.* **2007**, *36*, 920–921; c) H. Ozawa, K. Sakai, *Chem. Commun.* **2011**, *47*, 2227–2242.
- [128] J. Hawecker, J.-M. Lehn, R. Ziessel, *Helv. Chim. Acta* **1986**, *69*, 1990–2012.
- [129] M. R. Simond, K. Ballerat-Busserolles, Y. Coulier, L. Rodier, J.-Y. Coxam, *J. Solution Chem.* **2012**, *41*, 130–142.
- [130] L. zur Borg, A. L. Domanski, A. Breivogel, M. Bürger, R. Berger, K. Heinze, R. Zentel, *J. Mater. Chem. C* **2013**, *1*, 1223–1230.
- [131] a) M. Matsumoto, H. Miyazaki, K. Matsuhiro, Y. Kumashiro, Y. Takaoka, *Solid State Ionics* **1996**, *89*, 263–267; b) A. F. Nogueira, J. R. Durrant, M. A. De Paoli, *Adv. Mater.* **2001**, *13*, 826–830.
- [132] a) B. C. O'Regan, K. Walley, M. Juozapavicius, A. Anderson, F. Matar, T. Ghaddar, S. M. Zakeeruddin, C. Klein, J. R. Durrant, *J. Am. Chem. Soc.* **2009**, *131*, 3541–3548; b) B. C. O'Regan, I. López-Duarte, M. V. Martínez-Díaz, A. Forneli, J. Albero, A. Morandeira, E. Palomares, T. Torres, J. R. Durrant, *J. Am. Chem. Soc.* **2008**, *130*, 2906–2907; c) J. M. Gardner, J. M. Giaimuccio, G. J. Meyer, *J. Am. Chem. Soc.* **2008**, *130*, 17252–17253.
- [133] a) C.-C. Chou, K.-L. Wu, Y. Chi, W.-P. Hu, S. J. Yu, G.-H. Lee, C.-L. Lin, P.-T. Chou, *Angew. Chem. Int. Ed.* **2011**, *50*, 2054–2058; *Angew. Chem.* **2011**, *123*, 2102–2106; b) C.-C. Chou, F.-C. Hu, H.-H. Yeh, H.-P. Wu, Y. Chi, J. N. Clifford, E. Palomares, S.-H. Liu, P.-T. Chou, G.-H. Lee, *Angew. Chem. Int. Ed.* **2014**, *53*, 178–183; *Angew. Chem.* **2014**, *126*, 182–187; c) K.-L. Wu, C.-H. Li, Y. Chi, J. N. Clifford, L. Cabau, E. Palomares, Y.-M. Cheng, H.-A. Pan, P.-T. Chou, *J. Am. Chem. Soc.* **2012**, *134*, 7488–7496.
- [134] A. Breivogel, M. Park, D. Lee, S. Klassen, A. Kühnle, C. Lee, K. Char, K. Heinze, *Eur. J. Inorg. Chem.* **2014**, 288–295.
- [135] International Commission on Illumination (CIE), **1931**.
- [136] W. Y. Ng, X. Gong, W. K. Chan, *Chem. Mater.* **1999**, *11*, 1165–1170.
- [137] a) J. R. Butler, S. C. Quayle, *J. Organomet. Chem.* **1998**, *552*, 63–68; b) T. Okamura, K. Sakauye, N. Ueyama, A. Nakamura, *Inorg. Chem.* **1998**, *37*, 6731–6736; c) K. Heinze, M. Schlenker, *Eur. J. Inorg. Chem.* **2004**, 2974–2988; d) K. Heinze, M. Schlenker, *Eur. J. Inorg. Chem.* **2005**, 66–71; e) K. Heinze, M. Beckmann, *Eur. J. Inorg. Chem.* **2005**, 3450–3457; f) K. Heinze, U. Wild, M. Beckmann, *Eur. J. Inorg. Chem.* **2007**, 617–623; g) M. Čakić Semenčić, D. Siebler, K. Heinze, V. Rapić, *Organometallics* **2009**, *28*, 2028–2037; h) D. Siebler, C. Förster, K. Heinze, *Eur. J. Inorg. Chem.* **2010**, 523–527; i) M. Čakić Semenčić, K. Heinze, C. Förster, V. Rapić, *Eur. J. Inorg. Chem.* **2010**, 1089–1097; j) C. Förster, D. Siebler, K. Heinze, *Acta Crystallogr., Sect. C* **2010**, *66*, m235–m237; k) D. Siebler, M. Linseis, T. Gasi, L. M. Carrella, R. F. Winter, C. Förster, K. Heinze, *Chem. Eur. J.* **2011**, *17*, 4540–4551; l) D. Siebler, C. Förster, K. Heinze, *Dalton Trans.* **2011**, *40*, 3558–3575; m) C. Förster, M. Kovačević, L. Barišić, V. Rapić, K. Heinze, *Organometallics* **2012**, *31*, 3683–3694.
- [138] D. Siebler, C. Förster, T. Gasi, K. Heinze, *Organometallics* **2011**, *30*, 313–327.
- [139] a) S. L. Gould, G. Kodis, R. E. Palacios, L. de la Garza, A. Brune, D. Gust, T. A. Moore, A. L. Moore, *J. Phys. Chem. B* **2004**, *108*, 10566–10580; b) K. Heinze, A. Reinhart, *Dalton Trans.* **2008**, 469–480; c) J. Melomedov, A. Wünsche von Leupoldt, M. Meister, F. Laquai, K. Heinze, *Dalton Trans.* **2013**, *42*, 9727–9739.
- [140] K. Heinze, M. Beckmann, K. Hempel, *Chem. Eur. J.* **2008**, *14*, 9468–9480.

Received: May 26, 2014  
Published Online: August 15, 2014



## 1.2 EXCITED STATE DECAY MECHANISMS IN POLYPYRIDINE RUTHENIUM COMPLEXES

Polypyridine ligands typically are strong  $\pi$ -accepting ligands providing the lowest unoccupied molecular orbital (LUMO) in polypyridine ruthenium complexes. At the same time, the metal's  $d$  orbitals of the  $t_{2g}$  set (in idealized  $O_h$  symmetry) are good  $\pi$ -donors. Hence, upon irradiation into the low-energy absorption band (at around 500 nm) in the visible range of the electromagnetic spectrum, a singlet metal-to-ligand charge transfer ( $^1\text{MLCT}$ ) state is populated in such complexes.<sup>47</sup> The spin-orbit coupling caused by the heavy ruthenium atom leads to quantitative intersystem crossing (ISC) to the triplet potential surface populating a  $^3\text{MLCT}$  state.<sup>48,49</sup> This state typically is long-lived ( $\tau > 1$  ns) and has several decay pathways. These will be discussed in the following.

### 1.2.1 Phosphorescence

As an emissive excited state deactivation from the  $^3\text{MLCT}$  state to the singlet ground state ( $^1\text{GS}$ ) has to occur with spin inversion, phosphorescence is a spin-forbidden process. However, the presence of a heavy element lifts this restriction to some extent due to spin-orbit coupling. Physically, phosphorescence is described via the Einstein coefficient for spontaneous emission. In the Franck-Condon approximation, the decay rate constant for spontaneous emission is given by the following expression:<sup>50,51</sup>

$$k_r(^3\text{MLCT} \rightarrow ^1\text{GS}) = \frac{8\pi^2\eta^3}{3\epsilon_0\hbar} |\mathbf{M}_T(Q_0)|^2 \sum_{\tilde{\nu}} \tilde{\nu}^3 \int \left| \chi_{^1\text{GS},\nu'}^* \chi_{^3\text{MLCT},\nu''} \right|^2 \quad (1.1)$$

Hereby,  $\eta$  is the solvent's refractive index,  $\mathbf{M}_T(Q_0)$  is the transition dipole moment for the  $^3\text{MLCT} \rightarrow ^1\text{GS}$  transition at the  $^3\text{MLCT}$  geometry  $Q_0$  and  $\tilde{\nu}$  is the emission energy (in  $\text{cm}^{-1}$ ).  $\chi_{^1\text{GS},\nu'}$  and  $\chi_{^3\text{MLCT},\nu''}$  are the nuclear wavefunctions of the ground and excited state with quantum numbers  $\nu'$  and  $\nu''$ , respectively. The overlap integral  $\int \left| \chi_{^1\text{GS},\nu'}^* \chi_{^3\text{MLCT},\nu''} \right|^2$  between these vibrational wavefunctions is referred to as the Franck-Condon factor. Hence, the rate for spontaneous emission is directly proportional to the third power of the emission energy  $\tilde{\nu}$ .

$$\mathbf{M}_T(Q_0) = \sum_{j \in x,y,z} \left| \sum_m \frac{\langle ^3\text{MLCT} | \hat{H}_{\text{SOC}} | S_m \rangle}{E(S_m) - E(^3\text{MLCT})} \mathbf{M}_{S_m,j}(Q_0) \right|^2 \quad (1.2)$$

In first-order perturbation theory, the  $^3\text{MLCT} \rightarrow ^1\text{GS}$  transition dipole moment  $\mathbf{M}_T(Q_0)$  is dominated by the strength of the spin-orbit coupling ( $\langle ^3\text{MLCT} | \hat{H}_{\text{SOC}} | S_m \rangle$ ) and the singlet excited state ( $S_m$ )  $\rightarrow ^1\text{GS}$  transition dipole moments  $\mathbf{M}_{S_m,j}(Q_0)$  of energetically close-lying singlet states (equation 1.2).<sup>51</sup> These singlet states are typically  $^1\text{MLCT}$  states with relatively high transition dipole moments as the respective transitions are not symmetry-restricted.

The Franck-Condon factors are closely related to the distortion of the excited state with respect to the singlet ground state, but they do not affect the overall emission rate (or intensity). They only provide a weighing of the vibrational wavefunctions of the ground state: a larger distortion of the excited state with respect to the ground state yields an emission spectrum with a

pronounced vibronic progression whereas emission from an undistorted excited state is free of progressions.

For polypyridine complexes of ruthenium and osmium, the rate constants for phosphorescence are typically in the range of  $10^4 - 10^6 \text{ s}^{-1}$ .<sup>6,7,35,52</sup> A simple dependence between structure and rate of phosphorescence, however, cannot be drawn making the selective manipulation of the latter a difficult task.

### 1.2.2 Non-radiative Decay

The excited  $^3\text{MLCT}$  state of polypyridine ruthenium complexes can also evolve into the singlet ground state without emission of a photon. Two major relaxation pathways have been described theoretically which are referred to as the weak and the strong coupling limit (Figure 1.1).<sup>53</sup> They differ in the displacement of the excited state (ES) potential energy surface (PES) with respect to the ground state along the reaction coordinate, which comprises all geometric changes in the  $\text{GS} \rightarrow \text{ES}$  transition. In the weak coupling limit, the displacement of the ES surface is small leading to two parabolic potentials stacked vertically above one another (Figure 1.1 a).<sup>53</sup> In the strong coupling limit, on the other hand, the displacement of the ES is considerably larger. This yields a surface crossing point between the potential surfaces of the two states in the vicinity of the minimum of the upper state (Figure 1.1 b).<sup>53</sup> The consequences of the two limits for the excited state decay mechanisms will be discussed in the following.

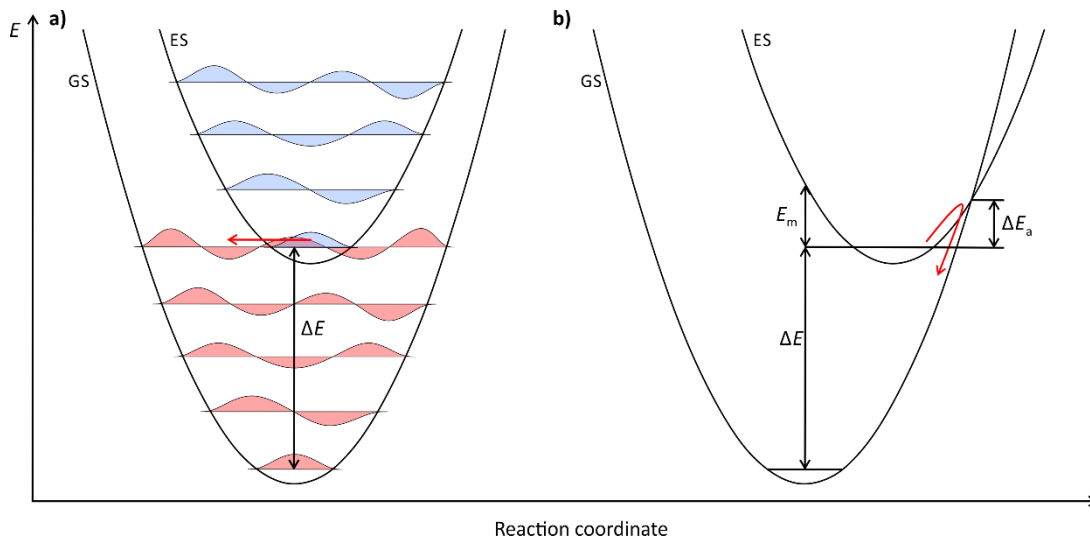


**Figure 1.1** Schematic potential energy surfaces in **a)** the weak coupling limit and **b)** the strong coupling limit.

#### Weak coupling limit

In the weak coupling limit (Figure 1.1 a), the transition probability for the  $\text{ES} \rightarrow \text{GS}$  transition is given by the following expression:<sup>7,51,53,54</sup>

$$k_{nr} = \left( \frac{2\pi H_{ab}^2}{\hbar} \right) (4\pi\lambda_s k_B T)^{-\frac{1}{2}} \sum_{n_M}^{\infty} \left[ \frac{S_M^{n_M}}{n_M!} \exp(-S_M) \exp\left(-\frac{(\Delta E - n_M \hbar \omega_M - \lambda_s)^2}{4\lambda_s k_B T}\right) \right] \quad (1.3)$$



Here,  $H_{ab}$  is the electronic coupling matrix element for the ES  $\rightarrow$  GS transition,  $\lambda_s$  is the solvent's reorganizational energy and  $S_M$  is the Huang-Rhys factor. This factor is a measure of the geometrical distortion between the equilibrium geometries of ground and excited state in terms of dimensionless fractional displacements along the complex's normal modes.  $\omega_M$  and  $n_M$  are the frequency and quantum number of high-frequency intraligand vibrational modes.  $\Delta E$  is approximately corresponds the energy difference between the ground and excited state.

Non-radiative decay in the weak coupling limit is a two-step process. Firstly, tunneling from the electronically excited state into the vibrationally excited ground state occurs (horizontal transition in the Jablonski diagram), followed by thermal cooling under emission of IR radiation (heat; vertical transition in the Jablonski diagram). From equation 1.3 follows, that predominantly C-H, N-H and O-H vibrations ( $\omega_M = 3000 - 3400 \text{ cm}^{-1}$ ) contribute to the non-radiative decay in the weak coupling limit, as they require overtones of significantly lower quantum numbers  $n_M$  to be in resonance with the excited state ( $\Delta E = 10000 - 20000 \text{ cm}^{-1}$ ) than intraligand C-C and C=C vibrations ( $\omega_M = 1200 - 1600 \text{ cm}^{-1}$ ).<sup>53</sup> Additionally, the displacement of the excited state with respect to the ground state plays a crucial role in promoting non-radiative decay.

The dependence of the rate of non-radiative decay on the energy gap  $\Delta E$  between ground and excited state has led to the often found reference "energy gap law".<sup>7,53,55</sup> In a series of structurally related complexes, in which variations of  $H_{ab}$  and  $S_m$  are small, the natural logarithm of the decay rate is proportional to  $-\Delta E$ .<sup>7,55</sup> Hence, in the weak coupling regime, non-radiative decay can be suppressed by raising the emission energy or by reducing the excited state distortion. In order to lower the energy of the high-frequency vibrations, deuteration of ligands and solvent is a viable, but synthetically challenging tool ( $\omega_{C-H} \approx 3000 \text{ cm}^{-1}$ ,  $\omega_{C-D} \approx 2200 \text{ cm}^{-1}$ ).<sup>56,57</sup>

### *Strong coupling limit*

In the strong coupling limit (Figure 1.1 b), the transition probability is given by the following expression:<sup>53</sup>

$$k_{nr} = \left(\frac{k_B T}{\hbar}\right) H_{ab}^2 \left(\frac{2\pi}{E_M(k_B T)^3}\right)^{\frac{1}{2}} \exp\left(-\frac{\Delta E_a}{k_B T}\right) \quad (1.4)$$

Again,  $k_{nr}$  depends on the electronic coupling matrix element  $H_{ab}$ .  $E_M$  is the Stokes shift between excitation and emission energy (of states with the same multiplicity, Figure 1.1 b). However, in this case,  $k_{nr}$  is temperature-dependent with an Arrhenius-like activation term involving the energy difference between the minimum of the excited state and the surface crossing point. Hence, an increasing temperature yields faster non-radiative decay in the strong coupling regime. As the activation barrier  $\Delta E_a$  depends on the excited state distortion, non-radiative decay can become barrier-free and very fast in the strong coupling limit.

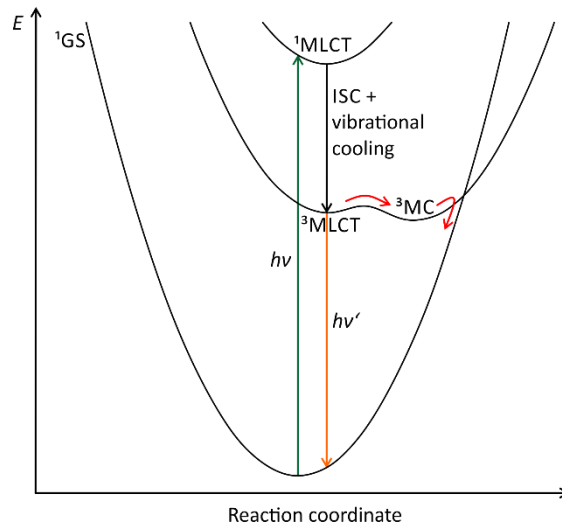


**Figure 1.2** Potential energy profile of  $[\text{Ru}(\text{bpy})_3]^{2+}$ . The green arrow indicates excitation, the orange arrow shows emissive relaxation, and the red arrows highlight the thermal population of the  $^3\text{MC}$  state followed by thermally activated surface crossing and ISC to the singlet ground state.

An intermediate case of weak and strong coupling limit was found for  $[\text{Ru}(\text{bpy})_3]^{2+}$  (bpy = 2,2'-bipyridine). Here, the emissive  $^3\text{MLCT}$  state is accompanied by a metal-centered ( $^3\text{MC}$ ) ligand-field excited state of very similar energy.<sup>4,6,8,58</sup> While the  $^3\text{MLCT}$  is only weakly displaced with respect to the  $^1\text{GS}$  geometry corresponding to the weak coupling limit, the  $^3\text{MC}$  state is substantially distorted and strongly coupled to the singlet PES (Figure 1.2). Both states are connected *via* a low-energy transition state allowing the population of the latter from the former and *vice versa*.<sup>6</sup> Hence, after excitation into a  $^1\text{MLCT}$  state and intersystem crossing (ISC) into the  $^3\text{MLCT}$  state, excited state decay can occur via emission  $h\nu'$ , tunneling to high-lying vibrationally excited singlet states (weak coupling limit) or thermal population of the  $^3\text{MC}$  state followed by surface crossing and ISC to the singlet ground state (strong coupling limit).

The lifetime  $\tau_0$  of an excited state is determined by the rate constants of all processes that depopulate this state, which typically is the radiative decay and several non-radiative decays:<sup>59,60</sup>

$$\tau_0 = \frac{1}{k_0} = \frac{1}{k_r + \sum k_{nr,i}} \quad (1.5)$$

The quantum efficiency  $\phi$  of the emission process thus is described as follows:<sup>59</sup>

$$\phi = \frac{k_r}{k_0} = \frac{k_r}{k_r + \sum k_{nr,i}} = k_r \tau_0 \quad (1.6)$$

In the case of  $[\text{Ru}(\text{bpy})_3]^{2+}$ , the decay via the  $^3\text{MC}$  state is associated with an activation barrier. As a consequence, the excited state lifetime (and the quantum yield) become temperature-dependent:<sup>6,8</sup>

$$\tau_0(T) = [k_r + k_{nr,MLCT \rightarrow GS} + k_{nr,MLCT \rightarrow MC}(T)]^{-1} = [k_1 + k_2^0 \exp(-\frac{\Delta E_a}{RT})]^{-1} \quad (1.7)$$

With  $k_1 = k_r + k_{nr,MLCT \rightarrow GS}$  describing the temperature-independent emissive and  $^3MLCT \rightarrow ^1GS$  tunneling processes and  $k_2^0 \exp\left(-\frac{\Delta E_a}{RT}\right)$  describing the  $^3MLCT \rightarrow ^3MC$  transition with  $\Delta E_a$  being the activation barrier of the  $^3MLCT \rightarrow ^3MC$  transition.

In fact, the temperature profile of the excited state lifetime of  $[Ru(bpy)_3]^{2+}$  is more accurately described by two thermally activated processes with different activation barriers. The second activated process ( $E_a \approx 100 \text{ cm}^{-1}$ ) is associated with a second emissive MLCT state of higher singlet character.<sup>2,3,8,58</sup>

### 1.2.3 Other Excited State Decay Channels

In addition to luminescence and non-radiative decay, which are both unimolecular deactivation channels, an excited state can also be quenched in a bimolecular fashion when its lifetime is sufficiently long ( $> 1 \text{ ns}$ ). These quenching processes either involve energy transfer to a molecule with an energetically suitable excited state or electron transfer from or to the excited molecule by an oxidant or reductant with suited redox potentials. Both processes will be discussed briefly from a mechanistic point of view.

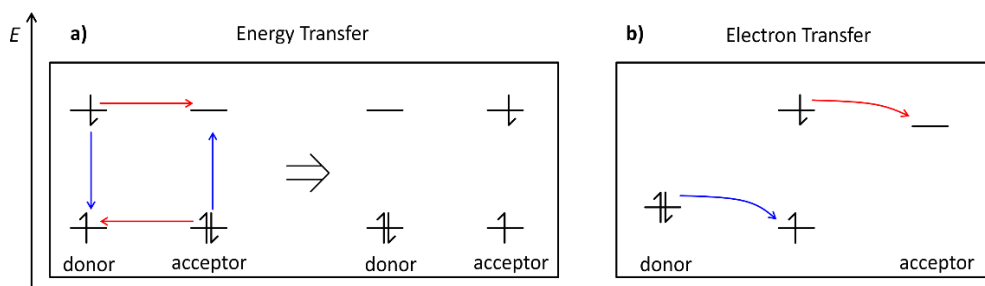


**Figure 1.3** Schematic representation of **a)** energy transfer between singlet excited and ground state molecules via Förster (blue) and Dexter energy transfer (red) and **b)** oxidative (red) and reductive (blue) electron transfer quenching of an excited singlet state.

#### Energy Transfer

In general, energy transfer can only occur when the excited states of a donor and an acceptor are in resonance, *i.e.* when the energy that the excited donor molecule emits is suitable to excite the acceptor molecule into one of its excited states. Quantum mechanically, the energy transfer rate is composed of two contributions accounting for through-space and through-bond interaction between the donor and acceptor molecule, respectively. Depending on which component dominates, energy transfer is referred to as Förster-type (through-space) or Dexter-type (through-bond, Figure 1.3 a).<sup>60-62</sup>

For a Förster-type through-space energy transfer, the rate constant is given by the following equation:<sup>60,61</sup>

$$k_{EnT} = 8.8 \cdot 10^{-25} \frac{\phi_0 \kappa^2}{\tau_0 r^6 \eta^4} J_F \quad (1.8)$$

$\phi_0$  and  $\tau_0$  are hereby the quantum yield and lifetime of the donor molecule in absence of an energy acceptor,  $\kappa$  is an orientation factor taking into account the transition dipole moments of

donor and acceptor molecule,  $r$  corresponds to the donor-acceptor distance and  $\eta$  is the solvent's refractive index. The factor  $J_F$  is known as Förster resonance integral and describes the spectral overlap of the donor's normalized emission spectrum and the acceptor's normalized absorption spectrum. The distance dependence  $r^{-6}$  results from that fact that this energy transfer effectively arises from the interaction of two transition dipoles. Typically, Förster resonance energy transfer (FRET) is encountered between different molecules provided all involved states have the same multiplicity.

Dexter-type energy transfer comes into play when the involved states differ in their multiplicity. As it is mediated either by direct orbital overlap of donor and acceptor or by the frontier orbitals of a bridge, its efficiency decreases exponentially with the donor-acceptor distance:<sup>60,62</sup>

$$k_{EnT} = \frac{2\pi}{\hbar} (H_{ab})^2 J_D \exp[-\beta_{EnT}(r - r_0)] \quad (1.9)$$

For Dexter energy transfer, the electronic coupling matrix element  $H_{ab}$  between the donor and acceptor states as well as the Dexter overlap integral  $J_D$  are crucial. The spectral overlap, however, does not nearly need to be as large as for Förster energy transfer. This is because formally, Dexter energy transfer is a double electron transfer between donor and acceptor and does not require the resonant transfer of a photon (Figure 1.3 a). Instead, the attenuation factor  $\beta_{EnT}$  takes the tunneling barriers for both electron transfer processes into account.

### Electron Transfer

The theory of thermal electron transfer reactions has been extensively studied by Marcus<sup>63-65</sup> and the so-called Marcus theory was extended to photochemical electron transfer by Hush.<sup>66,67</sup> The rate for thermal electron transfer is given by:<sup>60,68</sup>

$$k_{ET} = \nu_N \kappa_{el} \exp\left[-\frac{\Delta G^\ddagger}{RT}\right] \quad (1.10)$$

Here,  $\nu_N$  is the average nuclear frequency factor,  $\kappa_{el}$  is the electronic transmission factor and  $\Delta G^\ddagger$  corresponds to the activation energy required for electron transfer to occur. Generally, before an electron is transferred between a donor and an acceptor, their molecular geometries have to adjust in order to allow for barrier-free electron transfer. The average nuclear frequency factor gives effective frequency with which geometries appropriate for electron transfer are reached through molecular vibrations. The transmission coefficient is linked to the probability of electron transfer in the transition region. Marcus showed that the potential surfaces can be considered harmonic yielding a quadratic dependence of the activation barrier  $\Delta G^\ddagger$  on the thermodynamic driving force  $\Delta G_0$ :<sup>60</sup>

$$\Delta G^\ddagger = \frac{\lambda}{4} \left(1 + \frac{\Delta G_0}{\lambda}\right)^2 \quad (1.11)$$

Here,  $\lambda$  is the nuclear reorganizational energy. From equations 1.10 and 1.11 follows, that the electron transfer rate reaches a maximum when  $\Delta G_0 = -\lambda$ . This means that the rate will decrease when the electron transfer becomes too exergonic (Marcus-inverted region). In the endergonic and slightly exergonic range, however, the electron transfer rate increases with increasing driving force (Marcus-normal region).

Typically, electron transfer reactions in the Marcus-inverted region involve photo-excited molecules, since both their oxidative and reductive strength are substantially increased in the excited state (Figure 1.3 b). According to the Rehm-Weller equation, the excited state redox potentials  $E^*$  can be estimated from the ground state redox potentials  $E_{ox}/E_{red}$  and the energy gap  $E_{00}$  between the excited and ground state as follows:<sup>69</sup>

$$E_{ox}^* = E_{ox} - E_{00} \quad (1.12)$$

$$E_{red}^* = E_{red} + E_{00} \quad (1.13)$$

Spectroscopically, both electron and energy transfer quenching of excited states by an external quencher can be observed and quantified. This is typically done on the basis of the Stern-Volmer equation 1.14. It relates the dependence of the emission intensity on the concentration of an external quencher to a bimolecular quenching constant  $k_q$ , which incorporates both, the diffusion rate and the rate of electron/energy transfer:<sup>70</sup>

$$\frac{\phi_0}{\phi([Q])} = 1 + K_{SV}[Q] = 1 + k_q\tau_0[Q] \quad (1.14)$$

With  $\phi_0$  and  $\phi([Q])$  being the emission quantum yields in the absence and presence of a quencher of concentration  $[Q]$ ,  $K_{SV}$  being the Stern-Volmer constant and  $\tau_0$  being the emitter's lifetime in the absence of a quencher.

### 1.3 MIXED VALENCE AND OPTICAL ELECTRON TRANSFER

The expression “mixed valence” is usually utilized in the context of compounds that contain the same atom or fragment in two (or more) different oxidation states. These atoms or fragments may or may not interact depending on their respective electronic environments and the distance between them leading to interesting spectroscopic phenomena that are not observed for the independent fragments.

$[(\text{NH}_3)_5\text{Ru}(\mu\text{-pz})\text{Ru}(\text{NH}_3)_5]^{5+}$  (pz = pyrazine) constitutes a textbook example of such a mixed-valent complex formally containing two ruthenium atoms with an averaged oxidation state of +2.5. Depending on the spectroscopic method, however, the complex’s properties appear to reflect the presence of  $\text{Ru}^{2+}/\text{Ru}^{3+}$  or  $\text{Ru}^{2.5+}/\text{Ru}^{2.5+}$ . To classify mixed-valent compounds, Robin and Day introduced a classification based on the degree of interaction between the two fragments and the delocalization of the odd electron.<sup>71,72</sup> Hereby, Robin-Day class I describes entirely valence-localized complexes, while class III refers to a completely delocalized system. The intermediate class II consists of complexes with predominantly localized valences, but with measurable electronic coupling.<sup>72,73</sup>

As expected, electron transfer can occur between the two redox centers in different oxidation states in Robin-Day class II complexes. Starting from a system  $\text{A}^+-\text{L}-\text{A}'$ , with A and A’ being the redox-active sites and L being a bridging ligand, electron transfer yields the valence tautomer  $\text{A}-\text{L}-\text{A}'^+$ . This electron transfer can be driven thermally or optically. Figure 1.4 a) shows a potential energy diagram including the potential curves of the tautomers  $\text{A}^+-\text{L}-\text{A}'$  and  $\text{A}-\text{L}-\text{A}'^+$ . In this picture, the  $\text{A}-\text{L}-\text{A}'^+$  configuration is an electronically excited state at the  $\text{A}^+-\text{L}-\text{A}'$  geometry. Hence, optical excitation with a suitable energy, typically in the near infrared region of the electromagnetic spectrum, can promote electron transfer from the reduced to the oxidized fragment resulting in an intervalence charge transfer (IVCT) absorption.<sup>66,73,74</sup>

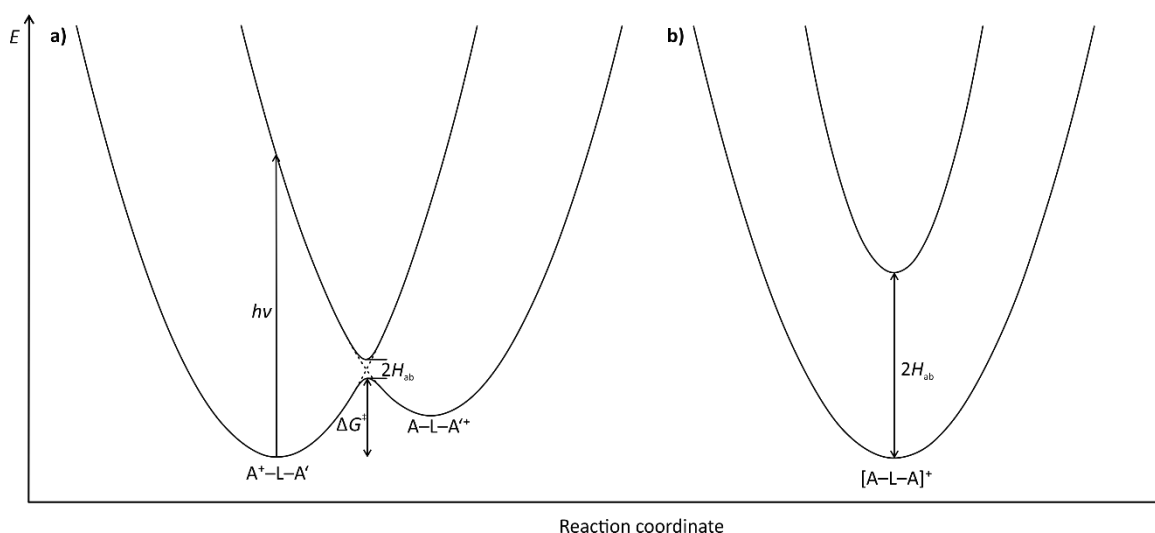


**Figure 1.4** Potential energy surfaces of **a)** a class II mixed-valent system and **b)** a delocalized class III system.

The electronic coupling  $H_{ab}$  between the redox centers in class II complexes can be deduced from energy and shape of the IVCT band:<sup>66</sup>

$$H_{ab} = \frac{2.05 \cdot 10^{-2} \sqrt{\epsilon_{max} \tilde{\nu}_{max} \tilde{\nu}_{1/2}}}{R} \quad (1.15)$$

With the maximum extinction coefficient of the IVCT band  $\epsilon_{max}$  in  $M^{-1} \text{ cm}^{-1}$ , the absorption maximum  $\tilde{\nu}_{max}$  in  $\text{cm}^{-1}$  and the full width at half maximum  $\tilde{\nu}_{1/2}$  in  $\text{cm}^{-1}$ .  $R$  describes the distance between the redox centers in Å.

In Robin-Day class III systems (Figure 1.4 b), no IVCT band is observed. Instead, optical excitation in the near infrared yields a charge-resonance transition that is associated with a substantially asymmetric absorption band broadened towards higher energies. The energy of this transition is directly correlated with the electronic coupling:<sup>66</sup>

$$H_{ab} = \frac{\tilde{\nu}_{max}}{2} \quad (1.16)$$

In an ideal mixed-valent system of class II, the theoretically expected full width at half maximum  $\tilde{\nu}_{1/2}$  depends on the energy of the absorption maximum  $\tilde{\nu}_{max}$ :<sup>73</sup>

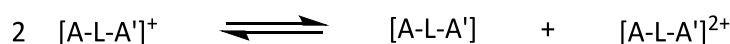
$$\tilde{\nu}_{1/2, theor} = \sqrt{2310 \tilde{\nu}_{max}} \quad (1.17)$$

This allows the introduction of a parameter  $\Gamma$  that allows to assign complexes to the different classes:<sup>73</sup>

$$\Gamma = 1 - (\tilde{\nu}_{1/2, obsvd} / \tilde{\nu}_{1/2, theor}) \quad (1.18)$$

For  $\Gamma = 0$ , the complex belongs to the very weakly coupled class I/II regime, at a value of 0.5 it is at the class II/III transition. Beyond that, a complex is considered entirely valence-delocalized.

Besides the IVCT band, also the splitting of the half-wave potentials  $\Delta E$  of consecutive redox processes with potentials  $E_1$  and  $E_2$  in the series  $A-L-A' \rightarrow [A-L-A']^+ \rightarrow [A-L-A']^{2+}$  is often consulted to evaluate the interaction between the redox centers. Frequently, the comproportionation constant is employed instead of the potential splitting:<sup>14,15,75</sup>



$$K_c = \frac{c^2([A-L-A']^+)}{c([A-L-A']) \cdot c([A-L-A']^{2+})} \quad (1.19)$$

$$K_c = \exp\left(-\frac{zF\Delta E}{RT}\right) \quad \text{with } \Delta E = E_2 - E_1 \quad (1.20)$$

However, the detection of a sizable splitting  $\Delta E$  cannot unambiguously be traced back to a large electronic coupling, as illustrated by equation 1.21:<sup>76</sup>

$$\Delta E = \Delta E_{stat} + \Delta E_{ind} + \Delta E_{ex} + \Delta E_{el} + \Delta E_{res} \quad (1.21)$$

Here,  $\Delta E_{stat}$  is the statistical contribution, which amounts to 36 mV in a system with two identical complex halves. The inductive contribution  $\Delta E_{ind}$  accounts for the influence that a redox process on one redox-active site has on all intramolecular bond strengths and thus on the redox potential

of the second redox center.  $\Delta E_{ex}$  accounts for the magnetic exchange contribution. The electrostatic contribution arising from the coulombic repulsion as a consequence of the accumulation of charges in a single molecule is taken into account with  $\Delta E_{el}$ . Only the resonance contribution  $\Delta E_{res}$  actually arises from the partial delocalization of the odd electron in the mixed-valent state but it is not accessible individually in electrochemical experiments. This is why the half-wave splitting  $\Delta E$  should not be used to estimate the electronic coupling in a mixed-valent system.<sup>76</sup>



## 1.4 CYCLOMETALATION

The concept of “cyclometalation” was introduced by Trofimenko in 1973<sup>77</sup> and refers to reactions of transition metal complexes, in which one of the ligands undergoes a metalation step yielding a chelate ring that contains a carbon-metal  $\sigma$ -bond.<sup>78</sup> Rather common are reactions at *ortho*-positions of phenyl rings attached to a ligand leading to the less common term “*ortho*-metalation”. Products of such cyclometalation reactions can be regarded as having a coordinating nitrogen formally exchanged by an isoelectronic carbon anion.

The cyclometalation step is usually accomplished under relatively mild conditions without the usage of highly reactive starting materials such as aryl lithium or Grignard reagents. Particularly in the last few decades, cyclometalation reactions have emerged as one of the most studied fields in organometallic chemistry since the products can show interesting luminescent properties or be suited as sensitizers in the dye-sensitized solar cell (DSSC, see section 1.5).<sup>46,79,80</sup> Despite that, the cyclometalation reaction itself still has some “black box” character to it, as the actual reaction mechanism is often unresolved.<sup>78,79</sup>

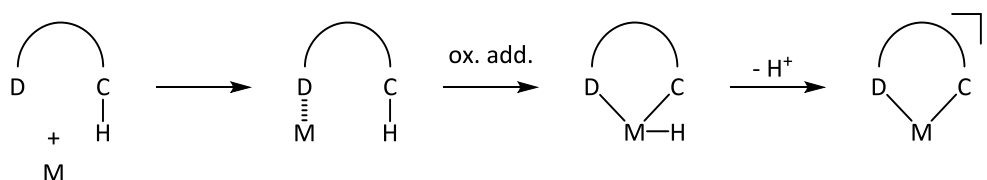


**Figure 1.5** Schematic representation of the cyclometalation of a C–H bond in the vicinity of a donor atom D.

Most commonly, aromatic C–H bonds in the proximity of a donor atom D are metalated. The accepted mechanism is sketched in Figure 1.5.<sup>79</sup> It involves coordination of the donor atom to the metal followed by oxidative addition of the pre-organized C–H bond yielding the metal in a twofold oxidized state as well as a carbanionic and a hydride ligand. The complex is deprotonated in the following giving the product with the metal in its original oxidation state. However, this mechanism is unlikely for cyclometalation reactions involving ruthenium(III) starting materials such as  $RuCl_3(tpy)$  ( $tpy = 2,2';6',2''$ -terpyridine), as the metal center would be forced to go through a  $Ru^V$  state. Instead, it is plausible that in the pre-organized state with an electropositive metal center in the vicinity, deprotonation occurs before or simultaneous to the M–C bond formation step circumventing the high oxidation state. The most frequently encountered metallacycle that is formed in these reactions is five-membered and entirely conjugated in the organic backbone. This probably results from a maximized degree of preorganization in these systems. Furthermore, cyclometalation of  $D^{\wedge}D^{\wedge}(C-H)$  ligands occurs much more readily than of  $D^{\wedge}(C-H)^{\wedge}D$  ligands which can be traced back to the chelating effect of the  $D^{\wedge}D$  anchor prior to cyclometalation.

In recent years, particularly cyclometalated polypyridine complexes of  $d^6$ ,  $d^8$  and  $d^{10}$  transition metal cations have gained much interest for their luminescent properties.<sup>79–82</sup> Additionally, cyclometalated polypyridine ruthenium(II) complexes have emerged as a new class of very promising class of DSSC sensitizers besides the benchmark thiocyanate-containing ruthenium dyes

(see section 1.5).<sup>42,46</sup> A few exemplary complexes are shown in Figure 1.6 along with the synthetic protocol of the respective cyclometalation step.

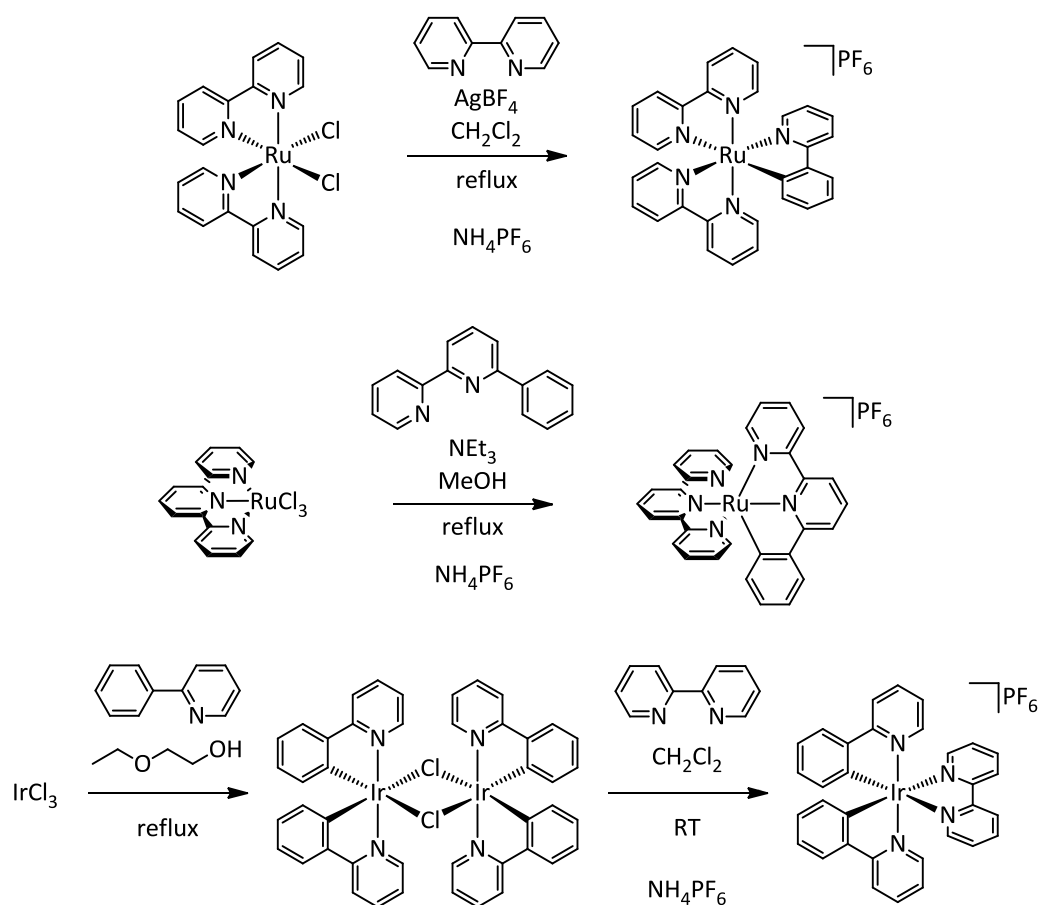


**Figure 1.6** Exemplary cyclometalation reactions yielding the prototype complexes  $[\text{Ru}(\text{bpy})_2(\text{ppy})]^+$ <sup>39</sup>,  $[\text{Ru}(\text{tpy})(\text{pbpy})]^+$ <sup>83,84</sup>,  $[\text{Ir}(\text{ppy})_2]_2\text{Cl}_2$ <sup>85</sup> and  $[\text{Ir}(\text{bpy})(\text{ppy})_2]^+$ <sup>86</sup> (ppyH = 2-phenylpyridine, pbpyH = 6-phenyl-2,2'-bipyridine).

Comparing the spectroscopic, electrochemical and electronic properties of cyclometalated polypyridine ruthenium complexes to those of their non-cyclometalated counterparts, a few general trends can be established:<sup>45,79,87,88</sup>

- Cyclometalation reduces the overall charge of the complex by one unit per cyclometalating site. This greatly affects the solubility of cyclometalated complexes.
- Cyclometalating ligands are less prone to nucleophilic ligand substitution under basic or neutral conditions but can be substituted in the presence of strong acids.
- The high  $\sigma$ -donor strength of cyclometalating ligands increases the ligand field splitting and pushes metal-centered excited states to higher energies.
- Due to the overall increase of electron density at the metal center, it is oxidized at substantially lower potentials than its non-cyclometalated pyridine analogue. Reduction of the remaining polypyridines on the other hand requires only slightly higher potentials. This is associated with an overall shift of the frontier orbitals to higher energies.

- Additionally, cyclometalation reduces the local symmetry around the metal center (e.g.  $\text{RuN}_5\text{C}$  instead of  $\text{RuN}_6$ ) which results in the metal's  $d$  orbitals to be shifted apart energetically. This is accompanied by a substantially broadened absorption spectrum as the number of allowed optical transitions is drastically increased and their transition energies are spread over a large portion of the visible range of the electromagnetic spectrum.

In summary, cyclometalation is a powerful tool to manipulate the electronic properties of a given complex. However, the synthesis can be challenging as the functional group tolerance of the cyclometalation step is limited.<sup>78</sup>

## 1.5 DYE-SENSITIZED SOLAR CELL

The dye-sensitized solar cell (DSSC) was first introduced by O'Regan and Grätzel in 1991.<sup>22</sup> Typically, it is composed of a light-harvesting dye, often referred to as sensitizer S, coated onto a nanoporous semiconducting carrier material such as TiO<sub>2</sub>. The semiconductor itself is mounted on a transparent conductor like fluorine-doped tin oxide (FTO) as anode. As cathode, usually silver or platinum is employed. The gap between the electrodes is filled with an electrolyte containing a redox shuttle. The working principle of a DSSC is depicted in Figure 1.7 a). Upon irradiation with visible light, the sensitizer is promoted into a photo-excited state S\*. This state has sufficient reducing power to inject an electron into the conducting band of the semiconductor (1). The injected electrons are collected at the anode and transferred into the electric circuit (2). At the sensitizer/electrolyte interface, the oxidized sensitizer S<sup>+</sup> is reduced to its original state S by the surrounding redox mediator (3). After diffusing to the cathode, the redox mediator is regenerated at the electrode surface closing the electric circuit (4). However, not only productive steps are possible within a DSSC. Several parasitic processes reducing the overall performance of a DSSC are known. The photo-excited sensitizer can evolve into its ground state without electron injection (5). Additionally, as the TiO<sub>2</sub> surface is in contact with the sensitizer and the electrolyte, recombination processes between injected electrons and oxidized dye (6) or redox mediator (7) molecules can occur. Finally, the photo-excited dye can recombine with oxidized redox mediator molecules (8). For an efficient performance of a DSSC, the rate constants of the productive steps 1 – 4 must surpass those of the recombination processes 5 – 8.<sup>23,46</sup>

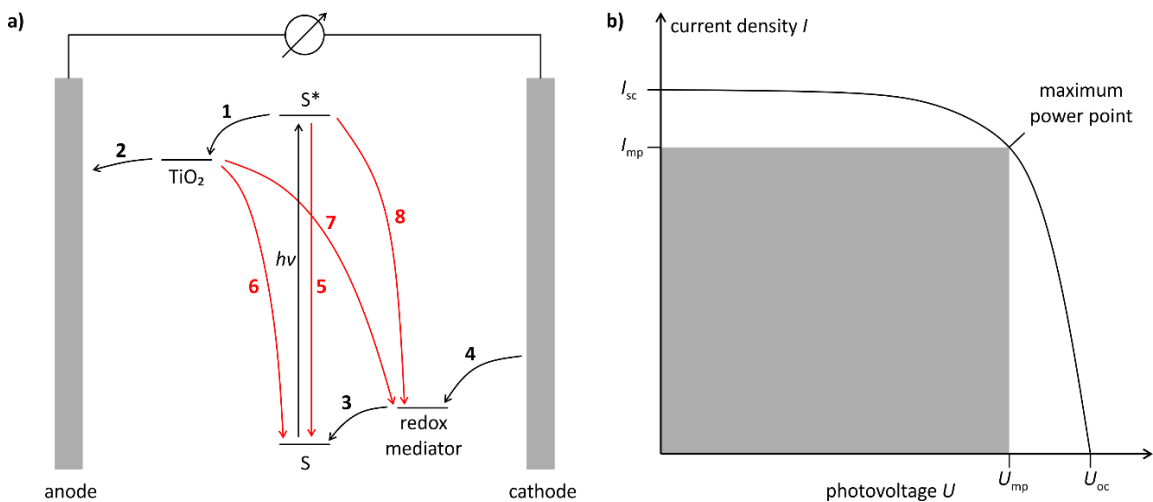


**Figure 1.7 a)** Schematic working principle of the DSSC. Black arrows indicate productive electron transfer steps, red arrows show parasitic recombination processes. **b)** Current density-voltage plot of a typical DSSC including short circuit and maximum power current  $I_{sc}$  and  $I_{mp}$ , open circuit and maximum power voltage  $U_{oc}$  and  $U_{mp}$  as well as maximum output power (area of the grey rectangle).

The efficiency  $\eta$  of a DSSC is measured in terms of the output power  $P_{out}$  with respect to the input power  $P_{in}$  and is usually given under standardized conditions with normalized solar light irradiation (Air Mass 1.5,  $P_{in} = 1000 \text{ W m}^{-2}$ ). The output power obtainable from a DSSC is given by

the product of photovoltage  $U$  and current density  $I$ , as displayed in the current density-voltage plot in Figure 1.7 b, maximizing at the maximum power point:

$$\eta = \frac{P_{out}}{P_{in}} = \frac{U_{mp}I_{mp}}{P_{in}} \quad (1.22)$$

The fill factor  $ff$  and the wavelength-dependent incident photon-to-current conversion efficiency (IPCE) are two further quantities characterizing the performance of a DSSC. The fill factor describes the shape of the current density-voltage curve and is given by:

$$ff = \frac{U_{mp}I_{mp}}{U_{oc}I_{sc}} \quad (1.23)$$

The IPCE is determined as the ratio between the number of electrons collected per number of photons irradiated at a given wavelength:<sup>23,46</sup>

$$IPCE(\lambda) = \frac{I_{sc}(\lambda)}{P_{in}(\lambda)} \frac{1}{\lambda} \frac{hc}{e} \quad (1.24)$$

Despite the sophisticated definition of all relevant parameters describing the performance of a DSSC, a standard reference dye is usually measured alongside the studied compounds as cell setup, solvents, additives or even impurities in any of the components vary from laboratory to laboratory making the obtained results usually difficult to compare.<sup>23,46</sup> In order to optimize the performance of a DSSC, all its components have to be adjusted to each other. Considering the amount of sensitizers, electrolytes, additives, co-adsorbents *etc.* known to date, finding the perfect DSSC configuration is a nearly impossible task especially because many of the key steps are interfacial reactions which are not too well understood. However, it is possible to establish criteria that make a certain component suitable for a DSSC application. In the following, these criteria will be discussed for the sensitizer.

First and foremost, a sensitizer needs to be capable of effectively harvesting solar light with a wavelength shorter than 900 nm to ensure maximum usage of the incident energy.<sup>23,25,46</sup> Additionally, it must provide one or more anchoring groups allowing for tight and irreversible binding to the semiconductor surface and to ensure efficient electron injection into the conduction band.<sup>46</sup> This is usually accomplished by introduction of  $-\text{CO}_2\text{H}$  or  $-\text{PO}_3\text{H}$  groups that are known to bind firmly to  $\text{TiO}_2$ . Moreover, the molecular frontier orbitals must be geometrically suited to allow efficient charge injection into  $\text{TiO}_2$  and charge recombination with the electrolyte.<sup>42</sup> This means, that the lowest unoccupied orbital (LUMO) should be found in proximity to the anchor groups on the anchoring ligand, while the highest occupied orbital (HOMO) points away from the semiconductor surface. Additionally, the energy of the LUMO must be higher than the Fermi edge of the semiconductor and the HOMO energy lower than that of the redox-active electrolyte to make sure electron transfer is thermodynamically feasible. Last, but not least, sensitizers must be thermally, photochemically, and electrochemically stable under the conditions present in the DSSC to avoid decomposition and loss of efficiency over time.

For ruthenium-based dyes, anchoring to the  $\text{TiO}_2$  surface is typically accomplished by 4,4'-dicarboxy-2,2'-bipyridine (dcbpy) or 4,4',4''-tricarboxy-2,2';6',2''-terpyridine (tctpy) ligands that also provide LUMOs with suited geometry and energy. On the opposite site facing away from the semiconductor surface, thiocyanato ligands seemed to be most suited for a long time. In this

category, the sensitizers with the best DSSC performances are **N719**<sup>89</sup> and the so-called black dye<sup>25</sup> (Figure 1.8 and Table 1.1) reaching external efficiencies of more than 10 %. In recent years, cyclometalated ruthenium complexes have entered the field. In these complexes, the cyclometalating ligand substitutes the thiocyanato ligands circumventing decomposition reactions arising from the presence of monodentate ligands to a great extent. **YE05** is the most prominent representative of this class with an efficiency of 10.1 % (Figure 1.8 and Table 1.1).<sup>42</sup> Also outside the field of ruthenium-based dyes, some remarkable compounds have been developed. The highest performance with an entirely metal-free sensitizer was reached with **C219** containing triarylamine and thiophene subunits ( $\eta = 10.1$  %).<sup>90</sup> However, the record holding class of sensitizers is that of zinc porphyrins. There, **SM315** is at the top of the list with an efficiency of 13.0 %<sup>91</sup> closely followed by **YD2-o-C8** ( $\eta = 12.3$  %).<sup>92</sup> All these sensitizers are depicted in Figure 1.8 and their performance parameters are summarized in Table 1.1.

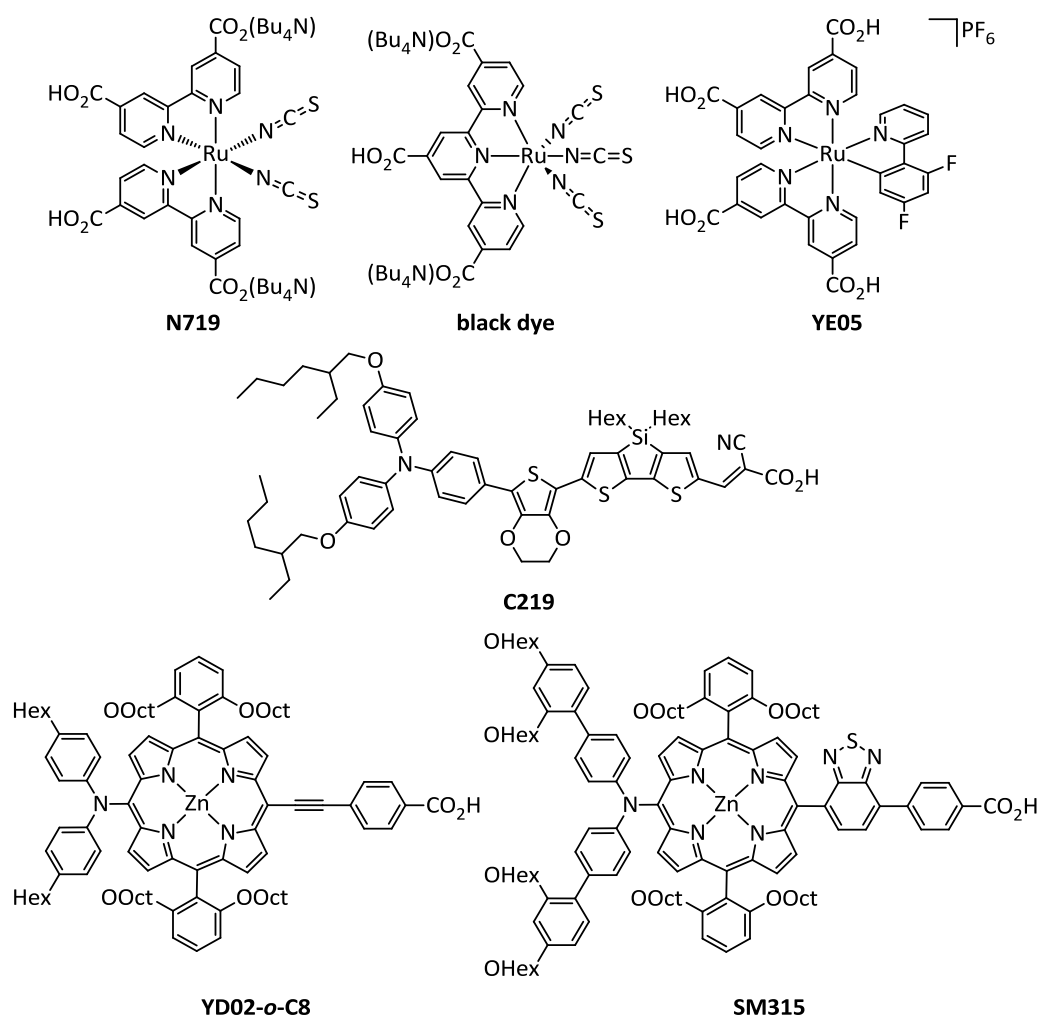


**Figure 1.8** Selected state-of-the-art DSSC sensitizers with efficiencies greater than 10 % reported in the literature (**N719**<sup>89</sup>, **black dye**<sup>25</sup>, **YE05**<sup>42</sup>, **C219**<sup>90</sup>, **YD02-o-C8**<sup>92</sup>, **SM315**<sup>91</sup>).



**Table 1.1** Performance parameters of selected state-of-the-art DSSC sensitizers reported in the literature (**N719**<sup>89</sup>, **black dye**<sup>25</sup>, **YE05**<sup>42</sup>, **C219**<sup>90</sup>, **YD02-o-C8**<sup>92</sup>, **SM315**<sup>91</sup>).

	$V_{oc}$ (V)	$I_{sc}$ / mA cm <sup>-2</sup>	$ff$	$\eta$ / %
<b>N719</b> <sup>89</sup>	0.846	17.73	0.72	11.2
<b>black dye</b> <sup>25</sup>	0.720	20.53	0.70	10.4
<b>YE05</b> <sup>42</sup>	0.800	17.00	0.74	10.1
<b>C219</b> <sup>90</sup>	0.770	17.94	0.73	10.1
<b>YD02-o-C8</b> <sup>92</sup>	0.935	17.66	0.74	12.3
<b>SM315</b> <sup>91</sup>	0.910	18.10	0.78	13.0



## 2 AIM OF THE WORK

The synthesis and study of mixed-valent complexes has intrigued chemists for a long time as it provides insight into the underlying physicochemical principles. Particularly interesting in this context are structurally asymmetric, but electronically symmetric complexes. Such systems were previously studied in the research group of Prof. Katja Heinze by means of the amide-bridged bis(terpyridine)ruthenium complexes **[I a]**<sup>5+</sup> and **[I b]**<sup>5+</sup> as well as several amide-bridged ferrocene oligomers **[II]**<sup>+</sup> (Figure 2.1).<sup>93–96</sup> While electronic coupling between the metal centers could be detected for the oligoferrocenes, no measurable electronic communication was found for the ruthenium complexes. This was mainly attributed to the bridge's frontier orbitals being energetically too separated from the metal  $d_{\pi}$  orbitals which leads to high tunneling barriers for thermal and optical electron transfer (see section 3.1).<sup>96</sup>

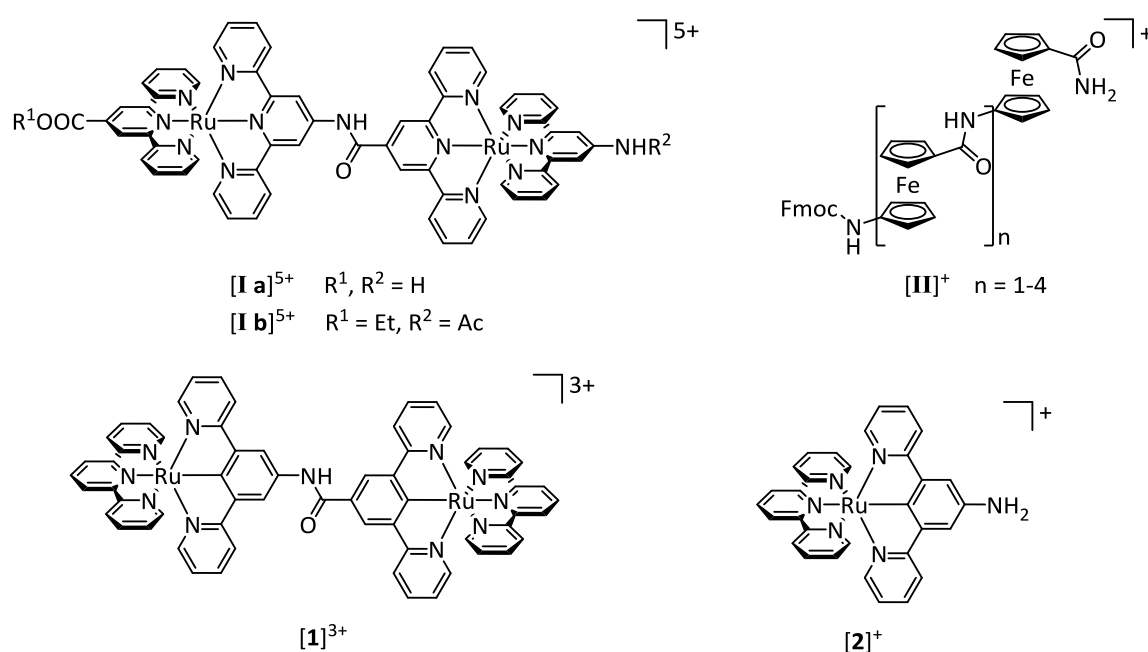


**Figure 2.1** Chemical structures of exemplary literature-known mixed-valent systems **[I a]**<sup>5+</sup>, **[I b]**<sup>5+</sup> and **[II]**<sup>+</sup> developed by the Heinze group)<sup>93–96</sup> as well as key objective structures of this work **[1]**<sup>3+</sup> and **[2]**<sup>+</sup>.

However, preliminary density functional theoretical results suggested that these tunneling barriers can be lowered using a bis(cyclometalating) bridging ligand as in **[1]**<sup>3+</sup> as this shifts the bridge's highest occupied orbital into the energy range of the metal  $d_{\pi}$  orbitals.

*A primary objective of this work is the synthesis and characterization of a dinuclear bis(cyclometalated) polypyridine ruthenium complex as shown in Figure 2.1.*

This requires the development of suitable synthon such as **[2]**<sup>+</sup> that allows the formation of an amide bond between the two complex halves as the final step. While the introduction of carboxy groups on cyclometalating ligands is well-established,<sup>87,88,97</sup> no primary or secondary amine or amide functional groups have been used on ligands involved in cyclometalation reactions to date.

*Hence, a robust synthetic protocol will be elaborated that enables the cyclometalation step in high yields and provides access to a cyclometalated bis(tridentate) ruthenium complex bearing a free  $-NH_2$  group.*

In contrast to the cyclometalated complexes of iridium, all literature-known cyclometalated polypyridine ruthenium complexes have been shown to be only very weakly emissive at room temperature.<sup>97–100</sup> Accomplishing the synthesis of  $-NH_2$  carrying mononuclear complexes also enlarges the pool of accessible functional groups to strongly electron donating ones and allows to study the dependence of the emission on the electronics of the substituents in more detail.

*By a combination of theoretical and spectroscopic techniques, the excited state properties of cyclometalated bis(tridentate) ruthenium complexes will be studied in close detail particularly investigating the dependence of occurring non-emissive deactivation channels on the functional groups. Additionally, the excited state properties of the known complex **[I b]**<sup>5+</sup> will be studied in more detail.*

*Ultimately, as cyclometalated polypyridine ruthenium complexes have been shown to be suited for sensitizing  $TiO_2$ , the impact of an amino group on the cyclometalating ligand will be studied.*

The redox-activity of the  $-NR_2$  group might help stabilize the complex after charge injection and suppress parasitic charge recombination processes.<sup>101</sup>

### 3 RESULTS AND DISCUSSION

All findings of this dissertation have been published/submitted as scientific articles in/to peer-reviewed chemistry journals. These articles will be reprinted in the following with permission of the respective publishers.

The synthesis and characterization of the dinuclear bis(terpyridine)ruthenium(II) complex **[I b]**<sup>4+</sup> with high electronic symmetry despite an intrinsic structural asymmetry is presented in section 3.1 *“Dual Emission and Excited-State Mixed-Valence in a Quasi-Symmetric Dinuclear Ru–Ru Complex”*. While the study of the ground state properties of **[I b]**<sup>4+</sup> and **[I b]**<sup>5+</sup> has already been carried out as part of the diploma thesis of Christoph Kreitner, the dual emission of photo-excited **[I b]**<sup>4+</sup> was discovered during the time of this dissertation. The unusual dual emission was traced back to two energetically close-lying and thermally equilibrated excited states, one being a <sup>3</sup>MLCT state and the second a triplet charge-separated (<sup>3</sup>CS) state. The electronic implications of this observation are discussed.

In section 3.2, *“Understanding the Excited State Behavior of Cyclometalated Bis(tridentate)ruthenium(II) Complexes: A Combined Experimental and Theoretical Study”*, the synthesis and characterization of the two cyclometalated complexes **[Ru(dpb-NHAc)(tpy-COOEt)]<sup>+</sup>** and **[Ru(dpb-COOEt)(tpy-NHAc)]<sup>+</sup>** is presented. The electronic transitions responsible for the visible range absorption bands of the UV-Vis spectrum are studied using a combination of resonance Raman spectroscopy and theoretical methods. Additionally, an attempt at understanding the different emissive properties of the two complexes is undertaken based on variable-temperature measurements of the emission quantum yields which are supported by density functional theory (DFT) calculations.

The synthesis of the target molecules **[1]**<sup>2+</sup> and **[2]**<sup>+</sup> is presented in section 3.3 along with several other substituted **[Ru(dpb-R)(tpy)]<sup>+</sup>** complexes (R = NHAc, NH<sub>2</sub>, COOEt and COOH, respectively). The article *“The Photochemistry of Mono- and Dinuclear Cyclometalated Bis(tridentate)ruthenium(II) Complexes: Dual Excited State Deactivation and Dual Emission”* focusses on the elucidation of the excited state deactivation processes on the basis of temperature-dependent emission quantum yield measurements and highlights how two parasitic triplet states flank the emissive <sup>3</sup>MLCT state to cause efficient emission quenching at room temperature in all complexes of the **[Ru(dpb)(tpy)]<sup>+</sup>** type. Furthermore, the dinuclear complex **[1]**<sup>3+</sup> was found to exhibit electronic communication between the metal centers in the mixed-valent state, while no coupling was found in the photo-excited state of **[1]**<sup>2+</sup>. The degree of electronic coupling in the mixed-valent state is estimated and the marked difference between mixed-valent **[1]**<sup>3+</sup> and photo-excited state of **[1]**<sup>2+</sup> is explained.

The article *“Strongly Coupled Cyclometalated Ruthenium Triarylamine Chromophores as Sensitizers for DSSCs”* in section 3.4 demonstrates the usage of **[Ru(dpb-NR<sub>2</sub>)(tpy(-COO)<sub>3</sub>)]<sup>2-</sup>** (R = aryl) complexes as sensitizers in TiO<sub>2</sub>-based DSSCs in combination with standard iodide/triiodide and novel polypyridine cobalt-based electrolytes and traces the trends in the solar cell efficiencies back to insufficiencies in the dye regeneration rates after charge injection into the semiconductor.

This publication was developed in a joint effort of Christoph Kreitner, who provided the ruthenium complexes, and Andreas Mengel, who synthesized the cobalt electrolytes and constructed and evaluated the solar cells.

Section 3.5, “*Excited State Decay of Cyclometalated Polypyridine Ruthenium Complexes: Insight from Theory and Experiment*” presents a perspective article following an invitation by the publishers of the journal *Dalton Transactions* of the Royal Society of Chemistry. It summarizes the current state of research in the field of luminescent cyclometalated ruthenium(II) complexes discussing common features and differences in the non-radiative decay between complexes with  $[\text{Ru}(\text{N}^{\wedge}\text{N})_2(\text{N}^{\wedge}\text{C})]^+$ ,  $[\text{Ru}(\text{N}^{\wedge}\text{N}^{\wedge}\text{N})(\text{N}^{\wedge}\text{C}^{\wedge}\text{N})]^+$  and  $[\text{Ru}(\text{N}^{\wedge}\text{N}^{\wedge}\text{N})(\text{N}^{\wedge}\text{N}^{\wedge}\text{C})]^+$  coordination cages. It recapitulates the findings presented in sections 3.2 and 3.3 and puts them into the context of other publications involving cyclometalated  $[\text{Ru}(\text{N}^{\wedge}\text{N}^{\wedge}\text{N})(\text{N}^{\wedge}\text{C}^{\wedge}\text{N})]^+$  complexes. Finally, predictions about the temperature-dependence of  $[\text{Ru}(\text{N}^{\wedge}\text{N})_2(\text{N}^{\wedge}\text{C})]^+$  and  $[\text{Ru}(\text{N}^{\wedge}\text{N}^{\wedge}\text{N})(\text{N}^{\wedge}\text{N}^{\wedge}\text{C})]^+$  complexes are made along with suggestions how to improve the quantum yields of such complexes in general.

Not only second and third row transition metal complexes are known for their manifold luminescent properties. Also first row complexes have been shown to emit at room temperature, but such observations are rarer. The article “[ $\text{Cr}(\text{ddpd})_2$ ]<sup>3+</sup>: A Molecular, Water-Soluble, Highly NIR-Emissive Ruby Analogue” in section 3.6 presents an example of a polypyridine chromium complex with an intense near-infrared emission. The synthetic and spectroscopic work shown in this publication has been carried out by Sven Otto, Christoph Kreitner assisted in the setup and evaluation of the DFT calculations particularly evolving around the accurate description of the doublet and quartet excited states.

### Comments on the DFT methodology

Since all presented findings rely heavily on the quality of the results obtained from quantum chemical calculations, a few thoughts on density functional theory and the choice of the level of theory will be collected here. The employed level of theory varies slightly between the DFT calculations presented in the different publications. Although there is no right or wrong level of theory, when it comes to DFT, several key components evolved during these studies as being crucial to ensure sufficiently accurate results. In general, B3LYP serves well in the description of transition metal complexes.<sup>102</sup> While geometry optimizations are typically less dependent on the choice of functional, particularly charge transfer processes are very sensitive to the amount of Hartree-Fock exchange considered in the respective functional.<sup>103</sup> This is why GGA functionals such as BPE or BP fail to describe the electronic transitions of polypyridine ruthenium complexes despite the proper description of their geometries (section 3.2). Interestingly, calculations on cyclometalated polypyridine ruthenium complexes using the popular range-separated CAM-B3LYP<sup>104</sup> functional yielded fairly inaccurate transitions judging from the vertical excitation energies and the orbital parentage of the respective transition. However, this is not true for all sorts of transition metal complexes.<sup>105</sup> The best description of the electronic transitions was obtained employing B3LYP and PBE0.<sup>106</sup> B3LYP was used in most calculations as the relative energies of different electronic states were found to be in better agreement with the experimental



data than with PBE0 (section 3.2). Concerning the choice of basis set, ideally it is as large as possible. For geometry optimizations and single point energies, a split-valence double- $\xi$  basis set including polarization functions on all non-hydrogen atoms is usually sufficient and manageable in terms of computational cost.<sup>107-109</sup> For the calculation of electronic properties (electronic transitions, EPR parameters etc.), it is highly advised to use larger basis sets of triple- $\xi$  quality.<sup>107-109</sup> To further improve the description of long-range charge-separated states such as  $^3\text{MLCT}$  or  $^3\text{LL}'\text{CT}$  states, an inclusion of a continuum solvation model is helpful and important, as it stabilizes the charge separation to some extent.<sup>103,110</sup> Additionally, relativistic effects must not be neglected for the heavy transition metal atoms. Inclusion of such can be done using the effective core potential approach<sup>111</sup>, or, more accurately, with the zeroth order regular approximation.<sup>112</sup> This typically also requires a refinement of the integration grids, as basis functions can become fairly steep in the proximity of a heavy atom. Interestingly, the incorporation of dispersion interactions in the calculation of the electronic properties of cyclometalated polypyridine ruthenium complexes does not seem to be necessary. In fact, geometries optimized with the D3BJ dispersion correction<sup>113</sup> differed more strongly from the crystal structure than those without dispersion correction (section 3.2).

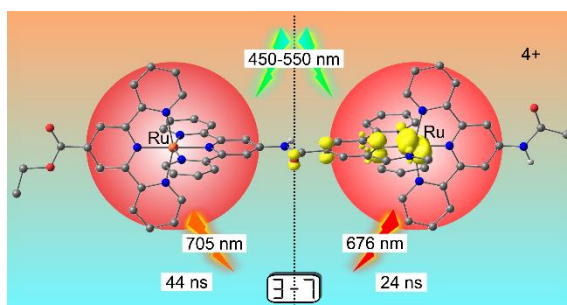
The individual contributions of all authors are expressed in more detail at the beginning of the section of the respective article.



### 3.1 DUAL EMISSION AND EXCITED-STATE MIXED-VALENCE IN A QUASI-SYMMETRIC DINUCLEAR RU–RU COMPLEX

Christoph Kreitner, Markus Grabolle, Ute Resch-Genger and Katja Heinze

*Inorg. Chem.* **2014**, *53*, 12947–12961.



The bimetallic dipeptide  $[(\text{EtOOC-tpy})\text{Ru}(\text{tpy-NHCO-tpy})\text{Ru}(\text{tpy-NHCOCH}_3)]^{4+}$  shows dual emission in fluid solution at room temperature arising from two equilibrating triplet states centered on the C- and N-terminal ruthenium sites. The  $\text{Ru}^{\text{II}}$  and  $\text{Ru}^{\text{III}}$  centers in these triplet valence isomers are electronically coupled through a bridging radical anion. In contrast the mixed-valent complex  $[(\text{EtOOC-tpy})\text{Ru}(\text{tpy-NHCO-tpy})\text{Ru}(\text{tpy-NHCOCH}_3)]^{5+}$  with a neutral bridging ligand is valence-localized. The equilibrating excited triplet states can be reduced by  $\text{PhNMe}_2$  via a  $\text{N}\cdots\text{HN}$  hydrogen bridge.

#### Author Contributions

The synthesis of complexes  $\mathbf{1}^{4+}$  and  $\mathbf{2}^{2+}$  and characterization of the ground state of  $\mathbf{2}^{2+}$ ,  $\mathbf{1}^{4+}$  and  $\mathbf{1}^{5+}$  has been conducted by Christoph Kreitner during his diploma thesis. However, DFT calculations and emission studies of  $\mathbf{1}^{4+}$  discovering the dual emission and excited-state mixed-valence have been performed by Christoph Kreitner during his PhD thesis. The excited state lifetime measurements which have been carried out by Markus Grabolle and Ute Resch-Genger at the *Bundesanstalt für Materialforschung und -prüfung* (BAM) in Berlin, Germany. Hence, the key findings of the manuscript were acquired during the PhD thesis. The manuscript was written by Christoph Kreitner (90 %) and Katja Heinze (10 %).

#### Supporting Information

for this article is found at pp. 175 (excluding Cartesian Coordinates of DFT-optimized geometries). For full Supporting Information, refer to <http://pubs.acs.org/doi/suppl/10.1021/ic5020362>.

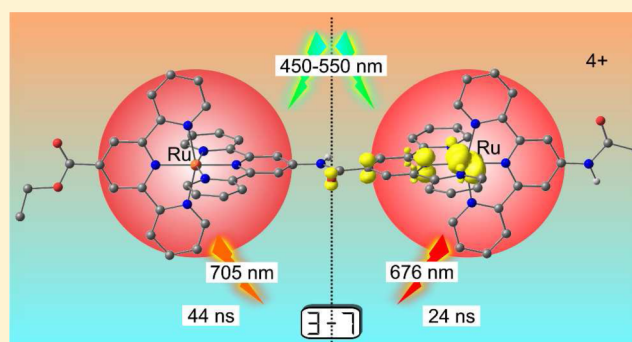
„Reprinted with permission from Kreitner, C.; Grabolle, M.; Resch-Genger, U.; Heinze, K. *Inorg. Chem.* 2014, *53*, 12947–12961. Copyright 2013 American Chemical Society.”

## Dual Emission and Excited-State Mixed-Valence in a Quasi-Symmetric Dinuclear Ru–Ru Complex

Christoph Kreitner,<sup>†,‡</sup> Markus Grabolle,<sup>§</sup> Ute Resch-Genger,<sup>§</sup> and Katja Heinze<sup>\*,†</sup><sup>†</sup>Institute of Inorganic and Analytical Chemistry, Johannes Gutenberg-University of Mainz, Duesbergweg 10–14, 55128 Mainz, Germany<sup>‡</sup>Graduate School Materials Science in Mainz, Staudingerweg 9, 55128 Mainz, Germany<sup>§</sup>Federal Institute for Materials Research and Testing (BAM), Division 1.5, Richard-Willstätter-Str. 11, 12489 Berlin, Germany

## Supporting Information

**ABSTRACT:** The synthesis and characterization of the new dinuclear dipeptide  $[(\text{EtOOC-tpy})\text{Ru}(\text{tpy-NHCO-tpy})\text{Ru}(\text{tpy-NHCOCH}_3)]^{4+}$   $3^{4+}$  of the bis(terpyridine)ruthenium amino acid  $[(\text{HOOC-tpy})\text{Ru}(\text{tpy-NH}_2)]^{2+}$   $1^{2+}$  are described, and the properties of the dipeptide are compared to those of the mononuclear complex  $[(\text{EtOOC-tpy})\text{Ru}(\text{tpy-NHCOCH}_3)]^{2+}$   $4^{2+}$  carrying the same functional groups.  $3^{4+}$  is designed to serve a high electronic similarity of the two ruthenium sites despite the intrinsic asymmetry arising from the amide bridge. This is confirmed via UV–vis absorption and NMR spectroscopy as well as cyclic voltammetry.  $4^{2+}$  and  $3^{4+}$  are emissive at room temperature, as expected. Moreover,  $3^{4+}$  exhibits dual emission from two different triplet states with different energies and lifetimes at room temperature. This is ascribed to the presence of a unique thermal equilibrium between coexisting  $[\text{Ru}^{\text{II}}(\text{tpy-NHCO-tpy}^-)\text{Ru}^{\text{III}}]$  and  $[\text{Ru}^{\text{III}}(\text{tpy-NHCO-tpy}^-)\text{Ru}^{\text{II}}]$  states leading to an unprecedented excited-state  $\text{Ru}^{\text{II}}\text{Ru}^{\text{III}}$  mixed-valent system via the radical anion bridge  $\text{tpy-NHCO-tpy}^-$ . The mixed-valent cation  $3^{5+}$ , on the other hand, shows no measurable interaction of the  $\text{Ru}^{\text{II}}\text{Ru}^{\text{III}}$  centers via the neutral bridge  $\text{tpy-NHCO-tpy}$  (Robin–Day class I). Reduction of  $3^{4+}$  to the radical cation  $3^{3+}$  by decamethylcobaltocene is bridge-centered as evidenced by rapid-freeze electron paramagnetic resonance spectroscopy. Interestingly, all attempts to observe  $3^{3+}$  via NMR and UV–vis absorption spectroscopy only led to the detection of the diamagnetic complex  $3\text{-H}^{3+}$  in which the bridging amide is deprotonated. Hence  $3\text{-H}^{3+}$  (and  $4\text{-H}^+$ ) appear to reduce protons to dihydrogen. The ease of single and double deprotonation of  $4^{2+}$  and  $3^{4+}$  to  $4\text{-H}^+$ ,  $3\text{-H}^{3+}$ , and  $3\text{-}2\text{H}^{2+}$  was demonstrated using a strong base and was studied using NMR and UV–vis absorption spectroscopies. The equilibrating excited triplet states of  $3^{4+}$  are reductively quenched by *N,N*-dimethylaniline assisted by hydrogen bonding to the bridging amide.



## INTRODUCTION

The controlled assembly of multinuclear metal complexes incorporating electrochemically and photochemically active moieties is of great interest for the fundamental understanding of energy and electron transfer<sup>1–3</sup> on a molecular level and the modeling of natural photosynthesis<sup>4</sup> as well as for the design of molecular wires<sup>5,6</sup> and switches,<sup>7,8</sup> photocatalysts,<sup>9–11</sup> and information storage devices.<sup>12</sup> (Polypyridine)ruthenium(II) complexes, especially the archetype compound  $[\text{Ru}(\text{bpy})_3]^{2+}$  (bpy = 2,2'-bipyridine), have found wide application in such arrays due to their high stability and outstanding photochemical properties. Further applications of this class of compounds comprise photosensitizers in dye-sensitized solar cells<sup>13</sup> and emitters in light-emitting electrochemical cells.<sup>14</sup>

$[\text{Ru}(\text{bpy})_3]^{2+}$  features unique optical and electrochemical properties.<sup>15,16</sup> The energetically low-lying  $\pi^*$  orbitals of the heteroaromatic ligands allow for a metal-to-ligand charge transfer ( $^1\text{MLCT}$ ) excitation upon irradiation. Rapid intersystem crossing (ISC) leads to population of  $^3\text{MLCT}$  states.<sup>17</sup>

The lowest of these  $^3\text{MLCT}$  excited states is emissive at room temperature and exhibits a reasonably long lifetime ( $\Phi = 0.095$ ,  $\tau = 855 \mu\text{s}$  at 298 K in  $\text{CH}_3\text{CN}$ ).<sup>16,18</sup> Because of the use of chelating ligands this complex has a fairly high thermal and chemical stability.<sup>19,20</sup>

The use of  $[\text{Ru}(\text{tpy})_2]^{2+}$  (tpy = 2,2':6',2''-terpyridine) instead of  $[\text{Ru}(\text{bpy})_3]^{2+}$  leads to structurally similar complexes,<sup>21,22</sup> but these compounds have been far less studied and applied in photochemical setups than their bpy analogues. This is due to low emission quantum yields and short excited-state lifetimes at room temperature in fluid solution because the  $^3\text{MLCT}$  states can undergo thermal depopulation via  $^3\text{MC}$  states followed by vibrational relaxation and ISC to the ground state.<sup>1,23–25</sup> This hampers the use of these complexes in the fields of photoelectron or energy transfer. Several attempts have been carried out to increase emission lifetimes and quantum

Received: August 21, 2014

Published: November 20, 2014

yields of bis(tridentate)ruthenium(II) complexes. Increasing the bite angle (N–Ru–N) within the ligands raises the energy of the  $^3\text{MC}$  states through better overlap of ligand and metal orbitals thus shifting the thermal population in favor of the  $^3\text{MLCT}$  states.<sup>26–30</sup> Functionalization of the parent  $[\text{Ru}(\text{tpy})_2]^{2+}$  in the 4' position with push–pull substituents has a similar effect: electron-withdrawing substituents lower the energy of the  $^3\text{MLCT}$  states, while electron-donating groups increase the energy of the  $^3\text{MC}$  states.<sup>24,25,31</sup> Emission can be intensified by several orders of magnitude via these approaches.

A major advantage of  $[\text{Ru}(\text{tpy})_2]^{2+}$  over  $[\text{Ru}(\text{bpy})_3]^{2+}$  for functionalization in the ligand backbone is the lack of a stereocenter in the former. This is important for the development of multinuclear assemblies as it simplifies synthesis and purification significantly. It becomes evident considering the stereogenic character of  $[\text{Ru}(\text{bpy})_3]^{2+}$ . Its  $D_3$  symmetry leads to enantiomers in the parent complex ( $\Delta$ ,  $\Lambda$ ). Complexes of the type  $[\text{Ru}(\text{bpy})(\text{bpy-R})(\text{bpy-R}') ]^{2+}$ , with  $\text{bpy-R}$  and  $\text{bpy-R}'$  carrying different functional groups, result in a mixture of diastereomers that requires sophisticated methods to be separated or avoided.<sup>32–35</sup> Employing  $[\text{Ru}(\text{bpy})_3]^{2+}$  in dinuclear systems gives rise to three stereoisomers ( $\Delta\Delta$ , meso- $\Delta\Lambda$ , and  $\Lambda\Lambda$ ) that can only be circumvented under certain conditions.<sup>33</sup>

This is why we employed donor- and acceptor-functionalized tpy ligands to develop emissive complexes of the type  $[(\text{R-tpy})\text{Ru}(\text{tpy-NHCO-tpy})\text{Ru}(\text{tpy-R}') ]^{2+}$ .<sup>31,36,37</sup> Using the functional groups  $\text{R} = \text{COOH}$  and  $\text{R}' = \text{NH}_2$  gives rise to the metallo amino acid  $1^{2+}$  in which the metal is placed in one line with the functional groups thus maximizing the ligands' electronic effects. Amino acid building blocks of this type allow the synthesis of oligopeptides in which ruthenium takes a unique position by enhancing the electronic communication between the building blocks,<sup>31,38–40</sup> which is not observed when the metal is placed in a side chain of the peptide structure.<sup>41–43</sup>

In the work presented herein, we demonstrate the synthesis and characterization of a protected dinuclear dipeptide  $[(\text{R-tpy})\text{Ru}(\text{tpy-NHCO-tpy})\text{Ru}(\text{tpy-R}') ]^{4+}$  of the ruthenium amino acid  $1^{2+}$ . Dinuclear mixed-valent ruthenium complexes have been widely studied in terms of electronic interaction between the metal centers. Symmetric complexes, especially the Creutz–Taube ion  $[(\text{NH}_3)_5\text{Ru}(\mu\text{-pz})\text{-Ru}(\text{NH}_3)_5]^{5+}$  ( $\text{pz} = \text{pyrazine}$ ) as prototype,<sup>44</sup> with identical electronic environments around both metal sites have been extensively examined,<sup>45–47</sup> and the theoretical background is well-understood.<sup>48–50</sup> The strength of the through-bond electronic interaction is dominated by the distance between the redox centers, as well as the planarity and appropriate symmetry of the bridging ligand.<sup>51</sup> Additionally, the frontier orbitals of the bridge need to be in a similar energy range as the involved metal orbitals for the interaction to be significant.<sup>45,47,51</sup> A classification into three classes (Robin–Day) distinguishes the degree of communication between the redox centers, with class I being ascribed to noninteracting and class III ascribed to strongly coupled systems.<sup>52–54</sup>

Directional electronic coupling through asymmetric bridging ligands has not been studied in great detail mainly because of the difficulty to generate distinct asymmetric structures<sup>55</sup> that meet the basic requirements for electronic interaction (planarity, sufficiently short distances). Electron transfer in natural systems, on the other hand, always occurs directionally with small driving forces.<sup>56</sup> This is why systematic synthesis and investigation of structurally asymmetric but nearly redox-symmetric mixed-valent systems is of general interest.

We had previously reported the unprotected dipeptide  $[(\text{R-tpy})\text{Ru}(\text{tpy-NHCO-tpy})\text{Ru}(\text{tpy-R}') ]^{4+}$ ,  $\text{R} = \text{COOH}$ ,  $\text{R}' = \text{NH}_2$ ,  $2^{4+}$ .<sup>57</sup> Its mixed-valent state  $2^{3+}$  features two electronically uncoupled ruthenium moieties due to differing local redox potentials leading to an intrinsic electronic asymmetry. No evidence of photochemical electron transfer from the  $\text{Ru}^{\text{II}}$  moiety onto the  $\text{Ru}^{\text{III}}$  species was found (Robin–Day class I). In contrast to  $1^{2+}$ ,  $2^{4+}$  containing both a carboxylic acid and an amino group has not been explored in terms of acid–base chemistry, although interesting properties can arise from the combination of redox and acid–base active centers in a single molecule (e.g., proton-coupled electron transfer).<sup>58–60</sup>

In this work, we present an intrinsically structurally asymmetric but, in terms of local redox potentials, highly symmetric derivative of  $2^{4+}$ , with  $\text{R} = \text{COOEt}$  and  $\text{R}' = \text{NHCOCH}_3$  ( $3^{4+}$ ). Its unique electronic and optical properties are studied in detail and are compared to a closely related mononuclear derivative of the ruthenium amino acid of the form  $[(\text{R-tpy})\text{Ru}(\text{tpy-R}') ]^{2+}$  ( $\text{R} = \text{COOEt}$ ,  $\text{R}' = \text{NHCOCH}_3$ ,  $4^{2+}$ ) with the same terminal functional groups as  $3^{4+}$ . The extent of electronic coupling between the redox moieties is evaluated in the neutral, singly oxidized, and singly reduced states as well as in the excited state.

Typically, aliphatic and aromatic amides exhibit only weakly acidic behavior ( $\text{p}K_{\text{a}} \approx 18\text{--}22$  in dimethyl sulfoxide).<sup>61</sup> However, inserting amide bonds in between charged polypyridine ruthenium(II) complexes leads to a substantial polarization of the amide and an acidification of the N–H bond, which is why the acid–base chemistry of  $3^{4+}$  is investigated as well.

## EXPERIMENTAL SECTION

**General Procedures.** Chemicals were obtained from commercial suppliers and were used without further purification. Bis(terpyridine)-ruthenium(II) complexes  $[(\text{HOOC-tpy})\text{Ru}(\text{tpy-NH}_2)](\text{PF}_6)_2$  **1** ( $\text{PF}_6$ )<sub>2</sub>,  $[(\text{EtOOC-tpy})\text{Ru}(\text{tpy-NHCOCH}_3)](\text{PF}_6)_2$  **4** ( $\text{PF}_6$ )<sub>2</sub>, and  $[(\text{EtOOC-tpy})\text{Ru}(\text{tpy-NH}_2)](\text{PF}_6)_2$  **5** ( $\text{PF}_6$ )<sub>2</sub> were synthesized according to literature-known procedures.<sup>31,36,37</sup> Air- or moisture-sensitive reactions and compounds were handled in dried glassware under an inert gas atmosphere (argon, quality 4.6). Acetonitrile was refluxed over  $\text{CaH}_2$  and distilled under argon prior to use in these reactions. IR spectra were recorded on a BioRad Excalibur FTS 3000 spectrometer using cesium iodide disks. UV–vis absorption spectra were recorded on a Varian Cary 5000 spectrometer in 1 cm cuvettes. Emission spectra were recorded on a Varian Cary Eclipse spectrometer. Quantum yields were determined by comparing the areas under the emission spectra recorded for solutions of the samples and a reference with matching absorbances on an energy scale ( $\phi([\text{Ru}(\text{bpy})_3]\text{Cl}_2) = 0.094$  in deaerated  $\text{CH}_3\text{CN}$ ).<sup>18</sup> Experimental uncertainty is estimated to be 15%. Luminescence decay curves of the samples in acetonitrile were measured under ambient conditions or under inert atmosphere by time-correlated single-photon counting (TCSPC) at 22 °C under magic-angle conditions with an Edinburgh Instruments lifetime spectrometer (FLS 920) equipped with a supercontinuum laser (SC400-PP, Fianium) in combination with a double monochromator, a MCP-PMT (R3809U-50, Hamamatsu), and a TCSPC module (TCC 900). The instrument response time was 200 ps; the repetition rate was 5 MHz. Sample excitation was at 504 and 492 nm, and fluorescence decays were measured at 684 and 690 nm for **3** ( $\text{PF}_6$ )<sub>4</sub> and **4** ( $\text{PF}_6$ )<sub>2</sub>, respectively. Decay times were obtained from single- or biexponential fits using the spectrometer software. Electrospray ionization (ESI<sup>+</sup>) and high-resolution (HR) ESI<sup>+</sup> mass spectra were recorded on a Micromass QToF Ultima API mass spectrometer with analyte solutions in acetonitrile. ESI<sup>+</sup> mass spectra are reported giving the  $m/z$  ratio and relative intensity of the most intense peak of the typical ruthenium isotope pattern, while HR ESI<sup>+</sup> numbers are given



for the lowest  $m/z$  ratio in a given ruthenium isotope pattern. Elemental analyses were performed by the microanalytical laboratory of the chemical institutes of the University of Mainz. NMR spectra were obtained with a Bruker Avance II 400 spectrometer at 400.31 ( $^1\text{H}$ ), 100.66 ( $^{13}\text{C}$ ), and 376.60 MHz ( $^{19}\text{F}$ ) at 25 °C. Chemical shifts  $\delta$  [ppm] are reported with respect to residual solvent signals as internal standards ( $^1\text{H}$ ,  $^{13}\text{C}$ ) or external standards ( $^{19}\text{F}$ ):  $\text{CD}_3\text{CN}$   $\delta(^1\text{H}) = 1.94$  ppm,  $\delta(^{13}\text{C}) = 1.32$  and 118.26 ppm,<sup>62</sup>  $\text{CFCl}_3$   $\delta(^{19}\text{F}) = 0.00$  ppm. Electrochemical experiments were performed with a BioLogic SP-50 voltammetric analyzer using platinum wire working and counter electrodes and a 0.01 M  $\text{Ag}/\text{AgNO}_3$  reference electrode. Measurements were carried out at a scan rate of 100  $\text{mV s}^{-1}$  for cyclic voltammetry experiments and at 10  $\text{mV s}^{-1}$  for square-wave voltammetry experiments using 0.1 M  $[\text{nBu}_4\text{N}][\text{PF}_6]$  as supporting electrolyte in acetonitrile. Potentials are given relative to the ferrocene/ferrocenium couple (0.40 V vs SCE,<sup>63</sup>  $E_{1/2} = 0.90 \pm 5$  mV under the given conditions). Electron paramagnetic resonance (EPR) spectra were recorded on a Miniscope MS 300 X-band CW spectrometer (Magnettech GmbH, Germany). Values of  $g$  are referenced to  $\text{Mn}^{2+}$  in ZnS as external standard ( $g = 2.118, 2.066, 2.027, 1.986, 1.946$ ). Simulations were performed with the EasySpin program package.<sup>64</sup>

Density functional theoretical (DFT) calculations were carried out using the Gaussian09/DFT series of programs<sup>65</sup> employing B3LYP as functional.<sup>66</sup> The choice of functional was made due to the vast abundance of publications using this functional in calculations on transition metal compounds. Previously published theoretical results on mono- and oligonuclear donor–acceptor functionalized  $[\text{Ru}(\text{tpy})_2]$  complexes were in good agreement with the experimental data.<sup>29,39,40,57</sup> The LANL2DZ implementation of Gaussian09 was used as basis set for all atoms. It comprises Dunning/Huzinaga's D95 V valence double- $\xi$  basis without polarization functions for hydrogen, carbon, nitrogen, and oxygen<sup>67</sup> and a Los Alamos effective core potential approach plus valence double- $\xi$  basis for ruthenium.<sup>68–70</sup> This rather small basis set combination was chosen to manage the computational effort of the large systems under study. To account for solvent effects a polarized continuum model modeling acetonitrile solution was used (IEFFCM, acetonitrile).<sup>71–73</sup> Explicit counterions and/or solvent molecules were not taken into account. All structures were characterized as local minima of the potential energy surface by vibrational analysis ( $N_{\text{imag}} = 0$ ). No symmetry constraints were imposed on the molecular geometries.

**Synthetic Procedures.** *Synthesis of 6*( $\text{PF}_6$ )<sub>2</sub>.<sup>57</sup>  $[(\text{HOOC-tpy})\text{Ru}(\text{tpy-NH}_2)](\text{PF}_6)_2$  **1**( $\text{PF}_6$ )<sub>2</sub><sup>31</sup> (339 mg, 0.370 mmol) was suspended in acetyl chloride (25 mL) and refluxed for 2 h giving a dark red solution. Acetyl chloride was distilled from this, and the residual solid was dissolved in acetonitrile. The crude product was triturated by addition of excess diethyl ether and collected via filtration. It was dissolved again in boiling water (250 mL) to cleave the mixed anhydride formed in the reaction of the carboxyl group with acetic anhydride and precipitated after addition of a solution of  $\text{NH}_4\text{PF}_6$  (250 mg) in water (1 mL). The precipitate was collected, washed with water, and dried under reduced pressure to give  $[(\text{HOOC-tpy})\text{Ru}(\text{tpy-NHCOCH}_3)](\text{PF}_6)_2$  **6**( $\text{PF}_6$ )<sub>2</sub> as a red powder. Yield: 330 mg (0.350 mmol, 95%). Anal. Calcd for  $\text{C}_{33}\text{H}_{25}\text{F}_{12}\text{N}_7\text{O}_3\text{P}_2\text{Ru}$  (958.6)·4 $\text{H}_2\text{O}$ : C, 38.46; H, 3.23; N, 9.51. Found: C, 38.63; H, 3.13; N, 9.68%. Mass spectrometry (MS) ( $\text{ESI}^+$ ):  $m/z$  (%) = 334.6 (30)  $[\text{M}-2\text{PF}_6]^{2+}$ , 814.1 (100)  $[\text{M}-\text{PF}_6]^+$ , 1293.1 (3)  $[\text{M}-\text{PF}_6]^{2+}$ , 1772.6 (3)  $[\text{M}-\text{PF}_6]^{2+}$ . HR-MS ( $\text{ESI}^+$ ,  $m/z$ ): calcd. for  $\text{C}_{33}\text{H}_{25}\text{F}_{12}\text{N}_7\text{O}_3\text{PRu}$   $[\text{M}-\text{PF}_6]^+$ : 808.0737; found: 808.0732.  $^1\text{H}$  NMR ( $\text{CD}_3\text{CN}$ ):  $\delta = 9.42$  (s, 1H, NH), 9.17 (s, 2H,  $\text{H}^2$ ), 8.94 (s, 2H,  $\text{H}^{2'}$ ), 8.62 (d,  $^3J_{\text{HH}} = 8$  Hz, 2H,  $\text{H}^3$ ), 8.37 (d,  $^3J_{\text{HH}} = 8$  Hz, 2H,  $\text{H}^{3'}$ ), 7.97–7.82 (m, 4H,  $\text{H}^6$ ,  $\text{H}^{6'}$ ), 7.46–7.41 (m, 2H,  $\text{H}^8$ ), 7.28–7.15 (m, 4H,  $\text{H}^7$ ,  $\text{H}^{8'}$ ), 7.12–7.06 (m, 2H,  $\text{H}^{7'}$ ), 2.35 (s, 3H,  $\text{CH}_3$ ).

*Synthesis of 7*( $\text{PF}_6$ )<sub>2</sub>.  $[(\text{HOOC-tpy})\text{Ru}(\text{tpy-NHCOCH}_3)](\text{PF}_6)_2$  **6**( $\text{PF}_6$ )<sub>2</sub> (200 mg, 0.209 mmol) was dissolved in absolute acetonitrile (15 mL), and pentafluorophenol (46.2 mg, 0.251 mmol) and  $N,N'$ -diisopropylcarbodiimide (31.7 mg, 0.251 mmol) were added. After it stirred at room temperature for 90 min, the reaction mixture was concentrated to 5 mL under reduced pressure, and the product was

triturated by addition of a solution of  $\text{NH}_4\text{PF}_6$  (297 mg) in water (70 mL). The product was collected via filtration, washed with small amounts of water and diethyl ether, and dried under reduced pressure to give  $[(\text{C}_6\text{F}_5\text{OOC-tpy})\text{Ru}(\text{tpy-NHCOCH}_3)](\text{PF}_6)_2$  **7**( $\text{PF}_6$ )<sub>2</sub> as red powder. Yield: 217.5 mg (0.193 mmol, 93%). Anal. Calcd for  $\text{C}_{39}\text{H}_{24}\text{F}_{17}\text{N}_7\text{O}_3\text{P}_2\text{Ru}$  (1124.6)·2 $\text{H}_2\text{O}$ : C, 40.36; H, 2.43; N, 8.45. Found: C, 40.24; H, 2.21; N, 8.61%. MS ( $\text{ESI}^+$ ):  $m/z$  (%) = 417.6 (15)  $[\text{M}-2\text{PF}_6]^{2+}$ , 834.1 (3)  $[\text{M}-2\text{PF}_6-\text{H}]^+$ , 980.1 (100)  $[\text{M}-\text{PF}_6]^+$ , 1542.6 (3)  $[\text{M}-\text{PF}_6]^{2+}$ , 2103.6 (3)  $[\text{M}-\text{PF}_6]^{2+}$ . HR-MS ( $\text{ESI}^+$ ,  $m/z$ ): calcd. for  $\text{C}_{39}\text{H}_{24}\text{F}_{17}\text{N}_7\text{O}_3\text{PRu}$   $[\text{M}-\text{PF}_6]^+$ : 974.0579; found: 974.0562.  $^1\text{H}$  NMR ( $\text{CD}_3\text{CN}$ ):  $\delta = 9.54$  (s, 1H, NH), 9.38 (s, 2H,  $\text{H}^2$ ), 9.01 (s, 2H,  $\text{H}^{2'}$ ), 8.70 (d,  $^3J_{\text{HH}} = 8$  Hz, 2H,  $\text{H}^3$ ), 8.42 (d,  $^3J_{\text{HH}} = 8$  Hz, 2H,  $\text{H}^{3'}$ ), 7.99 (t,  $^3J_{\text{HH}} = 8$  Hz, 2H,  $\text{H}^6$ ), 7.93 (t,  $^3J_{\text{HH}} = 8$  Hz, 2H,  $\text{H}^{6'}$ ), 7.51 (d,  $^3J_{\text{HH}} = 6$  Hz, 2H,  $\text{H}^8$ ), 7.32–7.26 (m, 4H,  $\text{H}^7$ ,  $\text{H}^{8'}$ ), 7.17–7.12 (m, 2H,  $\text{H}^{7'}$ ), 2.39 (s, 3H,  $\text{CH}_3$ ).  $^{13}\text{C}\{^1\text{H}\}$  NMR ( $\text{CD}_3\text{CN}$ ):  $\delta = 172.4$  (s,  $\text{NHCOCH}_3$ ), 160.6 (s,  $\text{COOC}_6\text{F}_5$ ), 157.8 (2s,  $\text{C}^4$ ,  $\text{C}^{4'}$ ), 157.0 (s,  $\text{C}^3$ ), 154.8 (s,  $\text{C}^{3'}$ ), 152.8 (s,  $\text{C}^{8'}$ ), 152.3 (s,  $\text{C}^8$ ), 147.3 (s,  $\text{C}^{1'}$ ), 138.7 (s,  $\text{C}^6$ ), 138.4 (s,  $\text{C}^{6'}$ ), 131.6 (s,  $\text{C}^1$ ), 128.3 (s,  $\text{C}^{7'}$ ), 127.6 (s,  $\text{C}^7$ ), 125.1 (s,  $\text{C}^5$ ), 124.8 (s,  $\text{C}^5$ ), 123.4 (s,  $\text{C}^2$ ), 113.5 (s,  $\text{C}^{2'}$ ), 24.0 (s,  $\text{NHCOCH}_3$ ), (carbon signals of  $\text{C}_6\text{F}_5$  not observed).<sup>74</sup>  $^{19}\text{F}$  NMR ( $\text{CD}_3\text{CN}$ ):  $\delta = -73.3$  (d,  $^1J_{\text{FP}} = 707$  Hz, 1F,  $\text{PF}_6$ ),  $-154.8$  (d,  $^3J_{\text{FF}} = 17$  Hz, 2F,  $o\text{-F}$ ),  $-159.0$  (t,  $^3J_{\text{FF}} = 21$  Hz, 1F,  $p\text{-F}$ ),  $-163.8$  (dd,  $^3J_{\text{FF}} = 21$ , 17 Hz, 2F,  $m\text{-F}$ ).

*Synthesis of 3*( $\text{PF}_6$ )<sub>4</sub>.  $[(\text{C}_6\text{F}_5\text{OOC-tpy})\text{Ru}(\text{tpy-NHCOCH}_3)](\text{PF}_6)_2$  **7**( $\text{PF}_6$ )<sub>2</sub> (59.5 mg, 0.053 mmol) and  $[(\text{EtOOC-tpy})\text{Ru}(\text{tpy-NH}_2)](\text{PF}_6)_2$  **5**( $\text{PF}_6$ )<sub>2</sub> (50 mg, 0.053 mmol) were each dissolved separately in acetonitrile (10 mL) under an atmosphere of argon and left to stand overnight over activated molecular sieves (3 Å) to remove crystal water. The solution of **5**( $\text{PF}_6$ )<sub>2</sub> then was added to a solution of phosphazene base *tert*-butylimino-tris(dimethylamino)phosphorane (25.8 mg, 0.110 mmol) in absolute acetonitrile (5 mL) and stirred for 45 min followed by the addition of the solution of **7**( $\text{PF}_6$ )<sub>2</sub>. After it was stirred at room temperature for 4 h, the reaction was quenched by the addition of a few drops of acetic acid and concentrated under reduced pressure to 5 mL. The product was precipitated by addition of  $\text{NH}_4\text{PF}_6$  (423 mg) and water (80 mL) and collected via filtration. The crude product was recrystallized from an ethanol/acetone mixture (20 mL, 3:1) and dried under reduced pressure to give  $[(\text{EtOOC-tpy})\text{Ru}(\text{tpy-NHCO-tpy})\text{Ru}(\text{tpy-NHCOCH}_3)](\text{PF}_6)_4$  **3**( $\text{PF}_6$ )<sub>4</sub> as red powder. Yield: 78.2 mg (0.042 mmol, 79%). Anal. Calcd for  $\text{C}_{66}\text{H}_{50}\text{F}_{24}\text{N}_{14}\text{O}_4\text{P}_4\text{Ru}_2$  (1885.2)·4 $\text{H}_2\text{O}$ : C, 40.50; H, 2.99; N, 10.02. Found: C, 40.61; H, 2.95; N, 9.78%. MS ( $\text{ESI}^+$ ):  $m/z$  (%) = 309.0 (5)  $[\text{M}-4\text{PF}_6-\text{EtAc}]^{4+}$ , 435.1 (15)  $[\text{M}-4\text{PF}_6-\text{H}]^{3+}$ , 725.1 (29)  $[\text{M}-3\text{PF}_6-\text{H}]^{2+}$ , 777.1 (6)  $[\text{M}-2\text{PF}_6-\text{Ac}]^{2+}$ , 798.1 (100)  $[\text{M}-2\text{PF}_6]^{2+}$ , 1741.3 (15)  $[\text{M}-\text{PF}_6]^+$ . HR-MS ( $\text{ESI}^+$ ,  $m/z$ ): calcd. for  $\text{C}_{66}\text{H}_{50}\text{F}_{24}\text{N}_{14}\text{O}_4\text{P}_4\text{Ru}_2$   $[\text{M}-2\text{PF}_6]^{2+}$ : 792.0788; found: 792.0782.  $^1\text{H}$  NMR ( $\text{CD}_3\text{CN}$ ):  $\delta = 10.42$  (s, 1H, tpy-CONH-tpy), 9.49 (s, 1H, CONH $\text{CH}_3$ ), 9.36 (s, 2H,  $\text{H}^{2'}$ ), 9.34 (s, 2H,  $\text{H}^{2''}$ ), 9.23 (s, 2H,  $\text{H}^2$ ), 9.01 (s, 2H,  $\text{H}^{2''}$ ), 8.75 (d,  $^3J_{\text{HH}} = 8$  Hz, 2H,  $\text{H}^{5''}$ ), 8.70 (d,  $^3J_{\text{HH}} = 8$  Hz, 2H,  $\text{H}^5$ ), 8.54 (d,  $^3J_{\text{HH}} = 8$  Hz, 2H,  $\text{H}^{5'}$ ), 8.44 (d,  $^3J_{\text{HH}} = 8$  Hz, 2H,  $\text{H}^{5''}$ ), 8.11–7.89 (m, 8H,  $\text{H}^6$ ,  $\text{H}^{6'}$ ,  $\text{H}^{6''}$ ,  $\text{H}^{6''}$ ), 7.62–7.50 (m, 4H,  $\text{H}^8$ ,  $\text{H}^{8''}$ ), 7.44–7.33 (m, 4H,  $\text{H}^{8'}$ ,  $\text{H}^{8''}$ ), 7.33–7.26 (m, 4H,  $\text{H}^7$ ,  $\text{H}^{7''}$ ), 7.24–7.14 (m, 4H,  $\text{H}^{7'}$ ,  $\text{H}^{7''}$ ), 4.67 (q, 2H,  $^3J_{\text{HH}} = 7$  Hz,  $\text{OCH}_2\text{CH}_3$ ), 2.39 (s, 3H,  $\text{NHCOCH}_3$ ), 1.59 (t, 3H,  $^3J_{\text{HH}} = 7$  Hz,  $\text{OCH}_2\text{CH}_3$ ).  $^{13}\text{C}\{^1\text{H}\}$  NMR ( $\text{CD}_3\text{CN}$ ):  $\delta = 171.6$  (s,  $\text{NHCOCH}_3$ ), 165.3 (s, tpy-CONH-tpy), 165.1 (s, tpy-COOEt), 158.8, 158.8, 158.7, 158.7, (s,  $\text{C}^4$ ,  $\text{C}^{4'}$ ,  $\text{C}^{4''}$ ,  $\text{C}^{4''}$ ), 157.5 (s,  $\text{C}^{3''}$ ), 157.4 (s,  $\text{C}^3$ ), 156.3 (s,  $\text{C}^{3'}$ ), 156.0 (s,  $\text{C}^{3''}$ ), 153.9, 153.8 (s,  $\text{C}^{8'}$ ,  $\text{C}^{8''}$ ), 153.5, 153.4 (s,  $\text{C}^8$ ,  $\text{C}^{8''}$ ), 148.2 (s,  $\text{C}^{1''}$ ), 147.4 (s,  $\text{C}^{1'}$ ), 140.0 (s,  $\text{C}^{1''}$ ), 139.5, 139.4 (s,  $\text{C}^{6'}$ ,  $\text{C}^{6''}$ ), 139.2, 139.2 (s,  $\text{C}^6$ ,  $\text{C}^{6''}$ ), 137.5 (s,  $\text{C}^1$ ), 129.0 (s,  $\text{C}^{7''}$ ), 128.9 (s,  $\text{C}^7$ ), 128.7 (s,  $\text{C}^{7'}$ ), 128.6 (s,  $\text{C}^{7''}$ ), 125.9 (s,  $\text{C}^5$ ), 125.8 (s,  $\text{C}^{5''}$ ), 125.6 (s,  $\text{C}^5$ ), 125.5 (s,  $\text{C}^{5''}$ ), 123.8 (s,  $\text{C}^2$ ), 122.7 (s,  $\text{C}^{2''}$ ), 115.2 (s,  $\text{C}^{2'}$ ), 114.0 (s,  $\text{C}^{2''}$ ), 63.9 (s,  $\text{OCH}_2\text{CH}_3$ ), 24.9 (s,  $\text{NHCOCH}_3$ ), 14.7 (s,  $\text{OCH}_2\text{CH}_3$ ).

**General Procedure for Removal of Crystal Water from the Complexes 4( $\text{PF}_6$ )<sub>2</sub> and **3**( $\text{PF}_6$ )<sub>4</sub>. The complex (100 mg) was suspended in chlorotrimethylsilane (5 mL) in an atmosphere of dry argon and left to stand for 15–20 min. After removal of excess silane and the formed siloxane under reduced pressure, the complex was dissolved in absolute acetonitrile (5 mL) and dried under reduced pressure again to remove residual acid. NMR analysis showed slight**

downfield shifts of amide proton resonances indicative of traces of remaining hydrochloric acid that could not be removed with this method.

## RESULTS AND DISCUSSION

**Synthesis of Dinuclear Amide.** The dinuclear ruthenium complex  $3^{4+}$  is extremely challenging to synthesize via amide coupling in a classical fashion because of the poor reactivity of the pyridylamine coordinated to the electron-withdrawing ruthenium(II), which is further augmented by the Coulombic repulsion of the doubly charged mononuclear precursors. The pyridylamine can be viewed as an iminium-like structure ( $=\text{NH}_2^+$ ) with rather acidic properties that can be deprotonated using strong bases.<sup>19,31,36</sup> Another possibility to acylate the amino group is by employing acid chlorides at elevated temperatures.<sup>57</sup>

The synthesis of the dinuclear dipeptide  $3^{4+}$  was effected in a four-step synthesis starting from the ethyl ester of the ruthenium amino acid  $5^{2+}$ . The first step was acidic cleavage of the ester to the amino acid  $1^{2+}$ .<sup>31</sup> Subsequent acetylation of the amino function with acetyl chloride leads to *N*-acetyl amide acid  $6^{2+}$  in a yield of 95%.<sup>57</sup> For the amide coupling of the two building blocks  $5^{2+}$  and  $6^{2+}$  to  $3^{4+}$  suitable conditions needed to be established. A broad range of typical conditions for amide couplings is known,<sup>75</sup> most of which employ active esters in different forms such as 1-hydroxybenzotriazolyl esters (OBt esters),<sup>76–78</sup> 1-hydroxy-7-azabenzotriazolyl esters (OAt esters),<sup>79</sup> pentafluorophenyl esters (OPfp esters),<sup>80,81</sup> and *p*-nitrophenylesters.<sup>82</sup> Intermediate activation can be achieved using acid chlorides<sup>83</sup> or *N,N'*-dicyclohexylcarbodiimide (DCC) adducts<sup>84</sup> as active species. More advanced and forcing activation procedures use aminium or phosphonium salt based coupling reagents.<sup>77,78,85</sup> We have recently shown that intermediate activation of ruthenium amino acids and coupling to amino-functionalized ferrocenes, ruthenium complexes, and bipyridines can be achieved using HOBt/DCC,<sup>31</sup> PyBOP,<sup>57</sup> and HATU,<sup>39</sup> respectively, when a strong base, typically a phosphazene base ( $\text{P}_1\text{-tBu}$ ) is present (PyBOP = benzotriazol-1-yl-oxytripyrrolidinophosphonium hexafluorophosphate; HATU = 1-[bis(dimethylamino)methylene]-1*H*-1,2,3-triazolo-[4,5-*b*]pyridinium 3-oxide hexafluorophosphate). The latter conditions even distinguish between aromatic amines and the pyridylamine present in the ruthenium amino acid  $1^{2+}$ , so that protection of the amino group of the complex is obsolete.<sup>39</sup>

In this work the active ester is isolated and purified to provide a well-defined starting material for the following amide coupling. Pentafluorophenol (PfpOH) is used in combination with *N,N'*-diisopropylcarbodiimide to activate the acid. The corresponding urea formed during the reaction is soluble in the water/acetonitrile mixture of the aqueous workup and thus is easily separated from the insoluble OPfp ester  $7^{2+}$ . The procedure is generalizable and also applicable to the amino acid  $1^{2+}$  affording the OPfp ester  $8^{2+}$ . This active ester does not exhibit any reactivity toward the free pyridylamino group present in the compound itself but rapidly reacts with aliphatic amines such as *tert*-butylamine giving the corresponding amide  $9^{2+}$  (for experimental procedures and  $^1\text{H}$  and  $^{13}\text{C}$  NMR spectra see Supporting Information, Figures S1 and S2).

The dried active ester  $7^{2+}$  readily reacts with the water-free amino ester  $5^{2+}$  after deprotonation of its amino function with  $\text{P}_1\text{-tBu}$  at ambient conditions in reasonable reaction times (4 h). Removal of residual crystal water in the starting materials was accomplished via storage of the respective compounds

dissolved in acetonitrile over 3 Å molecular sieves prior to setting up the reaction. During the coupling reaction a striking color change from red to purple was observed, which is attributed to the deprotonation of the generated dinuclear species (*vide infra*). Neither cleavage of the terminal ester nor the amine function was observed under the given water-free conditions (by NMR and ESI-MS).

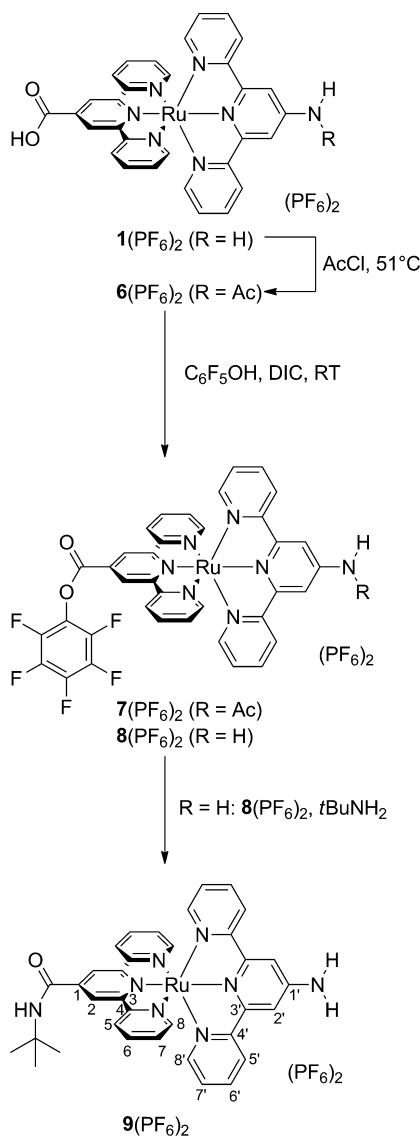
The synthesis of the corresponding protected mononuclear complex with identical capping functionalities  $4^{2+}$  was carried out via a literature-known procedure in good yields (Scheme 2).<sup>57</sup>

**Characterization of Mono- and Dinuclear Amides.** The successful formation of the pentafluorophenylesters of  $6^{2+}$  and  $1^{2+}$  is easily evidenced in the  $^1\text{H}$  NMR spectra of  $7^{2+}$  and  $8^{2+}$  because the resonances of the protons  $\text{H}^2$  are shifted downfield by  $\sim 0.15$  ppm. This is attributed to the stronger electron-withdrawing effect of the OPfp group compared to the free carboxylic acid or its ethyl ester (see Schemes 1 and 2 for atom numbering). The remainder of the  $^1\text{H}$  NMR spectra is rather unaffected from carboxylic acid activation. For example, in  $7^{2+}$  the amide proton resonates at 9.54 ppm, and proton  $\text{H}^{2'}$  resonates at 9.01 ppm; for  $8^{2+}$ , the protons of  $\text{NH}_2$  and  $\text{H}^{2'}$  are found at 6.04 and 8.00 ppm, respectively, which does not differ significantly from the parent compounds  $1^{2+}$  and  $6^{2+}$  (Supporting Information, Figures S3 and S6).  $^{13}\text{C}$  NMR chemical shifts (Supporting Information, Figures S4 and S7) are easily assigned via  $^1\text{H}^{13}\text{C}$  correlated techniques (except for the  $\text{C}_6\text{F}_5$  carbon signals, which are not detected under the given measurement settings).  $^{19}\text{F}$  NMR spectroscopy confirms the presence of a perfluorinated phenyl ring as well as of two  $\text{PF}_6^-$  counterions at typical chemical shifts (Supporting Information, Figures S5 and S8). ESI<sup>+</sup> mass spectra confirm the integrity of the OPfp esters  $7^{2+}$  and  $8^{2+}$  since only signals of intact cations with no or one counterions are observed.

As expected the NMR spectra of the dinuclear species  $3^{4+}$  are more complicated (Figure 1 and Supporting Information, Figures S9 and S10). The intended high electronic similarity of both complex subunits leads to a multitude of overlapping or close-lying resonances in both the  $^1\text{H}$  and the  $^{13}\text{C}$  NMR spectra. Nevertheless the success of the amide coupling reaction is most easily evidenced by the downfield shift of proton  $\text{H}^{2'}$  by  $\sim 1.3$  ppm now resonating at 9.36 ppm because the influence of the electron-donating amino group is lost. Four sets of signals consisting of one singlet, two doublets, and two doublets of doublets (ignoring  $^4J$  contributions) are expected with intensities of 1:1:1:1 originating from the four different terpyridine moieties present in  $3^{4+}$ . Especially the four singlets (protons  $\text{H}^2$ ,  $\text{H}^{2'}$ ,  $\text{H}^{2''}$ , and  $\text{H}^{2'''}$ ) are sufficiently separated and confirm the successful formation of  $3^{4+}$  (Figure 1). Significant downfield shifts of the proton resonances of the bridging ligand are observed due to the enhanced positive charge of  $3^{4+}$  and the stronger electron-withdrawing effect affecting particularly protons  $\text{H}^{2'}$  and  $\text{H}^{2''}$ . The high charge also affects the amide proton of the bridging amide: its resonance appears at 10.42 ppm and is shifted by 0.93 ppm compared to the terminal amide proton. In the high-field region of the spectrum the expected singlet of the acetyl group and quartet/triplet pattern of the ethyl ester group are observed at 2.39 and 4.67/1.59 ppm with correct integral ratios, respectively. Despite the overlapping of several signals full assignment of all  $^1\text{H}$  and  $^{13}\text{C}$  resonances was possible using  $^1\text{H}^{13}\text{C}$  correlation spectroscopy.



**Scheme 1. Pentafluorophenylester (OPfp Ester) Formation of Ruthenium Amino Acid 1(PF<sub>6</sub>)<sub>2</sub> and Its Acetyl Amide 6(PF<sub>6</sub>)<sub>2</sub> Leading to 7(PF<sub>6</sub>)<sub>2</sub> and 8(PF<sub>6</sub>)<sub>2</sub> and Subsequent Amidation of 8(PF<sub>6</sub>)<sub>2</sub> with *tert*-Butylamine to 9(PF<sub>6</sub>)<sub>2</sub><sup>a</sup>**



<sup>a</sup>Atom numbering for NMR assignment included.

ESI<sup>+</sup> mass spectra further confirm the formation of 3<sup>4+</sup>. Peaks attributable to [M-PF<sub>6</sub>]<sup>+</sup>, [M-2PF<sub>6</sub>]<sup>2+</sup>, [M-3PF<sub>6</sub>-H]<sup>2+</sup>, and [M-4PF<sub>6</sub>-H]<sup>3+</sup> dominate the mass spectrum. Presumably the proton that is lost is the bridging amide proton since its acidity is substantially increased due to the neighboring positively charged complex subunits (vide infra). Lower intensity signals of fragments lacking the acetyl and/or ethyl groups are observed as well. Since no other evidence for cleavage of the terminal amide and/or ester could be found, this fragmentation is believed to occur just during desolvation in the aerosol or during the ionization process. IR spectroscopy also reveals the integrity of the dinuclear complex 3<sup>4+</sup>. The NH and OH stretching vibrations from the amide groups and residual water show up at 3407 and 3649 cm<sup>-1</sup>. The ester and amide I carbonyl stretching vibrations appear as overlapping bands between 1723 and 1691 cm<sup>-1</sup>. Additionally the amide groups show typical NH deformation bands (amide II) at 1604 and

1589 cm<sup>-1</sup>. The PF<sub>6</sub><sup>-</sup> counterions are responsible for a broad intense band at 840 cm<sup>-1</sup>.

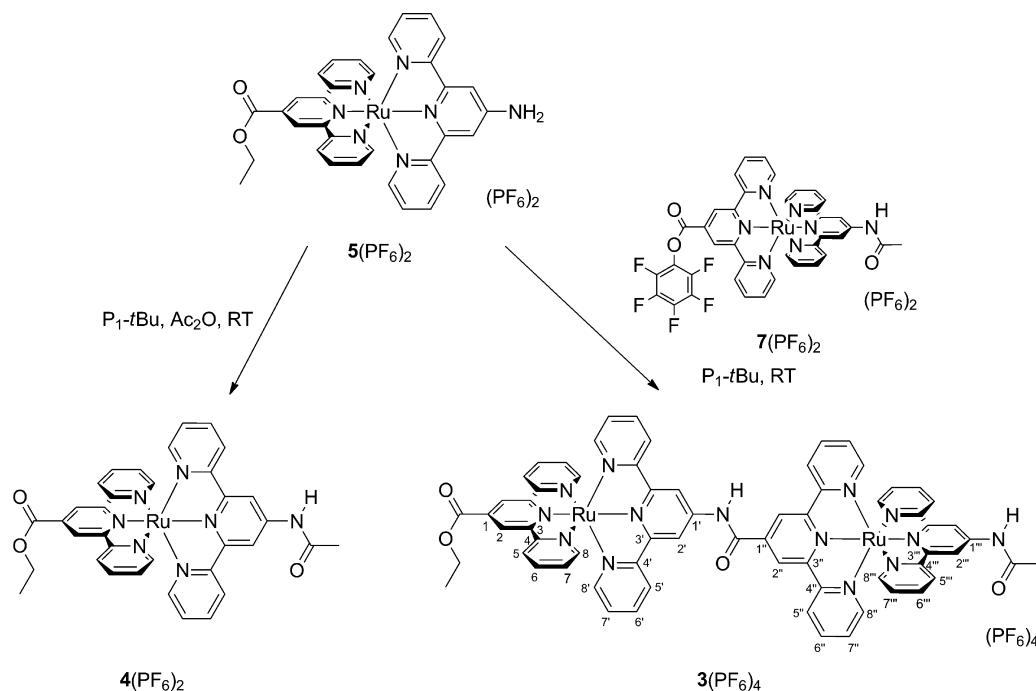
**Spectroscopic Properties of Mono- and Dinuclear Amides.** Both the mono- and the dinuclear bis(terpyridine)-ruthenium(II) complexes 4<sup>2+</sup> and 3<sup>4+</sup> exhibit a characteristic <sup>1</sup>MLCT transition in the UV-vis/NIR (NIR = near-infrared) absorption spectrum at ~500 nm (Figure 2). For the mononuclear complex 4<sup>2+</sup> this band is located at 492 nm in good agreement with wavelengths observed for similar bis(terpyridine)ruthenium(II) complexes carrying amido- and carboxylic acid functionalities.<sup>31,37,57</sup> For the dinuclear system 3<sup>4+</sup> this band is significantly shifted bathochromically to 504 nm. This shift can be attributed to the enhanced push-pull situation caused by the additional charge-carrying complex fragment on the one hand and to the enlarged conjugated aromatic π system on the other, both lowering the energy difference between the highest occupied and the lowest unoccupied orbital (HOMO-LUMO gap). This also affects the extinction coefficient of the <sup>1</sup>MLCT band of 3<sup>4+</sup>. The band is shifted hyperchromically and cannot be described as a simple superposition of two similar but independent bis(terpyridine)-ruthenium-based chromophores. The intraligand π-π\* transitions in the UV region of the absorption spectra of 4<sup>2+</sup> and 3<sup>4+</sup>, on the other hand, are very similar in shape and position to those of 3<sup>4+</sup> being roughly twice as intense as those of 4<sup>2+</sup>, which is in very good agreement with the doubled number of terpyridine ligands present in 3<sup>4+</sup>.

DFT calculations employing B3LYP as functional and LANL2DZ as basis set with acetonitrile as solvent in a polarized continuum model (IEFPCM) support the spectroscopic observations and assignments. The visible region is dominated mainly by two transitions, one originating from Ru<sup>II</sup> → tpy-CO transitions showing up at 490 nm for 3<sup>4+</sup> and at 476 nm for 4<sup>2+</sup>, consistent with the trend of the experimental <sup>1</sup>MLCT absorption maxima. The other band is based on transitions from Ru<sup>II</sup> into the more electron-rich tpy-NH ligands and is consequently found at higher energies (435 nm for 3<sup>4+</sup>, 431 nm for 4<sup>2+</sup>). This is in good agreement with the observed high-energy shoulders in the <sup>1</sup>MLCT bands for both compounds.

Both mononuclear 4<sup>2+</sup> as well as dinuclear 3<sup>4+</sup> are emissive at room temperature in fluid solution with emission quantum yields in the range of other bis(terpyridine)ruthenium(II) amino acid derivatives (Table 1, Figure 2). The quantum yield of dinuclear 3<sup>4+</sup> is lower than that of 4<sup>2+</sup> by a factor of 2. This might be attributed to the presence of a strongly polarized amide proton in the bridging ligand, which could allow for a more efficient radiationless deactivation pathway. The emission energy of 3<sup>4+</sup> is shifted slightly bathochromically with respect to 4<sup>2+</sup> matching the trend in the absorption spectra, which again supports the assumption of a smaller HOMO-LUMO gap in 3<sup>4+</sup>.

While the asymmetric shape of the emission band of 4<sup>2+</sup> at room temperature is typical for a ruthenium-based emission, the band shape of 3<sup>4+</sup> is significantly different: it is more symmetric and has a plateaulike maximum with nearly unchanged emission intensity over a range of 20 nm (Figure 2). On the other hand, the low-temperature emission spectra of 4<sup>2+</sup> and 3<sup>4+</sup> in a solid *n*PrCN matrix have essentially the same shape with maxima of 657 and 660 nm, respectively, and a pronounced shoulder at ~720 nm originating from a vibronic progression (Figure 3). We attribute this unusual room-temperature emission behavior to the coexistence of two

**Scheme 2. Amide Coupling of Amino Acid Ester 5(PF<sub>6</sub>)<sub>2</sub> and Acetyl Amido Acid Pentafluorophenyl (OPfp) Ester 7(PF<sub>6</sub>)<sub>2</sub> Giving Dinuclear Complex 3(PF<sub>6</sub>)<sub>4</sub> and Acylation of 5(PF<sub>6</sub>)<sub>2</sub> Leading to the Reference Compound 4(PF<sub>6</sub>)<sub>2</sub><sup>a</sup>**



<sup>a</sup>Atom numbering of 3(PF<sub>6</sub>)<sub>4</sub> for NMR assignment included.

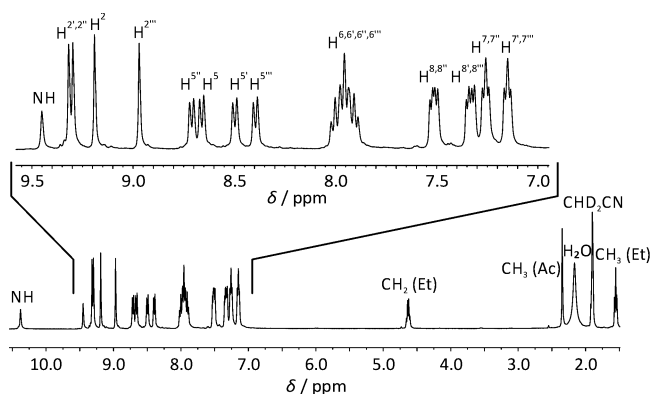


**Figure 1.** <sup>1</sup>H NMR spectrum of 3(PF<sub>6</sub>)<sub>4</sub> in CD<sub>3</sub>CN (lower), aromatic region (upper).

emissive triplet states in 3<sup>4+</sup>. This is in good agreement with the emission lifetimes of both complexes at room temperature. While 4<sup>2+</sup> exhibits an essentially monoexponential excited-state decay (the second component with 5% relative intensity is likely due to a strongly emissive but otherwise elusive impurity), the excited-state decay of 3<sup>4+</sup> is clearly biexponential.<sup>86</sup>

The room-temperature emission spectrum of the dinuclear complex 3<sup>4+</sup> can be fit by a simple superposition of two bands mimicking the emission band shape of a mononuclear complex. This was accomplished using the emission spectrum of 4<sup>2+</sup> twice at appropriate energies (676 and 705 nm, see Figure 4). The quality of this fit using weighing fractions of 71:29 for the two components, as indicated by the different measured emission lifetimes (Table 1), compared to the emission spectrum of 3<sup>4+</sup> is remarkable. This allows us to assign the 676 nm emission to  $\tau = 24$  ns (71%) and the low energy emission (705 nm) to  $\tau = 44$  ns (29%).

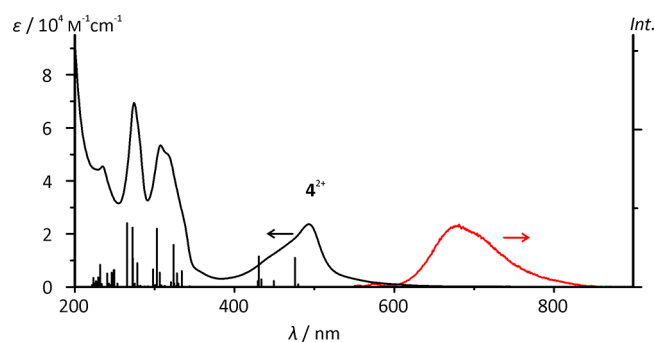
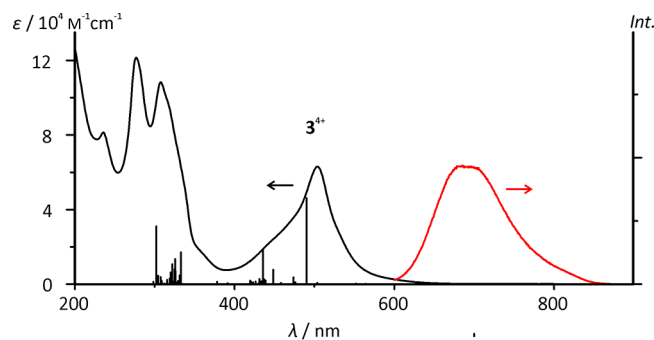


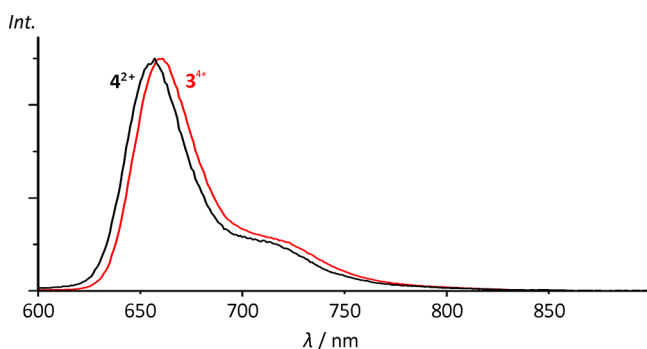
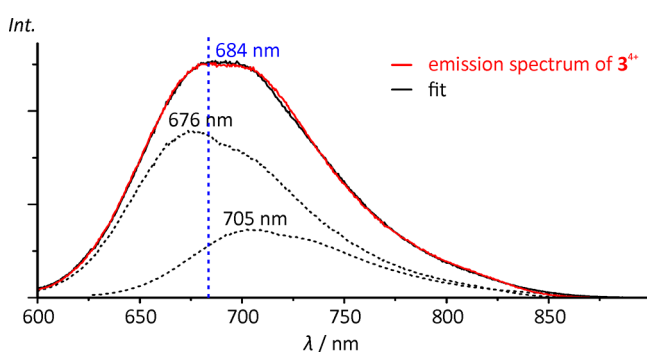
**Figure 2.** Experimental UV-vis absorption and normalized emission spectra of 3<sup>4+</sup> (upper) and 4<sup>2+</sup> (lower) at room temperature in deaerated CH<sub>3</sub>CN including oscillator strengths of computed optical transitions (time-dependent DFT: B3LYP, LANL2DZ, IEFPCM: CH<sub>3</sub>CN).

Furthermore, we were interested in the dependence of the shape of the emission spectrum of 3<sup>4+</sup> and hence the ratio of the emitting states as a function of the excitation wavelength (Supporting Information, Figure S11). The emission intensity follows that of the absorption spectrum, and the band shape is

**Table 1. Absorption and Emission Properties in Deaerated CH<sub>3</sub>CN at Room Temperature and Emission Properties of 3<sup>4+</sup> and 4<sup>2+</sup> in Deaerated nPrCN at 77 K**

	$\lambda_{\max}$ ( <sup>1</sup> MLCT) ( $\epsilon$ )	$\lambda_{\text{Em.}}$ ( $\lambda_{\text{Exc.}}$ ) at 298 K	$\lambda_{\text{Em.}}$ ( $\lambda_{\text{Exc.}}$ ) at 77 K	$\Phi^a$	$\tau^b$ (contribution)
4 <sup>2+</sup>	492 (22 100)	678 (492)	657 (499)	$5.9 \times 10^{-4}$	21 (95); 58 (5)
3 <sup>4+</sup>	504 (63 000)	684 (504)	660 (507)	$3.2 \times 10^{-4}$	24 (71); 44 (29)

<sup>a</sup>Quantum yields  $\Phi$  are determined at room temperature and given as fraction of emitted photons per absorbed photons. <sup>b</sup>Emission lifetimes  $\tau$  were determined at the respective emission maxima ( $\lambda_{\max}/\text{nm}$ ;  $\epsilon/\text{M}^{-1} \text{cm}^{-1}$ ;  $\lambda_{\text{Em.}}/\text{nm}$ ;  $\lambda_{\text{Exc.}}/\text{nm}$ ;  $\tau/\text{ns}$ , contribution/%).

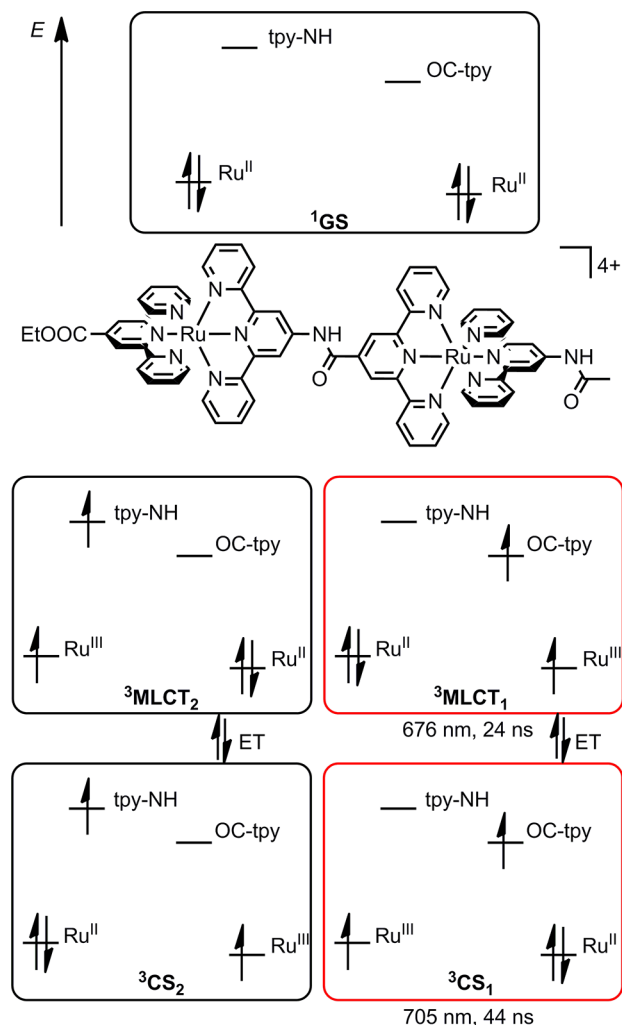
**Figure 3.** Normalized emission spectra of 3<sup>4+</sup> (red line) and 4<sup>2+</sup> (black line) at 77 K in butyronitrile.**Figure 4.** Normalized emission spectrum of 3<sup>4+</sup> at room temperature in deaerated CH<sub>3</sub>CN (red line), emission spectrum of 4<sup>2+</sup> (dashed lines) shifted to  $\lambda_{\max} = 676 \text{ nm}$  (contribution: 71%) and 705 nm (contribution: 29%), and their sum (solid black line). The blue vertical line indicates the detection wavelength of the emission lifetime measurements.

independent from the irradiation energy. As the relative abundances of the two emissive species are obviously independent from  $\lambda_{\text{exc}}$ , the two excited states are in thermal equilibrium in 3<sup>4+</sup>. As at 77 K only single emission is observed, both emissive states must be connected via a reaction path on the triplet hypersurface with a very low activation barrier to allow for thermal equilibration at room temperature and at 77 K state prior to emission.<sup>87</sup>

To allow for a rapid thermal exchange between the two relevant excited states even at low temperatures the transition between the two emissive states may only involve minor geometric changes. As an exciton transfer between the spatially separated <sup>3</sup>MLCT states involving Ru<sup>III</sup>(tpy<sup>-</sup>-CONH) and Ru<sup>III</sup>(tpy<sup>-</sup>-COOEt) requires the reorganization of various bond lengths the activation barrier between such two states is expected to be high. Accordingly, this process is unlikely to occur rapidly at 77 K in a frozen matrix, and these two states are ruled out as an origin for the dual emission. If such <sup>3</sup>MLCT states with a large activation barrier in between were involved in the emission process dual rather than a single emission would

be expected also at low temperatures. Consequently, the two emissive states likely involve Ru<sup>II</sup> → bridge-tpy-CO triplet states of both Ru<sup>II</sup> sites due to the spatial proximity of the involved centers.

Although the real electronic situation certainly is more complicated the simplified one-electron orbital representation in Scheme 3 helps to illustrate the processes leading to the observed dual emission. Four different excited states involving the bridging ligand and the two ruthenium centers of 3<sup>4+</sup> can be thought of according to this diagram. In this simple picture the four conceivable triplet states can be regarded as a Ru<sup>III</sup>Ru<sup>II</sup> mixed-valent system with a radical anion as bridging ligand.

**Scheme 3. Schematic Illustration of the Four <sup>3</sup>MLCT and <sup>3</sup>CS Excited States of 3<sup>4+</sup> Involving the Bridging Ligand<sup>a</sup>**

<sup>a</sup>The two electron configurations marked in red are most likely those involved in the room temperature emission of 3<sup>4+</sup>.

Two of these triplet states include an odd electron on the tpy-NH fragment of the bridge with one having the character of an MLCT state ( ${}^3\text{MLCT}_2$ ) and the other one having charge-separated state character ( ${}^3\text{CS}_2$ ). Because of the electron-donating effect of the  $-\text{NH}$  functionality their energies are substantially higher than those of the other two states involving the OC-tpy $^-$  moiety ( ${}^3\text{CS}_1$  and  ${}^3\text{MLCT}_1$ ). Consequently only the latter are relevant for excited-state emission according to Kasha's rule.<sup>87</sup> Electron transfer between the two ruthenium centers connects the two excited states  ${}^3\text{CS}_1$  and  ${}^3\text{MLCT}_1$ , which are thus valence-isomeric states. Since  ${}^3\text{CS}_1$  features a larger distance between the sites of the excited electron and the Ru<sup>III</sup> center, recombination/relaxation to the ground state might be slower. This fits to the assignment of a larger lifetime for  ${}^3\text{CS}_1$  ( $\tau = 44$  ns) as compared to that of  ${}^3\text{MLCT}_1$  ( $\tau = 24$  ns). The lowest-energy excited triplet state of  $3^{4+}$  was modeled by DFT calculations (B3LYP, LANL2DZ). Its spin density is localized on the bridging OC-tpy and the adjacent Ru<sup>III</sup> center (Supporting Information, Figure S12), which agrees with studies on the site of the first oxidation (experimental and theoretical, *vide infra*) and reduction (theoretical, *vide infra*). Hence triplet  $3^{4+}$  is described as an excited-state mixed-valent system ( $[\text{Ru}^{\text{II}}(\text{tpy-NHCO-tpy}^-)\text{Ru}^{\text{III}}]/[\text{Ru}^{\text{III}}(\text{tpy-NHCO-tpy}^-)\text{Ru}^{\text{II}}]$ ) of Robin–Day class II exhibiting substantial electronic coupling after optical population of a Ru<sup>II</sup>-bridge $^-$ -Ru<sup>III</sup> state.

Dual emission of polypyridine ruthenium(II) complexes has been observed very rarely. In mononuclear heteroleptic complexes it usually only arises with electronically very different  $\pi$ -accepting ligands such as in  $[\text{Ru}(\text{bpy})_2(\text{phen-4-R})]^{2+}$  (phen = 1,10-phenanthroline, R = phenylalkynyl)<sup>88</sup> allowing for two  ${}^3\text{MLCT}$  states with a high activation barrier in between so that both excited states emit simultaneously at room temperature and at 77 K.<sup>89–91</sup> Alternatively the presence of  ${}^3\text{MLCT}$  states as well as intraligand CT states ( ${}^3\text{ILCT}$ ) can be responsible for dual emission in bis(tridentate)ruthenium(II) complexes.<sup>92</sup> In dinuclear ruthenium(II) complexes dual emission has also been observed previously based on two  ${}^3\text{MLCT}$  states involving either phen or bpy as accepting ligands.<sup>93</sup> To the best of our knowledge no similar observation of dual emission of dinuclear complexes originating from two Ru<sup>III</sup>-tpy $^-$  triplet states involving the bridging ligand has been reported before. For a series of dinuclear bis(terpyridine)ruthenium(II) complexes, however, with either back-to-back or *para*-phenylene linkage ( $[(4'\text{-tolyl-tpy})\text{Ru}(\text{tpy}-(\text{C}_6\text{H}_4)_n\text{-tpy})\text{Ru}(\text{tpy-4'-tolyl})]^{4+}$  ( $n = 0, 1, 2$ )) it was shown that partial charge delocalization within the excited triplet state is responsible for a substantial extension of the luminescence lifetime (up to  $\tau = 570$  ns,  $n = 0$ ) along with a bathochromic shift of the emission just as observed in the case of  $3^{4+}$ .<sup>94</sup>

#### Acid–Base Chemistry of the Dinuclear Amide $3^{4+}$ .

While the acid–base chemistry of various derivatives of the mononuclear bis(terpyridine)ruthenium(II) amino acid has been previously discussed,<sup>19,31</sup> new reactivity arises from the dinuclear complex  $3^{4+}$  with two amides and a 4+ charge. The strongly polarizing effect of the 2-fold positively charged complex fragments on the bridging amide renders its proton significantly more acidic so that it can be readily abstracted using mild bases such as aliphatic tertiary amines in H<sub>2</sub>O/CH<sub>3</sub>CN mixtures. The two possible NH deprotonation reactions of  $3^{4+}$  have been studied via NMR and UV–vis absorption spectroscopy employing the strong phosphazene base P<sub>1</sub>-tBu under water-free conditions. In the UV–vis

absorption spectra (Figure 5) a two-step process is observed with two independent sets of isosbestic points, namely, at 512,

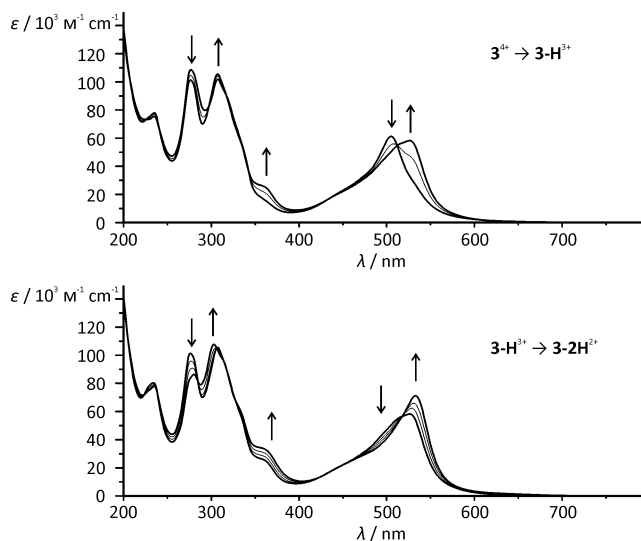


**Figure 5.** UV–vis absorption spectra of  $3^{4+}$  in dry CH<sub>3</sub>CN upon titration with a solution of phosphazene base P<sub>1</sub>-tBu in CH<sub>3</sub>CN (upper) 0 equiv  $\rightarrow$  1 equiv leading to  $3\text{-H}^{3+}$ , (lower) 1 equiv  $\rightarrow$  2.5 equiv leading to  $3\text{-2H}^{2+}$ . Arrows indicate most dominant spectral changes.

432, 343, 318, 297, 240, and 225 nm for the first step and at 519, 425, 326, 315, 306, 284, 239, and 223 nm for the second one. This observation is straightforwardly interpreted as the stepwise deprotonation of the complex with the first proton abstraction occurring at the strongly polarized bridging amide giving  $3\text{-H}^{3+}$  and the second one at the terminal NHCOCH<sub>3</sub> amide generating  $3\text{-2H}^{2+}$ . Notably, the second deprotonation is not accessible in the presence of water. The bathochromic shift of the  ${}^1\text{MLCT}$  absorption band from 504 nm in  $3^{4+}$  to 533 nm in  $3\text{-2H}^{2+}$  upon deprotonation is reflected by a color change from red to purple (*vide supra*) and can be traced back to changes in the geometry of the bridging ligand. As suggested by DFT calculations (B3LYP, LANL2DZ, IEFPCM: acetonitrile; *vide infra*) the tpy-NHCO-tpy bridge planarizes with dihedral angles at the bridging amide of  $\sim 0^\circ$  after deprotonation. This allows for a stronger  $\pi$  conjugation within the bridge leading to an enlargement of the chromophore and a lowering of the ligand-based LUMO energies. Additionally, the donor strength of the *N*-substituted terpyridine of the bridge is increased raising the energy of the ruthenium-based HOMO.

Support for a stepwise deprotonation mechanism is also obtained from  ${}^1\text{H}$  NMR spectroscopy (Figure 6). Upon addition of 1 equiv of P<sub>1</sub>-tBu to a solution of  $3^{4+}$  in CD<sub>3</sub>CN the resonance of the bridging amide proton at 10.5 ppm disappears, and several other resonances are shifted significantly with respect to the spectrum of  $3^{4+}$ . Major changes are observed for the resonances of the bridging ligand tpy-NHCO-tpy with the resonances of the tpy-NH fragment being shifted downfield, while the resonances of the tpy-CO fragment are found further upfield. This can be explained considering the stronger electron-donating effect of tpy-N $^-$  compared to tpy-NH increasing the electron density in this terpyridine. On the other side, the lowered dihedral angle (from  $-25^\circ$  to  $0^\circ$ ) between the carbonyl group and the proximal terpyridine increases the overlap of the  $\pi$  orbitals of these two fragments



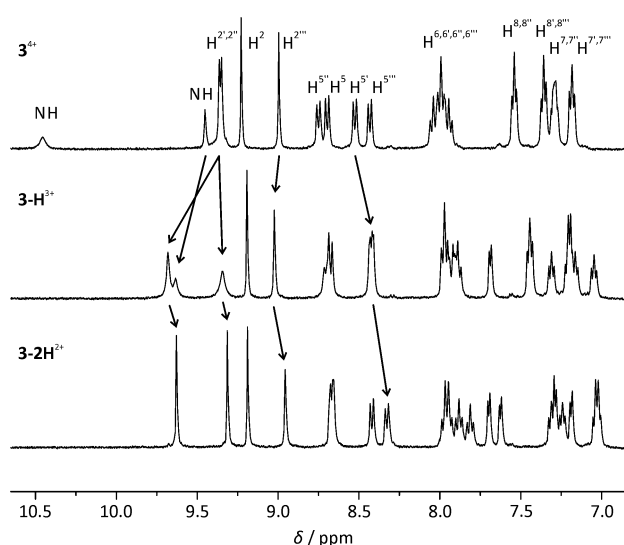


**Figure 6.**  $^1\text{H}$  NMR spectra of  $3^{4+}$  in  $\text{CD}_3\text{CN}$  (upper), after addition of 1 equiv of phosphazene base  $\text{P}_1\text{-tBu}$  (center;  $3\text{-H}^{3+}$ ) and after addition of 2 equiv of phosphazene base  $\text{P}_1\text{-tBu}$  (lower;  $3\text{-2H}^{2+}$ ). Arrows indicate shifts upon deprotonation.

resulting in a stronger  $-M$  effect of the carbonyl group. Upon addition of a second equivalent of base the resonance of the terminal amide proton disappears, and all aromatic signals are shifted upfield, except for those of the terminal  $\text{tpy-COOEt}$  ligand, which remain essentially unaltered. This is in agreement with an overall increase of the electron density within the complex upon deprotonation of the terminal amide. The pronounced acidity of the bridging amide will be relevant for the ground- and excited-state redox potentials of  $3^{4+}$  as well.

#### Redox Properties of Mono- and Dinuclear Amides.

The cyclic voltammograms of  $3^{4+}$  and  $4^{2+}$  in  $\text{CH}_3\text{CN}$  have a very similar shape (Figure 7, Table 2). Both complexes show a

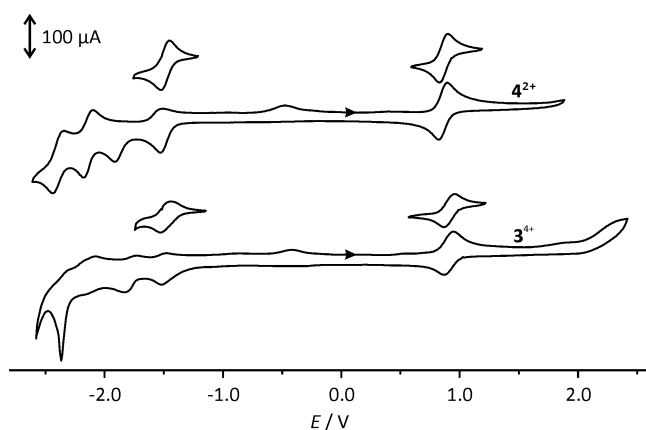


**Figure 7.** Cyclic voltammograms of 1 mM  $4^{2+}$  (upper) and  $3^{4+}$  (lower) in  $\text{CH}_3\text{CN}$  with 0.1 M  $[\text{nBu}_4][\text{NPF}_6]$  as supporting electrolyte referenced against the  $\text{FcH}/\text{FcH}^+$  couple. The first oxidation and reduction waves are shown individually.

reversible oxidation wave at  $\sim 0.9$  V versus  $\text{FcH}/\text{FcH}^+$ . For  $4^{2+}$  this wave represents the one-electron oxidation of  $\text{Ru}^{\text{II}}$  to  $\text{Ru}^{\text{III}}$  at 0.85 V. In  $3^{4+}$  both  $\text{Ru}^{\text{II}}$  centers are oxidized virtually at the same potential, leading to a two-electron oxidation wave at 0.91 V (referenced against 2 equiv of ferrocene as internal standard in the square-wave voltammogram, Supporting Information,

Figure S13). The slightly higher oxidation potential of  $3^{4+}$  compared to that of  $4^{2+}$  may be attributed to the unfavorable charge accumulation in  $3^{4+}$  (double oxidation affords a 6-fold positive charge). Interestingly, no separation of the oxidation waves of the two ruthenium centers is observed indicating no or only weak interaction between the metal sites using  $[\text{nBu}_4\text{N}][\text{PF}_6]$  as electrolyte<sup>95–97</sup> although potential differences are poor measures of electronic coupling.<sup>98–101</sup> Additionally  $4^{2+}$  exhibits four one-electron reduction waves, with the first two being reversible and the second two being quasireversible when examined individually. These are attributed to  $\text{tpy}/\text{tpy}^-$  and  $\text{tpy}^-/\text{tpy}^{2-}$  reductions starting with the acceptor-substituted  $\text{tpy-COOEt}$  ligand. In contrast,  $3^{4+/2+}$  shows only one reversible reduction wave, which accounts for a transfer of two electrons (referenced against internal ferrocene). It occurs essentially at the same potential as the first reduction of the mononuclear system  $4^{2+/+}$  ( $-1.49$  V vs  $-1.46$  V) and therefore is attributed to  $\text{tpy}/\text{tpy}^-$  reductions of both  $\text{tpy-CO}$  ligands. The second reduction is a quasireversible two-electron reduction ( $3^{2+/0}$ ). All further reductions overlap significantly so that a clear separation into individual reduction waves is impossible.

The irreversible peak at ca.  $-0.5$  V is a common feature of the cyclic voltammograms (CVs) of both complexes under study. It only arises in the CVs after reducing the respective compounds at potentials below  $-2.0$  V (quasi-reversible). Hence, it arises from the reoxidation of follow-up products of the reduced or doubly reduced state (vide infra for detailed discussion).

As can be seen from the oxidation potentials of  $4^{2+}$  and  $3^{4+}$  (Table 2), a strong oxidant is required to perform the oxidation of  $\text{Ru}^{\text{II}} \rightarrow \text{Ru}^{\text{III}}$ . Only few chemical redox reagents such as  $\text{Ce}^{\text{IV}}$  in acidic aqueous solution ( $E_{1/2} = 1.3$  V in  $\text{HClO}_4$ , 0.88 V in  $\text{H}_2\text{O}$ )<sup>63</sup> and the tris(2,4-dibromophenyl)aminium radical cation<sup>102</sup> in acetonitrile ( $E_{1/2} = 1.14$  V)<sup>63</sup> are capable to do so in a clean fashion. Reproducible UV–vis spectroscopic examination of the oxidation of  $4^{2+}$  and  $3^{4+}$  to  $4^{3+}$  and  $3^{6+}$ , respectively, was only possible in 0.5 M  $\text{H}_2\text{SO}_4(\text{aq})$  employing excess  $\text{Ce}(\text{SO}_4)_2$  as oxidant (Figure 8). A set of six isosbestic points is observed for the oxidation of  $3^{4+}$  to  $3^{6+}$  at 556, 421, 338, 298, 285, and 267 nm, indicative of a clean transformation without accumulation of  $3^{5+}$ . Even though an excess of oxidant is used, no additional band at  $\sim 400\text{--}420$  nm is observed originating from remaining  $\text{Ce}^{\text{IV}}$ , which is obviously consumed entirely immediately after addition. The  $^1\text{MLCT}$  absorption band of  $3^{4+}$  disappears completely, while a new broad and weak band appears with a maximum at 574 nm and a shoulder at  $\sim 720$  nm. The disappearance of the  $^1\text{MLCT}$  band indicates the complete oxidation of both  $\text{Ru}^{\text{II}}$  centers to  $\text{Ru}^{\text{III}}$  under these conditions. The new band is consequently ascribed to a  $^1\text{LMCT}$  transition from the donor-substituted  $\text{tpy-NH}$  ligand to  $\text{Ru}^{\text{III}}$ . Its intensity is rather low compared to, for example, the  $^1\text{LMCT}$  of  $[(\text{HOOC-tpy})\text{Ru}^{\text{III}}(\text{tpy-NH}_2)]^{3+}$  due to the less-pronounced donor effect of  $-\text{NHAc}$  as compared to that of  $-\text{NH}_2$ .<sup>19,57</sup> Performing the oxidation of  $4^{2+}$  to  $4^{3+}$  under the same conditions proved to be difficult since on the time scale of recording of the UV–vis absorption spectrum (minutes) after partial oxidation with  $\text{Ce}^{\text{IV}}$  substantial decomposition of the product was observed (absence of isosbestic points, loss of intensity). Only by addition of 10 equiv of oxidant followed by rapid measurement a reproducible spectrum of  $4^{3+}$  could be obtained (Figure 8, lower). It resembles that of the fully oxidized dinuclear complex  $3^{6+}$  ( $^1\text{LMCT}$  band, maxima at 590

**Table 2.** Ground- and Excited-State Electrochemical Properties of  $4^{2+}$  and  $3^{4+}$  in 0.1 M  $[n\text{Bu}_4][\text{NPF}_6]/\text{CH}_3\text{CN}$  at Room Temperature<sup>a</sup>

	$E_{\text{ox}}$ (Ru <sup>II</sup> /Ru <sup>III</sup> )	$E_{\text{red},1}$ (tpy/tpy <sup>-</sup> )	$E_{\text{red},2}$ (tpy/tpy <sup>-</sup> )	$E_{\text{ox}}^*$ (Ru <sup>II</sup> /Ru <sup>III</sup> ) <sup>b</sup>	$E_{\text{red},1}^*$ (tpy/tpy <sup>-</sup> ) <sup>c</sup>
$4^{2+}$	0.85 (68)	-1.46 (73)	-1.86	-1.04	0.43
$3^{4+}$	0.91 (84, 2e <sup>-</sup> )	-1.49 (81, 2e <sup>-</sup> )	-1.78 (2e <sup>-</sup> )	-0.97	0.39

<sup>a</sup>The peak-to-peak separations  $\Delta E_{\text{pp}}$  of the first oxidation and reduction waves are given in parentheses ( $E$ , V vs FcH/FcH<sup>+</sup> ( $E_{1/2}$  (FcH/FcH<sup>+</sup>) = 0.40 V vs SCE),  $\Delta E_{\text{pp}}$ , mV). <sup>b</sup> $E_{\text{ox}}^* = E_{\text{ox}} - E_{00}$ . <sup>c</sup> $E_{\text{red}}^* = E_{\text{red}} + E_{00}$ .  $E_{00}$  determined from emission spectra at 77 K.

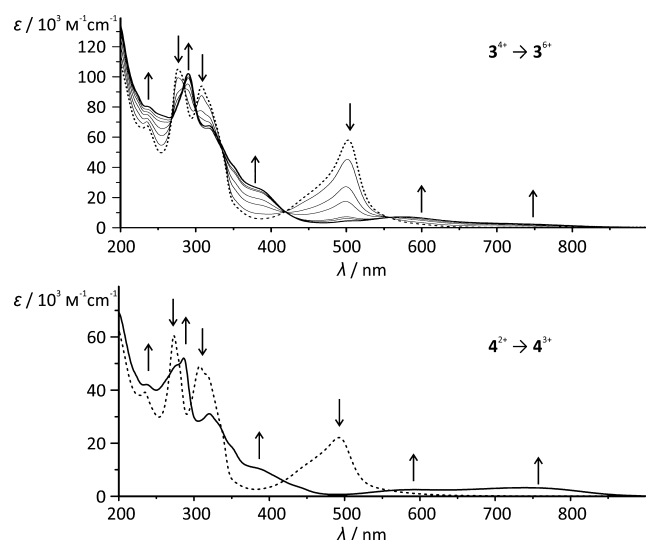


**Figure 8.** (upper) UV-vis absorption spectra of  $3^{4+}$  in 0.5 M  $\text{H}_2\text{SO}_4(\text{aq})$  upon titration with a solution of  $\text{Ce}(\text{SO}_4)_2$  in 0.5 M  $\text{H}_2\text{SO}_4(\text{aq})$  (0 equiv  $\rightarrow$  approximately 8 equiv). Arrows indicate spectral changes. (lower) UV-vis absorption spectra of  $4^{2+}$  and  $4^{3+}$  for comparison, obtained under the same conditions. Dashed lines indicate spectra of  $3^{4+}$  and  $4^{2+}$ , and bold lines show  $\text{Ru}^{\text{III}}$  complexes  $3^{6+}$  and  $4^{3+}$ .

and 739 nm) once again underlining the chemical similarity of  $4^{2+}$  and  $3^{4+}$ .

The mixed-valent  $\text{Ru}^{\text{II}}-\text{Ru}^{\text{III}}$  species  $3^{5+}$  is obtained in a statistical mixture with  $3^{4+}$  and  $3^{6+}$  due to facile disproportionation ( $2 \text{Ru}^{\text{II}}\text{Ru}^{\text{III}} \rightleftharpoons \text{Ru}^{\text{II}}\text{Ru}^{\text{II}} + \text{Ru}^{\text{III}}\text{Ru}^{\text{III}}$ ; statistical ratio of 1:2:1 for  $3^{4+}$ : $3^{5+}$ : $3^{6+}$ ). During the oxidation of  $3^{4+}$  to  $3^{6+}$ , no band attributable to an intervalence charge-transfer (IVCT) transition is observed in the NIR region of the spectrum up to 1350 nm (solvent absorption beyond 1350 nm prevented recording at longer wavelengths). Oxidation of  $3^{4+}$  in acetonitrile with substoichiometric amounts of tris(2,4-dibromophenyl)ammonium hexachloroantimonate did not show the appearance of a new IVCT band in the range between 1000 and 3000 nm. This is in agreement with results from cyclic voltammetry and allows the interpretation of  $3^{5+}$  as a valence-localized mixed-valent cation without observable electronic interaction between the ruthenium centers in different oxidation states (Robin-Day class I).<sup>45,48,52,101,103</sup>

This interpretation is in accordance with DFT calculations (B3LYP, LANL2DZ, IEFPCM:  $\text{CH}_3\text{CN}$ ) of the mixed-valent  $3^{5+}$  and the  $\text{Ru}^{\text{III}}\text{Ru}^{\text{III}}$   $3^{6+}$  complex (Figure 9). Spin density calculations performed on  $3^{5+}$  localize the unpaired electron on the *N*-terminal ruthenium atom. Upon oxidation to the  $\text{Ru}^{\text{III}}\text{Ru}^{\text{III}}$  species  $3^{6+}$  spin density is found on both metal centers. Time-dependent calculations on  $3^{5+}$  performed on the same level of theory predict no intensity for IVCT transitions of any kind in the NIR spectral region. Geometry optimizations failed to afford the valence-tautomeric mixed-valent  $\text{Ru}^{\text{II}}\text{Ru}^{\text{III}}$

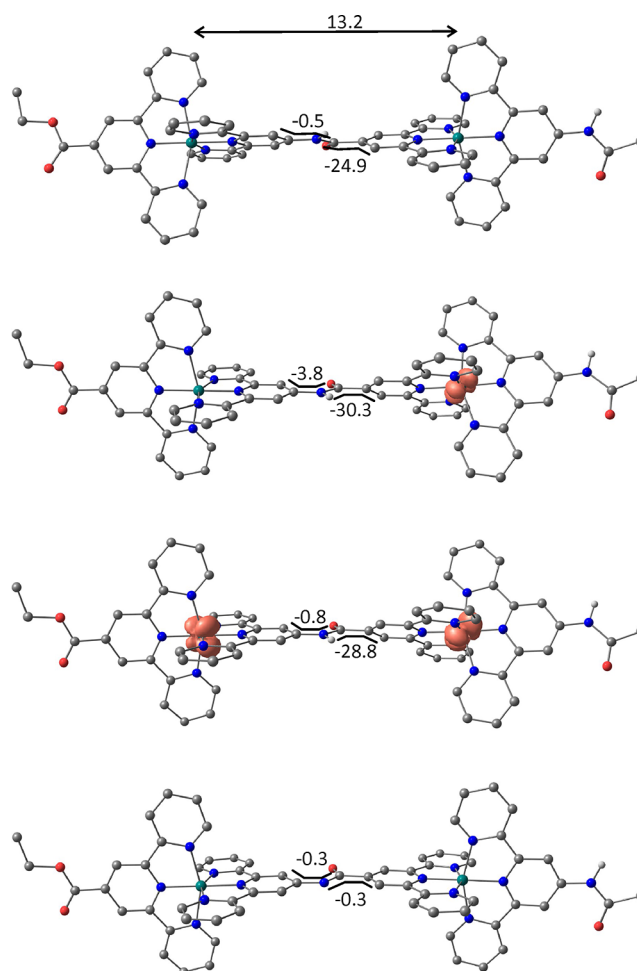


**Figure 9.** DFT (B3LYP, LANL2DZ, IEFPCM: acetonitrile) optimized geometric structures of  $3^{4+}$ ,  $3^{5+}$ ,  $3^{6+}$ , and  $3\text{-H}^{3+}$  (upper to lower), including tpy-NHCO-tpy dihedral angles (deg), Ru-Ru distance (Å), and calculated spin densities of  $3^{5+}$  (doublet) and  $3^{6+}$  (triplet). Contour value: 0.01, CH hydrogen atoms are omitted.

cation  $3^{5+}$  with the *C*-terminal ruthenium center being oxidized in repeated attempts suggesting that the  $\text{Ru}^{\text{II}}\text{Ru}^{\text{III}}$  species is lower in energy.

To further probe the hypothesis of noninteracting ruthenium centers and to localize the electron-hole oxidation, experiments were performed employing paramagnetic <sup>1</sup>H NMR spectroscopy.  $3^{4+}$  was titrated with substoichiometric amounts of tris(2,4-dibromophenyl)ammonium hexachloroantimonate as oxidant in deuterated acetonitrile (Figure 10). Paramagnetic line broadening and upfield shifts are observed only for certain proton resonances, namely, those assigned to the *N*-terminal bis(terpyridine)ruthenium(II) fragment. Especially pronounced is the shift of the resonances of  $\text{H}^{2''}$ ,  $\text{H}^{2'''}$ , and the bridging NH (highlighted with blue boxes in Figure 10), but also the proton resonances of  $\text{H}^{5''}$ ,  $\text{H}^{6''}$ ,  $\text{H}^{7''}$ ,  $\text{H}^{8''}$ ,  $\text{H}^{5'''}$ ,  $\text{H}^{6'''}$ ,  $\text{H}^{7'''}$ , and  $\text{H}^{8'''}$



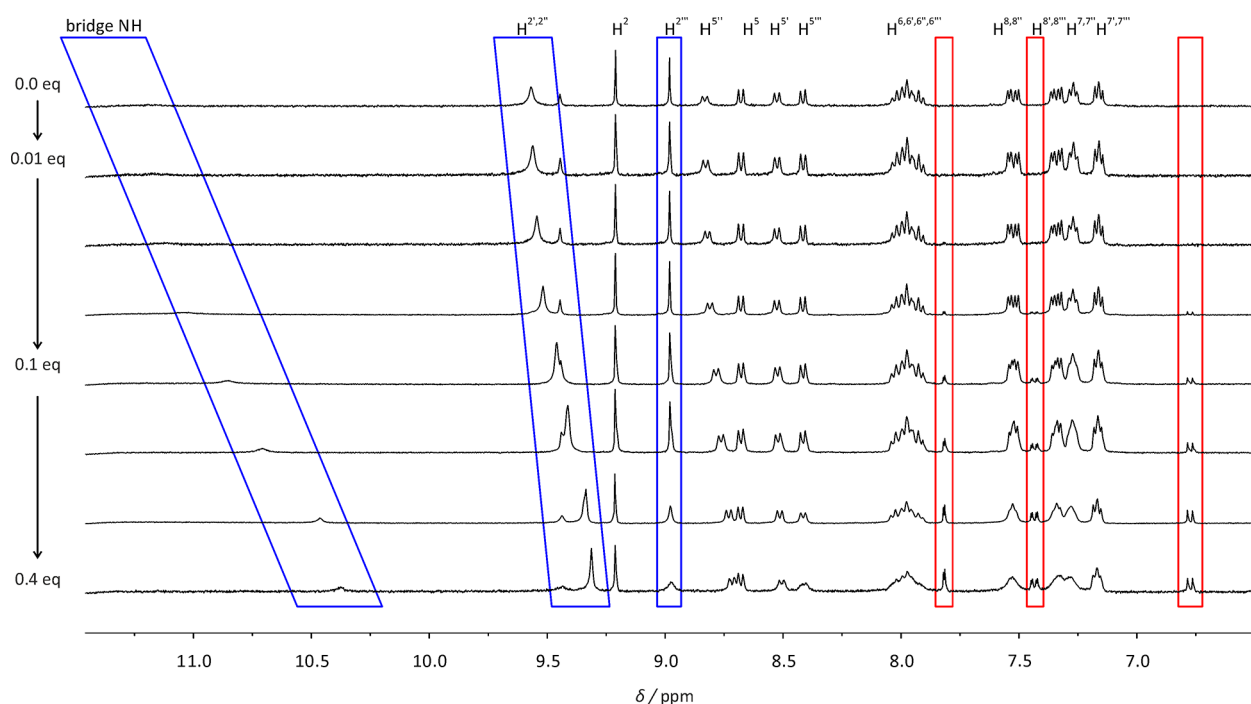


**Figure 10.**  $^1\text{H}$  NMR spectra of  $3^{4+}$  in  $\text{CD}_3\text{CN}$  upon partial oxidation to  $3^{5+}$  with substoichiometric amounts of tris(2,4-dibromophenyl)aminium hexachloroantimonate (resonances of the corresponding amine in red frames). Blue frames highlight most significant spectral changes.

respond to the partial oxidation of  $3^{4+}$ . At higher concentrations of oxidant ( $>0.2$  equiv) substantial broadening of the proton signals of the C-terminal complex fragment also becomes visible because then the concentration of the  $\text{Ru}^{\text{III}}\text{Ru}^{\text{III}}$  complex  $3^{6+}$  becomes spectroscopically significant due to disproportionation. The observation of the N-terminal bis(terpyridine)-ruthenium(II) fragment being the site of the first oxidation agrees with the theoretical results discussed above (Figure 9).

While a clean chemical oxidation of  $3^{4+}$  and  $4^{2+}$  is challenging to accomplish, the ligand-based reductions can easily be carried out using an acetonitrile solution of decamethylcobaltocene ( $E_{1/2} = -1.91$  V).<sup>63</sup> The ligand-centered radicals generated upon addition of 0.9 equiv of  $\text{CoCp}^*_2$  are examined using EPR spectroscopy after rapid-freezing to 77 K (Figure 11). The EPR spectra of the singly reduced species  $3^{3+}$  and  $4^{1+}$  are strikingly similar. Both show a rhombic signal pattern with one  $g$  value

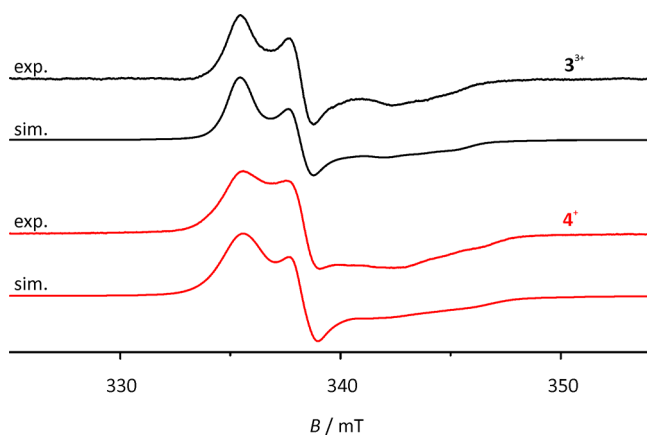


**Figure 11.** X-band EPR spectra of  $3^{3+}$  (black) and  $4^{1+}$  (red) in dry  $\text{CH}_3\text{CN}$  at 77 K after reduction with 0.9 equiv of  $\text{CoCp}^*_2$  including simulations.

greater and two lower than  $g_e$ . This is in agreement with an unpaired electron in the proximity of a low-spin  $\text{Ru}^{\text{II}}$  center. Interestingly, the signal occurring at the highest field is split by a hyperfine coupling to one nitrogen atom giving a 1:1:1 triplet ( $A(^{14}\text{N}) = 15\text{--}18$  G) suggesting that the unpaired electron is significantly localized on one of the coordinating nitrogen atoms. This is in agreement with the large  $g$  anisotropy of  $\sim\Delta g = 0.05$  and the substantial superhyperfine coupling to ruthenium required to fit the spectrum (see Table 3), which

**Table 3.** The  $g$  Values and Hyperfine and Superhyperfine Coupling Constants  $A$  of the Unpaired Electron in  $4^{1+}$  and  $3^{3+}$  Obtained by Simulation of the Experimental Spectra Recorded in Dry  $\text{CH}_3\text{CN}$  at 77 K Using EasySpin

	$g_{1,2,3}$	$\Delta g^a$	$A_{1,2,3} (^{99,101}\text{Ru})^b$	$A_{1,2,3} (^{14}\text{N})^b$
$4^{1+}$	2.0045, 1.9885, 1.9550	0.0495	2, 10, 24	1, 3, 18
$3^{3+}$	2.0057, 1.9892, 1.9580	0.0477	2, 8, 15	3, 2.5, 15

<sup>a</sup> $\Delta g = g_1 - g_3$ . <sup>b</sup>(A, G).

is in the range of other nitrogen-based radicals coordinated to a ruthenium(II) ion.<sup>39,40</sup> DFT calculations (B3LYP, LANL2DZ, IEFPCM: acetonitrile) support this interpretation: the spin density of the dinuclear complex  $3^{3+}$  is calculated to be spread mainly on the central pyridyl ring of the bridging tpy-CO ligand with a minor contribution from the coordinated ruthenium center (Supporting Information, Figure S12).

Interestingly, when measuring UV-vis absorption spectra while carrying out the reduction of  $4^{2+}$  and  $3^{4+}$  with up to 4 equiv of  $\text{CoCp}^*_2$  a clean transition with isosbestic points very similar to those observed upon deprotonation is obtained (Supporting Information, Figure S14). Furthermore, the spectra after addition of an excess of reductant (2 equiv for  $4^{2+}$ , 4 equiv for  $3^{4+}$ ) resemble those of the deprotonated species  $4\text{-H}^+$  and  $3\text{-H}^{3+}$  (see Figure 5). This cannot be interpreted as stepwise reductions of the respective complexes via  $4^{2+} \rightarrow 4^{1+} \rightarrow$

$4^0$  and  $3^{4+} \rightarrow 3^{3+} \rightarrow 3^{2+} \rightarrow 3^+ \rightarrow 3^0$ , respectively, since this should give several sets of isosbestic points in the UV–vis absorption spectra. However, these observations can be easily explained by a follow-up reaction after the initial reduction to  $4^+$  and  $3^{3+}$  (rapid-freeze EPR), namely, the irreversible reduction of protons to  $H_2$ . Alternatively, a direct reduction of protons by decamethylcobaltocene yielding dihydrogen is plausible.<sup>104</sup> The proton source could be residual crystal water generating  $OH^-$ , which deprotonates the amides. Excess of reductant is required due to varying amounts of water present in  $4^{2+}$  and  $3^{4+}$  (see Experimental Section). Spectral changes of similar shape have been observed previously with dinuclear amide conjugates in our group upon addition of decamethylcobaltocene as reductant.<sup>39,40</sup> The results obtained in the current study suggest that also in those cases the bridging amide is deprotonated in the presence of  $H_2O$  (UV–vis) after initial reduction of the complexes (rapid-freeze EPR).

The same process, namely, deprotonation of  $3^{4+}$ , is observed when monitoring the addition of  $CoCp^*_2$  via NMR spectroscopy (slow time scale). No paramagnetic signal broadening appears upon addition of reductant to a solution of  $3^{4+}$  (Supporting Information, Figure S15). This would have been indicative of the presence of a radical anion especially because the expected line broadening of the proton resonances is larger for a ligand-based radical as compared to a metal-based radical (Figure 10). The discrepancy between EPR results, on the one hand, where the unpaired electron originating from a complex-based reduction can be observed, and NMR and UV–vis absorption spectroscopy, on the other hand, which reveal follow-up products of this initial reduction, is ascribed to the different time scales of the respective experiments: because of the apparent instability of the radical formed in the presence of residual  $H_2O$ , rapid freezing of the solution of  $3^{4+}$  a few seconds after addition of  $CoCp^*_2$  allows detection of an EPR signal, while the NMR and UV–vis absorption measurements are carried out several minutes after the addition of reductant, allowing follow-up reactions to occur prior to measurement. CV experiments further support this interpretation: scanning just the potential range of the first ligand-based reduction of  $3^{4+}$  delivers a reversible redox wave. Scanning the full solvent window requires enough time to allow for further reactions of the complex after reduction. The reoxidation of the follow-up species then occurs at ca.  $-0.5$  V for both complexes  $4^{2+}$  and  $3^{4+}$  shifted by approximately 1 V to more positive values (Figure 7). This lends further support to a reaction sequence  $3^{4+} \rightarrow 3^{3+} \rightarrow 3\text{-H}^{3+} + 1/2H_2$ .

The excited-state redox potentials of the complexes  $4^{2+}$  and  $3^{4+}$  were calculated from  $E_{ox}^* = E_{ox} - E_{00}$  and  $E_{red}^* = E_{red} + E_{00}$  (Table 2).<sup>105,106</sup> As expected the complexes become stronger reductants and oxidants in the  $^3MLCT$  excited state. To probe the excited-state properties of  $4^{2+}$  and  $3^{4+}$  Stern–Volmer plots with various ferrocene derivatives and amines as potential weak electron donors were recorded (Table 4).<sup>107</sup> Employing ferrocene, ferrocenecarboxylic acid methyl ester, and 1,1'-ferrocenedicarboxylic acid dimethyl ester as electron donors for the reductive quenching of the  $^3MLCT$  state of  $4^{2+}$ , linear Stern–Volmer plots are obtained that show a clear dependence of the quenching rate  $k_q$  from the redox potential of the corresponding quencher (Supporting Information, Figure S16).<sup>108–111</sup> Lowering the driving force for the electron-transfer step reduces the efficiency of the reductive quenching significantly as expected from Marcus theory. Interestingly even if the electron-transfer step is estimated to be thermodynamically

**Table 4.** Excited-State Stern–Volmer Quenching Constants  $K_{sv}^a$  of  $4^{2+}$  and  $3^{4+}$  by Various Quenchers, Fraction  $f^b$  of Complex Accessible for Quencher, Bimolecular Quenching Rate Constants  $k_q^c$  and Quenching Fractions  $\eta_q^d$  by 0.1 M Quencher in  $CH_3CN$  at Room Temperature

		$4^{2+}$	$3^{4+}$
FcH ( $E_{1/2} = 0.00$ V) <sup>63</sup>	$K_{sv}(f)$	246 (100)	432 (100)
	$k_q$	$1.17 \times 10^{10}$	$1.80 \times 10^{10}$
	$\eta_q$	0.96	0.98
FcCOOMe ( $E_{1/2} = 0.30$ V) <sup>125</sup>	$K_{sv}(f)$	160 (100)	
	$k_q$	$7.62 \times 10^9$	
	$\eta_q$	0.94	
Fc(COOMe) <sub>2</sub> ( $E_{1/2} = 0.50$ V) <sup>126</sup>	$K_{sv}(f)$	147 (100)	399 (100)
	$k_q$	$7.00 \times 10^9$	$1.66 \times 10^{10}$
	$\eta_q$	0.94	0.98
Ph-NMe <sub>2</sub> ( $E_{1/2} = 0.39$ V) <sup>117</sup>	$K_{sv}(f)$	1.8 (100)	14.4 (57)
	$k_q$	$8.6 \times 10^7$	$6.00 \times 10^8$
	$\eta_q$	15	34

<sup>a</sup> $K_{sv}$ ,  $M^{-1}$ . <sup>b</sup> $f$ , %. <sup>c</sup> $k_q$ ,  $M^{-1} s^{-1} = K_{sv}/\tau$ . <sup>d</sup> $\eta_q$ , % =  $fK_{sv}[Q](1 + K_{sv}[Q])^{-1}$ .

ally slightly uphill by 70 mV as in the reaction of  $4^{2+}$  with Fc(COOMe)<sub>2</sub> very efficient quenching of the emission of  $4^{2+}$  is still observed. This cannot be accounted for solely with a contribution from a reductive electron-transfer step from the ferrocene to the ruthenium complex. An additional feasible path for radiationless deactivation is an energy transfer from the  $^3MLCT$  state of the Ru complex populating the nonemissive triplet excited state of the respective ferrocene derivative.<sup>31,112–114</sup> While stronger electron-withdrawing substituents on ferrocene lower its reduction potential, they also stabilize its triplet state facilitating energy transfer. It is worth noting that for both the mono- and the dinuclear complexes  $4^{2+}$  and  $3^{4+}$  very rapid quenching with formal bimolecular rate constants close to the diffusion limit ( $k = 1.9 \times 10^{10}$ , 298 K,  $CH_3CN$ )<sup>115</sup> is observed with all ferrocene derivatives without any detectable static quenching due to preorganization phenomena of the two components in their respective ground states. This emphasizes that a significant contribution of the excited-state quenching by ferrocene originates from energy transfer.

The choice of amines as electron sources for reductive electron transfer quenching of the complexes  $4^{2+}$  and  $3^{4+}$  is limited due to the facile deprotonation of the amide protons (vide supra). Using *N,N*-dimethylaniline, which is not sufficiently basic to abstract protons from the bridge of  $3^{4+}$  ( $pK_s = 5.1$ ,<sup>116</sup> substantiated by UV–vis absorption spectroscopy) as electron source ( $E_{1/2} = 0.39$  V vs FcH/FcH<sup>+</sup>),<sup>117</sup> it is possible to record Stern–Volmer plots for both complexes  $4^{2+}$  and  $3^{4+}$  (Figure 12). While its quenching efficiency with respect to  $4^{2+}$  is weak (2 orders of magnitude lower than that for Fc(COOMe)<sub>2</sub>; Table 4) it is increased by almost 1 order of magnitude in the  $3^{4+}$ /amine pair. This cannot be explained just by the marginally increased driving force for the electron transfer by 40 mV (Table 2). Additionally a curve bent downward toward the  $x$ -axis is obtained when  $(I_0/I - 1)$  is plotted against  $c_{\text{quencher}}$  indicating a precoordination of the quencher to the emissive species (Figure 12). An appropriate plot employing  $I_0/(I_0 - I) = (fK_{sv}[Q])^{-1} + f^{-1}$  gives the fraction  $f$  of the emissive species actively taking part in the bimolecular quenching process as well as the Stern–Volmer constant  $K_{sv}$  (Supporting Information, Figure S17).<sup>118</sup> We ascribe the substantial quenching fraction to an association of

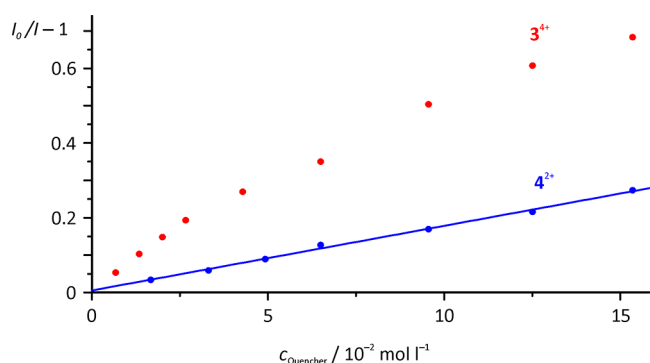
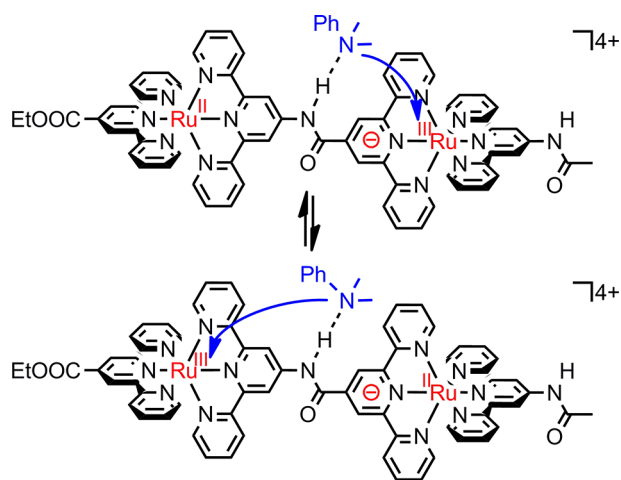


**Figure 12.** Stern–Volmer plots of the mono- and dinuclear complexes  $4^{2+}$  (blue) and  $3^{4+}$  (red) employing *N,N*-dimethylaniline as quencher. Plots were obtained using complex concentrations of  $c = 2 \times 10^{-5}$  mol  $L^{-1}$ .

the  $\text{PhNMe}_2$  nitrogen atom to the polarized proton of the bridging amide via a strong hydrogen bond. This facilitates inner-sphere reductive electron transfer into one of the excited states of the dinuclear complex as illustrated in Scheme 4. Similar observations of precoordination, especially via hydrogen bonds facilitating electron transfer from/to excited states, have been documented in the literature.<sup>119–124</sup>

**Scheme 4.** Reductive Electron Transfer from  $\text{PhNMe}_2$  to the Two Excited Triplet States of  $3^{4+}$



## CONCLUSION

The new dinuclear bis(terpyridine)ruthenium(II) complex  $3^{4+}$  with remarkable electronic symmetry despite an asymmetric bridge was synthesized and fully characterized. No electronic coupling is observed in the mixed-valent state  $3^{5+}$ . However, the similarity of the chemical environments of the ruthenium centers in  $3^{4+}$  enables a thermal electron transfer between  $\text{Ru}^{\text{II}}$  and  $\text{Ru}^{\text{III}}$  in the triplet excited states of  $3^{4+}$ . The two valence tautomers are observed via emission spectroscopy (dual emission) and excited-state lifetime measurements.

Reduction of  $3^{4+}$  with  $\text{CoCp}^*_2$  initially yields the radical localized on the bridge. This radical further reacts to finally give the deprotonated complex  $3\text{-H}^{3+}$  and presumably  $\text{H}_2$ .  $3\text{-H}^{3+}$  and  $3\text{-2H}^{2+}$  are prepared directly from strong bases and  $3^{4+}$ .  $\text{PhNMe}_2$  is not basic enough to deprotonate  $3^{4+}$  but coordinates to the bridging NH group via a hydrogen bond,

which facilitates reductive electron transfer from  $\text{PhNMe}_2$  to the excited complex  $3^{4+}$ . Further studies will be conducted to elucidate this process, namely, whether  $3^{4+}$  can act as an electro- or photocatalyst for the reduction of protons from water and which role the proton of the bridging amide plays in such a process.

## ASSOCIATED CONTENT

### Supporting Information

Experimental procedures for the syntheses of  $8(\text{PF}_6)_2$  and  $9(\text{PF}_6)_2$ ;  $^1\text{H}$  and  $^{13}\text{C}$  NMR spectra of  $7(\text{PF}_6)_2$ ,  $8(\text{PF}_6)_2$ , and  $9(\text{PF}_6)_2$ ;  $^{19}\text{F}$  NMR spectra of  $7(\text{PF}_6)_2$  and  $8(\text{PF}_6)_2$ ; CH-HSQC and CH-HMBC spectra of  $3(\text{PF}_6)_4$ ; emission spectra of  $3(\text{PF}_6)_4$  at different excitation wavelengths; figures of DFT-optimized geometries of  $3^{3+}$  and triplet  $3^{4+}$ ; UV-vis absorption spectra of  $3^{4+}$  and  $4^{2+}$  upon titration with  $\text{CoCp}^*_2$ ;  $^1\text{H}$  NMR spectra of  $3^{4+}$  upon deprotonation; Stern–Volmer plots of  $3^{4+}$  and  $4^{2+}$  with different ferrocene derivatives; Cartesian coordinates of DFT-optimized geometries of  $3^{4+}$ ,  $3^{5+}$ ,  $3^{6+}$ , triplet  $3^{4+}$ , and  $3^{3+}$ . This material is available free of charge via the Internet at <http://pubs.acs.org>.

## AUTHOR INFORMATION

### Corresponding Author

\*Fax: +49613127277. E-mail: [katja.heinze@uni-mainz.de](mailto:katja.heinze@uni-mainz.de).

### Author Contributions

The manuscript was written through contributions of all authors. All authors have given approval to the final version of the manuscript.

### Funding

This work was financially supported by the Deutsche Forschungsgemeinschaft (GSC 266, Materials Science in Mainz, scholarship for C.K.).

### Notes

The authors declare no competing financial interest.

## REFERENCES

- (1) Sauvage, J. P.; Collin, J. P.; Chambron, J. C.; Guillerez, S.; Coudret, C.; Balzani, V.; Barigelli, F.; Cola, L.; de Flamigni, L. *Chem. Rev.* **1994**, *94*, 993–1019.
- (2) D'Alessandro, D. M.; Keene, F. R. *New J. Chem.* **2006**, *30*, 228–237.
- (3) Chiorboli, C.; Indelli, M. T.; Scandola, F. *Top. Curr. Chem.* **2005**, *257*, 63–102.
- (4) Sun, L.; Hammarström, L.; Åkermark, B.; Styring, S. *Chem. Soc. Rev.* **2001**, *30*, 36–49.
- (5) Barigelli, F.; Flamigni, L. *Chem. Soc. Rev.* **2000**, *29*, 1–12.
- (6) Flores-Torres, S.; Hutchison, G. R.; Soltzberg, L. J.; Abruña, H. D. *J. Am. Chem. Soc.* **2006**, *128*, 1513–1522.
- (7) Akasaka, T.; Inoue, H.; Kuwabara, M.; Mutai, T.; Otsuki, J.; Araki, K. *Dalton Trans.* **2003**, 815–821.
- (8) Siebler, D.; Linseis, M.; Gasi, T.; Carrella, L. M.; Winter, R. F.; Förster, C.; Heinze, K. *Chem.—Eur. J.* **2011**, *17*, 4540–4551.
- (9) Ozawa, H.; Haga, M.; Sakai, K. *J. Am. Chem. Soc.* **2006**, *128*, 4926–4927.
- (10) Elvington, M.; Brown, J.; Arachchige, S. M.; Brewer, K. J. *J. Am. Chem. Soc.* **2007**, *129*, 10644–10645.
- (11) Takeda, H.; Koike, K.; Inoue, H.; Ishitani, O. *J. Am. Chem. Soc.* **2008**, *130*, 2023–2031.
- (12) Kumar, A.; Chhatwal, M.; Mondal, P. C.; Singh, V.; Singh, A. K.; Cristaldi, D. A.; Gupta, R. D.; Gulino, A. *Chem. Commun.* **2014**, *50*, 3783.
- (13) O'Regan, B.; Grätzel, M. *Nature* **1991**, *353*, 737–740.



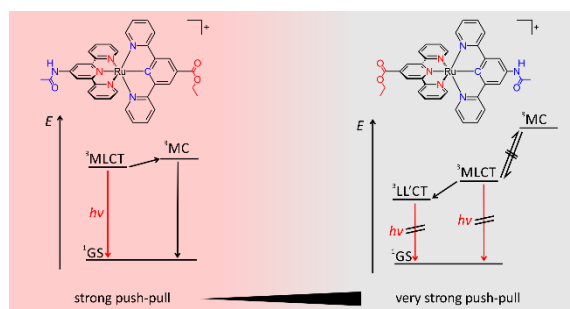
- (14) Bolink, H. J.; Cappelli, L.; Coronado, E.; Gaviña, P. *Inorg. Chem.* **2005**, *44*, 5966–5968.
- (15) Kalyanasundaram, K. *Coord. Chem. Rev.* **1982**, *46*, 159–244.
- (16) Caspar, J. V.; Meyer, T. J. *J. Am. Chem. Soc.* **1983**, *105*, 5583–5590.
- (17) Meyer, T. J. *Pure Appl. Chem.* **1986**, *58*, 1193–1206.
- (18) Suzuki, K.; Kobayashi, A.; Kaneko, S.; Takehira, K.; Yoshihara, T.; Ishida, H.; Shiina, Y.; Oishi, S.; Tobita, S. *Phys. Chem. Chem. Phys.* **2009**, *11*, 9850–9860.
- (19) Breivogel, A.; Kreitner, C.; Heinze, K. *Eur. J. Inorg. Chem.* **2014**, *2014*, 10.1002/ejic.201402466.
- (20) Breivogel, A.; Wooh, S.; Dietrich, J.; Kim, T. Y.; Kang, Y. S.; Char, K.; Heinze, K. *Eur. J. Inorg. Chem.* **2014**, 2720–2734.
- (21) Biner, M.; Buergi, H. B.; Ludi, A.; Roehr, C. *J. Am. Chem. Soc.* **1992**, *114*, 5197–5203.
- (22) Lashgari, K.; Kritikos, M.; Norrestam, R.; Norrby, T. *Acta Crystallogr., Sect. C: Cryst. Struct. Commun.* **1999**, *55*, 64–67.
- (23) Calvert, J. M.; Caspar, J. V.; Binstead, R. A.; Westmoreland, T. D.; Meyer, T. J. *J. Am. Chem. Soc.* **1982**, *104*, 6620–6627.
- (24) Maestri, M.; Armaroli, N.; Balzani, V.; Constable, E. C.; Thompson, A. M. W. C. *Inorg. Chem.* **1995**, *34*, 2759–2767.
- (25) Medlycott, E. A.; Hanan, G. S. *Chem. Soc. Rev.* **2005**, *34*, 133.
- (26) Abrahamsson, M.; Jäger, M.; Österman, T.; Eriksson, L.; Persson, P.; Becker, H.-C.; Johansson, O.; Hammarström, L. *J. Am. Chem. Soc.* **2006**, *128*, 12616–12617.
- (27) Schramm, F.; Meded, V.; Fliegl, H.; Fink, K.; Fuhr, O.; Qu, Z.; Klopper, W.; Finn, S.; Keyes, T. E.; Ruben, M. *Inorg. Chem.* **2009**, *48*, 5677–5684.
- (28) Breivogel, A.; Förster, C.; Heinze, K. *Inorg. Chem.* **2010**, *49*, 7052–7056.
- (29) Breivogel, A.; Meister, M.; Förster, C.; Laquai, F.; Heinze, K. *Chem.—Eur. J.* **2013**, *19*, 13745–13760.
- (30) Brown, D. G.; Sanguantrakun, N.; Schulze, B.; Schubert, U. S.; Berlinguette, C. P. *J. Am. Chem. Soc.* **2012**, *134*, 12354–12357.
- (31) Heinze, K.; Hempel, K.; Beckmann, M. *Eur. J. Inorg. Chem.* **2006**, 2040–2050.
- (32) Reynal, A.; Palomares, E. *Eur. J. Inorg. Chem.* **2011**, 4509–4526.
- (33) Sun, P.; Krishnan, A.; Yadav, A.; Singh, S.; MacDonnell, F. M.; Armstrong, D. W. *Inorg. Chem.* **2007**, *46*, 10312–10320.
- (34) Gong, L.; Mulcahy, S. P.; Harms, K.; Meggers, E. *J. Am. Chem. Soc.* **2009**, *131*, 9602–9603.
- (35) Meggers, E. *Chem.—Eur. J.* **2010**, *16*, 752–758.
- (36) Heinze, K.; Hempel, K.; Tschierlei, S.; Schmitt, M.; Popp, J.; Rau, S. *Eur. J. Inorg. Chem.* **2009**, 3119–3126.
- (37) Heinze, K.; Hempel, K.; Breivogel, A. *Z. Anorg. Allg. Chem.* **2009**, *635*, 2541–2549.
- (38) Heinze, K.; Hempel, K. *Chem.—Eur. J.* **2009**, *15*, 1346–1358.
- (39) Dietrich, J.; Thorenz, U.; Förster, C.; Heinze, K. *Inorg. Chem.* **2013**, *52*, 1248–1264.
- (40) Dietrich, J.; Wünsche von Leupoldt, A.; Grabolle, M.; Resch-Genger, U.; Heinze, K. *Eur. J. Inorg. Chem.* **2013**, 3009–3019.
- (41) Hurlay, D. J.; Roppe, J. R.; Tor, Y. *Chem. Commun.* **1999**, 993–994.
- (42) Bishop, B. M.; McCafferty, D. G.; Erickson, B. W. *Tetrahedron* **2000**, *56*, 4629–4638.
- (43) Kise, K. J.; Bowler, B. E. *Inorg. Chem.* **2002**, *41*, 379–386.
- (44) Creutz, C.; Taube, H. *J. Am. Chem. Soc.* **1969**, *91*, 3988–3989.
- (45) Kaim, W.; Klein, A.; Glöckle, M. *Acc. Chem. Res.* **2000**, *33*, 755–763.
- (46) Kaim, W.; Sarkar, B. *Coord. Chem. Rev.* **2007**, *251*, 584–594.
- (47) Kaim, W.; Lahiri, G. K. *Angew. Chem.* **2007**, *119*, 1808–1828; *Angew. Chem., Int. Ed.* **2007**, *46*, 1778–1796.
- (48) Hush, N. *Electrochim. Acta* **1968**, *13*, 1005–1023.
- (49) Fuerholz, U.; Buergi, H. B.; Wagner, F. E.; Stebler, A.; Ammeter, J. H.; Krausz, E.; Clark, R. J. H.; Stead, M. J.; Ludi, A. *J. Am. Chem. Soc.* **1984**, *106*, 121–123.
- (50) Zhang, L. T.; Ko, J.; Ondrechen, M. J. *J. Am. Chem. Soc.* **1987**, *109*, 1666–1671.
- (51) Hush, N. *Coord. Chem. Rev.* **1985**, *64*, 135–157.
- (52) Robin, M. B.; Day, P. *Adv. Inorg. Chem.* **1968**, *10*, 247–422.
- (53) Brunschwig, B. S.; Creutz, C.; Sutin, N. *Chem. Soc. Rev.* **2002**, *31*, 168–184.
- (54) D'Alessandro, D. M.; Topley, A. C.; Davies, M. S.; Keene, F. R. *Chem.—Eur. J.* **2006**, *12*, 4873–4884.
- (55) Crutchley, R. J. *Angew. Chem.* **2005**, *117*, 6610–6612; *Angew. Chem., Int. Ed.* **2005**, *44*, 6452–6454.
- (56) Moser, C. C.; Keske, J. M.; Warncke, K.; Farid, R. S.; Dutton, P. L. *Nature* **1992**, *355*, 796–802.
- (57) Breivogel, A.; Hempel, K.; Heinze, K. *Inorg. Chim. Acta* **2011**, *374*, 152–162.
- (58) Sortino, S.; Petralia, S.; Di Bella, S. *J. Am. Chem. Soc.* **2003**, *125*, 5610–5611.
- (59) Weinberg, D. R.; Gagliardi, C. J.; Hull, J. F.; Murphy, C. F.; Kent, C. A.; Westlake, B. C.; Paul, A.; Ess, D. H.; McCafferty, D. G.; Meyer, T. J. *Chem. Rev.* **2012**, *112*, 4016–4093.
- (60) Neidlinger, A.; Ksenofontov, V.; Heinze, K. *Organometallics* **2013**, *32*, 5955–5965.
- (61) Bordwell, F. G.; Ji, G. Z. *J. Am. Chem. Soc.* **1991**, *113*, 8398–8401.
- (62) Fulmer, G. R.; Miller, A. J. M.; Sherden, N. H.; Gottlieb, H. E.; Nudelman, A.; Stoltz, B. M.; Bercaw, J. E.; Goldberg, K. I. *Organometallics* **2010**, *29*, 2176–2179.
- (63) Connelly, N. G.; Geiger, W. E. *Chem. Rev.* **1996**, *96*, 877–910.
- (64) Stoll, S.; Schweiger, A. *J. Magn. Reson.* **2006**, *178*, 42–55.
- (65) Frisch, M. J.; Trucks, G. W.; Schlegel, H. B.; Scuseria, G. E.; Robb, M. A.; Cheeseman, J. R.; Scalmani, G.; Barone, V.; Mennucci, B.; Petersson, G. A.; Nakatsuji, H.; Caricato, M.; Li, X.; Hratchian, H. P.; Izmaylov, A. F.; Bloino, J.; Zheng, G.; Sonnenberg, J. L.; Hada, M.; Ehara, M.; Toyota, K.; Fukuda, R.; Hasegawa, J.; Ishida, M.; Nakajima, T.; Honda, Y.; Kitao, O.; Nakai, H.; Vreven, T.; Montgomery, J. J. A.; Peralta, J. E.; Ogliaro, F.; Bearpark, M.; Heyd, J. J.; Brothers, E.; Kudin, K. N.; Staroverov, V. N.; Kobayashi, R.; Normand, J.; Raghavachari, K.; Rendell, A.; Burant, J. C.; Iyengar, S. S.; Tomasi, J.; Cossi, M.; Rega, N.; Millam, J. M.; Klene, M.; Knox, J. E.; Cross, J. B.; Bakken, V.; Adamo, C.; Jaramillo, J.; Gomperts, R.; Stratmann, R. E.; Yazyev, O.; Austin, A. J.; Cammi, R.; Pomelli, C.; Ochterski, J. W.; Martin, R. L.; Morokuma, K.; Zakrzewski, V. G.; Voth, G. A.; Salvador, P.; Dannenberg, J. J.; Dapprich, S.; Daniels, A. D.; Farkas, Ö.; Foresman, J. B.; Ortiz, J. V.; Cioslowski, J.; Fox, D. J. *Gaussian09*, Rev. A.02; Gaussian, Inc.: Wallingford, CT, 2009.
- (66) Becke, A. D. *J. Chem. Phys.* **1993**, *98*, 5648.
- (67) Dunning, T. H.; Hay, P. J. in *Methods of Electronic Structure Theory*; Schaefer, H. F., Ed.; Springer: Boston, MA, 1977.
- (68) Hay, P. J.; Wadt, W. R. *J. Chem. Phys.* **1985**, *82*, 270.
- (69) Wadt, W. R.; Hay, P. J. *J. Chem. Phys.* **1985**, *82*, 284.
- (70) Hay, P. J.; Wadt, W. R. *J. Chem. Phys.* **1985**, *82*, 299.
- (71) Miertuš, S.; Scrocco, E.; Tomasi, J. *Chem. Phys.* **1981**, *55*, 117–129.
- (72) Miertuš, S.; Tomasi, J. *Chem. Phys.* **1982**, *65*, 239–245.
- (73) Pascual-ahuir, J. L.; Silla, E.; Tunon, I. *J. Comput. Chem.* **1994**, *15*, 1127–1138.
- (74) Rosales, A.; Muñoz-Bascón, J.; López-Sánchez, C.; Álvarez-Corral, M.; Muñoz-Dorado, M.; Rodríguez-García, I.; Oltra, J. E. *J. Org. Chem.* **2012**, *77*, 4171–4176.
- (75) Han, S.-Y.; Kim, Y.-A. *Tetrahedron* **2004**, *60*, 2447–2467.
- (76) König, W.; Geiger, R. *Chem. Ber.* **1970**, *103*, 788–798.
- (77) Coste, J.; Le-Nguyen, D.; Castro, B. *Tetrahedron Lett.* **1990**, *31*, 205–208.
- (78) Frérot, E.; Coste, J.; Pantaloni, A.; Dufour, M.-N.; Jouin, P. *Tetrahedron* **1991**, *47*, 259–270.
- (79) Carpino, L. A. *J. Am. Chem. Soc.* **1993**, *115*, 4397–4398.
- (80) Kisfaludy, L.; Schön, I. *Synthesis* **1983**, 325–327.
- (81) Atherton, E.; Cameron, L. R.; Sheppard, R. C. *Tetrahedron* **1988**, *44*, 843–857.
- (82) Gagnon, P.; Huang, X.; Therrien, E.; Keillor, J. W. *Tetrahedron Lett.* **2002**, *43*, 7717–7719.
- (83) Beyermann, M.; Bienert, M.; Niedrich, H.; Carpino, L. A.; Sadat-Aalae, D. *J. Org. Chem.* **1990**, *55*, 721–728.

- (84) Neises, B.; Steglich, W. *Angew. Chem.* **1978**, *90*, 556–557; *Angew. Chem., Int. Ed.* **1978**, *17*, 522–524.
- (85) Albericio, F.; Bofill, J. M.; El-Faham, A.; Kates, S. A. *J. Org. Chem.* **1998**, *63*, 9678–9683.
- (86) First interpretations of this observation were based on the presence of two different solvates of  $3^{4+}$ , one potentially an  $H_2O$  and the other one a  $CH_3CN$  solvate (via hydrogen bonds to the NH groups). Another interpretation included the simultaneous presence of contact ion pairs and solvent-separated ion pairs. These contact ion pairs were proposed as the complex cation  $3^{4+}$  and a strongly hydrogen-bonded  $PF_6^-$  counterion in the “binding pocket” of the bridging amide functionality as observed for other dinuclear amide-bridged complexes in our group.<sup>39,40</sup> To verify these interpretations lifetime measurements with varying concentrations of  $H_2O$  as good solvent and  $Cl^-$  ions as competing counterion were performed. These lifetime experiments showed that the ratio of the two emissive species and their emission lifetimes are essentially independent from these parameters excluding an interpretation of this kind.
- (87) Kasha, M. *Discuss. Faraday Soc.* **1950**, *9*, 14–19.
- (88) Glazer, E. C.; Magde, D.; Tor, Y. *J. Am. Chem. Soc.* **2007**, *129*, 8544–8551.
- (89) Chen, Y.; Zhou, X.; Wei, X.-H.; Yu, B.-L.; Chao, H.; Ji, L.-N. *Inorg. Chem. Commun.* **2010**, *13*, 1018–1020.
- (90) Siebert, R.; Schlütter, F.; Winter, A.; Presselt, M.; Görls, H.; Schubert, U. S.; Dietzek, B.; Popp, J. *Cent. Eur. J. Chem.* **2011**, *9*, 990–999.
- (91) Sen, R.; Koner, S.; Bhattacharjee, A.; Kusz, J.; Miyashita, Y.; Okamoto, K.-I. *Dalton Trans.* **2011**, *40*, 6952.
- (92) Song, L.-q.; Feng, J.; Wang, X.-s.; Yu, J.-h.; Hou, Y.-j.; Xie, P.-h.; Zhang, B.-w.; Xiang, J.-f.; Ai, X.-c.; Zhang, J.-p. *Inorg. Chem.* **2003**, *42*, 3393–3395.
- (93) Glazer, E. C.; Magde, D.; Tor, Y. *J. Am. Chem. Soc.* **2005**, *127*, 4190–4192.
- (94) Hammarström, L.; Barigelletti, F.; Flamigni, L.; Indelli, M. T.; Armaroli, N.; Calogero, G.; Guardigli, M.; Sour, A.; Collin, J.-P.; Sauvage, J.-P. *J. Phys. Chem. A* **1997**, *101*, 9061–9069.
- (95) Creutz, C. *Prog. Inorg. Chem.* **1983**, *30*, 1–73.
- (96) Richardson, D. E.; Taube, H. *Coord. Chem. Rev.* **1984**, *60*, 107–129.
- (97) Crutchley, R. J. *Adv. Inorg. Chem.* **1994**, *41*, 273–325.
- (98) LeSuer, R. J.; Buttolph, C.; Geiger, W. E. *Anal. Chem.* **2004**, *76*, 6395–6401.
- (99) LeSuer, R. J.; Geiger, W. E. *Angew. Chem.* **2000**, *112*, 254–256; *Angew. Chem., Int. Ed.* **2000**, *39*, 248–250.
- (100) D’Alessandro, D. M.; Keene, F. R. *Dalton Trans.* **2004**, 3950.
- (101) Winter, R. F. *Organometallics* **2014**, *33*, 4517–4536.
- (102) Yueh, W.; Bauld, N. L. *J. Am. Chem. Soc.* **1995**, *117*, 5671–5676.
- (103) Hush, N. S. *Prog. Inorg. Chem.* **1967**, *8*, 391–444.
- (104) Koelle, U.; Infelta, P. P.; Graetzel, M. *Inorg. Chem.* **1988**, *27*, 879–883.
- (105) Rehm, D.; Weller, A. *Ber. Bunsen-Ges.* **1969**, *73*, 834–839.
- (106) Bock, C. R.; Connor, J. A.; Gutierrez, A. R.; Meyer, T. J.; Whitten, D. G.; Sullivan, B. P.; Nagle, J. K. *J. Am. Chem. Soc.* **1979**, *101*, 4815–4824.
- (107) Stern, O.; Volmer, M. *Phys. Z.* **1919**, *20*, 183–188.
- (108) Marcus, R. A. *J. Chem. Phys.* **1956**, *24*, 979–989.
- (109) Marcus, R. A. *J. Chem. Phys.* **1956**, *24*, 966–978.
- (110) Marcus, R. A. *J. Chem. Phys.* **1965**, *43*, 2654–2657.
- (111) Marcus, R. A. *J. Chem. Phys.* **1965**, *43*, 679–701.
- (112) Farlow, B.; Nile, T. A.; Walsh, J. L.; McPhail, A. T. *Polyhedron* **1993**, *12*, 2891–2894.
- (113) Hutchison, K.; Morris, J. C.; Nile, T. A.; Walsh, J. L.; Thompson, D. W.; Petersen, J. D.; Schoonover, J. R. *Inorg. Chem.* **1999**, *38*, 2516–2523.
- (114) Siemeling, U.; Vor der Brüggen, J.; Vorfeld, U.; Neumann, B.; Stammeler, A.; Stammeler, H.-G.; Brockhinke, A.; Plessow, R.; Zanello, P.; Laschi, F.; Fabrizi de Biani, F.; Fontani, M.; Steenken, S.; Stapper, M.; Gurzadyan, G. *Chem.—Eur. J.* **2003**, *9*, 2819–2833.
- (115) McCleskey, T. M.; Winkler, J. R.; Gray, H. B. *J. Am. Chem. Soc.* **1992**, *114*, 6935–6937.
- (116) Burk, P.; Ruasse, M.-F.; Kaljurand, I.; Lilleorg, R.; Murumaa, A.; Mishima, M.; Koppel, I.; Koppel, I. A.; Leito, I. *J. Phys. Org. Chem.* **2013**, *26*, 171–181.
- (117) Andrew, T. L.; Swager, T. M. *J. Org. Chem.* **2011**, *76*, 2976–2993.
- (118) *Principles of Fluorescence Spectroscopy*; Lakowicz, J. R., Ed.; Springer: Boston, MA, 1983.
- (119) Tyson, D. S.; Luman, C. R.; Zhou, X.; Castellano, F. N. *Inorg. Chem.* **2001**, *40*, 4063–4071.
- (120) Zhao, G.-J.; Liu, J.-Y.; Zhou, L.-C.; Han, K.-L. *J. Phys. Chem. B* **2007**, *111*, 8940–8945.
- (121) Huynh, M. H. V.; Meyer, T. J. *Chem. Rev.* **2007**, *107*, 5004–5064.
- (122) Wenger, O. S. *Chem.—Eur. J.* **2011**, *17*, 11692–11702.
- (123) Nishino, T.; Hayashi, N.; Bui, P. T. *J. Am. Chem. Soc.* **2013**, *135*, 4592–4595.
- (124) Wenger, O. S. *Acc. Chem. Res.* **2013**, *46*, 1517–1526.
- (125) Abasq, M.-L.; Saidi, M.; Burgot, J.-L.; Darchen, A. *J. Organomet. Chem.* **2009**, *694*, 36–42.
- (126) Blankespoor, R. L. *Inorg. Chem.* **1985**, *24*, 1126–1128.

## 3.2 UNDERSTANDING THE EXCITED STATE BEHAVIOR OF CYCLOMETALATED BIS(TRIDENTATE)RUTHENIUM(II) COMPLEXES: A COMBINED EXPERIMENTAL AND THEORETICAL STUDY

Christoph Kreitner, Elisa Erdmann, Wolfram W. Seidel and Katja Heinze

*Inorg. Chem.* **2015**, *54*, 11088–11104.



The visible absorption bands of the isomers  $[\text{Ru}(\text{dpb-NHCOMe})(\text{tpy-COOEt})]^+$   $\mathbf{1}^+$  and  $[\text{Ru}(\text{dpb-COOEt})(\text{tpy-NHCOMe})]^+$   $\mathbf{2}^+$  (dpbH = 1,3-dipyridin-2-ylbenzene, tpy = 2,2';6,2''-terpyridine) arise from mixed Ru  $\rightarrow$  tpy/Ru  $\rightarrow$  dpb MLCT excitations according to resonance Raman spectroscopy and DFT calculations.  $\mathbf{2}^+$  is phosphorescent ( $^3\text{MLCT}$  state), while  $\mathbf{1}^+$  is nonemissive. Partial deactivation of the  $^3\text{MLCT}$  state of  $\mathbf{2}^+$  occurs via  $^3\text{MC}$  states 11 kJ mol $^{-1}$  higher in energy, while the  $^3\text{MLCT}$  state of  $\mathbf{1}^+$  is deactivated via a lower-lying  $^3\text{LLCT}$  state.

Partial deactivation of the  $^3\text{MLCT}$  state of  $\mathbf{2}^+$  occurs via  $^3\text{MC}$  states 11 kJ mol $^{-1}$  higher in energy, while the  $^3\text{MLCT}$  state of  $\mathbf{1}^+$  is deactivated via a lower-lying  $^3\text{LLCT}$  state.

### Author Contributions

The synthesis and characterization of the ruthenium complexes as well as all DFT calculations were performed by Christoph Kreitner. The resonance Raman spectroscopic studies were carried out by Elisa Erdmann and Wolfram Seidel at the University of Rostock, Germany. The manuscript was written by Christoph Kreitner (90 %) and Katja Heinze (10 %).

### Supporting Information

for this article is found at pp. 184 (excluding Cartesian Coordinates of DFT-optimized geometries). For full Supporting Information, refer to <http://pubs.acs.org/doi/suppl/10.1021/acs.inorgchem.5b01151>.

### Correction

A correction to this article was published as C. Kreitner, E. Erdmann, W. W. Seidel and K. Heinze, *Inorg. Chem.*, 2015, **54**, 12046 rectifying a mistake in the evaluation of the redox potentials of  $\mathbf{1}^+$ . This correction is printed after the original article.

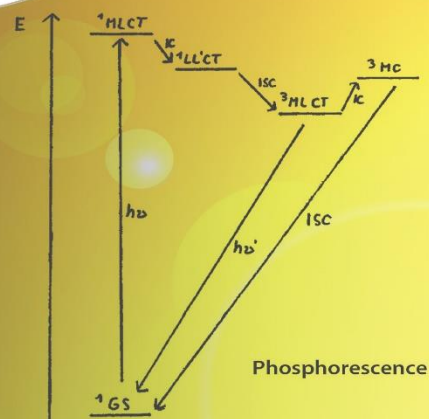
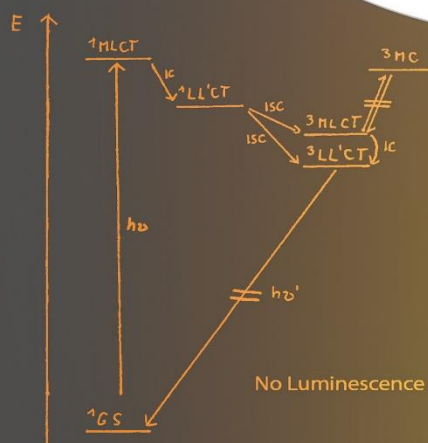
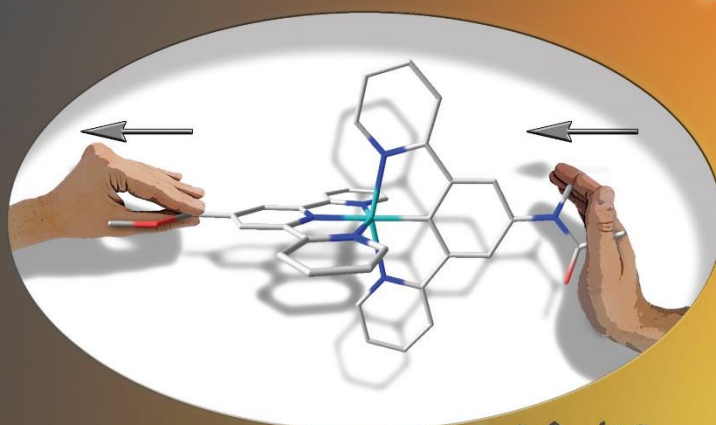
“This is an unofficial adaptation of an article that appeared in an ACS publication. ACS has not endorsed the content of this adaptation or the context of its use. Copyright 2015 American Chemical Society.”

# Inorganic Chemistry

including bioinorganic chemistry

December 7, 2015  
Volume 54, Number 23  
pubs.acs.org/IC

## Understanding the Excited State Behavior of Cyclometalated Ruthenium Complexes





# Understanding the Excited State Behavior of Cyclometalated Bis(tridentate)ruthenium(II) Complexes: A Combined Experimental and Theoretical Study

Christoph Kreitner,<sup>†,‡</sup> Elisa Erdmann,<sup>§</sup> Wolfram W. Seidel,<sup>§</sup> and Katja Heinze<sup>\*,†</sup>

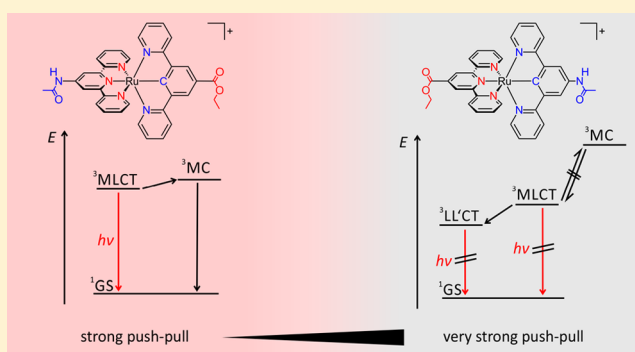
<sup>†</sup>Institute of Inorganic and Analytical Chemistry, Johannes Gutenberg-University of Mainz, Duesbergweg 10-14, 55128 Mainz, Germany

<sup>‡</sup>Graduate School Materials Science in Mainz, Staudingerweg 9, 55128 Mainz, Germany

<sup>§</sup>Institute of Chemistry, University of Rostock, Albert-Einstein-Straße 3a, 18059 Rostock, Germany

## Supporting Information

**ABSTRACT:** The synthesis and characterization of the donor–acceptor substituted cyclometalated ruthenium(II) polypyridine complex isomers [Ru(dpb-NHCOMe)(tpy-COOEt)](PF<sub>6</sub>) **1**(PF<sub>6</sub>) and [Ru(dpb-COOEt)(tpy-NHCOMe)](PF<sub>6</sub>) **2**(PF<sub>6</sub>) (dpbH = 1,3-dipyridin-2-ylbenzene, tpy = 2,2';6,2''-terpyridine) with inverted functional group pattern are described. A combination of resonance Raman spectroscopic and computational techniques shows that all intense visible range absorption bands arise from mixed Ru → tpy/Ru → dpb metal-to-ligand charge transfer (MLCT) excitations. **2**(PF<sub>6</sub>) is weakly phosphorescent at room temperature in fluid solution and strongly emissive at 77 K in solid butyronitrile matrix, which is typical for ruthenium(II) polypyridine complexes. Density functional theory calculations revealed that the weak emission of **2**(PF<sub>6</sub>) arises from a <sup>3</sup>MLCT state that is efficiently thermally depopulated via metal-centered (<sup>3</sup>MC) excited states. The activation barrier for the deactivation process was estimated experimentally from variable-temperature emission spectroscopic measurements as 11 kJ mol<sup>-1</sup>. In contrast, **1**(PF<sub>6</sub>) is nonemissive at room temperature in fluid solution and at 77 K in solid butyronitrile matrix. Examination of the electronic excited states of **1**(PF<sub>6</sub>) revealed a ligand-to-ligand charge-transfer (<sup>3</sup>LL'CT) as lowest-energy triplet state due to the very strong push–pull effect across the metal center. Because of the orthogonality of the participating ligands, emission from the <sup>3</sup>LL'CT is symmetry-forbidden. Hence, in this type of complex a stronger push–pull effect does not increase the phosphorescence quantum yields but completely quenches the emission.



## INTRODUCTION

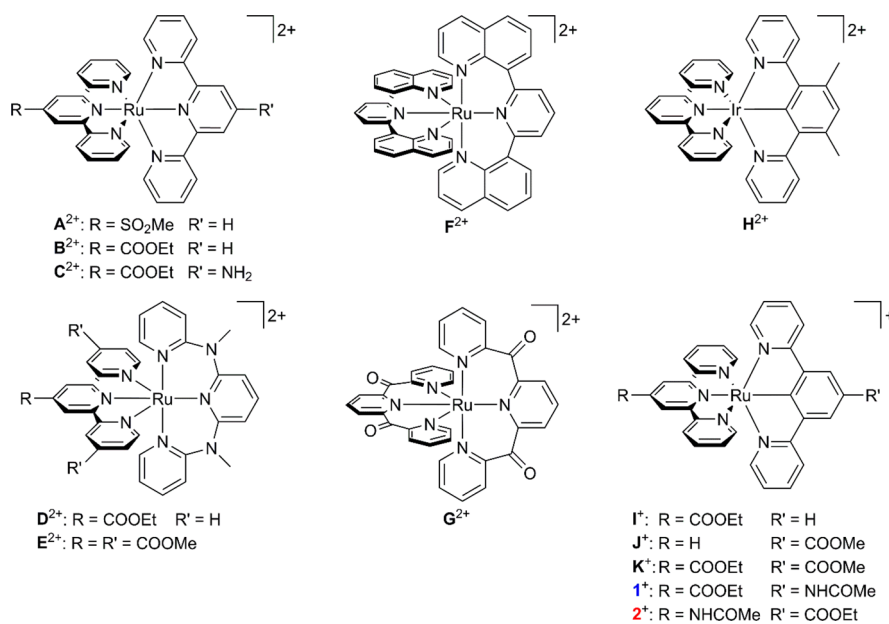
Polypyridine complexes of ruthenium have been studied extensively in the last 50 years.<sup>1</sup> Especially, the photophysics and photochemistry of their prototype [Ru(bipy)<sub>3</sub>]<sup>2+</sup> (bipy = 2,2'-bipyridine) are well understood.<sup>2–5</sup> The visible range of the absorption spectrum is dominated by an intense metal-to-ligand charge transfer (MLCT) absorption from ruthenium d-orbitals into the low-lying antibonding π\*-orbitals of the bipy ligands<sup>3,6</sup> with an absorption maximum at 452 nm and an extinction coefficient of 14 600 M<sup>-1</sup> cm<sup>-1</sup>.<sup>4</sup> The UV region is dominated by π–π\* transitions within the aromatic ligands.<sup>4</sup> Following Kasha's rule<sup>7</sup> rapid vibrational relaxation and internal conversion occur upon optical excitation populating the lowest-energy <sup>1</sup>MLCT state. From this state nearly quantitative intersystem crossing (ISC)<sup>8,9</sup> onto the triplet hypersurface occurs, which leads to population of the lowest-energy <sup>3</sup>MLCT state.<sup>10</sup> This state is highly phosphorescent<sup>10</sup> at room temperature (λ<sub>em</sub> = 621 nm, φ = 0.095 in acetonitrile)<sup>11</sup> and

has a long excited-state lifetime of 855 ns (in acetonitrile) due to the spin-forbidden character of the luminescence.<sup>5</sup>

A qualitatively similar picture of the excited-state mechanisms is gained for the meridionally coordinated<sup>12</sup> tridentate analogue of [Ru(bipy)<sub>3</sub>]<sup>2+</sup>, namely, [Ru(tpy)<sub>2</sub>]<sup>2+</sup> (tpy = 2,2';6',2''-terpyridine). MLCT absorption occurs at 474 nm slightly bathochromically and hyperchromically shifted (ε = 16 100 M<sup>-1</sup> cm<sup>-1</sup>)<sup>13</sup> due to the larger accepting π\*-orbitals of the terpyridine ligands. Upon ISC again <sup>3</sup>MLCT states are populated.<sup>14,15</sup> In contrast to the bipy counterpart an efficient deactivation pathway is available for this emissive <sup>3</sup>MLCT state: because of the smaller N–Ru–N bite angles in this tpy complex compared to the parent bipy complex the orbital overlap of the pyridine nitrogen lone pairs with the ruthenium d orbitals of the e<sub>g</sub> set (in idealized O<sub>h</sub> symmetry) is lowered. The loss in ligand-field splitting shifts d–d excited states (<sup>3</sup>MC states, MC

Received: May 27, 2015

Published: August 6, 2015

Scheme 1. Bis(tridentate)ruthenium(II) and Iridium(III) Polypyridine Complexes<sup>a</sup>

<sup>a</sup>By Constable (A<sup>2+</sup>),<sup>15</sup> van Koten (B<sup>2+</sup>, I<sup>+</sup>, J<sup>+</sup>, K<sup>+</sup>),<sup>20</sup> Heinze (C<sup>2+</sup>, D<sup>2+</sup>, E<sup>2+</sup>),<sup>21–23</sup> Hammarström (F<sup>2+</sup>),<sup>24</sup> Ruben (G<sup>2+</sup>),<sup>25</sup> Williams (H<sup>2+</sup>),<sup>26</sup> and from this work (1<sup>+</sup> and 2<sup>+</sup>).

= metal-centered) into the energy regime of the <sup>3</sup>MLCT states. These MC states are thermally populated at room temperature and lead to an efficient emission quenching in [Ru(tpy)<sub>2</sub>]<sup>2+</sup> (λ<sub>em</sub> = 629 nm, ϕ < 1 × 10<sup>-5</sup>).<sup>16</sup> At 77 K, the available thermal energy does not suffice to overcome the activation barrier for population of the <sup>3</sup>MC states, and an intense emission is regained (ϕ = 0.48).<sup>13</sup>

Just as this undesirable side effect also the major advantage of bis(terpyridine)ruthenium(II) complexes over their bipyridine analogues arises from their coordination geometry. The C<sub>2v</sub> symmetry of the core structure of this complex<sup>12</sup> prevents the formation of diastereomers even when heteroleptic complexes bearing ligands with different functional groups are formed. Syntheses of similarly substituted bipyridine complexes usually give mixtures of diastereomers that require elaborate methods to be purified<sup>17</sup> or to be circumvented.<sup>18,19</sup>

Several successful approaches improve the emissive behavior of bis(tridentate)ruthenium complexes by influencing the energies of the relevant excited states.<sup>27</sup> Introducing π-accepting functional groups (–SO<sub>2</sub>R, –COOR, Scheme 1, A<sup>2+</sup>, B<sup>2+</sup>) in the ligand backbone (typically in 4'-position) lowers the energy of the <sup>3</sup>MLCT states while leaving the energy of the <sup>3</sup>MC states unaltered. This hinders the thermal deactivation process to some extent and increases both excited-state lifetimes and quantum yields of such compounds (ϕ ≈ 1–5 × 10<sup>-4</sup>).<sup>15,28</sup> Alternatively, introducing σ-donating functional groups in the ligand's periphery directly influences the energy of the <sup>3</sup>MC states.<sup>15</sup> They are shifted to higher energies with respect to the <sup>3</sup>MLCT states again hampering thermal depopulation of the latter. Combining both approaches yields excited-state lifetimes of up to 50 ns (Scheme 1, A<sup>2+</sup>)<sup>15</sup> and quantum yields of up to 0.003 (Scheme 1, C<sup>2+</sup>)<sup>21,29</sup> but always at the cost of a lowered excited-state energy.<sup>27</sup>

The <sup>3</sup>MC states are even more efficiently shifted to higher energies by widening the N–Ru–N bite angles. This is achieved upon introduction of N–CH<sub>3</sub> in between the pyridine rings of the terpyridine ligand (N,N'-dimethyl-N,N'-dipyridin-

2-ylpyridine-2,6-diamine, ddpd).<sup>22</sup> The increased σ-donor strength of ddpd compared to tpy sufficiently separates the <sup>3</sup>MC states in the heteroleptic complex [Ru(ddpd)(tpy-COOEt)]<sup>2+</sup> D<sup>2+</sup> (Scheme 1) from the <sup>3</sup>MLCT states to allow [Ru(ddpd)(tpy)]<sup>2+</sup> to be emissive (ϕ = 0.0045) despite its much lower emission energy (λ<sub>em</sub> = 729 nm).<sup>22,23</sup> Gradually tuning the vertical <sup>3</sup>MLCT → <sup>1</sup>GS transition energy within a series of structurally similar [Ru(ddpd)(tpy)]<sup>2+</sup> complexes by variation of appended functional groups decreases the emission quantum yield with decreasing emission energy following the energy gap law as pointed out by Meyer and co-workers.<sup>30–32</sup> Similarly, Hammarström and co-workers used di(quinolin-8-yl)pyridine (dqp) as tridentate ligand forming six-membered chelate rings with ruthenium as metal center.<sup>24,33</sup> The homoleptic complex [Ru(dqp)<sub>2</sub>]<sup>2+</sup> F<sup>2+</sup> (Scheme 1) is phosphorescent at room temperature (ϕ = 0.02) with a remarkably long excited-state lifetime of 3.0 μs. Ruben and co-workers employed the carbonyl analogue of the ddpd ligand, 2,6-di(2-carboxypyridyl)pyridine (dcp) as chelating ligand with N–Ru–N bite angles of 90°. The homoleptic complex [Ru(dcp)<sub>2</sub>]<sup>2+</sup> G<sup>2+</sup> (Scheme 1) exhibits an extraordinary high room-temperature emission quantum yield of 0.30 with a long excited-state lifetime of 3.3 μs.<sup>25</sup>

Cyclometalation<sup>34,35</sup> (i.e., isoelectronic substitution of a nitrogen atom for a carbanion in the coordination sphere around the metal) is discussed as another option for raising the <sup>3</sup>MC states since the strong σ-donating effect of the anionic carbon greatly increases the ligand field splitting.<sup>20</sup> While for iridium(III) a large variety of highly phosphorescent cyclometalated complexes are known,<sup>36–39</sup> most cyclometalated ruthenium(II) complexes are barely emissive at room temperature.<sup>40–42</sup> For tris(bidentate)iridium(III) complexes with cyclometalating ligands of the type [Ir(bipy)<sub>n</sub>(ppy)<sub>3–n</sub>]<sup>n+</sup> (n = 1, 2; ppyH = 2-phenylpyridine) the excited-state mechanisms that are responsible for the efficient luminescence are well-understood.<sup>43</sup> The emissive excited state of Ir<sup>III</sup> complexes is a linear combination of a mixed <sup>3</sup>MLCT/<sup>3</sup>LL'/CT state (LL'/CT =

ligand-to-ligand charge-transfer state) and an energetically very similar ligand-centered ( $^3\text{LC}$ ) excited state due to the very high ligand field splitting of  $\text{Ir}^{\text{III}}$  combined with the ppy ligands. This state is well-separated from other states so that emission becomes very efficient.<sup>26,44–46</sup> Since most cyclometalated ruthenium complexes are essentially nonemissive at room temperature in solution it is much more difficult to obtain a profound understanding of the excited-state mechanisms in these systems. Berlinguette and co-workers showed that the energy gap law is obeyed in complexes of type  $[\text{Ru}(\text{bipy})_2(\text{ppy})]^+$  demonstrating that direct ISC onto the singlet hypersurface followed by vibrational cooling is the dominant deactivation pathway.<sup>41,42</sup>

Van Koten and co-worker recently discussed  $[\text{Ru}(\text{tpy-R})(\text{pbpy-R}')]^+$  ( $\text{pbpyH} = 6\text{-phenyl-2,2'-bipyridine}$ ) and  $[\text{Ru}(\text{tpy-R})(\text{dpb-R}')]^+$  ( $\text{dpbH} = 2,6\text{-di(pyrid-2'-yl)benzene}$ ) complexes and their application in dye-sensitized solar cells.<sup>20,47,48</sup> Electron-accepting anchor groups (COOR) were appended at either one of the two ligands or at both resulting in a series of weakly or nonemissive tridentate complexes (Scheme 1,  $\text{I}^+$ ,  $\text{J}^+$ , and  $\text{K}^+$ ). A structurally similar weakly emitting iridium(III) complex (Scheme 1,  $\text{H}^{2+}$ ) was synthesized by Williams and co-workers.<sup>26</sup> Despite the fact that the energy gap law is obeyed within these complex series luminescence quenching is discussed to arise from thermal depopulation of the very low-lying  $^3\text{MLCT}$  states via  $^3\text{MC}$  states. However, the latter should be high in energy due to the strong  $\sigma$ -donor strength of the cyclometalating ligand.<sup>20</sup> This apparent discrepancy will be addressed in this paper.

In this study we present an extension of our previous work on tridentate polypyridine ruthenium complexes bearing both electron-donating amino and electron-withdrawing carboxylic acid functionalities (such as  $\text{A}^{2+}$ , Scheme 1)<sup>21,27</sup> into the field of cyclometalated complexes and elucidate the excited-state deactivation mechanisms of these complexes in detail. In the isomeric  $[\text{Ru}(\text{dpb-R}')(\text{tpy-R})]^+$  complexes ( $\text{1}^+$ :  $\text{R} = \text{COOEt}$ ,  $\text{R}' = \text{NHCOMe}$ ;  $\text{2}^+$ :  $\text{R} = \text{NHCOMe}$ ,  $\text{R}' = \text{COOEt}$ ) the position of the functional groups with respect to the site of cyclometalation should have a strong impact on their electronic structure and excited-state ordering. The ground- and excited-state electronic structures as well as excited-state dynamics are elucidated by a combination of UV–vis, electron paramagnetic resonance (EPR), resonance Raman (rR), and emission spectroscopies and theoretical techniques to provide a better understanding of the unexplained low-emission efficiencies in cyclometalated bis(tridentate)ruthenium(II) complexes.

## EXPERIMENTAL SECTION

**General Procedures.** Chemicals were obtained from commercial suppliers and used without further purification. Air- or moisture-sensitive reactions were performed in dried glassware in an inert gas atmosphere (argon, quality 4.6). Acetonitrile and dichloromethane were refluxed over  $\text{CaH}_2$  and distilled under argon prior to use. Toluene and xylenes were refluxed over sodium and distilled prior to use. Palladium precatalyst  $[\text{Pd}]_2$ <sup>49</sup> and the ligand precursors 1-bromo-3,5-dipyridin-2-ylbenzene **LA**,<sup>50</sup> 4'-chloro-2,2':6',2''-terpyridine **LB**,<sup>51</sup> 4'-amino-2,2':6',2''-terpyridine **LC**,<sup>52</sup> and ethyl 3,5-dibromobenzoate **LD**<sup>53</sup> were synthesized following literature-known procedures. UV–vis spectra were recorded on a Varian Cary 5000 spectrometer in 1 cm cuvettes. Emission spectra were recorded on a Varian Cary Eclipse spectrometer. Quantum yields were determined by comparing the areas under the emission spectra on an energy scale recorded for solutions of the samples and a reference with matching absorbances ( $\phi([\text{Ru}(\text{bipy})_3]\text{Cl}_2) = 0.094$  in deaerated  $\text{CH}_3\text{CN}$ ).<sup>11</sup> Experimental

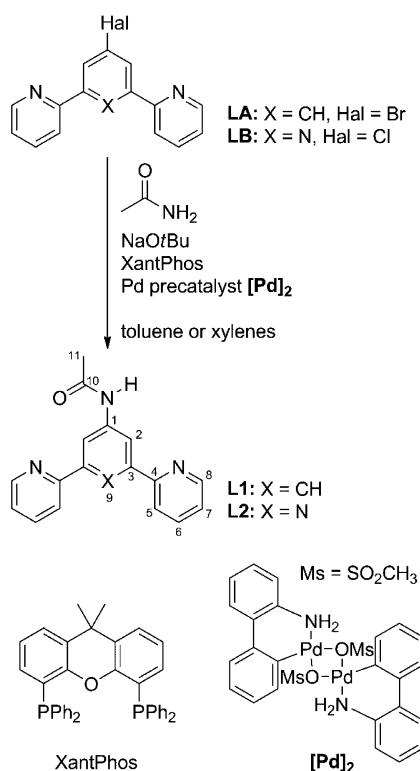
uncertainty is estimated to be 15%.  $\text{FD}^+$  mass spectra were recorded on a FD Finnigan MAT95 spectrometer. Electrospray ionization ( $\text{ESI}^+$ ) and high-resolution  $\text{ESI}^+$  mass spectra were recorded on a Micromass QToF Ultima API mass spectrometer with analyte solutions in acetonitrile. Elemental analyses were performed by the micro-analytical laboratory of the chemical institutes of the University of Mainz. NMR spectra were obtained with a Bruker Avance II 400 spectrometer at 400.31 ( $^1\text{H}$ ) and 100.66 ( $^{13}\text{C}$ ) at 25 °C. Chemical shifts  $\delta$  [parts per million] are reported with respect to residual solvent signals as internal standards ( $^1\text{H}$ ,  $^{13}\text{C}$ ):  $\text{CD}_3\text{CN}$   $\delta(^1\text{H}) = 1.94$  ppm,  $\delta(^{13}\text{C}) = 1.32$  and 118.26 ppm.<sup>54</sup> Electrochemical experiments were performed with a BioLogic SP-50 voltammetric analyzer at a sample concentration of  $1 \times 10^{-3}$  M using platinum wire working and counter electrodes and a 0.01 M  $\text{Ag}/\text{AgNO}_3$  reference electrode. Measurements were performed at a scan rate of 100  $\text{mV s}^{-1}$  for cyclic voltammetry experiments and at 10  $\text{mV s}^{-1}$  for square-wave voltammetry experiments using 0.1 M  $[\text{Bu}_4\text{N}][\text{PF}_6]$  as supporting electrolyte in acetonitrile. Potentials are given relative to the ferrocene/ferrocenium couple (0.40 V vs standard calomel electrode (SCE),  $E_{1/2} = 0.90 \pm 5$  mV under the given conditions).<sup>55</sup> EPR spectra were recorded on a Miniscope MS 300 X-band CW spectrometer (Magnettech GmbH, Germany). Values of  $g$  are referenced against  $\text{Mn}^{2+}$  in ZnS as external standard ( $g = 2.118, 2.066, 2.027, 1.986, 1.946$ ). Simulations were performed with the EasySpin program package.<sup>56</sup> A Horiba LabRAM HR Raman microscope was used for rR measurements with an object lens (10 $\times$  NA 0.25) from Olympus. Samples were optically excited with a red laser (633 nm, 17 mW, HeNe-laser), green laser (532 nm, 50 mW, air-cooled frequency-doubled Nd:YAG-solid state laser), or blue laser (473 nm, 20 mW, air-cooled solid-state laser). Samples were measured in acetonitrile (Chemsolute, for HPLC) solution in capillary tubes (80  $\times$  1.5 mm, Marienfeld-Superior).

Density functional theory (DFT) calculations were performed using the ORCA program package (version 3.0.2).<sup>57</sup> Tight convergence criteria were chosen for all calculations (keywords TightSCF and TightOpt, convergence criteria for the SCF part: energy change  $1.0 \times 10^{-8}$   $E_h$ ,  $1 - E_i$  energy change  $1.0 \times 10^{-5}$   $E_h$ , orbital gradient  $1.0 \times 10^{-5}$ , orbital rotation angle  $1.0 \times 10^{-5}$ , DIIS error  $5.0 \times 10^{-7}$ ; for geometry optimizations: energy change:  $1.0 \times 10^{-6}$   $E_h$ , maximum gradient  $1.0 \times 10^{-4}$   $E_h/\text{bohr}$ , root-mean-square (RMS) gradient  $3.0 \times 10^{-5}$   $E_h/\text{bohr}$ , maximum displacement  $1.0 \times 10^{-3}$  bohr, RMS displacement  $6.0 \times 10^{-4}$  bohr). All calculations employ the resolution of identity (Split-RI-J) approach for the coulomb term in combination with the chain-of-spheres approximation for the exchange term (COSX) where Hartree–Fock exchange is required.<sup>58,59</sup> Geometry optimizations were performed using the GGA functional PBE<sup>60,61</sup> in combination with Ahlrichs' split-valence double- $\xi$  basis set def2-SV(P) for all atoms except ruthenium, which comprises polarization functions for all non-hydrogen atoms.<sup>62,63</sup> For ruthenium a Stuttgart–Dresden effective core potential (ECP, def2-SD) was combined with Ahlrichs' def2-TZVP basis set for the valence electrons.<sup>64,65</sup> To account for solvent effects a conductor-like screening model (COSMO) modeling acetonitrile was used in all calculations except for excited-state gradients.<sup>66</sup> This proved to be particularly important for time-dependent DFT calculations (TD-DFT) where gas phase calculations lead to a substantial underestimation of excitation energies.<sup>67</sup> The optimized geometries were confirmed to be local minima on the respective potential energy surface by subsequent numerical frequency analysis ( $N_{\text{imag}} = 0$ ).

Calculation of EPR parameters and TD-DFT calculations were performed based on the PBE/def2-SV(P)/ECP(def2-TZVP) optimized geometry of the respective complex employing the triple- $\xi$  basis set def2-TVZP and several functionals with varying amounts of HF exchange:<sup>68</sup> PBE (0%), TPSSH (10%),<sup>69</sup> B3LYP (20%),<sup>70</sup> PBE0 (25%),<sup>71</sup> and CAM-B3LYP (19–65%).<sup>72</sup> The Douglas–Kroll–Hess (DKH) relativistic approximation<sup>73–76</sup> was used to describe relativistic effects in these calculations. The DKH keyword in ORCA automatically invokes adjusted basis sets (TZV\_DKH).<sup>77</sup> At least 50 vertical transitions were calculated in TD-DFT calculations. The electron  $g$  value and hyperfine coupling constants of the unpaired electron to the



ruthenium atom and all atoms coordinated to ruthenium were determined in EPR calculations. On the basis of the optimized <sup>1</sup>GS molecular geometries and the associated Hessian matrices excited-state gradients were calculated for the lowest 10 excitations at the B3LYP/def2-TZVP/DKH level of theory to generate excited-state displacements for the rR spectra simulation. The advanced spectra analysis tool provided with the ORCA program package (orca\_asa)<sup>78,79</sup> was employed to fit the absorption spectra of **1**(PF<sub>6</sub>) and **2**(PF<sub>6</sub>) and to simulate rR spectra. The Gibbs free energy was used to compare relative energies of the different triplet states of the complexes under study. Explicit counterions and/or solvent molecules were not taken into account in all cases. To reduce the computational cost methyl instead of ethyl groups were used throughout all calculations at the ester moiety.

Scheme 2<sup>a</sup>

<sup>a</sup>Buchwald–Hartwig amination of 1-bromo-3,5-di(pyridin-2-yl)benzene **LA** and 4'-chloro-2,2':6',2''-terpyridine **LB** with acetamide yielding *N*-acetyl-3,5-di(pyridin-2-yl)aniline **L1** and *N*-acetyl-4'-amino-2,2':6',2''-terpyridine **L2**. Atom numbering for NMR assignment is included.

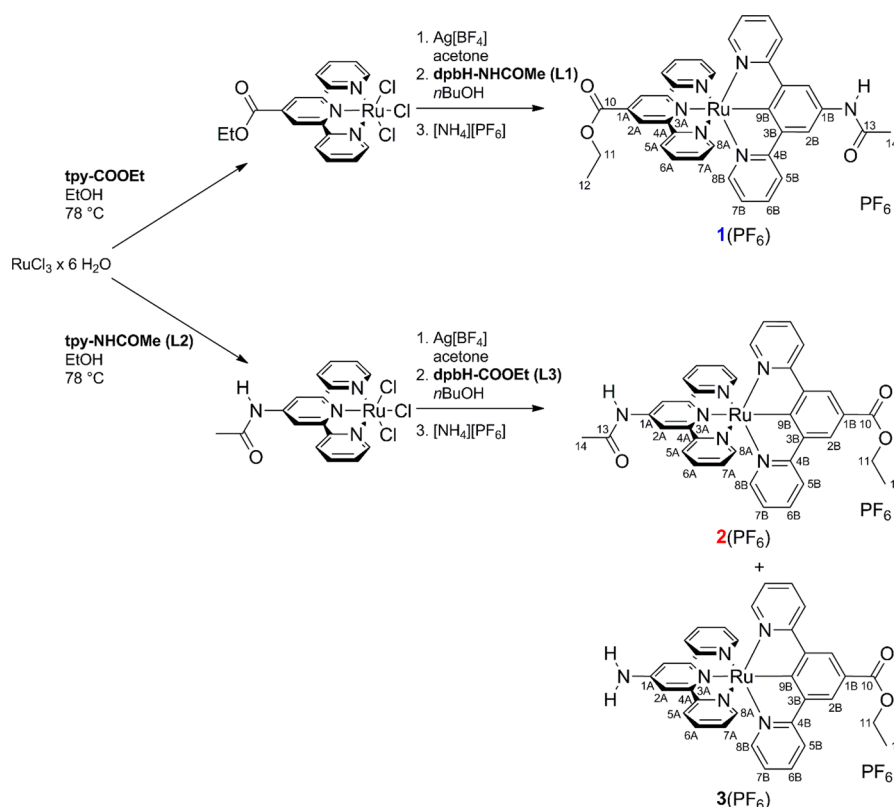
**Synthesis of *N*-Acetyl-3,5-di(pyridin-2-yl)aniline L1.** 4,5-Bis(diphenylphosphino)-9,9-dimethylxanthene (XantPhos, 64 mg, 111 μL, 3 mol %) and Pd precatalyst [Pd]<sub>2</sub> (14 mg, 19 μmol, 1.1 mol % based on Pd) were dissolved under argon in 15 mL of abs. toluene and left to stand. After 10 min 1-bromo-3,5-di(pyridin-2-yl)benzene **LA** (1.15 g, 3.70 mmol, 1 equiv), acetamide (273 mg, 4.62 mmol, 1.25 equiv), and sodium *tert*-butanolate (444 mg, 4.62 mmol, 1.25 equiv), dissolved in 15 mL of abs. toluene, were added, and the mixture was heated to reflux for 8 h. After the mixture cooled to room temperature, the solvent was removed under reduced pressure, and the remaining solid was dissolved in concentrated hydrochloric acid (20 mL), water (20 mL), and dichloromethane (50 mL). The phases were separated, and the aqueous phase was extracted twice with dichloromethane (2 × 50 mL). The aqueous phase was neutralized with dilute aqueous sodium hydroxide solution (pH = 9) followed by extraction with dichloromethane (3 × 50 mL). The organic fractions of the second extraction were dried over magnesium sulfate, and the solvent was

removed under reduced pressure to give 0.95 g of crude *N*-acetyl-3,5-di(pyridin-2-yl)aniline. After column chromatography on neutral Alox (Brockmann II, 3% water (w/w), solvent ethyl acetate) the product was obtained as colorless powder. Yield: 848 mg (2.90 mmol, 78%). Anal. Calcd C<sub>18</sub>H<sub>15</sub>N<sub>3</sub>O (289.33): C, 74.72; H, 5.23; N, 14.52. Found: C, 74.93; H, 4.98; N, 14.39%. MS(FD<sup>+</sup>): *m/z* (%) = 289.2 (100) [M]<sup>+</sup>, 579.4 (2) [2M+H]<sup>+</sup>. <sup>1</sup>H NMR (CD<sub>2</sub>Cl<sub>2</sub>): δ [ppm] = 8.67 (ddd, <sup>3</sup>J<sub>HH</sub> = 5 Hz, <sup>4</sup>J<sub>HH</sub> = 2 Hz, 1 Hz, 2H, H<sup>8</sup>), 8.38 (t, <sup>4</sup>J<sub>HH</sub> = 1 Hz, 1H, H<sup>9</sup>) 8.27 (d, <sup>4</sup>J<sub>HH</sub> = 1 Hz, 2H, H<sup>2</sup>), 8.25 (s, 1H, NH), 7.79 (ddd, <sup>3</sup>J<sub>HH</sub> = 8 Hz, <sup>4</sup>J<sub>HH</sub> = 1 Hz, 2H, H<sup>5</sup>), 7.74 (vtd, <sup>3</sup>J<sub>HH</sub> = 8, <sup>4</sup>J<sub>HH</sub> = 2 Hz, 2H, H<sup>6</sup>), 7.24 (ddd, <sup>3</sup>J<sub>HH</sub> = 8 Hz, 5 Hz, <sup>4</sup>J<sub>HH</sub> = 1.2 Hz, 2H, H<sup>7</sup>), 2.12 (s, 3H CH<sub>3</sub>). <sup>13</sup>C{<sup>1</sup>H} NMR (CD<sub>2</sub>Cl<sub>2</sub>): δ [ppm] = 169.3 (s, C<sup>10</sup>), 157.0 (s, C<sup>4</sup>), 150.1 (s, C<sup>8</sup>), 140.9 (s, C<sup>3</sup>), 140.0 (s, C<sup>1</sup>), 137.4 (s, C<sup>6</sup>), 123.1 (s, C<sup>7</sup>), 121.3 (s, C<sup>9</sup>), 121.1 (s, C<sup>5</sup>), 119.2 (s, C<sup>2</sup>), 24.9 (s, C<sup>11</sup>).

**Synthesis of *N*-Acetyl-4'-amino-2,2':6',2''-terpyridine L2. Procedure (a).** XantPhos (123 mg, 213 μmol, 9 mol %) and Pd precatalyst [Pd]<sub>2</sub> (39 mg, 53 μmol, 4.5 mol % based on Pd) were dissolved under argon in 15 mL abs. xylenes and left to stand. After 10 min 4'-chloro-2,2':6',2''-terpyridine **LB** (616 mg, 2.30 mmol, 1 equiv), acetamide (151 mg, 2.56 mmol, 1.1 equiv), and sodium *tert*-butanolate (246 mg, 2.56 mmol, 1.1 equiv) dissolved in additional 15 mL of abs. xylenes were added, and the mixture was heated to reflux for 20 h. Drying of all reagents prior to use is necessary since the resulting amide is prone to hydrolysis under the given reaction conditions in the presence of traces of water. The same workup routine as for *N*-acetyl-3,5-di(pyridin-2-yl)aniline was followed. Column chromatography on neutral Alox (Brockmann II, 3% water (w/w), solvent gradient ethyl acetate/hexanes 1:3 → 3:1) afforded pure *N*-acetyl-4'-amino-2,2':6',2''-terpyridine as off-white powder. Yield: 508 mg (1.75 mmol, 76%). Anal. Calcd C<sub>17</sub>H<sub>14</sub>N<sub>4</sub>O (290.32): C, 70.33; H, 4.86; N, 19.30. Found: C, 69.92; H, 4.81; N, 19.02%. MS(FD<sup>+</sup>): *m/z* (%) = 290.2 (100) [M]<sup>+</sup>, 313.1 (10) [M + Na]<sup>+</sup>, 603.3 (2) [2M+Na]<sup>+</sup>. <sup>1</sup>H NMR (0.5 mL of CD<sub>2</sub>Cl<sub>2</sub> + 0.1 mL of deuterated dimethyl sulfoxide): δ [ppm] = 10.23 (s, 1H, NH), 8.59 (s, 2H, H<sup>2</sup>), 8.58–8.53 (m, 2H, H<sup>8</sup>), 8.48 (d, <sup>3</sup>J<sub>HH</sub> = 8 Hz, 2H, H<sup>5</sup>), 7.76 (vtd, <sup>3</sup>J<sub>HH</sub> = 8 Hz, <sup>4</sup>J<sub>HH</sub> = 2 Hz, 2H, H<sup>6</sup>), 7.25 (ddd, <sup>3</sup>J<sub>HH</sub> = 8 Hz, 5 Hz, <sup>4</sup>J<sub>HH</sub> = 1 Hz, 2H, H<sup>7</sup>), 2.06 (s, 3H, CH<sub>3</sub>). <sup>13</sup>C{<sup>1</sup>H} NMR (CD<sub>2</sub>Cl<sub>2</sub>): δ [ppm] = 170.0 (s, C<sup>10</sup>), 156.3 (s, C<sup>4</sup>), 156.1 (s, C<sup>3</sup>), 149.0 (s, C<sup>8</sup>), 148.3 (s, C<sup>1</sup>), 137.0 (s, C<sup>6</sup>), 124.1 (s, C<sup>7</sup>), 121.0 (s, C<sup>5</sup>), 110.6 (s, C<sup>2</sup>), 24.5 (s, C<sup>11</sup>).

**Procedure (b).** To a solution of 4'-amino-2,2':6',2''-terpyridine **LC** (2.22 g, 8.94 mmol, 1 equiv) in dichloromethane (30 mL) was added a solution of acetyl chloride (10 mL, exc.) in dichloromethane (30 mL) dropwise over a period of 15 min. The resulting mixture was heated to reflux for 3 h. A slightly yellow precipitate formed during the heating. After the mixture cooled to room temperature, the solvent and the acetyl chloride were removed under reduced pressure. The remaining solid was dissolved in a mixture of water and tetrahydrofuran (1:1, 100 mL), and the pH was adjusted to 8 using aqueous sodium bicarbonate solution. The resulting colorless precipitate was collected via filtration yielding microanalytically pure *N*-acetyl-4'-amino-2,2':6',2''-terpyridine **L2** (1.09 g, 3.75 mmol). The aqueous phase was further extracted with dichloromethane (3 × 50 mL). The combined organic phases were dried over magnesium sulfate and evaporated to dryness. The crude product was purified via column chromatography on neutral Alox (Brockmann II, 3% water (w/w), solvent gradient ethyl acetate/hexanes 1:3 → 3:1) to give a second fraction of pure product as off-white solid (1.00 g, 3.44 mmol). Yield: 2.09 g (7.20 mmol, 81%). The <sup>1</sup>H NMR spectra of both fractions match those obtained from procedure a).

**Synthesis of RuCl<sub>3</sub>(R-tpy), R = COOC<sub>2</sub>H<sub>5</sub>, NHCOCH<sub>3</sub>.** A standard procedure was followed for the synthesis of the RuCl<sub>3</sub>(R-tpy) precursors.<sup>29,52</sup> Ruthenium(III) chloride hydrate (36% Ru (w/w); R = COOC<sub>2</sub>H<sub>5</sub>: 1.46 g, 5.20 mmol, 1.3 equiv; R = NHCOCH<sub>3</sub>: 566 mg, 2.01 mmol, 1.3 equiv) was dissolved in ethanol (50 mL), and the respective terpyridine (R = COOC<sub>2</sub>H<sub>5</sub>: 1.21 g, 3.96 mmol, 1 equiv; R = NHCOCH<sub>3</sub>: 450 mg, 1.55 mmol, 1 equiv) was added. The resulting mixture was heated to reflux for 3 h during which time the product precipitated as a red solid. It was filtered off and washed thoroughly with ethanol to remove residual RuCl<sub>3</sub>. The product was dried under reduced pressure and used without further purification. Yield: R =

Scheme 3. Synthetic Procedure<sup>a</sup>

<sup>a</sup>Starting from  $\text{RuCl}_3$  leading to the heteroleptic cyclometalated ruthenium complex isomers  $\mathbf{1}(\text{PF}_6)$  and  $\mathbf{2}(\text{PF}_6)$  as well as the amino complex  $\mathbf{3}(\text{PF}_6)$ . Numbering for NMR assignments is included.

$\text{COOC}_2\text{H}_5$ : 1.94 g (3.78 mmol, 96%).  $\text{R} = \text{NHCOCH}_3$ : 730 mg (1.47 mmol, 95%). Because of the poor solubility of  $\text{RuCl}_3(\text{tpy-R})$  no characterization was performed.

**Synthesis of  $[\text{Ru}(\text{dpb-NHCOCH}_3)(\text{tpy-COOC}_2\text{H}_5)](\text{PF}_6)$   $\mathbf{1}(\text{PF}_6)$ .**  $\text{RuCl}_3(\text{tpy-COOC}_2\text{H}_5)$  (100 mg, 0.195 mmol, 1 equiv) was suspended under argon in 20 mL of abs. acetone, and silver tetrafluoroborate (110 mg, 0.566 mmol, 2.9 equiv) was added. The resulting reaction mixture was heated to reflux for 2 h in the dark. After the mixture cooled to room temperature, the dark brown solution was filtered through a syringe filter to remove precipitated silver chloride prior to evaporation of the solvent. The dark, oily residue was dissolved in abs.  $n\text{BuOH}$  (20 mL), and  $\text{CH}_3\text{CONH-dpbH}$  L1 (68 mg, 0.234 mmol, 1.2 equiv) was added. The resulting dark brown to purple solution was heated to reflux for 16 h giving an intensely colored purple solution. After removal of the solvent under reduced pressure the remaining solid was dissolved in acetonitrile (5 mL), and a solution of ammonium hexafluorophosphate (125 mg, 0.78 mmol, 4 equiv) in water (1 mL) was added. Addition of more water (~80 mL) resulted in the precipitation of the crude product, which was filtered off. Column chromatography on silica gel (solvent gradient chloroform  $\rightarrow$  chloroform/methanol 7:1, after a yellow impurity was eluted) afforded pure  $[\text{Ru}(\text{dpb-NHCOCH}_3)(\text{tpy-COOC}_2\text{H}_5)](\text{PF}_6)$  as dark purple solid. Yield: 114 mg (0.136 mmol, 70%). Anal. Calcd for  $\text{C}_{36}\text{H}_{29}\text{F}_6\text{N}_6\text{O}_3\text{PRu}$  (839.7)·1.5 $\text{H}_2\text{O}$ : C, 49.89; H, 3.72; N, 9.70. Found: C, 50.01; H, 3.50; N, 9.53%. MS(ESI<sup>+</sup>):  $m/z$  (%) = 347.6 (1)  $[\text{M-PF}_6]^{2+}$ , 695.1 (100)  $[\text{M-PF}_6]^+$ , 1535.3 (3)  $[2\text{M-PF}_6]^+$ . HR-MS(ESI<sup>+</sup>):  $m/z$ : Calcd for  $\text{C}_{36}\text{H}_{29}\text{N}_6\text{O}_3\text{Ru}$   $[\text{M-PF}_6]^+$ : 695.1345; Found: 695.1336. <sup>1</sup>H NMR ( $\text{CD}_3\text{CN}$ ):  $\delta$  [ppm] = 9.21 (s, 2H,  $\text{H}^{2\text{A}}$ ), 8.69 (s, 1H, NH), 8.57 (d,  $^3J_{\text{HH}} = 8$  Hz, 2H,  $\text{H}^{5\text{A}}$ ), 8.45 (s, 2H,  $\text{H}^{2\text{B}}$ ), 8.06 (d,  $^3J_{\text{HH}} = 8$  Hz, 2H,  $\text{H}^{5\text{B}}$ ), 7.71 (vtd,  $^3J_{\text{HH}} = 8$  Hz,  $^4J_{\text{HH}} = 1$  Hz, 2H,  $\text{H}^{6\text{A}}$ ), 7.58 (vtd,  $^3J_{\text{HH}} = 8$  Hz,  $^4J_{\text{HH}} = 1$  Hz, 2H,  $\text{H}^{6\text{B}}$ ), 7.18 (d,  $^3J_{\text{HH}} = 5$  Hz, 2H,  $\text{H}^{8\text{A}}$ ), 7.04–6.95 (m, 2H,  $\text{H}^{7\text{A}}$ ), 6.93 (d,  $^3J_{\text{HH}} = 5$  Hz, 2H,  $\text{H}^{8\text{B}}$ ), 6.58 (vt,  $^3J_{\text{HH}} = 6$  Hz, 2H,  $\text{H}^{7\text{B}}$ ), 4.63 (q,  $^3J_{\text{HH}} = 7$  Hz, 2H,  $\text{H}^{11}$ ), 2.23 (s, 3H,  $\text{H}^{14}$ ), 1.57 (t,  $J = 7$  Hz, 3H,  $\text{H}^{12}$ ). <sup>13</sup>C{<sup>1</sup>H} NMR

( $\text{CD}_3\text{CN}$ ):  $\delta$  [ppm] = 215.8 (s,  $\text{C}^9$ ), 169.8 (s,  $\text{C}^{13}$ ), 169.3 (s,  $\text{C}^{4\text{B}}$ ), 166.0 (s,  $\text{C}^{10}$ ), 159.8 (s,  $\text{C}^{4\text{A}}$ ), 155.2 (s,  $\text{C}^{8\text{A}}$ ), 154.3 (s,  $\text{C}^{3\text{A}}$ ), 153.1 (s,  $\text{C}^{8\text{B}}$ ), 141.9 (s,  $\text{C}^{3\text{B}}$ ), 136.9 (s,  $\text{C}^{5\text{B}}$ ), 136.2 (s,  $\text{C}^{5\text{A}}$ ), 134.4 (s,  $\text{C}^{1\text{B}}$ ), 132.5 (s,  $\text{C}^{1\text{A}}$ ), 127.6 (s,  $\text{C}^{7\text{A}}$ ), 124.8 (s,  $\text{C}^{5\text{A}}$ ), 122.9 (s,  $\text{C}^{2\text{A}}$ ), 122.6 (s,  $\text{C}^{7\text{B}}$ ), 120.8 (s,  $\text{C}^{5\text{B}}$ ), 117.9 (s,  $\text{C}^{2\text{B}}$ ), 63.3 (s,  $\text{C}^{11}$ ), 24.4 (s,  $\text{C}^{14}$ ), 14.7 (s,  $\text{C}^{12}$ ). IR (KBr disk):  $\lambda^{-1}$  [ $\text{cm}^{-1}$ ] = 3435 (crystal water), 1723 ( $\text{C}=\text{O}_{\text{ester}}$ ), 1711 ( $\text{C}=\text{O}_{\text{amide}}$ ), 1600 ( $\text{C}=\text{C}$ ), 1518 (amide II), 845 (P–F). UV–vis (MeCN):  $\lambda_{\text{max}}$  ( $\epsilon$ ) [nm ( $1 \times 10^3 \text{ M}^{-1} \text{ cm}^{-1}$ )] = 241 (49.8), 282 (62.1), 319 (29.8), 378 (14.1), 418 (shoulder, 9.7), 506 (17.3), 555 (13.7).

**Synthesis of  $[\text{Ru}(\text{dpb-COOC}_2\text{H}_5)(\text{tpy-NHCOCH}_3)](\text{PF}_6)$   $\mathbf{2}(\text{PF}_6)$ .**  $\text{RuCl}_3(\text{tpy-NHCOCH}_3)$  (100 mg, 0.201 mmol, 1 equiv) was suspended in 20 mL of abs. acetone, and silver tetrafluoroborate (113 mg, 0.583 mmol, 2.9 equiv) was added. The resulting reaction mixture was heated to reflux for 2 h in the dark. After the mixture cooled to room temperature, the dark brown solution was filtered through a syringe filter to remove precipitated silver chloride prior to evaporation of the solvent. The dark, oily residue was dissolved in abs.  $n\text{BuOH}$  (20 mL), and  $\text{C}_2\text{H}_5\text{OOC-dpbH}$  L3 (73 mg, 0.241 mmol, 1.2 equiv) was added. The resulting dark brown to purple solution was heated to reflux for 16 h giving an intensely colored red solution. After removal of the solvent under reduced pressure the remaining solid was dissolved in acetonitrile (5 mL), and a solution of ammonium hexafluorophosphate (130 mg, 0.80 mmol, 4 equiv) in water (1 mL) was added. Addition of more water (~80 mL) resulted in the precipitation of the crude product, which subsequently was filtered off. Column chromatography on neutral Alox (Brockmann II, 3% water (w/w), solvent gradient chloroform  $\rightarrow$  chloroform/methanol 50:1, after a yellow impurity was eluted) afforded pure  $[\text{Ru}(\text{dpb-COOC}_2\text{H}_5)(\text{tpy-NHCOCH}_3)](\text{PF}_6)$  as dark solid. Yield: 87 mg (0.104 mmol, 52%) A second fraction consisting of  $[\text{Ru}(\text{dpb-COOEt})(\text{tpy-NH}_2)](\text{PF}_6)$   $\mathbf{3}(\text{PF}_6)$  was isolated as well (40 mg, 0.050 mmol, 25%). Anal. Calcd for  $\text{C}_{36}\text{H}_{29}\text{F}_6\text{N}_6\text{O}_3\text{PRu}$  (839.7): C, 51.49; H, 3.48; N, 10.01. Found: C, 51.46; H, 3.30; N, 9.73%. MS(ESI<sup>+</sup>):  $m/z$  (%) = 347.6 (1)

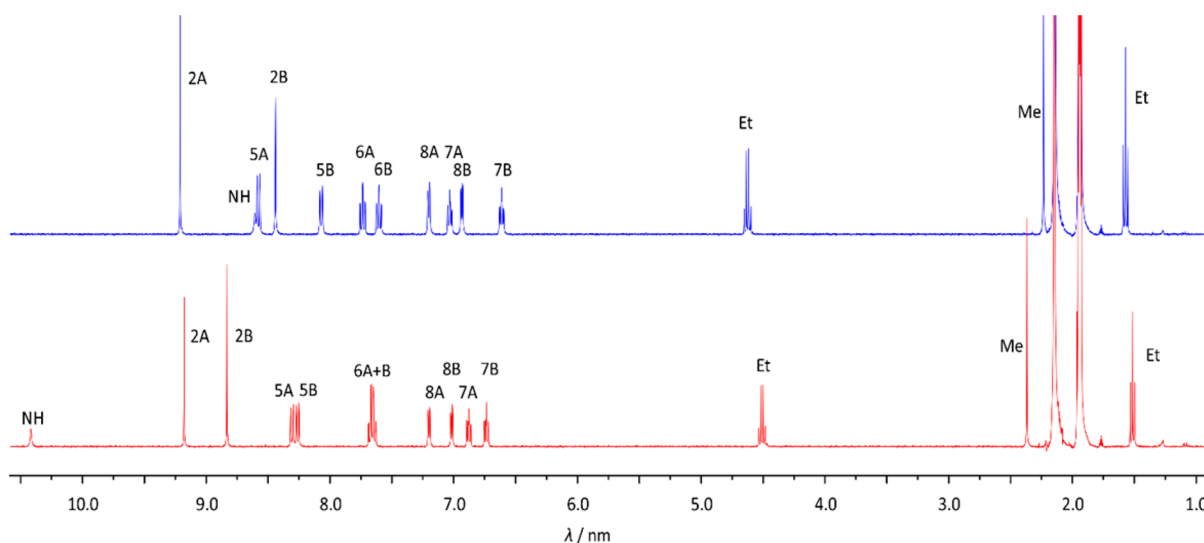


**Figure 1.**  $^1\text{H}$  NMR spectra of  $1(\text{PF}_6)$  (upper, blue) and  $2(\text{PF}_6)$  (lower, red) at room temperature in  $\text{CD}_3\text{CN}$  (for atom numbering see Scheme 3).

$[\text{M}-\text{PF}_6]^{2+}$ , 695.1 (100)  $[\text{M}-\text{PF}_6]^+$ , 1535.3 (6)  $[2\text{M}-\text{PF}_6]^+$ . HR-MS (ESI $^+$ ,  $m/z$ ): Calcd for  $\text{C}_{36}\text{H}_{29}\text{N}_6\text{O}_3\text{Ru}$   $[\text{M}-\text{PF}_6]^+$ : 695.1345; Found: 695.1342.  $^1\text{H}$  NMR ( $\text{CD}_3\text{CN}$ ):  $\delta$  [ppm] = 10.42 (s, 1H, NH), 9.12 (s, 2H,  $\text{H}^{2\text{A}}$ ), 8.83 (s, 2H,  $\text{H}^{2\text{B}}$ ), 8.30 (d,  $^3J_{\text{HH}} = 8$  Hz, 2H,  $\text{H}^{5\text{A}}$ ), 8.25 (d,  $^3J_{\text{HH}} = 8$  Hz, 2H,  $\text{H}^{5\text{B}}$ ), 7.70–7.60 (m, 4H,  $\text{H}^{6\text{A}}$ ,  $\text{H}^{6\text{B}}$ ), 7.18 (d,  $^3J_{\text{HH}} = 5$  Hz, 2H,  $\text{H}^{8\text{B}}$ ), 7.02 (d,  $^3J_{\text{HH}} = 5$  Hz, 2H,  $\text{H}^{8\text{A}}$ ), 6.91–6.82 (m, 2H,  $\text{H}^{7\text{A}}$ ), 6.76–7.66 (m, 2H,  $\text{H}^{7\text{B}}$ ), 4.51 (q,  $^3J_{\text{HH}} = 7$  Hz, 2H,  $\text{H}^{11}$ ), 2.36 (s, 3H,  $\text{H}^{14}$ ), 1.51 (t,  $^3J_{\text{HH}} = 7$  Hz, 3H,  $\text{H}^{12}$ ).  $^{13}\text{C}\{^1\text{H}\}$  NMR ( $\text{CD}_3\text{CN}$ ):  $\delta$  [ppm] = 233.7 (s,  $\text{C}^{9\text{B}}$ ), 171.3 (s,  $\text{C}^{13}$ ), 169.1 (s,  $\text{C}^{4\text{B}}$ ), 168.7 (s,  $\text{C}^{10}$ ), 159.8 (s,  $\text{C}^{4\text{A}}$ ), 155.6 (s,  $\text{C}^{8\text{A}}$ ), 153.7 (s,  $\text{C}^{3\text{A}}$ ), 152.8 (s,  $\text{C}^{8\text{B}}$ ), 145.7 (s,  $\text{C}^{1\text{A}}$ ), 143.4 (s,  $\text{C}^{3\text{B}}$ ), 136.5 (s,  $\text{C}^{6\text{A}}$ ), 136.4 (s,  $\text{C}^{6\text{B}}$ ), 127.3 (s,  $\text{C}^{7\text{A}}$ ), 124.5 (s,  $\text{C}^{5\text{A}}$ ), 124.5 (s,  $\text{C}^{2\text{B}}$ ), 123.0 (s,  $\text{C}^{7\text{B}}$ ), 122.7 (s,  $\text{C}^{1\text{B}}$ ), 120.8 (s,  $\text{C}^{5\text{B}}$ ), 112.8 (s,  $\text{C}^{2\text{A}}$ ), 61.5 (s,  $\text{C}^{11}$ ), 24.9 (s,  $\text{C}^{14}$ ), 15.0 (s,  $\text{C}^{12}$ ). IR (KBr disk):  $\lambda^{-1}$  [ $\text{cm}^{-1}$ ] = 1695 ( $\text{C}=\text{O}_{\text{ester,amide}}$ ), 1600 ( $\text{C}=\text{C}$ ), 1514 (amide II), 844 (P–F). UV–vis (MeCN):  $\lambda_{\text{max}}$  ( $\epsilon$ ) [nm ( $1 \times 10^3 \text{ M}^{-1} \text{ cm}^{-1}$ )] = 242 (49.2), 282 (69.4), 317 (32.4), 351 (16.9), 428 (8.7), 502 (15.2), 544 (shoulder, 11.8). (NMR and mass spectrometric data of  $3(\text{PF}_6)$  can be found in the Supporting Information.)

## RESULTS AND DISCUSSION

**Syntheses of Ru Complexes.** Details of the ligand syntheses can be found in the Experimental Section (L1, L2) and in the Supporting Information (L3). Several different experimental protocols have been reported for the synthesis of heteroleptic ruthenium complexes with terpyridine and dipyrrolylbenzene ligands. Complexation can be performed in water/methanol solution starting from  $\text{RuCl}_3(\text{tpy}-\text{R})$  at elevated temperatures and in the presence of a tertiary amine as sacrificial reductant.<sup>41</sup> This path resembles the microwave-assisted synthesis that we employed to obtain heteroleptic bis(terpyridine)ruthenium(II) complexes in high yields.<sup>21,27</sup> For cyclometalated complexes, this procedure gives practicable yields when the coordinating carbon atom is located at one of the peripheral aromatic rings of a multidentate ligand.<sup>20,41</sup> A more robust protocol was presented in 1991 by Sauvage and co-workers in the first report on the parent cyclometalated ruthenium(II) complex  $[\text{Ru}(\text{dpb})(\text{ttpy})]^+$  ( $\text{ttpy} = 4\text{'-tolylterpyridine}$ ):<sup>80</sup>  $\text{RuCl}_3(\text{ttpy})$  is activated via chloride abstraction with silver tetrafluoroborate. Upon addition of dpbH the desired cyclometalated complex forms readily at elevated temperatures in high yields.<sup>20,81</sup> We successfully adapted this protocol for the synthesis of the complexes presented herein (Scheme 3). Since acetylated amino groups are prone to hydrolysis and oxidation, all reactions were performed under

rigorous protective gas conditions, and only 2.9 equiv of  $\text{Ag}[\text{BF}_4]$  (instead of 3.6 equiv as usually found in the literature)<sup>20,81</sup> were employed to prevent undesired side reactions. Under these conditions, we obtained the complexes  $1(\text{PF}_6)$  and  $2(\text{PF}_6)$  in yields of 70% and 52%, respectively, besides small quantities of a side product with a hydrolyzed acetyl amino group ( $[\text{Ru}(\text{dpb}-\text{COOEt})(\text{tpy}-\text{NH}_2)](\text{PF}_6)$   $3(\text{PF}_6)$ ; see Scheme 3 and Supporting Information).

**Characterization of the Isomers.** Since both complexes  $1(\text{PF}_6)$  and  $2(\text{PF}_6)$  are constitutional isomers they share their elemental composition and show essentially identical mass spectra and isotope patterns (Supporting Information Figure S8). The most prominent differences are observed in the NMR spectra (Figure 1, Supporting Information Figures S9–S18). All tpy aromatic proton resonances (2A, 5A, 6A, 7A, and 8A) appear systematically further downfield in the  $^1\text{H}$  NMR spectrum (Figure 1, Scheme 3) compared to corresponding resonances of the dpb protons due to the electron-deficiency of the tpy ligand. Proton resonances of the functional groups (NHCOMe and COOEt) show the same trend. In  $1^+$ , with the tpy-COOEt ligand, the  $\text{CH}_2$  and  $\text{CH}_3$  resonances of the ethyl group are found at 4.63 and 1.57 ppm, respectively, whereas in the regioisomer  $2^+$  the corresponding protons of the dpb-COOEt ligand appear at 4.51 and 1.51 ppm, respectively. Similarly, the resonance of the acetyl  $\text{CH}_3$  protons is found at 2.23 ppm in  $1^+$  and at 2.36 ppm in  $2^+$ , underlining the electronic influence of the different ligands. This effect is most pronounced for the amide NH proton due to its proximity to the aromatic system in both complexes. The NH resonance of tpy-NHCOMe in  $2^+$  is found at very low field (10.42 ppm), while in  $1^+$ , the NH resonance of dpb-NHCOMe is found at 8.69 ppm. Similar trends are also observed in the  $^{13}\text{C}$  NMR spectra (Supporting Information Figures S10 and S15). The resonance of the carbon atom  $\text{C}^{9\text{B}}$  involved in the metal–carbon bond is found at 215.8 ppm in  $1^+$  with the dpb-NHCOMe ligand and at 233.7 ppm in  $2^+$  with the dpb-COOEt ligand.

Although the final complexation step requires harsh reaction conditions and long reaction times, the reaction proceeds in good yields without significant side reactions. The structural integrity of the complexes  $1^+$  and  $2^+$  with all functional groups is further confirmed by ESI mass spectrometry (Supporting



Information Figure S8). No significant mass peaks indicating cleavage of either the ester or the amide are detected. Interestingly, all mass spectra show a weak peak that can be assigned to  $[M-PF_6]^{2+}$  at  $m/z = 347.6$ . This is likely explained by the typically rather low oxidation potential of these electron-rich cyclometalated (polypyridine)ruthenium(II) complexes (vide infra). IR spectroscopy confirms the presence of both an ester group and a primary amide by characteristic bands for ester C=O and amide I stretching vibrations at 1723 and 1711  $cm^{-1}$  for  $1^+$  (DFT: 1733 and 1701  $cm^{-1}$ , respectively). For  $2^+$ , the IR stretching vibrations of the ester and amide carbonyl function are observed at 1697  $cm^{-1}$ . Indeed, DFT calculations predict essentially identical vibrational frequencies for both groups at  $\sim 1718$ – $1719$   $cm^{-1}$  for  $2^+$  reflecting the different electronic character of tpy and dpb (Supporting Information Figure S21). The NH deformation bands are found at  $\sim 1580$ – $1600$   $cm^{-1}$  for both isomers along with coupled C–C vibrations within the aromatic backbone (see rR spectra). The presence of the  $PF_6^-$  counterion is revealed by broad and intense P–F stretching bands at 840  $cm^{-1}$ .

**UV–vis Spectroscopic Properties of the Cyclometalated Isomers  $1^+$  and  $2^+$ .** The experimental UV–vis spectra of the two complexes  $1(PF_6)$  and  $2(PF_6)$  are depicted in Figure 2, and relevant spectroscopic data are summarized in the

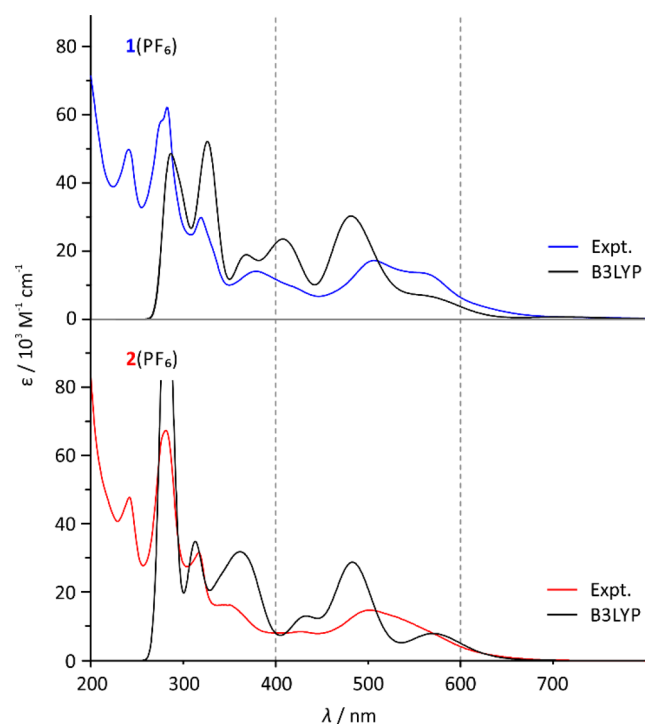


**Figure 2.** Experimental absorption spectra of  $1(PF_6)$  (upper, blue) and  $2(PF_6)$  (lower, red) in acetonitrile at room temperature;  $c = 2 \times 10^{-5}$  mol  $l^{-1}$  and calculated UV–vis spectra from TD-DFT calculations (B3LYP, black). The calculated spectra are shifted by  $1000$   $cm^{-1}$  to lower energies to match calculated and experimental  $\pi$ – $\pi^*$  absorption energies.

**Experimental Section.** Both complexes show absorption features of very similar shape, intensity, and energy between 200 and 325 nm. This is because of the identical ligand backbone of both complexes and is characteristic for  $[Ru(dpb)(tpy)]^+$ -type complexes.<sup>20,81</sup> Especially the sharp absorption band at  $\sim 320$  nm with an extinction coefficient of  $\sim 3.0 \times$

$10^4$   $M^{-1} cm^{-1}$  appears to be a characteristic marker for the cyclometalation in the central position of the tridentate ligand and is well-reproduced via theoretical calculations (vide infra).

The visible region of the absorption spectra of  $1(PF_6)$  and  $2(PF_6)$  is dominated by four absorption bands (Tables 1 and 2). The strongest absorption occurs at 506 nm in  $1(PF_6)$  and at 502 nm in  $2(PF_6)$  and is best described as  $^1MLCT$  transition involving the pyridine rings of both ligands as acceptors (vide infra).<sup>20</sup> In complex  $1(PF_6)$ , the donor and acceptor effect of the respective ligand and functional group reinforce one another. An additional absorption maximum appears at the low-energy side of this MLCT transition at 555 nm. On the contrary,  $2(PF_6)$  only shows a weak shoulder in this region (Figure 2). The overall bathochromic shift of the visible light absorption features of  $1(PF_6)$  compared to  $2(PF_6)$  is accompanied by an increase in absorption intensity. Both observations are best explained by the increased push–pull effect arising from the functional groups, which lowers the highest occupied molecular orbital–lowest unoccupied molecular orbital (HOMO–LUMO) gap (cf. MO diagram, Supporting Information Figure S22) and increases the transition dipole moments for the  $^1MLCT$  transitions in  $1(PF_6)$ . In  $2(PF_6)$  on the other hand, the donor strength of dpb and the acceptor strength of tpy are both partially canceled by the substituents leading to a larger HOMO–LUMO gap and weaker  $^1MLCT$  absorptions. As a consequence,  $1(PF_6)$  appears black in the solid state and deep purple in acetonitrile solution, while  $2(PF_6)$  is dark red in the solid state and in solution. This observation is in accordance with previous results for similar complexes.<sup>20</sup>

Both compounds show two more absorption bands between 340 and 450 nm with similar intensities as the  $^1MLCT$  absorptions. In the literature the origins of these bands are consistently discussed as MLCT transitions involving the cyclometalating ligand.<sup>20,41,81</sup> However, this interpretation contradicts the observed hypsochromic shift of this absorption from 378 nm ( $1(PF_6)$ ) to 351 nm ( $2(PF_6)$ ) upon exchanging the electron-donating N-acetyl amino group for an electron-accepting carboxy group. A more consistent explanation of these absorptions is gained from TD-DFT calculations and rR experiments.

Theoretical calculations were performed using geometries optimized at the PBE/def2-SV(P) level of theory with an effective core potential at ruthenium (def2-SD, def2-TZVP). This level of theory for the geometry optimization was chosen based on data obtained by screening multiple functionals and basis sets and by comparison to geometrical parameters obtained from crystal structures of three structurally related compounds ( $[Ru(dpb-COOMe)(tpy)](PF_6)$ ,  $[Ru(dpb)(tpy-COOEt)](PF_6)$ , and  $[Ru(pbp-COOMe)(tpy)](PF_6)$ ).<sup>20</sup> This evaluation showed only a marginal dependence of the geometrical parameters on the size of basis set allowing for usage of a rather small and computationally efficient basis set. The variation of the structural parameters with the choice of functional was larger, but still, qualitatively similar results were obtained with all functionals under study (BP, PBE, BLYP, TPSS, TPSSh, M06L, B3LYP, PBE0). Remarkably, within the mean deviation the hybrid functionals PBE0 and B3LYP yielded identical optimized geometries compared to the corresponding GGA functionals PBE and BLYP. Hence, the more economic GGA functional PBE was preferred over hybrid functionals for geometry optimizations.



**Table 1. Spectral Decomposition of the Absorption Bands of 1(PF<sub>6</sub>) in Acetonitrile Solution in the Range from 9000 to 29 000 cm<sup>-1</sup> Using the Advanced Spectral Analysis Tool of ORCA (orca\_asa)<sup>a</sup>**

experimental data					theoretical data			
state	$\lambda^{-1}$ , cm <sup>-1</sup>	$\lambda$ , nm	$f_{\text{osc}}$	$\epsilon_{\text{max}}$ M <sup>-1</sup> cm <sup>-1</sup>	state	$\lambda^{-1}$ , cm <sup>-1</sup>	$f_{\text{osc}}$	assignment
1	12 935	773	$1.39 \times 10^{-3}$	145				Ru→tpy <sup>3</sup> MLCT
2	15 438	648	$1.15 \times 10^{-2}$	714	2	15 095	$5.5 \times 10^{-3}$	Ru→tpy <sup>1</sup> MLCT
3	16 197	617	$1.48 \times 10^{-2}$	1940				
4	17 711	565	0.102	11 300	4	18 194	0.030	Ru→tpy
					5	19 150	0.040	<sup>1</sup> MLCT
5	18 694	535	$6.99 \times 10^{-3}$	1570				
6	19 687	508	0.107	11 700	6	20 914	0.091	Ru→dpb <sup>1</sup> MLCT
7	20 910	478	0.124	6200	7	21 962	0.213	Ru→tpy <sup>1</sup> MLCT
8	21 399	467	$4.13 \times 10^{-3}$	690	8	21 843	$2.6 \times 10^{-3}$	Ru→dpb <sup>1</sup> MLCT
9	23 871	419	$5.38 \times 10^{-2}$	5290				
10	25 166	397	$7.88 \times 10^{-3}$	1210				
11	26 500	377	0.234	14 700				

<sup>a</sup>Eleven Gaussian bands were required to reproduce the shape of the absorption profile, and  $\lambda^{-1}$ ,  $f_{\text{osc}}$  and  $\epsilon_{\text{max}}$  are obtained from the respective fitted bands. Theoretical data are obtained from TD-DFT calculations (B3LYP) and assigned to the experimental bands based on their energy and oscillator strengths.

**Table 2. Spectral Decomposition of the Absorption Bands of 2(PF<sub>6</sub>) in Acetonitrile Solution in the Range from 9000 to 29 000 cm<sup>-1</sup> Using the Advanced Spectral Analysis Tool of ORCA (orca\_asa)<sup>a</sup>**

experimental data					theoretical data			
state	$\lambda^{-1}$ , cm <sup>-1</sup>	$\lambda$ , nm	$f_{\text{osc}}$	$\epsilon_{\text{max}}$ M <sup>-1</sup> cm <sup>-1</sup>	state	$\lambda^{-1}$ , cm <sup>-1</sup>	$f_{\text{osc}}$	assignment
1	15 479	646	$1.29 \times 10^{-3}$	208				Ru→tpy <sup>3</sup> MLCT
2	17 345	577	$1.49 \times 10^{-3}$	331	4	18 332	0.014	Ru→tpy <sup>1</sup> MLCT
3	17 455	573	$3.25 \times 10^{-2}$	2530	5	18 593	0.060	Ru→tpy <sup>1</sup> MLCT
4	19 445	514	0.216	13 000	7	21 675	0.170	Ru→dpb <sup>1</sup> MLCT
					8	21 681	0.096	
5	20 269	493	$1.54 \times 10^{-2}$	2460				
6	21 472	466	$9.72 \times 10^{-3}$	1430				
7	23 244	430	$7.42 \times 10^{-2}$	6240	11	24 120	0.111	Ru→tpy,dpb <sup>1</sup> MLCT
8	24 575	407	$1.39 \times 10^{-4}$	56				
9	25 035	399	$1.12 \times 10^{-2}$	1480	16	26 366	0.026	Ru→tpy <sup>1</sup> MLCT
10	28 059	356	$1.16 \times 10^{-2}$	1250				
11	29 114	343	0.504	16 300				

<sup>a</sup>Eleven Gaussian bands were required to reproduce the shape of the absorption profile, and  $\lambda^{-1}$ ,  $f_{\text{osc}}$  and  $\epsilon_{\text{max}}$  are obtained from the respective fitted bands. Theoretical data are obtained from TD-DFT calculations (B3LYP) and assigned to the experimental bands based on their energy and oscillator strengths.

Vertical excitations were generated within the TD-DFT formalism with a triple- $\xi$  basis set (def2-TZVP) and the Douglas–Kroll–Hess relativistic approximation in combination with functionals of varying Hartree–Fock (HF) exchange (PBE, 0%; TPSSh, 10%; B3LYP, 20%; PBE0, 25%). Additionally, the range-separated CAM-B3LYP functional was employed. While PBE and CAM-B3LYP both gave unsatisfactory results, TPSSh, B3LYP, and PBE0 performed equally well in TD-DFT calculations of 1(PF<sub>6</sub>) and 2(PF<sub>6</sub>) compared to the corresponding experimental data (see Supporting Information, Figures S23 and S24). A systematic increase of all transition energies and transition probabilities (oscillator strengths) was observed with increasing HF exchange (TPSSh < B3LYP < PBE0).

In the following the TD-DFT calculations using B3LYP as functional and the corresponding spectra generated with orca\_mapspc (line width 1500 cm<sup>-1</sup>) will be discussed and correlated with the experimental absorption spectra of 1(PF<sub>6</sub>) and 2(PF<sub>6</sub>). The theoretical and experimental UV–vis spectra

match reasonably well in the UV region, when the entire theoretical spectrum is shifted by 1000 cm<sup>-1</sup> to lower energies (Figure 2). In the visible region, however, the agreement is somewhat lower for both 1(PF<sub>6</sub>) and 2(PF<sub>6</sub>). This is mostly because of the weakness of TD-DFT in the description of charge transfer excitations.<sup>68,82,83</sup> Difference density plots of the 10 lowest excitations and all further significant transitions ( $f > 0.01$ ) are shown for 1<sup>+</sup> and 2<sup>+</sup> in the Supporting Information, Tables S1 and S2. In both complexes the lowest-energy transition is a well-defined HOMO–LUMO excitation with no significant admixture of other orbitals. The LUMO in both complexes is a  $\pi^*$ -orbital located at the tpy ligand, while the HOMO is essentially a  $\pi$ -orbital of the dpb ligand. The lowest-energy excitation can formally be regarded as a LL'/CT transition although ruthenium d-orbitals of the t<sub>2g</sub> set are admixed into the frontier orbitals (mixed LL'/CT and MLCT character). To differentiate between these transitions and the MLCT transitions these states will be labeled LL'/CT. Since both ligands are perpendicular to each other so are the

contributing d-orbitals, which renders the metal contribution negligible. As a consequence, these HOMO–LUMO transitions for  $1^+$  and  $2^+$  are symmetry-forbidden excitations due to the vanishing overlap integral (oscillator strengths of  $1.1 \times 10^{-5}$  and  $7.1 \times 10^{-5}$  for  $1^+$  and  $2^+$ , respectively) and do not contribute to the absorption spectrum. The corresponding  $^3\text{LL}'\text{CT}$  states, however, might play a significant role for the excited-state behavior of  $1(\text{PF}_6)$  and  $2(\text{PF}_6)$ , as discussed below.

The higher-energy excitations predicted in the visible region are  $^1\text{MLCT}$  transitions from metal d-orbitals onto the ligands. Interestingly, these excitations do not only involve tpy  $\pi^*$ -orbitals. Already in the range above 400 nm dpb accepting orbitals play a major role for the absorption profile. The UV transitions in the range between 400 and 320 nm also consist of  $^1\text{MLCT}$  transitions onto both ligands. A distinct separation of  $\text{Ru} \rightarrow \text{tpy}$  and  $\text{Ru} \rightarrow \text{dpb}$  MLCT transitions, with the former being responsible for the low-energy absorption band between 600 and 450 nm and the latter yielding the UV band between 320 and 430 nm, is not valid.

To be able to match the experimentally obtained spectrum with the theoretical data spectral decompositions of the visible range of the absorption spectra were performed. This is of particular interest considering the predicted low intensity of the LL'CT transitions in  $1(\text{PF}_6)$  and  $2(\text{PF}_6)$ . The fit data are summarized in Tables 1 and 2 for  $1(\text{PF}_6)$  and  $2(\text{PF}_6)$ , respectively. Despite the high quality of the fit (see Supporting Information, Figure S25) the low-intensity LL'CT absorptions in the low-energy edge of the absorption spectrum were not detected in either case. An upper limit of the oscillator strengths of these transitions is estimated as  $f \leq 1 \times 10^{-4}$ , which is in agreement with the computational data. The decomposition of the absorption bands supports the qualitative discussion of the spectra above. A plausible assignment of TD-DFT excitations to the most intense bands was possible based on similarities in oscillator strengths and transition energies underlining that the computational method gives a reasonable estimate of the absorption spectrum. The lowest-energy excitation observed within the spectral decomposition ( $12\,935$  and  $15\,479 \text{ cm}^{-1}$  for  $1(\text{PF}_6)$  and  $2(\text{PF}_6)$ , respectively) could not be assigned to any calculated vertical singlet excitation. We ascribe these to  $^3\text{MLCT}$  absorptions that become partially spin-allowed due to spin–orbit coupling in the presence of ruthenium.<sup>4,5</sup> A complete assignment of all observed bands is of course out of reach at the presented level of theory and will generally be very difficult based on the complexity of the absorption characteristics of  $1(\text{PF}_6)$  and  $2(\text{PF}_6)$ .

**Resonance Raman Studies on  $1^+$  and  $2^+$ .** To further support this interpretation of the absorption characteristics of  $1(\text{PF}_6)$  and  $2(\text{PF}_6)$  in the visible region rR spectroscopic studies in acetonitrile solution were performed. This technique has proven to be useful just recently in the elucidation of the charge redistribution upon optical excitation in bis-(terpyridine)ruthenium(II) complexes.<sup>84,85</sup> The rR spectra of  $1(\text{PF}_6)$  and  $2(\text{PF}_6)$  with excitation at 473, 532, and 633 nm are shown in Figures 3 and 4, respectively. Since even the idealized core symmetry of these complexes ( $C_{2v}$ ) is rather low and the number of atoms is high ( $N = 76$ ), a multitude of Raman bands, many of them overlapping, is observed in the rR spectra. Qualitatively, the spectra appear very similar at the different excitation wavelengths with the only differences lying in the intensities of the bands. On one hand, the intensity of the rR

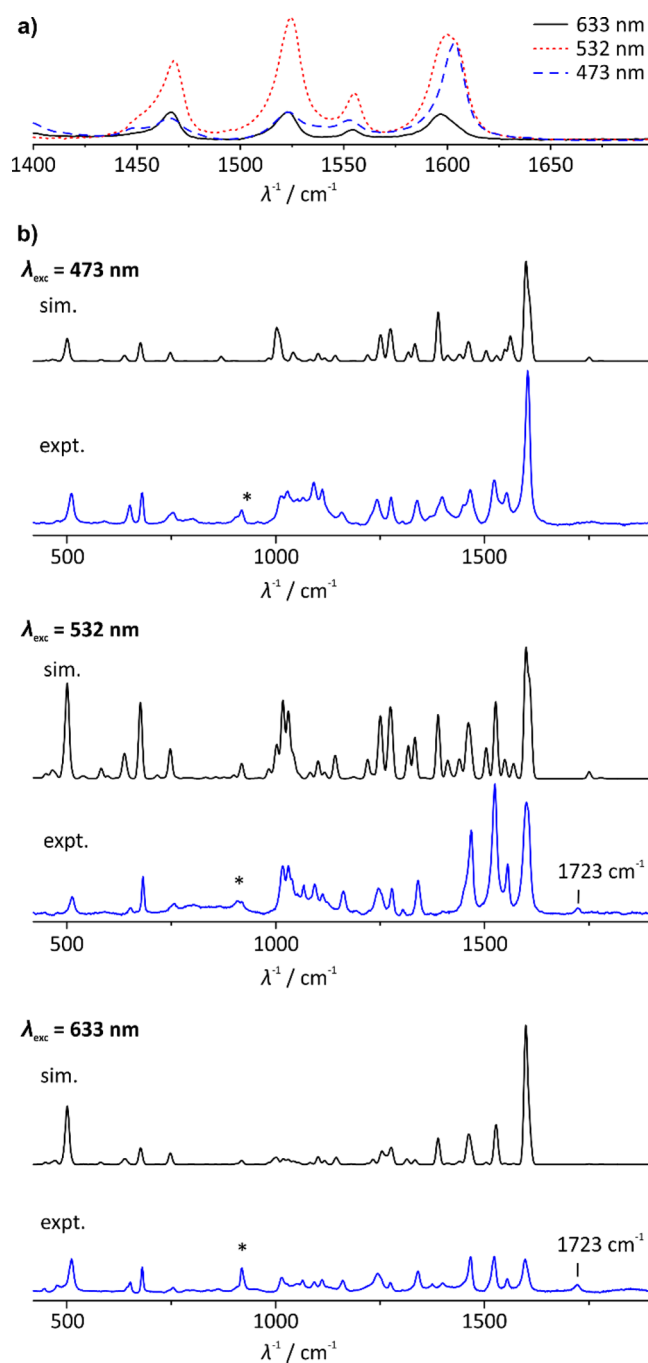


**Figure 3.** (a) Resonance Raman spectra of  $1(\text{PF}_6)$  in acetonitrile solution (298 K) in the range of  $1400\text{--}1700 \text{ cm}^{-1}$  at different excitation wavelengths. (b) Experimental (blue) and DFT-calculated (black, line width =  $10 \text{ cm}^{-1}$ ) rR spectra of  $1(\text{PF}_6)$  at 473, 532, and 633 nm excitation wavelength. Asterisks indicate Raman bands of  $\text{CH}_3\text{CN}$ .

spectra obviously directly depends on the extinction coefficient at the given irradiation wavelength so that a maximum in rR intensity is expected in the range of 530–470 nm for both complexes. On the other hand, the rR intensity depends on whether a given vibrational mode contributes to the geometrical reorganization associated with the given optical transition at the Franck–Condon point. Remarkably, the carbonyl stretching vibrations of both the ester and the amide functionality only play a subordinate role at all excitation wavelengths for both  $1(\text{PF}_6)$  and  $2(\text{PF}_6)$ . Since the common

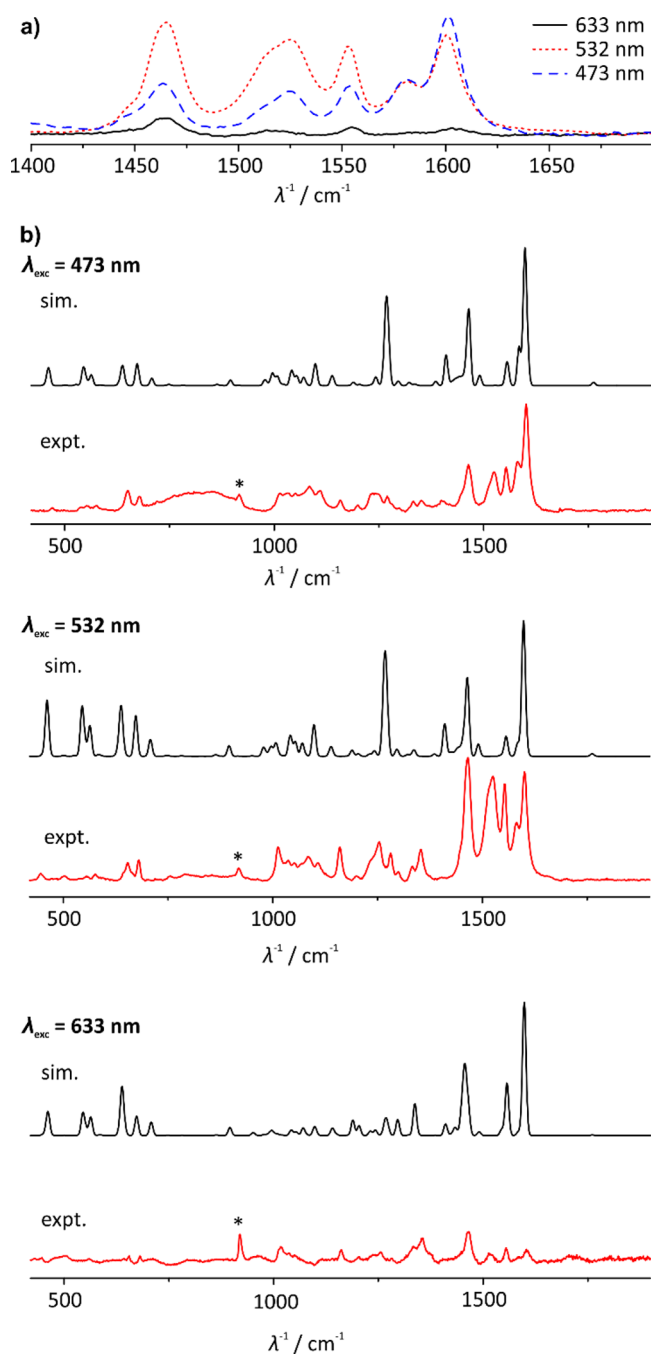


**Figure 4.** (a) Resonance Raman spectra of  $2(\text{PF}_6)$  in acetonitrile solution (298 K) in the range of 1400–1700  $\text{cm}^{-1}$  at different excitation wavelengths. (b) Experimental (red) and DFT-calculated (black, line width = 10  $\text{cm}^{-1}$ ) rR spectra of  $2(\text{PF}_6)$  at 473, 532, and 633 nm excitation wavelength. Asterisks indicate Raman bands of  $\text{CH}_3\text{CN}$ .

description of the intense visible range absorption band is that of a MLCT transition onto the terpyridine ligand the terpyridine ester  $\text{C}=\text{O}$  vibration at 1723  $\text{cm}^{-1}$  in  $1(\text{PF}_6)$  should be visible for all excitation wavelengths under study. At  $\lambda_{\text{exc}} = 633$  nm this is indeed true, but at higher energies ( $\lambda_{\text{exc}} = 532$  nm) the contribution of this vibration diminishes until disappearance at  $\lambda_{\text{exc}} = 473$  nm. At shorter wavelengths,  $\text{Ru} \rightarrow \text{dpb}$  MLCT excitations become increasingly relevant for the absorption characteristics. For  $2(\text{PF}_6)$ , no distinct  $\text{C}=\text{O}$

stretching bands are observed at any excitation wavelength (cf. IR spectrum, *vide supra*).

Since the MLCT transitions involve  $\pi^*$ -orbitals of the aromatic ligands the corresponding CC valence vibrations should be excited and give intense rR responses (see Figures 3a and 4a). They are assigned based on DFT-calculated ground-state vibrational frequencies. The bands at 1600  $\text{cm}^{-1}$  for  $1(\text{PF}_6)$  and  $2(\text{PF}_6)$  are assigned to the symmetric valence vibrations (local  $A_1$  symmetry) of the aromatic rings. While for  $1(\text{PF}_6)$ , all these vibrations are very close in energy (DFT: between 1597 and 1605  $\text{cm}^{-1}$ ) and overlap in the rR spectra at all excitation wavelengths, the symmetric vibration of the carboxy-substituted phenyl ring of  $2(\text{PF}_6)$  is shifted by 20  $\text{cm}^{-1}$  to lower energy yielding a well-resolved band in the rR spectra of  $2(\text{PF}_6)$  at 1581  $\text{cm}^{-1}$  (calculated at 1584  $\text{cm}^{-1}$ ) that is not present in  $1(\text{PF}_6)$ . The significant participation of the phenyl vibration in the rR spectra of  $2(\text{PF}_6)$  indicates substantial  $\text{Ru} \rightarrow \text{dpb}$  character of the MLCT absorption band at 532 nm and at 473 nm. This corroborates the findings of TD-DFT calculations that  $\text{Ru} \rightarrow \text{dpb}$  excitations are present even at energies below 450 nm. Since the corresponding vibration of the phenyl moiety of  $1(\text{PF}_6)$  overlaps with those of the pyridine rings a similar conclusion cannot be drawn for  $1(\text{PF}_6)$  although the width of the band suggests participation of all six totally symmetric aromatic vibrations. Similar behavior is observed for the antisymmetric (local  $B_2$  symmetry) CC valence vibrations at  $\sim 1525$   $\text{cm}^{-1}$ . While for  $1(\text{PF}_6)$  these vibrations overlap yielding one broad Raman band, a distinct shoulder at 1514  $\text{cm}^{-1}$  appears for  $2(\text{PF}_6)$ , which is assigned to the phenyl moiety again underlining the mixed  $\text{Ru} \rightarrow \text{tpy}/\text{Ru} \rightarrow \text{dpb}$  MLCT character of the absorption band at 473 and 533 nm.

The intensity of the bands between 1400 and 1550  $\text{cm}^{-1}$  increases substantially upon increasing  $\lambda_{\text{exc}}$  from 473 to 532 nm. Ground-state vibrational frequencies and Raman intensities provide no straightforward explanation for that. The independent mode-displaced harmonic oscillator (IMDHO) model was employed, which assumes harmonic ground- and excited-state potential energy surfaces (PES) and no frequency changes upon excitation. Additionally, the excited-state PES are considered as displaced with respect to the ground-state PES along certain (or all) normal modes. More evolved theoretical approaches have been employed previously in the description of rR spectra of large molecules,<sup>86</sup> but these require much more computational time and are limited to a small number (2–3) of electronically excited states that can be considered in the calculations.

At least three prerequisites must be met to yield a qualitatively good description of the rR behavior of a given compound: First, a high quality of the normal mode displacements is crucial for a reasonable description of the rR spectra since they determine the intensity of the corresponding Raman bands. These can be computed within the above-mentioned theoretical model from excited-state gradient calculations.<sup>78,87</sup> Second, the vibrational frequencies obtained from DFT calculations must correspond well to the experimentally observed ones since these define the normal modes and have a large impact on the displacement parameters. Third, the character of the calculated electronic excited states must match that of the actual transitions. This is the most challenging part, especially for charge transfer processes, since DFT has its weakness in describing such excitations.<sup>68,82,83</sup>

All calculations were performed based on the B3LYP/def2-SV(P)/DKH/COSMO(acetonitrile) optimized geometry of  $1^+$

and  $2^+$ . Vibrational frequencies were obtained at the same level of theory. Since ORCA does not support a solvation model for excited-state gradients, the 10 lowest vertical excitations and gradients were generated in the gas phase at the B3LYP/def2-TZVP/DKH level of theory. These 10 excitations describe the spectral range under study sufficiently well. The `orca_asa` software was then used to simulate the first-order rR spectra (higher-order Raman bands were considered but did not improve the quality of the simulations). A homogeneous line broadening of  $1200\text{ cm}^{-1}$  was assumed for all 10 excitations. The vibrational frequencies of both compounds were uniformly scaled by a factor of 0.967. This factor yields a maximum of agreement between the experimental and simulated spectra.

Neither the different MLCT optical excitations nor the molecular vibrations are energetically separated. Consequently, the rR spectrum at a given excitation wavelength is a superposition of rR profiles of the individual electronic excitations weighted by their contribution to the absorption spectrum at that wavelength. At the same time the individual Raman bands are a superposition of multiple vibrational modes. Despite the large number of approximations and assumptions the experimental rR spectra of  $1(\text{PF}_6)$  are remarkably well-reproduced by these simulations. This allows further confirmation of the character of respective absorption bands by assigning optical transitions to the respective absorption energies. The shape of the rR spectrum of  $1(\text{PF}_6)$  at  $633\text{ nm}$  is dominated by the most intense low-energy optical transitions 4 and 5 (see Table 1 and Supporting Information Table S1), which are Ru→tpy MLCT transitions. At  $\lambda_{\text{exc}} = 532\text{ nm}$ , the character of the involved absorptions changes and so does the rR spectrum. The range of  $1000\text{--}1300\text{ cm}^{-1}$  (in-plane deformation vibrations of the ligand backbones) is very characteristic for these changes, and a good agreement between simulation and experiment is obtained. The rR spectrum at  $\lambda_{\text{exc}} = 532\text{ nm}$  is dominated by the optical excitations 6 and 7 (Ru→tpy and Ru→dtpb; see Table 1 and Supporting Information Table S1). Consequently, the absorption region around the MLCT absorption maximum is composed of both Ru→tpy and Ru→dtpb MLCT transitions. This is in contrast to the widely accepted picture of this band as exclusively arising from Ru→tpy transitions. The quality of the rR simulation decreases somewhat at  $\lambda_{\text{exc}} = 473\text{ nm}$ . This is most likely because, at this wavelength, absorption bands of the second MLCT absorption (between  $450$  and  $320\text{ nm}$ ) contribute already. To keep the computational effort manageable these electronic transitions were neglected and thus are missing in the simulation. Consequently, the number of predicted rR bands is lower than experimentally observed. It is worth noting that the calculations also give an explanation for the missing resonant increase of the carbonyl stretching vibrations: For almost all major optical excitations the C=O fragment is located in a nodal plane of the involved orbitals and thus is only marginally affected by the rR effect.

$2(\text{PF}_6)$  gives a qualitatively very similar picture although the overall agreement between experiment and simulation is slightly lower (Figure 4). Especially, the  $B_2$  symmetric CC valence vibrations at  $1525\text{ cm}^{-1}$  seem to be missing in the simulation as they are calculated at higher energy at  $1556\text{ cm}^{-1}$ . At  $632\text{ nm}$  excitation wavelength essentially off-resonance excitation is achieved leading to a spectrum with a low signal-to-noise ratio. Still, the absorption characteristics at the different wavelengths are identical. While at  $632\text{ nm}$  low-energy MLCT transitions from ruthenium to the tpy ligand

prevail (excitations 4 and 5), the absorption at  $533\text{ nm}$  is dominated by excitation 5 (Ru→tpy MLCT; see Table 2 and Supporting Information Table S2). At  $\lambda_{\text{exc}} = 473\text{ nm}$  Ru→dtpb transitions come into play (state 7). Again, charge transfer processes into the electron-rich dtpb ligand occur at significantly lower energies than expected. In essence absorption bands between  $550$  and  $450\text{ nm}$  consist of MLCT absorptions from ruthenium onto both ligands in both complexes  $1(\text{PF}_6)$  and  $2(\text{PF}_6)$ .

**Emission Properties of  $1^+$  and  $2^+$ .** Cyclometalated polypyridine complexes of ruthenium usually exhibit only weak emission. The carboxy-substituted complex  $[\text{Ru}(\text{dtpb})(\text{tpy-COOR})]^+$  is nonemissive at room temperature, while its regioisomer  $[\text{Ru}(\text{dtpb-COOR})(\text{tpy})]^+$  shows weak room-temperature emission.<sup>20</sup> Similarly,  $[\text{Ru}(\text{pbpy})(\text{tpy-COOR})]^+$  is nonemissive at room temperature.<sup>20</sup>

$2(\text{PF}_6)$  emits at room temperature at  $751\text{ nm}$  with an emission quantum yield of  $1.4 \times 10^{-5}$  (Supporting Information Figure S26). At  $77\text{ K}$ , a much more intense emission is observed with an emission maximum at  $716\text{ nm}$  and a band shape typical for a ruthenium-based emission arising from a single vibronic progression (see Supporting Information Figure S27).<sup>27,88</sup>

The temperature dependence of the phosphorescence of  $2(\text{PF}_6)$  is shown in Figure 5. The emission intensity rapidly

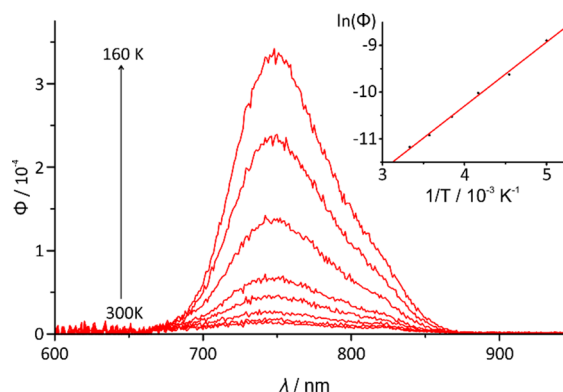


**Figure 5.** Emission quantum yield of  $2(\text{PF}_6)$  in fluid butyronitrile solution in the temperature range between 160 and 300 K (lower to upper). (inset) Plot of  $\ln(\phi)$  vs  $T^{-1}$  and the corresponding linear fit curve based on  $\ln(\phi) = \ln(k_r/k'_{nr}) + \Delta E'/R \cdot 1/T$  (see text for explanation).

increases upon lowering the temperature. This behavior is easily understood following the argumentation of van Houten and Watts<sup>2</sup> and later Meyer and co-workers.<sup>3</sup> The lifetime of the emissive  $^3\text{MLCT}$  state depends on the rates of radiative and nonradiative decay,  $k_r$  and  $k_{nr}$ . Additionally, irreversible thermal depopulation of the emissive  $^3\text{MLCT}$  states via  $^3\text{MC}$  states is a relevant nonradiative relaxation pathway in (polypyridine) ruthenium complexes. Because of the irreversibility of this process it can be accounted for by a third rate constant  $k'^0$  and an Arrhenius-like activation barrier  $\Delta E'$ . As the quantum yield is proportional to the lifetime of the emissive  $^3\text{MLCT}$  state and the rate constant for radiative decay,<sup>3</sup> the following relationship between  $\phi$  and  $T$  is obtained:

$$\phi = k_r / [k_r + k_{nr} + k'^0 \cdot \exp(-\Delta E'/RT)]$$

This equation gives a nonlinear relationship between  $\ln(\phi)$  and  $T^{-1}$ , as has been shown by Meyer and co-workers.<sup>3</sup> In the



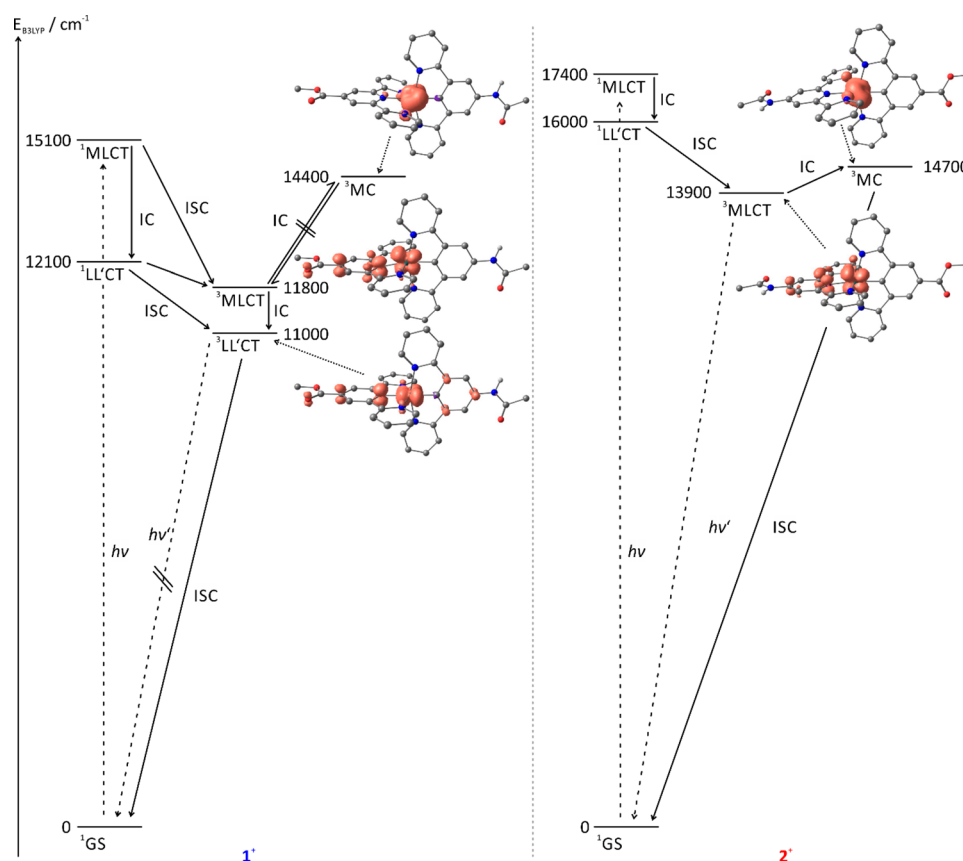


**Figure 6.** Jablonski diagrams and electronic spin densities of B3LYP-optimized triplet states of  $1^+$  and  $2^+$  (contour plots at 0.001 isosurface value).  $^1\text{MLCT}$  and  $^1\text{LL}'\text{CT}$  energies are obtained from TD-DFT calculations.  $^3\text{LL}'\text{CT}$  energy of  $1^+$  is obtained as energy difference from relaxed singlet and triplet geometries from DFT calculations. The  $^3\text{MLCT}$  energy of  $2^+$  is determined experimentally from the  $E_{00}$  emission at 77 K. Other triplet-state energies are obtained from B3LYP geometry optimizations.

present case, however (see inset of Figure 5), a linear relationship between  $\ln(\phi)$  and  $T^{-1}$  is obtained in the temperature range from 180 to 300 K. This can be explained assuming an efficient irreversible excited-state deactivation via low-lying  $^3\text{MC}$  states with a small barrier  $\Delta E'$ . With this assumption and at sufficiently high temperatures  $k_r$  and  $k_{nr}$  become negligible with respect to the exponential term associated with the rate constant  $k'^0$ , and  $\ln(\phi)$  indeed depends linearly on  $T^{-1}$ . From the linear regression, the thermal activation barrier for the  $^3\text{MLCT}$ – $^3\text{MC}$  surface crossing was determined to be  $\Delta E' = 11.4 \pm 0.5 \text{ kJ mol}^{-1}$ , which is just a fourth of the activation barrier found for  $[\text{Ru}(\text{bipy})_3]^{2+}$  ( $\Delta E' = 42.6 \text{ kJ mol}^{-1}$ ).<sup>3</sup>

To get a clearer picture of the involved excited-states, DFT calculations were performed. Using B3LYP or PBE0 as functional, one  $^3\text{MLCT}$  and one  $^3\text{MC}$  state could be localized for  $2^+$  (see Figure 6). The geometry of the  $^3\text{MLCT}$  state is essentially unaltered compared to the  $^1\text{GS}$  geometry. Because of the dipolar character of this excited state the electron-deficient ruthenium atom is slightly shifted by 3 pm toward the tpy ligand, while the dpb–tpy distance remains unaffected corresponding to a simple motion of ruthenium toward tpy in the fixed  $\text{N}_5\text{C}$  coordination sphere. A much stronger distortion with respect to the  $^1\text{GS}$  geometry is observed for the  $^3\text{MC}$  state since an antibonding metal orbital is occupied. The Ru– $\text{N}_{\text{tpy}}$  bond lengths are substantially elongated by  $\sim 20 \text{ pm}$ , and the peripheral pyridine rings of the tpy ligand are significantly twisted out of the plane of the central pyridine ring ( $\text{N}_{\text{central}}-$

C–C– $\text{N}_{\text{peripheral}}$  dihedral angles of  $\sim 9^\circ$ ). This nicely illustrates the dissociative character of this excited state that has previously been illustrated for a series of other bis(tridentate) ruthenium complexes<sup>23</sup> and that is responsible for the intrinsic photochemical reactivity of (polypyridine)ruthenium complexes.<sup>2,3,15</sup> The  $^3\text{MC}$ – $^3\text{MLCT}$  energy difference is determined as  $9.4 \text{ kJ mol}^{-1}$  and  $19.0 \text{ kJ mol}^{-1}$  (B3LYP and PBE0, respectively). Even though this energy difference is not directly related to the experimentally determined activation barrier  $\Delta E'$  of  $11.4 \text{ kJ mol}^{-1}$  it serves as a lower limit to the latter. The calculation using B3LYP as functional seems to give a good estimate to the  $^3\text{MLCT}$ – $^3\text{MC}$  energy difference, while PBE0 slightly overestimates this energy gap.

The  $^3\text{MLCT}$ – $^3\text{MC}$  energy difference calculated for  $2^+$  is significantly lower than that obtained for  $[\text{Ru}(\text{tpy}-\text{COOH})(\text{tpy}-\text{NH}_2)]^{2+}$  at a similar level of theory ( $26.8 \text{ kJ mol}^{-1}$ ).<sup>23</sup> This might be attributed to the fact that the strong  $\sigma$ -donating effect of dpb is partially diminished by the electron-accepting ester functionality in 4-position and the tpy ligand is a weaker electron acceptor. More importantly though, cyclometalation of the central phenyl ring only raises one of the three  $^3\text{MC}$  states that are responsible for the excited-state deactivation, while the other  $^3\text{MC}$  states remain low in energy and are efficiently populated at room temperature.<sup>20</sup>

In contrast to  $2(\text{PF}_6)$ ,  $1(\text{PF}_6)$  is nonemissive both at room temperature and at 77 K. This cannot be accounted for with a thermally activated deactivation mechanism of the excited state unless the activation barrier is close to zero. Hence another

mechanism must be responsible for the excited-state deactivation. As was shown above by TD-DFT calculations, symmetry-forbidden LL'/CT transitions exist at the low-energy edge of the absorption spectra of  $1(\text{PF}_6)$  and  $2(\text{PF}_6)$ . DFT calculations yielded a corresponding  $^3\text{LL}'\text{CT}$  excited state for  $1^+$  (see Figure 6) as well as  $^3\text{MLCT}$  and  $^3\text{MC}$  states with spin distributions similar to those of  $2^+$ . Remarkably, the complex core is essentially undistorted for the  $^3\text{LL}'\text{CT}$  state of  $1^+$  although the Ru–C<sub>dpb</sub> bond is slightly shortened by 3 pm and the central Ru–N<sub>tpy</sub> is elongated by 6 pm corresponding to the movement of ruthenium toward the dpb ligand within a fixed ligand framework. The  $^3\text{MLCT}$  state of  $1^+$ , however, is slightly distorted compared to the  $^1\text{GS}$  geometry of  $1^+$ : The central pyridine ring of the tpy ligand is somewhat shifted out of the plane perpendicular to the dpb ligand. Again, the ruthenium atom is closer to the tpy ligand because of the dipolar character of this excited state. The dissociative character of the  $^3\text{MC}$  state is also found for  $1^+$  with characteristically elongated Ru–N<sub>tpy</sub> bond lengths and a significant distortion of the peripheral pyridine rings away from the metal center. For emissive  $2^+$ , the  $^3\text{LL}'\text{CT}$  state could not be found. However, the corresponding  $^1\text{LL}'\text{CT}$  absorption is calculated to be  $\sim 3800\text{ cm}^{-1}$  ( $45\text{ kJ mol}^{-1}$ ) higher in energy as compared to that of  $1^+$  (Figure 6). Hence, we suggest that the  $^3\text{LL}'\text{CT}$  state does not play a significant role for the excited-state dynamics of  $2^+$ .

The order of these three states gives a straightforward explanation to the nonemissive behavior of  $1(\text{PF}_6)$ . The lowest-lying triplet excited state is the  $^3\text{LL}'\text{CT}$  state (Figure 6). Similar to the corresponding  $^1\text{LL}'\text{CT}$  transition in the absorption (vide supra), a  $^3\text{LL}'\text{CT} \rightarrow ^1\text{GS}$  emission process is symmetry-forbidden due to the orthogonality of the two ligands. The only available deactivation pathway is via radiationless ISC into the ground state followed by vibrational relaxation. The  $^3\text{MLCT}$  state that could evolve into the ground state radiatively is  $\sim 10\text{ kJ mol}^{-1}$  higher in energy than the  $^3\text{LL}'\text{CT}$  state and is only very inefficiently populated at room temperature.

Apart from the  $^3\text{LL}'\text{CT}$  state described by the strongly electron-accepting tpy and the electron-donating dpb ligand, the  $^3\text{MLCT}$ – $^3\text{MC}$  separation is calculated to be substantially larger in  $1^+$  than in  $2^+$  also due to the stronger push–pull substitution in  $1^+$  that stabilizes the tpy-based LUMO while at the same time destabilizing the metal-centered excited states.

In summary, the introduction of a carbon atom in the coordination sphere of ruthenium indeed increases the  $^3\text{MLCT}$ – $^3\text{MC}$  energy gap sufficiently to render  $[\text{Ru}(\text{dpb})(\text{tpy})]^+$  and  $2^+$  emissive at room temperature, while  $[\text{Ru}(\text{tpy})_2]^{2+}$  is silent. This effect is reinforced by attaching additional donor and acceptor functionalities in the ligand periphery that further increase this  $^3\text{MLCT}$ – $^3\text{MC}$  energy gap. Unfortunately, this push–pull approach suffers from the concomitant formation of a very low-lying  $^3\text{LL}'\text{CT}$  dark state when the donor–acceptor substitution becomes too strong.

**Electrochemical Properties of  $1(\text{PF}_6)$  and  $2(\text{PF}_6)$ .** The spatial orientation and symmetry of the frontier orbitals were further experimentally probed by electrochemical and EPR experiments. The cyclic voltammograms of the complexes  $1(\text{PF}_6)$  and  $2(\text{PF}_6)$  in acetonitrile using  $0.1\text{ M } [^n\text{Bu}_4\text{N}][\text{PF}_6]$  as supporting electrolyte are shown in Figure 7 and Supporting Information Figures S28 and S29. Both complexes show a reversible oxidation wave at a potential of  $0.02\text{ V}$  vs FcH/FcH $^+$  ( $1(\text{PF}_6)$ ) and  $0.14\text{ V}$  vs FcH/FcH $^+$  ( $2(\text{PF}_6)$ ); see Table 3). Additionally, an irreversible oxidation occurs for both complexes at higher potentials. The first oxidation is ascribed

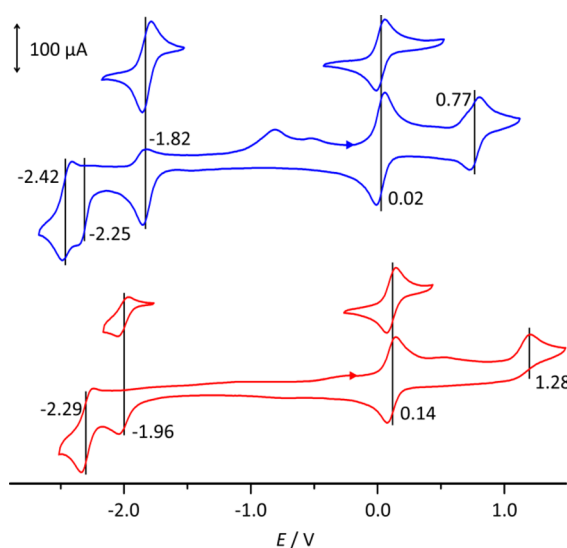


**Figure 7.** Cyclic voltammograms of  $1(\text{PF}_6)$  (upper, blue) and  $2(\text{PF}_6)$  (lower, red) ( $c = 1\text{ mM}$ ) in  $0.1\text{ M}$  acetonitrile solution of  $[^n\text{Bu}_4\text{N}][\text{PF}_6]$  at  $298\text{ K}$ . Potentials are referenced against the FcH/FcH $^+$  couple ( $E_{1/2} = 0.40\text{ V}$  vs SCE).

**Table 3. Electrochemical Data of  $1^+$ ,  $2^+$ , and  $[(\text{dpb})\text{Ru}(\text{tpy})]^+$  ( $1\text{ mM}$ ) in  $0.1\text{ M } [^n\text{Bu}_4\text{N}][\text{PF}_6]$  Electrolyte Solution<sup>a</sup>**

	$E_{\text{ox},1}$ , V	$E_{\text{ox},2}$ , V	$E_{\text{red},1}$ , V	$E_{\text{red},2}$ , V	$E_{\text{red},3}$ , V
$1^+$	0.02	0.77	−1.82	−2.25	−2.42
$2^+$	0.14	1.28	−1.96	−2.29	
$[\text{Ru}(\text{dpb})(\text{tpy})]^{+b}$	0.12	1.36	−1.95		

<sup>a</sup>Potentials are given in volts and referenced against the FcH/FcH $^+$  couple ( $E_{1/2} = 0.40\text{ V}$  vs SCE). <sup>b</sup>Values taken from the literature.<sup>20</sup>

to the Ru $^{\text{II}}$ /Ru $^{\text{III}}$  redox couple with contributions from the highest occupied  $\pi$ -orbital of the cyclometalating ligand (HOMO of  $1^+$  and  $2^+$ , Supporting Information Figure S22) as evidenced from Mulliken spin population analysis and spin density plots of  $1^{2+}$  and  $2^{2+}$  (Supporting Information Figures S30 and S31). The origin of the second oxidation process, however, is less clear. DFT calculations suggest a mixed oxidation of the metal center and cyclometalating ligand as primary step (see Supporting Information Figure S32), but the irreversibility of this process points to follow-up reactions, so that the final oxidation product remains unidentified. The Ru $^{\text{II}}$ /Ru $^{\text{III}}$  oxidation is shifted by  $0.6$ – $0.7\text{ V}$  to lower potentials compared to bis(terpyridine)ruthenium complexes bearing the same functional groups.<sup>89</sup> This illustrates the strong  $\sigma$ -donor character of the cyclometalating ligand that greatly increases the electron density at the metal center. The NHCome group at the cyclometalating ligand in  $1(\text{PF}_6)$  indeed leads to a further shift of the ruthenium-based oxidation by  $0.10\text{ V}$  to lower values as compared to  $[\text{Ru}(\text{tpy})(\text{dpb})]^+$ , while the COOEt substitution of the dpb ligand in  $2(\text{PF}_6)$  slightly increases this redox potential by  $0.02\text{ V}$ .

In the range accessible for reduction (up to  $-2.5\text{ V}$  vs FcH/FcH $^+$ ) three quasireversible or irreversible redox waves are found for  $1(\text{PF}_6)$ , while for  $2(\text{PF}_6)$  only two reduction waves are detected. These are assigned to ligand-centered reductions with the first one centered on the tpy ligand. The localization of this redox process on the ligand leads to a much stronger dependence of the corresponding redox potential on the tpy

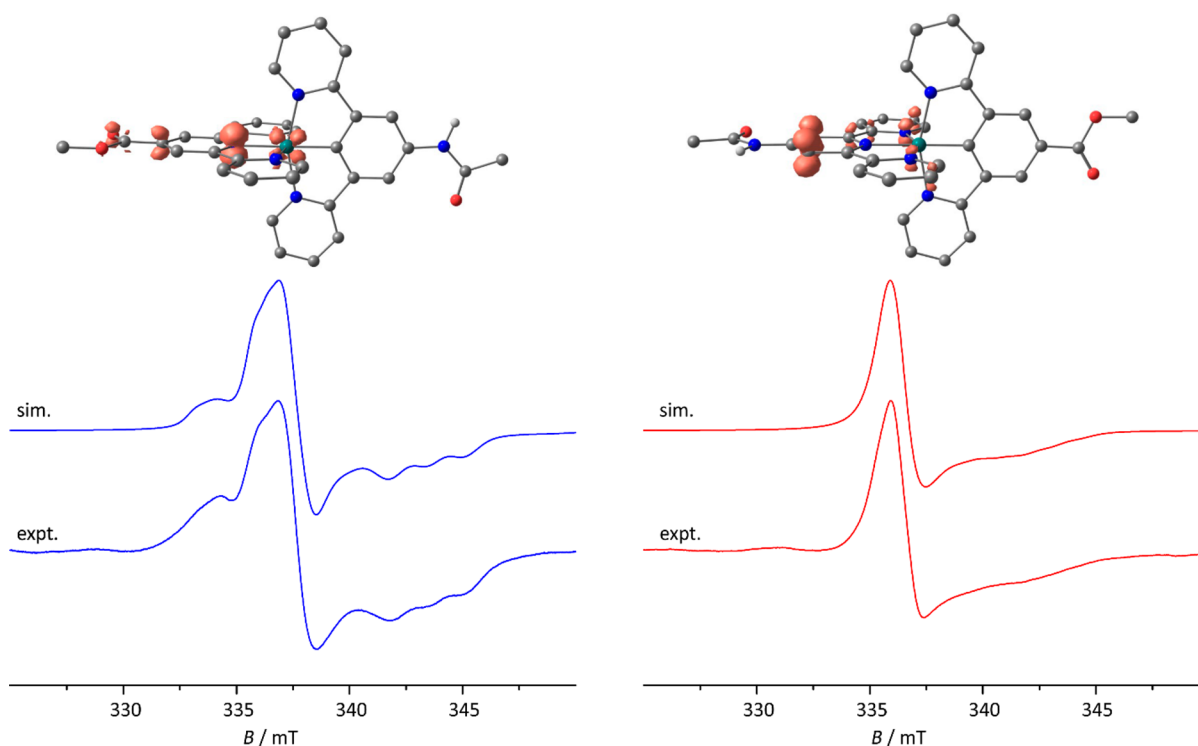


**Figure 8.** DFT-calculated spin densities (B3LYP/def2-TZVP/DKH/COSMO(acetonitrile), contour value: 0.01) of **1** (blue, left) and **2** (red, right) and experimental X-band EPR spectra ( $\nu \approx 9.4$  GHz) obtained from frozen acetonitrile solutions of **1** and **2** ( $c = 5$  mM) generated in situ with  $\text{Co}(\text{Cp}^*)_2$ . CH hydrogen atoms are omitted for clarity.

**Table 4. Electron Paramagnetic Resonance Spectroscopic Parameters of  $1^{2+}$ ,  $2^{2+}$ , **1**, and **2** Determined Experimentally (in Frozen Acetonitrile Solution at 77 K) and Theoretically (B3LYP, def2-TZVP, DKH, COSMO(Acetonitrile))<sup>a</sup>**

		$g_{1,2,3}$	$g_{\text{iso}}^b$	$\Delta g^c$	$A_{1,2,3}({}^{99,101}\text{Ru})/\text{MHz}$ ( $A_{\text{iso}}/\text{MHz}$ ) <sup>d</sup>	$A_{1,2,3}({}^{14}\text{N},1)/\text{MHz}$ ( $A_{\text{iso}}/\text{MHz}$ ) <sup>e</sup>	$A_{1,2,3}({}^{14}\text{N},2)/\text{MHz}$ ( $A_{\text{iso}}/\text{MHz}$ ) <sup>f</sup>
$1^{2+}$	expt.	2.238, 2.176, 2.045	2.153	0.193	84, 140, 112 (112)		
	calcd.	2.312, 2.172, 2.020	2.168	0.292	88, 162, 91 (114)		
$2^{2+}$	calcd.	2.586, 2.427, 2.021	2.345	0.565	94, 187, 103 (128)		
<b>1</b>	expt.	2.0008, 1.9921, 1.9594,	1.9841	0.0414	28, 36, 73 (46)	17, 10, 45 (24)	
	calcd.	2.0147, 2.0001, 1.9414	1.9854	0.0733	41, 41, 63 (48)	6, 5, 48 (19) <sup>e</sup>	
<b>2</b>	expt.	2.0008, 1.9998, 1.9685,	1.9897	0.0323	8, 8, 8 (8)	3, 7, 31 (14)	3, 6, 39 (16)
	calcd.	2.0034, 2.0009, 1.9963	2.0002	0.0071	11, 8, 6 (8)	0, 0, 29 (10) <sup>f</sup>	2, 1, 46 (16) <sup>f</sup>

<sup>a</sup>For theoretically determined hyperfine coupling constants  $A({}^{14}\text{N})$ , only the largest values ( $A_{\text{iso}}({}^{14}\text{N}) > 10$  MHz) are given. <sup>b</sup> $g_{\text{iso}} = (g_1 + g_2 + g_3)/3$ . <sup>c</sup> $\Delta g = g_1 - g_3$ . <sup>d</sup> $A_{\text{iso}} = (A_1 + A_2 + A_3)/3$ . <sup>e</sup>Hyperfine coupling to the central pyridine nitrogen atom of the tpy ligand. <sup>f</sup>Hyperfine coupling to one peripheral pyridine nitrogen atom of the tpy ligand.

functional groups than in the case of the metal-centered oxidation. Changing the functional group on the tpy ligand from ethyl carboxy (**1**(PF<sub>6</sub>)) to N-acetyl amino (**2**(PF<sub>6</sub>)) shifts the first reduction potential by 0.14 V to more negative values (cf. MO diagrams in Supporting Information Figure S22).

The oxidation steps in the potential range of  $-1.0$  to  $-0.5$  V for **1**(PF<sub>6</sub>) following the irreversible reduction processes are similar to those observed for bis(terpyridine)ruthenium(II) complexes bearing amide functional groups and might be associated with reduction of the NH proton at the terpyridine moiety to hydrogen.<sup>88</sup>

**Electron Paramagnetic Resonance Studies on Redox Products.** As evidenced from the cyclic voltammograms, both complexes can be oxidized to  $1^{2+}$  and  $2^{2+}$  using tris(4-bromophenyl)aminium hexachloridoantimonate as oxidant (0.67 V vs FcH/FcH<sup>+</sup> in acetonitrile, 0.70 V vs FcH/FcH<sup>+</sup> in dichloromethane) and reduced to **1** and **2** using decamethylcobaltocene  $\text{Co}(\text{Cp}^*)_2$  as reductant ( $-1.91$  V vs FcH/FcH<sup>+</sup> in

acetonitrile,  $-1.94$  V vs FcH/FcH<sup>+</sup> in dichloromethane). To study the nature of the oxidized and reduced species EPR spectra were recorded. Solutions were prepared at a 5 mM sample concentration with 0.9 equiv of the respective oxidant or reductant. While both complexes show EPR signals at 77 K after being reduced to **1** and **2** (see Figure 8), only  $1^{2+}$  is detected via X-band EPR spectroscopy at 77 K (see Supporting Information Figure S30). At room temperature in dichloromethane solution all samples were EPR-silent.

The EPR signal of  $1^{2+}$  (Supporting Information Figure S30; Table 4) is highly anisotropic ( $\Delta g = 0.193$ ) and very broad indicating a strong contribution of metal d-orbitals to the spin density. Hyperfine couplings are not resolved in the spectrum, but a good estimate of the coupling constants of the electronic spin to the nuclear spin of ruthenium ( ${}^{99}\text{Ru}$  and  ${}^{101}\text{Ru}$ :  $I = 5/2$ , natural abundance: 30%) is obtained by simulations. This coupling ( $A_{1,2,3}({}^{99,101}\text{Ru}) = 84, 140, 112$  MHz) is large underlining the strong metal contribution to the radical



character. Theoretical  $g$  tensor and hyperfine coupling parameter calculations on the DFT wave function generated at the B3LYP/def2-TZVP/DKH/COSMO(acetonitrile) level of theory are in excellent agreement with the experimentally determined quantities.  $2^{2+}$  is EPR-silent at 77 K and at room temperature, but theory predicts similar  $g$  values and hyperfine coupling constants to ruthenium as observed for  $1^{2+}$  (Table 4).

EPR spectra of **1** and **2** obtained upon reduction of the respective cations (Figure 8) are substantially sharper and better-resolved. The  $g$ -value anisotropy ( $\Delta g = 0.0414$  for **1**,  $\Delta g = 0.0323$  for **2**) is reduced by a factor of 5 compared to the EPR spectrum of  $1^{2+}$  indicating a significantly stronger ligand-based character of the radical. Hyperfine couplings to the ruthenium center and one or two nitrogen atoms for **1** and **2**, respectively, are well-resolved and were determined by simulations of the experimental spectra (see Table 4). The observed spectra are easily explained with the reduction occurring at the tpy ligand (cf. MO diagram in Supporting Information Figure S22). Spin density calculations for the neutral complexes **1** and **2** explain the occurrence of a single nitrogen hyperfine coupling in **1**, while **2** shows couplings to two chemically different nitrogen atoms. The unpaired electron in **1** is essentially localized at the central pyridine ring of the tpy-COOEt ligand with its highest coefficient at the nitrogen  $p-\pi$  orbital leading to strong anisotropic superhyperfine coupling to that nitrogen nucleus, which leads to a distinctive triplet splitting of the  $g_3$  signal (Table 4). In **2**, however, the unpaired electron is delocalized over the two peripheral pyridine rings of tpy-NHCOMe in **2** with a nodal plane orthogonal to the ligand plane containing the metal center. Consequently, the EPR signal is much less well-resolved especially because the superhyperfine coupling constants to the two peripheral nitrogen nuclei differ (Figure 8). This renders unambiguous determination of all superhyperfine and hyperfine coupling constants (except  $A_3$  of the two nitrogen atoms) in **2** rather challenging, so these are estimated from line width and broadening (Table 4). The electron-donating effect of the *N*-acetyl amino group attached to the terpyridine ligand in **2** increases the electron density at the central pyridine ring and consequently varies the character and symmetry of the singly occupied molecular orbital (SOMO). It resembles the LUMO+1 of  $2^+$  (see Supporting Information, Figure S22), whereas the SOMO of **1** is similar to the LUMO of  $1^+$  (DFT: B3LYP/def2-TZVP/DKH/COSMO(acetonitrile)). The superhyperfine coupling constants to nitrogen are smaller for **2** than for **1** because of this spin delocalization over two pyridine rings (spin dilution). Furthermore, the Ru-N<sub>terminal</sub> distances are larger than the Ru-N<sub>central</sub> distances leading to a reduction of the spin-orbit coupling affecting the unpaired electron and consequently a lowering of the ruthenium hyperfine coupling in **2** and the  $g$ -value anisotropy. Since the amide bridge is rigid and rotation about the N<sub>amide</sub>-C<sub>terpyridine</sub> bond is slow at the EPR time scale (especially in rigid matrix) the spin density is asymmetric, which explains the slight differences in coupling constants to the two peripheral coordinating nitrogen atoms.

## CONCLUSION

The key properties of the cyclometalated bis(tridentate)-ruthenium(II) complexes [Ru(dpb-NHCOMe)(tpy-COOEt)]<sup>+</sup> **1**<sup>+</sup> and [Ru(dpb-COOEt)(tpy-NHCOMe)]<sup>+</sup> **2**<sup>+</sup> were revealed by introduction of electron-donating and electron-accepting functional groups in the ligand periphery of [Ru(tpy)(dpb)]<sup>+</sup> complexes. For both isomers the visible-

range absorption spectrum is dominated by MLCT transitions to the electron-poor terpyridine (Ru → tpy) as well as the electron-rich dipyriddyphenyl ligand (Ru → dpb), which was evidenced by a combined DFT and rR spectroscopic approach. Theoretical calculations additionally suggest a symmetry-forbidden and hence experimentally undetected <sup>1</sup>LL'/CT as lowest spin-allowed optical transition in the red spectral range. The first oxidation is metal-centered in both complexes **1**(PF<sub>6</sub>) and **2**(PF<sub>6</sub>) with substantial contribution from the central phenyl ring of the dpb ligand, which corresponds to the ground state HOMO in both cases. The reduction is tpy-centered with the unpaired electron localized on the central pyridine ring in **1**(PF<sub>6</sub>), while it is delocalized over both peripheral pyridine rings of tpy in **2**(PF<sub>6</sub>). Reduction of  $2^+$  to **2** reverses the order of the unoccupied orbitals LUMO and LUMO+1 as they are close in energy in  $2^+$  resulting in a characteristic fingerprint in the respective EPR spectra.

While both isomers have similar absorption and electrochemical characteristics they differ fundamentally in their excited-state and emission behavior. **1**(PF<sub>6</sub>) is nonemissive both at room temperature and at 77 K, while **2**(PF<sub>6</sub>) shows a very weak emission at room temperature and a much stronger luminescence at 77 K. Temperature-dependent emission spectroscopy revealed that a very low activation barrier of ca. 11 kJ mol<sup>-1</sup> for the thermal deactivation of the emissive <sup>3</sup>MLCT state via a <sup>3</sup>MC state is responsible for the measurable, but low, emission quantum yield at room temperature.

For **1**(PF<sub>6</sub>) a completely different picture emerges. The stronger push-pull substitution substantially raises the <sup>3</sup>MC states in energy, which should lead to an increase in emission intensity compared to **2**(PF<sub>6</sub>). Indeed, DFT calculations find the <sup>3</sup>MC states high in energy. Hence, these do not contribute to the efficient excited-state deactivation in **1**(PF<sub>6</sub>). Instead, an unrecognized <sup>3</sup>LL'/CT state was found to be lower in energy than the <sup>3</sup>MLCT state in **1**(PF<sub>6</sub>). The <sup>3</sup>LL'/CT state undergoes radiationless deactivation as the radiative relaxation is symmetry-forbidden (dark state).

In essence, cyclometalation using dpb ligands shifts the <sup>3</sup>MC state above the <sup>3</sup>MLCT for  $1^+$  compared to [Ru(tpy)<sub>2</sub>]<sup>2+</sup> thus reducing the emission quenching via thermal depopulation through <sup>3</sup>MC states. At the same time it generates low-lying <sup>3</sup>LL'/CT states that evolve radiationless into the ground state due to the symmetry-forbidden character of the transition imposed by the orthogonality of the ligands. This quenching via a <sup>3</sup>LL'/CT state is dominant for push-pull substituted cyclometalated bis(tridentate)ruthenium(II) complexes of ruthenium, and the underlying mechanisms should be transferable to iridium(III) as well,<sup>26</sup> where similar nonemissive behavior has been observed.

Despite the fact that [Ru(dpb)(tpy)]<sup>+</sup> complexes are nonemissive or only weakly emissive at room temperature, the charge-separation at the Franck-Condon point and the high reducing potential of the excited state, both induced by the cyclometalation, render these complexes promising candidates as sensitizers in photoredox applications.

## ASSOCIATED CONTENT

### Supporting Information

Experimental procedure for the synthesis of **L3**; characterization of **3**(PF<sub>6</sub>); discussion of the synthetic procedures of **L1**, **L2** and **L3**; FD mass spectra, <sup>1</sup>H and <sup>13</sup>C NMR spectra of **L1**, **L2** and **L3**; ESI mass spectra, <sup>1</sup>H, <sup>13</sup>C, COSY, HSQC, and HMBC NMR spectra of **1**(PF<sub>6</sub>) and **2**(PF<sub>6</sub>); <sup>1</sup>H and <sup>13</sup>C NMR

spectra of  $3(\text{PF}_6)$ ; solid-state IR spectra and room-temperature emission spectra of  $1(\text{PF}_6)$  and  $2(\text{PF}_6)$ ; decomposition of the absorption spectra of  $1(\text{PF}_6)$  and  $2(\text{PF}_6)$ ; MO diagrams of  $1(\text{PF}_6)$  and  $2(\text{PF}_6)$ ; TD-DFT excitations of  $1(\text{PF}_6)$  and  $2(\text{PF}_6)$  with difference density plots; cyclic and square wave voltammograms of  $1(\text{PF}_6)$  and  $2(\text{PF}_6)$ ; EPR spectrum of  $1^{2+}$ ; DFT spin-density plots of  $2^{2+}$ ,  $2^{3+}$  and  $3^{3+}$ ; Cartesian coordinates of geometry-optimized  $1^+$ ,  $1^+$ ,  $2^{2+}$ ,  $1^{2+}$ ,  $2^{2+}$ ,  $1^{3+}$ ,  $2^{3+}$ ,  $1$ , and  $2$ , as well as of the triplet states  $^3\text{LL}'\text{CT}$ ,  $^3\text{MLCT}$ , and  $^3\text{MC}$  of  $1^+$  and  $^3\text{MLCT}$  and  $^3\text{MC}$  of  $2^+$ . The Supporting Information is available free of charge on the ACS Publications website at DOI: 10.1021/acs.inorgchem.5b01151.

## AUTHOR INFORMATION

### Corresponding Author

\*Fax: +49613127277. E-mail: [katja.heinze@uni-mainz.de](mailto:katja.heinze@uni-mainz.de).

### Author Contributions

The manuscript was written through contributions of all authors; rR spectra were measured by E.E. and W.W.S. All authors have given approval to the final version of the manuscript.

### Notes

The authors declare no competing financial interest.

## ACKNOWLEDGMENTS

Parts of this research were conducted using the supercomputer Mogon and advisory services offered by Johannes Gutenberg Univ. Mainz ([www.hpc.uni-mainz.de](http://www.hpc.uni-mainz.de)), which is a member of the AHRP and the Gauss Alliance e.V. This work was financially supported by the Deutsche Forschungsgemeinschaft (GSC 266, Materials Science in Mainz, scholarship for C.K.).

## REFERENCES

- Brandt, W. W.; Dwyer, F. P.; Gyrfas, E. D. *Chem. Rev.* **1954**, *54*, 959–1017.
- van Houten, J.; Watts, R. J. *Inorg. Chem.* **1978**, *17*, 3381–3385.
- Durham, B.; Caspar, J. V.; Nagle, J. K.; Meyer, T. J. *J. Am. Chem. Soc.* **1982**, *104*, 4803–4810.
- Kalyanasundaram, K. *Coord. Chem. Rev.* **1982**, *46*, 159–244.
- Caspar, J. V.; Meyer, T. J. *J. Am. Chem. Soc.* **1983**, *105*, 5583–5590.
- Meyer, T. J. *Pure Appl. Chem.* **1986**, *58*, 1193–1206.
- Kasha, M. *Discuss. Faraday Soc.* **1950**, *9*, 14–19.
- Demas, J. N.; Taylor, D. G. *Inorg. Chem.* **1979**, *18*, 3177–3179.
- Yoon, S.; Kukura, P.; Stuart, C. M.; Mathies, R. A. *Mol. Phys.* **2006**, *104*, 1275–1282.
- Lytle, F. E.; Hercules, D. M. *J. Am. Chem. Soc.* **1969**, *91*, 253–257.
- Suzuki, K.; Kobayashi, A.; Kaneko, S.; Takehira, K.; Yoshihara, T.; Ishida, H.; Shiina, Y.; Oishi, S.; Tobita, S. *Phys. Chem. Chem. Phys.* **2009**, *11*, 9850–9860.
- Lashgari, K.; Kritikos, M.; Norrestam, R.; Norrby, T. *Acta Crystallogr., Sect. C: Cryst. Struct. Commun.* **1999**, *55*, 64–67.
- Stone, M. L.; Crosby, G. A. *Chem. Phys. Lett.* **1981**, *79*, 169–173.
- Winkler, J. R.; Netzels, T. L.; Creutz, C.; Sutin, N. *J. Am. Chem. Soc.* **1987**, *109*, 2381–2392.
- Maestri, M.; Armaroli, N.; Balzani, V.; Constable, E. C.; Thompson, A. M. W. *Inorg. Chem.* **1995**, *34*, 2759–2767.
- Amini, A.; Harriman, A.; Mayeux, A. *Phys. Chem. Chem. Phys.* **2004**, *6*, 1157–1164.
- Sun, P.; Krishnan, A.; Yadav, A.; Singh, S.; MacDonnell, F. M.; Armstrong, D. W. *Inorg. Chem.* **2007**, *46*, 10312–10320.
- Gong, L.; Mulcahy, S. P.; Harms, K.; Meggers, E. *J. Am. Chem. Soc.* **2009**, *131*, 9602–9603.
- Meggers, E. *Chem. - Eur. J.* **2010**, *16*, 752–758.
- Wadman, S. H.; Lutz, M.; Tooke, D. M.; Spek, A. L.; Hartl, F.; Havenith, R. W. A.; van Klink, G. P. M.; van Koten, G. *Inorg. Chem.* **2009**, *48*, 1887–1900.
- Heinze, K.; Hempel, K.; Beckmann, M. *Eur. J. Inorg. Chem.* **2006**, *2006*, 2040–2050.
- Breivogel, A.; Förster, C.; Heinze, K. *Inorg. Chem.* **2010**, *49*, 7052–7056.
- Breivogel, A.; Meister, M.; Förster, C.; Laquai, F.; Heinze, K. *Chem. - Eur. J.* **2013**, *19*, 13745–13760.
- Abrahamsson, M.; Jäger, M.; Österman, T.; Eriksson, L.; Persson, P.; Becker, H.-C.; Johansson, O.; Hammarström, L. *J. Am. Chem. Soc.* **2006**, *128*, 12616–12617.
- Schramm, F.; Meded, V.; Fliegl, H.; Fink, K.; Fuhr, O.; Qu, Z.; Kloppe, W.; Finn, S.; Keyes, T. E.; Ruben, M. *Inorg. Chem.* **2009**, *48*, 5677–5684.
- Wilkinson, A. J.; Puschmann, H.; Howard, J. A. K.; Foster, C. E.; Williams, J. A. G. *Inorg. Chem.* **2006**, *45*, 8685–8699.
- Breivogel, A.; Kreitner, C.; Heinze, K. *Eur. J. Inorg. Chem.* **2014**, *2014*, 5468–5490.
- Bolink, H. J.; Cappelli, L.; Coronado, E.; Gaviña, P. *Inorg. Chem.* **2005**, *44*, 5966–5968.
- Heinze, K.; Hempel, K.; Breivogel, A. *Z. Anorg. Allg. Chem.* **2009**, *635*, 2541–2549.
- Englman, R.; Jortner, J. *Mol. Phys.* **1970**, *18*, 145–164.
- Caspar, J. V.; Kober, E. M.; Sullivan, B. P.; Meyer, T. J. *J. Am. Chem. Soc.* **1982**, *104*, 630–632.
- Caspar, J. V.; Meyer, T. J. *J. Phys. Chem.* **1983**, *87*, 952–957.
- Parada, G. A.; Fredin, L. A.; Santoni, M.-P.; Jäger, M.; Lomoth, R.; Hammarström, L.; Johansson, O.; Persson, P.; Ott, S. *Inorg. Chem.* **2013**, *52*, 5128–5137.
- Constable, E. C.; Holmes, J. M. *J. Organomet. Chem.* **1986**, *301*, 203–208.
- Beley, M.; Collin, J. P.; Sauvage, J. P. *Inorg. Chem.* **1993**, *32*, 4539–4543.
- King, K. A.; Spellane, P. J.; Watts, R. J. *J. Am. Chem. Soc.* **1985**, *107*, 1431–1432.
- King, K. A.; Watts, R. J. *J. Am. Chem. Soc.* **1987**, *109*, 1589–1590.
- Lamansky, S.; Djurovich, P.; Murphy, D.; Abdel-Razzaq, F.; Lee, H.-E.; Adachi, C.; Burrows, P. E.; Forrest, S. R.; Thompson, M. E. *J. Am. Chem. Soc.* **2001**, *123*, 4304–4312.
- Lowry, M. S.; Bernhard, S. *Chem. - Eur. J.* **2006**, *12*, 7970–7977.
- Constable, E. C.; Housecroft, C. E. *Polyhedron* **1990**, *9*, 1939–1947.
- Bomben, P. G.; Robson, K. C. D.; Sedach, P. A.; Berlinguette, C. P. *Inorg. Chem.* **2009**, *48*, 9631–9643.
- Bomben, P. G.; Koivisto, B. D.; Berlinguette, C. P. *Inorg. Chem.* **2010**, *49*, 4960–4971.
- Chirdon, D. N.; McCusker, C. E.; Castellano, F. N.; Bernhard, S. *Inorg. Chem.* **2013**, *52*, 8795–8804.
- Colombo, M. G.; Hauser, A.; Guedel, H. U. *Inorg. Chem.* **1993**, *32*, 3088–3092.
- Hay, P. J. *J. Phys. Chem. A* **2002**, *106*, 1634–1641.
- Flamigni, L.; Barbieri, A.; Sabatini, C.; Ventura, B.; Barigelletti, F. *Top. Curr. Chem.* **2007**, *281*, 143–203.
- Wadman, S. H.; Kroon, J. M.; Bakker, K.; Lutz, M.; Spek, A. L.; van Klink, G. P. M.; van Koten, G. *Chem. Commun.* **2007**, 1907–1909.
- Wadman, S. H.; Kroon, J. M.; Bakker, K.; Havenith, R. W. A.; van Klink, G. P. M.; van Koten, G. *Organometallics* **2010**, *29*, 1569–1579.
- Bruno, N. C.; Tudge, M. T.; Buchwald, S. L. *Chem. Sci.* **2013**, *4*, 916–920.
- Chavarot, M.; Pikramenou, Z. *Tetrahedron Lett.* **1999**, *40*, 6865–6868.
- Constable, E. C.; Ward, M. D. *J. Chem. Soc., Dalton Trans.* **1990**, 1405–1409.
- Fallahpour, R.-A. *Eur. J. Inorg. Chem.* **1998**, 1205–1207.
- Suda, K.; Akagi, K. *Macromolecules* **2011**, *44*, 9473–9488.

- (54) Fulmer, G. R.; Miller, A. J. M.; Sherden, N. H.; Gottlieb, H. E.; Nudelman, A.; Stoltz, B. M.; Bercaw, J. E.; Goldberg, K. I. *Organometallics* **2010**, *29*, 2176–2179.
- (55) Connelly, N. G.; Geiger, W. E. *Chem. Rev.* **1996**, *96*, 877–910.
- (56) Stoll, S.; Schweiger, A. J. *Magn. Reson.* **2006**, *178*, 42–55.
- (57) Neese, F. *WIREs Comput. Mol. Sci.* **2012**, *2*, 73–78.
- (58) Neese, F.; Wennmohs, F.; Hansen, A.; Becker, U. *Chem. Phys.* **2009**, *356*, 98–109.
- (59) Izsák, R.; Neese, F. *J. Chem. Phys.* **2011**, *135*, 144105.
- (60) Perdew, J. P.; Burke, K.; Ernzerhof, M. *Phys. Rev. Lett.* **1996**, *77*, 3865–3868.
- (61) Perdew, J. P.; Burke, K.; Ernzerhof, M. *Phys. Rev. Lett.* **1997**, *78*, 1396.
- (62) Schäfer, A.; Horn, H.; Ahlrichs, R. *J. Chem. Phys.* **1992**, *97*, 2571–2577.
- (63) Schäfer, A.; Huber, C.; Ahlrichs, R. *J. Chem. Phys.* **1994**, *100*, 5829–5835.
- (64) Andrae, D.; Häußermann, U.; Dolg, M.; Stoll, H.; Preuß, H. *Theoret. Chim. Acta* **1990**, *77*, 123–141.
- (65) Weigend, F.; Ahlrichs, R. *Phys. Chem. Chem. Phys.* **2005**, *7*, 3297–3305.
- (66) Sinnecker, S.; Rajendran, A.; Klamt, A.; Diedenhofen, M.; Neese, F. *J. Phys. Chem. A* **2006**, *110*, 2235–2245.
- (67) Vlček, A.; Zláliš, S. *Coord. Chem. Rev.* **2007**, *251*, 258–287.
- (68) Magyar, R. J.; Tretiak, S. *J. Chem. Theory Comput.* **2007**, *3*, 976–987.
- (69) Tao, J.; Perdew, J. P.; Staroverov, V. N.; Scuseria, G. E. *Phys. Rev. Lett.* **2003**, *91*, 146401.
- (70) Becke, A. D. *J. Chem. Phys.* **1993**, *98*, 5648–5652.
- (71) Adamo, C.; Barone, V. *J. Chem. Phys.* **1999**, *110*, 6158–6170.
- (72) Yanai, T.; Tew, D. P.; Handy, N. C. *Chem. Phys. Lett.* **2004**, *393*, 51–57.
- (73) Douglas, M.; Kroll, N. M. *Ann. Phys.* **1974**, *82*, 89–155.
- (74) Hess, B. *Phys. Rev. A: At., Mol., Opt. Phys.* **1985**, *32*, 756–763.
- (75) Hess, B. *Phys. Rev. A: At., Mol., Opt. Phys.* **1986**, *33*, 3742–3748.
- (76) Jansen, G.; Hess, B. *Phys. Rev. A: At., Mol., Opt. Phys.* **1989**, *39*, 6016–6017.
- (77) Pantazis, D. A.; Chen, X.-Y.; Landis, C. R.; Neese, F. *J. Chem. Theory Comput.* **2008**, *4*, 908–919.
- (78) Petrenko, T.; Neese, F. *J. Chem. Phys.* **2007**, *127*, 164319.
- (79) Petrenko, T.; Neese, F. *J. Chem. Phys.* **2012**, *137*, 234107.
- (80) Beley, M.; Collin, J. P.; Louis, R.; Metz, B.; Sauvage, J. P. *J. Am. Chem. Soc.* **1991**, *113*, 8521–8522.
- (81) Koivisto, B. D.; Robson, K. C. D.; Berlinguette, C. P. *Inorg. Chem.* **2009**, *48*, 9644–9652.
- (82) Dreuw, A.; Weisman, J. L.; Head-Gordon, M. *J. Chem. Phys.* **2003**, *119*, 2943.
- (83) Tozer, D. J. *J. Chem. Phys.* **2003**, *119*, 12697–12699.
- (84) Heinze, K.; Hempel, K.; Tschierlei, S.; Schmitt, M.; Popp, J.; Rau, S. *Eur. J. Inorg. Chem.* **2009**, *2009*, 3119–3126.
- (85) Preiß, J.; Jäger, M.; Rau, S.; Dietzek, B.; Popp, J.; Martínez, T.; Presselt, M. *ChemPhysChem* **2015**, *16*, 1395–1404.
- (86) Egidi, F.; Bloino, J.; Cappelli, C.; Barone, V. *J. Chem. Theory Comput.* **2014**, *10*, 346–363.
- (87) Heller, E. J.; Sundberg, R.; Tannor, D. *J. Phys. Chem.* **1982**, *86*, 1822–1833.
- (88) Kreitner, C.; Grabolle, M.; Resch-Genger, U.; Heinze, K. *Inorg. Chem.* **2014**, *53*, 12947–12961.
- (89) Breivogel, A.; Hempel, K.; Heinze, K. *Inorg. Chim. Acta* **2011**, *374*, 152–162.



## Correction to “Understanding the Excited State Behavior of Cyclometalated Bis(tridentate)ruthenium(II) Complexes: A Combined Experimental and Theoretical Study”

Christoph Kreitner, Elisa Erdmann, Wolfram W. Seidel, and Katja Heinze\*

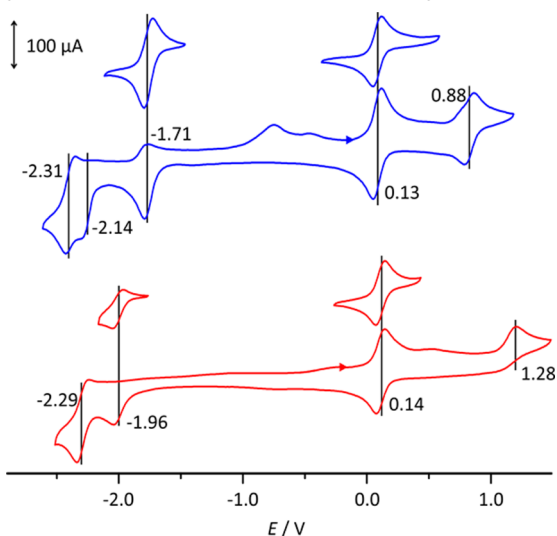
*Inorg. Chem.* **2015**, *54* (23), 11088–11104. DOI: [10.1021/acs.inorgchem.5b01151](https://doi.org/10.1021/acs.inorgchem.5b01151)

Pages 11100 and 11101. The electrochemical data of compound **1**<sup>+</sup> were erroneously referenced against the decamethylferrocene/decamethylferrocenium couple in dichloromethane instead of acetonitrile. This results in erroneously reported redox potentials for **1**<sup>+</sup> by 0.11 V.<sup>1</sup>

The corrected first row of Table 3 should read as follows:

	$E_{\text{ox},1}$ , V	$E_{\text{ox},2}$ , V	$E_{\text{red},1}$ , V	$E_{\text{red},2}$ , V	$E_{\text{red},3}$ , V
<b>1</b> <sup>+</sup>	0.13	0.88	−1.71	−2.14	−2.31

Figure 7 should be replaced by the following:



The sentence

“Both complexes show a reversible oxidation wave at a potential of 0.02 V vs FcH/FcH<sup>+</sup> (**1**(PF<sub>6</sub>)) and 0.14 V vs FcH/FcH<sup>+</sup> (**2**(PF<sub>6</sub>)) (see Table 3).”

should be replaced by

“Both complexes show a reversible oxidation wave at a potential of 0.13 V vs FcH/FcH<sup>+</sup> (**1**(PF<sub>6</sub>)) and 0.14 V vs FcH/FcH<sup>+</sup> (**2**(PF<sub>6</sub>)) (see Table 3).”

The sentence

“The NHCOMe group at the cyclometalating ligand in **1**(PF<sub>6</sub>) indeed leads to a further shift of the ruthenium-based oxidation by 0.10 V to lower values as compared to [Ru(tpy)(dpb)]<sup>+</sup>, while the COOEt substitution of the dpb ligand in **2**(PF<sub>6</sub>) slightly increases this redox potential by 0.02 V.”

should be deleted.

The sentence

“Changing the functional group on the tpy ligand from ethyl carboxy (**1**(PF<sub>6</sub>)) to N-acetyl amino (**2**(PF<sub>6</sub>)) shifts the

first reduction potential by 0.14 V to more negative values (cf. MO diagrams in Supporting Information Figure S22).” should be replaced by

“Changing the functional group on the tpy ligand from ethyl carboxy (**1**(PF<sub>6</sub>)) to N-acetyl amino (**2**(PF<sub>6</sub>)) shifts the first reduction potential by 0.25 V to more negative values (cf. MO diagrams in Supporting Information Figure S22).”

We regret the mistake, which does not affect the key findings reported in the paper, and sincerely apologize for any inconvenience.

### REFERENCES

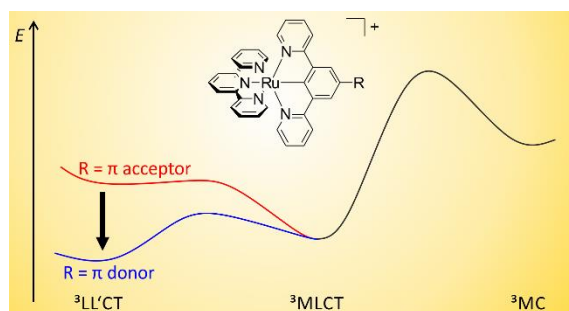
- (1) Connelly, N. G.; Geiger, W. E. *Chem. Rev.* **1996**, *96*, 877–910.



### 3.3 THE PHOTOCHEMISTRY OF MONO- AND DINUCLEAR CYCLOMETALATED BIS(TRIDENTATE)RUTHENIUM(II) COMPLEXES: DUAL EXCITED STATE DEACTIVATION AND DUAL EMISSION

Christoph Kreitner and Katja Heinze

*Dalton Trans.* **2016**, *45*, 5640–5658.



A low-energy  ${}^3\text{LL}'\text{CT}$  state efficiently depopulates the emissive  ${}^3\text{MLCT}$  state in cyclometalated  $[\text{Ru}(\text{dpb-R})(\text{tpy})]^+$  complexes (dpbH = 1,3-di(2-pyridyl)benzene, tpy = 2,2';6',2''-terpyridine).

#### Author Contributions

The synthesis and characterization of the ruthenium complexes as well as all DFT calculations were performed by Christoph Kreitner. The manuscript was written by Christoph Kreitner (90 %) and Katja Heinze (10 %).

#### Supporting Information

for this article is found at pp. 209 (excluding Cartesian Coordinates of DFT-optimized geometries). For full Supporting Information, refer to <http://www.rsc.org/suppdata/c6/dt/c6dt00384b/c6dt00384b1.pdf>.

„Kreitner, C.; Heinze, K. *Dalton Trans.* **2016**, *45*, 5640–5658. - Published by The Royal Society of Chemistry.”



Cite this: *Dalton Trans.*, 2016, **45**, 5640

## The photochemistry of mono- and dinuclear cyclometalated bis(tridentate)ruthenium(II) complexes: dual excited state deactivation and dual emission†

Christoph Kreitner<sup>a,b</sup> and Katja Heinze<sup>\*a</sup>

The synthesis and characterization of a series of weakly emissive mononuclear cyclometalated [Ru(dpb-R)(tpy)]<sup>+</sup> complexes with functional groups R of varying electron-donating characters at the dpb ligand are described (dpbH = 1,3-di(2-pyridyl)benzene, tpy = 2,2';6',2''-terpyridine, **1**<sup>+</sup>: R = NHCOMe, **2**<sup>+</sup>: R = NH<sub>2</sub>, **3**<sup>+</sup>: R = COOEt, **4**<sup>+</sup>: R = COOH). Steady-state emission spectroscopy in the temperature range between 298 K and 77 K revealed a previously unrecognized excited state deactivation pathway via low-lying triplet ligand-to-ligand (<sup>3</sup>LL'CT) charge transfer states in addition to the well-known pathway via <sup>3</sup>MC states. Thermal activation barriers for depopulation of the emissive metal-to-ligand charge transfer (<sup>3</sup>MLCT) states via the <sup>3</sup>MC (metal-centered) and <sup>3</sup>LL'CT states were determined experimentally for complexes **1**<sup>+</sup> and **3**<sup>+</sup>. The experimental results were further corroborated by calculating the respective <sup>3</sup>MLCT–<sup>3</sup>LL'CT and <sup>3</sup>MLCT–<sup>3</sup>MC transition states and their energies with density functional theoretical methods. The R substituent modifies the energy difference between the <sup>3</sup>MLCT and <sup>3</sup>LL'CT states and the corresponding activation barrier but leaves the analogous <sup>3</sup>MLCT/<sup>3</sup>MC energetics essentially untouched. Additionally, the dinuclear complex [(tpy)Ru(dpb-NHCO-dpb)Ru(tpy)]<sup>2+</sup>, **6**<sup>2+</sup>, containing a biscyclometalating bridge was devised. Despite the asymmetric nature induced by the amide bridge, the mixed-valent cation **6**<sup>3+</sup> is ascribed to Robin–Day class II with a broad and intense intervalence charge-transfer (IVCT) absorption ( $\lambda_{\text{max}} = 1165 \text{ nm}$ ). Upon optical excitation, the Ru<sup>II</sup>/Ru<sup>II</sup> complex **6**<sup>2+</sup> exhibits dual emission in liquid solution from two independently emitting <sup>3</sup>MLCT states localized at the two remote [Ru(tpy)] fragments. No equilibration via Dexter energy transfer is possible due to their large distance and short excited state lifetimes.

Received 27th January 2016,  
Accepted 16th February 2016

DOI: 10.1039/c6dt00384b

www.rsc.org/dalton

## Introduction

Polypyridine complexes of ruthenium(II) have been known and studied for the past sixty years.<sup>1,2</sup> Although the fundamentals of their photo- and electrochemical properties are well understood,<sup>3–7</sup> research efforts have not diminished over the last few years mainly due to a widespread potential for applications for this class of metal complexes. These vary from photoredox catalysis,<sup>8–12</sup> over light sensitization in dye-sensitized solar cells,<sup>13</sup> and sensing applications in biological<sup>14,15</sup> and chemical<sup>16</sup> contexts to optoelectronics.<sup>17</sup>

The prototype of this class of complexes is [Ru(bpy)<sub>3</sub>]<sup>2+</sup> (bpy = 2,2'-bipyridine), whose photophysical properties have been extensively studied and are well understood. Under visible light irradiation, excitation into a singlet metal-to-ligand charge transfer (<sup>1</sup>MLCT) state occurs ( $\lambda_{\text{max}} = 452 \text{ nm}$ ,  $\epsilon_{\text{max}} = 14.6 \text{ M}^{-1} \text{ cm}^{-1}$ ).<sup>1,3</sup> This state undergoes rapid and quantitative intersystem crossing onto the triplet hypersurface<sup>18,19</sup> populating a long-lived <sup>3</sup>MLCT state that is phosphorescent at room temperature ( $\lambda_{\text{em}} = 621 \text{ nm}$ ,  $\phi = 0.095$ ,  $\tau = 855 \text{ ns}$  in MeCN).<sup>20,21</sup> Upon cooling, both, emission quantum yield and excited state lifetime, increase drastically. Using lifetime measurements at varying temperatures, T. J. Meyer and co-workers showed that this temperature dependence is due to a thermally accessible d–d excited state (metal centered, <sup>3</sup>MC) that rapidly undergoes vibrational relaxation into the ground state (<sup>1</sup>GS).<sup>20,22</sup> Additionally, this excited state is dissociative in nature and enables [Ru(bpy)<sub>3</sub>]<sup>2+</sup> to undergo photosubstitution reactions.<sup>20,22,23</sup>

<sup>a</sup>Institute of Inorganic and Analytical Chemistry, Johannes Gutenberg University, Duesbergweg 10-14, D-55128 Mainz, Germany. E-mail: katja.heinze@uni-mainz.de

<sup>b</sup>Graduate School Materials Science in Mainz, Staudingerweg 9, D-55128 Mainz, Germany

† Electronic supplementary information (ESI) available. See DOI: 10.1039/c6dt00384b





To suppress these reactions and also to circumvent the chiral nature of  $[\text{Ru}(\text{bpy})_3]^{2+}$  stronger chelating, tridentate ligands such as tpy (tpy = 2,2',6',2''-terpyridine) were introduced in bis(tridentate)ruthenium(II) complexes.<sup>5,24</sup> Their meridional coordination geometry<sup>25</sup> allows the functionalization of the ligand periphery without resulting in stereoisomers. A major drawback of these complexes compared to their bpy counterparts is the almost complete lack of emission at room temperature ( $\phi = 5 \times 10^{-6}$ ).<sup>5,26</sup> Due to the weaker ligand field caused by the smaller bite angle of the terpyridine ligand (N–Ru–N  $\approx 79^\circ$ ), the emissive  $^3\text{MLCT}$  states of  $[\text{Ru}(\text{tpy})_2]^{2+}$  are very efficiently depopulated *via* low-lying  $^3\text{MC}$  states.<sup>24</sup> Upon cooling, thermal depopulation of the emissive state is retarded yielding bright luminescence at 77 K ( $\lambda_{\text{em}} = 599 \text{ nm}$ ,  $\phi = 0.48$ ,  $\tau = 110 \mu\text{s}$  in MeOH/EtOH).<sup>27</sup>

Various attempts have been made to regain room temperature luminescence from bis(tridentate)ruthenium(II) complexes. By introducing an electron-donating functional group on one of the terpyridine ligands, the energy of the  $^3\text{MC}$  state is increased with respect to the  $^3\text{MLCT}$  state energy rather selectively.<sup>5</sup> Similarly, electron-accepting functionalities lower the  $^3\text{MLCT}$  state energy.<sup>5</sup> Combining these two approaches in a push–pull system, the activation barrier for depopulation of the emissive  $^3\text{MLCT}$  state is increased. As a result, room temperature quantum yields of up to 0.003 and excited state lifetimes of 50 ns are achieved.<sup>5,28–31</sup> Since the coordination mode of the tpy ligand with five-membered chelate rings only allows for rather constrained geometries around the metal center with small bite angles, several research groups focussed on expanding the ligand backbone to increase the overlap between the ruthenium d orbitals of the  $e_g$  set and the nitrogen lone pairs. This yields an enlarged ligand field splitting and thus makes  $^3\text{MC}$  states as deactivation pathway thermally less accessible at room temperature.<sup>32–35</sup> Following this concept, bis(tridentate)ruthenium(II) complexes were synthesized with optical properties comparable to those of  $[\text{Ru}(\text{bpy})_3]^{2+}$  ( $\phi = 0.30$ ,  $\tau = 3.3 \mu\text{s}$ ).<sup>33</sup>

In a very similar approach, by introduction of very strong  $\sigma$ -donors in the coordination sphere, the ligand field splitting can be increased compared to  $[\text{Ru}(\text{tpy})_2]^{2+}$ . Conceptually, this was shown by Berlinguette and Schubert using N-heterocyclic carbene containing tridentate ligands ( $\text{C}^{\wedge}\text{N}^{\wedge}\text{C}$  coordination mode) with quantum yields of 0.11 and excited state lifetimes of up to 8  $\mu\text{s}$ .<sup>36</sup> Disappointingly, attempts using 1,3-di(2-pyridyl)benzene (dpbH), deprotonated in the 2-position of the central benzene ring, as a strong cyclometalating  $\sigma$ -donor ligand in conjunction with tpy as a  $\pi$ -accepting ligand ( $[\text{Ru}(\text{dpb})(\text{tpy})]^+$ ), gave only very weakly emissive complexes.<sup>30,37–40</sup> This was originally ascribed to a very small activation barrier for thermal depopulation of the emissive  $^3\text{MLCT}$  state *via* low-lying  $^3\text{MC}$  states since the cyclometalation at the central position of the dpb ligand merely shifts one of the  $^3\text{MC}$  states to a higher energy.<sup>30</sup> Recently, we have suggested that the introduction of a very strong push–pull arrangement across the metal center additionally gives rise to low-lying triplet ligand-to-ligand charge transfer ( $^3\text{LL}'\text{CT}$ )

states.<sup>40</sup> Since the involved ligands are orthogonal to one another in the meridional coordination geometry, so are the spin-carrying orbitals. Hence, emission from such  $^3\text{LL}'\text{CT}$  states is symmetry-forbidden and leads to efficient radiationless deactivation of the excited state.

To further study this phenomenon and to elaborate a general view, the work presented herein devised four cyclometalated ruthenium complexes  $[\text{Ru}(\text{dpb-R})(\text{tpy})]^+$  with varying substituents at the 5-position of the dpb ligand (R = NHCOMe, 1<sup>+</sup>; R = NH<sub>2</sub>, 2<sup>+</sup>; R = COOEt, 3<sup>+</sup>; R = COOH, 4<sup>+</sup>). Using these, it is possible to systematically study the impact of varying push–pull strengths across the metal center on the ground and excited state properties of these cyclometalated complexes. By employing steady-state emission spectroscopy, we demonstrate that the occurrence of low-energy  $^3\text{LL}'\text{CT}$  states is a common theme in cyclometalated bis(tridentate)ruthenium complexes providing a second excited state deactivation pathway in addition to the well-known pathway mediated by  $^3\text{MC}$  states.

Additionally, the presence of free amino and carboxylic acid groups allows the straightforward formation of a dinuclear complex with an amide-linked biscyclometalating bridging ligand ( $[(\text{tpy})\text{Ru}(\text{dpb-NHCO-dpb})\text{Ru}(\text{tpy})]^{2+}$  ( $6^{2+}$ ) that we synthesized and studied as well. Dinuclear bisruthenium complexes received wide interest since the discovery of the mixed-valent Creutz–Taube ion,  $[(\text{NH}_3)_5\text{Ru}(\mu\text{-pz})\text{Ru}(\text{NH}_3)_5]^{5+}$  (pz = pyrazine).<sup>41–43</sup> The ruthenium oxidation states within this mixed-valent complex cannot be assigned unambiguously. Depending on the spectroscopic method either 2+/3+ or 2.5+/2.5+ is obtained.<sup>44–47</sup> Dinuclear mixed-valent complexes are assigned to three different groups based on Robin's and Day's classification.<sup>48</sup> Systems with entirely localized valences and no electronic coupling between the redox centers in the mixed-valent state are referred to as Robin–Day class I, and systems with entirely delocalized valences are assigned as class III. Class II describes valence-localized complexes with measurable electronic interactions between the redox sites. The theoretical basis for an accurate physicochemical treatment of Robin–Day class II complexes was laid by Hush<sup>49–51</sup> describing the photochemical electron transfer occurring between the donor and acceptor sites  $[\text{M}^{n+} - \text{M}^{(n+1)+} \rightarrow \text{M}^{(n+1)+} - \text{M}^{n+}]$ . This process yields an intervalence charge transfer (IVCT) absorption that is typically observed in the Near Infrared (NIR) region of the electronic absorption spectrum of a Robin–Day class II compound. According to Marcus–Hush theory, this IVCT band is correlated with the electronic coupling parameter  $V_{\text{ab}}$  between the redox centers calculated as:  $V_{\text{ab}} = 2.06 \times 10^{-2} \tilde{\nu}_{\text{max}} \epsilon_{\text{max}} \tilde{\nu}_{1/2})^{1/2} r^{-1}$  with the absorption maximum  $\tilde{\nu}_{\text{max}}$  in  $\text{cm}^{-1}$ , the extinction coefficient  $\epsilon_{\text{max}}$  at  $\tilde{\nu}_{\text{max}}$  in  $\text{M}^{-1} \text{cm}^{-1}$ , the full width at half maximum  $\tilde{\nu}_{1/2}$  in  $\text{cm}^{-1}$  and the donor–acceptor distance  $r$  in  $\text{\AA}$ .<sup>47,52</sup>

Several amide-bridged dinuclear bis(terpyridine)ruthenium(II) complexes and their mixed-valent counterparts have been described in the literature.<sup>53–55</sup> While the back-to-back linked ( $n = 0$ ) or phenylene-extended ( $n = 1–2$ ) dinuclear bis(terpyridine)ruthenium(II) complexes  $[(\text{ttpy})\text{Ru}(\text{tpy}-(1,4\text{-C}_6\text{H}_4)_n\text{-tpy})\text{Ru}(\text{ttpy})]^{4+}$  (tpy = 4'-tolylterpyridine, 1,4-C<sub>6</sub>H<sub>4</sub> = *para*-phenylene)



## Paper

exhibit electronic coupling of the metal centers in the mixed-valent state to a small extent ( $n = 0$ :  $V_{ab} = 0.047$  eV,  $n = 1$ :  $V_{ab} = 0.030$  eV,  $n = 2$ :  $V_{ab} = 0.022$  eV),<sup>56,57</sup> the introduction of an amide bridge seems to reduce the molecular and redox-chemical symmetry enough to prevent the electronic interactions entirely.<sup>54,55</sup> In the cyclometalated analogue of the dinuclear back-to-back linked bis(terpyridine)ruthenium complex,  $[(\text{ttpy})\text{Ru}(\text{dpb-dpb})\text{Ru}(\text{tpy})]^{2+}$ , on the other hand, the metal-metal interaction is increased to  $V_{ab} = 0.127$  eV.<sup>58,59</sup> This increase was attributed to an energy shift of the bridge's frontier orbitals to better match those of the metal centers.<sup>59,60</sup> In this work, we study to what extent the insertion of an NHCO group into the bridge reduces the electronic coupling between the metal centers in the mixed-valent state  $6^{3+}$  and the interaction of the triplet excited states of  $6^{2+}$ .

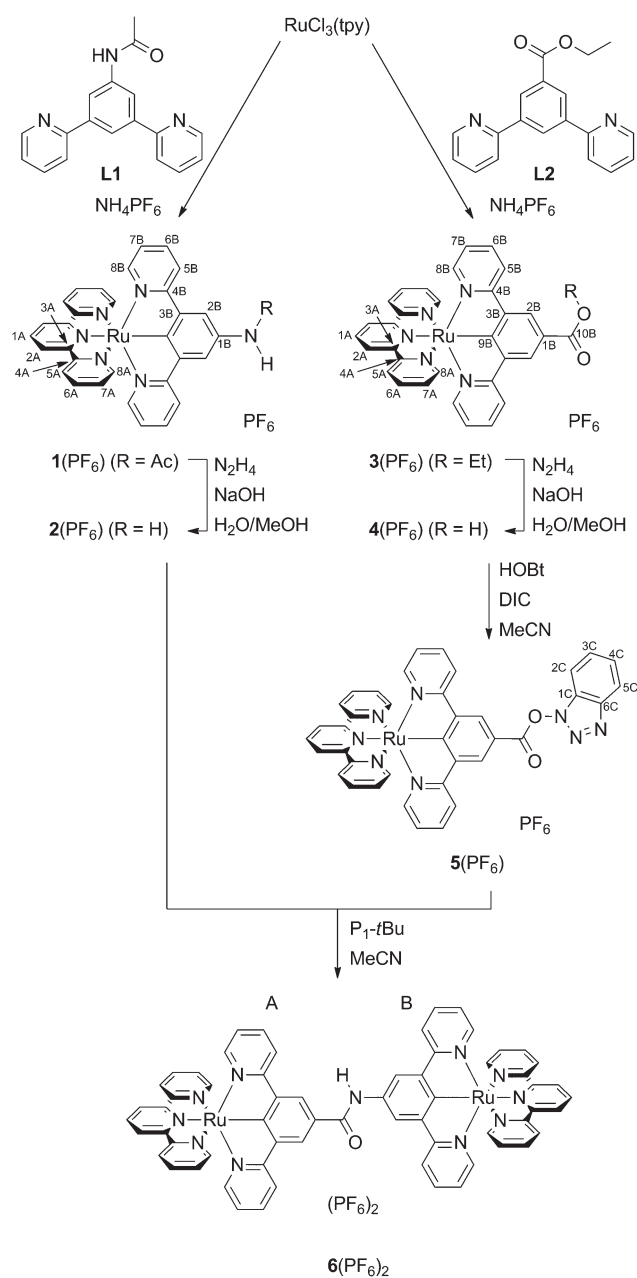
## Results and discussion

### Synthesis and characterization of mono- and dinuclear complexes

The synthesis (Scheme 1) of the target mononuclear complexes was carried out following a previously described synthetic route starting from  $\text{RuCl}_3(\text{tpy})$ .<sup>40,58</sup> In the first step, this precursor is activated by chloride abstraction using silver tetrafluoroborate. The resulting solvent complex intermediate was subsequently treated with the respective dipyriddybenzene ligand **L1** or **L2**<sup>40</sup> to give the amide or ester substituted  $[\text{Ru}(\text{dpb-R})(\text{tpy})]^+$  complexes **1**(PF<sub>6</sub>) and **3**(PF<sub>6</sub>) in good yields. Cleavage of the functional groups for the liberation of free amine or carboxylic acid was achieved in aqueous methanolic solutions using sodium hydroxide as a base and hydrazine as a reductant to prevent oxidative decomposition. This hydrolysis protocol gives comparable yields to the hydrolysis of structurally related ruthenium complexes by trimethylamine employed by Berlinguette and coworkers.<sup>61</sup>

In order to accomplish the coupling reaction between the free acid and the amine moieties of  $2^+$  and  $4^+$  to the dinuclear complex  $6^{2+}$ , activation of the acid component is necessary. This was achieved similarly to a previously employed technique using *N*-hydroxybenzotriazole (HOBt) and *N,N'*-diisopropylcarbodiimide (DIC).<sup>55,62</sup> Compared to the amide coupling reaction between bis(terpyridine)ruthenium(II) amino acid derivatives described previously,<sup>54,55</sup> the coupling had to be performed at elevated temperatures, possibly attributed to the reduced acidity of the OBt ester compared to other active esters.

All complexes were characterized using 1D- and 2D-NMR techniques (ESI, Fig. S1–S14†) as well as ESI and high-resolution ESI mass spectrometry (ESI, Fig. S15†). The purity of all compounds under study was confirmed by elemental analyses. Successful amide cleavage (**1**(PF<sub>6</sub>) → **2**(PF<sub>6</sub>)) is proven by the disappearance of the NH (8.62 ppm) and CH<sub>3</sub> (2.23 ppm) resonances in the proton NMR spectrum of **2**(PF<sub>6</sub>). Simultaneously, a new significantly broadened resonance



**Scheme 1** Synthesis of the mononuclear complexes **1**(PF<sub>6</sub>)–**5**(PF<sub>6</sub>) and the dinuclear complex **6**(PF<sub>6</sub>)<sub>2</sub> from  $\text{RuCl}_3(\text{tpy})$ . Atom numbering for NMR assignment is included.

appears at 4.24 ppm indicating the presence of a free amino group. Similarly, ester saponification (**3**(PF<sub>6</sub>) → **4**(PF<sub>6</sub>)) yields a loss of the characteristic CH<sub>2</sub> and CH<sub>3</sub> proton resonances of the ethyl group while essentially leaving the aromatic region of the <sup>1</sup>H NMR spectrum unaffected. For the hydroxybenzotriazole ester **5**(PF<sub>6</sub>), the resonances of the dipyriddybenzene ligand, predominantly those in the 2B-position, are shifted to a lower field. This is in agreement with the formation of a more electron-deficient species that is activated towards nucleophilic attack.



Interestingly, the functional group attached to the dpb ligand strongly affects the  $^{13}\text{C}$  chemical shift of the coordinating carbon atom. While this resonance is found at 239.5 ppm in complex  $5(\text{PF}_6)$  with the strongly electron-withdrawing COOBt substituent, it is shifted upfield to 233 ppm in complexes  $3(\text{PF}_6)$  and  $4(\text{PF}_6)$  with COOEt and COOH functional groups. In the *N*-substituted complexes, it is found at even lower chemical shifts, namely at 217.2 ppm for  $1(\text{PF}_6)$  and at 208.9 ppm for  $2(\text{PF}_6)$ . This also reflects the electrochemistry at the ruthenium center (*vide infra*).

Evidence for the success of the amide coupling between  $2(\text{PF}_6)$  and  $5(\text{PF}_6)$  is gained from the  $^1\text{H}$  NMR spectrum of  $6(\text{PF}_6)_2$ . The proton resonance at low field (9.63 ppm) with an integral of a single proton indicates the presence of an amide bridge. Additionally, all aromatic signal sets occur four times in a 1 : 1 : 1 : 1 ratio. Although the resonances of the two terpyridine ligands are distinguishable due to the different substituents at the remote dpb ligands, an unambiguous assignment to one of the two capping ligands is impossible. The ESI mass spectrum, which shows the required peaks at  $m/z = 586.6$  for  $6^{2+}$  and at 1318.3 for  $6(\text{PF}_6)^+$  with isotope patterns characteristic for a complex containing two ruthenium atoms, gives additional support to the successful formation of the dinuclear complex.

IR spectroscopy further confirms all structures under study (ESI, Fig. S16<sup>†</sup>). All the complexes exhibit an intense IR absorption at  $843\text{ cm}^{-1}$  arising from P–F stretching vibrations within the  $\text{PF}_6^-$  counterion. The amino-substituted complex  $2^+$  shows a broad, intense absorption at  $3420\text{ cm}^{-1}$  arising from N–H stretching vibrations of the  $\text{NH}_2$  group. The amide containing complexes  $1^+$  and  $6^{2+}$  exhibit a broad absorption band at around  $3220\text{--}3230\text{ cm}^{-1}$  ascribed to the N–H stretch along with intense C=O vibrations at  $1650\text{ cm}^{-1}$  and  $1635\text{ cm}^{-1}$ , respectively. Similar C=O vibrations are observed for the carboxy-substituted complexes  $3^+$  and  $4^+$ , with that of the ester occurring at  $1695\text{ cm}^{-1}$  and that of the carboxylic acid at  $1665\text{ cm}^{-1}$ . Additionally, the carboxylic acid  $4^+$  exhibits a broad absorption at  $3440\text{ cm}^{-1}$  (O–H stretch) along with absorptions in the range between  $3000$  and  $2300\text{ cm}^{-1}$  typical for carboxylic acids.

### Electrochemical properties of complexes $1(\text{PF}_6)$ – $4(\text{PF}_6)$ and $6(\text{PF}_6)_2$

The cyclic voltammograms of the complexes  $1(\text{PF}_6)$ – $4(\text{PF}_6)$  and  $6(\text{PF}_6)_2$  are depicted in Fig. 1 and the respective electrochemical data are summarized in Table 1. For all mononuclear complexes,  $1(\text{PF}_6)$ – $4(\text{PF}_6)$ , a single reversible oxidation is observed in the range between  $-0.2\text{ V}$  and  $0.28\text{ V}$  versus the ferrocene/ferrocenium redox couple. It is ascribed to the  $\text{Ru}^{\text{II}}/\text{Ru}^{\text{III}}$  couple. The electrochemical data of the ethyl ester-substituted complex  $3(\text{PF}_6)$  agree well with those of the methyl ester reported in the literature.<sup>30</sup> With increasing electron-accepting properties of the respective substituent, this redox process is shifted to higher potentials by almost 500 mV. This suggests a strong contribution of the dpb ligand to the highest occupied molecular orbital (HOMO) of these complexes.

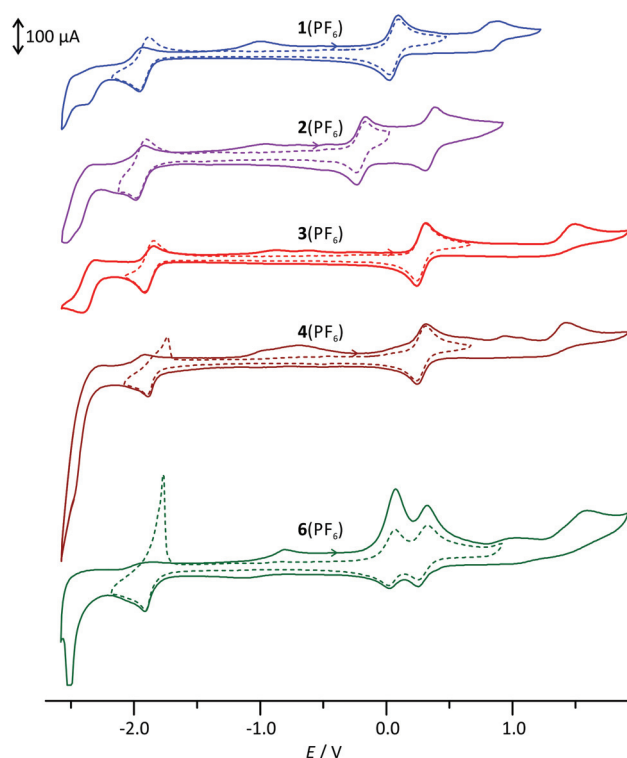


Fig. 1 Cyclic voltammograms of  $1(\text{PF}_6)$ – $4(\text{PF}_6)$  and  $6(\text{PF}_6)_2$  in MeCN with  $0.1\text{ mol l}^{-1}$   $[\text{nBu}_4\text{N}][\text{PF}_6]$  as the supporting electrolyte.

Density functional theory (DFT) calculations further illustrate and enlighten these experimental findings. We have shown previously<sup>40</sup> that the B3LYP functional<sup>63</sup> along with a split-valence double- $\xi$  basis set and polarization functions on all non-hydrogen atoms (def2-SV(P))<sup>64–66</sup> provides reasonable access to the electronic properties of the numerous charge transfer states of the complexes under study when combined with the ZORA relativistic approximation<sup>67</sup> and a continuum solvent model (COSMO).<sup>68</sup>

Indeed, DFT calculations for the singlet ground states of the respective cationic complexes nicely reproduce the dependence of the energy of the HOMO from the substitution pattern (Fig. 2). Additionally, the shape of the HOMO parallels that of the doublet spin density of the  $\text{Ru}^{\text{III}}$  complexes  $1^{2+}$ – $4^{2+}$  (ESI, Table S2<sup>†</sup>) supporting the fact that oxidation occurs on both the metal site and the dpb ligand. At substantially higher potentials, a second, irreversible oxidation is observed. It is again assigned to a mixed metal/dpb ligand oxidation yielding a  $[\text{Ru}(\text{dpb})]^{3+}$  state as suggested previously by DFT calculations for analogous complexes.<sup>40</sup> The dependence of this second oxidation from the substitution pattern is even more pronounced so that its potential ranges from  $0.35\text{ V}$  for amine-substituted  $2(\text{PF}_6)$  to  $1.49\text{ V}$  for ester-substituted  $3(\text{PF}_6)$ .

All four mononuclear complexes exhibit one reversible and several unresolved irreversible reductions. According to DFT calculations on the ground and the one-electron reduced states of  $1^+$ – $4^+$  ( $1^0$ – $4^0$ ), the first reduction is ascribed to a



**Table 1** Electrochemical data of complexes **1**(PF<sub>6</sub>)–**4**(PF<sub>6</sub>) and **6**(PF<sub>6</sub>)<sub>2</sub>, obtained from 0.1 mol l<sup>-1</sup> [nBu<sub>4</sub>N][PF<sub>6</sub>] containing acetonitrile solution. Potentials are referenced against the FcH/FcH<sup>+</sup> couple. Energy differences  $E_{\text{HOMO}} - E_{\text{LUMO}}$  are obtained from DFT calculations (see the MO diagram in Fig. 2)

	$E_{\text{ox},1}/\text{V}$	$E_{\text{ox},2}/\text{V}$	$E_{\text{ox},3}/\text{V}$	$E_{\text{red},1}/\text{V}$	$E_{\text{red},2}/\text{V}$	$E_{\text{ox},1} - E_{\text{red},1}/\text{V}$	$E_{\text{LUMO}} - E_{\text{HOMO}}/\text{eV}$
<b>1</b> (PF <sub>6</sub> )	0.06 ([Ru-dpb]/[Ru-dpb] <sup>+</sup> ) <sup>a</sup>	0.86 ([Ru-dpb] <sup>+</sup> /[Ru-dpb] <sup>2+</sup> ) <sup>b</sup>	—	-1.93 (tpy/tpy <sup>-</sup> ) <sup>a</sup>	-2.54 <sup>c</sup>	1.99	2.72
<b>2</b> (PF <sub>6</sub> )	-0.20 ([Ru-dpb]/[Ru-dpb] <sup>+</sup> ) <sup>a</sup>	0.35 ([Ru-dpb] <sup>+</sup> /[Ru-dpb] <sup>2+</sup> ) <sup>a</sup>	—	-1.95 (tpy/tpy <sup>-</sup> ) <sup>a</sup>	-2.48 <sup>c</sup>	1.75	2.48
<b>3</b> (PF <sub>6</sub> )	0.28 ([Ru-dpb]/[Ru-dpb] <sup>+</sup> ) <sup>a</sup>	1.49 ([Ru-dpb] <sup>+</sup> /[Ru-dpb] <sup>2+</sup> ) <sup>b</sup>	—	-1.87 (tpy/tpy <sup>-</sup> ) <sup>a</sup>	-2.40 <sup>c</sup>	2.15	2.98
<b>4</b> (PF <sub>6</sub> )	0.28 ([Ru-dpb]/[Ru-dpb] <sup>+</sup> ) <sup>a</sup>	1.42 ([Ru-dpb] <sup>+</sup> /[Ru-dpb] <sup>2+</sup> ) <sup>b</sup>	—	-1.86 (tpy/tpy <sup>-</sup> ) <sup>a</sup>	-2.50 <sup>c</sup>	2.14	2.99
<b>6</b> (PF <sub>6</sub> ) <sub>2</sub>	0.05 ([Ru-Ru]/[Ru-Ru] <sup>+</sup> ) <sup>a</sup>	0.29 ([Ru-Ru] <sup>+</sup> /[Ru-Ru] <sup>2+</sup> ) <sup>a</sup>	1.58 ([Ru-Ru] <sup>2+</sup> /[Ru-Ru] <sup>3+</sup> ) <sup>b</sup>	-1.85 (2 e <sup>-</sup> , tpy/tpy <sup>-</sup> ) <sup>a</sup>	-2.51 <sup>c</sup>	1.90	2.64

<sup>a</sup> Reversible,  $E_{1/2}$  given. <sup>b</sup> Irreversible, anodic peak potential given. <sup>c</sup> Irreversible, cathodic peak potential given.

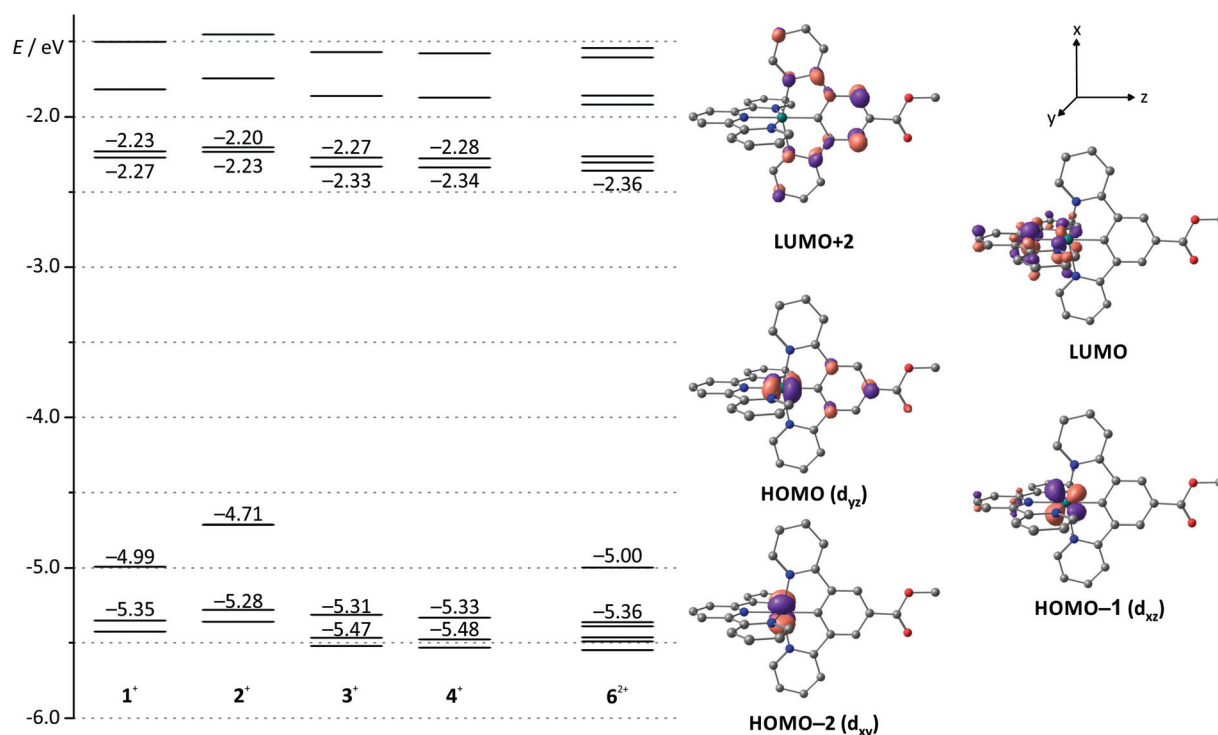


**Fig. 2** Molecular orbital energy diagram of complexes **1**(PF<sub>6</sub>)–**4**(PF<sub>6</sub>) and **6**(PF<sub>6</sub>)<sub>2</sub> obtained from DFT calculations (B3LYP, def2-SV(P), COSMO (acetonitrile), ZORA). Frontier orbitals are depicted exemplary for **3**(PF<sub>6</sub>) since the shape of the respective orbital varies only marginally among the mononuclear complexes (see also ESI, Table S1†). Hydrogen atoms are omitted for clarity.

tpy-centered reduction (ESI, Table S2†). The COOH-substituted complex **4**(PF<sub>6</sub>) shows a stripping peak upon reoxidation following the first reduction. We ascribe this phenomenon to precipitation of the neutral complex moiety [Ru<sup>II</sup>(dpb<sup>-</sup>-COOH)(tpy<sup>-</sup>)]<sup>0</sup> on the electrode surface and subsequent redissolution after reoxidation to **4**<sup>+</sup>.<sup>55</sup>

Due to the orthogonal *mer*-coordination of the two tridentate ligands, the electronic influence of the different functional groups attached to the dpb ligand on the tpy ligand is reduced

to a minor inductive effect. Consequently, the first reduction occurs at very similar potentials for all four complexes in the range between -1.86 (COOH-substituted **4**(PF<sub>6</sub>)) and -1.95 V (NH<sub>2</sub>-substituted **2**(PF<sub>6</sub>)) spanning just 90 mV. Accordingly, the HOMO–LUMO gap, which is closely correlated to the difference of the redox potentials of the first reduction and oxidation, varies considerably in the order  $4^+ \approx 3^+ > 1^+ > 2^+$  (Table 1). This trend is in excellent agreement with DFT calculations (Fig. 2 and Table 1).





All complexes exhibit follow-up oxidation peaks in the range between  $-1$  and  $-0.5$  V once reduction has been carried out beyond  $-2$  V. We had observed such behaviour previously both in mono- and dinuclear bis(terpyridine)ruthenium(II) complexes and cyclometalated ruthenium complexes bearing amide functionalities. We had suggested that these follow-up oxidations are associated with species that are formed after reduction of the substantially acidified amide NH proton (hydrogen formation).<sup>55</sup> The observation of similar processes in complexes such as **3**(PF<sub>6</sub>) and **4**(PF<sub>6</sub>) lacking NH functionalities contradicts this hypothesis. In fact, such more or less pronounced follow-up reoxidation peaks can be found for a large variety of tpy containing complexes of different metals such as chromium,<sup>69</sup> manganese,<sup>70</sup> and ruthenium,<sup>35</sup> once a sufficient number of reduction events have taken place at the tpy unit. The triplet spin densities of the twofold reduced complexes **1**<sup>1-</sup>–**4**<sup>1-</sup> do not provide further hints on possible follow-up reactions (ESI, Table S2†). Compared to the respective <sup>1</sup>GS structures, their geometries are undistorted with a spin density homogeneously distributed over all three pyridine rings of the terpyridine ligand.

For the dinuclear complex **6**(PF<sub>6</sub>)<sub>2</sub>, cyclic voltammetric studies reveal a single reversible two-electron reduction, as evidenced from square-wave voltammetry, followed by an intense stripping peak. Again, this stripping peak arises from precipitation of the large uncharged complex **6**<sup>0</sup> on the electrode surface and redissolution after reoxidation to **6**<sup>2+</sup>. The first, unsplit reduction processes are ascribed to tpy-centered reductions occurring at both terminal ligands of the bimetallic complex as evidenced from DFT calculated triplet spin densities of **6**<sup>0</sup> (ESI, Table S3 and Fig. S17†). Additionally, two reversible oxidation processes at 0.05 and 0.29 V, respectively, are observed. Based on the redox potentials of the mononuclear complexes, these can be ascribed to a primary oxidation of the NH-substituted complex fragment followed by oxidation of the CO-substituted moiety. Interestingly, the difference of the two oxidation potentials is slightly increased by 20 mV compared to that of the mononuclear complexes **1**<sup>+</sup> and **3**<sup>+</sup> (240 versus 220 mV, Table 1). This might be due to spatial charge accumulation or to a weak electronic communication between the two complex fragments in the mixed-valent state **6**<sup>3+</sup>. Missing shifts of the electrochemical potentials of asymmetric dinuclear complexes compared to similar mononuclear complexes or negligible splittings between the Ru<sup>II</sup>Ru<sup>II</sup>/Ru<sup>II</sup>Ru<sup>III</sup> and the Ru<sup>II</sup>Ru<sup>III</sup>/Ru<sup>III</sup>Ru<sup>III</sup> oxidation potentials in symmetrical complexes have already been observed with other bimetallic bis(tridentate)ruthenium complexes.<sup>53–55,57</sup> Some of these were accompanied by a weak electronic interaction between the Ru centers while others showed no metal–metal interaction. These examples illustrate that a clear conclusion as to whether electronic communication occurs between the metal centers of the complex fragments is impossible purely based on these electrochemical data.<sup>71</sup> UV-Vis spectroscopy studies on the mixed-valent species **6**<sup>3+</sup> will provide deeper insight into that matter (*vide infra*).

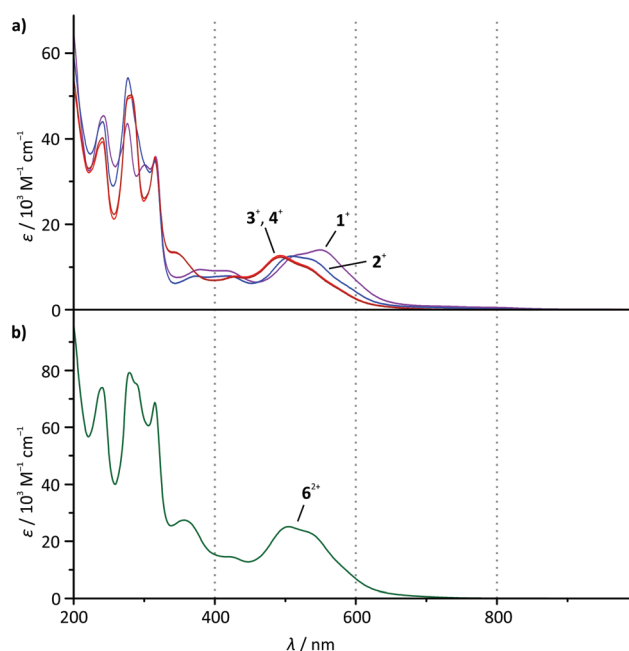


Fig. 3 UV-Vis absorption spectra of (a) **1**(PF<sub>6</sub>)–**4**(PF<sub>6</sub>) and (b) **6**(PF<sub>6</sub>)<sub>2</sub> in dry acetonitrile solution at room temperature ( $c = 2 \times 10^{-5}$  mol l<sup>-1</sup>).

#### UV-Vis spectroscopic properties of complexes **1**(PF<sub>6</sub>)–**4**(PF<sub>6</sub>) and **6**(PF<sub>6</sub>)<sub>2</sub>

The absorption spectra of all mononuclear complexes (Fig. 3) exhibit very similar features. Besides intense transitions in the UV region attributed to  $\pi$ – $\pi^*$  transitions within the ligands, four discernible absorption bands are observed in the visible range between 350 and 650 nm. DFT calculations<sup>30,39</sup> and resonance Raman spectroscopy studies<sup>40</sup> suggest that such bands characteristic for cyclometalated ruthenium complexes containing polypyridine and N<sup>+</sup>C, N<sup>+</sup>C<sup>+</sup>N or N<sup>+</sup>N<sup>+</sup>C ligands arise from metal-to-ligand charge transfer transitions (<sup>1</sup>MLCT) involving both the polypyridine and the cyclometalating ligand as electron accepting sites.

As the visible-range absorption bands are governed by <sup>1</sup>MLCT transitions involving both ligands, variation of the functional group on the cyclometalating ligand greatly affects the position of the low-energy absorption maximum (Table 2). While the ester- or acid-substituted complexes **3**<sup>+</sup> and **4**<sup>+</sup> exhibit absorption maxima at 493 nm, the respective maximum of amide-substituted **1**<sup>+</sup> is observed at 509 nm and that of the amine complex **2**<sup>+</sup> is found at 550 nm (Fig. 3). This trend is in good agreement with the HOMO–LUMO gap (Table 1 and Fig. 2) in this series of complexes. In contrast, DFT calculations reveal that the most intense Ru → tpy MLCT transitions (HOMO–1 ( $d_{xz}$ ) → LUMO) are not responsible for the observed trend since they appear at very similar energies for all four complexes (transition 5 in ESI, Tables S4–S7†). This is easily understood based on a closer examination of the orbitals of the complexes **1**<sup>+</sup>–**4**<sup>+</sup> involved in this transition (Fig. 2 and ESI, Table S1†): the symmetry of the LUMO (tpy) only allows for constructive interference with the  $d_{xz}$  orbital of the





**Table 2** Experimental UV-Vis absorption and emission data of the mononuclear complexes **1**(PF<sub>6</sub>), **2**(PF<sub>6</sub>), **3**(PF<sub>6</sub>), and **4**(PF<sub>6</sub>) as well as the dinuclear complex **6**(PF<sub>6</sub>)<sub>2</sub>. Absorption and emission data are obtained from (deaerated) acetonitrile solution, and low-temperature emission data are recorded in butyronitrile. Excitation wavelengths are given in parentheses where wavelength dependence of the emission maximum was observed, otherwise  $\lambda_{\text{exc}} = 500$  nm

	$\lambda_{\text{max}}/\text{nm}$ ( $\epsilon/10^3 \text{ M}^{-1} \text{ cm}^{-1}$ )	$\lambda_{\text{em}}/\text{nm}$ at 298 K	$\lambda_{\text{em}}/\text{nm}$ at 155 K	$\lambda_{\text{em}}/\text{nm}$ at 77 K	$\phi$ at 298 K
<b>1</b> (PF <sub>6</sub> )	533 (11.9, sh), 509 (12.5), 419 (7.9), 373 (7.9), 315 (34.8)	800	798	736	$8 \times 10^{-6}$
<b>2</b> (PF <sub>6</sub> )	550 (12.9), 519 (12.9, sh), 417 (9.1), 379 (9.4), 316 (35.8)	780	768	731	$<2 \times 10^{-6}$
<b>3</b> (PF <sub>6</sub> )	529 (9.9, sh), 493 (12.3), 428 (7.6), 343 (13.5), 315 (35.3)	744	738	708	$14 \times 10^{-6}$
<b>4</b> (PF <sub>6</sub> )	529 (10.2, sh), 493 (12.7), 429 (7.8), 343 (13.3), 315 (35.6)	744	738	709	$15 \times 10^{-6}$
<b>6</b> (PF <sub>6</sub> ) <sub>2</sub>	530 (23.4, sh), 504 (25.1), 422 (14.6), 356 (27.4), 315 (68.7)	756 (480), 772 (560)	746	736	$9 \times 10^{-6}$

metal (HOMO–1). On the other hand, both, HOMO–1 and LUMO are perpendicular to the Ru  $d_{yz}$  orbital and the dpb  $\pi$ -orbital which strongly contribute to the HOMO. Hence, the dpb functional group's impact on the involved orbitals is again reduced to a minor inductive effect explaining the weak dependence of the Ru  $\rightarrow$  tpy MLCT transitions on the dpb substituent.

The strong bathochromic shift of the experimental absorption maximum accompanying the more electron-donating *N*-acetyl amino and amino substituents at the dpb ligand in fact arises from symmetry-allowed  $d_{yz}(\text{Ru}) \rightarrow$  dpb MLCT transitions. Especially the HOMO  $\rightarrow$  LUMO+2 transition plays a key role within the absorption characteristics (transition 6 in Tables S4–S7†). These transitions are calculated at 486 (**1**<sup>+</sup>), 507 (**2**<sup>+</sup>), and 456 nm (**3**<sup>+</sup> and **4**<sup>+</sup>), respectively, and they nicely reproduce the trends within the absorption maxima of the respective complexes (Table 2). This fully confirms that the two main <sup>1</sup>MLCT transitions in the visible range of the electronic spectrum, namely  $d_{xz}(\text{Ru}) \rightarrow$  tpy and  $d_{yz}(\text{Ru}) \rightarrow$  dpb, are electronically decoupled for simple symmetry reasons.

At first sight, the absorption spectrum of the dinuclear complex **6**<sup>2+</sup> resembles the absorption spectra of the carboxy-substituted mononuclear complexes **3**<sup>+</sup> and **4**<sup>+</sup> with roughly doubled extinction coefficients due to its dinuclear nature (Fig. 3). A closer inspection reveals that the spectrum of the dinuclear complex is much better reproduced by a 1 : 1 superposition of the absorption spectra of the ester- and the amide-substituted mononuclear complexes **1**<sup>+</sup> and **3**<sup>+</sup> (Fig. 4). This suggests that the dinuclear compound **6**<sup>2+</sup> consists of two essentially non-interacting bis(tridentate)ruthenium(II) fragments connected *via* an amide bond. Indeed, this is underlined by time-dependent DFT calculations which reveal that all charge transfer excitations >400 nm between the two complex fragments have negligible oscillator strengths and should play no role in the observed absorption features (Table S8†). Similar observations have previously been made for other amide-linked dinuclear ruthenium(II) complexes with tridentate ligands.<sup>53–55</sup> Since in this study the visible absorption-spectroscopic fingerprints of the two subunits are more distinct than in the literature-known bimetallic examples, the superimposed nature of the absorption bands of **6**<sup>2+</sup> is more obvious. In principle, the two [Ru(dp)(tpy)]<sup>+</sup> subunits are essentially uncoupled in the Ru<sup>II</sup>Ru<sup>II</sup> state.

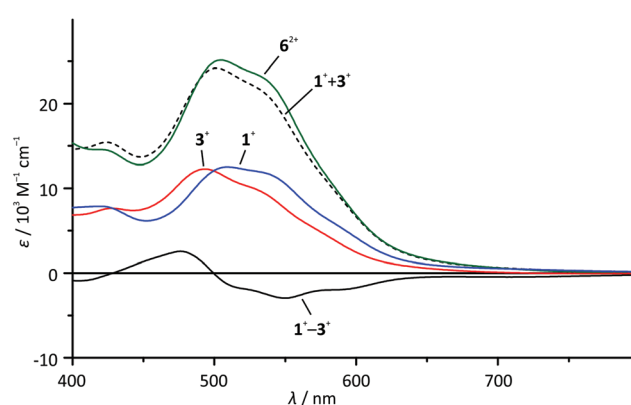


**Fig. 4** Visible range of the absorption spectra of **1**<sup>+</sup> (blue), **3**<sup>+</sup> (red) and **6**<sup>2+</sup> (green) in dry acetonitrile solution as well as superposition (**1**<sup>+</sup> + **3**<sup>+</sup>) (black, dashed line) and difference spectra (**3**<sup>+</sup> – **1**<sup>+</sup>) (black, solid line).

To probe the metal–metal interaction in the mixed-valent state **6**<sup>3+</sup>, careful *in situ* chemical oxidation of **6**(PF<sub>6</sub>)<sub>2</sub> in acetonitrile solution was carried out using (NH<sub>4</sub>)<sub>2</sub>[Ce(NO<sub>3</sub>)<sub>6</sub>] as an oxidant ( $E \approx 0.8\text{--}0.9$  V).<sup>72</sup> Its oxidation potential is high enough to allow for a stepwise double oxidation of **6**<sup>2+</sup> to the bis(ruthenium(III)) complex **6**<sup>4+</sup>. Absorption spectra (Fig. 5) were recorded each time after addition of 0.25 equivalents of the oxidant. A broad, symmetrical absorption band appears in the near infrared (NIR) region of the absorption spectrum upon addition of 0  $\rightarrow$  1 equivalents of the oxidant with an absorption maximum at 1165 nm (8585 cm<sup>–1</sup>,  $\epsilon_{\text{max}} = 2620 \text{ M}^{-1} \text{ cm}^{-1}$ , full width at half maximum  $\tilde{\nu}_{1/2} = 6020 \text{ cm}^{-1}$ ). Simultaneously, a second, significantly sharper band appears in the red region (maximum at 716 nm). A set of isosbestic points is observed for the oxidation of **6**<sup>2+</sup> to **6**<sup>3+</sup> at 233, 326, 335, 486, and 619 nm indicating a clean reaction without side products. Upon addition of more oxidant (1  $\rightarrow$  1.5 eq.), a new set of isosbestic points is observed at 273, 325, 335, 638, and 810 nm. Hence, the reaction **6**<sup>2+</sup>  $\rightarrow$  **6**<sup>3+</sup>  $\rightarrow$  **6**<sup>4+</sup> occurs stepwise as expected from the separation of the first and second oxidation waves in the cyclic voltammogram of **6**<sup>2+</sup>. Simultaneously, the intensity of the NIR band decreases while the band in the red region rises further. Interestingly, upon addition of more oxidant (1.5  $\rightarrow$  2 eq.), the isosbestic points are lost and a new absorption band appears at around 940 nm (ESI, Fig. S18†).



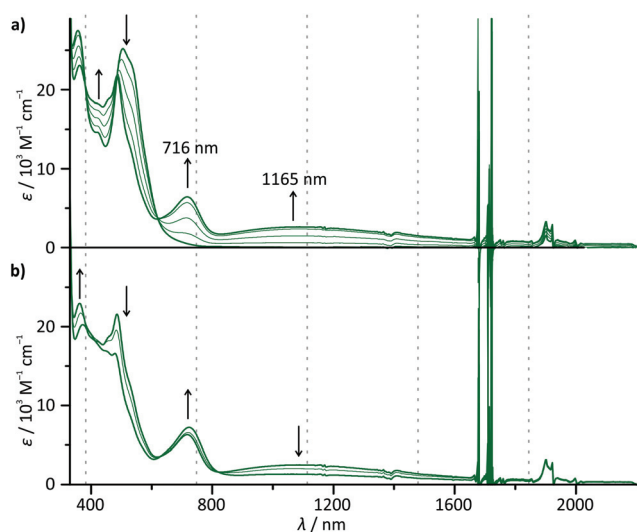


Fig. 5 UV-Vis-NIR absorption spectra of  $6^{2+}$  in acetonitrile solution upon addition (a) of 0  $\rightarrow$  1 equivalents of  $(\text{NH}_4)_2[\text{Ce}(\text{NO}_3)_6]$  as an oxidant and (b) of 1  $\rightarrow$  1.5 equivalents of  $(\text{NH}_4)_2[\text{Ce}(\text{NO}_3)_6]$  as an oxidant. Spectra are recorded after addition of 0.25 equivalents each time.

We ascribe this to the decomposition of the highly charged complex  $6^{4+}$  on the timescale of the measurement (about 45 minutes).

The fact, that the NIR band is only present in the mixed-valent state  $6^{3+}$ , allows for the conclusion that it arises from an intervalence charge transfer (IVCT) process between the two metal centers  $\text{Ru}^{\text{II}} \rightarrow \text{Ru}^{\text{III}}$ . The absorption band in the red spectral region on the other hand is ascribed to ligand-to-metal (LMCT) transitions in the newly formed  $\text{Ru}^{\text{III}}$  fragment ( $\text{dpb} \rightarrow \text{Ru}$ ). This is supported by TD-DFT calculations which predict such a symmetry allowed IVCT transition ( $d_{yz}(\text{Ru}) + \text{dpb-CO} \rightarrow d_{yz}(\text{Ru}) + \text{dpb-NH}$ ) to occur at a wavelength of 1395 nm and LMCT excitations at around 630 nm for  $6^{3+}$  (ESI, Table S9†). Additionally, the absorption spectra of the mononuclear complexes  $1^+$  and  $3^+$  exhibit very similar LMCT bands in the range between 600 and 800 nm upon oxidation under the same conditions (ESI, Fig. S19†). In particular, the excellent agreement between the LMCT maximum of  $1^{2+}$  (720 nm) and  $6^{3+}$  (716 nm) underlines that the first oxidation of  $6^{2+}$  occurs at the *N*-substituted  $[\text{Ru}(\text{dpb})(\text{tpy})]^+$  fragment.

Although a straight-forward Hush analysis of the band shape and energy of the IVCT band is formally not correct due to the energy difference  $\Delta G_0$  of the two valence isomers  $[(\text{tpy})\text{Ru}^{\text{II}}(\text{dpb-NHCO-dpb})\text{Ru}^{\text{III}}(\text{tpy})]^{3+}$  and  $[(\text{tpy})\text{Ru}^{\text{III}}(\text{dpb-NHCO-dpb})\text{Ru}^{\text{II}}(\text{tpy})]^{3+}$ , the latter being the lower energy isomer, we analysed the IVCT band to obtain a rough estimate of the electronic coupling parameter  $V_{\text{ab}}$  (ESI, Fig. S20†).<sup>49,73</sup> As the donor-acceptor distance  $r_{\text{MM}}$ , the Ru-Ru distance of 13.1 Å (from DFT calculation) was taken into account despite the fact that the involved orbitals are substantially delocalized towards the cyclometalated bridging ligand, thus rendering the effective charge transfer distance smaller.<sup>59,60,74-76</sup> As using a too large value for  $r_{\text{MM}}$  will underestimate the electronic coupling

parameter, the calculated  $V_{\text{ab}}$  value of  $580 \text{ cm}^{-1}$  represents a lower limit. This coupling in  $6^{3+}$  is roughly half as strong as in the back-to-back linked symmetrical dinuclear complex  $[(\text{tpy})\text{Ru}(\text{dpb-dpb})\text{Ru}(\text{tpy})]^{3+}$  ( $\text{tpy} = 4'$ -tolylterpyridine).<sup>59</sup> We attribute this weakening to the redox asymmetry introduced by the amide bridge in  $6^{3+}$ . Simultaneously, the NHCO group increases the donor-acceptor distance and reduces the orbital overlap between the two complex moieties. Clearly, the mixed-valent complex  $6^{3+}$  has to be assigned to the Robin-Day class II with localized valencies and a moderate electronic coupling between the complex subunits.<sup>48</sup> The activation barrier for thermal electron transfer can be calculated when the strength of electronic coupling and the energy difference  $\Delta G_0$  of the two valence isomers are known.<sup>52</sup> The latter can be estimated based on the difference in redox potentials of the  $\text{Ru}^{\text{II}}/\text{Ru}^{\text{III}}$  couple of the two complex subunits. Since for  $6^{2+}$ , this difference is shifted towards larger values due to charge accumulation and the resonance stabilization of the mixed-valent species  $6^{3+}$ , we used the difference in  $\text{Ru}^{\text{II}}/\text{Ru}^{\text{III}}$  redox potentials of the mononuclear complexes  $1^+$  and  $3^+$  to estimate  $\Delta G_0$  as 0.22 eV ( $1775 \text{ cm}^{-1}$ ,  $21 \text{ kJ mol}^{-1}$ ).<sup>52</sup> This yields an activation barrier of the electron transfer from  $[(\text{tpy})\text{Ru}^{\text{III}}(\text{dpb-NHCO-dpb})\text{Ru}^{\text{II}}(\text{tpy})]^{3+}$  to  $[(\text{tpy})\text{Ru}^{\text{II}}(\text{dpb-NHCO-dpb})\text{Ru}^{\text{III}}(\text{tpy})]^{3+}$  of  $2190 \text{ cm}^{-1}$  ( $26 \text{ kJ mol}^{-1}$ ).

The electronic coupling in  $6^{3+}$  is in contrast to the amide bridged dinuclear ruthenium complex  $[(\text{EtOOC-tpy})\text{Ru}^{\text{II}}(\text{tpy-NHCO-tpy})\text{Ru}^{\text{III}}(\text{tpy-NHCOMe})]^{5+}$ .<sup>55</sup> Based on a simple molecular orbital consideration, the electronic coupling occurs *via* a superexchange mechanism involving the bridge's frontier orbitals.<sup>77,78</sup> In the bis(terpyridine)ruthenium system, these are well separated in energy from the donor and acceptor orbitals at the metal centers. Thus, the tunnel barrier for electron transfer is much higher than in  $6^{3+}$  leading to no detectable electronic interaction in the former. In contrast, the mediating bridge orbitals of  $6^{3+}$  are already mixed into the ground state donor and acceptor orbitals of the metal centers, significantly increasing the electronic coupling in  $6^{3+}$ .<sup>55</sup> Obviously, cyclometalating bridging ligands enable electronic communication in mixed-valent  $\text{Ru}^{\text{II}}/\text{Ru}^{\text{III}}$  complexes.<sup>59,60,75,76</sup>

### Emission spectroscopy and triplet excited states of complexes $1(\text{PF}_6)-4(\text{PF}_6)$

All four mononuclear complexes  $1(\text{PF}_6)-4(\text{PF}_6)$  exhibit very weak room temperature emission in the red spectral range (Fig. 6 and Table 2). The carboxy-substituted complexes  $3^+$  and  $4^+$  show the highest energy emission along with the highest phosphorescence quantum yield. Both are in excellent agreement with the values for the methyl ester complex reported by van Koten and coworkers.<sup>30</sup> Interestingly, the phosphorescence of these complexes is not quenched by oxygen present during the measurement. This is attributed to very short excited state lifetimes in the picosecond range that are too short for bimolecular quenching processes by triplet oxygen to occur. Indeed, attempts to measure the luminescence lifetimes by time-correlated single photon counting failed underlining that the



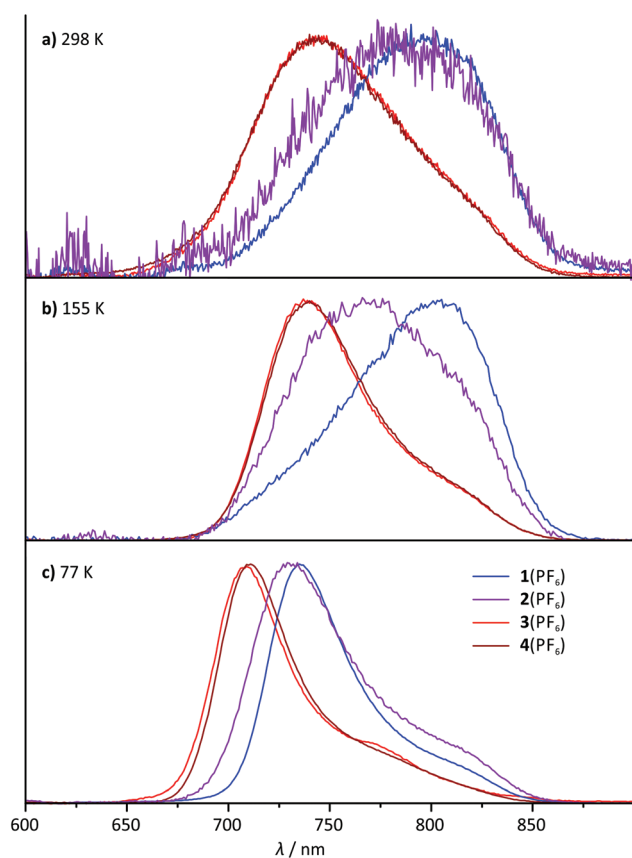


**Fig. 6** Normalized steady-state emission spectra of **1**(PF<sub>6</sub>)–**4**(PF<sub>6</sub>) ( $\lambda_{\text{exc}}$  = 500 nm) (a) at room temperature in degassed acetonitrile solution, (b) at 155 K in liquid butyronitrile solution and (c) at 77 K in a frozen butyronitrile matrix.

excited state lifetimes at room temperature are well below one nanosecond.

The shape of the emission band of the two COOR-substituted compounds **3**<sup>+</sup> and **4**<sup>+</sup> is very similar to that of many other (polypyridine)ruthenium(II) complexes with a vibronic progression resulting in a typical low-energy shoulder.<sup>2,27,31,40</sup> The emission band shape of the *N*-substituted complexes **1**<sup>+</sup> and **2**<sup>+</sup> on the other hand is different. Spectral decomposition in separate Gaussian shaped bands (ESI, Fig. S21†) suggests that 0–1 and especially 0–2 transitions dominate in these complexes at room temperature. The 0–0 transition, which typically is quite strong in other [Ru(dpb)(tpy)]<sup>+</sup>-complexes at room temperature, apparently is of less relevance in complexes with dpb-NHR ligands (ESI, Fig. S21†). Consequently, in a solid butyronitrile matrix at 77 K, a more pronounced hypsochromic shift is observed for complexes **1**<sup>+</sup> (1085 cm<sup>-1</sup>) and **2**<sup>+</sup> (860 cm<sup>-1</sup>) than for **3**<sup>+</sup> and **4**<sup>+</sup> (580 cm<sup>-1</sup>). At 77 K in frozen butyronitrile solution, the carboxy-substituted complexes **3**<sup>+</sup> and **4**<sup>+</sup> emit at a wavelength of 708–709 nm, while the amido- and amino-substituted complexes **1**<sup>+</sup> and **2**<sup>+</sup> emit at 736 and 731 nm, respectively. The similarity in the emission energy of the latter two complexes is remarkable and not straight-forwardly under-

stood from a simple consideration of the HOMO–LUMO gap of the respective complexes (Table 1).

In order to gain a deeper understanding of the excited state properties of the respective complexes, DFT calculations on the excited triplet states were performed. The symmetry allowed emission of (polypyridine)ruthenium(II) complexes arises from a low-energy <sup>3</sup>MLCT state. It exhibits spin density both at the metal site and the  $\pi$ -accepting polypyridine ligand. In fact, in cyclometalated complexes of the type [Ru(dpb-R<sup>1</sup>)(tpy-R<sup>2</sup>)],<sup>+</sup> the LUMO of the terpyridine is always involved in the <sup>3</sup>MLCT emissive state as well.<sup>40</sup> Consequently, geometry optimizations were performed on the triplet states of all complexes under study yielding the respective <sup>3</sup>MLCT states (Fig. 7). Despite the fact that these states are distorted to some extent compared to the singlet ground states (<sup>1</sup>GS) (*vide infra*), it is obvious from the respective spin densities that the <sup>3</sup>MLCT states are composed of HOMO–1 ( $d_{xz}(\text{Ru})$ ) as the electron donor and LUMO ( $\pi_{\text{tpy}}^*$ ) as the electron acceptor. Similar to the previous discussion concerning the <sup>1</sup>MLCT excitations (*vide supra*), this orbital parentage of the <sup>3</sup>MLCT state results in rather similar <sup>3</sup>MLCT–<sup>1</sup>GS energy gaps despite the strongly varying HOMO ( $d_{yz} + \pi_{\text{dpb}}$ )–LUMO gaps.

Insight into excited state deactivation pathways can be gained from temperature dependent measurements of excited state lifetimes or quantum yields. Seminal work by T. J. Meyer and co-workers<sup>22</sup> revealed a metal-centered <sup>3</sup>MC state as a thermally accessible state in [Ru(bpy)<sub>3</sub>]<sup>2+</sup>. This state depopulates the emissive <sup>3</sup>MLCT state and substantially shortens its lifetime at room temperature. In strongly push–pull substituted cyclometalated complexes such as [Ru(dpb-NHCOMe)(tpy-COOEt)]<sup>+</sup>, a second pathway *via* a low-energy ligand-to-ligand (dpb → tpy) charge transfer (<sup>3</sup>LL/CT) state is accessible that prevents emission entirely.<sup>40</sup>

Temperature-dependent steady-state emission spectra were recorded for complexes **1**(PF<sub>6</sub>) and **3**(PF<sub>6</sub>) in butyronitrile solution in the temperature range between 298 K and 155 K (Fig. 8). Due to the low quantum yield of complex **2**(PF<sub>6</sub>) and the spectroscopic similarity of **3**(PF<sub>6</sub>) and **4**(PF<sub>6</sub>), **2**(PF<sub>6</sub>) and **4**(PF<sub>6</sub>) were not considered in this variable temperature (VT) emission study. Interestingly, the VT emission plots  $\ln(\phi)$  vs.  $T^{-1}$  obtained for complexes **1**(PF<sub>6</sub>) and **3**(PF<sub>6</sub>) differ qualitatively from those of [Ru(bpy)<sub>3</sub>](PF<sub>6</sub>)<sub>2</sub> (ESI, Fig. S22 and S23†) and the structurally related complex [Ru(dpb-COOEt)(tpy-NHCOMe)](PF<sub>6</sub>)<sub>2</sub>.<sup>40</sup> The shape of the curves clearly is not linear as has been found for [Ru(dpb-COOEt)(tpy-NHCOMe)]<sup>+</sup>.<sup>40</sup> Meyer's equation<sup>22,23</sup> which assumes a single thermally activated deactivation pathway (<sup>3</sup>MC) for the emissive <sup>3</sup>MLCT state fails to reproduce the shape of the VT emission plots of **1**<sup>+</sup> and **3**<sup>+</sup> as well, while it perfectly fits the VT emission plot of [Ru(bpy)<sub>3</sub>]<sup>2+</sup> (ESI, Fig. S22 and S23†).

A rational explanation for this behaviour was found upon extended DFT examination of the triplet potential energy surface. Besides the emissive <sup>3</sup>MLCT state, two additional low-energy triplet states could be localized as local minima for all four complexes **1**<sup>+</sup>–**4**<sup>+</sup>. These are assigned as <sup>3</sup>MC states with a spin density essentially found on the metal site and as <sup>3</sup>LL/CT





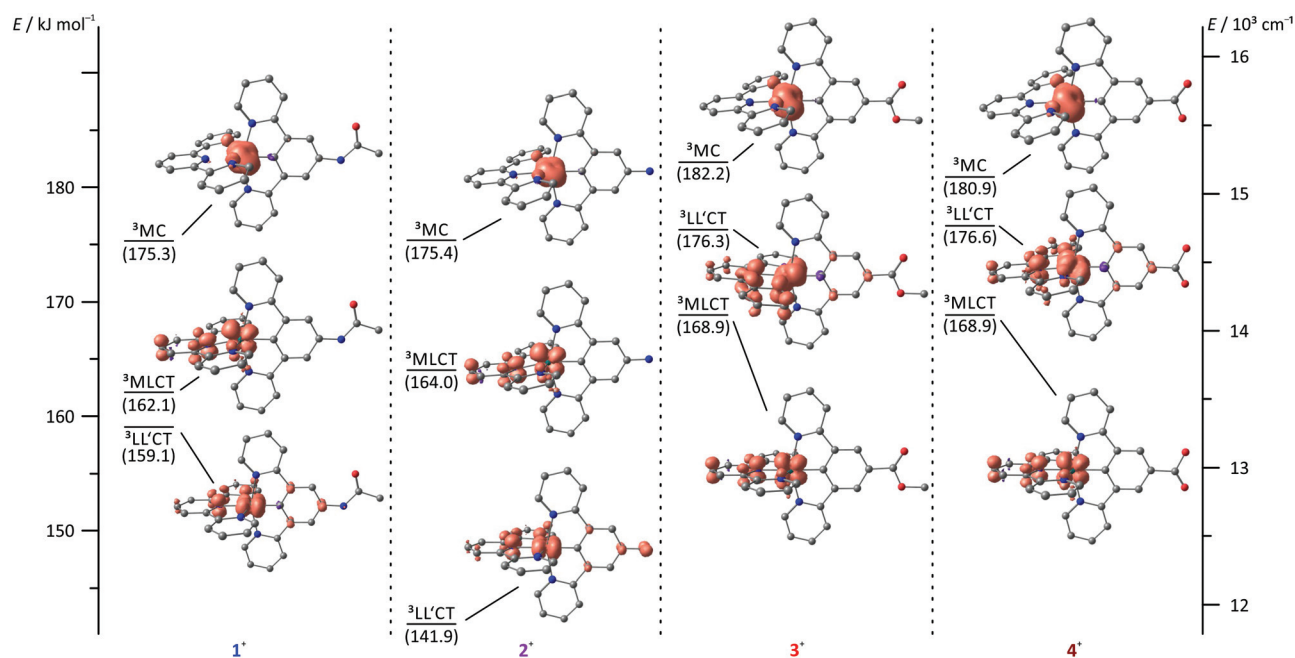


Fig. 7 Jablonski diagram of the triplet states of complexes 1<sup>+</sup>–4<sup>+</sup> including DFT spin density plots (B3LYP, def2-SV(P), COSMO (acetonitrile), ZORA; contour value: 0.01). <sup>3</sup>MLCT energies are given as experimental 0–0 emission energies, <sup>3</sup>LL'CT and <sup>3</sup>MC energies are calculated based on DFT derived Gibbs free energies relative to the respective <sup>3</sup>MLCT energy and given in kJ mol<sup>-1</sup>. Hydrogen atoms are omitted for clarity.

states in which the tpy ligand can be formally regarded as singly reduced while the Ru–dpb moiety carries an electron hole.<sup>40</sup> This latter low-energy state was considered responsible for the lack of emission from the strongly donor–acceptor substituted complex [Ru(dpb-NHCOME)(tpy-COOEt)]<sup>+</sup> because the orthogonality of the orbitals of the electron and hole prevents the radiative recombination from the <sup>3</sup>LL'CT state.<sup>40</sup>

Remarkably, all triplet states exhibit characteristic distortions compared to the geometry of the respective singlet ground state structures with a strong resemblance between the COOR-substituted complex on one side and the NHR-substituted complex on the other (Fig. 7). In the <sup>3</sup>MLCT states of complexes 3<sup>+</sup> and 4<sup>+</sup>, the arrangement of the ligand periphery is essentially unaltered while the metal center is shifted towards the tpy ligand. The Ru–N<sup>tpy</sup> central bond length is shortened by 2 pm (<sup>1</sup>GS: 204 pm, <sup>3</sup>MLCT: 206 pm for 3<sup>+</sup> and 4<sup>+</sup>) while the Ru–C<sup>dpb</sup> bond is elongated by 4 pm in both cases (<sup>1</sup>GS: 195 pm, <sup>3</sup>MLCT: 199 pm for 3<sup>+</sup> and 4<sup>+</sup>). This is in agreement with an increased coulombic interaction between the formally oxidized Ru and reduced tpy ligands upon population of the <sup>3</sup>MLCT state and has been described before for other polypyridine ruthenium complexes.<sup>35,40</sup> All Ru–N bonds involving the four peripheral pyridines are nearly unaffected with similar bond lengths between 210 pm and 212 pm in all cases. This is in stark contrast to the geometry of the <sup>3</sup>MLCT state of both 1<sup>+</sup> and 2<sup>+</sup>. Here, the ligand periphery is substantially distorted compared to the <sup>1</sup>GS geometry: the central pyridine ring of the tpy unit is offset from the plane perpendicular to the dpb ligand with a central N<sup>tpy</sup>–Ru–C<sup>dpb</sup> bond angle of just 167°. At the same time, one of the two peripheral pyridine

rings of the dpb unit is shifted away from the metal center to some extent yielding a long Ru–N bond of 219 pm while the *trans* Ru–N bond is shortened to 209 pm (from 212 pm in the <sup>1</sup>GS of 1<sup>+</sup> and 2<sup>+</sup>). A similar shift of the metal center towards the tpy ligand as observed for 3<sup>+</sup> and 4<sup>+</sup> is also found for 1<sup>+</sup> and 2<sup>+</sup>. This difference in the geometry of the <sup>3</sup>MLCT states between the NHR- and COOR-substituted complexes might explain the dominance of 0–2 transitions in the emission spectra of 1<sup>+</sup> and 2<sup>+</sup> as it corresponds to a larger horizontal offset on the <sup>1</sup>GS–<sup>3</sup>MLCT reaction coordinate.

In the <sup>3</sup>LL'CT states again a clear distinction is found between the geometries of complexes 1<sup>+</sup> and 2<sup>+</sup> on one side and 3<sup>+</sup> and 4<sup>+</sup> on the other. The <sup>3</sup>LL'CT geometries of complexes 1<sup>+</sup> and 2<sup>+</sup> appear essentially undistorted compared to the <sup>1</sup>GS structures with a slight elongation of the central Ru–N<sup>tpy</sup> bond by about 4 pm.<sup>40</sup> A similar shift is observed in the <sup>3</sup>LL'CT states of complexes 3<sup>+</sup> and 4<sup>+</sup>. Yet, in their <sup>3</sup>LL'CT geometries, the tpy ligand is twisted by about 8° out of the plane perpendicular to the dpb ligand.

The <sup>3</sup>MC states of all four complexes appear structurally similar with immensely elongated bond lengths between Ru and the tpy nitrogen atoms (central Ru–N<sup>tpy</sup> bonds: 225–227 pm, peripheral Ru–N<sup>tpy</sup> bonds: 235–237 pm). This distortion is accompanied by a tilt of the peripheral pyridine rings compared to the central one within the tpy unit by 9–11°. The dpb ligand on the other side is undistorted with typical Ru–dpb bond lengths (central Ru–C<sup>dpb</sup> bonds: 195–196 pm, peripheral Ru–N<sup>dpb</sup> bonds: 215–217 pm).

Based on DFT calculated Gibbs free energies, the <sup>3</sup>LL'CT state is the triplet ground state of the NHR-substituted com-



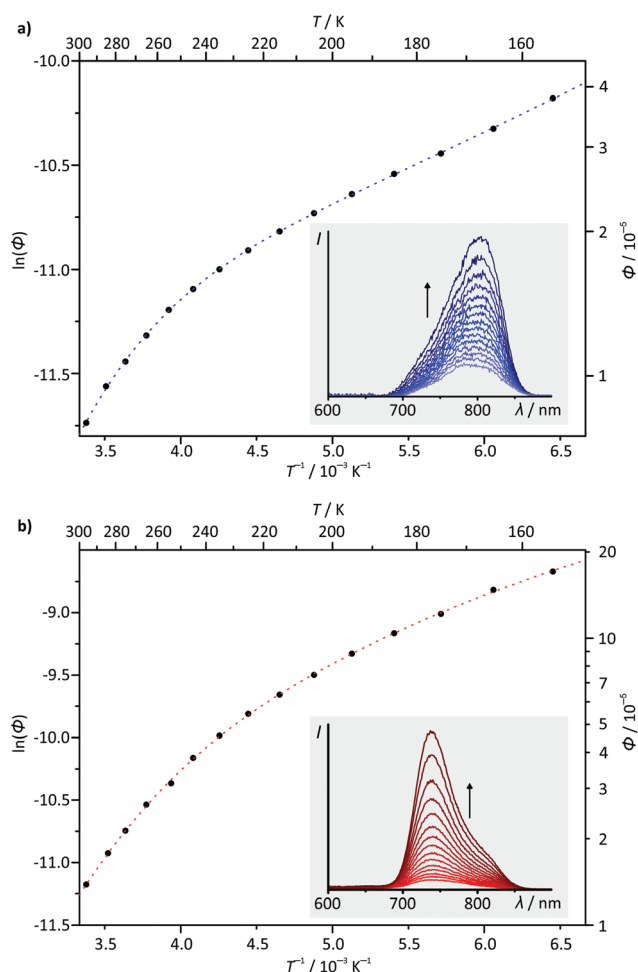


**Fig. 8** Variable-temperature emission plots of  $\ln(\phi)$  vs.  $T^{-1}$  for complexes (a) **1**(PF<sub>6</sub>) and (b) **3**(PF<sub>6</sub>) including fit curves (dashed lines; see the text for fit function and parameters). The insets show emission spectra in the range between 298 K and 155 K.

plexes **1**<sup>+</sup> and **2**<sup>+</sup> (Fig. 7) followed by the <sup>3</sup>MLCT and <sup>3</sup>MC states. This order is identical to that of the strongly donor-acceptor substituted complex [Ru(dpb-NHCOMe)(tpy-COOEt)]<sup>+</sup>.<sup>40</sup> In complexes **3**<sup>+</sup> and **4**<sup>+</sup>, in which the donor strength of the dpb ligand is weakened by the COOR substituents, the order of <sup>3</sup>MLCT and <sup>3</sup>LL/CT is inverted. Increasing the push-pull substitution of a given heteroleptic [Ru(dpb)(tpy)]<sup>+</sup> complex will lower the energy of a donor-acceptor charge-separated state, here the <sup>3</sup>LL/CT state, relative to the other excited states. Remarkably, the trends of the geometrical features of the various states can be related to their relative energies. While for **1**<sup>+</sup> and **2**<sup>+</sup>, the <sup>3</sup>LL/CT state is the least distorted compared to the <sup>1</sup>GS geometries, for **3**<sup>+</sup> and **4**<sup>+</sup> this is true for the <sup>3</sup>MLCT state instead.

Considering the relative energies of the various triplet states, it is apparent that the emissive <sup>3</sup>MLCT state is flanked by two non-emissive states (<sup>3</sup>MC and <sup>3</sup>LL/CT) for all four complexes. Both are thermally accessible, instead of just a single state (<sup>3</sup>MC) as in [Ru(bpy)<sub>3</sub>](PF<sub>6</sub>)<sub>2</sub>. The presence of a second

non-emissive state at low energy gives rise to an additional excited state deactivation pathway.<sup>40</sup> This is important for the interpretation of the temperature dependence of the emission spectra of **1**(PF<sub>6</sub>) and **3**(PF<sub>6</sub>) (Fig. 8). In fact, a second exponential term needs to be taken into account, compared to Meyer's original equation which accounts for a single depopulating state.<sup>22,23</sup> Including a second state yields the following equation (for derivation see the ESI<sup>†</sup>):

$$\ln(\phi) = \ln(k_r) - \ln[k_r + k_{nr} + k_1 \exp(-\Delta E_1/RT) + k_2 \exp(-\Delta E_2/RT)].$$

The rate constants  $k_r$  and  $k_{nr}$  describe the radiative and non-radiative decays (<sup>3</sup>MLCT → <sup>1</sup>GS),  $\Delta E_1$  corresponds to the activation barrier for surface crossing from the <sup>3</sup>MLCT to the <sup>3</sup>MC state ( $\Delta E_1 = \Delta G_1^\ddagger$ ) and  $k_1$  is the rate constant for this surface crossing at infinite temperature as shown by Meyer.<sup>22</sup>

An analogous equation was previously used by Balzani and coworkers to describe the photodynamics of complexes of the [Ru(bpy)<sub>3</sub>]<sup>2+</sup> family.<sup>79,80</sup> In these cases,  $\Delta E_1$  corresponds to the barrier for the thermally activated <sup>3</sup>MLCT → <sup>3</sup>MC surface crossing while  $\Delta E_2$  (typically <1 kJ mol<sup>-1</sup>) is interpreted as the energy separation between multiple close-lying <sup>3</sup>MLCT states split by spin-orbit coupling.<sup>80-82</sup>

In the present study,  $\Delta E_2$  can be interpreted either as the energy difference  $\Delta G_0$  of the <sup>3</sup>MLCT and <sup>3</sup>LL/CT states in thermal equilibrium or the activation barrier  $\Delta G_2^\ddagger$  for the surface crossing from the <sup>3</sup>MLCT to the <sup>3</sup>LL/CT state (see the ESI<sup>†</sup> for in-depth elaboration). This depends on the relative rate constants for the reverse internal conversion <sup>3</sup>LL/CT → <sup>3</sup>MLCT and the non-radiative intersystem crossing (ISC) to the ground state (<sup>3</sup>LL/CT → <sup>1</sup>GS). Upon cooling of solutions of all four mononuclear complexes, even complexes **1**<sup>+</sup> and **2**<sup>+</sup>, in which the emissive <sup>3</sup>MLCT state is not the triplet ground state, the emission intensity increases. This corroborates that <sup>3</sup>MLCT and <sup>3</sup>LL/CT cannot be in thermal equilibrium at least in complexes **1**<sup>+</sup> and **2**<sup>+</sup>. For complexes **3**<sup>+</sup> and **4**<sup>+</sup>, this conclusion cannot be drawn purely based on the temperature dependence of the emission quantum yield, since both, the energy difference of the <sup>3</sup>MLCT and <sup>3</sup>LL/CT states and the activation barrier  $\Delta G_2^\ddagger$ , are positive. Based on the DFT calculated energies of the activation barriers for the <sup>3</sup>MLCT-<sup>3</sup>LL/CT surface crossing and the experimentally determined  $\Delta E_2$  values (*vide infra*), however, it is plausible, that also for complexes **3**<sup>+</sup> and **4**<sup>+</sup>, the surface crossing into the <sup>3</sup>LL/CT state is irreversible and followed by rapid relaxation into the singlet ground state. Consequently,  $\Delta E_2$  is identified in analogy to  $\Delta E_1 = \Delta G_1^\ddagger$  as the activation barrier  $\Delta G_2^\ddagger$  for the thermal depopulation of the <sup>3</sup>MLCT *via* the <sup>3</sup>LL/CT states.

Based on the very similar 0-0 emission energies which should give similar rate constants for the non-radiative decay (<sup>3</sup>MLCT → <sup>1</sup>GS), the large differences in the phosphorescence quantum yields of the four complexes **1**<sup>+</sup>-**4**<sup>+</sup> are quite unexpected (Table 2).<sup>83-85</sup> Yet, combining the  $\ln(\phi)$  vs.  $T^{-1}$  plots with the relative energies of the involved states as determined by DFT provides an explanation. For complexes **3**<sup>+</sup> and **4**<sup>+</sup> the





relatively high quantum yield is associated with the emissive  $^3\text{MLCT}$  state being the triplet ground state. For  $1^+$  and  $2^+$  on the other hand, the non-emissive  $^3\text{LL}'\text{CT}$  state becomes the triplet ground state giving rise to a deactivation pathway with a potentially very low activation barrier  $\Delta G_1^\ddagger$ . Due to the small experimentally accessible temperature range, the fit using the biexponential equation given above is overparametrized. Consequently, quantitative results have to be considered very carefully. For  $1^+$ , activation barriers of  $\Delta G_1^\ddagger = 21.7$  and  $\Delta G_2^\ddagger = 2.1$   $\text{kJ mol}^{-1}$  are obtained from the fit, while for  $3^+$ , the activation barriers are  $\Delta G_1^\ddagger = 23.1$  and  $\Delta G_2^\ddagger = 6.2$   $\text{kJ mol}^{-1}$ . Based on the calculated energies of the various triplet states (Fig. 7), it is reasonable to assume that the higher activation barriers  $\Delta G_1^\ddagger$  of  $>20$   $\text{kJ mol}^{-1}$  are associated with the deactivation *via* the  $^3\text{MC}$  state (*vide infra*).  $\Delta G_2^\ddagger$  is very similar for both the NHR- and COOR-substituted complex types, corroborating that the substitution pattern at the cyclometalating ligand only has a marginal effect on the ligand field splitting in the  $[\text{Ru}(\text{dpb-R})(\text{tpy})]^+$  type of complexes. The second activation barrier  $\Delta G_2^\ddagger$  of  $1^+$  is only one third of that of  $3^+$ . Hence, thermal deactivation *via*  $^3\text{LL}'\text{CT}$  states is significantly accelerated by the presence of an electron donating substituent at the dpb ligand explaining the substantially lower quantum yield of the former. Substituents at the tpy ligand on the other hand are expected to influence both activation barriers but especially  $\Delta G_1^\ddagger$  between the  $^3\text{MLCT}$  and  $^3\text{MC}$  states since the substituents at the tpy ligand significantly impact the  $^3\text{MLCT}$  energy.

To gain a better understanding of the excited state processes, we performed DFT based geometry optimizations to find the transition states connecting the  $^3\text{MLCT}$  and the  $^3\text{MC}$  states on one side and the  $^3\text{MLCT}$  and  $^3\text{LL}'\text{CT}$  states on the other. All four transition states could be localized successfully and their nature confirmed by the presence of a single negative vibrational frequency representing the reaction coordinate of the respective transition (Fig. 9). Subsequent spin density calculations further confirmed the nature of the localized states as the desired transition states. For both complexes,  $1^+$  and  $3^+$ , the spin density of the  $^3\text{MLCT}$ - $^3\text{LL}'\text{CT}$  transition state shows contributions of both ligands and, predominantly, the metal center. Remarkably, the spin carrying orbital at the metal center neither corresponds to the  $d_{xy}$  orbital as in the  $^3\text{MLCT}$  state nor to the  $d_{yz}$  orbital as in the  $^3\text{LL}'\text{CT}$  state but is a linear combination of both. This further underlines the transition state character of the localized state. Similarly, the  $^3\text{MLCT}$ - $^3\text{MC}$  transition states of  $1^+$  and  $3^+$  show a substantial amount of spin density at the metal center (1.46 electrons based on Mulliken's spin population analysis). But instead of the nitrogen lone pairs, a tpy  $\pi^*$ -orbital (LUMO of  $1^+$  and  $3^+$ ) contributes to this transition state. The DFT calculated transition state energies  $\Delta G_1^\ddagger(\text{DFT})$  and  $\Delta G_2^\ddagger(\text{DFT})$  and  $G_1^\ddagger(\text{exp.})$  and  $\Delta G_2^\ddagger(\text{exp.})$  extracted from the fits of the  $\ln(\phi)$  vs.  $T^{-1}$  plots show remarkable agreement with deviation as small as  $\pm 2$   $\text{kJ mol}^{-1}$ . This suggests that despite the narrow temperature range of the VT measurement and their very low quantum yields and short excited state lifetimes, a very reasonable

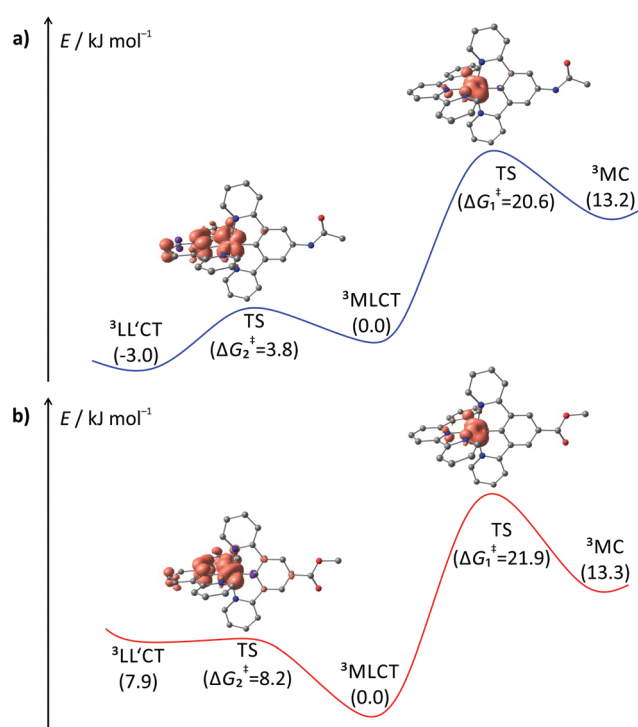


Fig. 9 Profile of the triplet hypersurface of (a)  $1^+$  and (b)  $3^+$  obtained from DFT calculations (B3LYP, def2-SV(P), ZORA, COSMO (acetonitrile)). Gibbs free energies are given in  $\text{kJ mol}^{-1}$  relative to the emissive  $^3\text{MLCT}$  state ( $G_{\text{MLCT}} = 0$   $\text{kJ mol}^{-1}$ ). Spin densities of the transition states (TS) are given at a contour value of 0.01. Hydrogen atoms are omitted for clarity.

description of the excited state deactivation processes can be obtained for these cyclometalated complexes.

In summary, dpb ligands in bis(tridentate)ruthenium(II) complexes indeed induce high-energy  $^3\text{MC}$  states, but give rise to low-energy  $^3\text{LL}'\text{CT}$  states. As for both states, emission is symmetry-forbidden, both contribute to the rapid excited state deactivation observed for these types of complexes. The combination of two  $[\text{Ru}(\text{dpb})(\text{tpy})]^+$  emitters is discussed in the next chapter.

### Emission spectroscopy and triplet excited states of complex $6(\text{PF}_6)_2$

For the dinuclear complex  $6^{2+}$ , a broadened emission spectrum is obtained at room temperature compared to the formally constituting mononuclear complexes  $1^+$  and  $3^+$  (Fig. 10). Additionally, the position of the emission maximum is dependent on the excitation wavelengths and shifts from 756 nm upon excitation at 480 nm to 772 nm when being irradiated at 560 nm (Fig. 10 and Table 2). Measurement at 155 K in butyronitrile yields substantially sharpened emission spectra with an emission maximum at 746 nm and a pronounced shoulder at 800 nm. The intensity of this shoulder increases upon increasing the excitation wavelength from 480 to 560 nm. The blue-shift of the emission maximum ( $180$   $\text{cm}^{-1}$ ) upon freezing the butyronitrile solution of  $6^{2+}$  is much smaller than that of all mononuclear complexes under study.



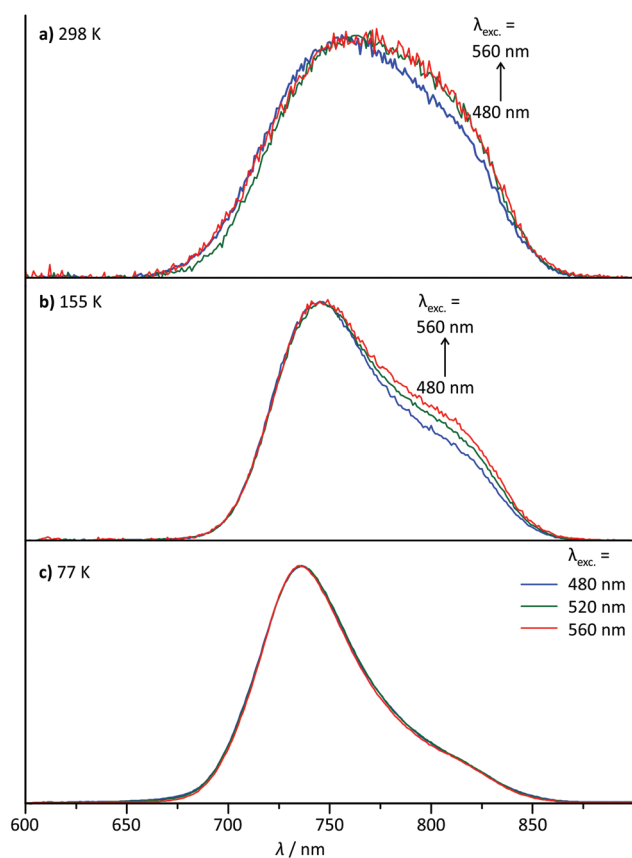


**Fig. 10** Normalized steady-state emission spectra of  $6(\text{PF}_6)_2$  at varying excitation wavelengths (a) at room temperature in degassed acetonitrile solution, (b) at 155 K in liquid butyronitrile solution and (c) at 77 K in a frozen butyronitrile matrix.

A wavelength dependence of the emission maximum from the excitation energy is very atypical for polypyridineruthenium(II) complexes. We ascribe this behaviour to two independent emission processes in solution involving the two complex subunits of  $6^{2+}$ . In fact, similar dual emission processes have previously been invoked to explain the emission wavelength dependence from the excitation energy.<sup>86–89</sup> Unfortunately, attempts to measure the excited state lifetimes by time-correlated single photon counting failed in this case due to the very rapid excited state decay of  $6^{2+}$ . Hence, no evidence for a biexponential character of the excited state decay, which would support the presence of a dual emission mechanism, could be obtained.

However, a reasonable explanation for the dual emission of  $6^{2+}$  can be given based on its absorption characteristics. As shown above, the visible range of the absorption spectrum of  $6^{2+}$  is composed of  $^1\text{MLCT}$  excitations localized on one of the two complex halves. Upon intersystem crossing and vibrational relaxation,  $d_{xz}(\text{Ru}) \rightarrow \text{tpy}$   $^3\text{MLCT}$  states are populated. Two such triplet excited states are conceivable, namely  $^3[(\text{tpy}^-)\text{Ru}^{\text{III}}(\text{dpb-NHCO-dpb})\text{Ru}^{\text{II}}(\text{tpy})]^{2+}$  and  $^3[(\text{tpy})\text{Ru}^{\text{II}}(\text{dpb-NHCO-dpb})\text{Ru}^{\text{III}}(\text{tpy}^-)]^{2+}$ , with the triplet spin density localized on opposing  $[\text{Ru}(\text{tpy})]$  fragments (ESI, Fig. S24<sup>†</sup>). Via double

electron transfer from  $\text{Ru}^{\text{II}}$  to  $\text{Ru}^{\text{III}}$  and from  $\text{tpy}^-$  to  $\text{tpy}$  (Dexter energy transfer), these states could interconvert.<sup>90,91</sup> Apparently, due to the large distance between the two  $[\text{Ru}(\text{tpy})]$  moieties ( $r_{\text{RuRu}} = 13 \text{ \AA}$ ,  $r_{\text{tpy,tpy}} \approx 20 \text{ \AA}$ ), Dexter energy transfer, whose rate constant decays exponentially with distance, is rather slow between the complex subunits. All other radiative and non-radiative relaxation pathways of triplet  $6^{2+}$  are extremely fast (below 1 ns as evidenced from time-resolved emission spectroscopy). Consequently, in fluid solution, emission occurs faster than thermal equilibration between the two emissive  $^3\text{MLCT}$  states. If equilibration was faster than emission, the  $^3[(\text{tpy}^-)\text{Ru}^{\text{III}}(\text{dpb-NHCO-dpb})\text{Ru}^{\text{II}}(\text{tpy})]^{2+}$  state would be favoured over  $^3[(\text{tpy})\text{Ru}^{\text{II}}(\text{dpb-NHCO-dpb})\text{Ru}^{\text{III}}(\text{tpy}^-)]^{2+}$  thermodynamically and would yield single emission at around 800 nm, but this is not observed.

Given that the two  $^3\text{MLCT}$  states are not in thermal equilibrium, it should be possible to selectively populate one or the other excited state by irradiation into one of the two complex subunits. Since in the absorption spectrum of  $6^{2+}$  the absorption bands of the two fragments  $[(\text{tpy})\text{Ru}(\text{dpb-NHR})]$  and  $[(\text{ROC-dpb})\text{Ru}(\text{tpy})]$  overlap substantially, it is not possible to excite them with 100% selectivity (Fig. 4). But by changing the excitation wavelength it is possible to gradually tune the ratio at which the two building blocks are excited. The difference spectrum of the two mononuclear complexes  $1^+$  and  $3^+$  carrying similar functional groups as the two subunits of  $6^{2+}$  (Fig. 4) gives an idea where a maximum difference of absorption can be expected between the NH- and CO-substituted  $[\text{Ru}(\text{dpb})(\text{tpy})]^+$  complex subunits. This difference spectrum reveals a maximized and minimized absorption of the COR-substituted complex at around 480 and 560 nm, respectively. This is in excellent agreement with the above mentioned minimum and maximum of the shoulder at 800 nm in the emission spectrum of  $6^{2+}$  at 155 K. Additionally, the difference spectrum of the emission spectra recorded at 155 K with  $\lambda_{\text{exc}} = 480$  and 560 nm reveals a band with a maximum at 800 nm (ESI, Fig. S25<sup>†</sup>) that resembles the emission band of  $1^+$  at that temperature (Fig. 6b). These observations strongly support that dual emission occurs from two uncoupled  $^3\text{MLCT}$  excited states of the dinuclear complex  $6^{2+}$  in solution.

The origin of this dual emission process is markedly different than that observed for the structurally similar amide-bridged dinuclear complex  $[(\text{EtOOC-tpy})\text{Ru}(\text{tpy-NHCO-tpy})\text{Ru}(\text{tpy-NHCOMe})]^{4+}$ .<sup>55</sup> In the latter, the involved emissive states are sufficiently long-lived and at a significantly shorter distance to allow for thermal equilibration prior to emission. Since the emissive states  $[(\text{EtOOC-tpy})\text{Ru}^{\text{II}}(\text{tpy-NHCO-tpy}^-)\text{Ru}^{\text{III}}(\text{tpy-NHCOMe})]^{4+}$  and  $[(\text{EtOOC-tpy})\text{Ru}^{\text{III}}(\text{tpy-NHCO-tpy}^-)\text{Ru}^{\text{II}}(\text{tpy-NHCOMe})]^{4+}$  are very similar in energy, occupation between the two is Boltzmann distributed leading to dual emission at room temperature.

Interestingly, upon freezing of the butyronitrile solution of  $6^{2+}$ , single emission is observed arising from the NHR-substituted subunit as judged from the position of the emission maximum as well as the independence of the emission band shape from the excitation wavelength (Fig. 10c). This loss of



dual emission can be traced back to the change in the rate constants involved with the excited state decay. Upon freezing the solvent matrix around a given luminescent dye, both non-radiative vibrational relaxation and emissive decay are slowed down substantially. This is because they are typically accompanied by geometrical rearrangements of the dye and the environment and such rearrangements are much more difficult in a rigid solvent cage. The rate for intramolecular Dexter energy transfer on the other hand is not significantly diminished upon freezing of the solvent.<sup>92,93</sup> Consequently, in frozen solution, the two <sup>3</sup>MLCT states of **6**<sup>2+</sup> equilibrate thermally prior to emission from the lower-energy <sup>3</sup>[(tpy<sup>-</sup>)Ru<sup>III</sup>(dpb-NHCO-dpb)Ru<sup>II</sup>(tpy)]<sup>2+</sup> state following Kasha's rule.<sup>94</sup>

## Experimental

### General procedures

Chemicals were obtained from commercial suppliers and used without further purification. Air- or moisture-sensitive reactions were performed in dried glassware under an inert gas atmosphere (argon, quality 4.6). Acetonitrile was refluxed over CaH<sub>2</sub> and distilled under argon prior to use. The ligands *N*-acetyl-3,5-dipyrid-2'-ylaniline **L1**<sup>40</sup> and ethyl 3,5-dipyrid-2'-ylbenzoate **L2**<sup>40</sup> as well as RuCl<sub>3</sub>(tpy)<sup>95</sup> were synthesized following the literature-known procedures. Infrared spectra were recorded on a Varian Excalibur Series 3100 FT-IR spectrometer using KBr disks. IR absorption band intensities are classified as s (strong), m (medium) and w (weak). UV/Vis spectra were recorded on a Varian Cary 5000 spectrometer in 1 cm cuvettes. Emission spectra were recorded on a Varian Cary Eclipse spectrometer. Quantum yields were determined by comparing the areas under the emission spectra on an energy scale recorded for solutions of the samples and a reference with matching absorbances ( $\phi$ ([Ru(bipy)<sub>3</sub>]Cl<sub>2</sub>) = 0.094 in deaerated MeCN).<sup>21</sup> Experimental uncertainty is estimated to be 15%. Low temperature emission spectra were recorded using an Oxford Instruments Optistat DN cryostat with cooling by liquid N<sub>2</sub>. ESI<sup>+</sup> and high resolution ESI<sup>+</sup> mass spectra were recorded on a Micromass QToF Ultima API mass spectrometer with analyte solutions in acetonitrile. Elemental analyses were performed in the microanalytical laboratory of the Chemical Institutes of the University of Mainz. NMR spectra were obtained with a Bruker Avance II 400 spectrometer at 400.31 (<sup>1</sup>H) and 100.66 (<sup>13</sup>C) at 25 °C. Chemical shifts  $\delta$  [ppm] are reported with respect to residual solvent signals as internal standards (<sup>1</sup>H, <sup>13</sup>C): CD<sub>3</sub>CN  $\delta$ (<sup>1</sup>H) = 1.94 ppm,  $\delta$ (<sup>13</sup>C) = 1.32 and 118.26 ppm.<sup>96</sup> Electrochemical experiments were performed with a BioLogic SP-50 voltammetric analyzer at a sample concentration of 10<sup>-3</sup> mol l<sup>-1</sup> using platinum wire as working and counter electrodes and a 0.01 mol l<sup>-1</sup> Ag/AgNO<sub>3</sub> reference electrode. Measurements were carried out at a scan rate of 100 mV s<sup>-1</sup> for cyclic voltammetry experiments and at 10 mV s<sup>-1</sup> for square-wave voltammetry experiments using 0.1 mol l<sup>-1</sup> [*n*Bu<sub>4</sub>N][PF<sub>6</sub>] as the supporting electrolyte in acetonitrile. Potentials are given relative to the ferrocene/ferrocenium

couple (0.40 V vs. SCE,  $E_{1/2} = 0.09 \pm 5$  mV under the given conditions).<sup>72</sup>

### Density functional theory calculations

DFT calculations were carried out using the ORCA program package (version 3.0.2).<sup>97</sup> Tight convergence criteria were chosen for all calculations (keywords TightSCF and TightOpt, convergence criteria for the SCF part: energy change  $1.0 \times 10^{-8}$  E<sub>h</sub>, 1-El. energy change  $1.0 \times 10^{-5}$  E<sub>h</sub>, orbital gradient  $1.0 \times 10^{-5}$ , orbital rotation angle  $1.0 \times 10^{-5}$ , DIIS error  $5.0 \times 10^{-7}$ ; for geometry optimizations: energy change:  $1.0 \times 10^{-6}$  E<sub>h</sub>, max. gradient  $1.0 \times 10^{-4}$  E<sub>h</sub> per bohr, RMS gradient  $3.0 \times 10^{-5}$  E<sub>h</sub> per bohr, max. displacement  $1.0 \times 10^{-3}$  bohr, RMS displacement  $6.0 \times 10^{-4}$  bohr). All calculations employ the resolution of identity (Split-RI-J) approach for the coulomb term in combination with the chain-of-spheres approximation for the exchange term (COSX).<sup>98,99</sup> All calculations were performed using the hybrid functional B3LYP<sup>63</sup> in combination with Ahlrichs' split-valence double- $\xi$  basis set def2-SV(P) which comprises polarization functions for all non-hydrogen atoms.<sup>64,65</sup> Relativistic effects were calculated at the zeroth order regular approximation (ZORA) niveau.<sup>67</sup> The ZORA keyword automatically invokes relativistically adjusted basis sets.<sup>100</sup> To account for solvent effects, a conductor-like screening model (COSMO) modelling acetonitrile was used in all calculations.<sup>68</sup> TD-DFT calculations with at least 50 vertical transitions were carried out based on the def2-SV(P) optimized geometry of the respective complex. Explicit counterions and/or solvent molecules were not taken into account in all cases. To reduce the computational cost, methyl instead of ethyl groups at the ester moiety were used throughout all calculations.

**Synthesis of [Ru(dpb-NHCOCH<sub>3</sub>)(tpy)](PF<sub>6</sub>) **1**(PF<sub>6</sub>).** RuCl<sub>3</sub>(tpy) (250 mg, 0.567 mmol, 1 eq.) and AgBF<sub>4</sub> (320 mg, 1.64 mmol, 2.9 eq.) were dissolved in dry acetone (20 ml) and heated to reflux for 2 h in the dark. The mixture was left to stand for 1 h and filtered through a syringe filter before removing the solvent under reduced pressure. The dark residue was dissolved in *n*BuOH (20 ml) and *N*-acetyl-3,5-dipyrid-2'-ylaniline **L1** (197 mg, 0.680 mmol, 1.2 eq.) was added. The resulting mixture was heated to reflux for 16 h to give a dark purple solution. After the removal of the solvent under reduced pressure, the residue was dissolved in a minimal amount of acetonitrile (5 ml). Upon addition of a solution of NH<sub>4</sub>PF<sub>6</sub> (220 mg, 1.35 mmol, 2.4 eq.) in water (1 ml) followed by slow addition of more water (80 ml), a black solid precipitated which was filtered off. Column chromatography on silica gel (CHCl<sub>3</sub>:MeOH = 7:1) afforded [Ru(dpb-NHCOCH<sub>3</sub>)(tpy)](PF<sub>6</sub>) **1**(PF<sub>6</sub>) as a dark purple solid. Yield: 175 mg (0.228 mmol, 40%). Anal. Calc. for C<sub>33</sub>H<sub>25</sub>F<sub>6</sub>N<sub>6</sub>OPRu (767.6)·H<sub>2</sub>O: C, 50.45; H, 3.46; N, 10.70. Found: C, 50.62; H, 3.31; N, 10.46. MS(ESI<sup>+</sup>): *m/z* (%) = 623.1 (100) [M - PF<sub>6</sub>]<sup>+</sup>. HR-MS(ESI<sup>+</sup>, *m/z*): Calcd for C<sub>33</sub>H<sub>25</sub>N<sub>6</sub>ORu [M - PF<sub>6</sub>]<sup>+</sup>: 617.1166; Found: 617.1177. <sup>1</sup>H NMR (CD<sub>3</sub>CN):  $\delta$  [ppm] = 8.73 (d, <sup>3</sup>J<sub>HH</sub> = 8 Hz, 2H, H<sup>2A</sup>), 8.62 (s, 1H, NH), 8.44–8.35 (m, 4H, H<sup>2B</sup>, H<sup>5A</sup>), 8.24 (t, <sup>3</sup>J<sub>HH</sub> = 8 Hz, 1H, H<sup>1A</sup>), 8.05 (d, <sup>3</sup>J<sub>HH</sub> = 8 Hz, 2H, H<sup>5B</sup>), 7.67 (dt, <sup>3</sup>J<sub>HH</sub> = 8 Hz, <sup>4</sup>J<sub>HH</sub> = 1 Hz, 2H, H<sup>6A</sup>), 7.59 (dt, <sup>3</sup>J<sub>HH</sub> = 8 Hz, <sup>4</sup>J<sub>HH</sub> = 1 Hz, 2H,





H<sup>6B</sup>), 7.11 (d, <sup>3</sup>J<sub>HH</sub> = 5 Hz, 2H, H<sup>8A</sup>), 7.01 (d, <sup>3</sup>J<sub>HH</sub> = 5 Hz, 2H, H<sup>8B</sup>), 6.94 (m, 2H, H<sup>7A</sup>), 6.64 (m, 2H, H<sup>7B</sup>), 2.23 (s, 3H, H<sup>11</sup>). <sup>13</sup>C{<sup>1</sup>H} NMR (CD<sub>3</sub>CN): δ [ppm] = 217.2 (C<sup>9B</sup>), 169.6 (C<sup>10</sup>), 169.4 (C<sup>4B</sup>), 160.1 (C<sup>4A</sup>), 155.3 (C<sup>8A</sup>), 154.0 (C<sup>3A</sup>), 152.9 (C<sup>8B</sup>), 142.5 (C<sup>3B</sup>), 136.4 (C<sup>6B</sup>), 135.9 (C<sup>6A</sup>), 133.6 (C<sup>1B</sup>), 132.7 (C<sup>1A</sup>), 127.2 (C<sup>7A</sup>), 124.4 (C<sup>5A</sup>), 123.2 (C<sup>2A</sup>), 122.5 (C<sup>7B</sup>), 120.6 (C<sup>5B</sup>), 117.8 (C<sup>2A</sup>), 24.3 (C<sup>11</sup>). IR (KBr disk):  $\tilde{\nu}$  [cm<sup>-1</sup>] = 3230 (m, N-H amide), 1650 (s, C=O amide), 1600 (m, C=C), 1520 (w, amide II), 843 (s, P-F).

**Synthesis of [Ru(dpb-NH<sub>2</sub>)(tpy)](PF<sub>6</sub>)<sub>2</sub> (2(PF<sub>6</sub>)).** [Ru(dpb-NHCOCH<sub>3</sub>)(tpy)](PF<sub>6</sub>)<sub>1</sub> (113 mg, 0.147 mmol) was added to a mixture of water (20 ml), methanol (20 ml), hydrazine monohydrate (1 ml) and sodium hydroxide (1 g) and heated to reflux for 16 h. After removal of the solvent under reduced pressure, the dark residue was dissolved in a minimal amount of acetonitrile (5 ml) followed by addition of a solution of NH<sub>4</sub>PF<sub>6</sub> (153 mg, 0.939 mmol, 6.75 eq.) in water (80 ml). The precipitate was filtered off and washed with water (2 × 5 ml) and diethyl ether (2 × 15 ml) giving [Ru(dpb-NH<sub>2</sub>)(tpy)](PF<sub>6</sub>)<sub>2</sub> (2(PF<sub>6</sub>)) as a purple solid. Yield: 92 mg (0.127 mmol, 86%). Anal. Calc. for C<sub>31</sub>H<sub>23</sub>F<sub>6</sub>N<sub>6</sub>PRu (725.6)-0.5H<sub>2</sub>O: C, 50.69; H, 3.29; N, 11.58. Found: C, 50.82; H, 3.05; N, 11.34. MS(ESI<sup>+</sup>): *m/z* (%) = 581.1 (100) [M - PF<sub>6</sub>]<sup>+</sup>. HR-MS(ESI<sup>+</sup>, *m/z*): Calcd for C<sub>31</sub>H<sub>23</sub>N<sub>6</sub>Ru [M - PF<sub>6</sub>]<sup>+</sup>: 575.1060; Found: 575.1071. <sup>1</sup>H NMR (CD<sub>3</sub>CN): δ [ppm] = 8.72 (d, <sup>3</sup>J<sub>HH</sub> = 8 Hz, 2H, H<sup>2A</sup>), 8.40 (d, <sup>3</sup>J<sub>HH</sub> = 8 Hz, 2H, H<sup>5A</sup>), 8.20 (t, <sup>3</sup>J<sub>HH</sub> = 8 Hz, 1H, H<sup>1A</sup>), 8.00 (d, <sup>3</sup>J<sub>HH</sub> = 8 Hz, 2H, H<sup>5B</sup>), 7.74 (s, 2H, H<sup>2B</sup>), 7.67 (t, <sup>3</sup>J<sub>HH</sub> = 8 Hz, 2H, H<sup>6A</sup>), 7.56 (t, <sup>3</sup>J<sub>HH</sub> = 8 Hz, 2H, H<sup>6B</sup>), 7.18 (d, <sup>3</sup>J<sub>HH</sub> = 5 Hz, 2H, H<sup>8A</sup>), 6.97 (dd, <sup>3</sup>J<sub>HH</sub> = 5 Hz, 8 Hz, 2H, H<sup>7A</sup>), 6.93 (d, <sup>3</sup>J<sub>HH</sub> = 5 Hz, 2H, H<sup>8B</sup>), 6.58 (dd, <sup>3</sup>J<sub>HH</sub> = 5 Hz, 8 Hz, 2H, H<sup>7B</sup>), 4.24 (s, 2H, NH<sub>2</sub>). <sup>13</sup>C{<sup>1</sup>H} NMR (CD<sub>3</sub>CN): δ [ppm] = 208.9 (C<sup>9B</sup>), 169.9 (C<sup>94B</sup>), 160.3 (C<sup>4A</sup>), 155.2 (C<sup>8A</sup>), 154.3 (C<sup>3A</sup>), 152.8 (C<sup>8B</sup>), 143.6 (C<sup>1B</sup>), 142.6 (C<sup>3B</sup>), 136.2 (C<sup>6B</sup>), 135.5 (C<sup>6A</sup>), 132.0 (C<sup>1A</sup>), 127.2 (C<sup>7A</sup>), 124.2 (C<sup>5A</sup>), 123.2 (C<sup>2A</sup>), 122.0 (C<sup>7B</sup>), 120.4 (C<sup>5B</sup>), 113.0 (C<sup>2B</sup>). IR (KBr disk):  $\tilde{\nu}$  [cm<sup>-1</sup>] = 3420 (m, N-H amine), 1600 (m, C=C), 843 (s, P-F).

**Synthesis of [Ru(dpb-COOC<sub>2</sub>H<sub>5</sub>)(tpy)](PF<sub>6</sub>)<sub>3</sub> (3(PF<sub>6</sub>)).** [RuCl<sub>3</sub>(tpy)] (250 mg, 0.567 mmol, 1 eq.) and AgBF<sub>4</sub> (320 mg, 1.64 mmol, 2.9 eq.) were dissolved in dry acetone (20 ml) and heated to reflux for 2 h in the dark. The mixture was left to stand for 1 h and filtered through a syringe filter before removing the solvent under reduced pressure. The dark residue was dissolved in *n*BuOH (20 ml) and ethyl 3,5-dipyrid-2'-ylbenzoate L2 (207 mg, 0.680 mmol, 1.2 eq.) was added. The resulting mixture was heated to reflux for 16 h to give a dark purple solution. After removal of the solvent under reduced pressure, the residue was dissolved in a minimal amount of acetonitrile (5 ml). Upon addition of a solution of NH<sub>4</sub>PF<sub>6</sub> (220 mg, 1.35 mmol, 2.4 eq.) in water (1 ml) followed by slow addition of more water (80 ml), a dark red solid precipitated that was filtered off and washed with water (2 × 5 ml) and diethyl ether (2 × 15 ml). Column chromatography on silica gel (CHCl<sub>3</sub>: MeOH = 7 : 1) afforded [Ru(dpb-COOC<sub>2</sub>H<sub>5</sub>)(tpy)](PF<sub>6</sub>)<sub>3</sub> (3(PF<sub>6</sub>)) as a dark red solid. Yield: 229 mg (0.293 mmol, 52%). Anal. Calc. for C<sub>34</sub>H<sub>26</sub>F<sub>6</sub>N<sub>5</sub>O<sub>2</sub>PRu (782.6): C, 52.18; H, 3.35; N, 8.95. Found: C, 52.01; H, 3.34; N, 8.65. MS(ESI<sup>+</sup>): *m/z* (%) = 638.1

(100) [M - PF<sub>6</sub>]<sup>+</sup>. HR-MS(ESI<sup>+</sup>, *m/z*): Calcd for C<sub>34</sub>H<sub>26</sub>N<sub>5</sub>O<sub>2</sub>Ru [M - PF<sub>6</sub>]<sup>+</sup>: 632.1162; Found: 632.1173. <sup>1</sup>H NMR (CD<sub>3</sub>CN): δ [ppm] = 8.85 (s, 2H, H<sup>1B</sup>), 8.74 (d, 2H, <sup>3</sup>J<sub>HH</sub> = 8 Hz, H<sup>2A</sup>), 8.42 (d, 2H, <sup>3</sup>J<sub>HH</sub> = 8 Hz, H<sup>5A</sup>), 8.30 (t, 1H, <sup>3</sup>J<sub>HH</sub> = 8 Hz, H<sup>1A</sup>), 8.27 (d, 2H, <sup>3</sup>J<sub>HH</sub> = 8 Hz, H<sup>5B</sup>), 7.74–7.56 (m, 4H, H<sup>6A</sup>, H<sup>6B</sup>), 7.13–7.04 (m, 4H, H<sup>8A</sup>, H<sup>8B</sup>), 6.91 (t, 2H, <sup>3</sup>J<sub>HH</sub> = 7 Hz, H<sup>7A</sup>), 6.72 (t, 2H, <sup>3</sup>J<sub>HH</sub> = 7 Hz, H<sup>7B</sup>), 4.52 (q, 2H, <sup>3</sup>J<sub>HH</sub> = 7 Hz, H<sup>11</sup>), 1.52 (t, 3H, <sup>3</sup>J<sub>HH</sub> = 7 Hz, H<sup>12</sup>). <sup>13</sup>C{<sup>1</sup>H} NMR (CD<sub>3</sub>CN): δ [ppm] = 232.8 (C<sup>9B</sup>), 168.9 (C<sup>4B</sup>), 168.6 (C<sup>10B</sup>), 159.8 (C<sup>4A</sup>), 155.4 (C<sup>8A</sup>), 153.5 (C<sup>3A</sup>), 152.8 (C<sup>8B</sup>), 143.1 (C<sup>3A</sup>), 136.7 (C<sup>6B</sup>), 136.4 (C<sup>6A</sup>), 133.8 (C<sup>1A</sup>), 127.3 (C<sup>7A</sup>), 124.6 (C<sup>2B</sup>), 124.5 (C<sup>6A</sup>), 123.3 (C<sup>2A</sup>), 123.0 (C<sup>7B</sup>), 120.9 (C<sup>1B</sup>), 61.5 (C<sup>11</sup>), 14.9 (C<sup>12</sup>). IR (KBr disk):  $\tilde{\nu}$  [cm<sup>-1</sup>] = 1695 (s, C=O ester), 1600, 1582 (m, C=C), 843 (s, P-F).

**Synthesis of [Ru(dpb-COOH)(tpy)](PF<sub>6</sub>)<sub>4</sub> (4(PF<sub>6</sub>)).** [Ru(dpb-COOC<sub>2</sub>H<sub>5</sub>)(tpy)](PF<sub>6</sub>)<sub>3</sub> (3(PF<sub>6</sub>)) (154 mg, 0.197 mmol) was added to a mixture of water (20 ml), methanol (20 ml), hydrazine monohydrate (1 ml) and sodium hydroxide (1 g) and heated to reflux for 16 h. After removal of the solvent under reduced pressure, the dark residue was dissolved in a minimal amount of acetonitrile (5 ml) followed by slow addition of 1 mol per l aqueous H<sub>2</sub>SO<sub>4</sub> to adjust the pH to 1. Upon addition of a solution of NH<sub>4</sub>PF<sub>6</sub> (145 mg, 0.890 mmol, 4.5 eq.) in water (40 ml) the product precipitated. The complex was filtered off and washed with water (2 × 5 ml) and diethyl ether (2 × 15 ml). Column chromatography on silica gel (CHCl<sub>3</sub>: MeOH = 5 : 1) afforded [Ru(dpb-COOH)(tpy)](PF<sub>6</sub>)<sub>4</sub> (4(PF<sub>6</sub>)) as a dark red solid. Yield: 82 mg (0.109 mmol, 55%). Anal. Calc. for C<sub>32</sub>H<sub>22</sub>F<sub>6</sub>N<sub>5</sub>O<sub>2</sub>PRu (754.6): C, 50.93; H, 2.94; N, 9.28. Found: C, 50.64; H, 2.51; N, 9.42. MS(ESI<sup>+</sup>): *m/z* (%) = 610.1 (100) [M - PF<sub>6</sub>]<sup>+</sup>. HR-MS(ESI<sup>+</sup>, *m/z*): Calcd for C<sub>32</sub>H<sub>22</sub>N<sub>5</sub>O<sub>2</sub>Ru [M - PF<sub>6</sub>]<sup>+</sup>: 604.0849; Found: 604.0873. <sup>1</sup>H NMR (CD<sub>3</sub>CN): δ [ppm] = 8.85 (s, 2H, H<sup>2B</sup>), 8.74 (d, <sup>3</sup>J<sub>HH</sub> = 8 Hz, 2H, H<sup>2A</sup>), 8.42 (d, <sup>3</sup>J<sub>HH</sub> = 8 Hz, 2H, H<sup>5A</sup>), 8.33–8.24 (m, 3H, H<sup>1A</sup>, H<sup>5B</sup>), 7.74–7.67 (m, 2H, H<sup>6A</sup>), 7.67–7.60 (m, 2H, H<sup>6B</sup>), 7.13–7.05 (m, 4H, H<sup>8A</sup>, H<sup>8B</sup>), 6.91 (ddd, <sup>3</sup>J<sub>HH</sub> = 7 Hz, 6 Hz, <sup>4</sup>J<sub>HH</sub> = 1 Hz, 2H, H<sup>7A</sup>), 6.72 (ddd, <sup>3</sup>J<sub>HH</sub> = 7 Hz, 6 Hz, <sup>4</sup>J<sub>HH</sub> = 1 Hz, 2H, H<sup>7B</sup>). <sup>13</sup>C{<sup>1</sup>H} NMR (CD<sub>3</sub>CN): δ [ppm] = 233.3 (C<sup>9B</sup>), 169.4 (C<sup>10</sup>), 168.9 (C<sup>4B</sup>), 159.8 (C<sup>4A</sup>), 155.5 (C<sup>8A</sup>), 153.5 (C<sup>3A</sup>), 152.8 (C<sup>8B</sup>), 143.2 (C<sup>3B</sup>), 136.7 (C<sup>6B</sup>), 136.4 (C<sup>6A</sup>), 133.9 (C<sup>1A</sup>), 127.4 (C<sup>7A</sup>), 125.0 (C<sup>2B</sup>), 124.6 (C<sup>5A</sup>), 123.4 (C<sup>2A</sup>), 123.1 (C<sup>7B</sup>), 122.4 (C<sup>1B</sup>), 121.0 (C<sup>5B</sup>). IR (KBr disk):  $\tilde{\nu}$  [cm<sup>-1</sup>] = 3440 (s, O-H acid), 1665 (s, C=O acid), 1602, 1579 (m, C=C), 843 (s, P-F).

**Synthesis of [Ru(dpb-COOBt)(tpy)](PF<sub>6</sub>)<sub>5</sub> (5(PF<sub>6</sub>)).** [Ru(dpb-COOC<sub>2</sub>H<sub>5</sub>)(tpy)](PF<sub>6</sub>)<sub>4</sub> (4(PF<sub>6</sub>)) (42 mg, 0.056 mmol, 1 eq.), *N,N'*-diisopropylcarbodiimide (15 mg, 0.119 mmol, 2.1 eq.) and *N*-hydroxybenzotriazole (HOBt, 18 mg, 0.117 mmol, 2.1 eq.) were dissolved in dry acetonitrile (20 ml) and stirred for 16 h at room temperature. After removal of the solvent under reduced pressure, the dark residue was dissolved in acetonitrile (5 ml). The product was precipitated by addition of NH<sub>4</sub>PF<sub>6</sub> (95 mg, 0.583 mmol, 10.4 eq.) and water (50 ml), filtered off and washed with water (2 × 5 ml) and diethyl ether (2 × 15 ml). [Ru(dpb-COOBt)(tpy)](PF<sub>6</sub>)<sub>5</sub> (5(PF<sub>6</sub>)) was obtained as a dark red solid. Yield: 45 mg (0.052 mmol, 92%). Anal. Calc. for C<sub>38</sub>H<sub>25</sub>F<sub>6</sub>N<sub>8</sub>O<sub>2</sub>PRu (871.69): C, 52.36; H, 2.89; N, 12.85.



Found: C, 52.42; H, 2.53; N, 12.54. MS(ESI<sup>+</sup>): *m/z* (%) = 699.1 (11) [M - PF<sub>6</sub> - N<sub>2</sub>]<sup>+</sup>, 727.1 (100) [M - PF<sub>6</sub>]<sup>+</sup>, 1599.2 (8) [2M - PF<sub>6</sub>]<sup>+</sup>. HR-MS(ESI<sup>+</sup>, *m/z*): Calcd for C<sub>38</sub>H<sub>25</sub>N<sub>8</sub>O<sub>2</sub>Ru [M - PF<sub>6</sub>]<sup>+</sup>: 721.1176; Found: 721.1192. <sup>1</sup>H NMR (CD<sub>3</sub>CN): δ [ppm] = 9.05 (s, 2H, H<sup>2B</sup>), 8.77 (d, 2H, <sup>3</sup>J<sub>HH</sub> = 8 Hz, H<sup>2A</sup>), 8.44 (d, 2H, <sup>3</sup>J<sub>HH</sub> = 8 Hz, H<sup>5A</sup>), 8.35 (t, 1H, <sup>3</sup>J<sub>HH</sub> = 8 Hz, H<sup>1A</sup>), 8.34 (d, 2H, <sup>3</sup>J<sub>HH</sub> = 8 Hz, H<sup>5B</sup>), 8.16 (d, 1H, <sup>3</sup>J<sub>HH</sub> = 9 Hz, H<sup>2C</sup>), 7.83 (d, 1H, <sup>3</sup>J<sub>HH</sub> = 8 Hz, H<sup>5C</sup>), 7.77–7.66 (m, 5H, H<sup>6A</sup>, H<sup>6B</sup>, H<sup>4C</sup>), 7.58 (t, 1H, H<sup>3C</sup>), 7.20 (d, 2H, <sup>3</sup>J<sub>HH</sub> = 5 Hz, H<sup>8B</sup>), 7.13 (d, 2H, <sup>3</sup>J<sub>HH</sub> = 5 Hz, H<sup>8A</sup>), 6.96 (t, 2H, <sup>3</sup>J<sub>HH</sub> = 6 Hz, H<sup>7A</sup>), 6.80 (t, 2H, <sup>3</sup>J<sub>HH</sub> = 6 Hz, H<sup>7B</sup>). <sup>13</sup>C {<sup>1</sup>H} NMR (CD<sub>3</sub>CN): δ [ppm] = 239.5 (C<sup>9B</sup>), 168.2 (C<sup>4B</sup>), 165.7 (C<sup>10</sup>), 159.7 (C<sup>4A</sup>), 155.5 (C<sup>8A</sup>), 153.3 (C<sup>3A</sup>), 152.9 (C<sup>8B</sup>), 144.5 (C<sup>1C</sup>), 144.2 (C<sup>3B</sup>), 137.0 (C<sup>6B</sup>), 136.9 (C<sup>6A</sup>), 134.8 (C<sup>1A</sup>), 130.1 (C<sup>4C</sup>), 127.5 (C<sup>7A</sup>), 126.2 (C<sup>3C</sup>), 124.9 (C<sup>2B</sup>), 124.8 (C<sup>5A</sup>), 123.6 (C<sup>7B</sup>), 123.5 (C<sup>2A</sup>), 121.3 (C<sup>2C</sup>), 121.1 (C<sup>6C</sup>), 115.4 (C<sup>1B</sup>), 110.0 (C<sup>5C</sup>).

**Synthesis of [(tpy)Ru(dpb-NHCO-dpb)Ru(tpy)](PF<sub>6</sub>)<sub>2</sub> 6(PF<sub>6</sub>)<sub>2</sub>.** In separate Schlenk flasks, [Ru(dpb-NH<sub>2</sub>)(tpy)](PF<sub>6</sub>) 2(PF<sub>6</sub>) (35 mg, 0.048 mmol, 1 eq.) and [Ru(dpb-COOBt)(tpy)](PF<sub>6</sub>) 5(PF<sub>6</sub>) (42 mg, 0.048 mmol, 1 eq.) were dissolved in dry acetonitrile (10 ml). Molecular sieves (3 Å) were added and the mixtures were left to stand overnight to remove crystal water. Both solutions were then combined in a third Schlenk flask and *tert*-butylimino-tris(dimethylamino)phosphorane (P<sub>1</sub>-*t*Bu) (34 mg, 0.144 mmol, 3 eq.) was added. The resulting solution was stirred at 50 °C for 16 h. After quenching the reaction by addition of NH<sub>4</sub>PF<sub>6</sub> (180 mg, 1.10 mmol, 23 eq.) dissolved in water (2 ml), the solution was concentrated to 5 ml and the product was triturated by addition of water (80 ml). The precipitate was filtered off, washed with water (2 × 5 ml) and diethyl ether (2 × 15 ml) and purified by column chromatography on silica gel (CHCl<sub>3</sub>:MeOH = 7:1) affording [(tpy)Ru(dpb-NHCO-dpb)Ru(tpy)](PF<sub>6</sub>)<sub>2</sub> 6(PF<sub>6</sub>)<sub>2</sub> as a dark red solid. Yield: 14 mg (0.0096 mmol, 20%). Anal. Calc. for C<sub>63</sub>H<sub>43</sub>F<sub>12</sub>N<sub>11</sub>OP<sub>2</sub>Ru<sub>2</sub> (1462.16)·4H<sub>2</sub>O: C, 49.32; H, 3.35; N, 10.04. Found: C, 49.39; H, 3.76; N, 10.36. MS(ESI<sup>+</sup>): *m/z* (%) = 296.6 (3) [M - 2PF<sub>6</sub>]<sup>4+</sup>, 390.8 (17) [M - 2PF<sub>6</sub>]<sup>3+</sup>, 586.6 (100) [M - 2PF<sub>6</sub>]<sup>2+</sup>, 1318.3 (5) [M - PF<sub>6</sub>]<sup>+</sup>. HR-MS(ESI<sup>+</sup>, *m/z*): Calcd for C<sub>63</sub>H<sub>43</sub>N<sub>11</sub>ORu<sub>2</sub> [M - 2PF<sub>6</sub>]<sup>2+</sup>: 586.5885; Found: 586.5884. <sup>1</sup>H NMR (CD<sub>3</sub>CN): δ [ppm] = 9.63 (s, 1H, NH), 9.09 (s, 2H, H<sup>2A</sup>), 8.83 (s, 2H, H<sup>2B</sup>), 8.80–8.74 (m, 4H, H<sup>2,1tpy</sup>), 8.44 (m, 4H, H<sup>5,1tpy</sup>), 8.39 (d, <sup>3</sup>J<sub>HH</sub> = 8 Hz, 2H, H<sup>5A</sup>), 8.32 (t, <sup>3</sup>J<sub>HH</sub> = 8 Hz, 1H, H<sup>1,1tpy</sup>), 8.28 (t, <sup>3</sup>J<sub>HH</sub> = 8 Hz, 1H, H<sup>1,1tpy</sup>), 8.18 (d, <sup>3</sup>J<sub>HH</sub> = 8 Hz, 2H, H<sup>5B</sup>), 7.76–7.65 (m, 6H, H<sup>6,1tpy</sup>, H<sup>6A</sup>), 7.65–7.59 (m, 2H, H<sup>6B</sup>), 7.19–7.10 (m, 6H, H<sup>8,1tpy</sup>, H<sup>8A</sup>), 7.07 (d, <sup>3</sup>J<sub>HH</sub> = 6 Hz, 2H, H<sup>8B</sup>), 6.96–6.88 (m, br, 4H, H<sup>7,1tpy</sup>), 6.75 (m, 2H, H<sup>7A</sup>), 6.68 (m, 2H, H<sup>7B</sup>). <sup>13</sup>C{<sup>1</sup>H} NMR (CD<sub>3</sub>CN): δ [ppm] = 230.3 (C<sup>9A</sup>), 217.9 (C<sup>9B</sup>), 169.6 (C<sup>5B</sup>), 169.3 (C<sup>5A</sup>), 168.0 (C<sup>10</sup>), 160.2, 160.0 (C<sup>4,1tpy</sup>), 155.3, 155.2 (C<sup>8,1tpy</sup>), 154.0, 153.6 (C<sup>3,1tpy</sup>), 153.0 (C<sup>8A</sup>, C<sup>8B</sup>), 143.2 (C<sup>3A</sup>), 142.7 (C<sup>3B</sup>), 136.8, 136.5, 136.4, 136.0 (C<sup>6,1tpy</sup>, C<sup>6A</sup>, C<sup>6B</sup>), 133.9 (C<sup>1B</sup>), 133.8, 132.9 (C<sup>1,1tpy</sup>), 127.9 (C<sup>1A</sup>), 127.3 (C<sup>7,1tpy</sup>), 124.6, 124.4 (C<sup>5,1tpy</sup>), 123.4, 123.3 (C<sup>2,1tpy</sup>), 123.3 (C<sup>2A</sup>), 123.0 (C<sup>7A</sup>), 122.6 (C<sup>7B</sup>), 120.9 (C<sup>8A</sup>), 120.7 (C<sup>8B</sup>), 118.9 (C<sup>2B</sup>). IR (KBr disk):  $\tilde{\nu}$  [cm<sup>-1</sup>] = 3220 (m, N–H amide), 1635 (s, C=O amide), 1599, 1582 (m, C=C), 1517 (w, amide II), 843 (s, P–F).

## Conclusions

The electrochemical, UV-Vis and excited state properties of a series of [Ru(dpb-R)(tpy)]<sup>+</sup> type of complexes was systematically studied. The visible range absorption bands of these complexes are dominated by two electronically decoupled <sup>1</sup>MLCT transitions either involving the dpb ligand (d<sub>yz</sub>(Ru) → dpb) or the tpy ligand (d<sub>xz</sub>(Ru) → tpy). These excitations are followed by intersystem crossing populating an emissive [Ru<sup>+</sup>(tpy<sup>-</sup>)] <sup>3</sup>MLCT state in all cases. This state, however, is rapidly depopulated at room temperature *via* two additional low-energy triplet excited states yielding very low luminescence quantum yields and short excited state lifetimes. VT steady-state emission spectroscopy and extended DFT calculations revealed their nature as <sup>3</sup>LL/CT and <sup>3</sup>MC states yielding a bi-exponential dependence of the quantum yield on the temperature. While the <sup>3</sup>MC state has been known as a parasitic channel for non-radiative decay in (polypyridine)ruthenium(II) complexes for over 30 years,<sup>22</sup> the observation of a <sup>3</sup>LL/CT state in such ruthenium complexes is unprecedented to the best of our knowledge. We previously referred to the <sup>3</sup>LL/CT state as a spectroscopically undetectable state (“dark” state).<sup>40</sup> However, the characteristic temperature dependence of the quantum yield clearly is spectroscopic evidence for its presence. Also for the bis(tridentate)iridium(III) complex [Ir(dpx)(tpy)]<sup>2+</sup> (dpxH = 1,5-di(2-pyridyl)-2,4-xylene), a <sup>3</sup>LL/CT state is suggested to be responsible for its low luminescence quantum yield.<sup>101</sup> Based upon the findings of this study, we believe that the excited state deactivation in this cyclometalated iridium complex occurs in an analogous manner *via* thermal depopulation of the emissive state *via* <sup>3</sup>LL/CT states.

Remarkably, for the acceptor-substituted complexes **3**<sup>+</sup> and **4**<sup>+</sup>, the <sup>3</sup>LL/CT state resides higher in energy than the <sup>3</sup>MLCT state, while for the donor-substituted complexes **1**<sup>+</sup> and **2**<sup>+</sup>, it is found to be the lowest triplet state. As a consequence, faster deactivation of the emissive <sup>3</sup>MLCT states is observed in the latter complexes associated with substantially lowered emission quantum yields compared to complexes **3**<sup>+</sup> and **4**<sup>+</sup>. But, since emission is observed for **1**<sup>+</sup> and **2**<sup>+</sup> with increasing quantum yields at lower temperatures, deactivation *via* the <sup>3</sup>LL/CT state is a thermally activated process and the <sup>3</sup>MLCT and <sup>3</sup>LL/CT states are not in thermal equilibrium.

Upon oxidation of the dinuclear complex **6**<sup>2+</sup> to its mixed-valent counterpart **6**<sup>3+</sup>, an intense NIR band is detected indicating a photochemical Ru<sup>II</sup> → Ru<sup>III</sup> charge transfer across the asymmetric biscyclometalating bridging ligand. Despite the substantial redox asymmetry of the two complex subunits bearing NH- and CO-substituents, a strong electronic communication between the donor and acceptor sites of **6**<sup>3+</sup> is observed. In the excited state of **6**<sup>2+</sup> however, the two complex fragments appear electronically uncoupled with dual emission occurring from <sup>3</sup>MLCT states localized at the two remote [Ru(tpy)] moieties. This “anti-Kasha” behaviour is explained based on the long metal–metal distance and the very rapid excited state decay (emissive and non-emissive) that prevents thermal equilibration in solution *via* energy transfer entirely.





Just upon freezing of the solution, the excited states become sufficiently long-lived to allow for thermalization, so that Kasha's rule is obeyed.

In summary, we were able to show spectroscopically and computationally that the introduction of N<sup>+</sup>C<sup>-</sup>N cyclometalating ligands in bis(tridentate)ruthenium(II) complexes gives rise to low-lying <sup>3</sup>LL/CT states that allow for efficient thermal depopulation of the emissive <sup>3</sup>MLCT state. Furthermore, we believe that the existence of <sup>3</sup>LL/CT states in polypyridine transition metal complexes is more general. As their energy is strongly dependent on the substitution pattern, they become particularly relevant in strong push-pull systems and can interfere with luminescence processes and shorten the excited state lifetimes substantially.

Additionally, in mixed-valent dinuclear ruthenium complexes such as **6**<sup>3+</sup>, the biscyclometalating bridge was shown to be an excellent mediator for photochemical electron transfer between the redox sites even in the presence of a substantial redox asymmetry. The triplet excited states of **6**<sup>2+</sup>, however, are electronically uncoupled due to the large spatial separation of the emissive [Ru(tpy)] moieties and their short excited state lifetimes induced by the cyclometalating bridge.

## Acknowledgements

Parts of this research were conducted using the supercomputer MOGON and advisory services offered by Johannes Gutenberg Univ. Mainz (<http://www.hpc.uni-mainz.de>), which is a member of the AHRP and the Gauss Alliance e.V. This work was financially supported by the Deutsche Forschungsgemeinschaft (GSC 266, Materials Science in Mainz, scholarship for C. K.).

## Notes and references

- J. P. Paris and W. W. Brandt, *J. Am. Chem. Soc.*, 1959, **81**, 5001–5002.
- F. E. Lytle and D. M. Hercules, *J. Am. Chem. Soc.*, 1969, **91**, 253–257.
- K. Kalyanasundaram, *Coord. Chem. Rev.*, 1982, **46**, 159–244.
- A. Juris, V. Balzani, F. Barigelletti, S. Campagna, P. Belser and A. von Zelewsky, *Coord. Chem. Rev.*, 1988, **84**, 85–277.
- M. Maestri, N. Armaroli, V. Balzani, E. C. Constable and A. M. W. C. Thompson, *Inorg. Chem.*, 1995, **34**, 2759–2767.
- V. Balzani and A. Juris, *Coord. Chem. Rev.*, 2001, **211**, 97–115.
- S. Campagna, F. Puntoriero, F. Nastasi, G. Bergamini and V. Balzani, *Top. Curr. Chem.*, 2007, **280**, 117–214.
- D. M. Hedstrand, W. H. Kruizinga and R. M. Kellogg, *Tetrahedron Lett.*, 1978, **19**, 1255–1258.
- H. D. Abruna, A. Y. Teng, G. J. Samuels and T. J. Meyer, *J. Am. Chem. Soc.*, 1979, **101**, 6745–6746.
- I. Okura and N. Kim-Thuan, *J. Mol. Catal.*, 1979, **5**, 311–314.
- J.-M. Lehn and R. Ziessel, *Proc. Natl. Acad. Sci. U. S. A.*, 1982, **79**, 701–704.
- J. W. Tucker and C. R. J. Stephenson, *J. Org. Chem.*, 2012, **77**, 1617–1622.
- B. O'Regan and M. Grätzel, *Nature*, 1991, **353**, 737–740.
- M. G. Sasso, F. H. Quina and E. J. Bechara, *Anal. Biochem.*, 1986, **156**, 239–243.
- K. K.-W. Lo, T. K.-M. Lee, J. S.-Y. Lau, W.-L. Poon and S.-H. Cheng, *Inorg. Chem.*, 2008, **47**, 200–208.
- P. D. Beer, Z. Chen, A. J. Goulden, A. Grieve, D. Heseck, F. Szemes and T. Wear, *J. Chem. Soc., Chem. Commun.*, 1994, 1269–1271.
- H. J. Bolink, L. Cappelli, E. Coronado and P. Gaviña, *Inorg. Chem.*, 2005, **44**, 5966–5968.
- J. N. Demas and D. G. Taylor, *Inorg. Chem.*, 1979, **18**, 3177–3179.
- S. Yoon, P. Kukura, C. M. Stuart and R. A. Mathies, *Mol. Phys.*, 2006, **104**, 1275–1282.
- J. V. Caspar and T. J. Meyer, *J. Am. Chem. Soc.*, 1983, **105**, 5583–5590.
- K. Suzuki, A. Kobayashi, S. Kaneko, K. Takehira, T. Yoshihara, H. Ishida, Y. Shiina, S. Oishi and S. Tobita, *Phys. Chem. Chem. Phys.*, 2009, **11**, 9850–9860.
- B. Durham, J. V. Caspar, J. K. Nagle and T. J. Meyer, *J. Am. Chem. Soc.*, 1982, **104**, 4803–4810.
- J. van Houten and R. J. Watts, *Inorg. Chem.*, 1978, **17**, 3381–3385.
- J. P. Sauvage, J. P. Collin, J. C. Chambron, S. Guillerez, C. Coudret, V. Balzani, F. Barigelletti, L. de Cola and L. Flamigni, *Chem. Rev.*, 1994, **94**, 993–1019.
- K. Lashgari, M. Kritikos, R. Norrestam and T. Norrby, *Acta Crystallogr., Sect. C: Cryst. Struct. Commun.*, 1999, **55**, 64–67.
- J. R. Winkler, T. L. Netzel, C. Creutz and N. Sutin, *J. Am. Chem. Soc.*, 1987, **109**, 2381–2392.
- M. L. Stone and G. A. Crosby, *Chem. Phys. Lett.*, 1981, **79**, 169–173.
- K. Heinze, K. Hempel and M. Beckmann, *Eur. J. Inorg. Chem.*, 2006, **2006**, 2040–2050.
- K. Heinze, K. Hempel and A. Breivogel, *Z. Anorg. Allg. Chem.*, 2009, **635**, 2541–2549.
- S. H. Wadman, M. Lutz, D. M. Tooke, A. L. Spek, F. Hartl, R. W. A. Havenith, G. P. M. van Klink and G. van Koten, *Inorg. Chem.*, 2009, **48**, 1887–1900.
- A. Breivogel, C. Kreitner and K. Heinze, *Eur. J. Inorg. Chem.*, 2014, **2014**, 5468–5490.
- M. Abrahamsson, M. Jäger, T. Österman, L. Eriksson, P. Persson, H.-C. Becker, O. Johansson and L. Hammarström, *J. Am. Chem. Soc.*, 2006, **128**, 12616–12617.
- F. Schramm, V. Meded, H. Fliegl, K. Fink, O. Fuhr, Z. Qu, W. Klopffer, S. Finn, T. E. Keyes and M. Ruben, *Inorg. Chem.*, 2009, **48**, 5677–5684.



- 34 A. Breivogel, C. Förster and K. Heinze, *Inorg. Chem.*, 2010, **49**, 7052–7056.
- 35 A. Breivogel, M. Meister, C. Förster, F. Laquai and K. Heinze, *Chem. – Eur. J.*, 2013, **19**, 13745–13760.
- 36 D. G. Brown, N. Sangantrakun, B. Schulze, U. S. Schubert and C. P. Berlinguette, *J. Am. Chem. Soc.*, 2012, **134**, 12354–12357.
- 37 M. Beley, J. P. Collin and J. P. Sauvage, *Inorg. Chem.*, 1993, **32**, 4539–4543.
- 38 S. H. Wadman, J. M. Kroon, K. Bakker, M. Lutz, A. L. Spek, G. P. M. van Klink and G. van Koten, *Chem. Commun.*, 2007, 1907–1909.
- 39 P. G. Bomben, K. C. D. Robson, P. A. Sedach and C. P. Berlinguette, *Inorg. Chem.*, 2009, **48**, 9631–9643.
- 40 C. Kreitner, E. Erdmann, W. W. Seidel and K. Heinze, *Inorg. Chem.*, 2015, **54**, 11088–11104.
- 41 C. Creutz and H. Taube, *J. Am. Chem. Soc.*, 1969, **91**, 3988–3989.
- 42 W. Kaim, A. Klein and M. Glöckle, *Acc. Chem. Res.*, 2000, **33**, 755–763.
- 43 W. Kaim and G. K. Lahiri, *Angew. Chem.*, 2007, **119**, 1808–1828, (*Angew. Chem., Int. Ed.*, 2007, **46**, 1778–1796).
- 44 U. Fuerholz, H. B. Büergi, F. E. Wagner, A. Stebler, J. H. Ammeter, E. Krausz, R. J. H. Clark, M. J. Stead and A. Ludi, *J. Am. Chem. Soc.*, 1984, **106**, 121–123.
- 45 L. T. Zhang, J. Ko and M. J. Ondrechen, *J. Am. Chem. Soc.*, 1987, **109**, 1666–1671.
- 46 S. P. Best, R. J. H. Clark, R. C. S. McQueen and S. Joss, *J. Am. Chem. Soc.*, 1989, **111**, 548–550.
- 47 B. S. Brunshwig, C. Creutz and N. Sutin, *Chem. Soc. Rev.*, 2002, **31**, 168–184.
- 48 M. B. Robin and P. Day, *Adv. Inorg. Chem.*, 1968, **10**, 247–422.
- 49 N. S. Hush, *Prog. Inorg. Chem.*, 1967, **8**, 391–444.
- 50 N. S. Hush, *Electrochim. Acta*, 1968, **13**, 1005–1023.
- 51 N. S. Hush, *Coord. Chem. Rev.*, 1985, **64**, 135–157.
- 52 B. S. Brunshwig and N. Sutin, *Coord. Chem. Rev.*, 1999, **187**, 233–254.
- 53 G. D. Storrier and S. B. Colbran, *Inorg. Chim. Acta*, 1999, **284**, 76–84.
- 54 A. Breivogel, K. Hempel and K. Heinze, *Inorg. Chim. Acta*, 2011, **374**, 152–162.
- 55 C. Kreitner, M. Grabolle, U. Resch-Genger and K. Heinze, *Inorg. Chem.*, 2014, **53**, 12947–12961.
- 56 E. C. Constable and M. D. Ward, *J. Chem. Soc., Dalton Trans.*, 1990, 1405–1409.
- 57 J.-P. Collin, P. Lainé, J.-P. Launay, J.-P. Sauvage and A. Sour, *J. Chem. Soc., Chem. Commun.*, 1993, 434–435.
- 58 M. Beley, J. P. Collin, R. Louis, B. Metz and J. P. Sauvage, *J. Am. Chem. Soc.*, 1991, **113**, 8521–8522.
- 59 C. Patoux, J.-P. Launay, M. Beley, S. Chodorowski-Kimmes, J.-P. Collin, S. James and J.-P. Sauvage, *J. Am. Chem. Soc.*, 1998, **120**, 3717–3725.
- 60 J.-Y. Shao and Y.-W. Zhong, *Chem. – Eur. J.*, 2014, **20**, 8702–8713.
- 61 K. C. D. Robson, B. D. Koivisto, A. Yella, B. Spornova, M. K. Nazeeruddin, T. Baumgartner, M. Grätzel and C. P. Berlinguette, *Inorg. Chem.*, 2011, **50**, 5494–5508.
- 62 W. König and R. Geiger, *Chem. Ber.*, 1970, **103**, 788–798.
- 63 A. D. Becke, *J. Chem. Phys.*, 1993, **98**, 5648–5652.
- 64 A. Schäfer, H. Horn and R. Ahlrichs, *J. Chem. Phys.*, 1992, **97**, 2571–2577.
- 65 A. Schäfer, C. Huber and R. Ahlrichs, *J. Chem. Phys.*, 1994, **100**, 5829–5835.
- 66 F. Weigend and R. Ahlrichs, *Phys. Chem. Chem. Phys.*, 2005, **7**, 3297–3305.
- 67 E. van Lenthe, E. J. Baerends and J. G. Snijders, *J. Chem. Phys.*, 1993, **99**, 4597–4610.
- 68 S. Sinnecker, A. Rajendran, A. Klamt, M. Diedenhofen and F. Neese, *J. Phys. Chem. A*, 2006, **110**, 2235–2245.
- 69 M. C. Hughes and D. J. Macero, *Inorg. Chem.*, 1976, **15**, 2040–2044.
- 70 S. Romain, C. Baffert, C. Duboc, J.-C. Leprêtre, A. Deronzier and M.-N. Collomb, *Inorg. Chem.*, 2009, **48**, 3125–3131.
- 71 R. F. Winter, *Organometallics*, 2014, **33**, 4517–4536.
- 72 N. G. Connelly and W. E. Geiger, *Chem. Rev.*, 1996, **96**, 877–910.
- 73 C. Creutz, M. D. Newton and N. Sutin, *J. Photochem. Photobiol., A*, 1994, **82**, 47–59.
- 74 J.-P. Launay, *Chem. Soc. Rev.*, 2001, **30**, 386–397.
- 75 L. Wang, W.-W. Yang, R.-H. Zheng, Q. Shi, Y.-W. Zhong and J. Yao, *Inorg. Chem.*, 2011, **50**, 7074–7079.
- 76 W.-W. Yang, L. Wang, Y.-W. Zhong and J. Yao, *Organometallics*, 2011, **30**, 2236–2240.
- 77 D. E. Richardson and H. Taube, *J. Am. Chem. Soc.*, 1983, **105**, 40–51.
- 78 M. Natali, S. Campagna and F. Scandola, *Chem. Soc. Rev.*, 2014, **43**, 4005–4018.
- 79 F. Barigelletti, A. Juris, V. Balzani, P. Belser and A. von Zelewsky, *Inorg. Chem.*, 1983, **22**, 3335–3339.
- 80 A. Juris, F. Barigelletti, V. Balzani, P. Belser and A. von Zelewsky, *Inorg. Chem.*, 1985, **24**, 202–206.
- 81 G. A. Crosby, *Acc. Chem. Res.*, 1975, **8**, 231–238.
- 82 F. Barigelletti, A. Juris, V. Balzani, P. Belser and A. von Zelewsky, *J. Phys. Chem.*, 1986, **90**, 5190–5193.
- 83 R. Englman and J. Jortner, *Mol. Phys.*, 1970, **18**, 145–164.
- 84 J. V. Caspar, E. M. Kober, B. P. Sullivan and T. J. Meyer, *J. Am. Chem. Soc.*, 1982, **104**, 630–632.
- 85 J. V. Caspar and T. J. Meyer, *J. Phys. Chem.*, 1983, **87**, 952–957.
- 86 K. A. King and R. J. Watts, *J. Am. Chem. Soc.*, 1987, **109**, 1589–1590.
- 87 T. E. Keyes, *Chem. Commun.*, 1998, 889–890.
- 88 E. C. Glazer, D. Magde and Y. Tor, *J. Am. Chem. Soc.*, 2007, **129**, 8544–8551.
- 89 Y. Chen, X. Zhou, X.-H. Wei, B.-L. Yu, H. Chao and L.-N. Ji, *Inorg. Chem. Commun.*, 2010, **13**, 1018–1020.
- 90 D. L. Dexter, *J. Chem. Phys.*, 1953, **21**, 836–850.



## Paper

## Dalton Transactions

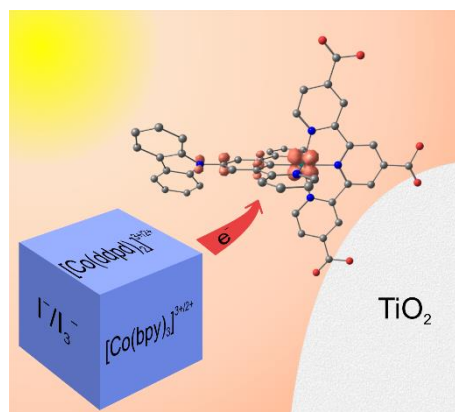
- 91 F. Barigelletti, L. Flamigni, V. Balzani, J.-P. Collin, J.-P. Sauvage, A. Sour, E. C. Constable and A. M. W. C. Thompson, *J. Am. Chem. Soc.*, 1994, **116**, 7692–7699.
- 92 V. Grosshenny, A. Harriman and R. Ziessel, *Angew. Chem.*, 1995, **107**, 1211–1214, (*Angew. Chem. Int. Ed.*, 1995, **34**, 1100–1102).
- 93 B. Schlicke, P. Belser, L. de Cola, E. Sabbioni and V. Balzani, *J. Am. Chem. Soc.*, 1999, **121**, 4207–4214.
- 94 M. Kasha, *Discuss. Faraday Soc.*, 1950, **9**, 14–19.
- 95 B. P. Sullivan, J. M. Calvert and T. J. Meyer, *Inorg. Chem.*, 1980, **19**, 1404–1407.
- 96 G. R. Fulmer, A. J. M. Miller, N. H. Sherden, H. E. Gottlieb, A. Nudelman, B. M. Stoltz, J. E. Bercaw and K. I. Goldberg, *Organometallics*, 2010, **29**, 2176–2179.
- 97 F. Neese, *Wiley Interdiscip. Rev.: Comput. Mol. Sci.*, 2012, **2**, 73–78.
- 98 F. Neese, F. Wennmohs, A. Hansen and U. Becker, *Chem. Phys.*, 2009, **356**, 98–109.
- 99 R. Izsák and F. Neese, *J. Chem. Phys.*, 2011, **135**, 144105.
- 100 D. A. Pantazis, X.-Y. Chen, C. R. Landis and F. Neese, *J. Chem. Theory Comput.*, 2008, **4**, 908–919.
- 101 A. J. Wilkinson, H. Puschmann, J. A. K. Howard, C. E. Foster and J. A. G. Williams, *Inorg. Chem.*, 2006, **45**, 8685–8699.



### 3.4 STRONGLY COUPLED CYCLOMETALATED RUTHENIUM TRIARYLAMINE CHROMOPHORES AS SENSITIZERS FOR DSSCs

Christoph Kreitner, Andreas K. C. Mengel, Tae Kyung Lee, Woohyung Cho, Kookheon Char, Yong Soo Kang and Katja Heinze

*Chem. Eur. J.* **2016**, published online: May, 19th, 2016, DOI: 10.1002/chem.201601001.



Anchor-functionalized cyclometalated bis(tridentate) ruthenium(II) triarylamine hybrids featuring mixed-valent states of varying resonance stabilization were employed in dye-sensitized solar cells in combination with different electrolytes. Together with cobalt-based electrolytes, the *N*-carbazole substituted dye surpasses the **N719** dye.

#### Author Contributions

The synthesis and characterization of the ruthenium complexes as well as all DFT calculations were performed by Christoph Kreitner. The cobalt electrolytes were synthesized and characterized by Andreas Mengel. After instruction from Prof. Dr. Yong Soo Kang and Prof. Dr. Kookheon Char the DSSCs were built and characterized by Andreas Mengel, Dr. Woohyung Cho and Tea-Kyung Lee. The evaluation of the DSSC results and the experimental arrangements were performed by Andreas Mengel. The manuscript was written by Christoph Kreitner (40 %) and Andreas Mengel (20 %) as well as Katja Heinze (40 %).

#### Supporting Information

for this article is found at pp. 240 (excluding Cartesian Coordinates of DFT-optimized geometries). For full Supporting Information, refer to [http://onlinelibrary.wiley.com/store/10.1002/chem.201601001/asset/supinfo/chem201601001-sup-0001-misc\\_information.pdf?v=1&s=24bd0e564e6a0c15c98a29abcb13226acfb50978](http://onlinelibrary.wiley.com/store/10.1002/chem.201601001/asset/supinfo/chem201601001-sup-0001-misc_information.pdf?v=1&s=24bd0e564e6a0c15c98a29abcb13226acfb50978).

„Reprinted with permission from Kreitner, C.; Heinze, K. *Chem. Eur. J.* **2016**. Copyright 2016 Jon Wiley and Sons.”

## Cyclometalated Complexes

# Strongly Coupled Cyclometalated Ruthenium Triarylamine Chromophores as Sensitizers for DSSCs

 Christoph Kreitner<sup>+, [a, d]</sup> Andreas K. C. Mengel<sup>+, [a]</sup> Tae Kyung Lee,<sup>[b]</sup> Woohyung Cho,<sup>[b]</sup> Kookheon Char,<sup>[c]</sup> Yong Soo Kang,<sup>[b]</sup> and Katja Heinze<sup>\*[a]</sup>

**Abstract:** A series of anchor-functionalized cyclometalated bis(tridentate) ruthenium(II) triarylamine hybrids [Ru(dbp-X)(tctpy)]<sup>2-</sup> [**2a**]<sup>2-</sup>–[**2c**]<sup>2-</sup> (H<sub>3</sub>tctpy = 2,2';6',2''-terpyridine-4,4',4''-tricarboxylic acid; dbpH = 1,3-dipyridylbenzene; X = N(4-C<sub>6</sub>H<sub>4</sub>OMe)<sub>2</sub> ([**2a**]<sup>2-</sup>), NPh<sub>2</sub> ([**2b**]<sup>2-</sup>), *N*-carbazolyl [**2c**]<sup>2-</sup>) was synthesized and characterized. All complexes show broad absorption bands in the range 300–700 nm with a maximum at about 545 nm. Methyl esters [Ru(Me<sub>3</sub>tctpy)(dpb-X)]<sup>+</sup> [**1a**]<sup>+</sup>–[**1c**]<sup>+</sup> are oxidized to the strongly coupled mixed-valent species [**1a**]<sup>2+</sup>–[**1c**]<sup>2+</sup> and the Ru<sup>III</sup>(aminium) complexes [**1a**]<sup>3+</sup>–[**1c**]<sup>3+</sup> at comparably low oxidation potentials. Theoretical calculations suggest an

increasing spin delocalization between the metal center and the triarylamine unit in the order [**1a**]<sup>2+</sup> < [**1b**]<sup>2+</sup> < [**1c**]<sup>2+</sup>. Solar cells were prepared with the saponified complexes [**2a**]<sup>2-</sup>–[**2c**]<sup>2-</sup> and the reference dye **N719** as sensitizers using the I<sub>3</sub><sup>-</sup>/I<sup>-</sup> couple and [Co(bpy)<sub>3</sub>]<sup>3+/2+</sup> and [Co(ddpd)<sub>2</sub>]<sup>3+/2+</sup> couples as [B(C<sub>6</sub>F<sub>5</sub>)<sub>4</sub>]<sup>-</sup> salts as electrolytes (bpy = 2,2'-bipyridine; ddpd = *N,N'*-dimethyl-*N,N'*-dipyridin-2-yl-pyridine-2,6-diamine). Cells with [**2c**]<sup>2-</sup> and I<sub>3</sub><sup>-</sup>/I<sup>-</sup> electrolyte perform similarly to cells with **N719**. In the presence of cobalt electrolytes, all efficiencies are reduced, yet under these conditions [**2c**]<sup>2-</sup> outperforms **N719**.

## Introduction

Pioneered by O'Regan and Grätzel in 1991,<sup>[1]</sup> the dye-sensitized solar cell (DSSC) has emerged as a promising light-to-energy conversion device.<sup>[2,3]</sup> Its setup has been optimized and standardized over the past 25 years. Typically, its central component is a molecular dye that is absorbed onto a mesoporous wide-bandgap semiconducting electrode, such as TiO<sub>2</sub> or ZnO.<sup>[3,4]</sup> Upon excitation by visible light, electrons are injected from the excited state of the dye into the conduction band of the semiconductor. The oxidized dye is then regenerated by a redox mediator, which transports the positive charge to the counter

electrode. The major advantages of dye sensitized solar cells over conventional silicon-based or inorganic thin film solar cells are lower costs and their modular architecture allowing for systematic optimization of all components (semiconductor, sensitizer, electrolyte) individually.<sup>[3–5]</sup>

Tremendous efforts have been put particularly into the development of new molecular dyes to optimize cell performance. An ideal sensitizer should be thermally and photochemically stable under working conditions, should rapidly inject electrons into the conduction band of the semiconductor after excitation and, most importantly, should efficiently absorb light between 400 and 900 nm. Among others, polypyridine complexes of iron,<sup>[6]</sup> copper,<sup>[7–9]</sup> platinum,<sup>[10,11]</sup> iridium,<sup>[12,13]</sup> and ruthenium<sup>[14]</sup> as well as polyaromatic and conjugated organic compounds,<sup>[15,16]</sup> porphyrins,<sup>[17–19]</sup> and quantum dots<sup>[20]</sup> have proven suitable for sensitization. Particularly, polypyridine complexes of ruthenium and osmium have emerged as a promising class of sensitizers due to their suitable photophysical properties.<sup>[21–24]</sup> The visible range of the electromagnetic spectrum of these complexes is dominated by characteristic metal-to-ligand charge transfer (MLCT) absorptions.<sup>[25–27]</sup> In these transitions, metal orbitals of the t<sub>2g</sub> set serve as electron donors, while the polypyridine π\* orbitals function as electron acceptors.

The most prominent and well-established sensitizers are the complexes [nBu<sub>4</sub>N]<sub>2</sub>[Ru(Hdcbpy)<sub>2</sub>(NCS)<sub>2</sub>], **N719** (H<sub>2</sub>dcbpy = 2,2'-bipyridine-4,4'-dicarboxylic acid, Scheme 1),<sup>[28,29]</sup> and the so-called “black dye” [nBu<sub>4</sub>N]<sub>3</sub>[Ru(Htctpy)(NCS)<sub>3</sub>] (H<sub>3</sub>tctpy = 2,2';6',2''-terpyridine-4,4',4''-tricarboxylic acid)<sup>[22]</sup> reaching power conversion efficiencies (PCE, η) of 10–11 % under full air mass 1.5 (AM 1.5) irradiation. In these complexes, the carboxy

[a] C. Kreitner,<sup>+</sup> A. K. C. Mengel,<sup>+</sup> Prof. Dr. K. Heinze  
Institute of Inorganic Chemistry and Analytical Chemistry  
Johannes Gutenberg-University of Mainz  
Duesbergweg 10–14, 55128 Mainz (Germany)  
Fax: (+49)6131-39-27-277  
E-mail: katja.heinze@uni-mainz.de

[b] T. K. Lee, W. Cho, Prof. Y. S. Kang  
The Department of Energy Engineering and Center for  
Next Generation Dye-Sensitized Solar Cells, Hanyang University  
222 Wangsimni-ro, Seongdong-gu, Seoul 133-791 (Korea)

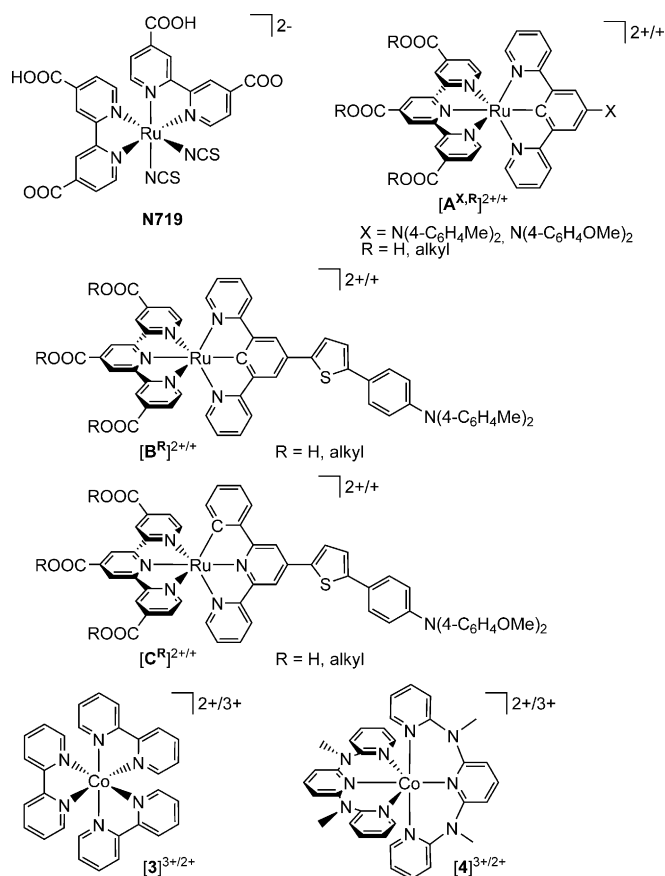
[c] Prof. Dr. K. Char  
The National Creative Research Initiative Center for Intelligent  
Hybrids, School of Chemical and Biological Engineering, Seoul  
National University, 1 Gwanak-ro, Gwanak-gu, Seoul 151-744 (Korea)

[d] C. Kreitner<sup>+</sup>  
Graduate School Materials Science in Mainz  
Staudingerweg 9, 55128 Mainz (Germany)

[\*] These authors contributed equally to the work.

Supporting information for this article is available on the WWW under  
<http://dx.doi.org/10.1002/chem.201601001>.





**Scheme 1.** N719 reference dye and amine-substituted cyclometalated ruthenium(II) dyes (top) and cobalt-based electrolytes (bottom).

groups serve as anchors to the  $TiO_2$  surface while the  $[NCS]^-$  ligands are responsible for an efficient charge transfer from the redox mediator onto the dye after charge injection (dye regeneration).<sup>[29]</sup> However, a major drawback of complexes containing monodentate ligands is their high lability towards  $[NCS]^-$  substitution in photoexcited or oxidized states hampering long-term application in photovoltaic devices.<sup>[30–33]</sup>

Recently, bi- and tridentate cyclometalating ligands emerged as viable and more robust alternatives for the labile  $[NCS]^-$  ligands. In 2007, van Koten and co-workers reported the successful sensitization of  $TiO_2$  by bis(tridentate)  $[Ru(pbpy)(tpy)]^+$  complexes ( $tpy = 2,2',6',2''$ -terpyridine,  $Hpbpy = 6$ -phenyl-2,2'-bipyridine).<sup>[34]</sup> Shortly thereafter, Grätzel and co-workers published a dye with record-breaking characteristics  $[Ru(H_2dcbpy)_2(ppy-F_2)]^+$  ( $\eta > 10\%$ ) based on a tris(bidentate) cyclometalating motif ( $Hppy-F_2 = 2$ -(2,4-difluorophenyl)pyridine).<sup>[35]</sup> Since then, much work has been dedicated towards the development of new cyclometalated ruthenium dyes both in the field of tris(bidentate) and bis(tridentate) complex architectures.<sup>[36–42]</sup> These studies indeed reveal several key benefits of the cyclometalating motif. The introduction of a Ru-C  $\sigma$  bond in the coordination environment reduces the local symmetry around the metal center. This yields a broad absorption band in the visible range resulting from multiple close-lying MLCT transitions involving both the polypyridine and cy-

clometalating ligands as electron acceptors.<sup>[37,38,43–48]</sup> Additionally, cyclometalation substantially increases the energy of the polypyridine-centered lowest unoccupied molecular orbital (LUMO) compared to non-cyclometalated counterparts. This should potentially accelerate charge injection into the  $TiO_2$  conduction band.<sup>[37,38,48]</sup> The highest occupied molecular orbital (HOMO) on the other side typically extends over the metal center and the anionic part of the cyclometalating ligand. This should facilitate dye regeneration after charge injection.<sup>[38,46,48]</sup>

Furthermore, the high  $\sigma$ -donating strength destabilizes the inherently photochemically reactive metal-centered ( $^3MC$ ) excited states.<sup>[38,48–52]</sup> The electron donating or withdrawing character of the cyclometalating ligands are easily tuned by further substitution (for example  $[A^{X,Me}]^+$ , Scheme 1) including hole-transport facilities ( $X = \text{amines}$ ).<sup>[38,48–52]</sup> Indeed, several approaches have been developed to incorporate electron donors into the dye structure to rapidly detract the positive charge remaining on the sensitizer after electron injection away from the semiconductor surface.<sup>[53–56]</sup> Attaching the reversible triphenylamine radical cation/triphenylamine redox couple ( $TPA^{+•}/TPA^0$ ) proved particularly successful in conjunction with several porphyrin dyes, for example, **YD2-o-C8**, yielding solar cells with  $\eta > 12\%$ .<sup>[19,57]</sup> Berlinguette and co-workers demonstrated that the overall cell performance can benefit from a TPA unit linked to a  $[Ru(pbpy)(tpy)]^+$  complex via a thiophene spacer. This architecture yields cell efficiencies of up to 8.0% (Scheme 1,  $[B^R]^+$ ,  $[C^H]^+$ ).<sup>[38]</sup> Through clever dye design and adjustment of relative oxidation potentials of  $Ru^{III/II}$  and  $TPA^{+•/0}$  an efficient transfer of the electron hole from the ruthenium center to the TPA unit is achieved after charge injection. This retards parasitic electron recombination processes with oxidized dyes in the DSSC.<sup>[38,58–60]</sup> The mixed-valent complexes  $[B^R]^{2+}$  are valence-localized and assigned to Robin–Day class II with measurable electronic coupling between the metal center and the TPA unit.<sup>[60,61]</sup> Recently, Zhong and co-workers presented a structurally related series of complexes combining bis(tridentate) cyclometalated ruthenium complexes with TPA units (Scheme 1,  $[A^{X,Me}]^{2+}/[A^{X,Me}]^+$ ) lacking the thiophene unit.<sup>[62,63]</sup> The mixed-valent state  $[A^{X,Me}]^{2+}$  is valence-delocalized (Robin–Day class III) between the metal center and the amine moiety as evidenced by the shape and bandwidth of the near infrared absorption band and by density functional theoretical calculations.<sup>[62–65]</sup> The parent complex  $[A^{H,H}]^+$  lacking the amine substituent ( $X = H$ ) has been reported recently as well.<sup>[66]</sup>

In contrast to reported dyes  $[B^R]^+$ , featuring a valence-isomeric description of the  $[B^R]^{2+}$  state (Robin–Day class II), potential DSSC sensitizers  $[A^{X,H}]^+$  with  $X = \text{amine}$  that provide a means of detracting the electron hole away from the semiconductor surface in a resonant fashion ( $[A^{X,H}]^{2+}$ ; Robin–Day class III) have not yet been reported. Saponifying the three methyl esters of  $[A^{X,Me}]^+$  type complexes should provide suitable sensitizers  $[A^{X,H}]^+$  with a class III mixed-valent state. Herein, we present a series of three complexes of the general structure  $[nBu_4N]_2[Ru(dpb-X)(tctpy)]$  ( $Hdpb-X = 5$ -substituted 1,3-di-(2-pyridyl)benzene) with different amine substituents  $X$  of increasing electron withdrawing power, namely  $N,N$ -bis(4-methoxyphenyl)amine ( $X = N(4-C_6H_4OMe)_2$ );  $[nBu_4N]_2[2a]$ ,  $N,N$ -diphenyl-

amine ( $X = N(C_6H_5)_2$ ;  $[nBu_4N]_2[2b]$ ) and carbazole ( $X = N$ -carbazolyl;  $[nBu_4N]_2[2c]$ ). We will discuss how the substituents at the dpb ligand affect the degree of valence-delocalization in the mixed-valent state  $[2]^-$  and to what extent such delocalization is beneficial for the application of such sensitizers in DSSCs.

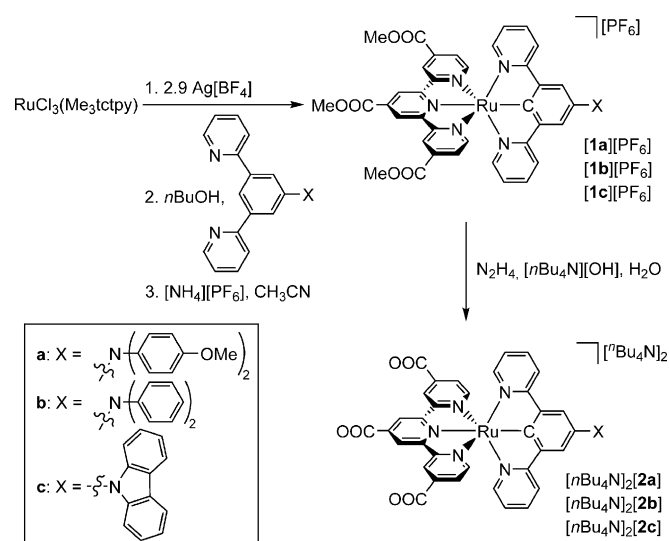
As outer-sphere cobalt-based electrolytes<sup>[67–80]</sup> should deliver higher open-circuit voltages  $V_{OC}$  due to their more positive redox potential as compared to the standard triiodide/iodide couple and as they perform extremely well in conjunction with TPA-appended porphyrin dyes (YD2-*o*-C8)<sup>[57]</sup> as well as with other potent TPA-appended dyes (Y123, D35),<sup>[72,73,74]</sup> we study the TPA-appended ruthenium(II) dyes  $[nBu_4N]_2[2a]$ – $[nBu_4N]_2[2c]$  with cobalt-based electrolytes in addition to the commonly used triiodide/iodide couple. Specifically, we employ the  $[Co(bpy)_3]^{3+/2+}$   $[3]^{3+/2+}$  and  $[Co(ddpd)]^{3+/2+}$   $[4]^{3+/2+}$  redox mediators (bpy = 2,2'-bipyridine, ddpd = *N,N'*-dimethyl-*N,N'*-dipyridin-2-yl-pyridine-2,6-diamine,<sup>[80]</sup> Scheme 1).<sup>[81–83]</sup> The DSSCs are studied by incident photon-to-current conversion efficiency measurements, by current-voltage characteristics under AM 1.5 irradiation and in the dark as well as by electron lifetime measurements.

## Results and Discussion

### Synthesis and characterization of chromophores

The 5-substituted 1,3-di-(2-pyridyl)benzene ligands  $L^a$  ( $R = N(4-C_6H_4OMe)_2$ ),  $L^b$  ( $R = N(C_6H_5)_2$ ) and  $L^c$  ( $R = N$ -carbazolyl) were synthesized starting from the previously reported 1-bromo-3,5-di-(2-pyridyl)benzene under Buchwald–Hartwig cross-coupling reaction conditions similar to a method we,<sup>[48]</sup> as well Zhong and co-workers employed previously.<sup>[63a]</sup> In the present study, the dimeric palladium(II) precatalyst bis( $\mu$ -mesylate)bis[(2-(2'-aminophenyl- $\kappa$ N)phenyl- $\kappa$ C')palladium(II)]  $[Pd]_2$ <sup>[84]</sup> was used along with the phosphane ligand 2-dicyclohexylphosphano-2',6'-diisopropoxybiphenyl<sup>[85]</sup> to provide a catalytically competent catalyst that afforded the ligands in yields of 82–98%. The identity of  $L^a$  was confirmed by comparison of its <sup>1</sup>H NMR spectrum with that reported before.<sup>[62,63a]</sup> The purity and integrity of the new ligands  $L^b$  and  $L^c$  were ascertained by <sup>1</sup>H and <sup>13</sup>C NMR spectroscopy, mass spectrometry, and elemental analyses (Experimental Section; Supporting Information, Figures S1–S4).

The heteroleptic ester-substituted  $[Ru(dpb)(tpy)]^+$  complexes  $[1a]^+–[1c]^+$  were prepared according to a previously employed synthetic method starting from  $RuCl_3(Me_3tctpy)$  (Scheme 2).<sup>[22,48]</sup> The two-step procedure includes chloride abstraction with silver tetrafluoroborate followed by complexation with the respective dipyriddybenzene ligand  $L^a–L^c$  under reducing conditions in *n*-butanol. Similar to observations made by Zhong and co-workers,<sup>[62,63a]</sup> we were not able to isolate the complexes  $[1a]^+–[1c]^+$  with high purity. Despite the reducing conditions during their synthesis, substantial amounts of the open-shell  $Ru^{III}$  complexes  $[1a]^{2+}–[1c]^{2+}$  were obtained, as evidenced from ESI mass spectra and the NMR silence of all three compounds (paramagnetic broadening).<sup>[62,63a]</sup> Additionally, the isolated products are black in solution and in the solid state instead of the dark purple color typically observed for



**Scheme 2.** Synthesis of  $[1a][PF_6]–[1c][PF_6]$  and  $[nBu_4N]_2[2a]–[nBu_4N]_2[2c]$ .

$[Ru(dpb)(tpy)]^+$  complexes, suggesting the presence of a second colored species. Yet, cyclic voltammograms confirm the purity of the synthesized complexes by absence of redox waves in the range of  $–3.0$  and  $1.5$  V other than the five expected reversible waves,<sup>[62,63a]</sup> namely for the  $[1]^{3+/2+}$ ,  $[1]^{2+/+}$ ,  $[1]^{+/0}$ ,  $[1]^{0/-}$  and  $[1]^{-2-}$  couples (Figure 1, Supporting Information, Figure S5).

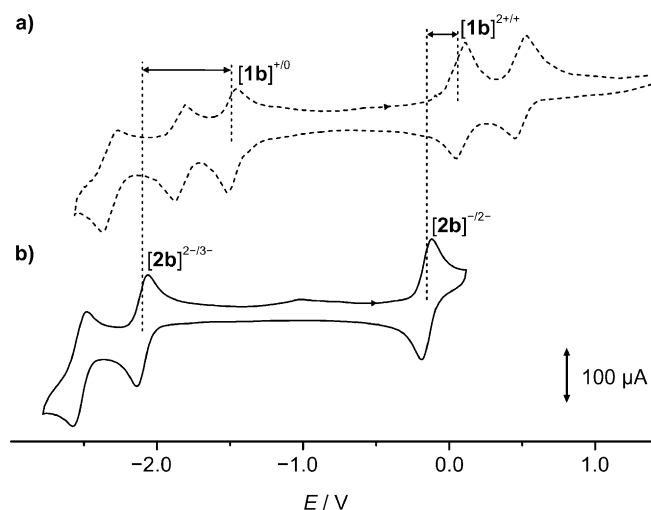


**Figure 1.** Cyclic voltammograms of a)  $[1b][PF_6]$  (----) and b)  $[nBu_4N]_2[2b]$  (—) dyes in  $[nBu_4N][PF_6]/CH_3CN$  ( $E$  vs.  $FcH/FcH^+$ ).

Subsequent saponification of the three methyl ester groups of  $[1a]^+–[1c]^+$  in aqueous solution using  $[nBu_4N][OH]$  as base and hydrazine as reductant yielded the corresponding carboxylates as tetrabutylammonium salts  $[nBu_4N]_2[2a]–[nBu_4N]_2[2c]$ . This method affords the fully deprotonated complexes  $[2a]^{2-}–[2c]^{2-}$ , in contrast to Berlinguette's procedure,<sup>[38]</sup> which yields the complexes in their neutral zwitterionic form with two protonated carboxy groups. Owing to the high solubility of the

tetrabutylammonium salts  $[n\text{Bu}_4\text{N}]_2[\mathbf{2a}]$ – $[n\text{Bu}_4\text{N}]_2[\mathbf{2c}]$  in organic solvents, the products are isolated straight-forwardly by extraction of the aqueous phase with dichloromethane. Co-extracted  $[n\text{Bu}_4\text{N}][\text{PF}_6]$  was removed by subsequent dissolution of the raw products in acetonitrile and addition of a diethylether/hexanes mixture that precipitates the desired complexes. The integrity of  $[n\text{Bu}_4\text{N}]_2[\mathbf{2a}]$ – $[n\text{Bu}_4\text{N}]_2[\mathbf{2c}]$  was confirmed by  $^1\text{H}$  NMR and  $^{13}\text{C}$  NMR spectra as well as by  $\text{ESI}^+$  and  $\text{ESI}^-$  mass spectra (Supporting Information, Figures S6–S19). All NMR spectra lack paramagnetic shifts or broadening, substantiating the absence of  $\text{Ru}^{\text{III}}$  in the pristine samples. The  $^1\text{H}$  NMR spectra confirm the presence of two equivalents of  $[n\text{Bu}_4\text{N}]^+$  cations per complex anion in all three cases corroborating the stoichiometry of the salt. IR spectra as KBr disk of the complexes  $[n\text{Bu}_4\text{N}]_2[\mathbf{2a}]$ – $[n\text{Bu}_4\text{N}]_2[\mathbf{2c}]$  lack the characteristic vibrations of  $[\text{PF}_6]^-$  ions at  $843\text{ cm}^{-1}$  (asym. stretch) and  $588\text{ cm}^{-1}$  (deformation) present in the parent complexes  $[\mathbf{1a}][\text{PF}_6]$ – $[\mathbf{1c}][\text{PF}_6]$  underlining the quantitative  $[\text{PF}_6]^-$  removal (Supporting Information, Figure S20). Additionally,  $^{19}\text{F}$  NMR spectra of  $[n\text{Bu}_4\text{N}]_2[\mathbf{2a}]$ – $[n\text{Bu}_4\text{N}]_2[\mathbf{2c}]$  confirm the absence of  $[\text{PF}_6]^-$ . Under the acidic and ionizing conditions of the  $\text{ESI}^+$  mass spectrometry technique, the complexes are observed in their fully protonated form as monocations  $[\mathbf{2} + 3\text{H}]^+$  with  $\text{Ru}^{\text{II}}$  metal sites or as dications  $[\mathbf{2} + 3\text{H}]^{2+}$  with  $\text{Ru}^{\text{III}}$  centers (Supporting Information, Figure S18). The  $\text{ESI}^-$  mass spectra (Supporting Information, Figure S19) show mass peaks at the expected  $m/z$  values for the dianions  $[\mathbf{2}]^{2-}$  ( $\text{Ru}^{\text{II}}$ ) and anions  $[\mathbf{2}]^-$  ( $\text{Ru}^{\text{III}}$ ) with typical ruthenium isotope patterns. Furthermore, several  $m/z$  peaks of decarboxylated complexes are found for all three complexes  $[n\text{Bu}_4\text{N}]_2[\mathbf{2a}]$ – $[n\text{Bu}_4\text{N}]_2[\mathbf{2c}]$ , confirming the presence of carboxylate substituents. The carboxylate groups are also evident from the characteristic IR CO stretching vibrations around  $1617\text{ cm}^{-1}$  (Supporting Information, Figure S20).

### Photophysical and electrochemical behavior

The absorption and emission spectra of the complexes  $[n\text{Bu}_4\text{N}]_2[\mathbf{2a}]$ – $[n\text{Bu}_4\text{N}]_2[\mathbf{2c}]$  are depicted in Figure 2 and data are summarized in Table 1 (Supporting Information, Figure S21). In the spectral range between 300 and 800 nm all dyes exhibit very similar absorption features. The absorption maximum around 536–549 nm is accompanied by three additional bands around 500, 425, and 375 nm. These bands characteristic for cyclometalated  $[\text{Ru}(\text{dpb})(\text{tpy})]^+$  complexes arise from metal-to-ligand charge transfer excitations involving both ligands as electron-

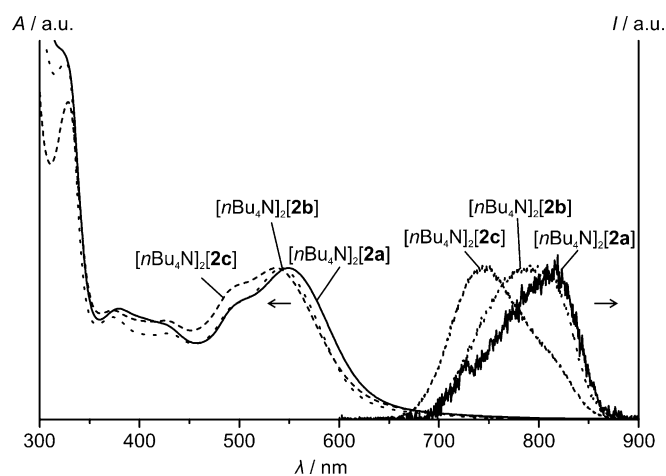


**Figure 2.** Normalized absorption and emission spectra of  $[n\text{Bu}_4\text{N}]_2[\mathbf{2a}]$  (—),  $[n\text{Bu}_4\text{N}]_2[\mathbf{2b}]$  (.....), and  $[n\text{Bu}_4\text{N}]_2[\mathbf{2c}]$  (-----) in  $\text{CH}_3\text{CN}$ .

accepting sites ( $d_{\text{Ru}} \rightarrow \pi_{\text{tpy}}^*$  and  $d_{\text{Ru}} \rightarrow \pi_{\text{dpb}}^*$ ).<sup>[38,48]</sup> Owing to the low local symmetry around the metal center, the number of absorption bands is larger than for the more symmetric systems containing all-nitrogen donor ligands such as  $[\text{Ru}(\text{tpy})_2]^{2+}$  or  $[\text{Ru}(\text{ddpd})(\text{tpy})]^{2+}$ , for example.<sup>[38,46,47,86]</sup> The lower symmetry yields substantially broadened absorption spectra and a more efficient light harvesting throughout the visible range of the electromagnetic spectrum.

The tris(carboxylate) complexes  $[n\text{Bu}_4\text{N}][\mathbf{2a}]$ – $[n\text{Bu}_4\text{N}][\mathbf{2c}]$  are very weakly emissive at room temperature (Figure 2, Table 1) with quantum yields below  $5 \times 10^{-6}$ . The wavelength of the emission maximum is shifted hypsochromically in the order  $[n\text{Bu}_4\text{N}][\mathbf{2a}] > [n\text{Bu}_4\text{N}][\mathbf{2b}] > [n\text{Bu}_4\text{N}][\mathbf{2c}]$  from 817 to 744 nm.

On the one hand, this trend is due to a more pronounced vibrational progression in  $[n\text{Bu}_4\text{N}][\mathbf{2a}]$  and  $[n\text{Bu}_4\text{N}][\mathbf{2b}]$  than in  $[n\text{Bu}_4\text{N}][\mathbf{2c}]$  similar to that observed for other  $[\text{Ru}(\text{dpb})(\text{tpy})]^+$  complexes with a strong push–pull substitution.<sup>[48]</sup> On the other hand, the energy of the emissive  $^3\text{MLCT}$  state increases with decreasing donor strength of the amine substituent, as this lowers the energy of the metal orbitals involved in the emission process while essentially maintaining the tctpy-centered LUMO energy (Figure 3; Supporting Information, Figure S22).<sup>[48]</sup>

Cyclovoltammetric studies of the ester-substituted complexes  $[\mathbf{1a}][\text{PF}_6]$ – $[\mathbf{1c}][\text{PF}_6]$  reveal multiple reversible redox processes (Figure 1, Table 1, Supporting Information, Figure S5).

Table 1. Optical and electrochemical data of $[\mathbf{1a}][\text{PF}_6]$ – $[\mathbf{1c}][\text{PF}_6]$ and $[n\text{Bu}_4\text{N}]_2[\mathbf{2a}]$ – $[n\text{Bu}_4\text{N}]_2[\mathbf{2c}]$ .			
	UV/Vis ( $\text{CH}_3\text{CN}$ ) $\lambda_{\text{max}}/\text{nm}$ ( $\epsilon/10^3\text{ M}^{-1}\text{ cm}^{-1}$ )	Emission ( $\text{CH}_3\text{CN}$ ) $\lambda_{\text{em}}/\text{nm}$ ( $\lambda_{\text{exc}}/\text{nm}$ )	Cyclic voltammetry E/V vs. FcH/FcH <sup>+</sup>
$[\mathbf{1a}][\text{PF}_6]$ <sup>[a]</sup>	323 (29), 339 (26), 420 (16), 507 (13), 583 (10)	– <sup>[b]</sup>	–1.87, –1.52, –0.05, +0.31
$[\mathbf{1b}][\text{PF}_6]$	– <sup>[b]</sup>	– <sup>[b]</sup>	–1.85, –1.49, +0.09, +0.49
$[\mathbf{1c}][\text{PF}_6]$	– <sup>[b]</sup>	– <sup>[b]</sup>	–1.83, –1.47, +0.34, +0.88
$[n\text{Bu}_4\text{N}]_2[\mathbf{2a}]$	549 (15.4), 503 (12.1), 424 (9.7), 379 (11.3), 323 (37.5), 289 (62.7)	817 (549) <sup>[c]</sup>	–2.52, –2.09, –0.21, – <sup>[d]</sup>
$[n\text{Bu}_4\text{N}]_2[\mathbf{2b}]$	543 (15.4), 501 (12.1), 428 (8.7), 374 (10.4), 325 (36.4), 288 (61.6)	791 (543) <sup>[c]</sup>	–2.54, –2.10, –0.15, – <sup>[d]</sup>
$[n\text{Bu}_4\text{N}]_2[\mathbf{2c}]$	536 (13.9), 499 (12.5), 426 (9.1), 373 (10.0), 328 (29.1), 283 (63.2)	744 (536) <sup>[c]</sup>	–2.51, –2.07, –0.06, – <sup>[d]</sup>

[a] From Ref. [63a]. [b] No optical data measured due to the presence of  $\text{Ru}^{\text{III}}$  species. [c] Quantum yield  $< 5 \cdot 10^{-6}$ . [d] No second oxidation potential was obtained due to precipitation of the neutral dye on the electrode surface.

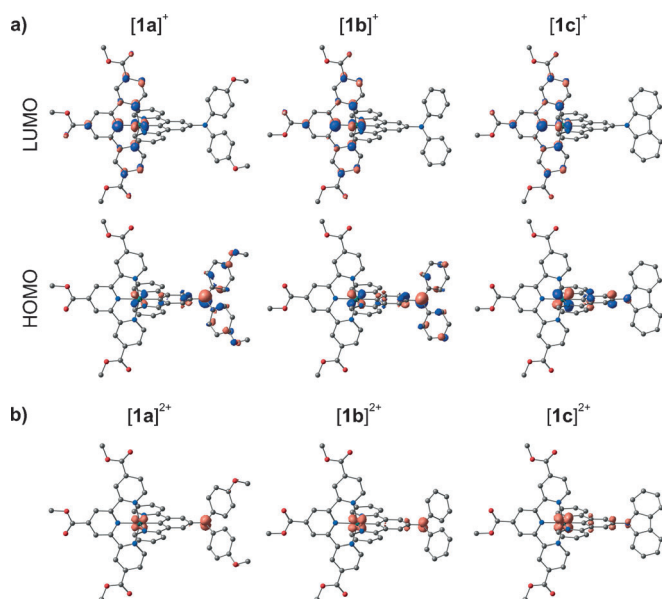


**Figure 3.** a) Frontier molecular orbitals of [1a]<sup>+</sup>, [1b]<sup>+</sup>, and [1c]<sup>+</sup> (contour value 0.06 a.u.) and b) spin densities of [1a]<sup>2+</sup>, [1b]<sup>2+</sup>, and [1c]<sup>2+</sup> (contour value 0.01 a.u.).

The complexes are oxidized at quite low potentials to the mixed-valent counterparts [1]<sup>2+</sup> (−0.05 to 0.34 V vs. FcH/FcH<sup>+</sup>). A second oxidation step occurs at higher potentials yielding the Ru<sup>III</sup>(aminium) complexes [1]<sup>3+</sup> (0.31 to 0.88 V vs. FcH/FcH<sup>+</sup>).<sup>[62]</sup> The trend of the first and the second oxidation potentials towards higher values in the order N(C<sub>6</sub>H<sub>4</sub>OCH<sub>3</sub>)<sub>2</sub> < N(C<sub>6</sub>H<sub>5</sub>)<sub>2</sub> < N-carbazole is in agreement with the decreasing +I effect of the respective amine substituent X. Additionally, the unpaired electron of the mixed-valent compounds [1]<sup>2+</sup> is substantially delocalized between the metal center and the triarylamine fragment via the 1,4-phenylene bridge.<sup>[62,63a]</sup> The electron donor strength of the dpb substituent<sup>[62,63a]</sup> strongly affects degree of delocalization as evidenced by DFT calculations (Figure 3b). Mulliken spin density analysis of [1a]<sup>2+</sup> indicates a balanced spin population of 0.26 and 0.25 at ruthenium and the amine nitrogen atom, respectively, while for [1b]<sup>2+</sup>, values of 0.43 (Ru) and 0.20 (N) are obtained. In [1c]<sup>2+</sup>, the spin density is further shifted towards the ruthenium atom with spin populations of 0.63 (Ru) and 0.07 (N). Thus, the degree of delocalization is reduced in this series from an essentially delocalized Robin–Day class III system in [1a]<sup>2+</sup> to a strongly coupled class II compound in [1c]<sup>2+</sup>.<sup>[61,63a]</sup> As a consequence, the resonance stabilization within complex [1a]<sup>2+</sup> is the largest, yielding the most pronounced negative shift of the first oxidation potential followed by complexes [1b]<sup>2+</sup> and [1c]<sup>2+</sup>. Additionally, two reversible reduction waves are observed for the ester-substituted complexes [1a][PF<sub>6</sub>]<sup>−</sup>–[1c][PF<sub>6</sub>]<sup>−</sup>. As these reductions are tpy-centered,<sup>[33b,46,48a,63a,87,88]</sup> their potentials are essentially independent from the substitution pattern at the dpb-X ligand with the first reduction occurring at −1.5 V and the second at −1.85 V vs. FcH/FcH<sup>+</sup> for all three complexes.

Deprotection and deprotonation of the ester functionalities, however, shifts the first and second reduction potentials by

600 mV towards more negative values (Figure 1, Table 1; Supporting Information, Figure S5). This is consistent with the substantial increase of negative charge density on the tctpy<sup>3−</sup> ligand in [2]<sup>2−</sup> and corroborates the tpy centered reduction. The oxidation waves shift to lower potentials as well, but to a lesser extent. This is mainly due to the fact, that the metal orbital involved with the oxidation process is orthogonal to the tpy ligand. However, a trend of the potential shifts is observed. While the first oxidation wave of [2a]<sup>2−</sup> occurs 160 mV below that of [1a]<sup>+</sup>, the first oxidation potentials of [2c]<sup>2−</sup> and [1c]<sup>+</sup> differ by 400 mV. Consequently, the first oxidation potentials of complexes [2a]<sup>2−</sup>–[2c]<sup>2−</sup> only differ by 150 mV as opposed to a difference of 390 mV between the esters [1a]<sup>+</sup>–[1c]<sup>+</sup>. This can be understood on the basis of the Mulliken spin populations of the metal center and the amine nitrogen atom in the mixed-valent anions [2]<sup>−</sup>: These amount to 0.49 (Ru)/0.17 (N) in [2a]<sup>−</sup>, 0.57 (Ru)/0.13 (N) in [2b]<sup>−</sup>, and 0.74 (Ru)/0.03 (N) in [2c]<sup>−</sup>. Apparently, the charge delocalization over the triarylamine fragment is significantly reduced and the spin densities of the mixed-valent anions [2]<sup>−</sup> are more valence-localized at the electron-rich metal center than their ester counterparts. Consequently, the resonance stabilization of the mixed-valent species [2]<sup>−</sup> is not as pronounced as that of [1]<sup>2+</sup> resulting in similar oxidation potentials for all three complexes. The strongest impact of deprotection and deprotonation is observed for [2c]<sup>2−</sup>, since its spin density is basically metal-centered. Accordingly, oxidation occurs in the closest proximity to the negatively charged tctpy<sup>3−</sup> ligand and is facilitated to the largest extent in the dye series [2]<sup>−</sup>.

Increasing the potential beyond 0.15 V vs FcH/FcH<sup>+</sup> results in a multitude of irreversible redox waves. We ascribe this to the deposition of the neutral Ru<sup>III</sup>(aminium) complexes [2]<sup>0</sup> on the platinum electrode surface, which impeded an unambiguous determination of the second oxidation potentials.

Combining all electrochemical and spectroscopic data of the dyes [1a]<sup>+</sup>–[1c]<sup>+</sup> and [2a]<sup>2−</sup>–[2c]<sup>2−</sup> with the redox data of the electrolytes I<sub>3</sub><sup>−</sup>/I<sup>−</sup>, 3<sup>3+/2+</sup> and 4<sup>3+/2+</sup> and the conduction band edge of TiO<sub>2</sub> yields the redox potential diagram depicted in Figure 4. Cyclic voltammetry of the dyes (see above) highlighted the strong dependence of the ground state oxidation potentials of the dyes from the degree of protonation of the carboxylic acids of the tpy ligand. For the setup of the DSSCs, the tris(carboxylate) dyes [2a]<sup>2−</sup>–[2c]<sup>2−</sup> were employed. Yet, under the given experimental conditions, partial protonation from water at the TiO<sub>2</sub> surface is conceivable. Additionally, the coadsorbent chenodeoxycholic acid (CDCA), as an organic acid, will modify the degree of protonation of the sensitizer. Hence, Figure 4 depicts redox potential ranges instead of distinct values for the redox potentials of the ruthenium dyes. An analogous range of ground state potentials is applied for N719 owing to the conceivable variation of the protonation state.<sup>[28]</sup> In a similar manner, the excited state <sup>1</sup>MLCT and <sup>3</sup>MLCT redox potentials span ranges.

It is apparent from Figure 4 that, similar to the reference dye N719, all cyclometalated dyes are thermodynamically capable of injecting an electron from both excited states into the conduction band of TiO<sub>2</sub>. Regeneration of the oxidized dyes by



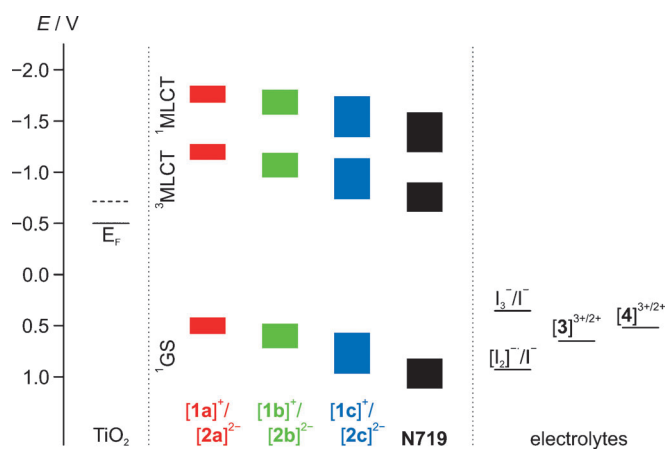


**Figure 4.** Diagram of the ground-state ( $^1GS$ ) and excited-state ( $^1MLCT$  and  $^3MLCT$ ) redox potentials of  $[1a]^+/[2a]^{2-}$ ,  $[1b]^+/[2b]^{2-}$ ,  $[1c]^+/[2c]^{2-}$ , and **N719**, the conduction band edge of  $TiO_2$ , and the redox potentials of the electrolytes.

the employed electrolytes on the other hand is not generally possible. While the carbazole-substituted ruthenium(III) complex  $[2c]^-$  is potentially regenerated by iodide even if the diiodide radical anion is formed as an intermediate,<sup>[89,90]</sup> this is not the case for the diarylamine-substituted dyes  $[2a]^{2-}$  and  $[2b]^{2-}$  in this simplified consideration of standard redox potentials. Hence, in a DSSC  $[2c]^{2-}$  is expected to outperform  $[2a]^{2-}$  and  $[2b]^{2-}$ . DSSC performances of all cyclometalated dyes in conjunction with the standard triiodide/iodide electrolyte and cobalt electrolytes will be discussed in the next section.

### Solar cell performance

Dye-sensitized solar cells were prepared from the carboxylate substituted dyes  $[nBu_4N]_2[2a]$ – $[nBu_4N]_2[2c]$  and the benchmark dye **N719**. The coadsorbent CDCA was employed to protect the  $TiO_2$  surface in several setups. Three different liquid electrolytes were utilized, namely the standard triiodide/iodide couple and two cobalt-based redox mediators.<sup>[67–69,82,83]</sup> The cobalt(III/II) complexes  $[Co(bpy)_3]^{3+/2+}$  and  $[Co(ddpd)_2]^{3+/2+}$  were prepared according to literature procedures.<sup>[74,78,82,91]</sup> Counter ion exchange was accomplished using  $Li[B(C_6F_5)_4]$  giving the cobalt salts  $[Co(bpy)_3][B(C_6F_5)_4]_2/[Co(bpy)_3][B(C_6F_5)_4]_3$  **[3]** $[B(C_6F_5)_4]_2/[3][B(C_6F_5)_4]_3$  and  $[Co(ddpd)_2][B(C_6F_5)_4]_2/[Co(ddpd)_2][B(C_6F_5)_4]_3$  **[4]** $[B(C_6F_5)_4]_2/[4][B(C_6F_5)_4]_3$ . NMR and mass spectrometric data confirm their compositions (Supporting Information, Figure S23–S31). The redox potential of  $[4]^{3+/2+}$  ( $E_{1/2} = 0.52$  V vs. NHE)<sup>[82]</sup> is intermediate of the  $I_3^-/I^-$  ( $E_{1/2} = 0.32 \pm 0.03$  V vs. NHE)<sup>[89]</sup> and the  $[3]^{3+/2+}$  ( $E_{1/2} = 0.65$  V vs. NHE)<sup>[92–94]</sup> couples (Figure 4).

The incident photon-to-current conversion efficiency (IPCE, Figure 5) depends on several individual key steps, namely light-harvesting, electron injection, dye regeneration, and charge collection.<sup>[67]</sup> The extinction coefficients around the MLCT maxima of  $[nBu_4N]_2[2a]$ – $[nBu_4N]_2[2c]$  (Figure 2, Experimental Section) are close to that of **N719** ( $\lambda = 535$  (14700), 395 (14300  $M^{-1} cm^{-1}$ ) nm.<sup>[28]</sup>). The achieved dye loadings of  $[nBu_4N]_2[2a]$ – $[nBu_4N]_2[2c]$  are consistently somewhat higher

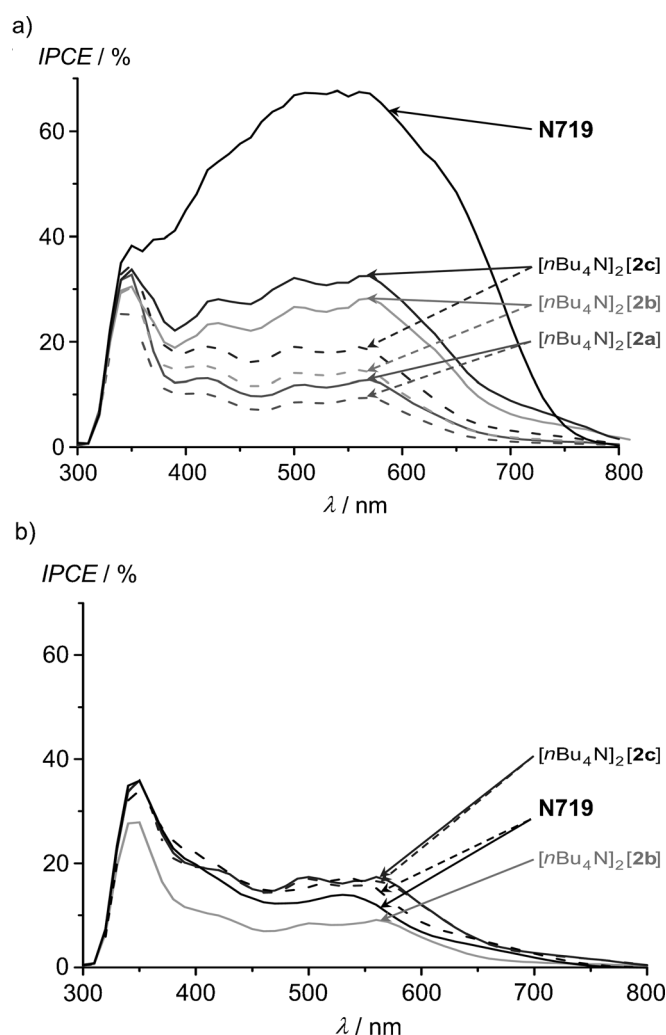


**Figure 5.** Photocurrent action spectra of cells with  $[nBu_4N]_2[2a]$ ,  $[nBu_4N]_2[2b]$ ,  $[nBu_4N]_2[2c]$ , and **N719**. a)  $I_3^-/I^-$  redox mediator with/without CDCA (—/– – – –); b)  $[3]^{3+/2+}$  (– – – –) and  $[4]^{3+/2+}$  (—) electrolytes.

than that found with **N719** (Experimental Section). Hence, we assume that the light-harvesting efficiencies of  $[nBu_4N]_2[2a]$ – $[nBu_4N]_2[2c]$  in the cells prepared are in the same range as that of the reference dye **N719**.

Concerning the injection efficiency, all dyes feature  $^1MLCT$  and  $^3MLCT$  levels well above the Fermi level of  $TiO_2$  (Figure 4). Hence, electron injection from the excited sensitizers should be feasible and fast for all dyes.<sup>[67]</sup> We assume rather similar injection efficiencies for all dyes.<sup>[67]</sup> Hence, the differences in DSSC performance in terms of power conversion efficiency  $\eta$  should predominantly relate to the dye regeneration efficiency, the charge collection efficiency (recombination losses) and the open-circuit voltage  $V_{OC}$ .

According to the electrochemical data of the dyes and the redox mediators, the  $Ru^{III}$  complex  $[2b]^-$  cannot be efficiently regenerated by the bipyridine cobalt(II) complex  $[3]^{2+}$ , while  $[2a]^-$  cannot be regenerated by both cobalt(II) complexes  $[3]^{2+}$  and  $[4]^{2+}$  (Figure 4). For all other dye/redox mediator combinations, dye regeneration is thermodynamically possible. In the electrolyte series, the highest driving force for dye re-



generation and hence the highest regeneration rate based on Marcus theory (Marcus normal region) is achieved with the  $I_3^-/I^-$  couple (although the  $[I_2]^-/I^-$  couple with a higher potential is responsible for the dye regeneration; Figure 4<sup>[89,90]</sup>). As the regeneration rate furthermore depends on the concentration of the reduced mediator,<sup>[67]</sup> the regeneration rate should decrease in the series  $I^-$  (0.550 M),  $[3]^{2+}$  (0.165 M), and  $[4]^{2+}$  (0.080 M). All of these factors strongly favor the  $I_3^-/I^-$  couple over cobalt-based couples.

Electron recombination with oxidized dyes (driving forces around 1.0–1.5 eV,<sup>[67]</sup> Figure 4) is reported to occur in the Marcus inverted region. However, the rates better correlate with the inverse distance of the positive charge in the dye and the  $TiO_2$  surface instead with the driving force.<sup>[67]</sup> In oxidized **N719** the positive charge is delocalized between Ru and the  $[NCS]^-$  ligands. In  $[1a]^{2+}-[1c]^{2+}$  the positive charge is efficiently delocalized onto the amine substituents of the dpb ligands (Robin–Day class III/class II behavior, see above). This is visualized in the DFT-calculated singly occupied molecular orbitals and corresponding spin densities of  $[1a]^{2+}-[1c]^{2+}$  spreading over the metal center and the amine substituent (see Figure 3). In this respect, amine substituted sensitizers should be somewhat advantageous as compared to **N719**. On the other hand, electron recombination with oxidized dyes depends on the lifetime of the oxidized dye and hence on its regeneration efficiency in the specific cell. Dye regeneration is very efficient for SCN-based ruthenium dyes and iodide, but often slowed down with other dye/electrolyte combinations for various reasons (lower electrolyte concentration, lower driving force, smaller electronic coupling, inner/outer sphere electron transfer).<sup>[67–69]</sup> Considering the slower dye regeneration using  $[2a]^{2+}-[2c]^{2+}$  sensitizers or cobalt redox mediators, the better performance of cells with the **N719**/ $I_3^-/I^-$  combination is quite expected (Figure 5a, Tables 2, Table 3). Interestingly, a lower electrolyte concentration decreases the efficiency of the **N719** cell to 5.8% but improves the efficiency of the cell with the  $[nBu_4N]_2[2c]$  sensitizer to 3.3% (Table 2). Obviously, the effects of electrolyte concentration on dye regeneration

**Table 2.** Photovoltaic data of cells using the  $I_3^-/I^-$  redox mediator with and without CDCA under AM1.5 light conditions (the data correspond to averaged values of several cells).

Dye	CDCA	$V_{oc}$ [V]	$J_{sc}$ [ $mA\,cm^{-2}$ ]	FF [%]	$\eta$ [%]
$[nBu_4N]_2[2a]$	–	0.50	1.77	63	0.6
$[nBu_4N]_2[2a]$	+	0.54	3.37	67	1.2
$[nBu_4N]_2[2b]$	–	0.53	2.91	67	1.1
$[nBu_4N]_2[2b]$	+	0.59	5.47	73	2.4
$[nBu_4N]_2[2c]$	–	0.57	5.06	72	2.1
$[nBu_4N]_2[2c]$	+	0.59	5.58	74	2.5
$[nBu_4N]_2[2c]^{[b]}$	+	0.70	6.74	70	3.3
<b>N719</b>	+	0.74	13.4	75	7.3
<b>N719</b> <sup>[b]</sup>	+	0.78	10.97	68	5.8
$[A^{H,H}]^{+ [66]}$	+	0.55	8.22	69	3.1
$[B^H]^{+ [38,a]}$	–	0.54	8.49	73	3.4
$[C^H]^{+ [38,a]}$	–	0.69	11.61	73	5.8

[a] Guanidinium thiocyanate was employed additionally in the electrolyte solution. [b] The electrolyte concentration was reduced to 0.100 M 1-methyl-3-propylimidazolium iodide and 0.020 M iodine in  $CH_3CN$ .

**Table 3.** Photovoltaic data of cells using the  $[3]^{3+/2+}$  and  $[4]^{3+/2+}$  redox mediators under AM1.5 light conditions.

Dye	Electrolyte	$V_{oc}$ [V]	$J_{sc}$ [ $mA\,cm^{-2}$ ]	FF [%]	$\eta$ [%]
$[nBu_4N]_2[2a]$	$[3]^{3+/2+}$	0.10	0.30	21	< 0.1
$[nBu_4N]_2[2a]$	$[4]^{3+/2+}$	0.59	1.07	66	0.4
$[nBu_4N]_2[2b]$	$[3]^{3+/2+}$	0.61	0.95	70	0.4
$[nBu_4N]_2[2b]$	$[4]^{3+/2+}$	0.66	1.90	73	0.9
$[nBu_4N]_2[2c]$	$[3]^{3+/2+}$	0.70	2.63	71	1.3
$[nBu_4N]_2[2c]$	$[4]^{3+/2+}$	0.66	3.06	71	1.4
<b>N719</b>	$[3]^{3+/2+}$	0.69	2.80	57	1.1
<b>N719</b>	$[4]^{3+/2+}$	0.64	2.68	62	1.1
<b>N719</b> <sup>[70a]</sup>	$[3]^{3+/2+}$	0.58	3.03	66	1.1
<b>N719</b> <sup>[92b]</sup>	$[3]^{3+/2+}$	0.62	3.80	76	1.8
<b>N719</b> <sup>[93c]</sup>	$[3]^{3+/2+}$	0.65	5.47	49	1.8

[a]  $[Co(bpy)_3][B(CN)_4]_2$  (0.22 M);  $[Co(bpy)_3][B(CN)_4]_3$  (0.05 M); 4-*tert*-butylpyridine (0.2 M) and lithium perchlorate (0.1 M) in  $CH_3CN$ ; [b]  $[Co(bpy)_3][PF_6]_2$  (0.2 M);  $[Co(bpy)_3][PF_6]_3$  (0.02 M); 4-*tert*-butylpyridine (0.5 M) and lithium perchlorate (0.1 M) in  $CH_3CN$ ; [c]  $[Co(bpy)_3][PF_6]_2$  (0.2 M);  $[Co(bpy)_3][PF_6]_3$  (0.02 M); 4-*tert*-butylpyridine (0.5 M) and lithium perchlorate (0.1 M) in  $CH_3CN$ .

and electron recombination kinetics differs for both dyes. This shows that the standard electrolyte concentration is optimized for **N719**, but the optimum electrolyte concentration needs to be determined for each dye individually. However, this is beyond the scope of this study.

Electron recombination of conduction band electrons with the oxidized mediator ( $I_3^-$ ,  $[3]^{3+}$ ,  $[4]^{3+}$ ) is a complex function of the driving force (Marcus normal or inverted region), the electronic coupling, and the presence of surface protection.<sup>[89]</sup> Recombination kinetics with  $I_3^-$  is slow,<sup>[89]</sup> yet all cells with  $[2]^{2+}/I_3^-/I^-$  combinations profit from the presence of CDCA as surface protecting agent and show higher short-circuit current densities (Table 2, Figure 5a, Figure 6a). With the  $I_3^-/I^-$  couple, the dark current for  $[2a]^{2+}-[2c]^{2+}$  sensitizers is higher than that of **N719** (Figure 6b). However this observation reverses for the cobalt-based electrolytes (Figure 7b). Obviously, cells with the tridentate cyclometalated complexes  $[2b]^{2+}$  and  $[2c]^{2+}$  cope with the cobalt-based electrolytes, but the cell performance with **N719** dyes and cobalt-based electrolytes is severely reduced. The poor performance of **N719** in combination with cobalt-based electrolytes can be traced back to the higher dark current densities and consequently a strongly diminished short-circuit current density (Figure 6b, 7b; Table 1 and Table 2). As a working hypothesis, the **N719** dye better shields  $TiO_2$  from  $I_2/I_3^-$ , but  $[2b]^{2+}$  and  $[2c]^{2+}$  better shield  $TiO_2$  from cobalt-based electrolytes. This effect is certainly related to molecular structure, packing density (cf. dye loadings, Table 4) and protonation state of the dyes.<sup>[28]</sup>

Comparing the influence of the two cobalt-based electrolytes on the dark current densities of the **N719** and  $[2c]^{2+}$  dyes, the bpy-based electrolyte  $[3]^{3+/2+}$  shows the lower dark current density (Figure 7b). For cobalt-based electrolytes with potentials above about 0.55 V vs. NHE, recombination with electrons in the conduction band should be in the Marcus inverted region.<sup>[67]</sup> In accordance with this reported limiting value, recombination with  $[3]^{3+}$  is hampered as compared to

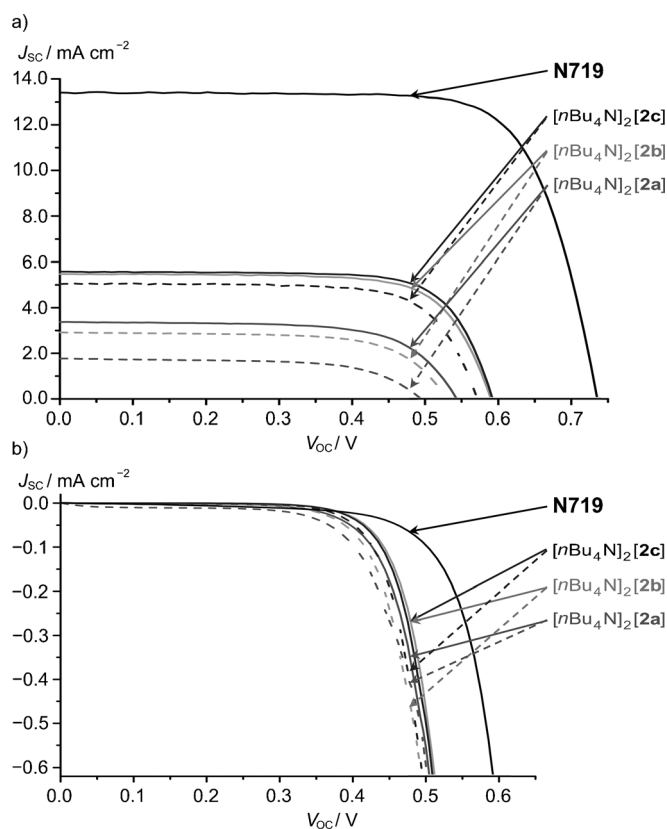


**Figure 6.** a) Current density–voltage characteristics of cells with  $[\text{nBu}_4\text{N}]_2[\mathbf{2a}]$ ,  $[\text{nBu}_4\text{N}]_2[\mathbf{2b}]$ ,  $[\text{nBu}_4\text{N}]_2[\mathbf{2c}]$ , and **N719** using the  $\text{I}_3^-/\text{I}^-$  redox mediator with/without CDCA (—/----) under illumination; b) corresponding dark current density–voltage measurements.

Table 4. Dye loadings.		
Dye	CDCA	$\text{mol cm}^{-2}$
$[\text{nBu}_4\text{N}]_2[\mathbf{2a}]$	–	$1.39 \times 10^{-7}$
$[\text{nBu}_4\text{N}]_2[\mathbf{2a}]$	+	$1.24 \times 10^{-7}$
$[\text{nBu}_4\text{N}]_2[\mathbf{2b}]$	–	$1.08 \times 10^{-7}$
$[\text{nBu}_4\text{N}]_2[\mathbf{2b}]$	+	$0.84 \times 10^{-7}$
$[\text{nBu}_4\text{N}]_2[\mathbf{2c}]$	–	$1.81 \times 10^{-7}$
$[\text{nBu}_4\text{N}]_2[\mathbf{2c}]$	+	$1.42 \times 10^{-7}$
<b>N719</b>	+	$0.55 \times 10^{-7}$

recombination with  $[\mathbf{4}]^{3+}$  accounting for the lower dark current density. For both low-spin cobalt(III) complexes  $[\mathbf{3}]^{3+}$  and  $[\mathbf{4}]^{3+}$  recombination with an electron initially yields low-spin cobalt(II) complexes corresponding to a metastable low-spin state which then undergoes spin crossover to the high spin state.<sup>[83,95]</sup> This effect might account for the favorable dark current densities of the cobalt-based electrolytes compared to the  $\text{I}_3^-/\text{I}^-$  couple for  $[\mathbf{2b}]^{2-}$  and  $[\mathbf{2c}]^{2-}$  (Figure 6b,7b).

Electron lifetimes were determined by the photovoltage response to a small amplitude light modulation as a function of the quasi Fermi level of  $\text{TiO}_2$  (Figure 8). All responses are linear in the semi-logarithmic plot, suggesting that recombination depends exponentially on the potential without participation of surface states.<sup>[68]</sup> As suggested above, CDCA retards recom-

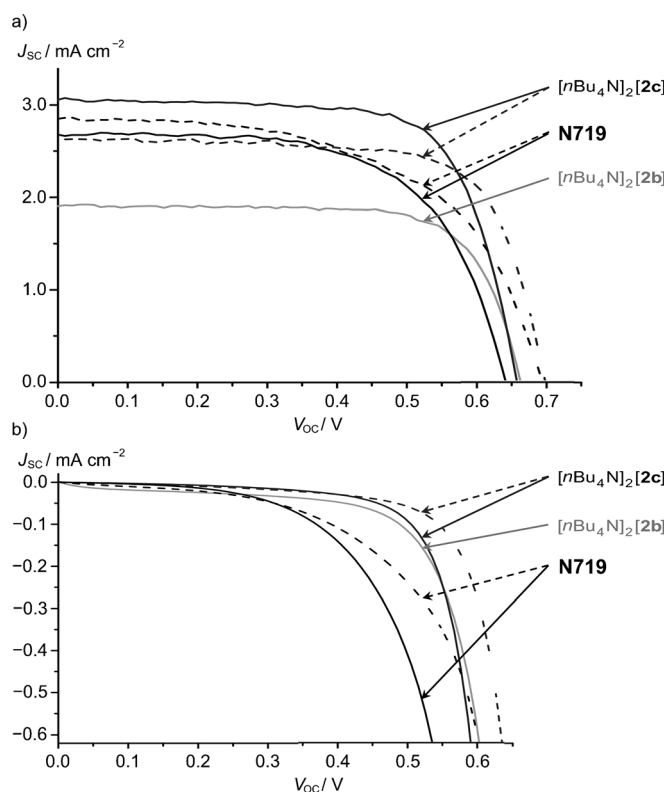


**Figure 7.** a) Current density–voltage characteristics of cells with  $[\text{nBu}_4\text{N}]_2[\mathbf{2b}]$ ,  $[\text{nBu}_4\text{N}]_2[\mathbf{2c}]$ , and **N719** using the  $[\mathbf{3}]^{3+/2+}$  (----) and  $[\mathbf{4}]^{3+/2+}$  (—) redox mediators under illumination; b) corresponding dark current density–voltage measurements.

bination with the iodine shuttle and increases the lifetime (Figure 8a). **N719** displays the highest lifetime with the  $\text{I}_3^-/\text{I}^-$  couple but performs poorly with the cobalt-based electrolytes (Figure 8). The slow dye regeneration kinetics of the cobalt-based electrolytes allowing for recombination with the oxidized dyes easily accounts for this observation. Slightly faster dye regeneration and/or better surface shielding with the dye/electrolyte combination  $[\mathbf{2c}]^{2-}/[\mathbf{3}]^{3+/2+}$  yields a higher electron lifetime (Figure 8b).

Finally, the open-circuit voltages  $V_{oc}$  should increase in the electrolyte series  $\text{I}_3^-/\text{I}^- < [\mathbf{3}]^{3+/2+} < [\mathbf{4}]^{3+/2+}$  according to the electrochemical data (Figure 4). Indeed,  $V_{oc}$  of the cobalt electrolytes is somewhat larger than that of the  $\text{I}_3^-/\text{I}^-$  couple for  $[\mathbf{2a}]^{2-}$ ,  $[\mathbf{2b}]^{2-}$ , and  $[\mathbf{2c}]^{2-}$  dyes, although the effect is less pronounced than expected from the redox potentials (Figure 4).

Overall, the combination of cobalt-based electrolytes with TPA-appended dyes, especially  $[\mathbf{2c}]^{2-}$  outperforms the standard dye **N719** with cobalt-based electrolytes. The absolute performance of **N719** and the  $\text{I}_3^-/\text{I}^-$  couple with optimized concentration is still unrivaled with the systems under study.

## Conclusion

The bis(tridentate) cyclometalated ruthenium complexes  $[\mathbf{1a}]$   $[\text{PF}_6]_2-[\mathbf{1c}][\text{PF}_6]$  as well as their saponified counterparts  $[\text{nBu}_4\text{N}]_2[\mathbf{2a}]-[\text{nBu}_4\text{N}]_2[\mathbf{2c}]$  were synthesized and characterized

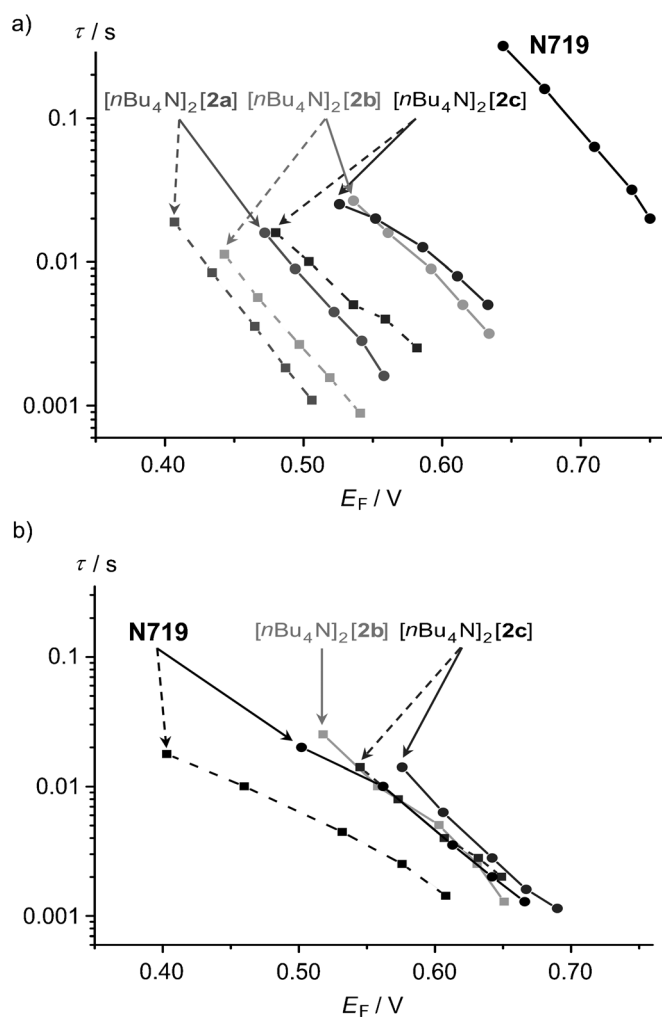


**Figure 8.** a) Electron recombination lifetimes ( $\tau$ ) of cells with  $[n\text{Bu}_4\text{N}]_2[2\text{a}]$ ,  $[n\text{Bu}_4\text{N}]_2[2\text{b}]$ ,  $[n\text{Bu}_4\text{N}]_2[2\text{c}]$ , and **N719** using a) the  $\text{I}_3^-/\text{I}^-$  redox mediator with/without CDCA ( $\square/\square$ ) and b) using the  $[3]^{3+/2+}$  ( $\circ$ ) and  $[4]^{3+/2+}$  ( $\square$ ) redox mediators.

using mass spectrometry, UV/Vis and emission spectroscopy, and electrochemical methods. Oxidation of  $[2\text{a}]^{2-}$ – $[2\text{c}]^{2-}$  yields strongly coupled mixed valent species  $[2\text{a}]^{-}$ – $[2\text{c}]^{-}$  with substantial charge delocalization between the metal center and the triarylamine fragment as evidenced from TD-DFT calculations.<sup>[62,63]</sup> Yet, the degree of this delocalization is reduced in the saponified complexes  $[2\text{a}]^{-}$ – $[2\text{c}]^{-}$  as compared to the corresponding esters  $[1\text{a}]^{2+}$ – $[1\text{c}]^{2+}$  due to an increased charge density at the metal center. Concomitantly, all redox potentials shift to substantially lower values. Charge delocalization should be beneficial for applications in dye-sensitized solar cells as it hampers undesired recombination processes. However, the low redox potentials, which result from the large resonance stabilization, poses a challenge in the selection of a suitable redox electrolyte for efficient dye regeneration. As a consequence, dye  $[2\text{c}]^{2-}$  with the highest oxidation potential yields the best cell performance of the cyclometalated complexes in this study in conjunction with triiodide/iodide ( $\eta=3.3\%$ ). The reference dye **N719**/triiodide/iodide combination remains un-

surpassed however ( $\eta=5.8\%$  under the same conditions). Compared to the triiodide/iodide cells, the efficiencies of the cells containing cobalt electrolytes are smaller by about a factor of three despite larger open-circuit voltages. We attribute this to the substantially slowed dye regeneration by the cobalt electrolytes which results in reduced short-circuit currents. In the presence of cobalt electrolytes, however, the cyclometalated dye with the carbazole substituent  $[2\text{c}]^{2-}$  ( $\eta=1.4\%$ ) surpasses the thiocyanato-based dye **N719** ( $\eta=1.1\%$ ). This once again underlines the exceptional suitability of the triiodide/iodide electrolyte for thiocyanate-based sensitizers. We aim to dedicate further work to the understanding of the opposing trends of overall cell performances with the cobalt and iodide based electrolytes.

## Experimental Section

Chemicals were obtained from commercial suppliers (Acros, Sigma-Aldrich, Solaronix SA, Wako, TCI, Boulder Scientific) and used without further purification. Air- or moisture-sensitive reactions were performed in dried glassware in an inert gas atmosphere (argon, quality 4.6). Acetonitrile was refluxed over  $\text{CaH}_2$  and distilled under argon prior to use. Toluene was refluxed over sodium and distilled under argon prior to use. The ligands trimethyl-2,2';6',2''-terpyridine-4,4',4''-tricarboxylate  $\text{Me}_3\text{tctpy}$ ,<sup>[22]</sup> 1-bromo-3,5-di(2-pyridyl)-benzene,<sup>[96]</sup>  $\text{ddpd}$ <sup>[81]</sup> as well as the ruthenium(III) complex  $\text{RuCl}_3(\text{Me}_3\text{tctpy})$ <sup>[22]</sup> and the palladium precatalyst  $[\text{Pd}]_2$ <sup>[84]</sup> were synthesized according to previously reported procedures. IR spectra were recorded on a Varian Excalibur Series 3100 FTIR spectrometer using KBr disks. IR absorption band intensities are classified as s (strong), m (medium), w (weak), and sh (shoulder). UV/Vis spectra were recorded on a Varian Cary 5000 spectrometer in 1 cm cuvettes. Emission spectra were recorded on a Varian Cary Eclipse spectrometer. Quantum yields were determined by comparing the areas under the emission spectra on an energy scale recorded for solutions of the samples and a reference with matching absorbances ( $\Phi([\text{Ru}(\text{bipy})_3\text{Cl}_2]=0.094$  in deaerated MeCN).<sup>[97]</sup> Experimental uncertainty is estimated to be 15%. ESI<sup>+</sup> and high-resolution ESI<sup>+</sup> mass spectra were recorded on a Micromass QToF Ultima API mass spectrometer with analyte solutions in acetonitrile. FD mass spectra were recorded on a Thermo Fisher DFS mass spectrometer with a LIFDI upgrade. Elemental analyses were performed by the micro-analytical laboratory of the chemical institutes of the University of Mainz. NMR spectra were obtained with a Bruker Avance II 400 spectrometer at 400.31 ( $^1\text{H}$ ), 100.66 ( $^{13}\text{C}$ ), 376.67 ( $^{19}\text{F}$ ) at 25 °C. Chemical shifts  $\delta$  [ppm] are reported with respect to residual solvent signals as internal standards ( $^1\text{H}$ ,  $^{13}\text{C}$ ):  $\text{CD}_3\text{CN}$   $\delta(^1\text{H})=1.94$  ppm,  $\delta(^{13}\text{C})=1.32$  and 118.26 ppm,<sup>[98]</sup>  $\text{CD}_2\text{Cl}_2$   $\delta(^1\text{H})=5.32$  ppm,  $\delta(^{13}\text{C})=53.84$  ppm<sup>[98]</sup> or external  $\text{CFCl}_3$  ( $^{19}\text{F}$ :  $\delta=0$  ppm). Electrochemical experiments were performed with a BioLogic SP-50 voltammetric analyzer at a sample concentration of  $10^{-3}$  M using platinum wire working and counter electrodes and a 0.01 M  $\text{Ag}/\text{AgNO}_3$  reference electrode. Measurements were carried out at a scan rate of  $100\text{ mVs}^{-1}$  for cyclic voltammetry experiments and at  $10\text{ mVs}^{-1}$  for square-wave voltammetry experiments using 0.1 M  $[n\text{Bu}_4\text{N}][\text{PF}_6]$  as supporting electrolyte in acetonitrile. Potentials are given relative to the ferrocene/ferrocenium couple (0.40 V vs. SCE,  $E_{1/2}=0.09\pm 5\text{ mV}$  under the given conditions).<sup>[99]</sup>

Current–voltage characteristics of the DSSCs were measured with a Keithley Model 2400 source meter and a solar simulator with a 300 W Xenon arc-lamp (Newport) under 1 sun illumination

(AM 1.5, 100 mW cm<sup>-2</sup>). A light shading mask, placed on the residual area of the front side of the FTO substrate (except for the 0.16 cm<sup>2</sup> TiO<sub>2</sub> active area), was employed to prevent overestimation of the power conversion efficiency. The quantum efficiencies of the DSSCs were measured by incident photon-to-current conversion efficiency (IPCE) measurements (PV Measurements, Inc.). UV/Vis spectra of the dye loading solutions were collected on a Jasco V-670 UV/Vis spectrometer. The electron lifetimes were obtained by intensity modulated photovoltage spectroscopy (IMVS) under open-circuit conditions as a function of light intensity using a controlled intensity modulated photo spectroscopy (CIMPS) system (Zahner).

**Density functional theory calculations:** DFT calculations were carried out using the ORCA program package (version 3.0.2).<sup>[100]</sup> Tight convergence criteria were chosen for all calculations (Keywords TightSCF and TightOpt). All calculations employ the resolution of identity (Split-RI-J) approach for the coulomb term in combination with the chain-of-spheres approximation for the exchange term (COSX).<sup>[101,102]</sup> All calculations were performed using the hybrid functional B3LYP<sup>[103]</sup> in combination with Ahlrichs' split-valence double- $\zeta$  basis set def2-SV(P), which comprises polarization functions for all non-hydrogen atoms.<sup>[104,105]</sup> Relativistic effects were calculated at the zeroth-order regular approximation (ZORA) niveau.<sup>[106]</sup> The ZORA keyword automatically invokes relativistically adjusted basis sets.<sup>[107]</sup> To account for solvent effects a conductor-like screening model (COSMO) modelling acetonitrile was used in all calculations.<sup>[108]</sup> Explicit counterions and/or solvent molecules were not taken into account in all cases.

**Synthesis of *N,N*-bis-(4-methoxyphenyl)-3,5-(di-2-pyridyl)aniline (dpbH-N(4-C<sub>6</sub>H<sub>4</sub>OMe)<sub>2</sub>) L<sup>a</sup>:** 2-Dicyclohexylphosphano-2',6'-diisopropoxybiphenyl (12 mg, 0.026 mmol, 0.04 equiv) and the precatalyst [Pd]<sub>2</sub> (8 mg, 0.011 mmol, 0.02 equiv) were suspended in dry toluene (10 mL) and stirred for 10 min followed by the addition of 1-bromo-3,5-di(2-pyridyl)benzene (200 mg, 0.643 mmol, 1 equiv), bis-(4-methoxyphenyl)amine (221 mg, 0.964 mmol, 1.50 equiv), sodium *tert*-butoxide (93 mg, 0.968 mmol, 1.51 equiv), and further dry toluene (40 mL). The resulting mixture was refluxed for 12 h. After cooling to room temperature, the solvent was removed under reduced pressure and the brown residue was purified by column chromatography on silica gel (eluent: dichloromethane/ethyl acetate 10:1→7:1), yielding L<sup>a</sup> as slightly yellow solid. Yield: 241 mg (0.524 mmol, 82%). NMR and mass spectrometric data agree with reported values.<sup>[62]</sup>

**Synthesis of *N,N*-diphenyl-3,5-(di-2-pyridyl)aniline (dpbH-NPh<sub>2</sub>) L<sup>b</sup>:** 2-Dicyclohexylphosphano-2',6'-diisopropoxybiphenyl (12 mg, 0.026 mmol, 0.04 equiv) and the precatalyst [Pd]<sub>2</sub> (7 mg, 0.009 mmol, 0.01 equiv) were suspended in dry toluene (10 mL) and stirred for 10 min followed by the addition of 1-bromo-3,5-di(2-pyridyl)benzene (200 mg, 0.643 mmol, 1 equiv), diphenylamine (163 mg, 0.964 mmol, 1.50 equiv), sodium *tert*-butoxide (93 mg, 0.968 mmol, 1.51 equiv) and further dry toluene (40 mL). The resulting mixture was refluxed for 12 h. After cooling to room temperature, the solvent was removed under reduced pressure and the brown residue was purified by column chromatography on silica gel (eluent: dichloromethane/ethyl acetate 10:1) yielding L<sup>b</sup> as slightly yellow solid. Yield: 222 mg (0.556 mmol, 86%). Anal. calcd. for C<sub>28</sub>H<sub>21</sub>N<sub>3</sub> (399.49): C 84.18, H 5.30, N 10.52; found: C 83.86, H 5.39, N 10.39. MS(FD<sup>+</sup>): *m/z* (%) = 399.1 (100) [L<sup>b</sup>]<sup>+</sup>. <sup>1</sup>H NMR (CD<sub>2</sub>Cl<sub>2</sub>):  $\delta$  [ppm] = 8.64 (d, <sup>3</sup>J<sub>HH</sub> = 5 Hz, 2H, H<sup>8</sup>), 8.32 (s, 1H, H<sup>9</sup>), 7.80 (s, 2H, H<sup>2</sup>), 7.76–7.71 (m, 4H, H<sup>5</sup>, H<sup>6</sup>), 7.29 (t, <sup>3</sup>J<sub>HH</sub> = 8 Hz, 4H, H<sup>13</sup>), 7.24 (dd, <sup>3</sup>J<sub>HH</sub> = 9 Hz, 5 Hz, 2H, H<sup>7</sup>), 7.17 (d, <sup>3</sup>J<sub>HH</sub> = 8 Hz, 4H, H<sup>11</sup>), 7.06 (t, <sup>3</sup>J<sub>HH</sub> = 7 Hz, 2H, H<sup>13</sup>). <sup>13</sup>C{<sup>1</sup>H} NMR (CD<sub>2</sub>Cl<sub>2</sub>):  $\delta$  [ppm] = 157.1 (C<sup>4</sup>), 150.0 (C<sup>8</sup>), 149.4 (C<sup>1</sup>), 148.3 (C<sup>10</sup>), 141.5 (C<sup>3</sup>), 137.1 (C<sup>6</sup>),

129.7 (C<sup>12</sup>), 124.7 (C<sup>11</sup>), 123.5 (C<sup>2</sup>), 123.3 (C<sup>13</sup>), 122.8 (C<sup>7</sup>), 120.9 (C<sup>5</sup>), 120.3 (C<sup>9</sup>). IR (KBr disk):  $\tilde{\nu}$  [cm<sup>-1</sup>] = 3054 (w, aromatic C-H), 1584 (s, C=C), 1566 (s, C=C), 1492 (s), 1352 (s), 1255 (s), 779 (s), 749 (s), 700 (s).

**Synthesis of 1-(*N*-carbazolyl)-3,5-(di-2-pyridyl)benzene (dpbH-N-carbazole) L<sup>c</sup>:** 2-Dicyclohexylphosphano-2',6'-diisopropoxybiphenyl (12 mg, 0.026 mmol, 0.04 equiv) and the precatalyst [Pd]<sub>2</sub> (7 mg, 0.009 mmol, 0.01 equiv) were suspended in dry toluene (10 mL) and stirred for 10 min followed by the addition of 1-bromo-3,5-di(2-pyridyl)benzene (200 mg, 0.643 mmol, 1 equiv), carbazole (161 mg, 0.964 mmol, 1.50 equiv), sodium *tert*-butoxide (93 mg, 0.968 mmol, 1.51 equiv), and further dry toluene (40 mL). The resulting mixture was refluxed for 12 h. After cooling to room temperature, the solvent was removed under reduced pressure and the brown residue was purified by column chromatography on silica gel (eluent: dichloromethane/ethyl acetate 20:1) yielding L<sup>c</sup> as slightly yellow solid. Yield: 251 mg (0.556 mmol, 98%). Anal. calcd. for C<sub>28</sub>H<sub>19</sub>N<sub>3</sub> (397.47) -0.5H<sub>2</sub>O: C 82.73, H 4.96, N 10.34; found: C 82.96, H 4.53, N 10.04. MS(FD<sup>+</sup>): *m/z* (%) = 198.6 (1.5) [L<sup>c</sup>]<sup>2+</sup>, 397.1 (100) [L<sup>c</sup>]<sup>+</sup>. <sup>1</sup>H NMR (CD<sub>2</sub>Cl<sub>2</sub>):  $\delta$  [ppm] = 8.85 (s, 1H, H<sup>9</sup>), 8.73 (d, <sup>3</sup>J<sub>HH</sub> = 4 Hz, 2H, H<sup>8</sup>), 8.31 (s, 2H, H<sup>2</sup>), 8.19 (d, *J* = 8 Hz, 2H, H<sup>14</sup>), 7.92 (d, *J* = 8 Hz, 2H, H<sup>5</sup>), 7.83 (t, <sup>3</sup>J<sub>HH</sub> = 8 Hz, 2H, H<sup>6</sup>), 7.54 (d, <sup>3</sup>J<sub>HH</sub> = 8 Hz, 2H, H<sup>11</sup>), 7.44 (t, <sup>3</sup>J<sub>HH</sub> = 7 Hz, 2H, H<sup>12</sup>), 7.29–7.35 (m, 4H, H<sup>7</sup>, H<sup>13</sup>). <sup>13</sup>C{<sup>1</sup>H} NMR (CD<sub>2</sub>Cl<sub>2</sub>):  $\delta$  [ppm] = 156.4 (C<sup>4</sup>), 150.3 (C<sup>8</sup>), 142.2 (C<sup>3</sup>), 141.4 (C<sup>10</sup>), 139.1 (C<sup>1</sup>), 137.3 (C<sup>6</sup>), 126.5 (C<sup>12</sup>), 126.2 (C<sup>2</sup>), 124.6 (C<sup>9</sup>), 123.8 (C<sup>15</sup>), 123.2 (C<sup>7</sup>), 121.0 (C<sup>5</sup>), 120.7 (C<sup>14</sup>), 120.4 (C<sup>13</sup>), 110.3 (C<sup>11</sup>). IR (KBr disk):  $\tilde{\nu}$  [cm<sup>-1</sup>] = 3049 (w, aromatic C-H), 1587 (s, C=C), 1566 (s, C=C), 1448 (s), 1228 (s), 779 (s), 747 (s), 723 (s).

**Synthesis of [Ru(L<sup>a</sup>)(Me<sub>3</sub>tctpy)][PF<sub>6</sub>]<sub>2</sub> [1a][PF<sub>6</sub>]<sub>2</sub>:**<sup>[63a]</sup> RuCl<sub>3</sub>(Me<sub>3</sub>tctpy) (222 mg, 0.361 mmol, 1 equiv) and AgBF<sub>4</sub> (204 mg, 1.05 mmol, 2.9 equiv) were dissolved in dry acetonitrile (15 mL) and refluxed in the dark for 3 h. After cooling to room temperature, the mixture was filtered through a syringe filter (0.2  $\mu$ m) and the solvent removed under reduced pressure. The dark residue was dissolved in deaerated *n*-butanol (20 mL) and L<sup>a</sup> (200 mg, 0.435 mmol, 1.2 equiv) was added. The mixture was refluxed for 13 h followed by removal of the solvent under reduced pressure. The raw product was redissolved in MeCN (5 mL) and triturated by addition of a solution of [NH<sub>4</sub>][PF<sub>6</sub>] (177 mg, 1.08 mmol, 3 equiv) in H<sub>2</sub>O (2 mL). The black precipitate was filtered off and washed with diethyl ether and hexanes. After purification via column chromatography on silica gel (eluent: chloroform/methanol 1:0→7:1), [1a][PF<sub>6</sub>]<sub>2</sub> was obtained as black powder. Yield: 364 mg (0.327 mmol, 91%). MS(ESI<sup>+</sup>): *m/z* (%) = 967.1 (100) [1a]<sup>+</sup>. Traces of the paramagnetic Ru<sup>III</sup> complex [1a][PF<sub>6</sub>]<sub>2</sub> broaden all NMR resonances of [1a][PF<sub>6</sub>]<sub>2</sub> due to the presence of a fast self-exchange reaction.<sup>[62,63a]</sup>

**Synthesis of [nBu<sub>4</sub>N]<sub>2</sub>[Ru(L<sup>a</sup>)(H<sub>3</sub>tctpy)] [nBu<sub>4</sub>N]<sub>2</sub>[2a]:** Complex [1a][PF<sub>6</sub>]<sub>2</sub> (360 mg, 0.324 mmol) was suspended in deaerated H<sub>2</sub>O (35 mL) and *n*Bu<sub>4</sub>NOH (1.5 M in H<sub>2</sub>O, 5 mL) and hydrazine (1 mL) were added. After refluxing for 13 h, the mixture was extracted with dichloromethane (3×50 mL). The organic phases were combined, dried over MgSO<sub>4</sub>, and the solvent was removed under reduced pressure. The purple residue was dissolved in MeCN (10 mL) and triturated by adding a 1:1 mixture of diethyl ether and hexanes (50 mL), yielding [nBu<sub>4</sub>N]<sub>2</sub>[2a] as purple powder. Yield: 347 mg (0.247 mmol, 66%). Anal. calcd. for C<sub>80</sub>H<sub>104</sub>N<sub>8</sub>O<sub>8</sub>Ru (1406.8) -8H<sub>2</sub>O: C 61.95, H 7.80, N 7.22; found: C 62.24, H 7.88, N 7.22. MS(ESI<sup>+</sup>): *m/z* (%) = 242.3 (100) [nBu<sub>4</sub>N]<sup>+</sup>, 462.6 (12) [2a + 3H]<sup>2+</sup>, 925.1 (48) [2a + 3H]<sup>+</sup>. HR-MS(ESI<sup>+</sup>, *m/z*): Calcd. for C<sub>48</sub>H<sub>35</sub>N<sub>6</sub>O<sub>8</sub><sup>96</sup>Ru [2a + 3H]<sup>+</sup>: 919.1592; Found: 919.1578. MS(ESI<sup>-</sup>): *m/z* (%) = 439.4 (85) [2a-CO<sub>2</sub>]<sup>2-</sup>, 461.4 (56) [2a]<sup>2-</sup>, 834.9 (17) [2a-2CO<sub>2</sub>]<sup>-</sup>, 878.8 (100) [2a-CO<sub>2</sub>]<sup>-</sup>, 922.8 (19) [2a]<sup>-</sup>, 1163.8 (77) ([nBu<sub>4</sub>N][2a])<sup>-</sup>. <sup>1</sup>H NMR (CD<sub>3</sub>CN):  $\delta$  [ppm] = 9.25 (s, 2H, H<sup>2A</sup>), 8.86 (s, 2H, H<sup>5A</sup>), 8.03 (s, 2H,



H<sup>2B</sup>), 7.90 (d, <sup>3</sup>J<sub>HH</sub> = 8 Hz, 2H, H<sup>5B</sup>), 7.47 (t, <sup>3</sup>J<sub>HH</sub> = 7 Hz, 2H, H<sup>6B</sup>), 7.37 (d, <sup>3</sup>J<sub>HH</sub> = 6 Hz, 2H, H<sup>7A</sup>), 7.20 (d, <sup>3</sup>J<sub>HH</sub> = 9 Hz, 4H, H<sup>12A</sup>), 7.07 (d, <sup>3</sup>J<sub>HH</sub> = 6 Hz, 2H, H<sup>8A</sup>), 7.05 (d, <sup>3</sup>J<sub>HH</sub> = 6 Hz, 2H, H<sup>8B</sup>), 6.92 (d, <sup>3</sup>J<sub>HH</sub> = 9 Hz, 4H, H<sup>12B</sup>), 6.58 (t, <sup>3</sup>J<sub>HH</sub> = 6 Hz, 2H, H<sup>7B</sup>), 3.79 (s, 6H, H<sup>14B</sup>), 3.19–3.00 (m, 16H, H<sup>1</sup>), 1.68–1.44 (m, 16H, H<sup>2</sup>), 1.38–1.21 (m, 16H, H<sup>3</sup>), 0.93 (t, <sup>3</sup>J<sub>HH</sub> = 7 Hz, 24H, H<sup>4</sup>). <sup>13</sup>C{<sup>1</sup>H} NMR (CD<sub>3</sub>CN): δ [ppm] = 219.0 (C<sup>9B</sup>), 169.1 (C<sup>4B</sup>), 168.3 (C<sup>10A</sup>), 167.1 (C<sup>11A</sup>), 160.2 (C<sup>4A</sup>), 155.7 (C<sup>13B</sup>), 154.5 (C<sup>8A</sup>), 153.7 (C<sup>3A</sup>), 152.9 (C<sup>8B</sup>), 147.9 (C<sup>6A</sup>), 143.9 (C<sup>9B</sup>), 143.5 (C<sup>3B</sup>), 142.8 (C<sup>1B</sup>), 136.0 (C<sup>6B</sup>), 126.6 (C<sup>7A</sup>), 124.8 (C<sup>11B</sup>), 123.6 (C<sup>5A</sup>), 123.4 (C<sup>2B</sup>), 122.9 (C<sup>2A</sup>), 122.4 (C<sup>7B</sup>), 120.4 (C<sup>5B</sup>), 115.6 (C<sup>12B</sup>), 59.3 (C<sup>1</sup>), 56.1 (C<sup>14B</sup>), 24.3 (C<sup>2</sup>), 20.3 (C<sup>3</sup>), 13.8 (C<sup>4</sup>). IR (KBr disk):  $\tilde{\nu}$  [cm<sup>-1</sup>] = 3440 (s, O-H crystal water), 3065 (w, aromatic C-H), 2960, 2873, 2843 (m, aliphatic C-H), 1620 (s, C=O carboxylate), 1598 (sh, C=C), 1465 (m, aliphatic C-N), 1341 (s, aromatic C-N), 1237 (s, C-O-C).

**Synthesis of [Ru(L<sup>b</sup>)(Me<sub>3</sub>tctpy)](PF<sub>6</sub>) [1b][PF<sub>6</sub>]:** RuCl<sub>3</sub>(Me<sub>3</sub>tctpy) (263 mg, 0.429 mmol, 1 equiv) and AgBF<sub>4</sub> (243 mg, 1.25 mmol, 2.9 equiv) were dissolved in dry acetonitrile (15 mL) and refluxed in the dark for 3 h. After cooling to room temperature, the mixture was filtered through a syringe filter (0.2 μm) and the solvent removed under reduced pressure. The dark residue was dissolved in deaerated *n*-butanol (20 mL) and L<sup>b</sup> (206 mg, 0.516 mmol, 1.2 equiv) was added. The mixture was refluxed for 13 h followed by removal of the solvent under reduced pressure. The raw product was redissolved in MeCN (5 mL) and triturated by addition of a solution of [NH<sub>4</sub>][PF<sub>6</sub>] (210 mg, 1.29 mmol, 3 equiv) in H<sub>2</sub>O (2 mL). The black precipitate was filtered off and washed with diethyl ether and hexanes. After purification via column chromatography on silica gel (eluent: chloroform/methanol 1:0→7:1), [1b][PF<sub>6</sub>] was obtained as a black powder. Yield: 389 mg (0.370 mmol, 86%). MS(ESI<sup>+</sup>): *m/z* (%) = 453.6 (12) [1b]<sup>2+</sup>, 907.1 (100) [1b]<sup>+</sup>. HR-MS(ESI<sup>+</sup>, *m/z*): Calcd. for C<sub>49</sub>H<sub>37</sub>N<sub>6</sub>O<sub>6</sub><sup>96</sup>Ru [1b]<sup>+</sup>: 901.1851; Found: 901.1857. Traces of the paramagnetic Ru<sup>III</sup> complex [1b][PF<sub>6</sub>]<sub>2</sub> broaden all NMR resonances of [1b][PF<sub>6</sub>] due to the presence of a fast self-exchange reaction.<sup>[62,63a]</sup> IR (KBr disk):  $\tilde{\nu}$  [cm<sup>-1</sup>] = 3041 (w, aromatic C-H), 1725 (s, C=O ester), 1599 (m, C=C), 1243 (s), 843 (s, P-F), 588 (m, PF<sub>def</sub>).

**Synthesis of [nBu<sub>4</sub>N]<sub>2</sub>[Ru(L<sup>b</sup>)(H<sub>3</sub>tctpy)] [nBu<sub>4</sub>N]<sub>2</sub>[2b]:** Complex [1b][PF<sub>6</sub>] (279 mg, 0.265 mmol) was suspended in deaerated H<sub>2</sub>O (35 mL), and [nBu<sub>4</sub>N][OH] (1.5 M in H<sub>2</sub>O, 5 mL) and hydrazine (1 mL) were added. After refluxing for 13 h, the mixture was extracted with dichloromethane (3×50 mL). The organic phases were combined, dried over MgSO<sub>4</sub>, and the solvent was removed under reduced pressure. The purple residue was dissolved in MeCN (10 mL) and triturated by adding a 1:1 mixture of diethyl ether and hexanes (50 mL), yielding [nBu<sub>4</sub>N]<sub>2</sub>[2b] as purple powder. Yield: 312 mg (0.323 mmol, 87%). Anal. calcd. for C<sub>78</sub>H<sub>100</sub>N<sub>6</sub>O<sub>6</sub>Ru (1346.8)·6H<sub>2</sub>O: C 64.39, H 7.76, N 7.70; found: C 64.06, H 7.40, N 7.53. MS(ESI<sup>+</sup>): *m/z* (%) = 242.3 (100) [nBu<sub>4</sub>N]<sup>+</sup>, 432.6 (9) [2b+3H]<sup>2+</sup>, 865.2 (8) [2b+3H]<sup>+</sup>. HR-MS(ESI<sup>+</sup>, *m/z*): Calcd. for C<sub>46</sub>H<sub>31</sub>N<sub>6</sub>O<sub>6</sub><sup>96</sup>Ru [2b+3H]<sup>+</sup>: 859.1381; Found: 859.1390. MS(ESI<sup>-</sup>): *m/z* (%) = 387.5 (13) [2b-2CO<sub>2</sub>]<sup>2-</sup>, 409.4 (47) [2b-CO<sub>2</sub>]<sup>2-</sup>, 431.4 (15) [2b]<sup>2-</sup>, 775.0 (28) [2b-2CO<sub>2</sub>]<sup>-</sup>, 818.9 (67) [2b-CO<sub>2</sub>]<sup>-</sup>, 862.9 (13) [2b]<sup>-</sup>, 1103.7 (100) ([nBu<sub>4</sub>N][2b])<sup>-</sup>. <sup>1</sup>H NMR (CD<sub>3</sub>CN): δ [ppm] = 9.20 (s, 2H, H<sup>2A</sup>), 8.80 (s, 2H, H<sup>5A</sup>), 8.10 (s, 2H, H<sup>2B</sup>), 7.96 (d, <sup>3</sup>J<sub>HH</sub> = 8 Hz, 2H, H<sup>5B</sup>), 7.49 (t, <sup>3</sup>J<sub>HH</sub> = 8 Hz, 2H, H<sup>6B</sup>), 7.40–7.26 (m, 10H, H<sup>7A</sup>, H<sup>11B</sup>, H<sup>12B</sup>), 7.11 (d, <sup>3</sup>J<sub>HH</sub> = 5 Hz, 2H, H<sup>8B</sup>), 7.06–6.95 (m, 4H, H<sup>8A</sup>, H<sup>13B</sup>), 6.61 (t, <sup>3</sup>J<sub>HH</sub> = 6 Hz, 2H, H<sup>7B</sup>), 3.19–3.00 (m, 16H, H<sup>1</sup>), 1.67–1.49 (m, 16H, H<sup>2</sup>), 1.41–1.21 (m, 16H, H<sup>3</sup>), 0.94 (t, <sup>3</sup>J<sub>HH</sub> = 7 Hz, 24H, H<sup>4</sup>). <sup>13</sup>C{<sup>1</sup>H} NMR (CD<sub>3</sub>CN): δ [ppm] = 218.8 (C<sup>9B</sup>), 169.1 (C<sup>4B</sup>), 167.6 (C<sup>9A</sup>), 166.6 (C<sup>10A</sup>), 160.2 (C<sup>4A</sup>), 154.4 (C<sup>8A</sup>), 153.6 (C<sup>3A</sup>), 152.9 (C<sup>8B</sup>), 149.9 (C<sup>6A</sup>), 149.9 (C<sup>10B</sup>), 149.4 (C<sup>1A</sup>), 144.0 (C<sup>3B</sup>), 141.0 (C<sup>1B</sup>), 135.9 (C<sup>6B</sup>), 130.3 (C<sup>11B</sup>), 126.5 (C<sup>7A</sup>), 124.7 (C<sup>2B</sup>), 123.5 (C<sup>5A</sup>), 123.1 (C<sup>12B</sup>), 122.7 (C<sup>2A</sup>), 122.5 (C<sup>7B</sup>), 122.4 (C<sup>13B</sup>), 120.4 (C<sup>5B</sup>), 59.3 (C<sup>1</sup>), 24.3 (C<sup>2</sup>), 20.3 (C<sup>3</sup>), 13.8 (C<sup>4</sup>). IR (KBr

disk):  $\tilde{\nu}$  [cm<sup>-1</sup>] = 3440 (s, O-H crystal water), 3065 (w, aromatic C-H), 2960, 2873 (m, aliphatic C-H), 1617 (s, C=O carboxylate), 1598 (sh, C=C), 1465 (m, aliphatic C-N), 1351 (s, aromatic C-N).

**Synthesis of [Ru(L<sup>c</sup>)(Me<sub>3</sub>tctpy)](PF<sub>6</sub>) [1c][PF<sub>6</sub>]:** RuCl<sub>3</sub>(Me<sub>3</sub>tctpy) (257 mg, 0.418 mmol, 1 equiv), and AgBF<sub>4</sub> (237 mg, 1.22 mmol, 2.9 equiv) were dissolved in dry acetonitrile (15 mL) and refluxed in the dark for 3 h. After cooling to room temperature, the mixture was filtered through a syringe filter (0.2 μm) and the solvent removed under reduced pressure. The dark residue was dissolved in deaerated *n*-butanol (20 mL) and L<sup>c</sup> (200 mg, 0.503 mmol, 1.2 equiv) was added. The mixture was refluxed for 13 h followed by removal of the solvent under reduced pressure. The raw product was redissolved in MeCN (5 mL) and triturated by addition of a solution of [NH<sub>4</sub>][PF<sub>6</sub>] (204 mg, 1.25 mmol, 3 equiv) in H<sub>2</sub>O (2 mL). The black precipitate was filtered off and washed with diethyl ether and hexanes. After purification via column chromatography on silica gel (eluent: chloroform/methanol 1:0→7:1) [1c][PF<sub>6</sub>] was obtained as black powder. Yield: 385 mg (0.366 mmol, 88%). MS(ESI<sup>+</sup>): *m/z* (%) = 905.1 (100) [1c]<sup>+</sup>. HR-MS(ESI<sup>+</sup>, *m/z*): Calcd. for C<sub>49</sub>H<sub>35</sub>N<sub>6</sub>O<sub>6</sub><sup>96</sup>Ru [1c]<sup>+</sup>: 899.1694; Found: 899.1725. Traces of paramagnetic Ru<sup>III</sup> complex [1c][PF<sub>6</sub>]<sub>2</sub> broaden all NMR resonances of [1c][PF<sub>6</sub>] due to the presence of a fast self-exchange reaction.<sup>[62,63a]</sup> IR (KBr disk):  $\tilde{\nu}$  [cm<sup>-1</sup>] = 3052 (w, aromatic C-H), 1725 (s, C=O ester), 1599 (m, C=C), 1249 (s), 842 (s, P-F), 588 (m, PF<sub>def</sub>).

**Synthesis of [nBu<sub>4</sub>N]<sub>2</sub>[Ru(L<sup>c</sup>)(H<sub>3</sub>tctpy)] [nBu<sub>4</sub>N]<sub>2</sub>[2c]:** Complex [1c][PF<sub>6</sub>] (233 mg, 0.222 mmol) was suspended in deaerated H<sub>2</sub>O (35 mL), and [nBu<sub>4</sub>N][OH] (1.5 M in H<sub>2</sub>O, 5 mL) and hydrazine (1 mL) were added. After refluxing for 13 h, the mixture was extracted with dichloromethane (3×50 mL). The organic phases were combined, dried over MgSO<sub>4</sub>, and the solvent was removed under reduced pressure. The purple residue was dissolved in MeCN (10 mL) and triturated by adding a 1:1 mixture of diethyl ether and hexanes (50 mL), yielding [nBu<sub>4</sub>N]<sub>2</sub>[2c] as purple powder. Yield: 159 mg (0.118 mmol, 53%). Anal. calcd. for C<sub>78</sub>H<sub>98</sub>N<sub>6</sub>O<sub>6</sub>Ru (1344.7)·8H<sub>2</sub>O: C 63.69, H 7.68, N 7.62; found: C 63.77, H 8.03, N 7.55. MS(ESI<sup>+</sup>): *m/z* (%) = 242.3 (100) [nBu<sub>4</sub>N]<sup>+</sup>, 431.6 (3) [2a+3H]<sup>2+</sup>, 863.1 (89) [2a+3H]<sup>+</sup>. HR-MS(ESI<sup>+</sup>, *m/z*): Calcd. for C<sub>46</sub>H<sub>29</sub>N<sub>6</sub>O<sub>6</sub><sup>96</sup>Ru [2c+3H]<sup>+</sup>: 857.1225; Found: 857.1218. MS(ESI<sup>-</sup>): *m/z* (%) = 386.5 (26) [2c-2CO<sub>2</sub>]<sup>2-</sup>, 408.4 (74) [2c-CO<sub>2</sub>]<sup>2-</sup>, 430.4 (20) [2c]<sup>2-</sup>, 773.0 (40) [2c-2CO<sub>2</sub>]<sup>-</sup>, 816.9 (80) [2c-CO<sub>2</sub>]<sup>-</sup>, 860.9 (13) [2c]<sup>-</sup>, 1101.7 (100) ([nBu<sub>4</sub>N][2c])<sup>-</sup>. <sup>1</sup>H NMR (CD<sub>3</sub>CN): δ [ppm] = 9.25 (s, 2H, H<sup>2A</sup>), 8.85 (s, 2H, H<sup>5A</sup>), 8.39 (s, <sup>3</sup>J<sub>HH</sub> = 9 Hz, 2H, H<sup>2B</sup>), 8.29 (d, <sup>3</sup>J<sub>HH</sub> = 8 Hz, 2H, H<sup>14B</sup>), 8.11 (d, <sup>3</sup>J<sub>HH</sub> = 8 Hz, 2H, H<sup>5B</sup>), 7.72 (d, <sup>3</sup>J<sub>HH</sub> = 8 Hz, 2H, H<sup>11B</sup>), 7.60–7.50 (m, 4H, H<sup>6B</sup>, H<sup>12B</sup>), 7.41–7.31 (m, 4H, H<sup>7A</sup>, H<sup>13B</sup>), 7.21–7.12 (m, 4H, H<sup>8A</sup>, H<sup>8B</sup>), 6.67 (t, <sup>3</sup>J<sub>HH</sub> = 6 Hz, 2H, H<sup>7B</sup>), 3.16–3.00 (m, 16H, H<sup>1</sup>), 1.63–1.51 (m, 16H, H<sup>2</sup>), 1.40–1.24 (m, 16H, H<sup>3</sup>), 0.92 (t, <sup>3</sup>J<sub>HH</sub> = 7 Hz, 24H, H<sup>4</sup>). <sup>13</sup>C{<sup>1</sup>H} NMR (CD<sub>3</sub>CN): δ [ppm] = 223.7 (C<sup>9B</sup>), 169.0 (C<sup>4B</sup>), 167.9 (C<sup>9A</sup>), 166.9 (C<sup>10A</sup>), 160.2 (C<sup>4A</sup>), 154.7 (C<sup>8A</sup>), 153.6 (C<sup>3A</sup>), 153.0 (C<sup>8B</sup>), 148.8 (C<sup>6A</sup>), 146.8 (C<sup>1A</sup>), 144.1 (C<sup>3B</sup>), 143.2 (C<sup>10B</sup>), 136.1 (C<sup>6B</sup>), 130.3 (C<sup>1B</sup>), 127.1 (C<sup>7A</sup>), 126.5 (C<sup>15B</sup>), 123.8 (C<sup>2B</sup>), 123.6 (C<sup>5A</sup>), 123.6 (C<sup>12B</sup>), 122.8 (C<sup>2A</sup>), 122.7 (C<sup>7B</sup>), 121.3 (C<sup>14B</sup>), 120.7 (C<sup>5B</sup>), 120.6 (C<sup>13B</sup>), 111.3 (C<sup>11B</sup>), 59.2 (C<sup>1</sup>), 24.3 (C<sup>2</sup>), 20.3 (C<sup>3</sup>), 13.8 (C<sup>4</sup>). IR (KBr disk):  $\tilde{\nu}$  [cm<sup>-1</sup>] = 3440 (s, O-H crystal water), 3065 (w, aromatic C-H), 2960 (m, aliphatic C-H), 2873 (m, aliphatic C-H), 1614 (s, C=O carboxylate), 1598 (sh, C=C), 1465 (m, aliphatic C-N), 1353 (s, aromatic C-N).

**Synthesis of [Co(bpy)<sub>3</sub>][B(C<sub>6</sub>F<sub>5</sub>)<sub>4</sub>]<sub>2</sub> [3][B(C<sub>6</sub>F<sub>5</sub>)<sub>4</sub>]<sub>2</sub>:** The bpy ligand (2.27 g, 14.6 mmol, 3.2 equiv), dissolved in CH<sub>3</sub>CN (50 mL) was added to a solution of Co(BF<sub>4</sub>)<sub>2</sub>·6H<sub>2</sub>O (1.55 g, 4.55 mmol, 1.0 equiv) in CH<sub>3</sub>CN (50 mL) and the mixture was stirred for 6 h at room temperature. The complex was precipitated by addition of Et<sub>2</sub>O (200 mL) and filtered off, washed with Et<sub>2</sub>O (100 mL), and dried under reduced pressure. The yellow powder was dissolved in a minimum amount of CH<sub>3</sub>CN and Li[B(C<sub>6</sub>F<sub>5</sub>)<sub>4</sub>]<sub>2</sub>·Et<sub>2</sub>O (13.8 g, 18.2 mmol,



4.0 equiv) was added. The volume of the solvent was reduced under reduced pressure and the product was precipitated by addition of water to give a yellow crystalline solid (6.52 g, 3.46 mmol, 76%).  $^1\text{H NMR}$  ( $\text{CD}_3\text{CN}$ ):  $\delta$  [ppm] = 88.3 (bs, 1H), 85.0 (s, 1H), 46.5 (s, 1H), 14.7 (s, 1H).  $^{19}\text{F NMR}$  ( $\text{CD}_3\text{CN}$ ):  $\delta$  [ppm] = -134.04 (bs, 2F), -164.20 (pt, 1F,  $^3J_{\text{FF}} = 19.7$  Hz), -168.68 (pt, 2F,  $^3J_{\text{FF}} = 16.8$  Hz). The  $^1\text{H NMR}$  data match literature values of  $[\text{Co}(\text{bpy})_2][\text{PF}_6]_2$ .<sup>[91]</sup> MS( $\text{ESI}^+$ ):  $m/z$  (%) = 185.6 (7)  $[\text{Co}(\text{bpy})_2]^{2+}$ , 1206.2 (100)  $[\text{Co}(\text{bpy})_3 + \text{B}(\text{C}_6\text{F}_5)_4]^+$ , 2149.3 (17)  $[3 \times (\text{Co}(\text{bpy})_3) + 4 \times (\text{B}(\text{C}_6\text{F}_5)_4)]^{2+}$ , 3092.44 (19)  $[4 \times (\text{Co}(\text{bpy})_3) + 6 \times (\text{B}(\text{C}_6\text{F}_5)_4)]^{2+}$ . HR-MS( $\text{ESI}^+$ ,  $m/z$ ): Calcd. for  $\text{C}_{54}\text{H}_{24}^{10}\text{BCoF}_{20}\text{N}_6$ : 1205.1204; found: 1205.1224.

**Synthesis of  $[\text{Co}(\text{bpy})_3][\text{B}(\text{C}_6\text{F}_5)_4]_3$   $[\text{3}][\text{B}(\text{C}_6\text{F}_5)_4]_3$ :**  $[\text{Co}(\text{bpy})_3](\text{BF}_4)_2$  (2.94 g, 4.20 mol, 1.0 equiv) was dissolved in  $\text{CH}_3\text{CN}$  (100 mL) and 2,3-dichloro-5,6-dicyano-1,4-benzoquinone (1.43 g, 6.30 mmol, 1.5 equiv) was added. The solution was stirred for 5 h at room temperature.  $\text{Li}[\text{B}(\text{C}_6\text{F}_5)_4]\cdot\text{Et}_2\text{O}$  (12.8 g, 16.8 mol, 4.0 equiv) was added and the mixture was diluted with water (200 mL). The precipitate was filtered off, washed with water (200 mL), and dried under reduced pressure to give a slightly orange crystalline solid (7.65 g, 2.98 mmol, 71%).  $^1\text{H NMR}$  ( $\text{CD}_3\text{CN}$ ):  $\delta$  [ppm] = 8.71 (d, 1H,  $^3J_{\text{HH}} = 7.8$  Hz), 8.49 (pt, 1H,  $^3J_{\text{HH}} = 7.7$  Hz), 7.76 (pt, 1H,  $^3J_{\text{HH}} = 6.5$  Hz), 7.31 (d, 1H,  $^3J_{\text{HH}} = 5.5$  Hz).  $^{19}\text{F NMR}$  ( $\text{CD}_3\text{CN}$ ):  $\delta$  [ppm] = -134.07 (bs, 2F), -164.22 (pt, 1F,  $^3J_{\text{FF}} = 19.7$  Hz), -168.65 (bs, 2F). MS( $\text{ESI}^+$ ):  $m/z$  (%) = 185.6 (20)  $[\text{Co}(\text{bpy})_2]^{2+}$ , 263.6 (6)  $[\text{Co}(\text{bpy})_3]^{2+}$ , 371.1 (46)  $[\text{Co}(\text{bpy})_2]^+$ , 423.1 (74), 1054.2 (14), 1206.2 (31)  $[\text{Co}(\text{bpy})_3 + \text{B}(\text{C}_6\text{F}_5)_4]^+$ , 1885.2 (100)  $[\text{Co}(\text{bpy})_3 + 2 \times (\text{B}(\text{C}_6\text{F}_5)_4)]^+$ , 2526.8 (6)  $[\text{Co}(\text{bpy})_3 + 3 \times (\text{B}(\text{C}_6\text{F}_5)_4 - 2\text{F})]^+$ , 2740.6 (7), 3168.3 (8)  $[3 \times (\text{Co}(\text{bpy})_3) + 7 \times (\text{B}(\text{C}_6\text{F}_5)_4)]^{2+}$ . HR-MS( $\text{ESI}^+$ ,  $m/z$ ): Calcd. for  $\text{C}_{78}\text{H}_{24}^{10}\text{B}_2\text{CoF}_{40}\text{N}_6$ : 1883.1014; found: 1883.1052.

**Synthesis of  $[\text{Co}(\text{ddpd})][\text{B}(\text{C}_6\text{F}_5)_4]_2$   $[\text{4}][\text{B}(\text{C}_6\text{F}_5)_4]_2$ :** The ddpd ligand (2.53 g, 8.68 mol, 2.2 equiv), dissolved in  $\text{CH}_3\text{CN}$  (50 mL), was added to a solution of  $\text{Co}(\text{BF}_4)_2 \cdot 6\text{H}_2\text{O}$  (1.34 g, 3.95 mmol, 1.0 equiv) in  $\text{CH}_3\text{CN}$  (50 mL) and the mixture was stirred for 6 h at room temperature. The complex was precipitated by addition of  $\text{Et}_2\text{O}$  (400 mL) and filtered off, washed with  $\text{Et}_2\text{O}$  (100 mL), and dried under reduced pressure. The yellow powder was dissolved in a minimum amount of  $\text{CH}_3\text{CN}$ , and  $\text{Li}[\text{B}(\text{C}_6\text{F}_5)_4]\cdot\text{Et}_2\text{O}$  (12.0 g, 15.7 mmol, 4.0 equiv) was added. The volume of the solvent was reduced under reduced pressure and the product was precipitated by addition of water to give a yellow crystalline solid (7.18 g, 3.51 mmol, 89%).  $^1\text{H NMR}$  ( $\text{CD}_3\text{CN}$ ):  $\delta$  [ppm] = 75.0 (s, 2H), 69.0 (s, 2H), 34.6 (bs, 2H), 34.2 (s, 2H), 22.5 (s, 6H), 21.9 (s, 1H), 2.7 (s, 2H).  $^{19}\text{F NMR}$  ( $\text{CD}_3\text{CN}$ ):  $\delta$  [ppm] = -134.07 (bs, 2F), -164.22 (pt, 1F,  $^3J_{\text{FF}} = 19.7$  Hz), -168.67 (pt, 2F,  $^3J_{\text{FF}} = 16.8$  Hz). The  $^1\text{H NMR}$  data match reported values of  $[\text{Co}(\text{ddpd})_2][\text{BF}_4]_2$ .<sup>[82]</sup> MS( $\text{ESI}^+$ ):  $m/z$  (%) = 292.1 (14)  $[\text{ddpd} + \text{H}]^+$ , 320.6 (18)  $[\text{Co}(\text{ddpd})_2]^{2+}$ , 1320.1 (100)  $[\text{Co}(\text{ddpd})_2 + \text{B}(\text{C}_6\text{F}_5)_4]^+$ , 2320.3 (13)  $[3 \times (\text{Co}(\text{ddpd})_2) + 4 \times (\text{B}(\text{C}_6\text{F}_5)_4)]^{2+}$ , 3320.3 (18)  $[4 \times (\text{Co}(\text{ddpd})_2) + 6 \times (\text{B}(\text{C}_6\text{F}_5)_4)]^{2+}$ . HR-MS( $\text{ESI}^+$ ,  $m/z$ ): Calcd. for  $\text{C}_{58}\text{H}_{34}^{10}\text{BCoF}_{20}\text{N}_{10}$ : 1319.2110; found: 1319.2106.

**Synthesis of  $[\text{Co}(\text{ddpd})][\text{B}(\text{C}_6\text{F}_5)_4]_3$   $[\text{4}][\text{B}(\text{C}_6\text{F}_5)_4]_3$ :**  $[\text{Co}(\text{ddpd})_2](\text{BF}_4)_2$  (3.24 g, 3.83 mmol, 1.0 equiv) was dissolved in  $\text{CH}_3\text{CN}$  (100 mL) and 2,3-dichloro-5,6-dicyano-1,4-benzoquinone (1.30 g, 5.75 mmol, 1.5 equiv) was added. The solution was stirred for 5 h at room temperature.  $\text{Li}[\text{B}(\text{C}_6\text{F}_5)_4]\cdot\text{Et}_2\text{O}$  (11.6 g, 15.3 mmol, 4.0 equiv) was added and the mixture was diluted with water (200 mL). The precipitate was filtered off, washed with water (200 mL), and dried under reduced pressure to give a pinkish powder (8.32 g, 3.06 mmol, 86%).  $^1\text{H NMR}$  ( $\text{CD}_3\text{CN}$ ):  $\delta$  [ppm] = 8.33 (pt, 1H,  $^3J_{\text{HH}} = 8.1$  Hz), 8.13 (pt, 2H,  $^3J_{\text{HH}} = 7.8$  Hz), 7.38–7.43 (m, 4H), 7.01 (pt, 2H,  $^3J_{\text{HH}} = 6.7$  Hz), 6.90 (d, 2H,  $^3J_{\text{HH}} = 5.7$  Hz), 3.12 (s, 6H).  $^{19}\text{F NMR}$  ( $\text{CD}_3\text{CN}$ ):  $\delta$  [ppm] = -134.07 (s), -164.22 (pt), -168.68 (pt). The  $^1\text{H NMR}$  data match reported values of  $[\text{Co}(\text{ddpd})_2][\text{BF}_4]_3$ .<sup>[82]</sup> MS( $\text{ESI}^+$ ):  $m/z$  (%) = 175.1 (10)  $[\text{Co}(\text{ddpd})]^{2+}$ , 184.1 (10)  $[\text{Co}(\text{ddpd}) + \text{F}]^{2+}$ , 291.2 (12)  $[\text{ddpd}]^+$ , 320.6

(56)  $[\text{Co}(\text{ddpd})_2]^{2+}$ , 1320.2 (8)  $[\text{Co}(\text{ddpd})_2 + \text{B}(\text{C}_6\text{F}_5)_4]^+$ , 1999.2 (100)  $[\text{Co}(\text{ddpd})_2 + 2 \times (\text{B}(\text{C}_6\text{F}_5)_4)]^+$ , 2535.5 (18), 2669.6 (20)  $[5 \times (\text{Co}(\text{ddpd})_2) + 11 \times (\text{B}(\text{C}_6\text{F}_5)_4)]^{4+}$ , 2892.8 (7)  $[4 \times (\text{Co}(\text{ddpd})_2) + 9 \times (\text{B}(\text{C}_6\text{F}_5)_4)]^{3+}$ , 3071.4 (12), 3339.4 (12)  $[3 \times (\text{Co}(\text{ddpd})_2) + 7 \times (\text{B}(\text{C}_6\text{F}_5)_4)]^{2+}$ . HR-MS( $\text{ESI}^+$ ,  $m/z$ ): Calcd. for  $\text{C}_{82}\text{H}_{34}^{11}\text{B}_2\text{CoF}_{40}\text{N}_{10}$ : 1999.1847; found: 1999.1809.

**TiO<sub>2</sub> electrode preparation:** Fluorine-doped tin oxide (FTO) glass plates ( Pilkington-TEC8) were cleaned using an ultrasonic bath with 2 vol% of Helmanex in deionized water and ethanol. A doctor-bladed layer of 35 nm TiO<sub>2</sub> particles (PST-35 NR, CCIC) was used as photoelectrode. A 8  $\mu\text{m}$  thick transparent film and an additional 4  $\mu\text{m}$  scattering TiO<sub>2</sub> film (PST-400C, CCIC, particle size ca. 400 nm) were coated on the top of the conducting glass electrode. The TiO<sub>2</sub> electrodes were heated to 450 °C for 30 min, treated with a 0.5 mM TiCl<sub>4</sub> solution in deionized water for 20 min at 70 °C, followed by an annealing process for 30 min at 450 °C. Following the heat treatment, these electrodes were immersed into the sensitizer/CDCA solutions ( $2.95 \times 10^{-4}$  M of  $[\text{nBu}_4\text{N}][\mathbf{2a}]$ ,  $3.01 \times 10^{-4}$  M of  $[\text{nBu}_4\text{N}][\mathbf{2b}]$ ,  $3.01 \times 10^{-4}$  M of  $[\text{nBu}_4\text{N}][\mathbf{2c}]$ , and  $3.11 \times 10^{-4}$  M of **N719** solution ( $\text{CH}_3\text{CN}/t\text{BuOH}$ ) (1:1, volume ratio) with or without  $5.99 \times 10^{-4}$  M CDCA (Dyesol) and kept at room temperature for 6 h, 16 h or 24 h, respectively. The TiO<sub>2</sub> electrodes were rinsed with  $\text{CH}_3\text{CN}$  and dried.

**Electrolyte solutions:** The triiodide/iodide electrolyte solutions were prepared from 1-methyl-3-propylimidazolium iodide (0.600 M) and iodine (0.050 M) in  $\text{CH}_3\text{CN}$ . The  $\text{Co}^{\text{III/II}}$  electrolytes were employed as 0.035/0.165 M and 0.020/0.080 M  $\text{CH}_3\text{CN}$  solutions of  $[\mathbf{3}]^{3+}/[\mathbf{3}]^{2+}$  and  $[\mathbf{4}]^{3+}/[\mathbf{4}]^{2+}$ , respectively. Owing to the employed relative concentrations the redox potentials shift to lower values by 0.061, 0.039, and 0.036 V for  $\text{I}_3^-/\text{I}^-$ ,  $[\mathbf{3}]^{3+}/[\mathbf{3}]^{2+}$  and  $[\mathbf{4}]^{3+}/[\mathbf{4}]^{2+}$ , respectively. The absolute concentrations of the redox couples are 0.6 M, 0.2 M and 0.1 M for  $\text{I}_3^-/\text{I}^-$ ,  $[\mathbf{3}]^{3+}/[\mathbf{3}]^{2+}$  and  $[\mathbf{4}]^{3+}/[\mathbf{4}]^{2+}$ , respectively. 4-*tert*-Butylpyridine (0.8 M) and lithium perchlorate (0.1 M) were used in all cells.

**Counter electrode preparation:** The Pt electrode was prepared by spin-coating of 10 mM  $\text{H}_2\text{PtCl}_6$  (Sigma-Aldrich) in 2-propanol and then sintered at 450 °C for 30 min. The cells were sealed using 60  $\mu\text{m}$  Surllyn. The electrolyte solutions were introduced through holes on the counter electrode.

**Dye loading:** TiO<sub>2</sub>/FTO electrodes were immersed in a 0.1 M KOH  $\text{H}_2\text{O}/\text{CH}_3\text{CN}$  1:1 solution for at least 5 min. From the UV/Vis absorption spectra of the resulting dye solutions, the concentrations of the attached dyes were calculated (Table 4).

## Acknowledgements

A.K.C.M. thanks the International Research Training Group (IRTG 1404) Self Organized Materials for Optoelectronics supported by the Deutsche Forschungsgemeinschaft (DFG) for funding. This work was financially supported by the Deutsche Forschungsgemeinschaft (GSC 266, Materials Science in Mainz, scholarship for C.K.). Parts of this research were conducted using the supercomputer MOGON and advisory services offered by Johannes Gutenberg Univ. Mainz ([www.hpc.uni-mainz.de](http://www.hpc.uni-mainz.de)), which is a member of the AHRP and the Gauss Alliance e.V. We thank Johannes Moll for preparative assistance.

**Keywords:** cobalt electrolytes • cyclometalated complexes • dye-sensitized solar cells • mixed valency • ruthenium

- [1] B. O'Regan, M. Grätzel, *Nature* **1991**, 353, 737–740.
- [2] M. A. Green, *Solar Energy* **2004**, 76, 3–8.
- [3] M. Grätzel, *J. Photochem. Photobiol. C* **2003**, 4, 145–153.
- [4] A. Hagfeldt, G. Boschloo, L. Sun, L. Kloo, H. Pettersson, *Chem. Rev.* **2010**, 110, 6595–6663.
- [5] R. McConnell, *Renewable Sustainable Energy Rev.* **2002**, 6, 271–293.
- [6] S. Ferrere, B. A. Gregg, *J. Am. Chem. Soc.* **1998**, 120, 843–844.
- [7] N. Alonso-Vante, J.-F. Nierengarten, J.-P. Sauvage, *J. Chem. Soc. Dalton Trans.* **1994**, 1649–1654.
- [8] T. Bessho, E. C. Constable, M. Graetzel, A. Hernandez Redondo, C. E. Housecroft, W. Kylberg, M. K. Nazeeruddin, M. Neuburger, S. Schaffner, *Chem. Commun.* **2008**, 3717–3719.
- [9] C. E. Housecroft, E. C. Constable, *Chem. Soc. Rev.* **2015**, 44, 8386–8398.
- [10] E. A. M. Geary, N. Hirata, J. Clifford, J. R. Durrant, S. Parsons, A. Dawson, L. J. Yellowlees, N. Robertson, *Dalton Trans.* **2003**, 3757–3762.
- [11] E. C.-H. Kwok, M.-Y. Chan, K. M.-C. Wong, W. H. Lam, V. W.-W. Yam, *Chem. Eur. J.* **2010**, 16, 12244–12254.
- [12] E. I. Mayo, K. Kilså, T. Tirrell, P. I. Djurovich, A. Tamayo, M. E. Thompson, N. S. Lewis, H. B. Gray, *Photochem. Photobiol. Sci.* **2006**, 5, 871–873.
- [13] E. Baranoff, J. Yum, I. Jung, R. Vulcano, M. Grätzel, M. K. Nazeeruddin, *Chem. Asian J.* **2010**, 5, 496–499.
- [14] J. B. Asbury, E. Hao, Y. Wang, T. Lian, *J. Phys. Chem. B* **2000**, 104, 11957–11964.
- [15] S. Kim, J. K. Lee, S. O. Kang, J. Ko, J.-H. Yum, S. Fantacci, F. de Angelis, D. Di Censo, M. K. Nazeeruddin, M. Grätzel, *J. Am. Chem. Soc.* **2006**, 128, 16701–16707.
- [16] A. Mishra, M. K. R. Fischer, P. Bäuerle, *Angew. Chem. Int. Ed.* **2009**, 48, 2474–2499; *Angew. Chem.* **2009**, 121, 2510–2536.
- [17] W. M. Campbell, K. W. Jolley, P. Wagner, K. Wagner, P. J. Walsh, K. C. Gordon, L. Schmidt-Mende, M. K. Nazeeruddin, Q. Wang, M. Grätzel, D. L. Officer, *J. Phys. Chem. C* **2007**, 111, 11760–11762.
- [18] L.-L. Li, E. W.-G. Diau, *Chem. Soc. Rev.* **2013**, 42, 291–304.
- [19] S. Mathew, A. Yella, P. Gao, R. Humphry-Baker, B. F. E. Curchod, N. Ashari-Astani, I. Tavernelli, U. Rothlisberger, M. K. Nazeeruddin, M. Grätzel, *Nat. Chem.* **2014**, 6, 242–247.
- [20] S. Rühle, M. Shalom, A. Zaban, *ChemPhysChem* **2010**, 11, 2290–2304.
- [21] M. K. Nazeeruddin, A. Kay, I. Rodicio, R. Humphry-Baker, E. Mueller, P. Liska, N. Vlachopoulos, M. Graetzel, *J. Am. Chem. Soc.* **1993**, 115, 6382–6390.
- [22] M. K. Nazeeruddin, P. Péchy, T. Renouard, S. M. Zakeeruddin, R. Humphry-Baker, P. Comte, P. Liska, L. Cevey, E. Costa, V. Shklover, L. Spiccia, G. B. Deacon, C. A. Bignozzi, M. Grätzel, *J. Am. Chem. Soc.* **2001**, 123, 1613–1624.
- [23] S. Altobello, R. Argazzi, S. Caramori, C. Contado, S. Da Fré, P. Rubino, C. Choné, G. Larramona, C. A. Bignozzi, *J. Am. Chem. Soc.* **2005**, 127, 15342–15343.
- [24] T. W. Rees, E. Baranoff, *Polyhedron* **2014**, 82, 37–49.
- [25] G. A. Crosby, *Acc. Chem. Res.* **1975**, 8, 231–238.
- [26] M. L. Stone, G. A. Crosby, *Chem. Phys. Lett.* **1981**, 79, 169–173.
- [27] J. R. Winkler, T. L. Netzel, C. Creutz, N. Sutin, *J. Am. Chem. Soc.* **1987**, 109, 2381–2392.
- [28] M. K. Nazeeruddin, S. M. Zakeeruddin, R. Humphry-Baker, M. Jirousek, P. Liska, N. Vlachopoulos, V. Shklover, C.-H. Fischer, M. Grätzel, *Inorg. Chem.* **1999**, 38, 6298–6305.
- [29] M. K. Nazeeruddin, F. de Angelis, S. Fantacci, A. Selloni, G. Viscardi, P. Liska, S. Ito, B. Takeru, M. Grätzel, *J. Am. Chem. Soc.* **2005**, 127, 16835–16847.
- [30] M. Nazeeruddin, M. Grätzel, *J. Photochem. Photobiol. A* **2001**, 145, 79–86.
- [31] H. T. Nguyen, H. M. Ta, T. Lund, *Sol. Energy Mater. Sol. Cells* **2007**, 91, 1934–1942.
- [32] a) T. P. Brewster, W. Ding, N. D. Schley, N. Hazari, V. S. Batista, R. H. Crabtree, *Inorg. Chem.* **2011**, 50, 11938–11946; b) S. Kämper, A. Paretzki, J. Fiedler, S. Zális, W. Kaim, *Inorg. Chem.* **2012**, 51, 2097–2104.
- [33] a) A. Breivogel, S. Wooh, J. Dietrich, T. Y. Kim, Y. S. Kang, K. Char, K. Heinze, *Eur. J. Inorg. Chem.* **2014**, 2720–2734; b) A. Breivogel, C. Kreitner, K. Heinze, *Eur. J. Inorg. Chem.* **2014**, 5468–5490.
- [34] S. H. Wadman, J. M. Kroon, K. Bakker, M. Lutz, A. L. Spek, G. P. M. van Klink, G. van Koten, *Chem. Commun.* **2007**, 1907–1909.
- [35] T. Bessho, E. Yoneda, J.-H. Yum, M. Guglielmi, I. Tavernelli, H. Imai, U. Rothlisberger, M. K. Nazeeruddin, M. Grätzel, *J. Am. Chem. Soc.* **2009**, 131, 5930–5934.
- [36] B. D. Koivisto, K. C. D. Robson, C. P. Berlinguette, *Inorg. Chem.* **2009**, 48, 9644–9652.
- [37] S. H. Wadman, J. M. Kroon, K. Bakker, R. W. A. Havenith, G. P. M. van Klink, G. van Koten, *Organometallics* **2010**, 29, 1569–1579.
- [38] a) K. C. D. Robson, B. D. Koivisto, A. Yella, B. Spornova, M. K. Nazeeruddin, T. Baumgartner, M. Grätzel, C. P. Berlinguette, *Inorg. Chem.* **2011**, 50, 5494–5508; b) P. G. Bomben, T. J. Gordon, E. Schott, C. P. Berlinguette, *Angew. Chem. Int. Ed.* **2011**, 50, 10682–10685; *Angew. Chem.* **2011**, 123, 10870–10873.
- [39] J.-J. Kim, H. Choi, S. Paek, C. Kim, K. Lim, M.-J. Ju, H. S. Kang, M.-S. Kang, J. Ko, *Inorg. Chem.* **2011**, 50, 11340–11347.
- [40] P. G. Bomben, K. C. Robson, B. D. Koivisto, C. P. Berlinguette, *Coord. Chem. Rev.* **2012**, 256, 1438–1450.
- [41] T. Funaki, H. Funakoshi, O. Kitao, N. Onozawa-Komatsuzaki, K. Kasuga, K. Sayama, H. Sugihara, *Angew. Chem. Int. Ed.* **2012**, 51, 7528–7531; *Angew. Chem.* **2012**, 124, 7646–7649.
- [42] B. Schulze, D. G. Brown, K. C. D. Robson, C. Friebe, M. Jäger, E. Birkner, C. P. Berlinguette, U. S. Schubert, *Chem. Eur. J.* **2013**, 19, 14171–14180.
- [43] E. C. Constable, J. M. Holmes, *J. Organomet. Chem.* **1986**, 301, 203–208.
- [44] E. C. Constable, C. E. Housecroft, *Polyhedron* **1990**, 9, 1939–1947.
- [45] M. Beley, J. P. Collin, R. Louis, B. Metz, J. P. Sauvage, *J. Am. Chem. Soc.* **1991**, 113, 8521–8522.
- [46] S. H. Wadman, M. Lutz, D. M. Tooke, A. L. Spek, F. Hartl, R. W. A. Havenith, G. P. M. van Klink, G. van Koten, *Inorg. Chem.* **2009**, 48, 1887–1900.
- [47] P. G. Bomben, K. C. D. Robson, P. A. Sedach, C. P. Berlinguette, *Inorg. Chem.* **2009**, 48, 9631–9643.
- [48] a) C. Kreitner, E. Erdmann, W. W. Seidel, K. Heinze, *Inorg. Chem.* **2015**, 54, 11088–11104; b) C. Kreitner, K. Heinze, *Dalton Trans.* **2016**, 45, 5640–5658.
- [49] B. Durham, J. V. Caspar, J. K. Nagle, T. J. Meyer, *J. Am. Chem. Soc.* **1982**, 104, 4803–4810.
- [50] K. Kalyanasundaram, *Coord. Chem. Rev.* **1982**, 46, 159–244.
- [51] M. Maestri, N. Armadori, V. Balzani, E. C. Constable, A. M. W. C. Thompson, *Inorg. Chem.* **1995**, 34, 2759–2767.
- [52] V. Balzani, A. Juris, *Coord. Chem. Rev.* **2001**, 211, 97–115.
- [53] T. Edvinsson, C. Li, N. Pschirer, J. Schöneboom, F. Eickemeyer, R. Sens, G. Boschloo, A. Herrmann, K. Müllen, A. Hagfeldt, *J. Phys. Chem. C* **2007**, 111, 15137–15140.
- [54] A. Abboto, C. Barolo, L. Bellotto, F. de Angelis, M. Grätzel, N. Manfredi, C. Marini, S. Fantacci, J.-H. Yum, M. K. Nazeeruddin, *Chem. Commun.* **2008**, 5318–5320.
- [55] M. Ishida, S. W. Park, D. Hwang, Y. B. Koo, J. L. Sessler, D. Y. Kim, D. Kim, *J. Phys. Chem. C* **2011**, 115, 19343–19354.
- [56] J.-H. Yum, S.-J. Moon, C. S. Karthikeyan, H. Wietasch, M. Thelakkat, S. M. Zakeeruddin, M. Nazeeruddin, M. Grätzel, *Nano Energy* **2012**, 1, 6–12.
- [57] A. Yella, H.-W. Lee, H. N. Tsao, C. Yi, A. K. Chandiran, M. K. Nazeeruddin, E. W.-G. Diau, C.-Y. Yeh, S. M. Zakeeruddin, M. Grätzel, *Science* **2011**, 334, 629–634.
- [58] K. C. D. Robson, B. D. Koivisto, T. J. Gordon, T. Baumgartner, C. P. Berlinguette, *Inorg. Chem.* **2010**, 49, 5335–5337.
- [59] K. C. D. Robson, B. Spornova, B. D. Koivisto, E. Schott, D. G. Brown, C. P. Berlinguette, *Inorg. Chem.* **2011**, 50, 6019–6028.
- [60] K. Hu, K. C. D. Robson, P. G. Johansson, C. P. Berlinguette, G. J. Meyer, *J. Am. Chem. Soc.* **2012**, 134, 8352–8355.
- [61] M. B. Robin, P. Day, *Adv. Inorg. Chem.* **1968**, 10, 247–422.
- [62] C.-J. Yao, R.-H. Zheng, Q. Shi, Y.-W. Zhong, J. Yao, *Chem. Commun.* **2012**, 48, 5680–5682.
- [63] a) C.-J. Yao, H.-J. Nie, W.-W. Yang, J.-Y. Shao, J. Yao, Y.-W. Zhong, *Chem. Eur. J.* **2014**, 20, 17466–17477; b) B.-B. Cui, Y.-W. Zhong, J. Yao, *J. Am. Chem. Soc.* **2015**, 137, 4058–4061.
- [64] Y.-W. Zhong, Z.-L. Gong, J.-Y. Shao, J. Yao, *Coord. Chem. Rev.* **2016**, 312, 22–40.
- [65] B. S. Brunshwig, C. Creutz, N. Sutin, *Chem. Soc. Rev.* **2002**, 31, 168–184.

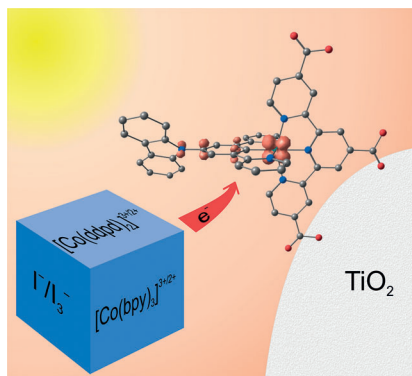
- [66] R. K. Chitumalla, K. S. V. Gupta, C. Malapaka, R. Fallahpour, A. Islam, L. Han, B. Kotamarthi, S. P. Singh, *Phys. Chem. Chem. Phys.* **2014**, *16*, 2630–2640.
- [67] S. M. Feldt, P. W. Lohse, F. Kessler, M. K. Nazeeruddin, M. Grätzel, G. Boschloo, A. Hagfeldt, *Phys. Chem. Chem. Phys.* **2013**, *15*, 7087–7097.
- [68] J. W. Ondersma, T. W. Hamann, *Coord. Chem. Rev.* **2013**, *257*, 1533–1543.
- [69] M. Wang, C. Grätzel, S. M. Zakeeruddin, M. Grätzel, *Energy Environ. Sci.* **2012**, *5*, 9394–9405.
- [70] E. Mosconi, J.-H. Yum, F. Kessler, C. J. G. García, C. Zuccaccia, A. Cinti, M. K. Nazeeruddin, M. Grätzel, F. D. Angelis, *J. Am. Chem. Soc.* **2012**, *134*, 19438–19453.
- [71] T. W. Hamann, *Dalton Trans.* **2012**, *41*, 3111–3115.
- [72] J.-H. Yum, E. Baranoff, F. Kessler, T. Moehl, S. Ahmad, T. Bessho, A. Marchioro, E. Ghadiri, J.-E. Moser, C. Yi, M. K. Nazeeruddin, M. Grätzel, *Nat. Commun.* **2012**, *3*, 631; DOI: 10.1038/ncomms1655.
- [73] S. M. Feldt, G. Wang, G. Boschloo, A. Hagfeldt, *J. Phys. Chem. C* **2011**, *115*, 21500–21507.
- [74] S. M. Feldt, E. A. Gibson, E. Gabrielsson, L. Sun, G. Boschloo, A. Hagfeldt, *J. Am. Chem. Soc.* **2010**, *132*, 16714–16724.
- [75] S. Caramori, J. Husson, M. Beley, C. A. Bignozzi, R. Argazzi, P. C. Gros, *Chem. Eur. J.* **2010**, *16*, 2611–2618.
- [76] B. M. Klahr, T. W. Hamann, *J. Phys. Chem. C* **2009**, *113*, 14040–14045.
- [77] J. J. Nelson, T. J. Amick, C. M. Elliott, *J. Phys. Chem. C* **2008**, *112*, 18255–18263.
- [78] H. Nusbaumer, S. M. Zakeeruddin, J.-E. Moser, M. Grätzel, *Chem. Eur. J.* **2003**, *9*, 3756–3763.
- [79] S. A. Sapp, C. Elliott, C. Contado, S. Caramori, C. A. Bignozzi, *J. Am. Chem. Soc.* **2002**, *124*, 11215–11222.
- [80] H. Nusbaumer, J.-E. Moser, S. M. Zakeeruddin, M. K. Nazeeruddin, M. Grätzel, *J. Phys. Chem. B* **2001**, *105*, 10461–10464.
- [81] A. Breivogel, C. Förster, K. Heinze, *Inorg. Chem.* **2010**, *49*, 7052–7056.
- [82] C. Förster, K. Mack, L. M. Carrella, V. Ksenofontov, E. Rentschler, K. Heinze, *Polyhedron* **2013**, *52*, 576–581.
- [83] A. K. C. Mengel, W. Cho, A. Breivogel, K. Char, Y. S. Kang, K. Heinze, *Eur. J. Inorg. Chem.* **2015**, 3299–3306.
- [84] N. C. Bruno, M. T. Tudge, S. L. Buchwald, *Chem. Sci.* **2013**, *4*, 916–920.
- [85] M. D. Charles, P. Schultz, S. L. Buchwald, *Org. Lett.* **2005**, *7*, 3965–3968.
- [86] A. Breivogel, M. Meister, C. Förster, F. Laquai, K. Heinze, *Chem. Eur. J.* **2013**, *19*, 13745–13760.
- [87] C. Kreitner, M. Grabolle, U. Resch-Genger, K. Heinze, *Inorg. Chem.* **2014**, *53*, 12947–12961.
- [88] K. Heinze, K. Hempel, *Chem. Eur. J.* **2009**, *15*, 1346–1358.
- [89] G. Boschloo, A. Hagfeldt, *Acc. Chem. Res.* **2009**, *42*, 1819–1826.
- [90] X. Wang, D. M. Stanbury, *Inorg. Chem.* **2006**, *45*, 3415–3423.
- [91] T. L. J. Huang, D. G. Brewer, *Can. J. Chem.* **1981**, *59*, 1689–1700.
- [92] Y. Liu, J. R. Jennings, Y. Huang, Q. Wang, S. M. Zakeeruddin, M. Grätzel, *J. Phys. Chem. C* **2011**, *115*, 18847–18855.
- [93] D. K. Lee, K.-S. Ahn, S. Thogiti, J. H. Kim, *Dyes Pigm.* **2015**, *117*, 83–91.
- [94] V. V. Pavlishchuk, A. W. Addison, *Inorg. Chim. Acta* **2000**, *298*, 97–102.
- [95] I. Krivokapic, M. Zerara, M. L. Dakua, A. Vargas, C. Enachescu, C. Ambrusc, P. Tregenna-Piggott, N. Amstutz, E. Krausz, A. Hauser, *Coord. Chem. Rev.* **2007**, *251*, 364–378.
- [96] M. Chavarot, Z. Pikramenou, *Tetrahedron Lett.* **1999**, *40*, 6865–6868.
- [97] K. Suzuki, A. Kobayashi, S. Kaneko, K. Takehira, T. Yoshihara, H. Ishida, Y. Shiina, S. Oishi, S. Tobita, *Phys. Chem. Chem. Phys.* **2009**, *11*, 9850–9860.
- [98] G. R. Fulmer, A. J. M. Miller, N. H. Sherden, H. E. Gottlieb, A. Nudelman, B. M. Stoltz, J. E. Bercaw, K. I. Goldberg, *Organometallics* **2010**, *29*, 2176–2179.
- [99] N. G. Connelly, W. E. Geiger, *Chem. Rev.* **1996**, *96*, 877–910.
- [100] F. Neese, *WIREs Comput. Mol. Sci.* **2012**, *2*, 73–78.
- [101] F. Neese, F. Wennmohs, A. Hansen, U. Becker, *Chem. Phys.* **2009**, *356*, 98–109.
- [102] R. Izsák, F. Neese, *J. Chem. Phys.* **2011**, *135*, 144105.
- [103] A. D. Becke, *J. Chem. Phys.* **1993**, *98*, 5648–5652.
- [104] A. Schäfer, H. Horn, R. Ahlrichs, *J. Chem. Phys.* **1992**, *97*, 2571–2577.
- [105] A. Schäfer, C. Huber, R. Ahlrichs, *J. Chem. Phys.* **1994**, *100*, 5829–5835.
- [106] E. van Lenthe, E. J. Baerends, J. G. Snijders, *J. Chem. Phys.* **1993**, *99*, 4597–4610.
- [107] D. A. Pantazis, X.-Y. Chen, C. R. Landis, F. Neese, *J. Chem. Theory Comput.* **2008**, *4*, 908–919.
- [108] S. Sinnecker, A. Rajendran, A. Klamt, M. Diedenhofen, F. Neese, *J. Phys. Chem. A* **2006**, *110*, 2235–2245.

Received: March 2, 2016

Published online on ■■■■■, 0000

## FULL PAPER

**Anchor-functionalized** cyclometalated bis(tridentate) ruthenium(II) triarylamine hybrids featuring mixed-valent states of varying resonance stabilization were employed in dye-sensitized solar cells in combination with different electrolytes. Together with cobalt-based electrolytes, the *N*-carbazole substituted dye surpasses the **N719** dye.



### Cyclometalated Complexes

C. Kreitner, A. K. C. Mengel, T. K. Lee, W. Cho, K. Char, Y. S. Kang, K. Heinze\*



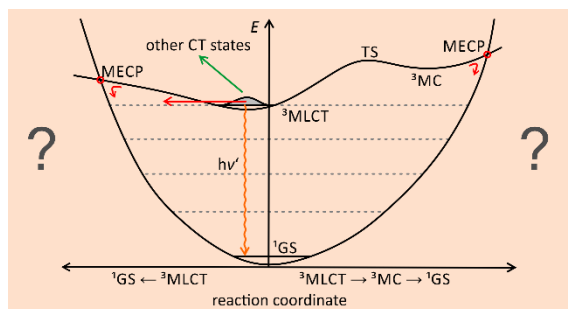
**Strongly Coupled Cyclometalated Ruthenium Triarylamine Chromophores as Sensitizers for DSSCs**



### 3.5 EXCITED STATE DECAY OF CYCLOMETALATED POLYPYRIDINE RUTHENIUM COMPLEXES: INSIGHT FROM THEORY AND EXPERIMENT

*Christoph Kreitner and Katja Heinze*

*Submitted to Dalton Transactions, 2016.*



This perspective article tackles the open question why cyclometalated polypyridine ruthenium(II) complexes typically only emit very weakly at room temperature and delivers answers beyond the standard schemes involving  $^3MC$  and tunneling decay channels.

#### Author Contributions

All DFT calculations were performed by Christoph Kreitner. The manuscript was written by Christoph Kreitner (90 %) and Katja Heinze (10 %).

#### Supporting Information

for this article is found at pp. 259.



## EXCITED STATE DECAY OF CYCLOMETALATED POLYPYRIDINE RUTHENIUM COMPLEXES: INSIGHT FROM THEORY AND EXPERIMENT

Christoph Kreitner<sup>a,b</sup> and Katja Heinze<sup>a</sup>

Deactivation pathways of the triplet metal-to-ligand charge transfer (<sup>3</sup>MLCT) excited state of cyclometalated polypyridine ruthenium complexes with [RuN<sub>5</sub>C]<sup>+</sup> coordination are discussed on the basis of the available experimental data and a series of density functional theory calculations. Three different complex classes are considered, namely with [Ru(N<sup>^</sup>N)<sub>2</sub>(N<sup>^</sup>C)]<sup>+</sup>, [Ru(N<sup>^</sup>N<sup>^</sup>N)(N<sup>^</sup>C<sup>^</sup>N)]<sup>+</sup> and [Ru(N<sup>^</sup>N<sup>^</sup>N)(N<sup>^</sup>N<sup>^</sup>C)]<sup>+</sup> coordination modes. Excited state deactivation in these complex types proceeds *via* five distinct decay channels. Vibronic coupling of the <sup>3</sup>MLCT state to high-energy oscillators of the singlet ground state (<sup>1</sup>GS) allows tunneling to the ground state followed by vibrational relaxation (path **A**). A ligand field excited state (<sup>3</sup>MC) is thermally accessible via a <sup>3</sup>MLCT → <sup>3</sup>MC transition state with the <sup>3</sup>MC state being strongly coupled to the <sup>1</sup>GS surface via a low-energy minimum energy crossing point (path **B**). Furthermore, a <sup>3</sup>MLCT → <sup>1</sup>GS surface crossing point directly couples the triplet and singlet potential energy surfaces (path **C**). Charge transfer states either with higher singlet character or with different orbital parentage and intrinsic symmetry restrictions are thermally populated which promote non-radiative decay via tunneling to the <sup>1</sup>GS state (path **D**). Finally, the excited state can decay via phosphorescence (path **E**). The dominant deactivation pathways differ for the three individual complex classes. The implications of these findings for isoelectronic iridium(III) or iron(II) complexes are discussed. Ultimately, strategies for optimizing the emission efficiencies of cyclometalated polypyridine complexes of d<sup>6</sup>-metal ions, especially Ru<sup>II</sup>, are suggested.

### Introduction

Polypyridine complexes of a wide range of transition metals have received great interest from coordination chemists and materials scientists over the last few decades due to their versatile applicability. For example, such complexes of copper(I)<sup>1–3</sup>, iron(II)<sup>4–6</sup>, osmium(II)<sup>7,8</sup>, iridium(III)<sup>9,10</sup> and, particularly, ruthenium(II)<sup>11–19</sup> were successfully applied as sensitizers in dye sensitized solar cells. Additionally, a wide range of complexes of this type has been successfully used as sensitizers in photoredox catalysis.<sup>20–31</sup>

Moreover, the most fascinating and thoroughly studied property observed for a large number of polypyridine transition metal complexes is their luminescence.<sup>32,33</sup> The first polypyridine complex reported to exhibit luminescence was [Ru(bpy)<sub>3</sub>]<sup>2+</sup> (bpy = 2,2'-bipyridine).<sup>34</sup> Since then, luminescent polypyridine complexes have been described for second and third row transition metal ions with d<sup>6</sup>, d<sup>8</sup> and d<sup>10</sup> electron configuration<sup>35–37</sup>, namely for rhenium(I)<sup>38–41</sup>, osmium(II)<sup>42–45</sup>, rhodium(III)<sup>46–48</sup>, iridium(III)<sup>41,42,49–51</sup>, palladium(II)<sup>52</sup>, platinum(II)<sup>52–55</sup>, and gold(III)<sup>56,57</sup>. Even a few luminescent first row transition metal polypyridine complexes are known of chromium(III)<sup>58–62</sup>, copper(I)<sup>63–68</sup> and zinc(II)<sup>69</sup>.

**a** Institute of Inorganic and Analytical Chemistry, Johannes Gutenberg University, Duesbergweg 10-14, D-55128 Mainz, Germany, E-mail: katja.heinze@uni-mainz.de

**b** Graduate School Materials Science in Mainz, Staudingerweg 9, D-55128 Mainz, Germany

As such luminescence was first observed for ruthenium, most of the effort understanding the underlying electronic processes evolved around this element and in particular around  $[\text{Ru}(\text{bpy})_3]^{2+}$  as the prototype.<sup>70–72</sup> Its key features are an electron-rich low-spin  $d^6$  metal center with  $(t_{2g})^6$  electron configuration in idealized  $O_h$  symmetry and strongly  $\pi$ -accepting chelate ligands. Upon irradiation with visible light ( $\lambda_{\text{max}} = 452 \text{ nm}$ )<sup>70</sup>,  $[\text{Ru}(\text{bpy})_3]^{2+}$  is excited into its lowest excited singlet state which has metal-to-ligand charge transfer (MLCT) character.<sup>73–75</sup> As MLCT transitions are not restricted in terms of parity selection rules, the corresponding absorption bands are typically very intense. Due to the spin-orbit coupling induced by the ruthenium atom, the excited  $^1\text{MLCT}$  state undergoes very efficient intersystem crossing ( $\phi_{\text{ISC}} \approx 1$ ) onto the triplet hypersurface populating a  $^3\text{MLCT}$  state.<sup>76,77</sup> At low temperatures in solid matrix, this state either evolves into the ground state without emission *via* tunnelling to the singlet energy surface and vibrational cooling or *via* phosphorescent emission of a photon ( $\lambda_{\text{em}} = 621 \text{ nm}$ ,  $\phi_{\text{em}} = 0.095$  at 298 K).<sup>74,78–81</sup> The rate of non-radiative excited state decay is hereby governed by the so-called energy gap law.<sup>82–85</sup> In a series of structurally related compounds, the rate increases with decreasing excited state energy. At room temperature however, a third deactivation pathway *via* metal centered (MC) d-d excited states ( $(t_{2g})^5(e_g)^1$  electron configuration) is thermally accessible dramatically quenching the emission.<sup>81,86–88</sup> The activation barrier for this thermally activated depopulation was determined to be about  $45 \text{ kJ mol}^{-1}$  for  $[\text{Ru}(\text{bpy})_3]^{2+}$ .<sup>87,88</sup>

This general scheme for  $[\text{Ru}(\text{bpy})_3]^{2+}$  is applicable to other ruthenium polypyridine complexes as well. It enables a fine-tuning of their emissive properties by manipulation of the  $^3\text{MLCT}$  energies *via* introduction of functional groups or extension of the aromatic backbone of the pyridine ligands.<sup>72,89–93</sup> This allowed the design of specifically tailored complexes for luminescent sensing applications<sup>94,95</sup> and for optoelectronics.<sup>96–99</sup>

The concept was successfully transferred to polypyridine complexes of other transition metals. For example, cyclometalated polypyridine complexes of iridium(III) proved to be exceptionally well suited for PHOLED applications as their room temperature emission is typically very intense and can be tuned throughout the visible range of the electromagnetic spectrum.<sup>41,100–103</sup> Cyclometalation hereby refers to the exchange of one or multiple nitrogen atoms of the polypyridine's coordination sphere by isoelectronic carbon anions. This substitution typically yields a reduction of the overall charge of the complex moiety as well as a substantial shift of all redox processes to lower potentials.

Due to the fact that the isoelectronic cyclometalated complexes of ruthenium(II) perform very well as sensitizers in dye sensitized solar cells, they have also received increasing interest in the last years.<sup>16,17,19,104–106</sup> Additionally, cyclometalated bridging ligands enhance the electronic coupling between the redox centers in mixed-valent Ru/Ru complexes<sup>107–109</sup> and Ru/organic hybrid structures.<sup>110–113</sup> Despite the large variety of cyclometalated polypyridine ruthenium complexes synthesized up-to-date, however, no phosphorescence comparable to  $[\text{Ru}(\text{bpy})_3]^{2+}$  has yet been achieved. Furthermore, a general explanation for the striking difference in the luminescence properties between the isoelectronic complexes of iridium(III) and ruthenium(II) is still missing.<sup>114–</sup>

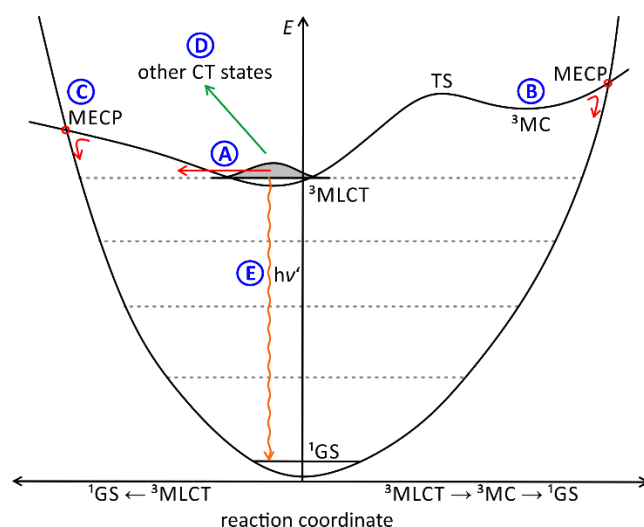


**Figure 1** Schematic representation of the energy landscape of a polypyridine ruthenium complex including all relevant deactivation pathways of an emissive  $^3\text{MLCT}$  state: **A**) Tunneling into high-energy vibrationally excited singlet states; **B**) thermally activated decay into a  $^3\text{MC}$  state followed by surface crossing at a minimum energy crossing point (MECP), **C**) direct thermally activated surface crossing from the  $^3\text{MLCT}$  state to the singlet ground state, **D**) decay *via* non-emissive charge transfer states, and **E**) phosphorescence.

Hence, this issue will be addressed in this perspective. We will discuss the excited state deactivation processes of cyclometalated polypyridine complexes beyond the  $^3\text{MLCT}/^3\text{MC}$  and energy gap law schemes by picking illustrative examples from the literature and elaborate why these are weak emitters at room temperature. Several decay pathways of the emissive  $^3\text{MLCT}$  state are known for polypyridine ruthenium complexes, and their individual contribution to the excited state decay of cyclometalated polypyridine ruthenium complexes will be discussed (Figure 1):

Decay path **A**) tunneling into high-lying vibrational levels of the singlet state.<sup>83–85</sup> This channel is always available and its efficiency depends on the Franck-Condon overlap of the vibrational wavefunctions of the  $^3\text{MLCT}$  and singlet ground states ( $^1\text{GS}$ ).

Decay path **B**) *via* a thermally accessible  $^3\text{MC}$  state. Population of this state is followed by rapid surface crossing to the singlet potential energy surface *via* a close-lying minimum energy crossing point (MECP) and vibrational cooling. The energy of the  $^3\text{MC}$  state mainly depends on the ligand field strength.

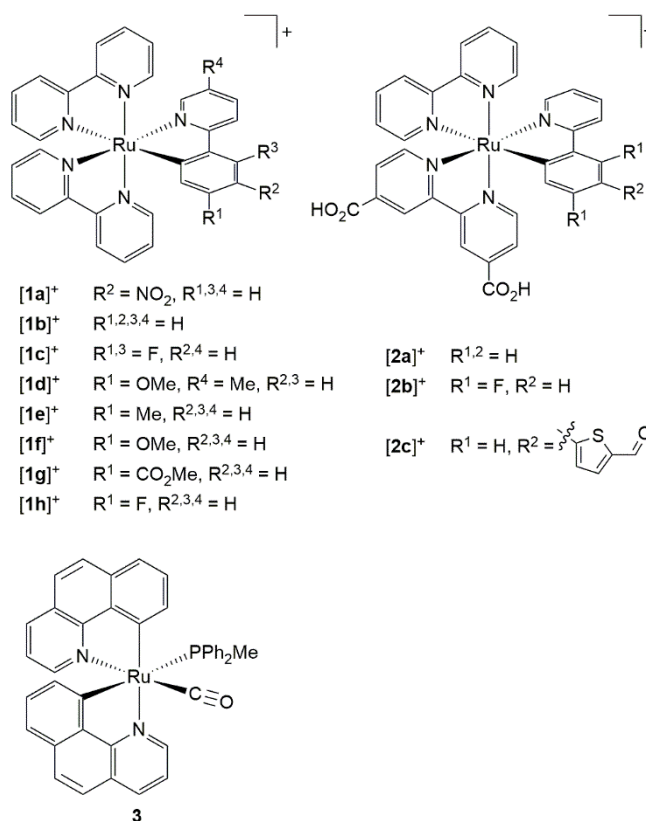
Decay path **C**) direct surface crossing from the  $^3\text{MLCT}$  state to the singlet potential surface *via* a low-lying surface crossing point. The energy of this MECP depends on the degree of  $^3\text{MLCT}$  state distortion and the energy of the  $^3\text{MLCT}$  state itself.

Decay path **D**) *via* other non-emissive triplet states or states with higher singlet character as in  $[\text{Ru}(\text{tpy})_2]^{2+}$  and  $[\text{Ru}(\text{bpy})_3]^{2+}$  that allow efficient tunnelling into high-lying singlet states.<sup>74,80,88,117</sup>

Decay path **E**) phosphorescence.

In the following, we will divide the discussion into tris(bidentate) complexes with  $[\text{Ru}(\text{N}^{\wedge}\text{N})_2(\text{N}^{\wedge}\text{C})]^+$  coordination sphere and bis(tridentate) complexes with either  $[\text{Ru}(\text{N}^{\wedge}\text{N}^{\wedge}\text{N})(\text{N}^{\wedge}\text{C}^{\wedge}\text{N})]^+$  or  $[\text{Ru}(\text{N}^{\wedge}\text{N}^{\wedge}\text{N})(\text{N}^{\wedge}\text{N}^{\wedge}\text{C})]^+$  motifs to highlight similarities and differences between the different classes. Finally, we will suggest strategies how to improve the room temperature emission of such complexes and how our conclusions might impact the photophysics of cyclometalated polypyridine complexes of still elusive iron(II)<sup>6,118–120</sup> and well-known iridium(III) emitters<sup>42,49,121</sup> as well.

### Tris(bidentate) ruthenium complexes



**Scheme 1** Literature-known tris(bidentate) cyclometalated (polypyridine)ruthenium(II) complexes relevant to this work (**[1a]**<sup>+</sup><sup>122</sup>, **[1b]**<sup>+</sup><sup>123–125</sup>, **[1c]**<sup>+</sup> – **[1d]**<sup>+</sup><sup>124</sup>, **[1e]**<sup>+</sup> – **[1h]**<sup>+</sup><sup>125</sup>, **[2a]**<sup>+</sup> – **[2c]**<sup>+</sup><sup>126</sup>, **3**<sup>127</sup>).

The first cyclometalated (polypyridine)ruthenium complex,  $[\text{Ru}(\text{bpy})_2(\text{ppy}-\text{NO}_2)]^+$  **[1a]**<sup>+</sup> (Hppy = 2-phenylpyridine, R<sup>2</sup> = NO<sub>2</sub>), was reported in 1985 by Reveno *et al.* (Scheme 1).<sup>122</sup> Shortly thereafter, the syntheses of unsubstituted  $[\text{Ru}(\text{bpy})_2(\text{ppy})]^+$  **[1b]**<sup>+</sup><sup>123</sup> and the bis(tridentate) counterparts  $[\text{Ru}(\text{ttpy})(\text{dpb})]^+$  (ttpy = 4'-p-tolyl-2,2';6',2''-terpyridine, dpbH = 1,3-di-(2'-pyridyl)benzene)<sup>128</sup> and  $[\text{Ru}(\text{tpy}-4'-\text{Cl})(\text{pbpy})]^+$  (tpy = 2,2';6',2''-terpyridine, pbpyH = 6-phenyl-2,2'-bipyridine)<sup>129</sup> were presented (*vide supra*). However, deeper interest in cyclometalated (polypyridine)ruthenium(II) complexes did not evolve until the discovery of their excellent performance as solar cell sensitizers in 2007.<sup>16,17</sup> Since then, more effort has been put into the understanding of the photophysical properties of this class of compounds.<sup>104,106,114–116,124,130–132</sup>

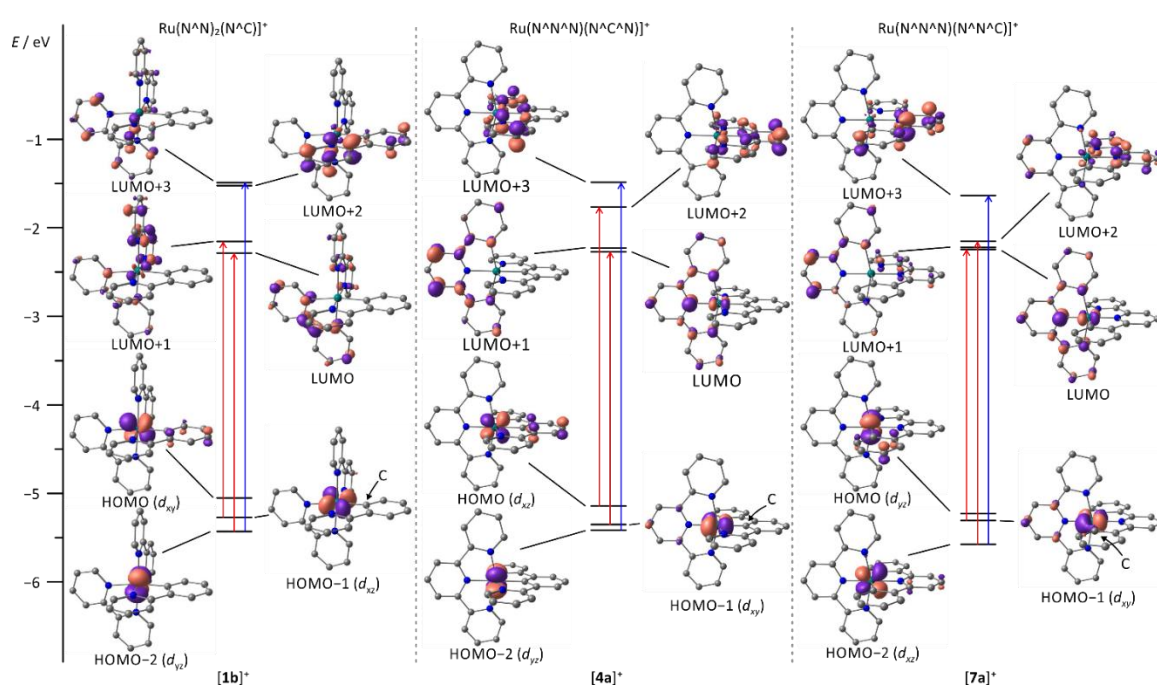


**Figure 2** MO diagram of the parent cyclometalated (polypyridine)ruthenium(II) complexes **[1b]<sup>+</sup>**, **[4a]<sup>+</sup>** and **[7a]<sup>+</sup>** obtained from DFT calculations (B3LYP, def2-SVP, ZORA, COSMO(acetonitrile), contour value: 0.07). H atoms are omitted for clarity. The most important orbitals involved in the dominant transitions around 500 nm and 400 nm are highlighted in red and blue, respectively.

The visible range of the absorption spectrum of  $[\text{Ru}(\text{bpy})_2(\text{ppy})]^+$ -type complexes typically is dominated by two broad structured absorption bands, one appearing between 320 and 450 nm and the second between 470 and 650 nm.<sup>104,124,130–132</sup> The broadness of the visible range absorption features has been attributed to the low symmetry around the metal center which breaks the degeneracy of the metal's *d* orbitals. Additionally, the lowest unoccupied molecular orbital (LUMO) of the ppy unit (LUMO+2) is substantially higher in energy than the bpy LUMO (Figure 2). Hence, Berlinguette and coworkers assigned these bands to Ru→ppy (at 400 nm) and Ru→bpy (at 500 nm) MLCT transitions.<sup>3,104,124,132</sup> Grätzel, however, suggested that all visible range absorption bands predominantly arise from Ru→bpy MLCT transitions with varying contributions from the highest occupied molecular orbital (HOMO) of  $\pi$ -symmetry at the cyclometalating phenyl ring.<sup>17</sup> Indeed, the theoretical data published by Berlinguette<sup>104</sup> show that all Ru→ppy transitions are weak in intensity and do not contribute to the absorption spectrum which supports Grätzel's interpretation. Additionally, the shift of the absorption bands induced by the functional groups attached to either the ppy ligand or the bpy units further underlines Grätzel's assignment of all bands as Ru→bpy transitions.<sup>3,104,124,132</sup>



**Table 1** Emission wavelengths  $\lambda_{em}$  and wavenumbers  $\tilde{\nu}_{em}$  as well as excited state lifetimes  $\tau$  of selected tris(bidentate) cyclometalated (polypyridine)ruthenium(II) complexes at room temperature in solution.

	$\lambda_{em} / \text{nm}$ ( $\tilde{\nu}_{em} / \text{cm}^{-1}$ )	$\tau / \text{ns}$		$\lambda_{em} / \text{nm}$ ( $\tilde{\nu}_{em} / \text{cm}^{-1}$ )	$\tau / \text{ns}$
<b>[1b]</b> <sup>+</sup> <sup>124</sup>	821 (12180)	13	<b>[1g]</b> <sup>+</sup> <sup>125</sup>	781 (12800)	-
<b>[1c]</b> <sup>+</sup> <sup>124</sup>	778 (12850)	35	<b>[1h]</b> <sup>+</sup> <sup>125</sup>	776 (12890)	-
<b>[1d]</b> <sup>+</sup> <sup>124</sup>	824 (12140)	13	<b>[2a]</b> <sup>+</sup> <sup>126</sup>	787 (12710)	9
<b>[1e]</b> <sup>+</sup> <sup>125</sup>	805 (12420)	-	<b>[2b]</b> <sup>+</sup> <sup>126</sup>	761 (13140)	27
<b>[1f]</b> <sup>+</sup> <sup>125</sup>	800 (12500)	-	<b>[2c]</b> <sup>+</sup> <sup>126</sup>	779 (12840)	14

For most tris(bidentate) complexes of this type, weak room temperature emission in the range between 720 and 820 nm is reported (Table 1).<sup>104,124–126,130,132</sup> The emissive state is considered to be a Ru→bpy <sup>3</sup>MLCT state.<sup>104,130</sup> This is corroborated by the influence of functional groups on the emission energy. In a series of [Ru(bpy)<sub>2</sub>(ppy-R)]<sup>+</sup> complexes (**[1e]**<sup>+</sup> – **[1h]**<sup>+</sup>, Scheme 1) with functional groups in *meta*-position to the cyclometalating carbon atom, the emission energy decreases with increasing electron donating character strength of the respective substituent as this destabilizes the metal *d* orbitals (Table 1).<sup>125</sup> Similarly, functionalization of the bpy ligands with electron accepting substituents such as COOR groups shifts the emission bathochromically as a consequence of the lowered LUMO energy (Table 1).<sup>130</sup> However, missing low-temperature emission data ( $\lambda_{em}$ ,  $\phi$ ,  $\tau$ ) currently impede a quantification of the respective effects.

To the best of our knowledge, no quantum yields have been determined neither at room temperature nor at 77 K for any of the reported tris(bidentate) cyclometalated complexes due to their very weakly emissive character and the associated instrumental limitations.<sup>124,125</sup> Castellano and coworkers estimated the phosphorescence quantum yields to be  $\phi < 0.005$ <sup>124</sup>, while Housecroft and coworkers reported yields below 0.01 for compounds **[1e]**<sup>+</sup> – **[1h]**<sup>+</sup>.<sup>125</sup> However, Berlinguette<sup>126</sup> and Castellano<sup>124</sup> provided lifetime data of the emissive excited states for two series of complexes **[2a]**<sup>+</sup> – **[2c]**<sup>+</sup> and **[1b]**<sup>+</sup> – **[1d]**<sup>+</sup>, respectively (Scheme 1, Table 1). The lifetimes are in the nanosecond range for all complexes and correlate nicely with the emission energy: The excited state lifetimes become smaller with decreasing emission energy. In (polypyridine)ruthenium(II) complexes, the emissive <sup>3</sup>MLCT state typically is depopulated to some extent *via* a <sup>3</sup>MC state (path **B**, *vide supra*).<sup>81,86–88</sup> However, cyclometalation substantially increases the <sup>3</sup>MC energy, as pointed out by Dixon<sup>133</sup> and van Koten<sup>134</sup>, efficiently retarding emission quenching *via* this pathway.<sup>115</sup> In fact, we were able to localize the respective <sup>3</sup>MLCT and <sup>3</sup>MC states of **[1b]**<sup>+</sup> *via* DFT calculations (Figure 3). The <sup>3</sup>MC state (Mulliken spin population at Ru: 1.87) is located 66 kJ mol<sup>-1</sup> above the <sup>3</sup>MLCT level while for [Ru(bpy)<sub>3</sub>]<sup>2+</sup>, the <sup>3</sup>MLCT–<sup>3</sup>MC energy gap was calculated to be –7.7 kJ mol<sup>-1</sup> in favour of the <sup>3</sup>MC state.<sup>135–137</sup> Remarkably, the nitrogen donor atom N1 of the cyclometalating ligand as well as the *trans* nitrogen atom N4 are essentially decoordinates in the <sup>3</sup>MC state of **[1b]**<sup>+</sup> with Ru–N distances of 2.48 and 2.39 Å, respectively (Figure 4). This tetragonal distortion along the N1–Ru–N4 axis underlines the strongly dissociative

character of the  $^3\text{MC}$  state similar to that described for biscyclometalated tris(bidentate) iridium complexes<sup>138–140</sup> and for  $[\text{Ru}(\text{bpy})_3]^{2+}$ .<sup>135–137</sup> It resembles the Jahn-Teller mode of  $d^7$  low-spin  $\text{Co}^{\text{II}}$  complexes due to the  $(e_g^*)^1$  electron configuration.<sup>141,142</sup>

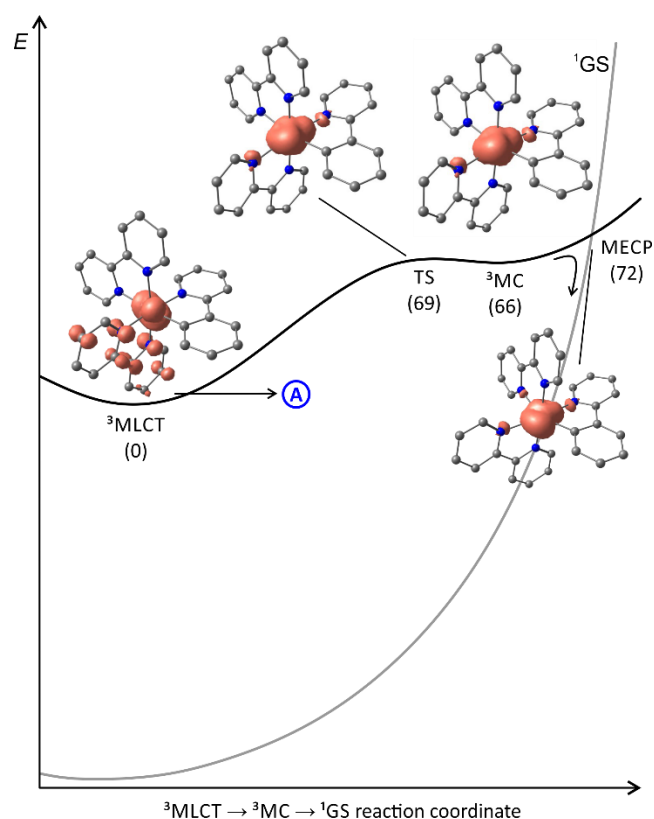


**Figure 3** Schematic representation of the energy landscape of  $[\mathbf{1b}]^+$  including spin density contour plots (contour value: 0.01) of the  $^3\text{MLCT}$  and the  $^3\text{MC}$  states as well as the  $^3\text{MLCT} \rightarrow ^3\text{MC}$  transition state and the  $^3\text{MC} \rightarrow ^1\text{GS}$  minimum energy surface crossing point. H atoms are omitted for clarity. Energies ( $\text{kJ mol}^{-1}$ ) are given in parentheses. The  $^3\text{MLCT} - ^1\text{GS}$  energy difference is taken from DFT calculations.

The transition state between the  $^3\text{MC}$  and  $^3\text{MLCT}$  state was localized on the potential surface with an energy of  $69 \text{ kJ mol}^{-1}$  above the  $^3\text{MLCT}$  state (Figure 3). Hence, in contrast to the isoelectronic complex  $[\text{Ru}(\text{bpy})_3]^{2+}$ , the  $^3\text{MC}$  state of  $[\mathbf{1b}]^+$  is thermally inaccessible. The comparably low quantum yields of  $[\mathbf{1b}]^+$  are attributed to an increased thermal relaxation into the ground state. Non-emissive excited state decay occurs *via* vibronic coupling to high-energy oscillators (path **A**) or *via* a thermally activated surface crossing to the ground state potential surface (path **C**).<sup>83</sup> The latter requires a low-energy surface crossing point. We attempted to localize such a minimum energy crossing point (MECP) between the  $^3\text{MLCT}$  and  $^1\text{GS}$  potential surfaces. However, the lowest  $^3\text{MLCT} \rightarrow ^1\text{GS}$  MECP we could find was localized at  $120 \text{ kJ mol}^{-1}$  above the  $^3\text{MLCT}$  level. An analogous  $^3\text{MC} \rightarrow ^1\text{GS}$  MECP on the other hand is localized at  $72 \text{ kJ mol}^{-1}$  merely  $6 \text{ kJ mol}^{-1}$  above the  $^3\text{MC}$  state (path **B**, Figure 3). However, since all of these states are thermally inaccessible at room temperature or below, surface crossing to the singlet ground state is irrelevant for the excited state deactivation of  $[\mathbf{1b}]^+$ . As a consequence, emission quenching in  $[\mathbf{1b}]^+$  appears to occur exclusively *via* tunnelling into high-energy oscillators of the ground state (path **A**). According

to the energy gap law, the vibronic coupling of the  $^3\text{MLCT}$  state and  $^1\text{GS}$  becomes stronger, the smaller the  $^3\text{MLCT}$ – $^1\text{GS}$  energy gap is.<sup>83–85</sup> Secondly, a more pronounced distortion of the  $^3\text{MLCT}$  excited state compared to the ground state geometry increases the non-radiative decay rate as it results in a higher Franck-Condon overlap of the vibronic wavefunctions of the ground and excited state.<sup>83–85,124,143,144</sup> Indeed, inspection of the DFT-optimized geometries of the  $^3\text{MLCT}$  and  $^1\text{GS}$  states reveals a sizable distortion of the former (Figure 4) allowing for more efficient radiationless deactivation compared to other (polypyridine)ruthenium(II) based near-IR emitters. This distortion is mainly localized at the bpy ligand *trans* to Ru–C. The Ru–N2 and Ru–N3 bonds are significantly elongated as a consequence of the formal oxidation of ruthenium to +III in the  $^3\text{MLCT}$  state and the *trans* influence of the cyclometalating phenyl ring. However, while the Ru–N2 and Ru–N3 bonds are elongated, the formal negative charge on the second bpy ligand compensates the repulsion yielding essentially unaltered Ru–N4 and Ru–N5 bond lengths.

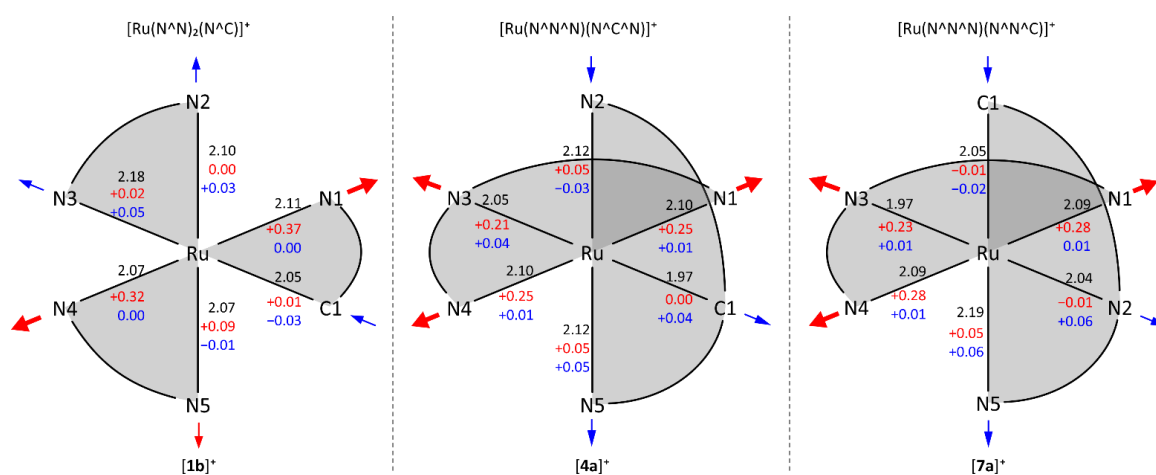


**Figure 4** Schematic representation of the  $^1\text{GS}$  geometries of **[1b]<sup>+</sup>**, **[4a]<sup>+</sup>** and **[7a]<sup>+</sup>** including Ru–X bond lengths in Å (black). The bond length changes in Å in the  $^3\text{MC}$  (red) and  $^3\text{MLCT}$  states (blue) are given with respect to the  $^1\text{GS}$  state. Arrows indicate major molecular distortions of the respective states.

In summary, the high energy of the  $^3\text{MC}$  state is very favourable for efficient emitters because it eliminates one pathway for excited state deactivation and concomitantly prevents photodecomposition reactions, that typically occur from the dissociative  $^3\text{MC}$  state.<sup>87,145</sup> However, in order to increase phosphorescence quantum yields of cyclometalated (polypyridine)ruthenium, radiationless deactivation *via* vibronic coupling has to be suppressed. This can be approached in two ways: The distortion of the  $^3\text{MLCT}$  state compared to the  $^1\text{GS}$  has to be reduced and the emission energy has to be blueshifted as far as possible. Chou and coworkers provided a beautiful example successfully implementing both approaches.<sup>127</sup> Clever molecular design yielded systems with Ru→ppy MLCT states as lowest triplet excited states. This is straight-forwardly accomplished by making the cyclometalating ppy<sup>−</sup> ligand the strongest  $\pi$ -acceptor in the complex. Chou and coworkers achieved this with carbon monoxide and phosphanes which are rather poor  $\pi$ -acceptors towards Ru<sup>II</sup> in biscyclometalated complexes of the type Ru(bq)<sub>2</sub>(CO)(PPh<sub>2</sub>Me) **3** (bqH = benzo-[h]quinoline, Scheme 1).<sup>127</sup> As the LUMO of bq<sup>−</sup> is much higher in energy than that of bpy (Figure 2), the emission from the corresponding Ru→bq  $^3\text{MLCT}$  state is blueshifted substantially

to 575 nm with a quantum yield of  $\phi = 0.24$ . Additionally, as the excited state involves a cyclometalating ligand, its distortion compared to the ground state geometry should be less pronounced as in complex **[1b]**<sup>+</sup>. Similar observations were made for the isoelectronic osmium complexes.<sup>146</sup>

These findings suggest that with careful choice of suitable, very weakly  $\pi$ -accepting polypyridine ligands, cyclometalated (polypyridine)ruthenium complexes with similar emission behaviour arising from high-energy Ru $\rightarrow$ ppy <sup>3</sup>MLCT states are accessible. Another way of improving the emission behaviour of cyclometalated (polypyridine)ruthenium complexes could be by introducing tridentate chelate ligands as this potentially suppresses excited state distortions while maintaining the high energies of parasitic <sup>3</sup>MC states. This should yield nested states with poorer Franck-Condon overlap (weakly coupling limit) which reduces tunnelling processes into high-energy singlet states (path **A**). We will discuss the possibilities and consequences of bis(tridentate) coordination spheres on the phosphorescence properties of cyclometalated ruthenium complexes in the next section.

### Bis(tridentate) ruthenium complexes

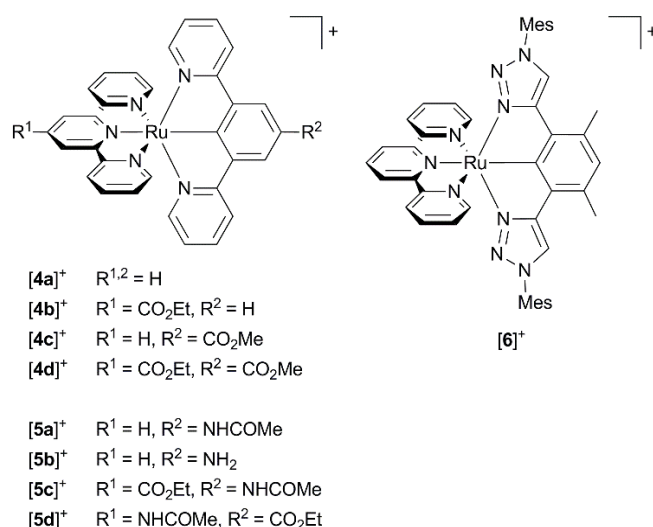
Considering cyclometalated bis(tridentate) complexes, a distinction between  $[\text{Ru}(\text{N}^{\wedge}\text{N}^{\wedge}\text{N})(\text{N}^{\wedge}\text{C}^{\wedge}\text{N})]^+$  and  $[\text{Ru}(\text{N}^{\wedge}\text{N}^{\wedge}\text{N})(\text{N}^{\wedge}\text{N}^{\wedge}\text{C})]^+$  coordination environments is reasonable. The next two sections will highlight similarities between the two classes of bis(tridentate) complexes as well as important differences and compare these findings to those concerning tris(bidentate) complexes (*vide supra*).

### The $[\text{Ru}(\text{N}^{\wedge}\text{N}^{\wedge}\text{N})(\text{N}^{\wedge}\text{C}^{\wedge}\text{N})]^+$ coordination sphere

Similar to tris(bidentate) complexes, the visible range of the absorption spectrum of bis(tridentate) complexes with central cyclometalation is dominated by intense and broad absorption bands that have been assigned to MLCT transitions. Again, two bands are observed, one in the range of 350 – 450 nm and a second between 470 and 650 nm. Van Koten<sup>134,147</sup> and Berlinguette<sup>104</sup> assigned the high energy MLCT band to Ru $\rightarrow$ dpb transitions and the low-energy band to Ru $\rightarrow$ tpy excitations based on relative orbital energies of the lowest  $\pi^*$ -orbitals of the respective ligands (Figure 2). Schubert and coworkers<sup>114,148</sup> on the other hand assigned the low-energy band to mixed MLCT and ligand-to-ligand charge transfer (LL'CT) transitions arising from a HOMO-LUMO transition while the blue absorption band was attributed to mixed MLCT/LL'CT and MC transitions. We examined several  $[\text{Ru}(\text{dpb}-\text{R}^1)(\text{tpy}-\text{R}^2)]^+$  complexes and demonstrated experimentally (resonance Raman spectroscopy) and theoretically that the low energy absorption arises from both Ru $\rightarrow$ tpy and Ru $\rightarrow$ dpb excitations (Figure 2).<sup>115,149</sup> Excitation into the tpy-centered LUMO is only possible from the HOMO-1, while the dpb-centered LUMO+2 can be reached from the HOMO as evidenced from time-dependent DFT calculations. Both excitations occur at very similar energy and contribute comparably to the absorption band at 500 nm. The higher energy absorption features result from MLCT transitions targeting the higher  $\pi^*$  orbitals of the tpy ligand. In fact, a LL'CT transition as suggested by Schubert<sup>114</sup> is symmetry-forbidden as it

involves two mutually perpendicular  $\pi$  orbitals. This symmetry argument will become important for the emission properties as well.

Weak emission is observed under ambient conditions for most bis(tridentate) complexes with central cyclometalation in the range between 700 and 800 nm while the parent  $[\text{Ru}(\text{tpy})_2]^{2+}$  complex is virtually non-emissive at room temperature.<sup>104,106,115,116,134,148</sup> Van Koten<sup>134</sup> and we<sup>115,116</sup> determined extremely low quantum yields in the range of  $10^{-5}$  for complexes of type  $[\text{Ru}(\text{dpb}-\text{R}^1)(\text{tpy}-\text{R}^2)]^+$ . In contrast to the tris(bidentate) series, however, no excited state lifetimes were reported so far (Table 2). Our attempts to obtain lifetimes suggested that they are in the picosecond range.<sup>116</sup>



**Scheme 2** Literature-known  $[\text{Ru}(\text{N}^{\wedge}\text{N}^{\wedge}\text{N})(\text{N}^{\wedge}\text{C}^{\wedge}\text{N})]^+$  complexes relevant to this work (**[4a]**<sup>+</sup><sup>104,134</sup>, **[4b]**<sup>+</sup> – **[4d]**<sup>+</sup><sup>134</sup>, **[5a]**<sup>+</sup> and **[5b]**<sup>+</sup><sup>116</sup>, **[5c]**<sup>+</sup> and **[5d]**<sup>+</sup><sup>115</sup>, **[6]**<sup>+</sup><sup>114</sup>).

**Table 2** Emission wavelengths  $\lambda_{\text{em}}$  and wavenumbers  $\tilde{\nu}_{\text{em}}$  as well as quantum yields  $\phi$  of selected  $[\text{Ru}(\text{N}^{\wedge}\text{N}^{\wedge}\text{N})(\text{N}^{\wedge}\text{C}^{\wedge}\text{N})]^+$  complexes at room temperature.

	$\lambda_{\text{em}} / \text{nm}$ ( $\tilde{\nu}_{\text{em}} / \text{cm}^{-1}$ )	$\phi$		$\lambda_{\text{em}} / \text{nm}$ ( $\tilde{\nu}_{\text{em}} / \text{cm}^{-1}$ )	$\phi$
<b>[4a]</b> <sup>+</sup> <sup>134</sup>	781 (12800)	$9.4 \cdot 10^{-6}$	<b>[5b]</b> <sup>+</sup> <sup>116</sup>	780 (12820)	$< 2 \cdot 10^{-6}$
<b>[4b]</b> <sup>+</sup> <sup>134</sup>	-	-	<b>[5c]</b> <sup>+</sup> <sup>115</sup>	-	-
<b>[4c]</b> <sup>+</sup> <sup>134</sup>	743 (13460)	$1.5 \cdot 10^{-5}$	<b>[5d]</b> <sup>+</sup> <sup>115</sup>	751 (13320)	$1.4 \cdot 10^{-5}$
<b>[4d]</b> <sup>+</sup> <sup>134</sup>	789 (12670)	$4 \cdot 10^{-7}$	<b>[6]</b> <sup>+</sup> <sup>114</sup>	751 (13320)	$6.1 \cdot 10^{-5}$
<b>[5a]</b> <sup>+</sup> <sup>116</sup>	800 (12500)	$8 \cdot 10^{-6}$			

Van Koten<sup>134</sup> studied complexes of the type  $[\text{Ru}(\text{dpb}-\text{R}^1)(\text{tpy}-\text{R}^2)]^+$  bearing carboxy-substituents on either or both ligands (Scheme 2, **[4a]**<sup>+</sup> – **[4d]**<sup>+</sup>). The effect of the functional groups on the respective emission energy (Table 2) points to a <sup>3</sup>MLCT emissive state. In fact, a COOR substituent at the tpy ligand (**[4b]**<sup>+</sup>) leads to complexes that are non-emissive at room temperature due to its stabilizing influence on the tpy-centered LUMO. Since the phosphorescence quantum yields



decrease with increasing emission wavelength following the energy gap law, van Koten suggested vibrational relaxation as main source of emission quenching.<sup>134</sup> We extended this study by also introducing electron-donating substituents such as NH<sub>2</sub> and NHCOMe to the dpb ligand (Scheme 2, [5a]<sup>+</sup> – [5c]<sup>+</sup>) and the tpy ligand ([5d]<sup>+</sup>).<sup>115,116</sup> Using theoretical methods we showed, that the emissive state is in fact a <sup>3</sup>MLCT state. The two singly occupied orbitals (SOMOs) in this state correspond to the *d*<sub>xy</sub> (HOMO–1) and the tpy LUMO, respectively (Figure 2). No dpb ligand participation was observed. However, we localized a second charge transfer state with LL'CT character (dpb→tpy, HOMO→LUMO orbital parentage) on the triplet potential energy surface. The mutually perpendicular SOMOs make this state spectroscopically undetectable and non-emissive (dark state). As third type of triplet states, the <sup>3</sup>MC states were found (Figure 5 and Table 3). While the <sup>3</sup>LL'CT state is essentially undistorted compared to the ground state with only a small displacement of ruthenium towards C1 and a concomitant elongation of the Ru–N3 bond, the <sup>3</sup>MLCT state exhibits substantial distortions within the tpy ligand. It is inclined with respect to the plane perpendicular to the dpb ligand by 12° (Figure 5). At the same time the Ru–C and Ru–N5 bonds are slightly elongated while the Ru–N2 bond shortens (Figure 4). In the <sup>3</sup>MC state on the other hand, the peripheral pyridine rings of the tpy ligand are tilted away from the metal center forming dihedral angles of about 11° with the central pyridine ring, respectively. Furthermore, the all Ru–N<sub>tpy</sub> bonds Ru–N1, Ru–N3 and Ru–N4 are substantially elongated (Figure 4) underlining the dissociative character of the <sup>3</sup>MC state.

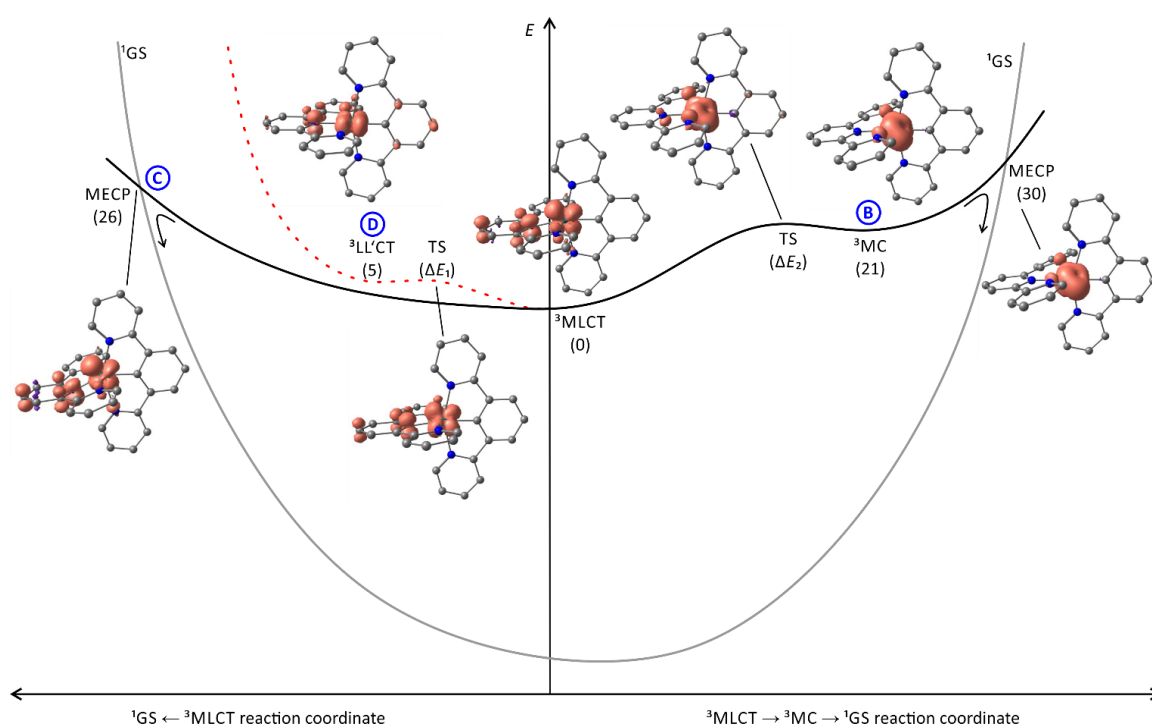


**Figure 5** Schematic representation of the energy landscape of [Ru(dpb)(tpy)]<sup>+</sup> type of complexes including spin density contour plots (contour value: 0.01) of the <sup>3</sup>LL'CT, <sup>3</sup>MLCT and <sup>3</sup>MC states of [4a]<sup>+</sup>, the <sup>3</sup>MLCT → <sup>3</sup>MC and <sup>3</sup>MLCT → <sup>3</sup>LL'CT transition states as well as the minimum energy points for the <sup>3</sup>MLCT → <sup>1</sup>GS and the <sup>3</sup>MC → <sup>1</sup>GS surface crossing. H atoms are omitted for clarity. Energies (kJ mol<sup>-1</sup>) of the respective states are given in parentheses. The <sup>3</sup>MLCT – <sup>1</sup>GS energy difference is taken from DFT calculations.

**Table 2** DFT-calculated Gibbs free enthalpies (in  $\text{kJ mol}^{-1}$ ) of the  ${}^3\text{LL}'\text{CT}$  and  ${}^3\text{MC}$  states as well as the  ${}^3\text{MLCT} \rightarrow {}^3\text{LL}'\text{CT}$  ( $\Delta E_1$ ) and  ${}^3\text{MLCT} \rightarrow {}^3\text{MC}$  ( $\Delta E_2$ ) transition states of complexes  $[\mathbf{4a}]^+$ ,  $[\mathbf{4c}]^+$ ,  $[\mathbf{5a}]^+$ ,  $[\mathbf{5b}]^+$ ,  $[\mathbf{5d}]^+$  and  $[\mathbf{6}]^+$  relative to the respective  ${}^3\text{MLCT}$  state energy. Experimentally determined activation barriers are given in parentheses.

	$E({}^3\text{LL}'\text{CT})$	$\Delta E_1$	$E({}^3\text{MC})$	$\Delta E_2$
$[\mathbf{4a}]^+$	5	5	21	23
$[\mathbf{4c}]^+$	-3	4 (2)	13	21 (22)
$[\mathbf{5a}]^+$	8	8 (6)	13	22 (23)
$[\mathbf{5c}]^+$	-10	-	31	-
$[\mathbf{5d}]^+$	-	-	9	(11)
$[\mathbf{6}]^+$	-	-(4)	-	-(22)

The calculated relative energies of the triplet states (Figure 5) of  $[\mathbf{5a}]^+ - [\mathbf{5d}]^+$  as well as the transition states connecting them are summarized in Table 3. The emissive  ${}^3\text{MLCT}$  state is flanked by two thermally accessible quenching states, namely the  ${}^3\text{LL}'\text{CT}$  and  ${}^3\text{MC}$  states. The lowering of the relative  ${}^3\text{MC}$  energy from  $66 \text{ kJ mol}^{-1}$  in  $[\mathbf{1b}]^+$  to  $10 - 30 \text{ kJ mol}^{-1}$  in these bis(tridentate) complexes is attributed to the smaller N-Ru-N bite angles and the weaker overlap of the nitrogen lone pairs with the  $e_g$  metal orbitals which results in a smaller ligand field splitting. The distortion of the  ${}^3\text{MC}$  state allows for tunnelling to the  ${}^1\text{GS}$  and for a surface crossing point (MECP) that is just  $9 \text{ kJ mol}^{-1}$  above the  ${}^3\text{MC}$  level providing an accessible non-emissive deactivation channel for the  ${}^3\text{MLCT}$  state (path **B**, Figure 5).

Interestingly, a direct  ${}^3\text{MLCT} \rightarrow {}^1\text{GS}$  MECP was found for  $[\mathbf{4a}]^+$  as well at a moderate energy ( $26 \text{ kJ mol}^{-1}$  above the  ${}^3\text{MLCT}$  state). It is qualitatively similarly distorted as the  ${}^3\text{MLCT}$  state but the degree of the distortion is larger. Thus, the geometry of this crossing point can be regarded as a high-amplitude distortional vibration along the  ${}^1\text{GS} \rightarrow {}^3\text{MLCT}$  vibrational mode ( ${}^3\text{MLCT} \rightarrow {}^1\text{GS}$  reaction coordinate, Figure 5). Hence, the  ${}^3\text{MLCT}$  distortion of  $[\mathbf{4a}]^+$  opens up this low-energy deactivation channel (path **C**), that is absent for  $[\mathbf{1b}]^+$ . However, experimental evidence for such a quenching channel is difficult to obtain as its activation barrier is similar to that of the  ${}^3\text{MC}$  deactivation channel and hence a similar temperature-dependent emission behaviour is expected.

The  ${}^3\text{LL}'\text{CT}$  state is connected to the  ${}^3\text{MLCT}$  state *via* a transition state with a very low activation barrier (Table 3). As the  ${}^3\text{LL}'\text{CT}$  state is barely distorted compared to the  ${}^1\text{GS}$  geometry (*vide supra*) it is considered a nested state. Indeed, attempts to localize a  ${}^3\text{LL}'\text{CT} \rightarrow {}^1\text{GS}$  MECP, that would provide a non-emissive decay channel, failed. Because emission from the  ${}^3\text{LL}'\text{CT}$  state is symmetry-forbidden, its only decay pathway proceeds *via* tunnelling into the vibrationally excited singlet state followed by thermal relaxation (path **D**, Figure 5).

Hence both, the  ${}^3\text{LL}'\text{CT}$  and  ${}^3\text{MC}$  states (and potentially also the  ${}^3\text{MLCT} \rightarrow {}^1\text{GS}$  MECP) are responsible for the efficient phosphorescence quenching at room temperature. This DFT-based

interpretation was evidenced experimentally by recording the temperature dependence of the quantum yield. The respective  $\ln(\phi)$  vs.  $T^{-1}$  data of  $[4c]^+$  and  $[5a]^+$  were reproduced using a fit function accounting for two thermally activated deactivation pathways. The activation barriers obtained from the fit are in excellent agreement with the computed transition state energies (Table 3).

Schubert and coworkers<sup>114</sup> published very similar results on structurally related complexes such as  $[Ru(dtp)(tpy)]^+$  (dtbH = 1,3-di-(1,2,3-triazol-4-yl)benzene, Scheme 2,  $[6]^+$ ). Two Arrhenius-like activation parameters were required to properly reproduce the temperature-dependent lifetime data yielding very similar activation energies compared to our findings for  $[4c]^+$  and  $[5a]^+$ . In contrast to our assignments, however, they attributed the two deactivation channels of  $[6]^+$  to an irreversible  ${}^3MLCT \rightarrow {}^3MC$  surface crossing and an internal conversion to a higher-lying MLCT state of increased singlet character. The latter is a common feature of non-cyclometalated (polypyridine)ruthenium(II) complexes.<sup>74,80,88,150</sup> In the light of our results and the electronic similarity of the studied structures, it seems plausible that the second deactivation channel in  $[6]^+$  actually is *via* a state of  ${}^3LL'CT$  nature as well. In fact, their DFT-optimization of a triplet state of  $[6]^+$  afforded a  ${}^3CT$  state with orthogonal SOMOs.<sup>114</sup> Even if the cyclometalating ligand does not contribute significantly to the spin density of this state, its emissive relaxation is symmetry-forbidden.

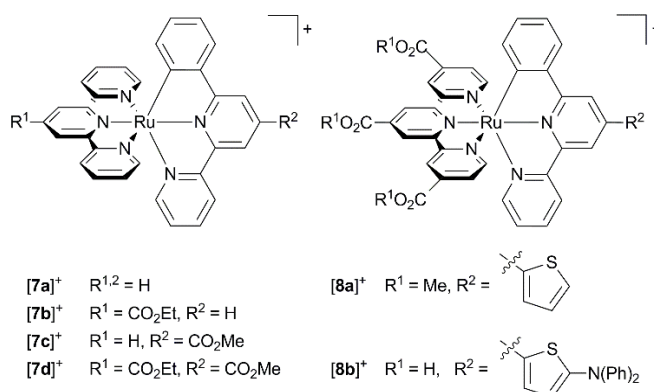
To summarize, the combination of orthogonal ligands with strongly differing electronic properties, one being an excellent  $\pi$ -acceptor and the second a strong  $\pi$ -donor typically yields a low-lying  ${}^3CT$  state. Even though this state is not directly populated after optical excitation into a  ${}^1MLCT$  state and subsequent intersystem crossing onto the triplet manifold it serves as a further low-barrier channel for radiationless deactivation of the emissive  ${}^3MLCT$  state (path **D**) besides the  ${}^3MC$  state (path **B**). Recent reports underline that these results are transferable to structurally similar complexes of other transition metals with orthogonal tridentate ligands. In fact, Williams and coworkers suggested that a  ${}^3LL'CT$  state plays a key role in the excited state deactivation of isostructural and isoelectronic  $[Ir(N^{\wedge}N^{\wedge}N)(N^{\wedge}C^{\wedge}N)]^{2+}$  complexes.<sup>151</sup> A beautiful theoretical study on the excited state deactivation pathways in biscyclometalated gold(III) complexes of the general formula  $[Au(C^{\wedge}N^{\wedge}C)(acetylide)]$  revealed a  ${}^3LL'CT$  state which efficiently contributed to the radiationless deactivation of the emissive state.<sup>152</sup> Its substantial distortion compared to the ground state increased the rate of non-radiative decay.

In order to optimize the emissive properties of bis(tridentate) cyclometalated ruthenium complexes, circumventing the low-energy non-emissive  ${}^3LL'CT$  state is a key objective, for example by removing the axial symmetry. This can be achieved using a  $N^{\wedge}N^{\wedge}C$  coordination mode on the cyclometalating ligand which will be discussed in the next section (*vide infra*). However, the kinetic parameters extracted by Schubert and coworkers<sup>114</sup> from the temperature-dependent lifetime data suggest, that at room temperature the  ${}^3LL'CT$  state (path **D**) with an activation barrier  $\Delta E_2$  of just  $4.2 \text{ kJ mol}^{-1}$  is only responsible for the quenching of about 25 % of the excited molecules of  $[6]^+$  and structurally similar complexes. At the same time, the  ${}^3MC$  state with a considerably higher barrier  $\Delta E_1$  of  $21.9 \text{ kJ mol}^{-1}$  is responsible for about 75 % of the excited state deactivation (path **B** and potentially path **C**), while direct radiationless decay into the ground state only contributes 0.1

% (path **A**). Hence, even avoiding the  $^3\text{LL}'\text{CT}$  state by clever molecular design will not *per se* yield strong emitters. The strong electronic coupling of the  $^3\text{MLCT}$  and  $^3\text{MC}$  states [ $k_0(^3\text{MLCT}\rightarrow^3\text{MC}) = 10^{11} - 10^{13} \text{ s}^{-1}$ ;  $k_0(^3\text{MLCT}\rightarrow^3\text{LL}'\text{CT}) \approx 10^8 \text{ s}^{-1}$ ]<sup>114</sup> renders the former the dominant deactivating state despite the substantially higher activation barrier. The appreciably weaker coupling of the  $^3\text{MLCT}$  and  $^3\text{LL}'\text{CT}$  states can be traced back to the two states still being electronically nearly orthogonal (*vide supra*). Concluding, despite the occurrence of a  $^3\text{LL}'\text{CT}$  state in this kind of bis(tridentate) complexes the important states to manipulate for improving emission efficiencies remain the  $^3\text{MC}$  and  $^3\text{MLCT}$  states. Some well-thought-out examples have been provided in the recent literature employing ligand bite angle manipulation<sup>91,92,153,154</sup> and push-pull concepts<sup>90,154,155</sup> to increase the  $^3\text{MLCT}$ – $^3\text{MC}$  gap in bis(tridentate) ruthenium complexes which in principle are applicable to cyclometalated complexes as well. However, these conceptual approaches are beyond the scope of this perspective. Recently, Dixon and coworkers<sup>156–158</sup> suggested on a computational basis, that two cyclometalating sites in *cis*-position could be beneficial to increase the ligand field splitting of iron(II) complexes and provide a tool for controlling the relative  $^3\text{MLCT}$  and  $^3\text{MC}$  energies. This concept should be transferable to cyclometalated ruthenium complexes as well (c.f. **3**) although it is likely accompanied with synthetic challenges.<sup>102,127,159,160</sup> An alternative approach could again involve attaching very weakly  $\pi$ -accepting ligands *trans* to a  $\text{N}^{\wedge}\text{C}^{\wedge}\text{N}$  ligand to yield potentially highly luminescent  $\text{Ru}\rightarrow\text{N}^{\wedge}\text{C}^{\wedge}\text{N}$   $^3\text{MLCT}$  states.

### The $[\text{Ru}(\text{N}^{\wedge}\text{N}^{\wedge}\text{N})(\text{N}^{\wedge}\text{N}^{\wedge}\text{C})]^+$ coordination sphere

The absorption spectrum of  $[\text{Ru}(\text{tpy})(\text{pbpy})]^+$  type complexes resembles that of  $[\text{Ru}(\text{bpy})_2(\text{ppy})]^+$  with two absorption bands, one around 400 nm, and a second around 500–600 nm. Again, the low-energy band is composed of MLCT transitions both involving the tpy and the cyclometalating ligand. However, the  $\pi^*$  orbital of the coordinating phenyl ring (LUMO+3) is not involved in any of the low-energy transitions, as its energy is substantially higher than the frontier orbitals (Figure 2).<sup>104</sup> Due to the near-degeneracy of the three lowest unoccupied orbitals (LUMO – LUMO+2), the absorption band at 500 nm is markedly sharper than that of  $[\text{Ru}(\text{dpb})(\text{tpy})]^+$  and  $[\text{Ru}(\text{bpy})_2(\text{ppy})]^+$  complexes. The feature around 400 nm is dominated by an intense  $\text{Ru}\rightarrow\text{phenyl}$  (LUMO+3) transition (Figure 2).<sup>104</sup>



**Scheme 3** Literature-known  $[\text{Ru}(\text{N}^{\wedge}\text{N}^{\wedge}\text{N})(\text{N}^{\wedge}\text{N}^{\wedge}\text{C})]^+$  complexes relevant to this work ( $[\mathbf{7a}]^+ - [\mathbf{7d}]^+$ <sup>104,134</sup>,  $[\mathbf{8a}]^+$ <sup>131</sup>,  $[\mathbf{8b}]^+$ <sup>161</sup>).

**Table 4** Emission wavelengths  $\lambda_{em}$  and wavenumbers  $\tilde{\nu}_{em}$  as well as quantum yields  $\phi$  of selected  $[\text{Ru}(\text{N}^{\wedge}\text{N}^{\wedge}\text{N})(\text{N}^{\wedge}\text{N}^{\wedge}\text{C})]^+$  complexes at room temperature in solution.

	$\lambda_{em} / \text{nm}$ ( $\tilde{\nu}_{em} / \text{cm}^{-1}$ )	$\phi$
<b>[7a]</b> <sup>+ 134</sup>	797 (12550)	$5.1 \cdot 10^{-6}$
<b>[7b]</b> <sup>+ 134</sup>	-	-
<b>[7c]</b> <sup>+ 134</sup>	780 (12820)	$1.3 \cdot 10^{-5}$
<b>[7d]</b> <sup>+ 134</sup>	807 (12390)	$4 \cdot 10^{-7}$
<b>[8a]</b> <sup>+ 131</sup>	810 (12350)	-
<b>[8b]</b> <sup>+ 161</sup>	549 (18210)	0.27

Unfortunately, accounts on emission properties of these  $[\text{Ru}(\text{tpy})(\text{pbpy})]^+$  complexes are very limited.<sup>104,104,131,161</sup> A few examples are summarized in Scheme 3 and Table 4. In the series **[7a]**<sup>+</sup> – **[7d]**<sup>+</sup> with carboxy substituents at either or both ligands, the quantum yields and trends in the emission energies are similar to those of the isomeric  $[\text{Ru}(\text{tpy})(\text{dpb})]^+$  complexes **[4a]**<sup>+</sup> – **[4d]**<sup>+</sup>. Again, carboxy-substitution at the tpy ligand lowers the LUMO energy sufficiently to yield non-emissive (**[7b]**<sup>+</sup>) or essentially non-emissive (**[7d]**<sup>+</sup>) complexes at room temperature due to the energy gap law.<sup>134</sup> However, carboxy-substitution at the pbpy ligand (**[7c]**<sup>+</sup>) does not blueshift the emission energy compared to the unsubstituted complex **[7a]**<sup>+</sup> ( $270 \text{ cm}^{-1}$ ) as much as in the case of the  $[\text{Ru}(\text{dpb})(\text{tpy})]^+$  complexes **[4c]**<sup>+</sup> and **[4a]**<sup>+</sup> ( $660 \text{ cm}^{-1}$ ).<sup>134</sup> This was traced back to a change of the orbital parentage of the emissive <sup>3</sup>MLCT state. Instead of being a Ru→tpy state as in **[7a]**<sup>+</sup>, emission of **[7c]**<sup>+</sup> arises from a Ru→(pbpy–COOR) <sup>3</sup>MLCT state. This is accompanied by an altered energy ordering of the lowest unoccupied orbitals and reflects their energetic similarity (Figure 2). This example highlights that in  $[\text{Ru}(\text{N}^{\wedge}\text{N}^{\wedge}\text{N})(\text{N}^{\wedge}\text{N}^{\wedge}\text{C})]^+$  type complexes Ru→N<sup>^</sup>N<sup>^</sup>C <sup>3</sup>MLCT states are obtained by tuning the respective frontier orbital energies of the ligands. However, the cyclometalating phenyl ring does not contribute as  $\pi$ -accepting moiety and the excited electron is entirely localized on the bipyridine fragment of the pbpy ligand. Consequently, the phosphorescence efficiency is not affected significantly (Table 4).

Interestingly, Berlinguette and coworkers reported on a series of  $[\text{Ru}(\text{tpy})(\text{pbpy})]^+$  based complexes with diarylamine groups appended *via* a thiophene linker such as **[8b]**<sup>+</sup>. These are highly emissive (quantum yields in the range of 0.1 – 0.3) in some cases, but emit at much higher energy than typically observed for these complexes.<sup>161</sup> In fact, the analogous thiophene substituted complex **[8a]**<sup>+</sup> without the diarylamine functionality lacks the strong emission.<sup>131</sup> However, Berlinguette showed that the emissive behaviour of **[8b]**<sup>+</sup> actually arises from a singlet intraligand charge transfer state (<sup>1</sup>ILCT) involving the diarylamine unit as electron donor and the polypyridine moiety as electron acceptor.<sup>162,163</sup> An identical emission energy was observed for the free ligand with even higher fluorescence quantum yields ( $\phi = 0.91$ ,  $\tau = 3.4 \text{ ns}$ ) explaining the untypically high emission energy and quantum yield of **[8b]**<sup>+</sup>.<sup>161–163</sup>



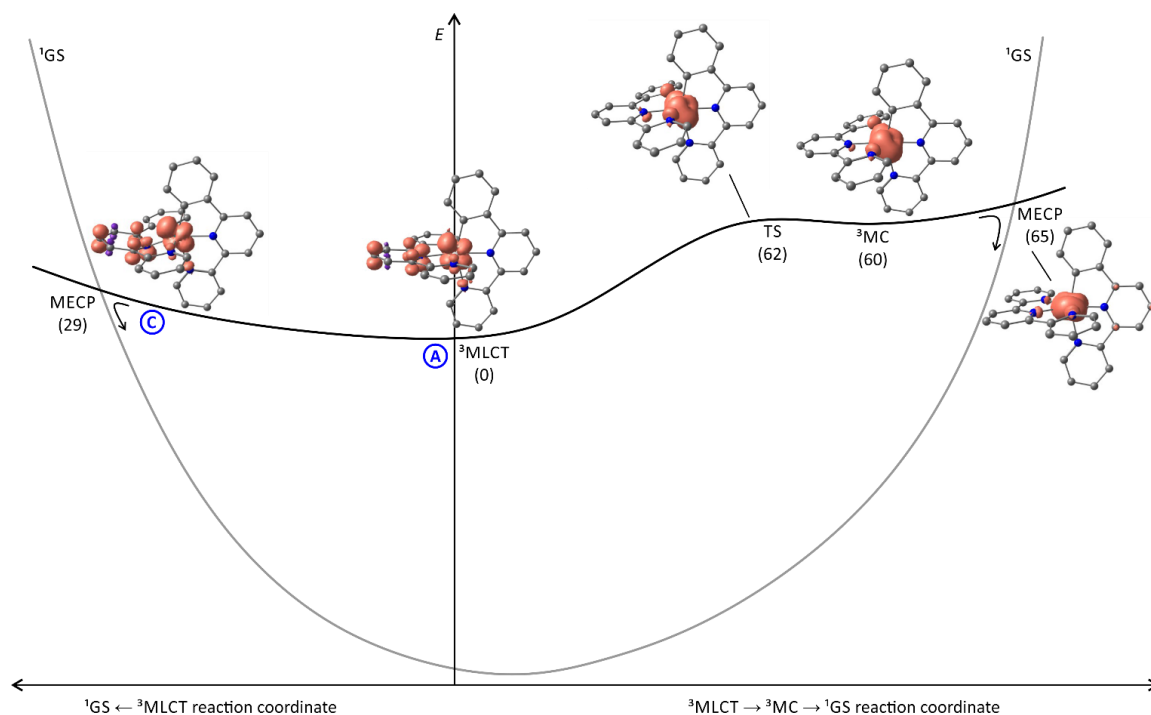


**Figure 6** Schematic representation of the energy landscape of  $[\text{Ru}(\text{tpy})(\text{pbpy})]^+$  type of complexes including spin density contour plots (contour value: 0.01) of the  $^3\text{MLCT}$  and  $^3\text{MC}$  states of  $[\mathbf{7a}]^+$ , the  $^3\text{MLCT} \rightarrow ^3\text{MC}$  transition state as well as the minimum energy points for the  $^3\text{MLCT} \rightarrow ^1\text{GS}$  and the  $^3\text{MC} \rightarrow ^1\text{GS}$  surface crossing. H atoms are omitted for clarity. Energies ( $\text{kJ mol}^{-1}$ ) of the respective states are given in parentheses. The  $^3\text{MLCT} - ^1\text{GS}$  energy difference is taken from DFT calculations.

To get a better understanding of the states involved in the excited state deactivation of  $[\text{Ru}(\text{tpy})(\text{pbpy})]^+$  complexes, we studied the triplet potential energy surface of  $[\mathbf{7a}]^+$  using DFT calculations. Inspecting the  $^3\text{MLCT}$  state geometry and spin density of  $[\mathbf{7a}]^+$  reveals a striking similarity to  $[\mathbf{4a}]^+$  (Figures 4, 5 and 6). In fact, a similar distortion of the tpy ligand with an offset central pyridine ring is found in both cases (*vide supra*). Additionally, the bond length changes of the  $^3\text{MLCT}$  states compared to the respective  $^1\text{GS}$  geometries of  $[\mathbf{4a}]^+$  and  $[\mathbf{7a}]^+$  are very similar (Figure 4). Given the similar quantum yields of the isoelectronic classes of complexes  $[\text{Ru}(\text{dpb})(\text{tpy})]^+$  and  $[\text{Ru}(\text{tpy})(\text{pbpy})]^+$  this suggests excited state deactivation channels with similar barriers are dominant in both cases. However, the  $^3\text{MC}$  state (path **B**) is found to be  $60 \text{ kJ mol}^{-1}$  ( $^3\text{MLCT} \rightarrow ^3\text{MC}$  transition state at  $62 \text{ kJ mol}^{-1}$ ) higher in energy than the  $^3\text{MLCT}$  state and thus it is thermally inaccessible at room temperature. As a consequence, its contribution to the excited state deactivation of  $[\mathbf{7a}]^+$  is negligible. The marked increase of the  $^3\text{MC} - ^3\text{MLCT}$  energy gap by about  $30 \text{ kJ mol}^{-1}$  by exchanging  $\text{N}^{\wedge}\text{C}^{\wedge}\text{N}$  by  $\text{N}^{\wedge}\text{N}^{\wedge}\text{C}$  chelate ligands in bis(tridentate) complexes (Figure 6) was also found for the isoelectronic iron(II) complexes by Dixon and coworkers.<sup>158</sup> They argued that the cyclometalating ligand does not only act as a strong  $\sigma$ -donor but also as a  $\pi$ -donor. In the iron(II) complex  $[\text{Fe}(\text{dpb})(\text{tpy})]^+$  the  $\pi$ -donor strength is the dominant influence yielding a net reduction of the effective ligand field strength and hence a stabilization of the  $^3\text{MC}$  state compared to the non-cyclometalated complex  $[\text{Fe}(\text{tpy})_2]^{2+}$ . In  $[\text{Fe}(\text{tpy})(\text{pbpy})]^+$  on the other hand, the  $\pi$ -overlap between the peripheral cyclometalating phenyl ring and the metal  $d$  orbitals is not

as pronounced. As a consequence of the  $\sigma$ -overlap an increased ligand field splitting and a higher  $^3\text{MC}$  energy compared to  $[\text{Fe}(\text{dpb})(\text{tpy})]^+$  are calculated. At the same time, the  $^3\text{MLCT}$  energies of  $[\text{Fe}(\text{tpy})(\text{pbpy})]^+$  and  $[\text{Fe}(\text{dpb})(\text{tpy})]^+$  are essentially identical yielding an overall higher  $^3\text{MLCT}$ – $^3\text{MC}$  energy gap by about  $30 \text{ kJ mol}^{-1}$  for  $[\text{Fe}(\text{tpy})(\text{pbpy})]^+$ . As for ruthenium, the  $d$  orbitals are more diffuse than for iron, the destabilization of the  $t_{2g}$  orbitals *via*  $\pi$ -donor interactions is much less pronounced yielding  $^3\text{MC}$  states well above the  $^3\text{MLCT}$  level in all cyclometalating complexes, but the same principles apply explaining the trends we observe for the isoelectronic ruthenium complexes.<sup>158</sup>

In principle, a  $^3\text{LL}'\text{CT}$  state similar to that described for  $[\text{Ru}(\text{dpb})(\text{tpy})]^+$  complexes (*vide supra*) is also conceivable for complexes of the  $[\text{Ru}(\text{N}^{\wedge}\text{N}^{\wedge}\text{N})(\text{N}^{\wedge}\text{N}^{\wedge}\text{C})]^+$  class. However, an analogous symmetry restriction as discussed above for the former does not apply in this case due to the lowered molecular symmetry. Although we tried to localize such a  $^3\text{LL}'\text{CT}$  state it remained elusive. Whether such a state actually contributes to the excited state deactivation of  $[\text{Ru}(\text{N}^{\wedge}\text{N}^{\wedge}\text{N})(\text{N}^{\wedge}\text{N}^{\wedge}\text{C})]^+$  complexes has to be evaluated based on experimental emission data at variable temperatures. This exceeds the scope of this article.

Since the  $^3\text{MLCT}$  state of  $[\mathbf{7a}]^+$  is electronically very similar to the  $^3\text{MLCT}$  state of the tris(bidentate) complex  $[\mathbf{1b}]^+$ , an argumentation based on emission quenching *via* vibronic coupling to the ground state (path **A**) is insufficient to account for the substantially lower emission quantum yields of the former ( $10^{-6} - 10^{-5}$  as compared to  $10^{-4} - 10^{-3}$ ). Additionally, deactivation channels *via* low-lying  $^3\text{MC}$  (path **B**) or  $^3\text{LL}'\text{CT}$  states (path **D**) as found for  $[\text{Ru}(\text{dpb})(\text{tpy})]^+$  complexes do not contribute to the efficient non-emissive excited state decay of  $[\text{Ru}(\text{tpy})(\text{pbpy})]^+$  complexes. A surface crossing point between the  $^3\text{MLCT}$  and  $^1\text{GS}$  potential energy surfaces (path **C**), however, similar to that found for  $[\mathbf{4a}]^+$  (Figure 5), would provide a concise explanation for the marked difference between the tris(bidentate) and bis(tridentate) complexes. Indeed, we localized a thermally accessible  $^3\text{MLCT} \rightarrow ^1\text{GS}$  surface crossing point that is only  $29 \text{ kJ mol}^{-1}$  higher in energy than the  $^3\text{MLCT}$  state (Figure 6). Remarkably, the geometry and energy of this crossing point is similar to that of the  $^3\text{MLCT} \rightarrow ^1\text{GS}$  MECP of  $[\mathbf{4a}]^+$ . Again, the distortion of the  $^3\text{MLCT}$  state provides an excited state deactivation pathway for polypyridine ruthenium complexes. This finding has some predictive value as well. The  $^3\text{MC}$  state is thermally inaccessible at temperatures below 298 K in  $[\mathbf{7a}]^+$  and does not contribute to the excited state decay. Hence, the temperature dependence of the emission of  $[\mathbf{7a}]^+$  can provide information on the contribution of a minimum energy surface crossing point in proximity to the relaxed  $^3\text{MLCT}$  geometry to the emission quenching. An increasing emission intensity upon cooling would support this hypothesis. Additionally, as the dissociative anti-bonding  $^3\text{MC}$  state is out of reach at room temperature, no photosubstitution reactions should occur for  $[\mathbf{7a}]^+$  in contrast to  $[\text{Ru}(\text{bpy})_3]^{2+}$  which is very prone to such reactivity.<sup>87</sup> We will devote future work into elucidating these predictions.

In conclusion, it does not suffice to reduce the molecular symmetry and circumvent the parasitic  $^3\text{LL}'\text{CT}$  state to increase phosphorescence quantum yields in bis(tridentate) cyclometalated complexes. Bis(tridentate)  $[\text{Ru}(\text{N}^{\wedge}\text{N}^{\wedge}\text{N})(\text{N}^{\wedge}\text{N}^{\wedge}\text{C})]^+$  complexes with peripheral cyclometalation suffer from the same distortion and low energy of the  $^3\text{MLCT}$  state as the analogous tris(bidentate) complexes. As the relative  $^3\text{MC}$  state energy of  $[\text{Ru}(\text{tpy})(\text{pbpy})]^+$  complexes is substantially higher

than for comparable  $[\text{Ru}(\text{N}^{\wedge}\text{N}^{\wedge}\text{N})(\text{N}^{\wedge}\text{C}^{\wedge}\text{N})]^+$  complexes, its contribution to the excited state decay can be neglected (path **B**). Hence, similar strategies are applicable for increasing the luminescence quantum yields as suggested before for tris(bidentate) complexes. These should focus on reducing the excited state distortion yielding a nested emissive state and shutting down the deactivation *via* direct  $^3\text{MLCT} \rightarrow ^1\text{GS}$  surface crossing (path **C**). This might be achieved by shifting the LUMO to higher energies and making the  $\pi^*$  orbital of the cyclometalating moiety the acceptor site of the lowest  $^3\text{MLCT}$  state. At the same time, a lower excited state distortion would shift the energy of the  $^3\text{MLCT} \rightarrow ^1\text{GS}$  MECP to higher energies as well. This could potentially be accomplished by a combination of a very weakly  $\pi$ -accepting spectator ligand with a cyclometalating ligand that also contains a weakly  $\pi$ -accepting site such as an *N*-heterocyclic carbene.<sup>164,165</sup>

## Experimental Section

### Density functional theory calculations

DFT calculations were carried out using the ORCA program package (version 3.0.2).<sup>166</sup> Tight convergence criteria were chosen for all calculations (Keywords TightSCF and TightOpt). All calculations were performed using the hybrid functional B3LYP<sup>167</sup> and employ the RIJCOSX approximation.<sup>168,169</sup> Relativistic effects were calculated at the zeroth order regular approximation (ZORA) level. The ZORA keyword automatically invokes relativistically adjusted basis sets.<sup>170</sup> To account for solvent effects, a conductor-like screening model (COSMO) modelling acetonitrile was used in all calculations.<sup>171</sup> Geometry, transition state and minimum energy crossing point optimizations were performed using Ahlrichs' split-valence double- $\xi$  basis set def2-SV(P) which comprises polarization functions for all non-hydrogen atoms.<sup>172,173</sup> Optimized geometries were confirmed to be minima or first-order saddle points by subsequent frequency analysis ( $n_{\text{imag}} = 0$  or 1, respectively). Computed free Gibbs enthalpies were used to compare the relative energies of all structures. Explicit counterions and/or solvent molecules were not taken into account in any case.

## Conclusions

Cyclometalated polypyridineruthenium(II) complexes with  $\text{N}_5\text{C}$  coordination sphere typically exhibit very weak room temperature emission in the near infrared range (700-800 nm) of the electromagnetic spectrum. The reasons for the weak emission are various and depend on the chelate coordination sphere around the metal center. In tris(bidentate)  $[\text{Ru}(\text{N}^{\wedge}\text{N})_2(\text{N}^{\wedge}\text{C})]^+$  complexes, the  $^3\text{MC}$  state (path **B**) that is typically a major channel for excited state decay in polypyridineruthenium(II) complexes<sup>81,86,87</sup>, does not contribute in these systems as it is thermally inaccessible ( $\Delta E(^3\text{MLCT} \rightarrow ^3\text{MC}) = 60 - 70 \text{ kJ mol}^{-1}$ ) at room temperature. Furthermore, no low energy  $^3\text{MLCT} \rightarrow ^1\text{GS}$  surface crossing point was found (path **C**) which suggests that tunnelling into high-energy vibrationally excited singlet states is the main channel of excited state deactivation (path **A**).

In contrast, the emission quenching of  $[\text{Ru}(\text{N}^{\wedge}\text{N}^{\wedge}\text{N})(\text{N}^{\wedge}\text{C}^{\wedge}\text{N})]^+$  complexes is dominated by two thermally accessible triplet states, that flank the emissive  $^3\text{MLCT}$  state, namely the  $^3\text{MC}$  state (path **B**,  $\Delta E(^3\text{MLCT} \rightarrow ^3\text{MC}) = 10 - 30 \text{ kJ mol}^{-1}$ ) and a  $^3\text{LL}'\text{CT}$  state (path **D**,  $\Delta E(^3\text{MLCT} \rightarrow ^3\text{LL}'\text{CT}) < 10 \text{ kJ mol}^{-1}$ ).<sup>114–116</sup> The  $^3\text{LL}'\text{CT}$  state is a peculiarity of  $C_2$ -symmetric cyclometalated complexes and provides a second, unprecedented non-emissive deactivation channel. Additionally, a  $^3\text{MLCT} \rightarrow ^1\text{GS}$  surface crossing point provides another decay channel (path **C**) whose contribution yet needs to be quantified. These three channels B, C and D are responsible for almost 100 % of the emission quenching. Although significantly faster than the emission process itself, direct non-emissive decay *via*  $^3\text{MLCT} \rightarrow ^1\text{GS}$  tunnelling (path **A**) only plays a subordinate role simply because excited state decay *via* paths B, C and D is so efficient. This is reflected by the very low excited state lifetimes below the nanosecond range.

In  $[\text{Ru}(\text{N}^{\wedge}\text{N}^{\wedge}\text{N})(\text{N}^{\wedge}\text{N}^{\wedge}\text{C})]^+$  complexes, the  $^3\text{MC}$  states are thermally inaccessible ( $\Delta E(^3\text{MLCT} \rightarrow ^3\text{MC}) \approx 60 \text{ kJ mol}^{-1}$ ) and no quenching  $^3\text{LL}'\text{CT}$  states are relevant. However, the triplet and singlet potential surfaces intersect close to the relaxed  $^3\text{MLCT}$  state providing an efficient deactivation channel (path **C**) with an activation barrier of only about  $30 \text{ kJ mol}^{-1}$ . This explains the similarly low emission quantum yields of bis(tridentate) complexes with central and peripheral cyclometalating site despite the markedly different triplet states relevant to the two systems. However, the amount of emission quenching *via* tunneling (path **A**) in  $[\text{Ru}(\text{N}^{\wedge}\text{N}^{\wedge}\text{N})(\text{N}^{\wedge}\text{N}^{\wedge}\text{C})]^+$  complexes remains unclear until temperature-dependent lifetime data are acquired.

Strategies for increasing the phosphorescence quantum yields are proposed. In  $[\text{Ru}(\text{N}^{\wedge}\text{N})_2(\text{N}^{\wedge}\text{C})]^+$  complexes emission quenching is dominated the very low emission energies and the efficient tunnelling into high-energy singlet states following the energy gap law (path **A**). Hence, improving the emission efficiency is very challenging and only achieved by structurally restraining the already small excited state distortions or increasing the emission energy drastically. The latter is possible by making the cyclometalating ligand the  $\pi$ -accepting site of the  $^3\text{MLCT}$  state as shown by Chou and coworkers.<sup>127</sup>

In bis(tridentate) cyclometalated ruthenium complexes, emission quenching predominantly arises from the distortion of the  $^3\text{MLCT}$  state compared to the ground state. The triplet potential energy surface is relatively flat around the  $^3\text{MLCT}$  geometry leading to a  $^3\text{MLCT}/^1\text{GS}$  surface intersection less than  $30 \text{ kJ mol}^{-1}$  above the emissive  $^3\text{MLCT}$  state giving rise to a deactivation channel *via* a direct  $^3\text{MLCT} \rightarrow ^1\text{GS}$  surface crossing. Minimizing the excited state distortion *via* structural constraints could circumvent this channel. Additionally, by making the cyclometalating ligand the  $\pi$ -accepting site within the  $^3\text{MLCT}$  state *via* tuning the energy levels of the lowest unoccupied molecular orbitals, a substantial increase of the  $^3\text{MLCT}$  state energy can be achieved which would be beneficial for suppressing the  $^3\text{MLCT} \rightarrow ^1\text{GS}$  surface crossing as well. This will, however, also shift the emission well into the visible range of the electronic spectrum.

Furthermore, it is crucial to avoid orthogonal  $\pi$ -donor and  $\pi$ -acceptor sites in *trans* position across the metal center as in  $[\text{Ru}(\text{N}^{\wedge}\text{N}^{\wedge}\text{N})(\text{N}^{\wedge}\text{C}^{\wedge}\text{N})]^+$  because this inherently invokes orthogonal, non-emissive  $^3\text{LL}'\text{CT}$  states as quenching channels and also lowers the energy of the  $^3\text{MC}$  states into a thermally accessible region due to a lower ligand field splitting.

In order to elucidate the excited state properties of cyclometalated complexes, temperature-dependent excited state lifetime or emission quantum yield measurements provide an invaluable tool.<sup>114–116</sup> Additionally, quantum chemical approaches can deliver lots of information about energies and geometries of relevant excited states. Tong, Che and coworkers (*vide supra*) demonstrated this on luminescent cyclometalated gold(III) complexes.<sup>152</sup> They assessed the radiative and non-radiative decay rates from a computational standpoint and quantified key processes that yield or prevent efficient emission in these species. Similarly, Dixon and coworkers studied mono- and bis(cyclometalated) iron(II) complexes using DFT calculations.<sup>156–158</sup> The <sup>3</sup>MC state in [Fe(pbpy)(tpy)]<sup>+</sup> with peripheral cyclometalation is substantially higher in energy than in [Fe(dpb)(tpy)]<sup>+</sup> with central cyclometalation, very similar to the results presented here for the ruthenium homologues. Furthermore, they highlighted, that bis(cyclometalated) iron(II) complexes such as [Fe(dpb)(pbpy)] and [Fe(pbpy)<sub>2</sub>] have very low-lying <sup>3</sup>MLCT states that are, in the case of [Fe(dpb)(pbpy)], only marginally distorted compared to the ground state geometry. We suggest that these findings apply to the analogous ruthenium complexes potentially opening a route to highly luminescent near-IR emitters. However, since only very few bis(cyclometalated) polypyridine ruthenium complexes are known so far<sup>127,159,160</sup> and none of them contain tridentate ligands, the synthesis of Ru(dpb)(pbpy) and Ru(pbpy)<sub>2</sub> complexes might be challenging. We will devote future work to the design and synthesis of ruthenium-based emitters with cyclometalating ligands to improve and exploit their excited state properties.

### Acknowledgements

Parts of this research were conducted using the supercomputer MOGON and advisory services offered by Johannes Gutenberg Univ. Mainz (<http://www.hpc.uni-mainz.de>), which is a member of the AHRP and the Gauss Alliance e.V. This work was financially supported by the Deutsche Forschungsgemeinschaft (GSC 266, Materials Science in Mainz, scholarship for C.K.).

### Authors

#### Christoph Kreitner



is currently working on his PhD thesis in the research group of Prof. Dr. Katja Heinze at the Johannes Gutenberg-University in Mainz, Germany (since 2013). There, his research focusses on the synthesis and understanding of new cyclometalated ruthenium complexes and their application in dye-sensitized solar cells. He studied chemistry at the Johannes Gutenberg-University of Mainz, Germany where he received his diploma degree in 2012. During his studies he spent one semester at the University of Toronto, Toronto, Canada (2010/2011), working in the Department of Inorganic Chemistry in the group of Prof. Douglas W. Stephan on Frustrated Lewis Pairs and their reactions with lactones and lactide. For his PhD thesis, he received a scholarship of the



Graduate School of Excellence “Materials Science in Mainz” (2013) and became junior member of the Gutenberg Academy of the Johannes Gutenberg-University Mainz, Germany (2014). His research interests particularly aim at the understanding of electron and energy transfer as well as optoelectronic mechanisms in molecular systems.

### Katja Heinze



is professor of organometallic and bioinorganic chemistry at the Johannes Gutenberg-University of Mainz, Germany. After receiving a diploma degree (1995) and a Ph.D. degree (1998) from the Ruprecht Karls University of Heidelberg, Germany (G. Huttner), she went for a postdoctoral stay to the University of Zurich, Zurich, Switzerland (1999). She was appointed Privatdozent in 2004 at the University of Heidelberg, Germany, and Full Professor in 2008 at the Johannes Gutenberg-University of Mainz, Germany. She received the Lieseberg award of the Faculty of Chemistry and Earth Sciences, University of Heidelberg (2002), the Heisenberg fellowship from the Deutsche Forschungsgemeinschaft (2004), the Hengstberger Award of the University of Heidelberg (2007) and the Interregional Research Price of the Greater Region (2014). Currently she serves as chair of the Institute of Inorganic Chemistry and Analytical Chemistry, University of Mainz. From 2011 to 2015 she has served as a member of the International Advisory Board of Organometallics. Her key research interests comprise functional complex systems based on coordination and organometallic compounds with special emphasis on molecular wires, light-harvesting systems, bistable systems, emitters, switches and sensors as well as on (biomimetic) catalysts. She has authored more than 130 international refereed papers.

### References

- 1 N. Alonso-Vante, J.-F. Nierengarten and J.-P. Sauvage, *J. Chem. Soc., Dalton Trans.*, 1994, 1649–1654.
- 2 T. Bessho, E. C. Constable, M. Graetzel, A. Hernandez Redondo, C. E. Housecroft, W. Kylberg, M. K. Nazeeruddin, M. Neuburger and S. Schaffner, *Chem. Commun.*, 2008, 3717–3719.
- 3 C. E. Housecroft and E. C. Constable, *Chem. Soc. Rev.*, 2015, **44**, 8386–8398.
- 4 S. Ferrere and B. A. Gregg, *J. Am. Chem. Soc.*, 1998, **120**, 843–844.
- 5 S. Ferrere, *Chem. Mater.*, 2000, **12**, 1083–1089.
- 6 T. C. B. Harlang, Y. Liu, O. Gordivska, L. A. Fredin, C. S. Ponceca, P. Huang, P. Chábera, K. S. Kjaer, H. Mateos, J. Uhlig, R. Lomoth, R. Wallenberg, S. Styring, P. Persson, V. Sundström and K. Wärnmark, *Nature Chem.*, 2015, **7**, 883–889.

- 7 G. Sauvé, M. E. Cass, S. J. Doig, I. Lauermaun, K. Pomykal and N. S. Lewis, *J. Phys. Chem. B*, 2000, **104**, 3488–3491.
- 8 T. Kinoshita, J.-i. Fujisawa, J. Nakazaki, S. Uchida, T. Kubo and H. Segawa, *J. Phys. Chem. Lett.*, 2012, 394–398.
- 9 E. I. Mayo, K. Kilså, T. Tirrell, P. I. Djurovich, A. Tamayo, M. E. Thompson, N. S. Lewis and H. B. Gray, *Photochem. Photobiol. Sci.*, 2006, **5**, 871–873.
- 10 E. Baranoff, J. Yum, I. Jung, R. Vulcano, M. Grätzel and M. K. Nazeeruddin, *Chem. Asian J.*, 2010, **5**, 496–499.
- 11 B. O'Regan and M. Grätzel, *Nature*, 1991, **353**, 737–740.
- 12 M. K. Nazeeruddin, A. Kay, I. Rodicio, R. Humphry-Baker, E. Mueller, P. Liska, N. Vlachopoulos and M. Graetzel, *J. Am. Chem. Soc.*, 1993, **115**, 6382–6390.
- 13 M. K. Nazeeruddin, S. M. Zakeeruddin, R. Humphry-Baker, M. Jirousek, P. Liska, N. Vlachopoulos, V. Shklover, C.-H. Fischer and M. Grätzel, *Inorg. Chem.*, 1999, **38**, 6298–6305.
- 14 M. K. Nazeeruddin, P. Péchy, T. Renouard, S. M. Zakeeruddin, R. Humphry-Baker, P. Comte, P. Liska, Le Cevey, E. Costa, V. Shklover, L. Spiccia, G. B. Deacon, C. A. Bignozzi and M. Grätzel, *J. Am. Chem. Soc.*, 2001, **123**, 1613–1624.
- 15 M. Grätzel, *J. Photochem. Photobiol. C*, 2003, **4**, 145–153.
- 16 S. H. Wadman, J. M. Kroon, K. Bakker, M. Lutz, A. L. Spek, G. P. M. van Klink and G. van Koten, *Chem. Commun.*, 2007, 1907–1909.
- 17 T. Bessho, E. Yoneda, J.-H. Yum, M. Guglielmi, I. Tavernelli, H. Imai, U. Rothlisberger, M. K. Nazeeruddin and M. Grätzel, *J. Am. Chem. Soc.*, 2009, **131**, 5930–5934.
- 18 A. Hagfeldt, G. Boschloo, L. Sun, L. Kloo and H. Pettersson, *Chem. Rev.*, 2010, **110**, 6595–6663.
- 19 P. G. Bomben, K. C. Robson, B. D. Koivisto and C. P. Berlinguette, *Coord. Chem. Rev.*, 2012, **256**, 1438–1450.
- 20 H. D. Abruna, A. Y. Teng, G. J. Samuels and T. J. Meyer, *J. Am. Chem. Soc.*, 1979, **101**, 6745–6746.
- 21 I. Okura and N. Kim-Thuan, *J. Mol. Catal.*, 1979, **5**, 311–314.
- 22 J.-M. Lehn and R. Ziessel, *Proc. Natl. Acad. Sci.*, 1982, **79**, 701–704.
- 23 J. Hawecker, J.-M. Lehn and R. Ziessel, *J. Chem. Soc., Chem. Commun.*, 1983, 536.
- 24 H. Ozawa, M. Haga and K. Sakai, *J. Am. Chem. Soc.*, 2006, **128**, 4926–4927.
- 25 S. Rau, B. Schäfer, D. Gleich, E. Anders, M. Rudolph, M. Friedrich, H. Görls, W. Henry and J. G. Vos, *Angew. Chem.*, 2006, **118**, 6361–6364. *Angew. Chem. Int. Ed.*, 2006, **45**, 6215–6218.
- 26 A. Fihri, V. Artero, M. Razavet, C. Baffert, W. Leibl and M. Fontecave, *Angew. Chem.*, 2008, **120**, 574–577. *Angew. Chem. Int. Ed.*, 2008, **47**, 564–567.
- 27 J. W. Tucker and C. R. J. Stephenson, *J. Org. Chem.*, 2012, **77**, 1617–1622.
- 28 J. W. Tucker, Y. Zhang, T. F. Jamison and C. R. J. Stephenson, *Angew. Chem.*, 2012, **124**, 4220–4223. *Angew. Chem. Int. Ed.*, 2012, **51**, 4144–4147.
- 29 M. Majek and A. Jacobi von Wangelin, *Angew. Chem.*, 2013, **125**, 6033–6035. *Angew. Chem. Int. Ed.*, 2013, **52**, 5919–5921.
- 30 S. Paria and O. Reiser, *ChemCatChem*, 2014, **6**, 2477–2483.

- 31 S. M. Stevenson, M. P. Shores and E. M. Ferreira, *Angew. Chem.*, 2015, **127**, 6606–6610. *Angew. Chem. Int. Ed.*, 2015, **54**, 6506–6510.
- 32 V. Balzani and S. Campagna, *Top. Curr. Chem.*, 2007, **280**, 1–273.
- 33 V. Balzani and S. Campagna, *Top. Curr. Chem.*, 2007, **281**, 1–327.
- 34 J. P. Paris and W. W. Brandt, *J. Am. Chem. Soc.*, 1959, **81**, 5001–5002.
- 35 V. W.-W. Yam and K. M.-C. Wong, *Chem. Commun.*, 2011, **47**, 11579–11592.
- 36 H. Xiang, J. Cheng, X. Ma, X. Zhou and J. J. Chruma, *Chem. Soc. Rev.*, 2013, **42**, 6128–6185.
- 37 H. Xu, R. Chen, Q. Sun, W. Lai, Q. Su, W. Huang and X. Liu, *Chem. Soc. Rev.*, 2014, **43**, 3259–3302.
- 38 S. M. Fredericks, J. C. Luong and M. S. Wrighton, *J. Am. Chem. Soc.*, 1979, **101**, 7415–7417.
- 39 A. Juris, S. Campagna, I. Bidd, J. M. Lehn and R. Ziessel, *Inorg. Chem.*, 1988, **27**, 4007–4011.
- 40 R. A. Kirgan, B. P. Sullivan and D. P. Rillema, *Top. Curr. Chem.*, 2007, **281**, 45–100.
- 41 K. K.-W. Lo, M.-W. Louie and K. Y. Zhang, *Coord. Chem. Rev.*, 2010, **254**, 2603–2622.
- 42 J. N. Demas, E. W. Harris, C. M. Flynn and D. Diemente, *J. Am. Chem. Soc.*, 1975, **97**, 3838–3839.
- 43 C. Creutz, M. Chou, T. L. Netzel, M. Okumura and N. Sutin, *J. Am. Chem. Soc.*, 1980, **102**, 1309–1319.
- 44 J. P. Sauvage, J. P. Collin, J. C. Chambron, S. Guillerez, C. Coudret, V. Balzani, F. Barigelletti, L. de Cola and L. Flamigni, *Chem. Rev.*, 1994, **94**, 993–1019.
- 45 D. Kumaresan, K. Shankar, S. Vaidya and R. H. Schmehl, *Top. Curr. Chem.*, 2007, **281**, 101–142.
- 46 D. Carstens and G. Crosby, *J. Mol. Spectros.*, 1970, **34**, 113–135.
- 47 A. Zilian, U. Maeder, A. von Zelewski and H. U. Guedel, *J. Am. Chem. Soc.*, 1989, **111**, 3855–3859.
- 48 M. T. Indelli, C. Chiorboli and F. Scandola, *Top. Curr. Chem.*, **280**, 215–255.
- 49 K. A. King, P. J. Spellane and R. J. Watts, *J. Am. Chem. Soc.*, 1985, **107**, 1431–1432.
- 50 M. G. Colombo, A. Hauser and H. U. Guedel, *Inorg. Chem.*, 1993, **32**, 3088–3092.
- 51 L. Flamigni, A. Barbieri, C. Sabatini, B. Ventura and F. Barigelletti, *Top. Curr. Chem.*, 2007, **281**, 143–203.
- 52 F. Barigelletti, D. Sandrini, M. Maestri, V. Balzani, A. von Zelewsky, L. Chassot, P. Jolliet and U. Maeder, *Inorg. Chem.*, 1988, **27**, 3644–3647.
- 53 H.-K. Yip, L.-K. Cheng, K.-K. Cheung and C.-M. Che, *J. Chem. Soc., Dalton Trans.*, 1993, 2933–2938.
- 54 D. R. McMillin and J. J. Moore, *Coord. Chem. Rev.*, 2002, **229**, 113–121.
- 55 J. A. G. Williams, *Top. Curr. Chem.*, 2007, **281**, 205–268.
- 56 V. Wing-Wah Yam and E. Chung-Chin Cheng, *Top. Curr. Chem.*, 2007, **281**, 269–309.
- 57 C. Bronner and O. S. Wenger, *Dalton Trans.*, 2011, **40**, 12409–12420.
- 58 N. A. P. Kane-Maguire and C. H. Langford, *J. Chem. Soc. D*, 1971, 895–896.

- 59 M. Maestri, F. Bolletta, L. Moggi, V. Balzani, M. S. Henry and M. Z. Hoffman, *J. Am. Chem. Soc.*, 1978, **100**, 2694–2701.
- 60 A. D. Kirk and G. B. Porter, *J. Phys. Chem.*, 1980, **84**, 887–891.
- 61 N. A. P. Kane-Maguire, *Top. Curr. Chem.*, 2007, **280**, 37–67.
- 62 S. Otto, M. Grabolle, C. Förster, C. Kreitner, U. Resch-Genger and K. Heinze, *Angew. Chem.*, 2015, **127**, 11735–11739. *Angew. Chem. Int. Ed.*, 2015, **54**, 11572–11576.
- 63 A. Juris and R. Ziessel, *Inorg. Chim. Acta*, 1994, **225**, 251–254.
- 64 N. Armaroli, *Chem. Soc. Rev.*, 2001, **30**, 113–124.
- 65 N. Armaroli, G. Accorsi, F. Cardinali and A. Listorti, *Top. Curr. Chem.*, 2007, **280**, 69–115.
- 66 M. Iwamura, S. Takeuchi and T. Tahara, *Acc. Chem. Res.*, 2015, **48**, 782–791.
- 67 J. Nitsch, C. Kleeberg, R. Fröhlich and A. Steffen, *Dalton Trans*, 2015, **44**, 6944–6960.
- 68 M. W. Mara, K. A. Fransted and L. X. Chen, *Coord. Chem. Rev.*, 2015, **282–283**, 2–18.
- 69 L.-Y. Zhang, G.-F. Liu, S.-L. Zheng, B.-H. Ye, X.-M. Zhang and X.-M. Chen, *Eur. J. Inorg. Chem.*, 2003, **2003**, 2965–2971.
- 70 K. Kalyanasundaram, *Coord. Chem. Rev.*, 1982, **46**, 159–244.
- 71 A. Juris, V. Balzani, F. Barigelletti, S. Campagna, P. Belser and A. von Zelewsky, *Coord. Chem. Rev.*, 1988, **84**, 85–277.
- 72 V. Balzani and A. Juris, *Coord. Chem. Rev.*, 2001, **211**, 97–115.
- 73 J. R. Winkler, T. L. Netzel, C. Creutz and N. Sutin, *J. Am. Chem. Soc.*, 1987, **109**, 2381–2392.
- 74 G. D. Hager and G. A. Crosby, *J. Am. Chem. Soc.*, 1975, **97**, 7031–7037.
- 75 T. J. Meyer, *Pure Appl. Chem.*, 1986, **58**, 1193–1206.
- 76 J. N. Demas and D. G. Taylor, *Inorg. Chem.*, 1979, **18**, 3177–3179.
- 77 S. Yoon, P. Kukura, C. M. Stuart and R. A. Mathies, *Mol. Phys.*, 2006, **104**, 1275–1282.
- 78 K. Suzuki, A. Kobayashi, S. Kaneko, K. Takehira, T. Yoshihara, H. Ishida, Y. Shiina, S. Oishi and S. Tobita, *Phys. Chem. Chem. Phys.*, 2009, **11**, 9850–9860.
- 79 G. A. Crosby, *Acc. Chem. Res.*, 1975, **8**, 231–238.
- 80 G. D. Hager, R. J. Watts and G. A. Crosby, *J. Am. Chem. Soc.*, 1975, **97**, 7037–7042.
- 81 J. van Houten and R. J. Watts, *J. Am. Chem. Soc.*, 1976, **98**, 4853–4858.
- 82 M. Kasha, *Discuss. Faraday Soc.*, 1950, **9**, 14–19.
- 83 R. Englman and J. Jortner, *Mol. Phys.*, 1970, **18**, 145–164.
- 84 J. V. Caspar, E. M. Kober, B. P. Sullivan and T. J. Meyer, *J. Am. Chem. Soc.*, 1982, **104**, 630–632.
- 85 J. V. Caspar and T. J. Meyer, *J. Phys. Chem.*, 1983, **87**, 952–957.
- 86 J. van Houten and R. J. Watts, *Inorg. Chem.*, 1978, **17**, 3381–3385.
- 87 B. Durham, J. V. Caspar, J. K. Nagle and T. J. Meyer, *J. Am. Chem. Soc.*, 1982, **104**, 4803–4810.
- 88 F. Barigelletti, A. Juris, V. Balzani, P. Belser and A. von Zelewsky, *Inorg. Chem.*, 1983, **22**, 3335–3339.

- 89 G. H. Allen, R. P. White, D. P. Rillema and T. J. Meyer, *J. Am. Chem. Soc.*, 1984, **106**, 2613–2620.
- 90 M. Maestri, N. Armaroli, V. Balzani, E. C. Constable and A. M. W. C. Thompson, *Inorg. Chem.*, 1995, **34**, 2759–2767.
- 91 M. Abrahamsson, M. Jäger, T. Österman, L. Eriksson, P. Persson, H.-C. Becker, O. Johansson and L. Hammarström, *J. Am. Chem. Soc.*, 2006, **128**, 12616–12617.
- 92 F. Schramm, V. Meded, H. Fliegl, K. Fink, O. Fuhr, Z. Qu, W. Klopper, S. Finn, T. E. Keyes and M. Ruben, *Inorg. Chem.*, 2009, **48**, 5677–5684.
- 93 A. Breivogel, C. Kreitner and K. Heinze, *Eur. J. Inorg. Chem.*, 2014, **2014**, 5468–5490.
- 94 R. D. Gerardi, N. W. Barnett and S. W. Lewis, *Anal. Chim. Acta*, 1999, **378**, 1–41.
- 95 S. Ji, W. Wu, W. Wu, P. Song, K. Han, Z. Wang, S. Liu, H. Guo and J. Zhao, *J. Mater. Chem.*, 2010, **20**, 1953–1963.
- 96 F. G. Gao and A. J. Bard, *J. Am. Chem. Soc.*, 2000, **122**, 7426–7427.
- 97 H. J. Bolink, L. Cappelli, E. Coronado and P. Gaviña, *Inorg. Chem.*, 2005, **44**, 5966–5968.
- 98 H. J. Bolink, L. Cappelli, E. Coronado, M. Grätzel and M. K. Nazeeruddin, *J. Am. Chem. Soc.*, 2006, **128**, 46–47.
- 99 H. J. Bolink, L. Cappelli, E. Coronado, M. Grätzel, E. Ortí, R. D. Costa, P. M. Viruela and M. K. Nazeeruddin, *J. Am. Chem. Soc.*, 2006, **128**, 14786–14787.
- 100 X. Yang, D. Neher, D. Hertel and T. K. Däubler, *Adv. Mater.*, 2004, **16**, 161–166.
- 101 M. S. Lowry and S. Bernhard, *Chem. Eur. J.*, 2006, **12**, 7970–7977.
- 102 Y. Chi and P.-T. Chou, *Chem. Soc. Rev.*, 2010, **39**, 638–655.
- 103 C.-H. Yang, M. Mauro, F. Polo, S. Watanabe, I. Muenster, R. Fröhlich and L. de Cola, *Chem. Mater.*, 2012, **24**, 3684–3695.
- 104 P. G. Bomben, K. C. D. Robson, P. A. Sedach and C. P. Berlinguette, *Inorg. Chem.*, 2009, **48**, 9631–9643.
- 105 T. Funaki, H. Funakoshi, O. Kitao, N. Onozawa-Komatsuzaki, K. Kasuga, K. Sayama and H. Sugihara, *Angew. Chem.*, 2012, **124**, 7646–7649. *Angew. Chem. Int. Ed.*, 2012, **51**, 7528–7531.
- 106 C. Kreitner, A. K. C. Mengel, T. K.-M. Lee, W. Cho, K. Char, Y. S. Kang and K. Heinze, *Chem. Eur. J.*, 2016.
- 107 M. Beley, J. P. Collin and J. P. Sauvage, *Inorg. Chem.*, 1993, **32**, 4539–4543.
- 108 C. Patoux, J.-P. Launay, M. Beley, S. Chodorowski-Kimmes, J.-P. Collin, S. James and J.-P. Sauvage, *J. Am. Chem. Soc.*, 1998, **120**, 3717–3725.
- 109 W.-W. Yang, J. Yao and Y.-W. Zhong, *Organometallics*, 2012, **31**, 1035–1041.
- 110 C.-J. Yao, R.-H. Zheng, Q. Shi, Y.-W. Zhong and J. Yao, *Chem. Commun.*, 2012, **48**, 5680–5682.
- 111 C.-J. Yao, H.-J. Nie, W.-W. Yang, J.-Y. Shao, J. Yao and Y.-W. Zhong, *Chem. Eur. J.*, 2014, **20**, 17466–17477.
- 112 J.-J. Shen and Y.-W. Zhong, *Sci. Rep.*, 2015, **5**, 13835.
- 113 Y.-W. Zhong, Z.-L. Gong, J.-Y. Shao and J. Yao, *Coord. Chem. Rev.*, 2016, **312**, 22–40.
- 114 B. Schulze, D. Escudero, C. Friebe, R. Siebert, H. Görls, S. Sinn, M. Thomas, S. Mai, J. Popp, B. Dietzek, L. González and U. S. Schubert, *Chem. Eur. J.*, 2012, **18**, 4010–4025.



- 115 C. Kreitner, E. Erdmann, W. W. Seidel and K. Heinze, *Inorg. Chem.*, 2015, **54**, 11088–11104.
- 116 C. Kreitner and K. Heinze, *Dalton Trans.*, 2016, **45**, 5640–5658.
- 117 A. C. Benniston, G. Chapman, A. Harriman, M. Mehrabi and C. A. Sams, *Inorg. Chem.*, 2004, **43**, 4227–4233.
- 118 L. A. Fredin, M. Pápai, E. Rozsályi, G. Vankó, K. Wärnmark, V. Sundström and P. Persson, *J. Phys. Chem. Lett.*, 2014, **5**, 2066–2071.
- 119 L. L. Jamula, A. M. Brown, D. Guo and J. K. McCusker, *Inorg. Chem.*, 2014, **53**, 15–17.
- 120 A. K. C. Mengel, C. Förster, A. Breivogel, K. Mack, J. R. Ochsmann, F. Laquai, V. Ksenofontov and K. Heinze, *Chem. Eur. J.*, 2015, **21**, 704–714.
- 121 K. A. King and R. J. Watts, *J. Am. Chem. Soc.*, 1987, **109**, 1589–1590.
- 122 P. Reveco, J. H. Medley, A. R. Garber, N. S. Bhacca and J. Selbin, *Inorg. Chem.*, 1985, **24**, 1096–1099.
- 123 E. C. Constable and J. M. Holmes, *J. Organomet. Chem.*, 1986, **301**, 203–208.
- 124 M. L. Muro-Small, J. E. Yarnell, C. E. McCusker and F. N. Castellano, *Eur. J. Inorg. Chem.*, 2012, **2012**, 4004–4011.
- 125 C. D. Ertl, D. P. Ris, S. C. Meier, E. C. Constable, C. E. Housecroft, M. Neuburger and J. A. Zampese, *Dalton Trans.*, 2015, **44**, 1557–1570.
- 126 P. G. Bomben, K. D. Thériault and C. P. Berlinguette, *Eur. J. Inorg. Chem.*, 2011, **2011**, 1806–1814.
- 127 E. Y. Li, Y.-M. Cheng, C.-C. Hsu, P.-T. Chou, G.-H. Lee, I.-H. Lin, Y. Chi and C.-S. Liu, *Inorg. Chem.*, 2006, **45**, 8041–8051.
- 128 M. Beley, J. P. Collin, R. Louis, B. Metz and J. P. Sauvage, *J. Am. Chem. Soc.*, 1991, **113**, 8521–8522.
- 129 E. C. Constable, A. M. W. C. Thompson and S. Greulich, *J. Chem. Soc., Chem. Commun.*, 1993, 1444–1446.
- 130 P. G. Bomben, B. D. Koivisto and C. P. Berlinguette, *Inorg. Chem.*, 2010, **49**, 4960–4971.
- 131 H. Kisserwan, A. Kamar, T. Shoker and T. H. Ghaddar, *Dalton Trans.*, 2012, **41**, 10643–10651.
- 132 Z. Ji, G. Natu, Z. Huang, O. Kokhan, X. Zhang and Y. Wu, *J. Phys. Chem. C*, 2012, **116**, 16854–16863.
- 133 I. M. Dixon, F. Alary and J.-L. Heully, *Dalton Trans.*, 2010, **39**, 10959–10966.
- 134 S. H. Wadman, M. Lutz, D. M. Tooke, A. L. Spek, F. Hartl, R. W. A. Havenith, G. P. M. van Klink and G. van Koten, *Inorg. Chem.*, 2009, **48**, 1887–1900.
- 135 F. Alary, J.-L. Heully, L. Bijeire and P. Vicendo, *Inorg. Chem.*, 2007, **46**, 3154–3165.
- 136 J.-L. Heully, F. Alary and M. Boggio-Pasqua, *J. Chem. Phys.*, 2009, **131**, 184308.
- 137 T. Guillon, M. Boggio-Pasqua, F. Alary, J.-L. Heully, E. Lebon, P. Sutra and A. Igau, *Inorg. Chem.*, 2010, **49**, 8862–8872.
- 138 R. D. Costa, E. Ortí, D. Tordera, A. Pertegás, H. J. Bolink, S. Graber, C. E. Housecroft, L. Sachno, M. Neuburger and E. C. Constable, *Adv. Energy Mater.*, 2011, **1**, 282–290.

- 139 F. Monti, A. Baschieri, I. Gualandi, J. J. Serrano-Pérez, J. M. Junquera-Hernández, D. Tonelli, A. Mazzanti, S. Muzzioli, S. Stagni, C. Roldan-Carmona, A. Pertegás, H. J. Bolink, E. Ortí, L. Sambri and N. Armaroli, *Inorg. Chem.*, 2014, **53**, 7709–7721.
- 140 S. Yi, J.-H. Kim, Y.-J. Cho, J. Lee, T.-S. Choi, D. W. Cho, C. Pac, W.-S. Han, H.-J. Son and S. O. Kang, *Inorg. Chem.*, 2016, **55**, 3324–3331.
- 141 I. Krivokapic, M. Zerara, M. L. Daku, A. Vargas, C. Enachescu, C. Ambrus, P. Tregenna-Piggott, N. Amstutz, E. Krausz and A. Hauser, *Coord. Chem. Rev.*, 2007, **251**, 364–378.
- 142 R. G. Miller, S. Narayanaswamy, J. L. Tallon and S. Brooker, *New J. Chem.*, 2014, **38**, 1932–1941.
- 143 J. P. Claude and T. J. Meyer, *J. Phys. Chem.*, 1995, **99**, 51–54.
- 144 N. H. Damrauer, T. R. Boussie, M. Devenney and J. K. McCusker, *J. Am. Chem. Soc.*, 1997, **119**, 8253–8268.
- 145 J. V. Caspar and T. J. Meyer, *J. Am. Chem. Soc.*, 1983, **105**, 5583–5590.
- 146 K.-C. Hwang, J.-L. Chen, Y. Chi, C.-W. Lin, Y.-M. Cheng, G.-H. Lee, P.-T. Chou, S.-Y. Lin and C.-F. Shu, *Inorg. Chem.*, 2008, **47**, 3307–3317.
- 147 S. H. Wadman, J. M. Kroon, K. Bakker, R. W. A. Havenith, G. P. M. van Klink and G. van Koten, *Organometallics*, 2010, **29**, 1569–1579.
- 148 B. Schulze, D. G. Brown, Robson, Kiyoshi C D, C. Friebe, M. Jäger, E. Birckner, C. P. Berlinguette and U. S. Schubert, *Chem. Eur. J.*, 2013, **19**, 14171–14180.
- 149 C. Kreitner, M. Grabolle, U. Resch-Genger and K. Heinze, *Inorg. Chem.*, 2014, **53**, 12947–12961.
- 150 F. Barigelletti, P. Belser, A. von Zelewsky, A. Juris and V. Balzani, *J. Phys. Chem.*, 1985, **89**, 3680–3684.
- 151 A. J. Wilkinson, H. Puschmann, Howard, Judith A K, C. E. Foster and J. A. G. Williams, *Inorg. Chem.*, 2006, **45**, 8685–8699.
- 152 G. S. Ming Tong, K. T. Chan, X. Chang and C.-M. Che, *Chem. Sci.*, 2015, **6**, 3026–3037.
- 153 A. Breivogel, C. Förster and K. Heinze, *Inorg. Chem.*, 2010, **49**, 7052–7056.
- 154 A. Breivogel, M. Meister, C. Förster, F. Laquai and K. Heinze, *Chem. Eur. J.*, 2013, **19**, 13745–13760.
- 155 K. Heinze, K. Hempel and M. Beckmann, *Eur. J. Inorg. Chem.*, 2006, **2006**, 2040–2050.
- 156 I. M. Dixon, F. Alary, M. Boggio-Pasqua and J.-L. Heully, *Inorg. Chem.*, 2013, **52**, 13369–13374.
- 157 I. M. Dixon, S. Khan, F. Alary, M. Boggio-Pasqua and J.-L. Heully, *Dalton Trans.*, 2014, **43**, 15898–15905.
- 158 I. M. Dixon, F. Alary, M. Boggio-Pasqua and J.-L. Heully, *Dalton Trans.*, 2015, **44**, 13498–13503.
- 159 J. M. Patrick, A. H. White, M. I. Bruce, M. J. Beatson, D. C. St. Black, G. B. Deacon and N. C. Thomas, *J. Chem. Soc., Dalton Trans.*, 1983, 2121–2123.
- 160 M. I. Bruce, M. J. Liddell, G. N. Pain, M. A. Bennett and H. Neumann, *Inorg. Synth.*, 1989, **26**, 171–180.
- 161 K. C. D. Robson, B. D. Koivisto, A. Yella, B. Spornova, M. K. Nazeeruddin, T. Baumgartner, M. Grätzel and C. P. Berlinguette, *Inorg. Chem.*, 2011, **50**, 5494–5508.

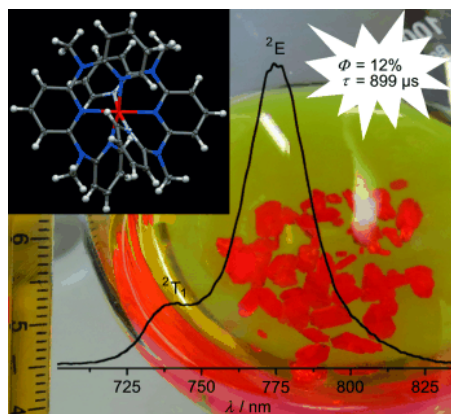
- 
- 162 K. C. D. Robson, B. D. Koivisto, T. J. Gordon, T. Baumgartner and C. P. Berlinguette, *Inorg. Chem.*, 2010, **49**, 5335–5337.
- 163 K. C. D. Robson, B. Sporinova, B. D. Koivisto, E. Schott, D. G. Brown and C. P. Berlinguette, *Inorg. Chem.*, 2011, **50**, 6019–6028.
- 164 W. A. Herrmann and C. Köcher, *Angew. Chem.*, 1997, **109**, 2256–2282. *Angew. Chem. Int. Ed. Engl.*, 1997, **36**, 2162–2187.
- 165 Y.-M. Zhang, J.-Y. Shao, C.-J. Yao and Y.-W. Zhong, *Dalton Trans.*, 2012, **41**, 9280–9282.
- 166 F. Neese, *WIREs Comput Mol Sci*, 2012, **2**, 73–78.
- 167 A. D. Becke, *J. Chem. Phys.*, 1993, **98**, 5648–5652.
- 168 F. Neese, F. Wennmohs, A. Hansen and U. Becker, *Chem. Phys.*, 2009, **356**, 98–109.
- 169 R. Izsák and F. Neese, *J. Chem. Phys.*, 2011, **135**, 144105.
- 170 D. A. Pantazis, X.-Y. Chen, C. R. Landis and F. Neese, *J. Chem. Theory Comput.*, 2008, **4**, 908–919.
- 171 S. Sinnecker, A. Rajendran, A. Klamt, M. Diedenhofen and F. Neese, *J. Phys. Chem. A*, 2006, **110**, 2235–2245.
- 172 A. Schäfer, H. Horn and R. Ahlrichs, *J. Chem. Phys.*, 1992, **97**, 2571–2577.
- 173 A. Schäfer, C. Huber and R. Ahlrichs, *J. Chem. Phys.*, 1994, **100**, 5829–5835.



### 3.6 [Cr(DDPD)<sub>2</sub>]<sup>3+</sup>: A MOLECULAR, WATER-SOLUBLE, HIGHLY NIR-EMISSIVE RUBY ANALOGUE

Sven Otto, Markus Grabolle, Christoph Förster, Christoph Kreitner, Ute Resch-Genger and Katja Heinze

*Angew. Chem.* **2015**, *127*, 11735–11739. *Angew. Chem. Int. Ed.* **2015**, *54*, 11572–11576.



Strong, long-lived, and sharp NIR phosphorescence (775 nm,  $\Phi = 12\%$ ,  $\tau = 899 \mu\text{s}$ ) is achieved in the soluble chromium(III) complex [Cr(ddpd)<sub>2</sub>]<sup>3+</sup> (ddpd = *N,N'*-dimethyl-*N,N'*-dipyridin-2-ylpyridine-2,6-diamine) by ligand-field tuning through optimization of the ligand's bite angle and  $\sigma$ -donor strength. <sup>3</sup>O<sub>2</sub> quenches the emission, allowing for optical oxygen sensing. The highly stable complex is easy to prepare in high yields from inexpensive starting materials.

#### Author Contributions

Sven Otto synthesized and characterized the chromium complexes presented in this manuscript and carried out the electrochemical, UV-Vis and emission spectroscopic experiments. Markus Grabolle and Ute Resch-Genger determined the emission quantum yields and excited state lifetimes at the *Bundesanstalt für Materialforschung und -prüfung* in Berlin, Germany. The crystal structures were solved and refined by Christoph Förster. Sven Otto and Christoph Kreitner performed the DFT calculations of the relevant doublet and quartet states. The English version of the manuscript was written by Katja Heinze and the German translation was prepared by Sven Otto and Christoph Kreitner.

#### Supporting Information

for this article is found at pp. 281 (excluding Cartesian Coordinates of DFT-optimized geometries). For full Supporting Information, refer to [http://onlinelibrary.wiley.com/store/10.1002/anie.201504894/asset/supinfo/anie\\_201504894\\_sm\\_miscellaneous\\_information.pdf?v=1&s=f8f85e07854a6b1185612016cad863dcc2d9645c](http://onlinelibrary.wiley.com/store/10.1002/anie.201504894/asset/supinfo/anie_201504894_sm_miscellaneous_information.pdf?v=1&s=f8f85e07854a6b1185612016cad863dcc2d9645c).

„Reprinted with permission from Otto, S.; Grabolle, M.; Förster, C.; Kreitner, C.; Resch-Genger, U.; Heinze, K. *Angew. Chem. Int. Ed.* **2015**, *54*, 11572–11575. Copyright 2016 Jon Wiley and Sons.”





## [Cr(ddpd)<sub>2</sub>]<sup>3+</sup>: A Molecular, Water-Soluble, Highly NIR-Emissive Ruby Analogue

Sven Otto, Markus Grabolle, Christoph Förster, Christoph Kreitner, Ute Resch-Genger,\* and Katja Heinze\*

**Abstract:** Bright, long-lived emission from first-row transition-metal complexes is very challenging to achieve. Herein, we present a new strategy relying on the rational tuning of energy levels. With the aid of the large N-Cr-N bite angle of the tridentate ligand ddpd (N,N'-dimethyl-N,N'-dipyridine-2-ylpyridine-2,6-diamine) and its strong  $\sigma$ -donating capabilities, a very large ligand-field splitting could be introduced in the chromium(III) complex [Cr(ddpd)<sub>2</sub>]<sup>3+</sup>, that shifts the deactivating and photoreactive <sup>4</sup>T<sub>2</sub> state well above the emitting <sup>2</sup>E state. Prevention of back-intersystem crossing from the <sup>2</sup>E to the <sup>4</sup>T<sub>2</sub> state enables exceptionally high near-infrared phosphorescence quantum yields and lifetimes for this 3d metal complex. The complex [Cr(ddpd)<sub>2</sub>](BF<sub>4</sub>)<sub>3</sub> is highly water-soluble and very stable towards thermal and photo-induced substitution reactions and can be used for fluorescence intensity- and lifetime-based oxygen sensing in the NIR.

Dyes with room-temperature emission in the near infrared (NIR) spectral region (> 650 nm) have emerged as promising candidates for NIR organic light emitting diodes (OLEDs), fiber-optic telecommunication applications, night-vision readable displays, security inks for identification systems, oxygen sensing, and in vivo imaging.<sup>[1–7]</sup> Essentially, all currently employed (water-)soluble, NIR emissive dyes are based on lanthanide complexes,<sup>[4–7]</sup> complexes of the second- and third-row metal ions,<sup>[8–10]</sup> complex organic scaffolds,<sup>[11]</sup> or a combination of them.<sup>[12]</sup> All of them feature specific advantages, such as long-lived emissive states and large energy differences between absorption and emission maxima (lanthanides, 4d/5d metal complexes), medium to high quantum yields, and rational tuning of the emission energy (organic dyes). Typical drawbacks are, however, multi-step syntheses and poor water solubility and dye aggregation for the more extended  $\pi$ -systems required for NIR emission (organic dyes),<sup>[11b]</sup> short


lifetimes in the range of 1–10 ns (organic dyes, many transition-metal complexes), or high costs (e.g. Eu, Rh, Ir, Ru, Os, Pd, Pt, Au). Furthermore, NIR emitters typically suffer from radiationless relaxation to the ground state (energy gap law).<sup>[13]</sup> An emerging class of luminophores comprises first-row transition-metal complexes. They are, however, limited to complexes of d<sup>10</sup> ions (Zn<sup>II</sup>, Cu<sup>I</sup>), such as [Zn(tpp)] or [Cu(PPh<sub>3</sub>)<sub>2</sub>(phen)]<sup>+</sup> (tpp = meso-tetraphenylporphyrinato, phen = 1,10-phenanthroline) derivatives with quantum yields around 2–3%, lifetimes in the nanosecond range,<sup>[1]</sup> and in most cases emission in the visible. Although considerable progress has been made in the field of Cu<sup>I</sup> complexes,<sup>[14]</sup> octahedral Cr<sup>III</sup> complexes<sup>[15]</sup> have been also suggested as NIR emitters partly because the Cr<sup>III</sup> emission in solid materials, such as chromium-doped sapphire (ruby), has led to the historically important development of the ruby laser in 1960.<sup>[16]</sup> The phosphorescence quantum efficiencies for most of these complexes were, however, too low ( $\Phi < 0.1\%$ ) for practical applications<sup>[1]</sup> despite the fascinating photo-physical aspects observed in [Cr(ox)<sub>3</sub>]<sup>3-</sup> (ox = oxalato) polymeric networks<sup>[17a,b]</sup> and the use of Cr<sup>III</sup> complexes as energy donors for lanthanide emission in heterometallic complexes.<sup>[17c–e]</sup> [Cr(bpy)<sub>3</sub>]<sup>3+</sup> and [Cr(phen)<sub>3</sub>]<sup>3+</sup> (bpy = 2,2'-bipyridine) complexes have recently found renewed interest as photo-redox catalysts.<sup>[18]</sup>

The reasons for the poor quantum yields of Cr<sup>III</sup> complexes can be understood from ligand field theory.<sup>[15]</sup> The desired luminescence of octahedral d<sup>3</sup> Cr<sup>III</sup> complexes with a (t<sub>2g</sub>)<sup>3</sup>(e<sub>g</sub>)<sup>0</sup> electron configuration occurs from a transition from doublet states (<sup>2</sup>E and <sup>2</sup>T<sub>1</sub>) to the quartet ground state (<sup>4</sup>A<sub>2</sub>), in the red to near-infrared spectral region (for simplicity, we use the O<sub>h</sub> point-group classification). The <sup>2</sup>E and <sup>2</sup>T<sub>1</sub> spectroscopic terms as well as the <sup>4</sup>A<sub>2</sub> ground term arise from the (t<sub>2g</sub>)<sup>3</sup> electron configuration and hence, the geometric reorganization is very minor, yielding sharp emission bands like the ruby emission.<sup>[16]</sup> At low ligand-field strength, the doublet states lie above the <sup>4</sup>T<sub>2</sub> state of electron configuration (t<sub>2g</sub>)<sup>2</sup>(e<sub>g</sub>)<sup>1</sup> yielding weak, broad fluorescence from <sup>4</sup>T<sub>2</sub> instead.<sup>[19]</sup> Even for classical strong-field ligands, such as bpy, phen, or 2,2':6',2''-terpyridine (tpy), the energy difference between <sup>4</sup>T<sub>2</sub> and the emitting <sup>2</sup>E/<sup>2</sup>T<sub>1</sub> states is so small that back-intersystem crossing occurs, strongly reducing phosphorescence quantum yields and lifetimes.<sup>[1,15]</sup> Furthermore, the <sup>4</sup>T<sub>2</sub> state is prone to photosubstitution and hence, its back-population should be avoided.<sup>[15,20]</sup> To increase the phosphorescence quantum yield, the energy difference between the <sup>4</sup>T<sub>2</sub> and <sup>2</sup>E states should be large to prevent back-intersystem crossing to the detrimental <sup>4</sup>T<sub>2</sub> state. This should be achievable by using a strong ligand-field to shift

[\*] S. Otto, Dr. C. Förster, C. Kreitner, Prof. K. Heinze  
Institute of Inorganic and Analytical Chemistry  
Johannes Gutenberg-University of Mainz  
Duesbergweg 10–14, 55128 Mainz (Germany)  
E-mail: katja.heinze@uni-mainz.de

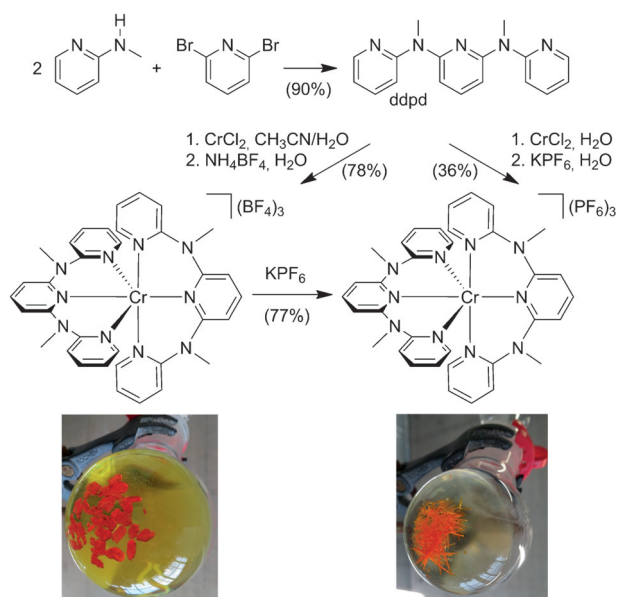
Dr. M. Grabolle, Dr. U. Resch-Genger  
Division 1.10  
Federal Institute for Materials Research and Testing (BAM)  
Richard-Willstätter-Strasse 11, 12489 Berlin (Germany)  
E-mail: ute.resch@bam.de

C. Kreitner  
Graduate School Materials Science in Mainz  
Staudingerweg 9, 55128 Mainz (Germany)

 Supporting information for this article is available on the WWW under <http://dx.doi.org/10.1002/anie.201504894>.

the  $^4T_2$  state to higher energy in conjunction with a strong nephelauxetic effect lowering the energy of the doublet states  $^2E$  and  $^2T_1$  and hence should be made possible by proper ligand design.

Recently, we introduced the tridentate ddpd ligand (*N,N*-dimethyl-*N,N'*-dipyridin-2-ylpyridine-2,6-diamine) with a large bite angle N-M-N of around  $90^\circ$  in six-coordinate metal complexes to optimize metal–ligand orbital overlap and to induce a stronger ligand field compared to bpy or tpy (Scheme 1).<sup>[21]</sup> Also, ddpd is a poor  $\pi$ -acceptor ligand, that is,



**Scheme 1.** High-yield syntheses of  $\mathbf{1}(X)_3$  and photographs of crystals of  $\mathbf{1}(X)_3$  grown from  $\text{CH}_3\text{CN}$  solutions.

rather electron rich and difficult to reduce, but a quite strong  $\sigma$ -donor ligand.<sup>[21]</sup> With these properties of ddpd in mind, we envisaged that ddpd could increase the energy of the  $^4T_2$  state in a  $[\text{Cr}(\text{ddpd})_2]^{3+}$  complex  $\mathbf{1}^{3+}$  (Scheme 1) and simultaneously decrease the energy of the  $^2E$  state, resulting in an enlarged  $^4T_2/{}^2E$  energy gap, which impedes back-intersystem crossing.

$[\text{Cr}(\text{bpy})_3]^{3+}$  and  $[\text{Cr}(\text{tpy})_2]^{3+}$  are substitutionally labile under alkaline conditions giving the hydroxido complexes  $[\text{Cr}(\text{bpy})_2(\text{OH})_2]^+$  and  $[\text{Cr}(\text{tpy})(\text{OH})_x]^{(3-x)+}$ .<sup>[22]</sup> Possibly, the  $\pi$ -accepting ligands bpy and tpy reduce the electron density between the ligand axes by back-donation from  $t_{2g}$  orbitals, facilitating a nucleophilic attack of hydroxide. The  $\pi$ -accepting nature of bpy/tpy also accounts for the special redox properties, as reduction of  $[\text{Cr}^{\text{III}}(\text{bpy})_3]^{3+}$  or  $[\text{Cr}^{\text{III}}(\text{tpy})_2]^{3+}$  does not yield  $\text{Cr}^{\text{II}}$ ,  $\text{Cr}^{\text{I}}$ ,  $\text{Cr}^0$ ,  $\text{Cr}^{-1}$  oxidation states but is ligand centered.<sup>[23]</sup> The envisaged ddpd complex  $\mathbf{1}^{3+}$  should resist ligand-centered reductions and nucleophilic attack at the metal center due to the strong electron donating power of ddpd.

The synthesis of  $\mathbf{1}^{3+}$  is straightforward from  $\text{CrCl}_2$  and ddpd<sup>[21a]</sup> in water. Ion exchange with  $(\text{BF}_4)^-$  or  $(\text{PF}_6)^-$  gives the bright orange salts  $\mathbf{1}(\text{BF}_4)_3$  and  $\mathbf{1}(\text{PF}_6)_3$  (Scheme 1, Supporting Information). Both were obtained as single

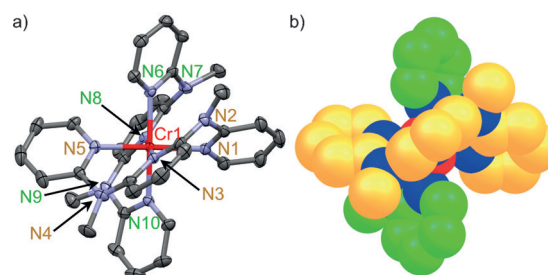


**Figure 1.** a) Molecular structure of the cation of  $\mathbf{1}(\text{BF}_4)_3$  in the solid state (thermal ellipsoids set at 50% probability); b) space-filling representation of  $\mathbf{1}^{3+}$  with the two ligands are shown in yellow and green, respectively (hydrogen atom omitted for clarity).

crystals suitable for X-ray diffraction analysis (Figure 1, Supporting Information, Figure S1). The complex cations feature an essentially octahedral  $\text{CrN}_6$  coordination geometry with Cr–N distances of 2.028–2.054 Å and N–Cr–N angles close to  $90^\circ$  and  $180^\circ$  as required for a large ligand-field splitting. Similar to structurally comparable  $[\text{M}(\text{ddpd})_2]^{2+}$  complexes, the ligands are wrapped around the metal center (Figure 1) and the counter ions fill the pockets between the ligands with Cr···B/P distances between 5.3 and 7.0 Å (Supporting Information, Figure S1).<sup>[21]</sup>

Magnetic susceptibility and EPR data are consistent with a quartet ground state ( $\chi T = 1.833 \text{ cm}^3 \text{ K mol}^{-1}$  at 300 K;  $g_{\text{av}} = 1.990$  at 77 K, Figure S14, Supporting Information) similar to  $[\text{Cr}(\text{tpy})_3]^{3+}$ .<sup>[24]</sup> A reversible  $\text{Cr}^{\text{III/II}}$  reduction is observed at  $-1.11 \text{ V}$  versus ferrocene (Supporting Information, Figure S13). Compared to  $[\text{Cr}(\text{bpy})_3]^{3+}$  ( $E_{1/2} = -0.63 \text{ V}$ ) and  $[\text{Cr}(\text{tpy})_2]^{3+}$  ( $E_{1/2} = -0.53 \text{ V}$ ), this reduction occurs at much more negative potential.<sup>[23]</sup> DFT calculations (B3LYP, RIJ-COSX, Def2-SVP/J, Def2-SVP, ZORA) confirm the metal-centered reduction to  $\text{Cr}^{\text{II}}$  (Supporting Information, Figure S25,S26). The next reduction at  $E_p = -1.94 \text{ V}$  is irreversible as coordinated ddpd cannot be reduced to its radical anion. Interestingly,  $\mathbf{1}(\text{BF}_4)_3$  is highly soluble in water ( $0.0479 \text{ mol L}^{-1}$ ) while  $\mathbf{1}(\text{PF}_6)_3$  is more soluble in  $\text{CH}_3\text{CN}$  ( $0.208 \text{ mol L}^{-1}$ ), enabling different applications of the two salts. The absorption spectra of  $\mathbf{1}^{3+}$  in  $\text{H}_2\text{O}$  or  $\text{CH}_3\text{CN}$  show maxima at 220(sh), 302, 315(sh), 350(sh), and 435 nm (Figure 2, Supporting Information, Figure S5) which can be assigned to  $\pi\pi^*$ , ligand-to-metal charge transfer (LMCT) and mixed metal-centered (MC)/LMCT excitations according to time-dependent DFT calculations (Supporting Information, Figure S20). No metal-to-ligand charge transfer (MLCT) transitions were identified in this energy region because of the weak electron-accepting properties of ddpd and the inaccessible  $\text{Cr}^{\text{III/IV}}$  oxidation. The low-energy absorption maximum is ascribed to the  ${}^4A_2 \rightarrow {}^4T_2$  transition (TD-DFT: 427.7, 436.9, and 439.0 nm) and an LMCT (Supporting Information, Figure S20). Three Laporte- and spin-forbidden transitions are found at 697, 736, and 776 nm in the single-crystal absorption spectrum of  $\mathbf{1}(\text{BF}_4)_3$ . These are assigned to  ${}^4A_2 \rightarrow {}^2T_2$  (tentative),  ${}^2T_1$ , and  ${}^2E$  excitations (Supporting Information, Figure S10). Excitation of a solution of  $\mathbf{1}(\text{BF}_4)_3$  in water or  $\text{CH}_3\text{CN}$  (Supporting Information, Figure S8) at 435 nm leads to emission spectra that can be superimposed, as

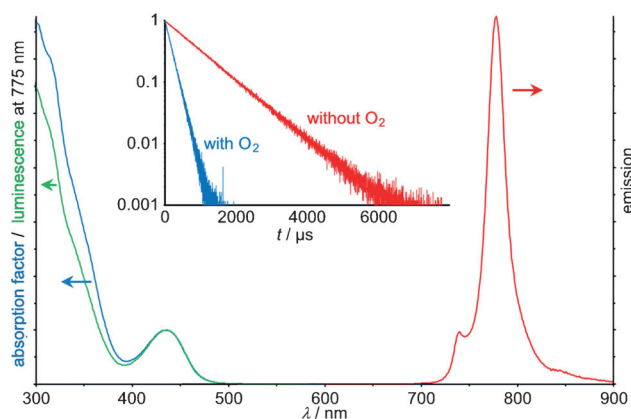


**Figure 2.** Absorption factor (blue), excitation ( $\lambda_{\text{obs}} = 775$  nm, green) and emission spectrum ( $\lambda_{\text{exc}} = 435$  nm, red) of  $\mathbf{1}(\text{BF}_4)_3$  in deaerated  $\text{H}_2\text{O}$  at room temperature; the inset shows the emission decay curves of  $\mathbf{1}(\text{BF}_4)_3$  in  $\text{H}_2\text{O}$  with and without  $\text{O}_2$ .

depicted in Figure 2 for  $\text{CH}_3\text{CN}$ . The strong, sharp emission band at 775 nm (full width at half maximum height (FWHM) =  $420\text{ cm}^{-1}$ ) is ascribed to the  ${}^2\text{E}$  emission and the weaker band at 738 nm to the  ${}^2\text{T}_1$  emission.<sup>[15,25]</sup> A single crystal of  $\mathbf{1}(\text{BF}_4)_3$  emits at 740 and 778 nm (Supporting Information, Figure S11). Clearly, these two intraconfigurational doublet states equilibrate at room temperature both in solution and in the solid state. At 100 K in a frozen butyronitrile glass, only the  ${}^2\text{E}$  emission at 779 nm is observed (Supporting Information, Figure S9). The emission of  $\mathbf{1}^{3+}$  is considerably red shifted relative to  $[\text{Cr}(\text{bpy})_3]^{3+}$  (727 nm) and  $[\text{Cr}(\text{phen})_3]^{3+}$  (730 nm), but similar to that of  $[\text{Cr}(\text{tpy})_2]^{3+}$  (770 nm).<sup>[1,15]</sup> The solid material ruby emits at 694 nm.<sup>[16]</sup>

The luminescence quantum yields ( $\Phi$ ) of  $\mathbf{1}^{3+}$  in deaerated  $\text{CH}_3\text{CN}$  and  $\text{H}_2\text{O}$  were determined absolutely with an integrating-sphere setup to  $\Phi = 12.1\%$  and  $11.0\%$ , respectively. In  $\text{D}_2\text{O}$ ,  $\Phi$  increases to  $14.2\%$ . To our knowledge, these  $\Phi$  values are by far the highest values reported for  $\text{Cr}^{\text{III}}$  complexes in solution at room temperature to date.<sup>[1,15]</sup> For instance,  $[\text{Cr}(\text{bpy})_3]^{3+}$ ,  $[\text{Cr}(\text{phen})_3]^{3+}$ , and  $[\text{Cr}(\text{tpy})_2]^{3+}$  have  $\Phi = 0.089\%$ ,  $0.15\%$ , and  $< 0.00089\%$  in water.<sup>[1]</sup> The lifetimes ( $\tau$ ) of the emitting doublet states of  $\mathbf{1}^{3+}$  were determined to  $\tau = 899$ ,  $898$ , and  $1164\ \mu\text{s}$  in deaerated  $\text{CH}_3\text{CN}$ , in  $\text{H}_2\text{O}$ , and in  $\text{D}_2\text{O}$ , respectively. Again, these are the highest values reported to date for a molecular  $\text{Cr}^{\text{III}}$  complex in solution at room temperature. The lifetimes of  $[\text{Cr}(\text{bpy})_3]^{3+}$ ,  $[\text{Cr}(\text{phen})_3]^{3+}$ , and  $[\text{Cr}(\text{tpy})_2]^{3+}$  are  $\tau = 63\ \mu\text{s}$ ,  $270\ \mu\text{s}$ , and  $\leq 30\ \mu\text{s}$ , respectively.<sup>[1]</sup> The solid laser material ruby has  $\tau = 4270\ \mu\text{s}$ <sup>[16]</sup> while a single crystal of  $\mathbf{1}(\text{BF}_4)_3$  reveals  $\tau = 443\ \mu\text{s}$ .

Excitation spectra recorded at 775 nm in  $\text{CH}_3\text{CN}$  and  $\text{H}_2\text{O}$  perfectly match with the absorption spectrum around the 435 nm maximum (Figure 2, Supporting Information, Figure S8) suggesting efficient population of the  ${}^2\text{E}/{}^2\text{T}_1$  states from these  ${}^4\text{T}_2$  ligand-field and LMCT states. At higher energies, the excitation spectra deviate from the absorption factor suggesting that not all high-energy states of  $\mathbf{1}^{3+}$  populate the  ${}^2\text{E}/{}^2\text{T}_1$  states. Excitation at 435 nm also yields a very weak broad emission band around 500 nm with  $\tau$  of 3 ns, independent of the presence of  $\text{O}_2$  (Supporting Information, Figure S7). As ddpd emits at 398 nm in  $\text{CH}_3\text{CN}$  ( $\Phi =$

$8.0\%$ ,  $\tau = 3.0$  ns; Supporting Information, Figure S12), the weak 500 nm emission cannot be assigned to ddpd fluorescence but is ascribed to the spontaneous  ${}^4\text{T}_2 \rightarrow {}^4\text{A}_2$  fluorescence of  $\mathbf{1}^{3+}$ . Delayed  ${}^4\text{T}_2 \rightarrow {}^4\text{A}_2$  fluorescence<sup>[15,19]</sup> fed by back-intersystem crossing from  ${}^2\text{E}/{}^2\text{T}_1$  states is ruled out on the basis of the short lifetime. Hence, back-intersystem crossing is efficiently prevented in  $\mathbf{1}^{3+}$  which accounts for its exceptionally high quantum yield and lifetime. The minimal energy difference between the relaxed  ${}^2\text{E}$  and  ${}^4\text{T}_2$  states is estimated at around  $7100\text{ cm}^{-1}$  ( $0.88\text{ eV}$ ;  $85\text{ kJ mol}^{-1}$ ) from the emission spectra. Although the geometry of the  ${}^2\text{E}$  state is close to that of the  ${}^4\text{A}_2$  ground state, a large reorganization energy barrier is expected as the relaxed  ${}^4\text{T}_2$  state features a Jahn–Teller distorted octahedron with  $\text{Cr}-\text{N}_{\text{ax}}$  bonds elongated by approximately  $0.3\ \text{\AA}$  according to DFT calculations (Supporting Information, Figure S24–S26).<sup>[26]</sup> For back-intersystem crossing ( ${}^2\text{E} \rightarrow {}^4\text{T}_2$ ), the large energy gap and the reorganizational barrier must be overcome which is clearly impossible at room temperature (Figure 3).<sup>[15]</sup> Direct intersystem crossing from  ${}^4\text{T}_2$  to the vibrationally excited  ${}^2\text{T}_1/{}^2\text{E}$  states or to the  ${}^2\text{T}_2$

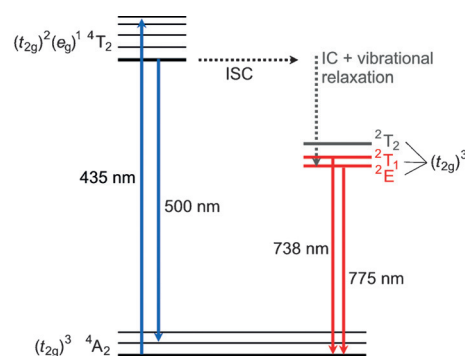


**Figure 3.** Jablonski diagram of  $\mathbf{1}^{3+}$  constructed from experimental solution data ( ${}^2\text{T}_2$  state tentatively from single-crystal absorption). ISC = intersystem crossing, IC = internal conversion.

state and subsequent internal conversion is conceivable (Figure 3). For  $\text{Cr}(\text{acac})_3$  (acac = acetylacetonato), McCusker et al. have shown that intersystem crossing to  ${}^2\text{E}$  is faster than vibrational cooling within the  ${}^4\text{T}_2$  state along the Jahn–Teller modes.<sup>[27]</sup> Intersystem crossing might also occur from vibrationally hot states in  $\mathbf{1}^{3+}$  before the Jahn–Teller distortion. Independent of the details of the intersystem crossing processes, the use of the strong-field ddpd ligand is very efficient in inducing high phosphorescence quantum yields and lifetimes as a result of the large barrier for back-intersystem crossing.<sup>[15]</sup>

As expected, the phosphorescence quantum yield is sensitive to the presence of  $\text{O}_2$ .<sup>[28,29]</sup> In air,  $\Phi$  is reduced by factors of 5.2 ( $\text{H}_2\text{O}$ ) and 17 ( $\text{CH}_3\text{CN}$ ) and the lifetimes are correspondingly shortened from  $898\ \mu\text{s}$  to  $177\ \mu\text{s}$  ( $\text{H}_2\text{O}$ ) and  $51\ \mu\text{s}$  ( $\text{CH}_3\text{CN}$ ) (Figure 2). The bimolecular  $\text{O}_2$  quenching constant has been estimated from a Stern–Volmer plot of  $\mathbf{1}(\text{BF}_4)_3$  in  $\text{H}_2\text{O}$  as  $k_q = 1.77 \times 10^7\text{ M}^{-1}\text{s}^{-1}$  and the Stern–Volmer constant as  $K_{\text{SV}} = k_d \times \tau = 1.59 \times 10^4\text{ M}^{-1}$  (Supporting Information, Figure S15). These quenching efficiencies<sup>[29]</sup> suggest possible applications of  $\mathbf{1}^{3+}$  in optical oxygen sensors.<sup>[2,30]</sup>



with the large difference between excitation and emission easing the combination with a spectrally distinguishable O<sub>2</sub>-inert reference dye. The quenching efficiency is explained on the basis of the very long <sup>2</sup>E lifetime and on the basis of spin statistics, although *k<sub>q</sub>* is not particularly large.<sup>[29c]</sup> The *k<sub>q</sub>* value might be associated with an effective shielding of Cr<sup>III</sup> by the ligands and the counterions (Figure 1, Figure S1). Commonly employed optical oxygen sensors are based on the quenching of their dye's excited triplet states, for example, <sup>3</sup>MLCT or <sup>3</sup>ππ\*, by <sup>3</sup>O<sub>2</sub> yielding the dye's singlet ground state and <sup>1</sup>O<sub>2</sub>.<sup>[2,30]</sup> For these triplet states, spin statistics predict that 1/9 (11%) of the possible encounters (quintet, triplet, singlet: 9 possibilities), namely the singlets, are productive. For the <sup>2</sup>E state of **1**<sup>3+</sup> and <sup>3</sup>O<sub>2</sub>, a quartet and a doublet encounter complex is conceivable giving six microstate possibilities. The quartet encounter is productive giving the <sup>4</sup>A<sub>2</sub> state of **1**<sup>3+</sup> and <sup>1</sup>O<sub>2</sub>. Hence, 4/6 (67%) of the encounters should yield <sup>1</sup>O<sub>2</sub> which explains the O<sub>2</sub> sensitivity of Cr<sup>III</sup> complexes in general.

The substitutional stability of **1**(BF<sub>4</sub>)<sub>3</sub> was probed in aqueous solution (pH 7) as well as in the presence of HCl (pH 2.1) and NaOH (pH 11.9). The cation **1**<sup>3+</sup> is stable for at least 2.5 months according to UV/Vis spectroscopy (Figure S16, S17). This stability is in stark contrast to the lability of [Cr(bpy)<sub>3</sub>]<sup>3+</sup> and [Cr(tpy)<sub>2</sub>]<sup>3+</sup>.<sup>[22]</sup> Also, **1**<sup>3+</sup> is perfectly stable in 0.1 M [nBu<sub>4</sub>N]Cl and in [nBu<sub>4</sub>N](OH) (pH 11.4) H<sub>2</sub>O/CH<sub>3</sub>CN (1:1) solution under illumination with LEDs at 430 nm in air according to absorption and emission spectra while an isoabsorptive solution of [Cr(bpy)<sub>3</sub>]<sup>3+</sup> undergoes complete photosubstitution within a few hours (Figure S18).<sup>[15]</sup> These experiments demonstrate the superior stability of **1**<sup>3+</sup> compared to [Cr(bpy)<sub>3</sub>]<sup>3+</sup> in aqueous solution.

Thanks to the difficult Cr<sup>III</sup>/Cr<sup>II</sup> reduction and the low <sup>2</sup>E energy, the oxidative power of the <sup>2</sup>E state of **1**<sup>3+</sup> is rather small [*E*(Cr<sup>III/II</sup>)\* = *E*(Cr<sup>III/II</sup>) + *E*<sub>00</sub>(<sup>2</sup>E) = -1.11 V + 1.60 V = 0.49 V versus ferrocene (+1.12 V vs. normal hydrogen electrode (NHE))]. Hence, no photooxidative damage to organic material is expected. In contrast [Cr(bpy)<sub>3</sub>]<sup>3+</sup> or [Cr(tpy)<sub>2</sub>]<sup>3+</sup> photooxidize dGMP and hence, cleave DNA in their excited states (ttpy = *p*-tolylterpyridine, dGMP = deoxyguanosine monophosphate).<sup>[31]</sup> Indeed, dGMP (*E* = 1.29 V vs. NHE) quenches the emission of [Cr(bpy)<sub>3</sub>]<sup>3+</sup> under our conditions but not that of **1**<sup>3+</sup> (Figure S19).

Based upon rational ligand design, we could obtain the first molecular, water- or CH<sub>3</sub>CN-soluble ruby analogues **1**(BF<sub>4</sub>)<sub>3</sub> and **1**(PF<sub>6</sub>)<sub>3</sub> with excellent phosphorescence quantum yields. Together with their high stability, their simple high-yield synthesis, their large excitation/emission energy gap and long lifetime these properties will allow a plethora of applications, such as time-gated imaging, the design of optical probes, and integration into multiplexed sensing schemes. We aim to explore their full potential in the near future.

### Acknowledgements

We thank Luca Carrella and Eva Rentschler for collecting the SQUID data of **1**(PF<sub>6</sub>)<sub>3</sub>. Parts of this research were conducted using the supercomputer Mogon and advisory services offered by Johannes Gutenberg University Mainz

(www.hpc.uni-mainz.de), which is a member of the AHRP and the Gauss Alliance e.V. This work was financially supported by the Deutsche Forschungsgemeinschaft (GSC 266, Materials Science in Mainz, scholarship for C.K.).

**Keywords:** chromium complexes · intersystem crossing · ligand-field splitting · NIR luminescence · photophysics

**How to cite:** *Angew. Chem. Int. Ed.* **2015**, *54*, 11572–11576  
*Angew. Chem.* **2015**, *127*, 11735–11739

- [1] H. Xiang, J. Cheng, X. Ma, X. Zhou, J. Chruma, *Chem. Soc. Rev.* **2013**, *42*, 6128–6185.
- [2] M. Quaranta, S. M. Borisov, I. Klimant, *Bioanal. Rev.* **2012**, *4*, 115–157.
- [3] a) “Luminescent lanthanide complex, and articles and inks containing the luminescent complex”: F. Thomas, C. Laporte, PCT Int. Appl. WO 2014048702A1, **2014**; b) “Secure document comprising luminescent chelates”: V. Aboutanos, T. Tiller, C. Reinhard, S. Rascagnères, PCT Int. Appl. WO 2010130681A1, **2010**.
- [4] A. J. Amoroso, S. J. A. Pope, *Chem. Soc. Rev.* **2015**, *44*, 4723–4742.
- [5] E. Pershagen, K. E. Borbas, *Coord. Chem. Rev.* **2014**, *273*–274, 30–46.
- [6] E. J. New, D. Parker, D. G. Smith, J. W. Walton, *Curr. Opin. Chem. Biol.* **2010**, *14*, 238–246.
- [7] S. V. Eliseeva, J.-C. G. Bünzli, *Chem. Soc. Rev.* **2010**, *39*, 189–227.
- [8] a) Q. Zhao, C. Huanga, F. Li, *Chem. Soc. Rev.* **2011**, *40*, 2508–2524; b) O. S. Wenger, *Chem. Rev.* **2013**, *113*, 3686–3733.
- [9] V. W.-W. Yam, K. M.-C. Wong, *Chem. Commun.* **2011**, *47*, 11579–11592.
- [10] P.-T. Chou, Y. Chi, *Chem. Eur. J.* **2007**, *13*, 380–395.
- [11] Selection of examples: a) S. Wiktorowski, C. Rosazza, M. J. Winterhalder, E. Daltrozzo, A. Zumbusch, *Chem. Commun.* **2014**, *50*, 4755–4758; b) T. Marks, E. Daltrozzo, A. Zumbusch, *Chem. Eur. J.* **2014**, *20*, 6494–6504; c) D. Frath, J. Massue, G. Ulrich, R. Ziessel, *Angew. Chem. Int. Ed.* **2014**, *53*, 2290–2310; *Angew. Chem.* **2014**, *126*, 2322–2342; d) J. C. Er, C. Leong, C. L. Teoh, Q. Yuan, P. Merchant, M. Dunn, D. Sulzer, D. Sames, A. Bhinghe, D. Kim, S.-M. Kim, M.-H. Yoon, L. W. Stanton, S. H. Je, S.-W. Yun, Y.-T. Chang, *Angew. Chem. Int. Ed.* **2015**, *54*, 2442–2446; *Angew. Chem.* **2015**, *127*, 2472–2476; e) S. Wiktorowski, E. Daltrozzo, A. Zumbusch, *RSC Adv.* **2015**, *5*, 29420–29423; f) D. Jansch, C. Li, L. Chen, M. Wagner, K. Müllen, *Angew. Chem. Int. Ed.* **2015**, *54*, 2285–2289; *Angew. Chem.* **2015**, *127*, 2314–2319; g) E. Heyer, P. Lory, J. Leprince, M. Moreau, A. Romieu, M. Guardigli, A. Roda, R. Ziessel, *Angew. Chem. Int. Ed.* **2015**, *54*, 2995–2999; *Angew. Chem.* **2015**, *127*, 3038–3042; h) U. Resch-Genger, M. Grabolle, S. Cavaliere-Jaricot, R. Nitschke, T. Nann, *Nat. Methods* **2008**, *5*, 763–775.
- [12] M. Schulze, A. Steffen, F. Würthner, *Angew. Chem. Int. Ed.* **2015**, *54*, 1570–1573; *Angew. Chem.* **2015**, *127*, 1590–1593.
- [13] a) J. V. Caspar, E. M. Kober, B. P. Sullivan, T. J. Meyer, *J. Am. Chem. Soc.* **1982**, *104*, 630–632; b) J. V. Caspar, T. J. Meyer, *J. Am. Chem. Soc.* **1983**, *105*, 5583–5590; c) J. V. Caspar, T. J. Meyer, *J. Phys. Chem.* **1983**, *87*, 952–957; d) T. J. Meyer, *Pure Appl. Chem.* **1986**, *58*, 1193–1206.
- [14] a) N. Armaroli, G. Accorsi, F. Cardinali, A. Listorti, *Top. Curr. Chem.* **2007**, *280*, 69–115; b) C. E. McCusker, F. N. Castellano, *Inorg. Chem.* **2013**, *52*, 8114–8120; c) M. S. Lazorski, F. N. Castellano, *Polyhedron* **2014**, *33*, 57–70.
- [15] a) A. D. Kirk, *Chem. Rev.* **1999**, *99*, 1607–1640; b) L. S. Forster, *Coord. Chem. Rev.* **2002**, *227*, 59–92; c) N. A. P. Kane-Maguire, *Top. Curr. Chem.* **2007**, *280*, 37–67; d) V. Balzani, P. Ceroni, A.

- Juris, *Photochemistry and Photophysics*, Wiley-VCH, Weinheim, **2014**, pp. 216–219; e) M. A. Jamieson, N. Serpone, M. Z. Hoffman, *Coord. Chem. Rev.* **1981**, *39*, 121–179; f) C. K. Ryu, J. F. Endicott, *Inorg. Chem.* **1988**, *27*, 2203–2214.
- [16] a) T. H. Maiman, *Nature* **1960**, *187*, 493–494; b) C. Degli Esposti, L. Bizzocchi, *J. Chem. Educ.* **2007**, *84*, 1316–1318.
- [17] a) A. Hauser, M. E. Von Arx, R. Pellaux, S. Decurtins, *Mol. Cryst. Liq. Cryst.* **1996**, *286*, 225–230; b) M. Milos, S. Kairouani, S. Rabaste, A. Hauser, *Coord. Chem. Rev.* **2008**, *252*, 2540–2551; c) L. Aboshyan-Sorgho, H. Nozary, A. Aebischer, J.-C. G. Bünzli, P.-Y. Morgantini, K. R. Kittilstved, A. Hauser, S. V. Eliseeva, S. Petoud, C. Piguet, *J. Am. Chem. Soc.* **2012**, *134*, 12675–12684; d) M. Cantuel, F. Gumy, J.-C. G. Bünzli, C. Piguet, *Dalton Trans.* **2006**, 2647–2660; e) S. Torelli, D. Imbert, M. Cantuel, G. Bernardinelli, S. Delahaye, A. Hauser, J.-C. G. Bünzli, C. Piguet, *Chem. Eur. J.* **2005**, *11*, 3228–3242.
- [18] S. M. Stevenson, M. P. Shores, E. M. Ferreira, *Angew. Chem. Int. Ed.* **2015**, *54*, 6506–6510; *Angew. Chem.* **2015**, *127*, 6606–6610.
- [19] a) H. Yersin, P. Huber, G. Gietl, D. Trümbach, *Chem. Phys. Lett.* **1992**, *199*, 1–9; b) F. Castelli, L.-S. Forster, *J. Am. Chem. Soc.* **1975**, *97*, 6306–6309.
- [20] a) N. Sabbatini, V. Balzani, *J. Am. Chem. Soc.* **1972**, *94*, 7587–7589; b) H. F. Wasgestian, *J. Phys. Chem.* **1972**, *76*, 1947–1951.
- [21] a) A. Breivogel, C. Förster, K. Heinze, *Inorg. Chem.* **2010**, *49*, 7052–7056; b) K. Mack, A. Wünsche von Leupoldt, C. Förster, M. Ezhevskaya, D. Hinderberger, K. W. Klinkhammer, K. Heinze, *Inorg. Chem.* **2012**, *51*, 7851–7858; c) A. Breivogel, M. Meister, C. Förster, F. Laquai, K. Heinze, *Chem. Eur. J.* **2013**, *19*, 13745–13760; d) C. Förster, K. Mack, L. M. Carrella, V. Ksenofontov, E. Rentschler, K. Heinze, *Polyhedron* **2013**, *52*, 576–581; e) A. Breivogel, M. Park, D. Lee, S. Klassen, A. Kühnle, C. Lee, K. Char, K. Heinze, *Eur. J. Inorg. Chem.* **2014**, 288–295; f) A. Breivogel, C. Kreitner, K. Heinze, *Eur. J. Inorg. Chem.* **2014**, 5468–5490; g) A. K. C. Mengel, C. Förster, A. Breivogel, K. Mack, J. R. Ochsmann, F. Laquai, V. Ksenofontov, K. Heinze, *Chem. Eur. J.* **2015**, *21*, 704–714.
- [22] a) M. Maestri, F. Bolletta, N. Serpone, L. Moggi, V. Balzani, *Inorg. Chem.* **1976**, *15*, 2048–2051; b) E. C. Constable, C. E. Housecroft, M. Neuburger, J. Schönle, J. A. Zampese, *Dalton Trans.* **2014**, *43*, 7227–7235.
- [23] a) C. C. Scarborough, K. M. Lancaster, S. DeBeer, T. Weyhermüller, S. Sproules, K. Wieghardt, *Inorg. Chem.* **2012**, *51*, 3718–3732; b) C. C. Scarborough, S. Sproules, T. Weyhermüller, S. Serena DeBeer, K. Wieghardt, *Inorg. Chem.* **2011**, *50*, 12446–12462.
- [24] U. Casellato, R. Graziani, R. P. Bonomo, A. J. Di Bilio, *J. Chem. Soc. Dalton Trans.* **1991**, 23–31.
- [25] N. A. P. Kane-Maguire, J. Conway, C. H. Langford, *J. Chem. Soc. Chem. Commun.* **1974**, 801–802.
- [26] a) F. Gilardoni, J. Weber, K. Bellafrouh, C. Daul, H. U. Güdel, *J. Chem. Phys.* **1996**, *104*, 7624–7632; b) O. S. Wenger, H. U. Güdel, *J. Chem. Phys.* **2001**, *114*, 5832–5841.
- [27] a) E. A. Juban, J. K. McCusker, *J. Am. Chem. Soc.* **2005**, *127*, 6857–6865; b) E. A. Juban, A. L. Smeigh, J. E. Monat, J. K. McCusker, *Coord. Chem. Rev.* **2006**, *250*, 1783–1791.
- [28] a) N. Serpone, M. A. Jamieson, M. S. Henry, M. Z. Hoffman, F. Bolletta, M. Maestri, *J. Am. Chem. Soc.* **1979**, *101*, 2907–2916; b) B. Brunshwig, N. Sutin, *J. Am. Chem. Soc.* **1978**, *100*, 7568–7577.
- [29] a) M. Isaacs, A. G. Sykes, S. Ronco, *Inorg. Chim. Acta* **2006**, *359*, 3847–3854; b) K. D. Barker, K. A. Barnett, S. M. Connell, J. W. Glaeser, A. J. Wallace, J. Wildsmith, B. J. Herbert, J. F. Wheeler, N. A. P. Kane-Maguire, *Inorg. Chim. Acta* **2001**, *316*, 41–49; c) M. Z. Hoffman, F. Bolletta, L. Moggi, G. L. Hug, *J. Phys. Chem. Ref. Data* **1989**, *18*, 219–543.
- [30] J. Napp, T. Behnke, L. Fischer, C. Würth, M. Wottawa, D. M. Katschinski, F. Alves, U. Resch-Genger, M. Schäferling, *Anal. Chem.* **2011**, *83*, 9039–9046.
- [31] a) R. T. Watson, N. Desai, J. Wildsmith, J. F. Wheeler, N. A. P. Kane-Maguire, *Inorg. Chem.* **1999**, *38*, 2683–2687; b) V. G. Vaidyanathan, B. U. Nair, *Eur. J. Inorg. Chem.* **2004**, 1840–1846.

Received: May 29, 2015

Published online: August 12, 2015



## 4 SUMMARY AND OUTLOOK

In this work, the successful synthesis and characterization of novel mono- and dinuclear *push-pull* substituted polypyridine ruthenium complexes is presented. The dinuclear bis(terpyridine)ruthenium complex  $[(\text{EtOOC-tpy})\text{Ru}(\text{tpy-NHCO-tpy})\text{Ru}(\text{tpy-NHAc})]^{4+}$  [**I b**]<sup>4+</sup> (section 3.1) does not exhibit any measurable electronic coupling between the metal centers in the mixed valent state [**I b**]<sup>5+</sup>. This was attributed to high tunneling barriers for electron transfer as the bridge's frontier orbitals differ drastically from the metal  $d_{\pi}$  orbitals in their energies. In contrast, in the photo-excited state of [**I b**]<sup>4+</sup>, the bridging ligand is reduced by one electron, while one of the metal centers is oxidized. The resulting mixed-valent system is partially delocalized between the two valence isomers  $[(\text{EtOOC-tpy})\text{Ru}^{\text{II}}(\text{tpy-NHCO-tpy}^{-})\text{Ru}^{\text{III}}(\text{tpy-NHAc})]^{4+}$  and  $[(\text{EtOOC-tpy})\text{Ru}^{\text{III}}(\text{tpy-NHCO-tpy}^{-})\text{Ru}^{\text{II}}(\text{tpy-NHAc})]^{4+}$ . Both valence isomers are in thermal equilibrium mediated by electron transfer between the two metal sites. This is possible as the formal reduction of the bridge in the photo-excited state opens up additional electron transfer channels that are not accessible in [**I b**]<sup>5+</sup>, leading to the detection of dual emission at room temperature.

Furthermore, several mononuclear cyclometalated polypyridine ruthenium complexes with a  $[\text{Ru}(\text{N}^{\wedge}\text{N}^{\wedge}\text{N})(\text{N}^{\wedge}\text{C}^{\wedge}\text{N})]^{+}$  coordination cage were synthesized and studied (sections 3.2 and 3.3). The UV-Vis absorption properties of these  $[\text{Ru}(\text{dpb-R}')(\text{tpy-R}'')]^{+}$  systems were examined on a theoretical level and the obtained results verified using resonance Raman spectroscopy: The low-energy absorption band in the range of 470-600 nm consists of Ru→tpy and Ru→dpb transitions to a similar extent in all cases, while 350-450 nm band is predominantly composed of Ru→tpy excitations involving higher unoccupied orbitals at the tpy ligand.

All of the studied  $[\text{Ru}(\text{dpb-R}')(\text{tpy-R}'')]^{+}$  complexes are weakly emissive at room temperature with quantum yields in the range of  $10^{-6}$  –  $10^{-5}$  excluding  $[\text{Ru}(\text{dpb-NHAc})(\text{tpy-COOEt})]^{+}$  (sections 3.2 and 3.3). The latter is non-emissive both at room temperature and at 77 K. The lack of emission was attributed to the strong push-pull substitution induced by the cyclometalation which is further amplified by the carboxy and amide substituents. This reduces the emission energy to an extent that non-radiative decay via tunneling into vibrationally excited states of the singlet ground state becomes very efficient leading to complete quenching of the excited state via this channel (section 3.2). Using temperature-dependent quantum yield measurements complemented with quantum chemical results, it was shown for the luminescent complexes, that the emissive <sup>3</sup>MLCT state is flanked by two parasitic triplet states that promote radiationless excited state decay, namely a <sup>3</sup>MC state and a <sup>3</sup>LL'CT state. Both states are thermally accessible with activation barriers of around 25 and 5 kJ mol<sup>-1</sup>, respectively, leading to a biexponential dependence of the emission quantum yield on the temperature. The experimentally determined activation barriers were correlated with the electronic <sup>3</sup>MLCT→<sup>3</sup>MC and <sup>3</sup>MLCT→<sup>3</sup>LL'CT transitions based on the excellent agreement with the energies of the DFT-calculated transition states with deviations as small as ± 2 kJ mol<sup>-1</sup> (section 3.3).

The dinuclear cyclometalated polypyridine ruthenium complex  $[(\text{tpy})\text{Ru}(\text{dpb-NHCO-dpb})\text{Ru}(\text{tpy})]^{2+}$  [**1**]<sup>2+</sup> with an amide-containing bridging ligand was synthesized and characterized as well (section 3.3). As suggested by preliminary DFT results, the odd electron is predominantly

located at the carboxy-substituted complex fragment in the mixed-valent state:  $[[(\text{tpy})\text{Ru}(\text{dpb-NHCO-dpb})\text{Ru}^{\text{III}}(\text{tpy})]^{3+} \mathbf{[1]}^{3+}$ . However, the UV-Vis-NIR spectrum of  $\mathbf{[1]}^{3+}$  shows an NIR absorption band at 1100 nm characteristic for an IVCT transition. This indicates that  $\mathbf{[1]}^{3+}$  belongs to Robin-Day class II in contrast to the similar non-cyclometalated class I complex  $\mathbf{[I b]}^{5+}$ . Also the emissive properties of  $\mathbf{[1]}^{2+}$  differ from those of  $\mathbf{[I b]}^{4+}$ . At room temperature, dual emission is observed arising from two  $\text{Ru}^{\text{III}}(\text{tpy}^-)^3\text{MLCT}$  states localized at the two capping fragments, respectively. However, these states are spatially so far apart that thermal equilibration to the lower-energy  $[(\text{tpy}^-)\text{Ru}^{\text{III}}(\text{dpb-NHCO-dpb})\text{Ru}^{\text{II}}(\text{tpy})]^{2+}$  state via Dexter energy transfer is very slow. Hence, on the timescale of the excited state lifetime, which is estimated to be well below 1 ns, energy transfer does not occur. Only in frozen solution at 77 K, single emission from the *N*-substituted complex fragment is observed, as the transition to the solid phase slows down all non-emissive decay channels thus allowing energy transfer to occur prior to emission.

Finally,  $[\text{Ru}(\text{dpb-NR}_2)(\text{tpy}(-\text{COO})_3)]^{2-}$  complexes bearing diarylamine substituents at the cyclometalating dipyridylbenzene ligand were synthesized (section 3.4). These are known to exhibit substantial charge delocalization between the metal center and the amine functionality in the mixed-valent state  $[\text{Ru}(\text{dpb-NR}_2)(\text{tpy-COO})]^{2-}$  (Robin-Day class II/III regime). The suitability of such mesomeric charge delocalization away from the semiconductor surface was tested with respect to an application in DSSCs. Unfortunately, the charge delocalization in the mixed-valent state yields a resonance-stabilization that hampers the dye regeneration by the employed electrolytes. Nonetheless, the carbazole-substituted dye reached an external efficiency of  $\eta = 3.3\%$  using the iodide/triiodide electrolyte while benchmark dye **N719** reached  $\eta = 5.8\%$  using the same cell setup. In the presence of cobalt electrolytes, on the other hand, the performances of the carbazole-substituted cyclometalated dye and **N719** are very similar with efficiencies just above 1%.

In summary, the photophysical properties of cyclometalated polypyridine ruthenium complexes with a  $[\text{Ru}(\text{N}^{\wedge}\text{N}^{\wedge}\text{N})(\text{N}^{\wedge}\text{C}^{\wedge}\text{N})]^{+}$  coordination cage have been illustrated using a variety of experimental and theoretical techniques. Especially the discovery that the  $^3\text{MLCT}$  and  $^1\text{GS}$  potential energy surfaces intersect in the proximity of the minimum  $^3\text{MLCT}$  geometry, sheds new light on the research of highly emissive ruthenium-based NIR emitters (section 3.5). This surface crossing seems to be a common feature of cyclometalated bis(tridentate) complexes, as it was also found for  $[\text{Ru}(\text{tpy})(\text{pbpy})]^{+}$  with a  $[\text{Ru}(\text{N}^{\wedge}\text{N}^{\wedge}\text{N})(\text{N}^{\wedge}\text{N}^{\wedge}\text{C})]^{+}$  environment. However, an evaluation of the importance of this phenomenon for the excited state deactivation of cyclometalated ruthenium complexes definitely requires future work for example by studying the temperature dependence of the quantum yield of  $[\text{Ru}(\text{tpy})(\text{pbpy})]^{+}$ . The  $^3\text{MC}$  state of this complex is thermally inaccessible at room temperature and its responsibility in thermally activated emission quenching be excluded. If this research suggests, that a direct  $^3\text{MLCT} \rightarrow ^1\text{GS}$  surface crossing is indeed a viable excited state decay channel in cyclometalated bis(tridentate) ruthenium complexes this will mean that not only the energies of  $^3\text{MC}$  and potential  $^3\text{LL}'\text{CT}$  states need to be adjusted in order to improve the emission quantum yield of such systems. Additionally, the energy of this surface crossing point will have to be taken into consideration. As it is inherently linked to the distortion of the excited state with respect to the ground state, more strained systems might provide a possible solution. For example, annulated ligands such as 2-pyrid-2'-yl-benzo[h]quinoline

as  $N^{\wedge}N^{\wedge}C$  ligand or 9-pyrid-2'-yl-benzo[h]chinoline as  $N^{\wedge}C^{\wedge}N$  ligand might render excited state distortions more energetically demanding. This could be combined with very weakly  $\pi$ -accepting ligands to force  $Ru \rightarrow (\text{cyclometalating ligand})^3MLCT$  states as lowest triplet excited states, which might be considerably less distorted than  $Ru \rightarrow (\text{polypyridine ligand})$  excited states in cyclometalated complexes. Two such exemplary complexes are given in Figure 4.1. Additionally, bis(cyclometalation) could be a potential path to luminescent cyclometalated ruthenium complexes as suggested previously.<sup>114</sup>

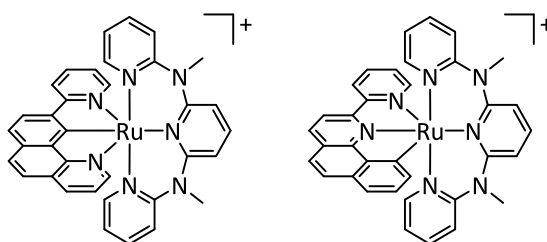


**Figure 4.1** Potentially luminescent ruthenium complexes with more restrained cyclometalating ligands.

However, before synthetic efforts in any of the directions are undertaken, quantum chemical calculations can already provide valuable information about the energies and geometries of all excited states. The work presented herein has highlighted, that the predictive power of DFT calculation is sufficient to acquire a profound understanding of the photophysical properties of a cyclometalated polypyridine ruthenium complex without actually synthesizing it. This allows to scan for electronically suited structures or motives that then can be tackled synthetically. In conclusion, this work has provided insight into the photophysical properties of  $[Ru(N^{\wedge}N^{\wedge}N)(N^{\wedge}C^{\wedge}N)]^+$  complexes and given answers to the question why these complexes are so weakly emissive. This should lay the foundation for more in-depth studies in this field that might yield luminescent complexes



## 5 REFERENCES

- 1 J. P. Paris and W. W. Brandt, *J. Am. Chem. Soc.*, 1959, **81**, 5001–5002.
- 2 G. D. Hager and G. A. Crosby, *J. Am. Chem. Soc.*, 1975, **97**, 7031–7037.
- 3 G. D. Hager, R. J. Watts and G. A. Crosby, *J. Am. Chem. Soc.*, 1975, **97**, 7037–7042.
- 4 J. van Houten and R. J. Watts, *Inorg. Chem.*, 1978, **17**, 3381–3385.
- 5 M. Maestri, F. Bolletta, L. Moggi, V. Balzani, M. S. Henry and M. Z. Hoffman, *J. Am. Chem. Soc.*, 1978, **100**, 2694–2701.
- 6 B. Durham, J. V. Caspar, J. K. Nagle and T. J. Meyer, *J. Am. Chem. Soc.*, 1982, **104**, 4803–4810.
- 7 J. V. Caspar, E. M. Kober, B. P. Sullivan and T. J. Meyer, *J. Am. Chem. Soc.*, 1982, **104**, 630–632.
- 8 F. Barigelletti, A. Juris, V. Balzani, P. Belser and A. von Zelewsky, *Inorg. Chem.*, 1983, **22**, 3335–3339.
- 9 C. Chiorboli, M. T. Indelli and F. Scandola, *Top. Curr. Chem.*, 2005, **257**, 63–102.
- 10 S. Campagna, G. Denti, S. Serroni, M. Ciano and V. Balzani, *Inorg. Chem.*, 1991, **30**, 3728–3732.
- 11 K. Heinze, K. Hempel and M. Beckmann, *Eur. J. Inorg. Chem.*, 2006, **2006**, 2040–2050.
- 12 J. M. Calvert, J. V. Caspar, R. A. Binstead, T. D. Westmoreland and T. J. Meyer, *J. Am. Chem. Soc.*, 1982, **104**, 6620–6627.
- 13 C. Creutz and H. Taube, *J. Am. Chem. Soc.*, 1969, **91**, 3988–3989.
- 14 W. Kaim, A. Klein and M. Glöckle, *Acc. Chem. Res.*, 2000, **33**, 755–763.
- 15 W. Kaim and G. K. Lahiri, *Angew. Chem.*, 2007, **119**, 1808–1828. *Angew. Chem. Int. Ed.*, 2007, **46**, 1778–1796.
- 16 S. Campagna, F. Puntoriero, F. Nastasi, G. Bergamini and V. Balzani, *Top. Curr. Chem.*, 2007, **280**, 117–214.
- 17 H. D. Abruna, A. Y. Teng, G. J. Samuels and T. J. Meyer, *J. Am. Chem. Soc.*, 1979, **101**, 6745–6746.
- 18 J.-M. Lehn and R. Ziessel, *Proc. Natl. Acad. Sci.*, 1982, **79**, 701–704.
- 19 J. Hawecker, J.-M. Lehn and R. Ziessel, *J. Chem. Soc., Chem. Commun.*, 1983, 536.
- 20 H. Ozawa, M. Haga and K. Sakai, *J. Am. Chem. Soc.*, 2006, **128**, 4926–4927.
- 21 S. Ji, W. Wu, W. Wu, P. Song, K. Han, Z. Wang, S. Liu, H. Guo and J. Zhao, *J. Mater. Chem.*, 2010, **20**, 1953–1963.
- 22 B. O'Regan and M. Grätzel, *Nature*, 1991, **353**, 737–740.
- 23 M. Grätzel, *J. Photochem. Photobiol. C*, 2003, **4**, 145–153.
- 24 M. A. Green, *Solar Energy*, 2004, **76**, 3–8.



- 25 M. K. Nazeeruddin, P. Péchy, T. Renouard, S. M. Zakeeruddin, R. Humphry-Baker, P. Comte, P. Liska, Le Cevey, E. Costa, V. Shklover, L. Spiccia, G. B. Deacon, C. A. Bignozzi and M. Grätzel, *J. Am. Chem. Soc.*, 2001, **123**, 1613–1624.
- 26 M. K. Nazeeruddin, A. Kay, I. Rodicio, R. Humphry-Baker, E. Mueller, P. Liska, N. Vlachopoulos and M. Graetzel, *J. Am. Chem. Soc.*, 1993, **115**, 6382–6390.
- 27 M. K. Nazeeruddin, S. M. Zakeeruddin, R. Humphry-Baker, M. Jirousek, P. Liska, N. Vlachopoulos, V. Shklover, C.-H. Fischer and M. Grätzel, *Inorg. Chem.*, 1999, **38**, 6298–6305.
- 28 G. Sauvé, M. E. Cass, S. J. Doig, I. Lauermann, K. Pomykal and N. S. Lewis, *J. Phys. Chem. B*, 2000, **104**, 3488–3491.
- 29 T. Bessho, E. C. Constable, M. Graetzel, A. Hernandez Redondo, C. E. Housecroft, W. Kylberg, M. K. Nazeeruddin, M. Neuburger and S. Schaffner, *Chem. Commun.*, 2008, 3717–3719.
- 30 T. Kinoshita, J.-i. Fujisawa, J. Nakazaki, S. Uchida, T. Kubo and H. Segawa, *J. Phys. Chem. Lett.*, 2012, 394–398.
- 31 C. E. Housecroft and E. C. Constable, *Chem. Soc. Rev.*, 2015, **44**, 8386–8398.
- 32 H. J. Bolink, L. Cappelli, E. Coronado and P. Gaviña, *Inorg. Chem.*, 2005, **44**, 5966–5968.
- 33 H. J. Bolink, L. Cappelli, E. Coronado, M. Grätzel and M. K. Nazeeruddin, *J. Am. Chem. Soc.*, 2006, **128**, 46–47.
- 34 M. Maestri, N. Armaroli, V. Balzani, E. C. Constable and A. M. W. C. Thompson, *Inorg. Chem.*, 1995, **34**, 2759–2767.
- 35 M. Abrahamsson, M. Jäger, T. Österman, L. Eriksson, P. Persson, H.-C. Becker, O. Johansson and L. Hammarström, *J. Am. Chem. Soc.*, 2006, **128**, 12616–12617.
- 36 F. Schramm, V. Meded, H. Fliegl, K. Fink, O. Fuhr, Z. Qu, W. Klopper, S. Finn, T. E. Keyes and M. Ruben, *Inorg. Chem.*, 2009, **48**, 5677–5684.
- 37 A. Breivogel, C. Förster and K. Heinze, *Inorg. Chem.*, 2010, **49**, 7052–7056.
- 38 P. Revecó, J. H. Medley, A. R. Garber, N. S. Bhacca and J. Selbin, *Inorg. Chem.*, 1985, **24**, 1096–1099.
- 39 E. C. Constable and J. M. Holmes, *J. Organomet. Chem.*, 1986, **301**, 203–208.
- 40 M. Beley, J. P. Collin, R. Louis, B. Metz and J. P. Sauvage, *J. Am. Chem. Soc.*, 1991, **113**, 8521–8522.
- 41 S. H. Wadman, J. M. Kroon, K. Bakker, M. Lutz, A. L. Spek, G. P. M. van Klink and G. van Koten, *Chem. Commun.*, 2007, 1907–1909.
- 42 T. Bessho, E. Yoneda, J.-H. Yum, M. Guglielmi, I. Tavernelli, H. Imai, U. Rothlisberger, M. K. Nazeeruddin and M. Grätzel, *J. Am. Chem. Soc.*, 2009, **131**, 5930–5934.
- 43 I. M. Dixon, F. Alary and J.-L. Heully, *Dalton Trans.*, 2010, **39**, 10959–10966.
- 44 I. M. Dixon, F. Alary, M. Boggio-Pasqua and J.-L. Heully, *Dalton Trans.*, 2015, **44**, 13498–13503.

- 45 K. C. D. Robson, B. D. Koivisto, A. Yella, B. Sporinova, M. K. Nazeeruddin, T. Baumgartner, M. Grätzel and C. P. Berlinguette, *Inorg. Chem.*, 2011, **50**, 5494–5508.
- 46 P. G. Bomben, K. C. Robson, B. D. Koivisto and C. P. Berlinguette, *Coord. Chem. Rev.*, 2012, **256**, 1438–1450.
- 47 K. Kalyanasundaram, *Coord. Chem. Rev.*, 1982, **46**, 159–244.
- 48 J. N. Demas and D. G. Taylor, *Inorg. Chem.*, 1979, **18**, 3177–3179.
- 49 S. Yoon, P. Kukura, C. M. Stuart and R. A. Mathies, *Mol. Phys.*, 2006, **104**, 1275–1282.
- 50 S. J. Strickler and R. A. Berg, *J. Chem. Phys.*, 1962, **37**, 814–822.
- 51 G. S. Ming Tong, K. T. Chan, X. Chang and C.-M. Che, *Chem. Sci.*, 2015, **6**, 3026–3037.
- 52 D. G. Brown, N. Sangantrakun, B. Schulze, U. S. Schubert and C. P. Berlinguette, *J. Am. Chem. Soc.*, 2012, **134**, 12354–12357.
- 53 R. Englman and J. Jortner, *Mol. Phys.*, 1970, **18**, 145–164.
- 54 B. S. Brunshwig and N. Sutin, *Comments Inorg. Chem.*, 1987, **6**, 209–235.
- 55 J. V. Caspar and T. J. Meyer, *J. Phys. Chem.*, 1983, **87**, 952–957.
- 56 T. E. Keyes, F. Weldon, E. Müller, P. Pechy, M. Grätzel and J. G. Vos, *J. Chem. Soc., Dalton Trans.*, 1995, 2705–2706.
- 57 M. Schulz, J. Hirschmann, A. Draksharapu, G. Singh Bindra, S. Soman, A. Paul, R. Groarke, M. T. Pryce, S. Rau, W. R. Browne and J. G. Vos, *Dalton Trans.*, 2011, **40**, 10545–10552.
- 58 F. Barigelletti, P. Belser, A. von Zelewsky, A. Juris and V. Balzani, *J. Phys. Chem.*, 1985, **89**, 3680–3684.
- 59 J. R. Lakowicz, ed., *Principles of Fluorescence Spectroscopy*, Springer US, Boston, MA, 1983.
- 60 V. Balzani, G. Bergamini, S. Campagna and F. Puntoriero, *Top. Curr. Chem.*, 2007, **280**, 1–36.
- 61 T. Förster, *Ann. Phys.*, 1948, **437**, 55–75.
- 62 D. L. Dexter, *J. Chem. Phys.*, 1953, **21**, 836–850.
- 63 R. A. Marcus, *J. Chem. Phys.*, 1956, **24**, 979–989.
- 64 R. A. Marcus, *J. Chem. Phys.*, 1965, **43**, 679–701.
- 65 R. Marcus and N. Sutin, *Biochim. Biophys. Acta - Bioenergetics*, 1985, **811**, 265–322.
- 66 N. S. Hush, *Prog. Inorg. Chem.*, 1967, **8**, 391–444.
- 67 N. S. Hush, *Coord. Chem. Rev.*, 1985, **64**, 135–157.
- 68 J. T. Hupp and M. J. Weaver, *J. Electroanal. Chem. Interfacial Electrochem.*, 1983, **152**, 1–14.
- 69 D. Rehm and A. Weller, *Ber. Bunsenges. Phys. Chem.*, 1969, **73**, 834–839.
- 70 O. Stern and M. Volmer, *Physik. Z.*, 1919, **20**, 183–188.
- 71 G. C. Allen and N. S. Hush, *Prog. Inorg. Chem.*, 1967, **8**, 357–389.
- 72 M. B. Robin and P. Day, *Adv. Inorg. Chem.*, 1968, **10**, 247–422.
- 73 B. S. Brunshwig, C. Creutz and N. Sutin, *Chem. Soc. Rev.*, 2002, **31**, 168–184.
- 74 B. S. Brunshwig and N. Sutin, *Coord. Chem. Rev.*, 1999, **187**, 233–254.

- 75 W. Kaim and B. Sarkar, *Coord. Chem. Rev.*, 2007, **251**, 584–594.
- 76 R. F. Winter, *Organometallics*, 2014, **33**, 4517–4536.
- 77 S. Trofimenko, *Inorg. Chem.*, 1973, **12**, 1215–1221.
- 78 M. I. Bruce, *Angew. Chem.*, 1977, **89**, 75–89. *Angew. Chem. Int. Ed.*, 1977, **16**, 73–86.
- 79 Y. Chi and P.-T. Chou, *Chem. Soc. Rev.*, 2010, **39**, 638–655.
- 80 V. W.-W. Yam and K. M.-C. Wong, *Chem. Commun.*, 2011, **47**, 11579–11592.
- 81 V. Balzani and S. Campagna, *Top. Curr. Chem.*, 2007, **280**, 1–273.
- 82 V. Balzani and S. Campagna, *Top. Curr. Chem.*, 2007, **281**, 1–327.
- 83 E. C. Constable and M. J. Hannon, *Inorg. Chim. Acta*, 1993, **211**, 101–110.
- 84 E. C. Constable, A. M. W. C. Thompson and S. Greulich, *J. Chem. Soc., Chem. Commun.*, 1993, 1444–1446.
- 85 S. Sprouse, K. A. King, P. J. Spellane and R. J. Watts, *J. Am. Chem. Soc.*, 1984, **106**, 6647–6653.
- 86 Y. Ohsawa, S. Sprouse, K. A. King, M. K. DeArmond, K. W. Hanck and R. J. Watts, *J. Phys. Chem.*, 1987, **91**, 1047–1054.
- 87 P. G. Bomben, K. C. D. Robson, P. A. Sedach and C. P. Berlinguette, *Inorg. Chem.*, 2009, **48**, 9631–9643.
- 88 B. D. Koivisto, K. C. D. Robson and C. P. Berlinguette, *Inorg. Chem.*, 2009, **48**, 9644–9652.
- 89 M. K. Nazeeruddin, F. de Angelis, S. Fantacci, A. Selloni, G. Viscardi, P. Liska, S. Ito, B. Takeru and M. Grätzel, *J. Am. Chem. Soc.*, 2005, **127**, 16835–16847.
- 90 W. Zeng, Y. Cao, Y. Bai, Y. Wang, Y. Shi, M. Zhang, F. Wang, C. Pan and P. Wang, *Chem. Mater.*, 2010, **22**, 1915–1925.
- 91 S. Mathew, A. Yella, P. Gao, R. Humphry-Baker, B. F. E. Curchod, N. Ashari-Astani, I. Tavernelli, U. Rothlisberger, M. K. Nazeeruddin and M. Grätzel, *Nat. Chem.*, 2014, **6**, 242–247.
- 92 A. Yella, H.-W. Lee, H. N. Tsao, C. Yi, A. K. Chandiran, M. K. Nazeeruddin, E. W.-G. Diao, C.-Y. Yeh, S. M. Zakeeruddin and M. Grätzel, *Science*, 2011, **334**, 629–634.
- 93 D. Siebler, M. Linseis, T. Gasi, L. M. Carrella, R. F. Winter, C. Förster and K. Heinze, *Chem. Eur. J.*, 2011, **17**, 4540–4551.
- 94 D. Siebler, C. Förster and K. Heinze, *Dalton Trans.*, 2011, **40**, 3558–3575.
- 95 A. Breivogel, K. Hempel and K. Heinze, *Inorg. Chim. Acta*, 2011, **374**, 152–162.
- 96 C. Kreitner, *Diploma thesis*, 2012.
- 97 S. H. Wadman, M. Lutz, D. M. Tooke, A. L. Spek, F. Hartl, R. W. A. Havenith, G. P. M. van Klink and G. van Koten, *Inorg. Chem.*, 2009, **48**, 1887–1900.
- 98 M. L. Muro-Small, J. E. Yarnell, C. E. McCusker and F. N. Castellano, *Eur. J. Inorg. Chem.*, 2012, **2012**, 4004–4011.
- 99 B. Schulze, D. Escudero, C. Friebe, R. Siebert, H. Görls, S. Sinn, M. Thomas, S. Mai, J. Popp, B. Dietzek, L. González and U. S. Schubert, *Chem. Eur. J.*, 2012, **18**, 4010–4025.

- 
- 100 C. D. Ertl, D. P. Ris, S. C. Meier, E. C. Constable, C. E. Housecroft, M. Neuburger and J. A. Zampese, *Dalton Trans.*, 2015, **44**, 1557–1570.
- 101 C.-J. Yao, H.-J. Nie, W.-W. Yang, J.-Y. Shao, J. Yao and Y.-W. Zhong, *Chem. Eur. J.*, 2014, **20**, 17466–17477.
- 102 A. D. Becke, *J. Chem. Phys.*, 1993, **98**, 5648–5652.
- 103 A. Viček and S. Zálíš, *Coord. Chem. Rev.*, 2007, **251**, 258–287.
- 104 T. Yanai, D. P. Tew and N. C. Handy, *Chem. Phys. Lett.*, 2004, **393**, 51–57.
- 105 J. Preiß, M. Jäger, S. Rau, B. Dietzek, J. Popp, T. Martínez and M. Presselt, *ChemPhysChem*, 2015, **16**, 1395–1404.
- 106 C. Adamo and V. Barone, *J. Chem. Phys.*, 1999, **110**, 6158–6170.
- 107 A. Schäfer, H. Horn and R. Ahlrichs, *J. Chem. Phys.*, 1992, **97**, 2571–2577.
- 108 A. Schäfer, C. Huber and R. Ahlrichs, *J. Chem. Phys.*, 1994, **100**, 5829–5835.
- 109 F. Weigend and R. Ahlrichs, *Phys. Chem. Chem. Phys.*, 2005, **7**, 3297–3305.
- 110 S. Sinnecker, A. Rajendran, A. Klamt, M. Diedenhofen and F. Neese, *J. Phys. Chem. A*, 2006, **110**, 2235–2245.
- 111 D. Andrae, U. Häußermann, M. Dolg, H. Stoll and H. Preuß, *Theoret. Chim. Acta*, 1990, **77**, 123–141.
- 112 E. van Lenthe, E. J. Baerends and J. G. Snijders, *J. Chem. Phys.*, 1993, **99**, 4597–4610.
- 113 S. Grimme, S. Ehrlich and L. Goerigk, *J. Comput. Chem.*, 2011, **32**, 1456–1465.
- 114 E. Y. Li, Y.-M. Cheng, C.-C. Hsu, P.-T. Chou, G.-H. Lee, I.-H. Lin, Y. Chi and C.-S. Liu, *Inorg. Chem.*, 2006, **45**, 8041–8051.



## 6 APPENDIX

### 6.1 SUPPORTING INFORMATION TO 1.1: REDOX AND PHOTOCHEMISTRY OF BIS(TERPYRIDINE) RUTHENIUM(II) AMINO ACIDS AND THEIR AMIDE CONJUGATES – FROM UNDERSTANDING TO APPLICATIONS

**General procedures:** Et<sub>2</sub>O was distilled from sodium, CH<sub>3</sub>CN and CH<sub>2</sub>Cl<sub>2</sub> from CaH<sub>2</sub> and THF from potassium under an argon atmosphere. TentaGel-Wang resin and Fmoc-Gly-OH were purchased from IRIS Biotech. DIC, PyBOP and HOBT were purchased from Fluka (DIC = *N,N'*-diisopropylcarbodiimide, PyBOP = benzotriazole-1-yloxy)tripyrrolidinophosphonium hexafluorophosphate, HOBT = 1-hydroxybenzotriazole). All other reagents were used without further treatment from commercial suppliers (Acros and Sigma-Aldrich). Microwave heating was performed in a Discover Benchmate Plus (CEM Synthesis) single-mode microwave cavity, producing continuous irradiation at 2.455 GHz with 100 W (maximum power). The temperature and irradiation power were monitored during the course of the reaction. NMR spectra were recorded on a Bruker Avance DRX 400 spectrometer at 400.31 MHz (<sup>1</sup>H) and 100.66 MHz (<sup>13</sup>C{<sup>1</sup>H}). All resonances are reported in ppm versus the solvent signal as an internal standard (CH<sub>3</sub>CN (<sup>1</sup>H,  $\delta$  = 1.94; <sup>13</sup>C,  $\delta$  = 1.24 ppm). Figure S1 shows the SPPS of **[36]**(PF<sub>6</sub>)<sub>2</sub> and **[37]**(PF<sub>6</sub>)<sub>2</sub> as well as the atom numbering for NMR signal assignment. IR spectra were recorded on a BioRad Excalibur FTS 3100 spectrometer as CsI disks. Electrochemical experiments were carried out with a Bio Logic SP-50 voltammetric analyzer using platinum wires as counter- and working electrodes and 0.01 M Ag/AgNO<sub>3</sub> as reference electrode. The measurements were performed with a scan rate of 50 – 333 mV s<sup>-1</sup> for cyclic voltammetry experiments and 100 – 200 mV s<sup>-1</sup> for square-wave voltammetry experiments using 0.1 M [*n*-Bu<sub>4</sub>N](PF<sub>6</sub>) as the supporting electrolyte and a 10<sup>-3</sup> M solution of the sample in dry and degassed CH<sub>3</sub>CN. Potentials are referenced to the ferrocene/ferrocenium couple ( $E_{1/2}$  = 85 ± 5 mV under our experimental conditions). UV/Vis/near-IR spectra were recorded on a Varian Cary 5000 spectrometer using 1.0 cm cells (Hellma, Suprasil). Emission spectra were recorded on a Varian Cary Eclipse spectrometer. Quantum yields were determined by comparing the areas under the emission spectra on an energy scale (cm<sup>-1</sup>) recorded for optically matched solutions of the sample and the reference [Ru(bpy)<sub>3</sub>]Cl<sub>2</sub> ( $\Phi$  = 9.4% in deaerated CH<sub>3</sub>CN).<sup>1</sup> ESI mass spectra were recorded on a Micromass Q-TOF-Ultima spectrometer. Elemental analyses were performed by the microanalytical laboratory of the chemical institutes of the University of Mainz.

<sup>1</sup> K. Suzuki, A. Kobayashi, S. Kaneko, K. Takehira, T. Yoshihara, H. Ishida, Y. Shiina, S. Oishi, S. Tobita, *Phys. Chem. Chem. Phys.* **2009**, *11*, 9850–9860.



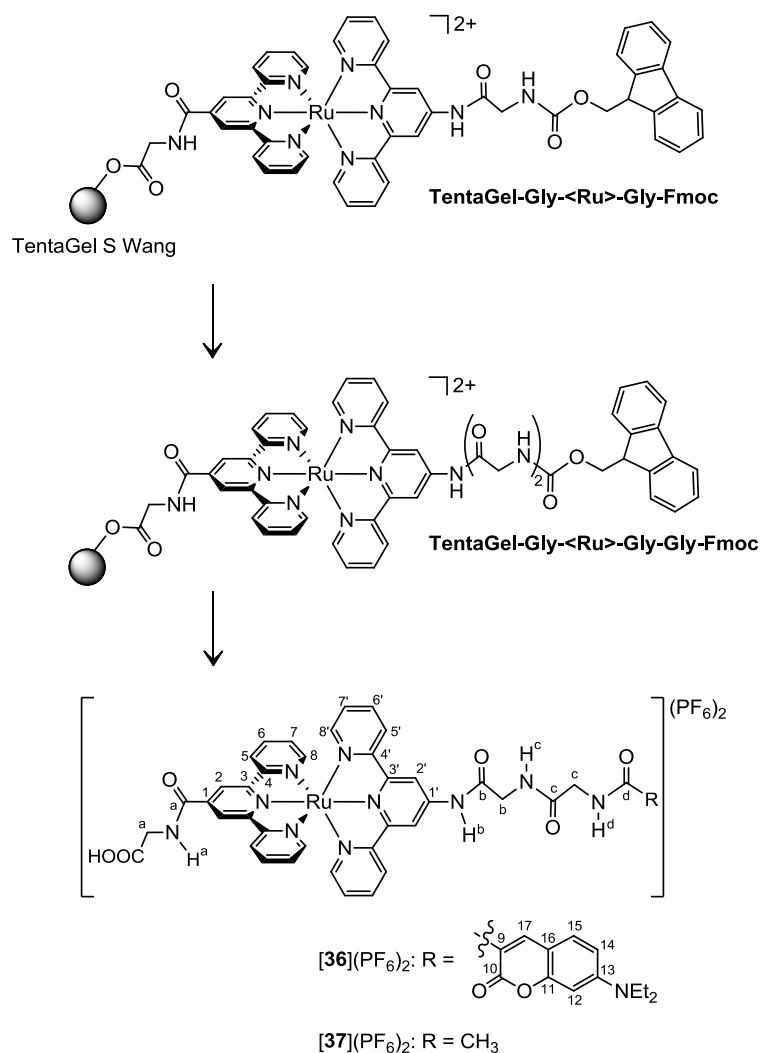


**Figure S1** SPPS of complexes  $[36](PF_6)_2$  and  $[37](PF_6)_2$ .

**Tentagel-Gly-<Ru>-Gly-Fmoc** was synthesized according to a literature procedure.<sup>2</sup> The progress of the reaction was monitored by treating a small portion of **Tentagel-Gly-<Ru>-Gly-Fmoc** (2 – 3 mg) with TFA (4 ml) and stirring for 30 min. The solvent was removed under reduced pressure, the product was re-dissolved in CH<sub>3</sub>CN (2 ml) and filtered. ESI mass spectra of the resulting solution showed signals for the Fmoc-protected tripeptide  $[H\text{-Gly-<Ru>-Gly-Fmoc}]^{2+} = [M]^{2+}$  at  $m/z = 481.6$  (100%)  $[M]^{2+}$ , 962.2 (29%)  $[M-H]^+$ .

**Tentagel-Gly-<Ru>-Gly-Gly-Fmoc:** **Tentagel-Gly-<Ru>-Gly-Fmoc** (0.167 mmol active centers, 1.0 equiv) was shaken in a piperidine/CH<sub>2</sub>Cl<sub>2</sub> (1:5, 15 ml) mixture for 30 min. After filtration and washing with CH<sub>2</sub>Cl<sub>2</sub> (3 × 15 ml) the residue was dried under reduced pressure. A solution of Fmoc-Gly-OH (209.5 mg, 0.705 mmol, 4.2 equiv), HOBT (118.5 mg, 0.877 mmol, 5.2 equiv) and DIC (0.15 ml, 0.97 mmol, 5.8 equiv) in DMF (20 ml) was prepared, stirred for 30 min and added. The mixture was shaken for 16 h, filtered and washed with DMF (3 × 15 ml) and with CH<sub>2</sub>Cl<sub>2</sub> (3 × 15 ml). The

<sup>2</sup> K. Heinze, K. Hempel, *Chem. Eur. J.* **2009**, *15*, 1346–1358.

dark red product was dried under reduced pressure. The progress of the reaction was monitored by treating a small portion of **Tentagel-Gly-<Ru>-Gly-Gly-Fmoc** (2 – 3 mg) with TFA (4 ml) and stirring for 30 min. The solvent was removed under reduced pressure, the product was re-dissolved in CH<sub>3</sub>CN (2 ml) and filtered. ESI mass spectra of the resulting solution showed signals for the Fmoc-protected tetrapeptide [**H-Gly-<Ru>-Gly-Gly-Fmoc**]<sup>2+</sup> = [M]<sup>2+</sup> at *m/z* = 510.1 (100%) [M]<sup>2+</sup>, 1019.3 (49%) [M-H]<sup>+</sup>.

**[36](PF<sub>6</sub>)<sub>2</sub>: Tentagel-Gly-<Ru>-Gly-Gly-Fmoc** (0.167 mmol active centers, 1.0 equiv) was shaken in a piperidine/CH<sub>2</sub>Cl<sub>2</sub> (1:5, 15 ml) mixture for 30 min. After filtration and washing with CH<sub>2</sub>Cl<sub>2</sub> (3 × 15 ml) the residue was dried under reduced pressure. A solution of 7-diethylaminocoumarin-3-carboxylic acid (104.1 mg, 0.398 mmol, 2.4 equiv), PyBOP (235.0 mg, 0.452 mmol, 2.7 equiv) and pyridine (0.20 ml, 2.5 mmol, 15 equiv) in CH<sub>2</sub>Cl<sub>2</sub> (20 ml) was prepared, stirred for 30 min and added. The mixture was shaken for 40 h, filtered and washed with CH<sub>2</sub>Cl<sub>2</sub> (6 × 15 ml). The red product was dried under reduced pressure. Trifluoroacetic acid (10 ml) was added, the mixture was shaken for 45 min, filtered and washed with CH<sub>3</sub>CN (2 × 10 ml). The solvent of the combined filtrates was removed under reduced pressure. The dark red powder was dissolved in CH<sub>3</sub>CN (2 ml). Water was added (10 ml) and the product precipitated upon adding an aqueous solution of [NH<sub>4</sub>](PF<sub>6</sub>) (194.4 mg, 1.19 mmol, 7.1 equiv, 3 ml H<sub>2</sub>O). After filtration the dark red product was washed with cold water and dried under reduced pressure. Yield: 140.0 mg (0.105 mmol, 63%).  
<sup>1</sup>H NMR (CD<sub>3</sub>CN, 300 K): δ = 9.93 (s, 1 H, NH<sup>b</sup>), 9.43 (t, <sup>3</sup>J<sub>HH</sub> = 5.2 Hz, 1 H, NH<sup>d</sup>), 9.25 (s, 2 H, H<sup>2</sup>), 9.08 (s, 2 H, H<sup>2</sup>), 8.69 (s, 1 H, H<sup>17</sup>), 8.59 (d, <sup>3</sup>J<sub>HH</sub> = 8.0 Hz, 2 H, H<sup>5</sup>), 8.41 (d, <sup>3</sup>J<sub>HH</sub> = 8.0 Hz, 2 H, H<sup>5</sup>), 8.10 (t, <sup>3</sup>J<sub>HH</sub> = 5.6 Hz, 1 H, NH<sup>a</sup>), 7.94 (m, 2 H, H<sup>6</sup>), 7.87 (m, 2 H, H<sup>6</sup>), 7.57 (t, <sup>3</sup>J<sub>HH</sub> = 5.2 Hz, 1 H, NH<sup>c</sup>), 7.47 (d, <sup>3</sup>J<sub>HH</sub> = 5.2 Hz, 2 H, H<sup>8</sup>), 7.32 (d, <sup>3</sup>J<sub>HH</sub> = 5.2 Hz, 2 H, H<sup>8</sup>), 7.18 (m, 2 H, H<sup>7</sup>), 7.12 (m, 2 H, H<sup>7</sup>), 7.08 (m, <sup>3</sup>J<sub>HH</sub> = 9.6 Hz, 1 H, H<sup>15</sup>), 6.55 (m, 2 H, H<sup>12,14</sup>), 4.32 (d, <sup>3</sup>J<sub>HH</sub> = 5.6 Hz, 2 H, CH<sub>2</sub><sup>a</sup>), 4.16 (d, <sup>3</sup>J<sub>HH</sub> = 5.2 Hz, 2 H, CH<sub>2</sub><sup>b</sup>), 4.13 (d, <sup>3</sup>J<sub>HH</sub> = 5.2 Hz, 2 H, CH<sub>2</sub><sup>c</sup>), 3.44 (q, <sup>3</sup>J<sub>HH</sub> = 7.0 Hz, 4 H, CH<sub>2</sub><sup>ethyl</sup>), 1.15 ppm (t, <sup>3</sup>J<sub>HH</sub> = 7.0 Hz, 6 H, CH<sub>3</sub>), no resonance for OH was observed. <sup>13</sup>C{<sup>1</sup>H} NMR (CD<sub>3</sub>CN, 300 K): δ = 171.4 (CO<sup>b</sup>), 170.9 (COOH), 168.4 (CO<sup>d</sup>), 166.2 (CO<sup>c</sup>), 165.2 (CO<sup>a</sup>), 163.3 (C<sup>10</sup>), 158.9 (C<sup>9</sup>), 158.8 (C<sup>4</sup>), 158.7 (C<sup>4</sup>), 157.2 (C<sup>3</sup>), 156.0 (C<sup>3</sup>), 154.1 (C<sup>16</sup>), 153.8 (C<sup>8</sup>), 153.4 (C<sup>8</sup>), 148.9 (C<sup>17</sup>), 147.5 (C<sup>11</sup>), 140.4 (C<sup>1</sup>), 139.2 (C<sup>6</sup>), 139.0 (C<sup>6</sup>), 132.2 (C<sup>15</sup>), 128.6 (C<sup>7</sup>), 128.4 (C<sup>7</sup>), 125.5 (C<sup>5</sup>), 125.3 (C<sup>5</sup>), 122.2 (C<sup>2</sup>), 114.6 (C<sup>2</sup>), 111.2 (C<sup>14</sup>), 109.9 (C<sup>11</sup>), 108.7 (C<sup>13</sup>), 97.1 (C<sup>12</sup>), 45.6 (CH<sub>2</sub><sup>ethyl</sup>), 45.1, 44.7 (CH<sub>2</sub><sup>b</sup>, CH<sub>2</sub><sup>c</sup>), 42.3 (CH<sub>2</sub><sup>a</sup>), 12.6 ppm (CH<sub>3</sub>). MS (ESI<sup>+</sup>): *m/z* 520.6 (65%) [M – 2 PF<sub>6</sub>]<sup>2+</sup>, 1186.3 (100%) [M – PF<sub>6</sub>]<sup>+</sup>. HR-MS (ESI<sup>+</sup>): *m/z* calcd for C<sub>51</sub>H<sub>45</sub>N<sub>11</sub>O<sub>8</sub><sup>96</sup>Ru<sup>2+</sup>: 517.6264; found: 517.6273; calcd for C<sub>51</sub>H<sub>45</sub>F<sub>6</sub>N<sub>11</sub>O<sub>8</sub>P<sup>96</sup>Ru<sup>+</sup>: 1180.2170; found: 1180.2195. IR (Csl):  $\tilde{\nu}$  = 3425 (br, m, OH, NH), 3101 (w, CH), 2963 (w, CH), 2930 (w, CH), 2874 (w, CH), 2858 (w, CH), 1699 (m, C=O), 1616 (s, C=N, amide I), 1580 (m, C=N, amide II), 1512 (s, C=N), 1475 (m), 1427 (m), 1354 (s), 1288 (m), 1232 (s), 1190 (m), 1165 (w), 1134 (m), 1096 (m), 1036 (w), 845 (vs, PF), 791 (m), 756 (w), 613 (m), 559 (m) cm<sup>-1</sup>. UV/Vis (CH<sub>3</sub>CN): λ<sub>abs</sub>(ε) = 490 (17100), 422 (33700), 309 (42200), 275 (56300), 236 (33500), 207 nm (62300 m<sup>-1</sup>cm<sup>-1</sup>). Emission (CH<sub>3</sub>CN, 295 K, λ<sub>exc</sub> = 490 nm): λ<sub>emiss</sub> = 668 nm. Φ(CH<sub>3</sub>CN, λ<sub>exc</sub> = 456 nm, 295 K): 0.12%. CV (CH<sub>3</sub>CN): E<sub>1/2</sub> = +0.89 (1e, rev.), +0.75 (1e, rev.), -1.15 (1e, irrev.), -1.55 (2e, irrev.) V vs. FcH/FcH<sup>+</sup>. Elemental analysis calcd (%) for C<sub>51</sub>H<sub>45</sub>F<sub>12</sub>N<sub>11</sub>O<sub>8</sub>P<sub>2</sub>Ru × 10 H<sub>2</sub>O: C 41.03, H 4.25, N 10.32; found: C 41.12, H 3.97, N 9.21.

**[37](PF<sub>6</sub>)<sub>2</sub>: Tentagel-Gly-<Ru>-Gly-Gly-Fmoc** (0.183 mmol reaction centers, 1.0 equiv) was shaken in a piperidine/CH<sub>2</sub>Cl<sub>2</sub> (1:5, 15 ml) mixture for 30 min. After filtration and washing with CH<sub>2</sub>Cl<sub>2</sub> (3 × 15 ml) the residue was dried under reduced pressure. A solution of acetyl chloride (0.10 ml, 1.4 mmol, 7.7 equiv) and pyridine (0.40 ml, 5.0 mmol, 27 equiv) in CH<sub>2</sub>Cl<sub>2</sub> (15 ml) was added. The mixture was shaken for 12 h, filtered and washed with CH<sub>2</sub>Cl<sub>2</sub> (5 × 15 ml). Trifluoroacetic acid (10 ml) was added, the mixture was shaken for 45 min, filtered and washed with CH<sub>3</sub>CN (2 × 10 ml). The solvent of the filtrate was removed under reduced pressure. The dark red powder was dissolved in CH<sub>3</sub>CN (2 ml). Water was added (10 ml) and the product precipitated upon adding an aqueous solution of [NH<sub>4</sub>](PF<sub>6</sub>) (194.4 mg, 1.09 mmol, 5.9 equiv, 3 ml H<sub>2</sub>O). After filtration the dark red product was washed with cold water and dried under reduced pressure. The product was dissolved in CH<sub>3</sub>CN (2 ml), precipitated by the addition of Et<sub>2</sub>O (30 ml), filtered and dried at 90 °C for 2 h. Yield: 125.5 mg (0.111 mmol, 61%). <sup>1</sup>H NMR (CD<sub>3</sub>CN, 300 K): δ = 9.93 (s, 1 H, NH<sup>b</sup>), 9.34 (s, 2 H, H<sup>2i</sup>), 9.09 (s, 2 H, H<sup>2</sup>), 8.59 (d, <sup>3</sup>J<sub>HH</sub> = 8.0 Hz, 2 H, H<sup>5</sup>), 8.36 (d, <sup>3</sup>J<sub>HH</sub> = 8.2 Hz, 2 H, H<sup>5i</sup>), 8.16 (t, <sup>3</sup>J<sub>HH</sub> = 5.4 Hz, 1 H, NH<sup>a</sup>), 7.94 (m, 2 H, H<sup>6</sup>), 7.90 (m, 2 H, H<sup>6i</sup>), 7.51 (t, <sup>3</sup>J<sub>HH</sub> = 6.1 Hz, 1 H, NH<sup>c</sup>), 7.47 (d, <sup>3</sup>J<sub>HH</sub> = 5.5 Hz, 2 H, H<sup>8</sup>), 7.35 (t, <sup>3</sup>J<sub>HH</sub> = 5.0 Hz, 1 H, NH<sup>d</sup>), 7.31 (d, <sup>3</sup>J<sub>HH</sub> = 4.8 Hz, 2 H, H<sup>8i</sup>), 7.21 (m, 2 H, H<sup>7</sup>), 7.11 (m, 2 H, H<sup>7i</sup>), 4.32 (d, <sup>3</sup>J<sub>HH</sub> = 5.4 Hz, 2 H, CH<sub>2</sub><sup>a</sup>), 4.15 (d, <sup>3</sup>J<sub>HH</sub> = 6.1 Hz, 2 H, CH<sub>2</sub><sup>b</sup>), 3.84 (d, <sup>3</sup>J<sub>HH</sub> = 5.0 Hz, 2 H, CH<sub>2</sub><sup>c</sup>), 2.18 ppm (s, 3 H, CH<sub>3</sub>). <sup>13</sup>C{<sup>1</sup>H} NMR (CD<sub>3</sub>CN, 300 K): δ = 174.3 (CO<sup>d</sup>), 171.2; 171.1 (3 C) (CO<sup>b</sup>, CO<sup>c</sup>, COOH), 165.3 (CO<sup>a</sup>), 158.8 (C<sup>4i</sup>), 158.7 (C<sup>4</sup>), 157.2 (C<sup>3</sup>), 156.0 (C<sup>3i</sup>), 153.8 (C<sup>8i</sup>), 153.4 (C<sup>8</sup>), 147.6 (C<sup>1i</sup>), 140.4 (C<sup>1</sup>), 139.2 (C<sup>6i</sup>), 139.0 (C<sup>6</sup>), 128.7 (C<sup>7</sup>), 128.4 (C<sup>7i</sup>), 125.5 (C<sup>5</sup>), 125.2 (C<sup>5i</sup>), 122.2 (C<sup>2</sup>), 114.3 (C<sup>2i</sup>), 45.1 (CH<sub>2</sub><sup>c</sup>), 44.5 (CH<sub>2</sub><sup>b</sup>), 42.4 (CH<sub>2</sub><sup>a</sup>), 23.2 ppm (CH<sub>3</sub>). MS (ESI<sup>+</sup>): *m/z* 420.1 (30%) [*M* – 2 PF<sub>6</sub>]<sup>2+</sup>, 985.2 (100%) [*M* – PF<sub>6</sub>]<sup>+</sup>. HR-MS (ESI<sup>+</sup>): *m/z* calcd for C<sub>39</sub>H<sub>34</sub>F<sub>6</sub>N<sub>10</sub>O<sub>6</sub><sup>96</sup>Ru<sup>2+</sup>: 979.1381; found: 979.1395. IR (Csl):  $\tilde{\nu}$  = 3433 (br, m, OH, NH), 3341 (w, NH), 3102 (w, CH), 2931 (w, CH), 1661 (s, C=O), 1604 (m, C=N, amide I), 1529 (m, C=N, amide II), 1477 (m, C=N), 1358 (s), 1292 (m), 1232 (s), 1165 (w), 1097 (m), 1036 (w), 1028 (w), 841 (vs, PF), 791 (m), 764 (w), 756 (w), 613 (m), 559 (s), 405 (w) cm<sup>-1</sup>. UV/Vis (CH<sub>3</sub>CN):  $\lambda_{\text{abs}}(\epsilon)$  = 490 (16500), 308 (38900), 275 (49700), 235 (27200), 204 nm (41500 M<sup>-1</sup>cm<sup>-1</sup>). Emission (CH<sub>3</sub>CN, 295 K,  $\lambda_{\text{exc}}$  = 490 nm):  $\lambda_{\text{emiss}}$  = 667 nm.  $\Phi$ (CH<sub>3</sub>CN,  $\lambda_{\text{exc}}$  = 447 nm, 295 K): 0.080%. CV (CH<sub>3</sub>CN): *E*<sub>1/2</sub> = +0.88 (1e, rev.), –1.14 (1e, irrev.), –1.49 (2e, irrev.) V vs. FcH/FcH<sup>+</sup>. Elemental analysis calcd (%) for C<sub>39</sub>H<sub>34</sub>F<sub>12</sub>N<sub>10</sub>O<sub>6</sub>P<sub>2</sub>Ru·2.5 HPF<sub>6</sub>: C 31.34, H 2.46, N 9.37; found: C 31.56, H 2.46, N 9.19.

## 6.2 SUPPORTING INFORMATION TO 3.1: DUAL EMISSION AND EXCITED-STATE MIXED-VALENCE IN A QUASI-SYMMETRIC DINUCLEAR RU–RU COMPLEX

**Synthesis of 8(PF<sub>6</sub>)<sub>2</sub>:** [(HOOC-tpy)Ru(tpy-NH<sub>2</sub>)](PF<sub>6</sub>)<sub>2</sub> **1**(PF<sub>6</sub>)<sub>2</sub> (202 mg, 0.221 mmol) was dissolved in abs. acetonitrile (15 ml) and pentafluorophenol (53.4 mg, 0.290 mmol) and *N,N'*-diisopropylcarbodiimide (39.0 mg, 0.310 mmol) were added. After stirring at room temperature for 60 min the reaction mixture was concentrated to 5 ml under reduced pressure and the product triturated by addition of a solution of NH<sub>4</sub>PF<sub>6</sub> (263 mg) in water (70 ml). The product was collected via filtration, washed with a small amount of water and diethyl ether and dried under reduced pressure to give [(C<sub>6</sub>F<sub>5</sub>OOC-tpy)Ru(tpy-NH<sub>2</sub>)](PF<sub>6</sub>)<sub>2</sub> **8**(PF<sub>6</sub>)<sub>2</sub> as red powder. Yield: 203.5 mg (0.188 mmol, 85%). Anal. Calc. C<sub>37</sub>H<sub>22</sub>F<sub>17</sub>N<sub>7</sub>O<sub>2</sub>P<sub>2</sub>Ru (1086.6)·1.5H<sub>2</sub>O: C, 40.05; H, 2.27; N, 8.84. Found: C, 40.06; H, 2.22; N, 8.84%. MS (ESI<sup>+</sup>): *m/z* (%) = 396.6 (83) [M-2PF<sub>6</sub>]<sup>2+</sup>, 938.1 (100) [M-PF<sub>6</sub>]<sup>+</sup>, 1479.1 (3) [3M-2PF<sub>6</sub>]<sup>2+</sup>. HR-MS (ESI<sup>+</sup>, *m/z*): calcd. for C<sub>37</sub>H<sub>22</sub>F<sub>11</sub>N<sub>7</sub>O<sub>2</sub>PRu [M-PF<sub>6</sub>]<sup>+</sup>: 932.0473; found: 932.0459. <sup>1</sup>H NMR (CD<sub>3</sub>CN): δ = 9.33 (s, 2H, H<sup>2</sup>), 8.67 (d, <sup>3</sup>J<sub>HH</sub> = 8 Hz, 2H, H<sup>5</sup>), 8.28 (d, <sup>3</sup>J<sub>HH</sub> = 8 Hz, 2H, H<sup>5'</sup>), 8.01 - 7.95 (m, 4H, H<sup>2'</sup>, H<sup>6</sup>), 7.86 (td, <sup>3</sup>J<sub>HH</sub> = 8 Hz, <sup>4</sup>J<sub>HH</sub> = 1.5 Hz, 2H, H<sup>6'</sup>), 7.60 (d, <sup>3</sup>J<sub>HH</sub> = 5 Hz, 2H, H<sup>8</sup>), 7.35 - 7.28 (m, 2H, H<sup>7</sup>), 7.19 (d, <sup>3</sup>J<sub>HH</sub> = 5 Hz, 2H, H<sup>8'</sup>), 7.07 - 7.02 (m, 2H, H<sup>7'</sup>), 6.04 (s, 2H, NH<sub>2</sub>). <sup>13</sup>C{<sup>1</sup>H} NMR (CD<sub>3</sub>CN): δ = 162.1 (s, COOC<sub>6</sub>F<sub>5</sub>), 159.2 (s, C<sup>4'</sup>), 158.6, 158.7 (2s, C<sup>4</sup>, C<sup>3</sup>), 154.7, 154.7 (2s, C<sup>1'</sup>, C<sup>3'</sup>), 153.9 (s, C<sup>8</sup>), 153.1 (s, C<sup>8'</sup>), 139.3 (s, C<sup>6'</sup>), 138.9 (s, C<sup>6</sup>), 131.3 (s, C<sup>1</sup>), 129.1 (s, C<sup>7</sup>), 128.0 (s, C<sup>7'</sup>), 125.8 (s, C<sup>5</sup>), 124.9 (s, C<sup>5'</sup>), 124.2 (s, C<sup>2</sup>), 109.7 (s, C<sup>2'</sup>), (C<sub>6</sub>F<sub>5</sub>-C-atoms not observed). <sup>19</sup>F NMR (CD<sub>3</sub>CN): δ = -73.3 (d, <sup>1</sup>J<sub>FP</sub> = 705 Hz, 12F, PF<sub>6</sub>), -154.8 (d, <sup>3</sup>J<sub>FF</sub> = 17 Hz, 2F, *o*-F), -159.0 (t, <sup>3</sup>J<sub>FF</sub> = 21 Hz, 1F, *p*-F), -163.8 (dd, <sup>3</sup>J<sub>FF</sub> = 21, 17 Hz, 2F, *m*-F).

**Synthesis of 9(PF<sub>6</sub>)<sub>2</sub>:** [(C<sub>6</sub>F<sub>5</sub>OOC-tpy)Ru(tpy-NH<sub>2</sub>)](PF<sub>6</sub>)<sub>2</sub> **8**(PF<sub>6</sub>)<sub>2</sub> (71 mg, 0.066 mmol) was dissolved in abs. acetonitrile (15 ml) and *tert*-butylamine (0.2 ml, 1.9 mmol, excess) was added. After stirring the mixture for 60 min at room temperature water (80 ml) was added. Addition of NH<sub>4</sub>PF<sub>6</sub> (113 mg) in water (2 ml) precipitated the product which was filtered off, washed with small amounts of water and diethyl ether and dried under reduced pressure to give [(*t*BuHNOC-tpy)Ru(tpy-NH<sub>2</sub>)](PF<sub>6</sub>)<sub>2</sub> **9**(PF<sub>6</sub>)<sub>2</sub> as red powder. Yield: 31.6 mg (0.033 mmol, 50%). Anal. Calc. C<sub>35</sub>H<sub>32</sub>F<sub>12</sub>N<sub>8</sub>OP<sub>2</sub>Ru (971.7)·2.5H<sub>2</sub>O: C, 41.35; H, 3.67; N, 11.02. Found: C, 41.26; H, 3.34; N, 10.82%. MS (ESI<sup>+</sup>): *m/z* (%) = 341.1 (100) [M-2PF<sub>6</sub>]<sup>2+</sup>, 827.2 (57) [M-PF<sub>6</sub>]<sup>+</sup>. HR-MS (ESI<sup>+</sup>, *m/z*): calcd. for C<sub>35</sub>H<sub>32</sub>F<sub>6</sub>N<sub>8</sub>OPRu [M-PF<sub>6</sub>]<sup>+</sup>: 792.0788; found: 792.0782. <sup>1</sup>H NMR (CD<sub>3</sub>CN): δ = 8.98 (s, 2H, H<sup>2</sup>), 8.60 (d, <sup>3</sup>J<sub>HH</sub> = 8 Hz, 2H, H<sup>5</sup>), 8.26 (d, <sup>3</sup>J<sub>HH</sub> = 8 Hz, 2H, H<sup>5'</sup>), 8.00 - 7.88 (m, 4H, H<sup>2'</sup>, H<sup>6</sup>), 7.84 (t, <sup>3</sup>J<sub>HH</sub> = 7 Hz, 2H, H<sup>6'</sup>), 7.54 (d, <sup>3</sup>J<sub>HH</sub> = 5 Hz, 2H, H<sup>8</sup>), 7.28 (s, 1H, CONH), 7.27 - 7.20 (m, 2H, H<sup>7</sup>), 7.18 (d, <sup>3</sup>J<sub>HH</sub> = 5 Hz, 2H, H<sup>8'</sup>), 7.07 - 6.99 (m, 2H, H<sup>7'</sup>), 5.97 (s, 2H, NH<sub>2</sub>), 1.61 (3, 9H, CH<sub>3</sub>). <sup>13</sup>C{<sup>1</sup>H} NMR (CD<sub>3</sub>CN): δ = 164.5 (s, CONH*t*Bu), 159.4 (s, C<sup>4</sup>), 159.1 (s, C<sup>4'</sup>), 157.5 (s, C<sup>3</sup>), 156.9 (s, C<sup>1'</sup>), 155.1 (s, C<sup>3'</sup>), 153.6 (s, C<sup>8</sup>), 153.1 (s, C<sup>8'</sup>), 141.9 (c, C<sup>1</sup>), 139.0 (s, C<sup>6</sup>), 138.7 (s, C<sup>6'</sup>), 128.7 (s, C<sup>7</sup>), 127.9 (s, C<sup>7'</sup>), 125.4 (s, C<sup>5</sup>), 124.8 (s, C<sup>5'</sup>), 122.2 (s, C<sup>2</sup>), 109.6 (s, C<sup>2'</sup>), 53.4 (s, C(CH<sub>3</sub>)<sub>3</sub>), 28.9 (s, C(CH<sub>3</sub>)<sub>3</sub>).

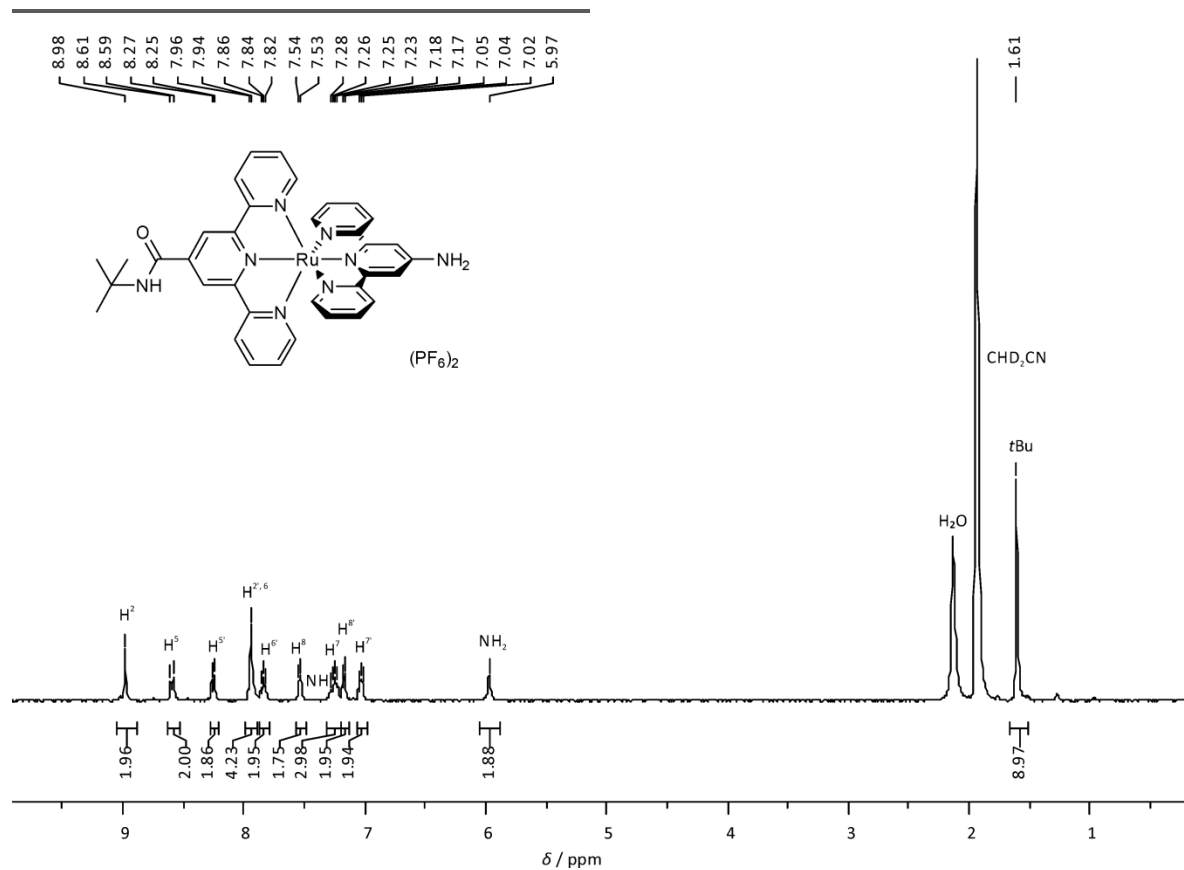


Figure S1. <sup>1</sup>H NMR spectrum of **9**(PF<sub>6</sub>)<sub>2</sub> in CD<sub>3</sub>CN.

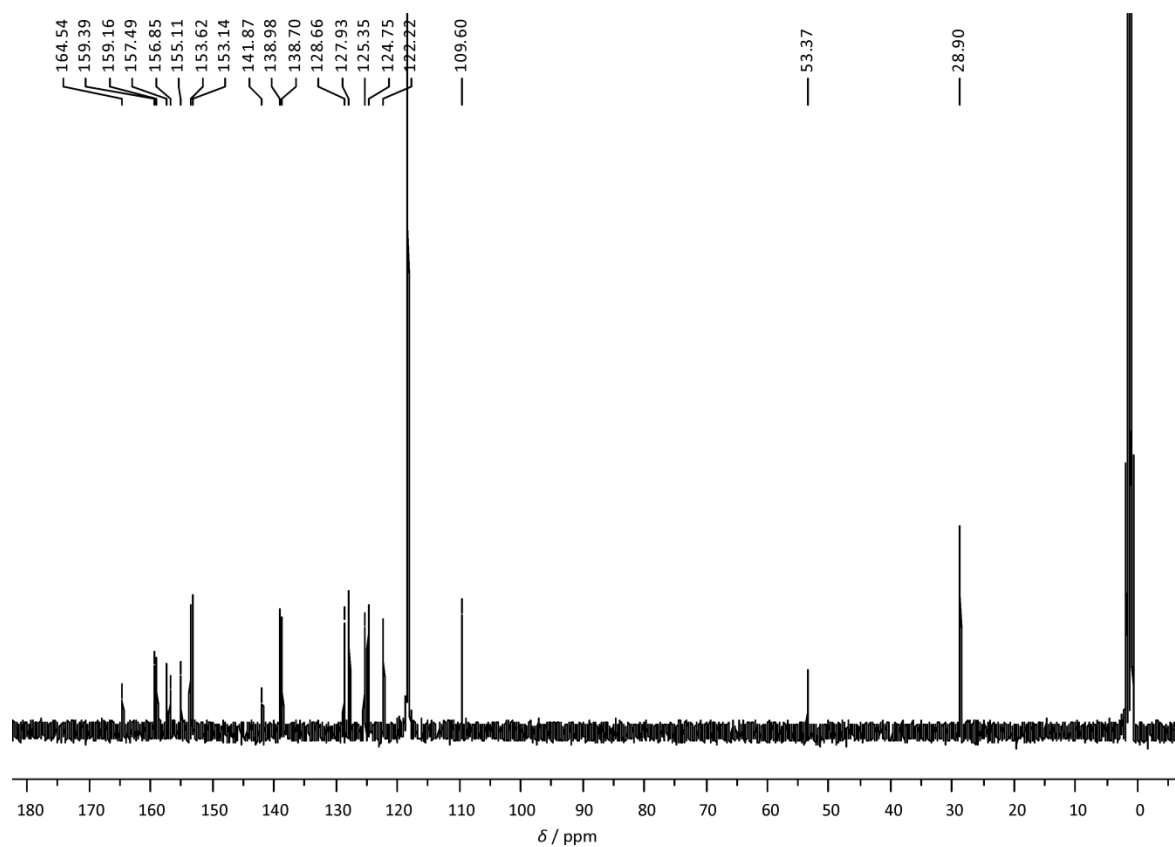


Figure S2. <sup>13</sup>C NMR spectrum of **9**(PF<sub>6</sub>)<sub>2</sub> in CD<sub>3</sub>CN.

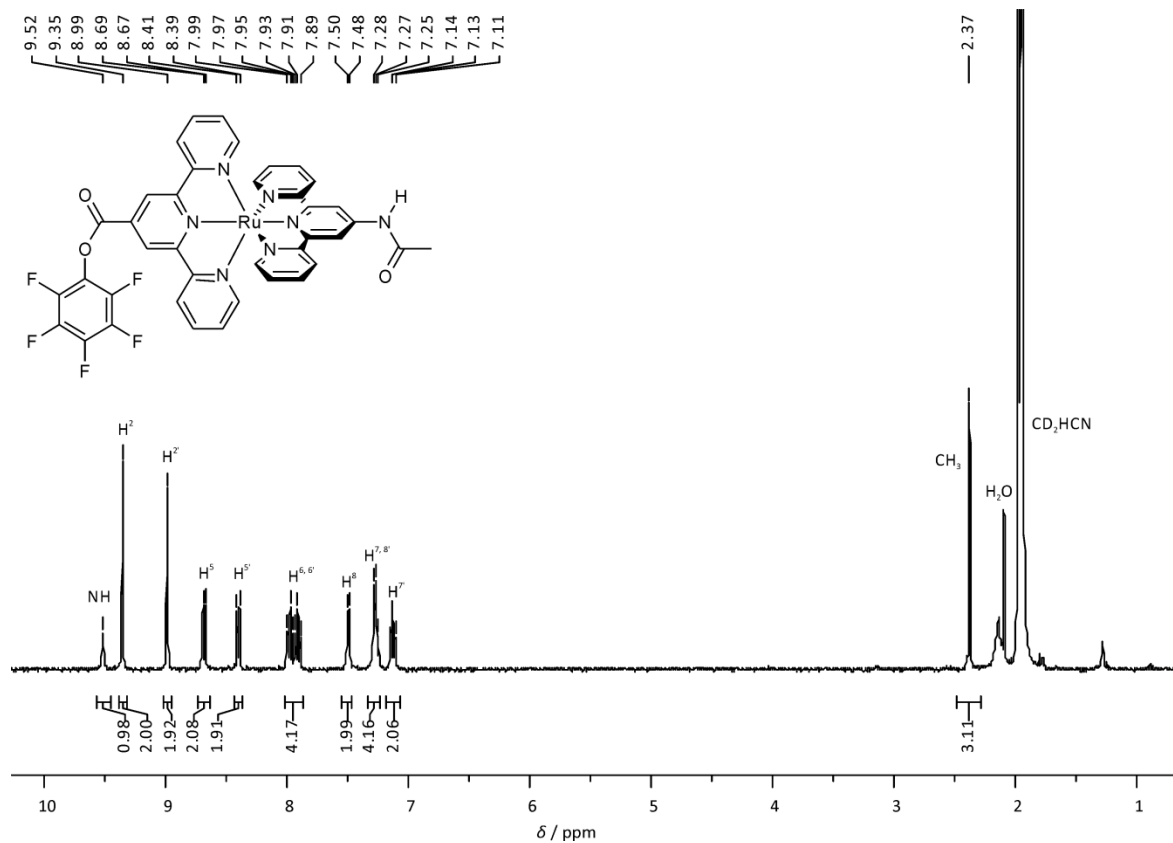


Figure S3. <sup>1</sup>H NMR spectrum of **7**(PF<sub>6</sub>)<sub>2</sub> in CD<sub>3</sub>CN.

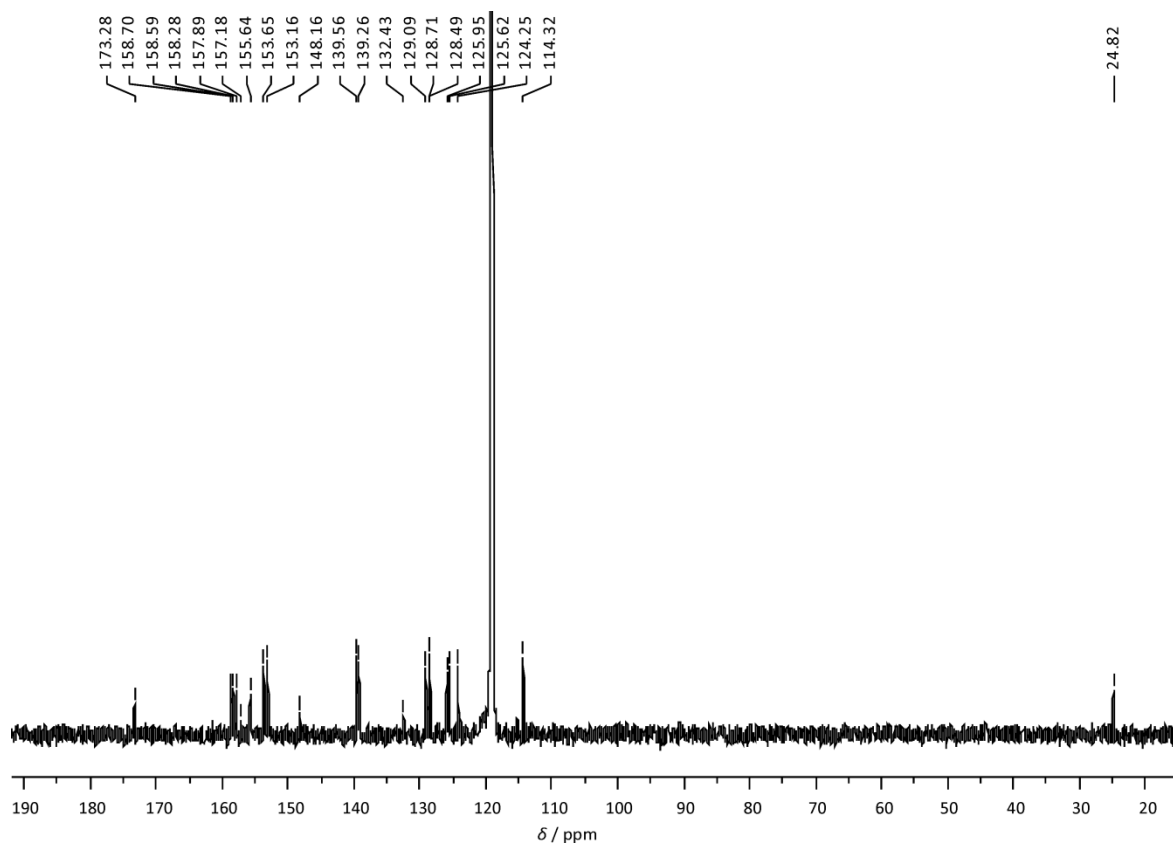


Figure S4. <sup>13</sup>C NMR spectrum of **7**(PF<sub>6</sub>)<sub>2</sub> in CD<sub>3</sub>CN.



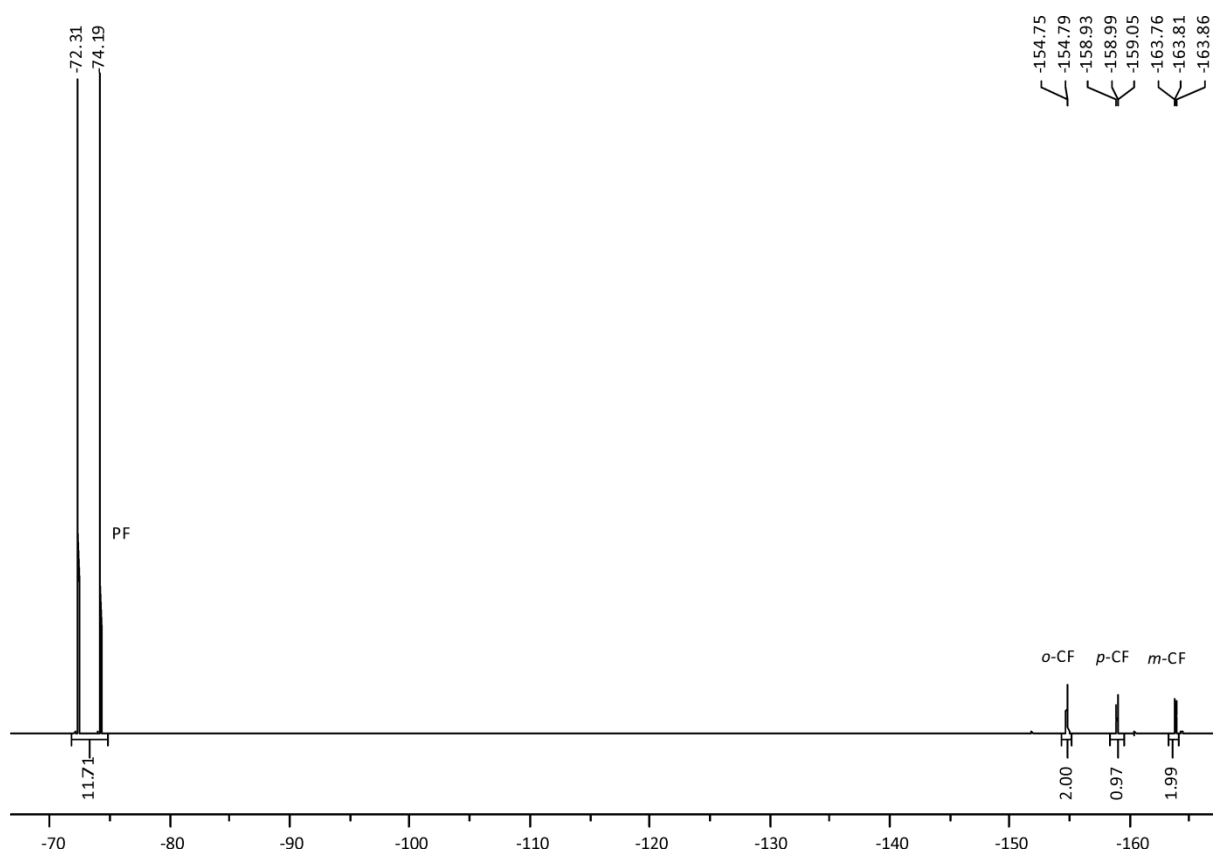


Figure S5.  $^{19}\text{F}$  NMR spectrum of **7**(PF<sub>6</sub>)<sub>2</sub> in CD<sub>3</sub>CN.

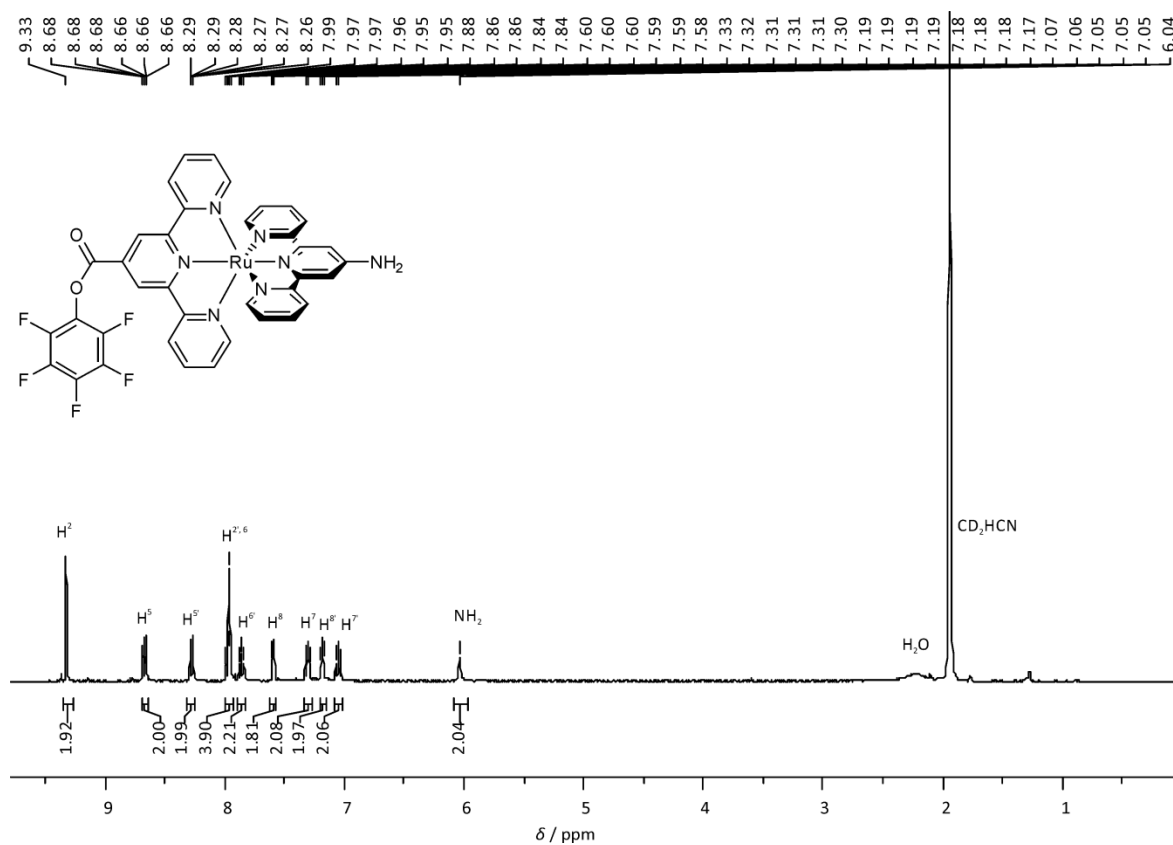


Figure S6.  $^1\text{H}$  NMR spectrum of **8**(PF<sub>6</sub>)<sub>2</sub> in CD<sub>3</sub>CN.

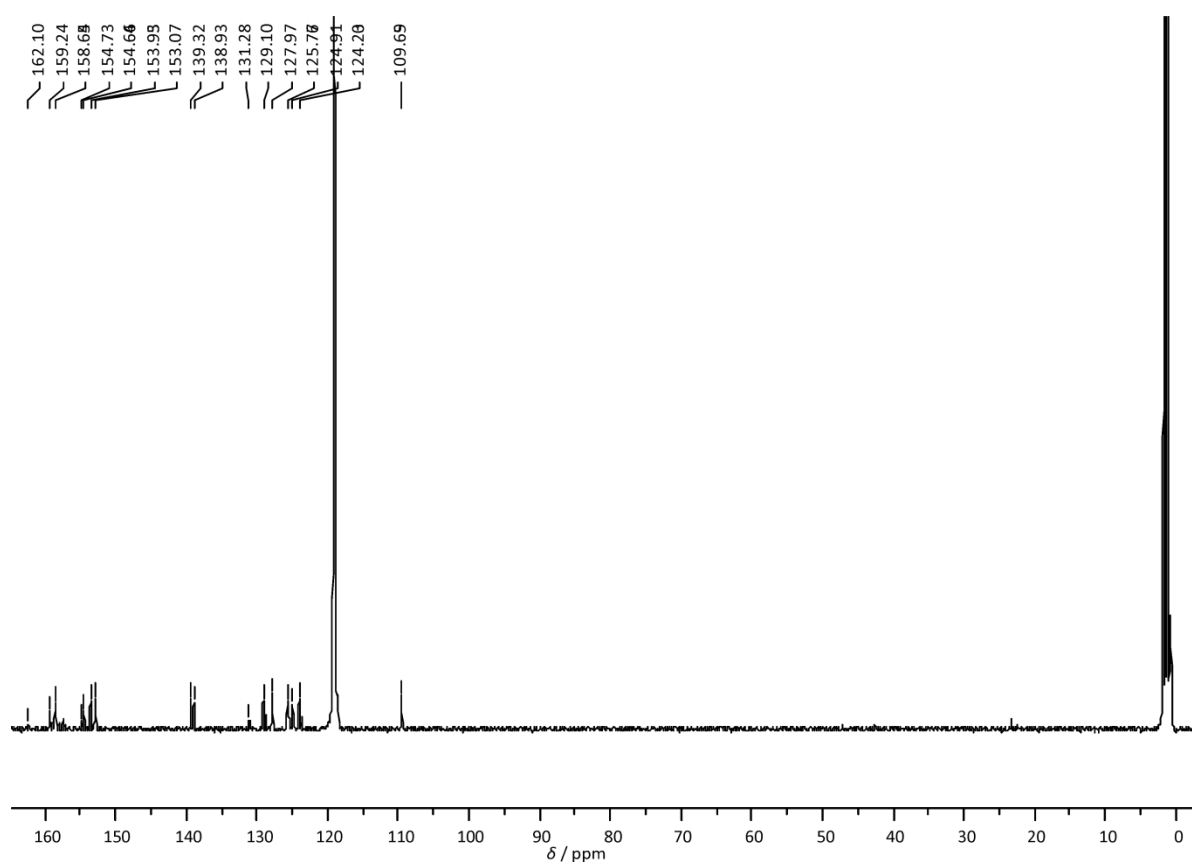


Figure S7.  $^{13}\text{C}$  NMR spectrum of  $\mathbf{8}(\text{PF}_6)_2$  in  $\text{CD}_3\text{CN}$ .

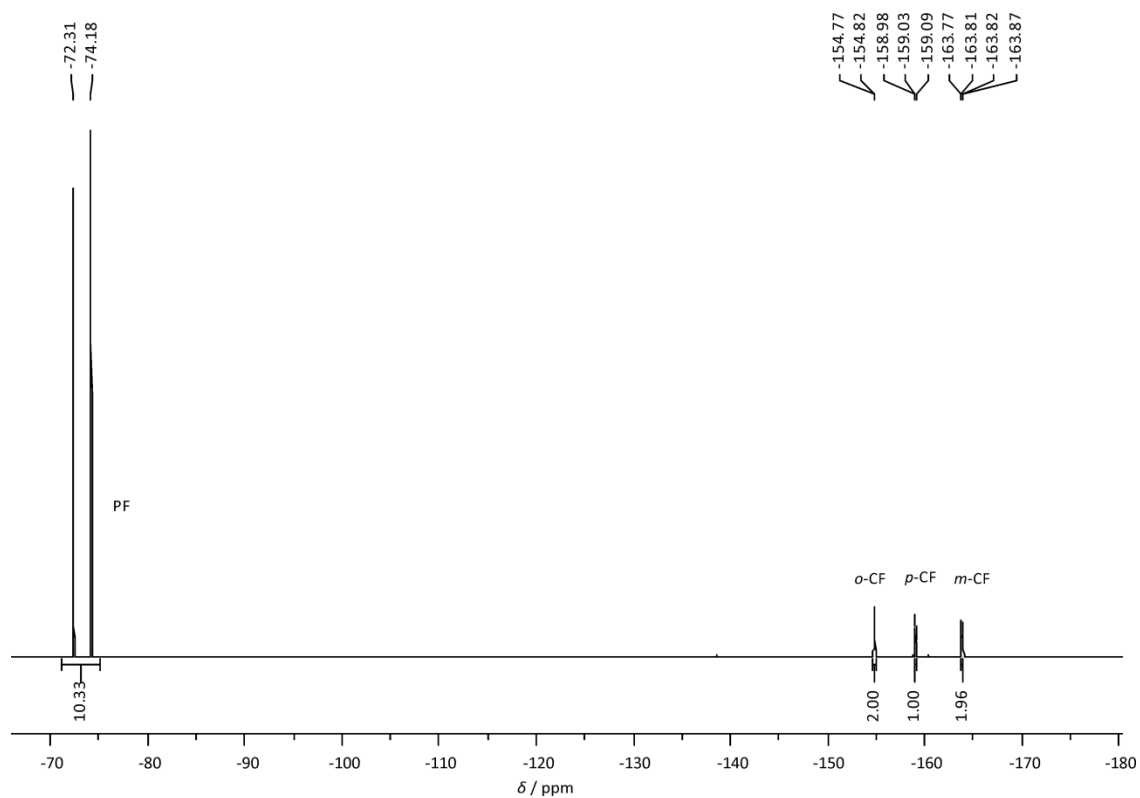
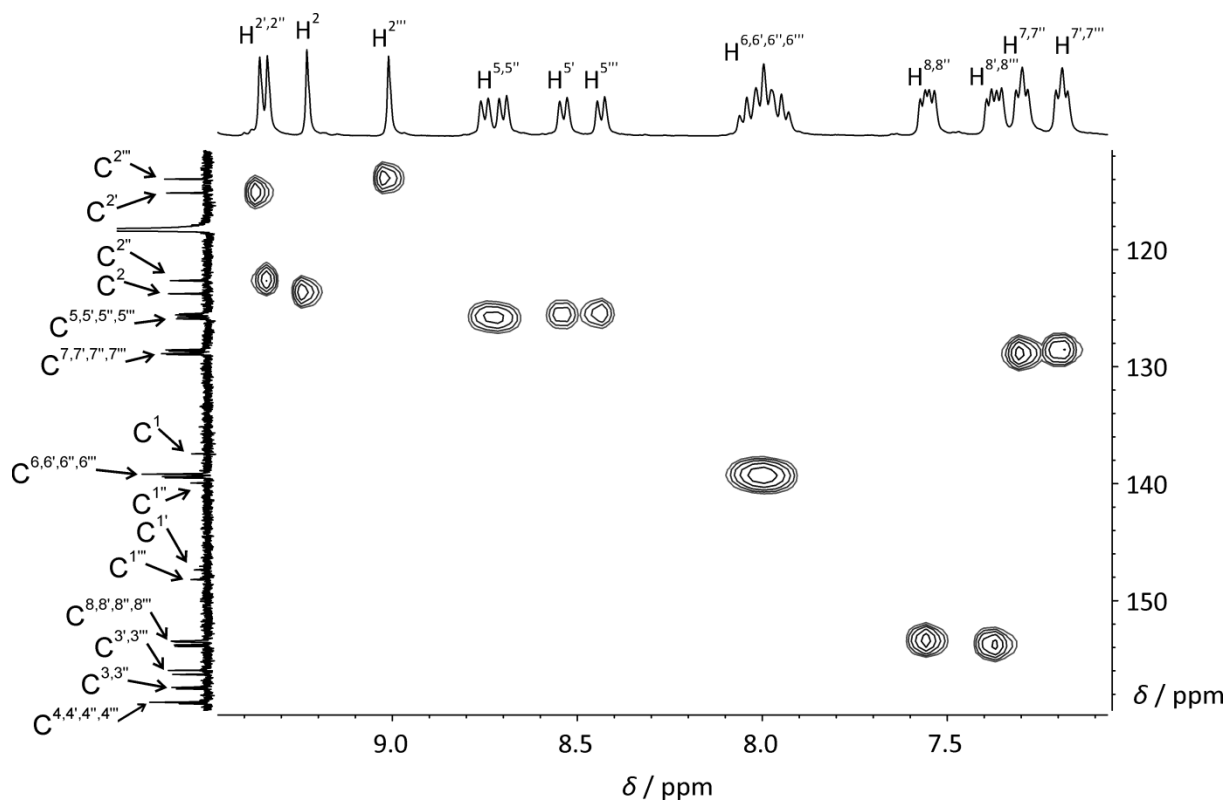
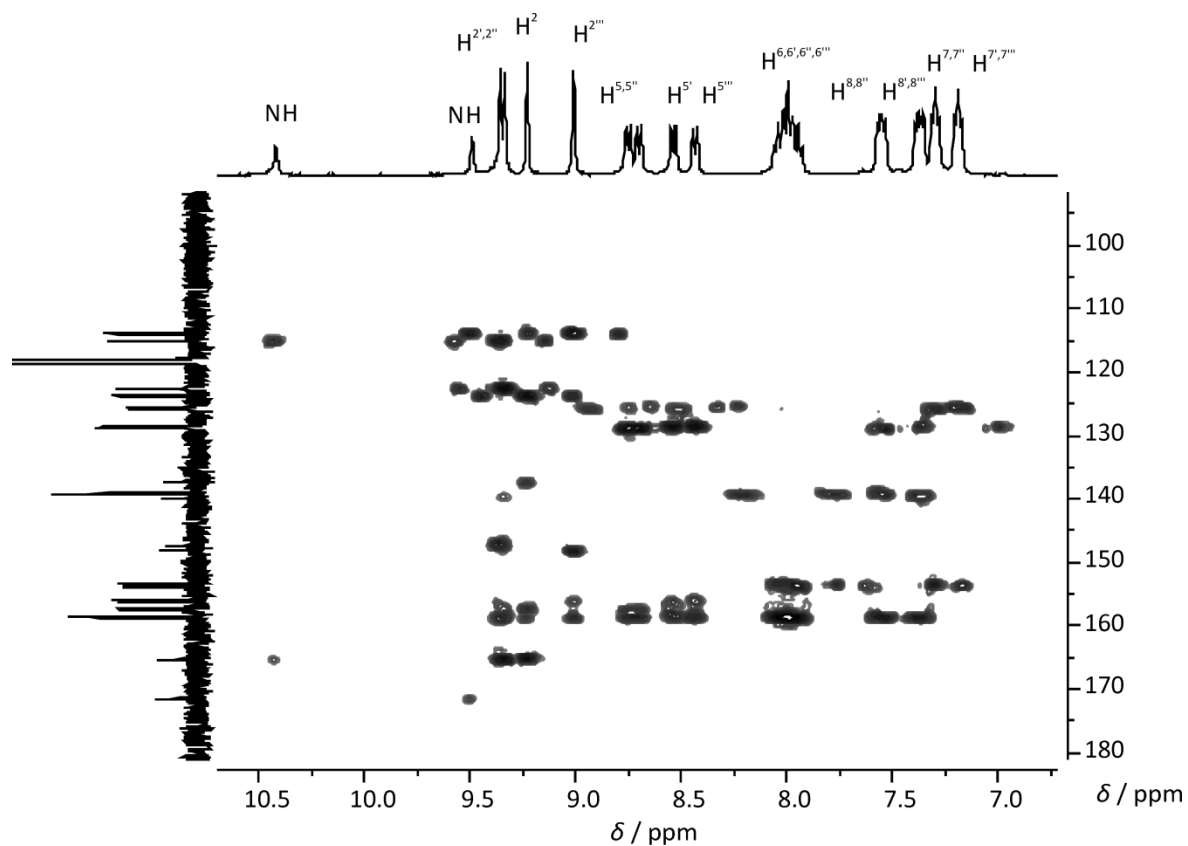


Figure S8.  $^{19}\text{F}$  NMR spectrum of  $\mathbf{8}(\text{PF}_6)_2$  in  $\text{CD}_3\text{CN}$ .



**Figure S9.** CH-HSQC spectrum of the aromatic region of  $3(\text{PF}_6)_4$  in  $\text{CD}_3\text{CN}$ .



**Figure S10.** CH-HMBC spectrum of the aromatic region of  $3(\text{PF}_6)_4$  in  $\text{CD}_3\text{CN}$ .

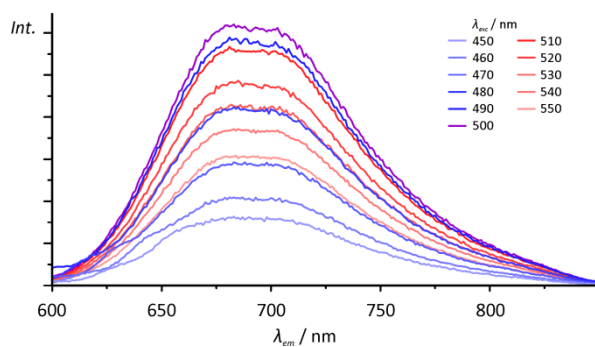


**Figure S11.** Emission spectra of  $3^{4+}$  at room temperature in deaerated  $\text{CH}_3\text{CN}$  with varying excitation wavelength.

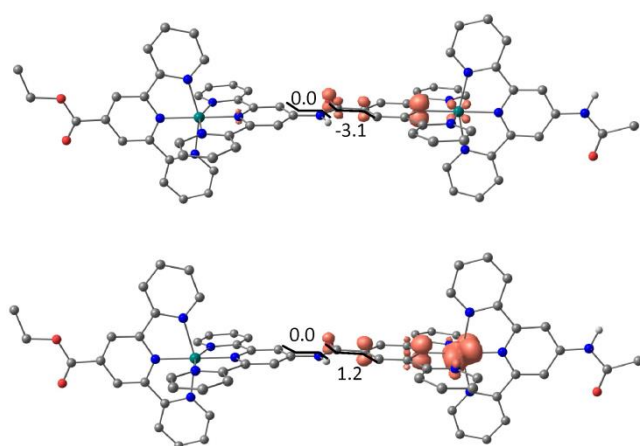


**Figure S12.** DFT (B3LYP, LANL2DZ) optimized geometric structures of  $3^{3+}$  (doublet, IEFPCM: acetonitrile) and  $3^{4+}$  (triplet, gasphase) including tpy-NHCO-tpy dihedral angles ( $^\circ$ ) and calculated spin densities. Contour value: 0.01, CH hydrogen atoms are omitted.

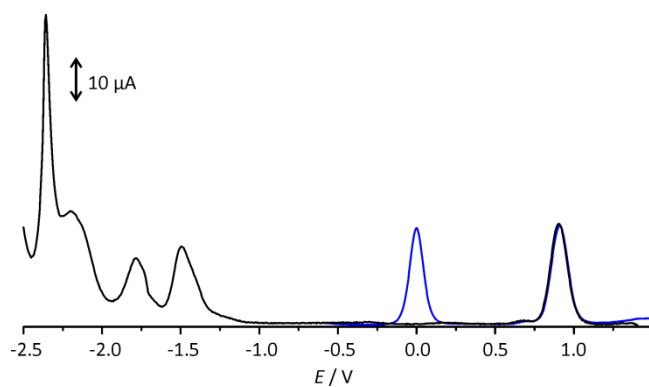


**Figure S13.** Square wave voltammogram of  $3^{4+}$  in the presence of 0.1 M  $[\text{nBu}_4\text{N}][\text{PF}_6]$  as supporting electrolyte in acetonitrile. Black line shows the SWV in the absence of ferrocene, blue line in the presence of 2 eq. of ferrocene as internal standard for referencing.

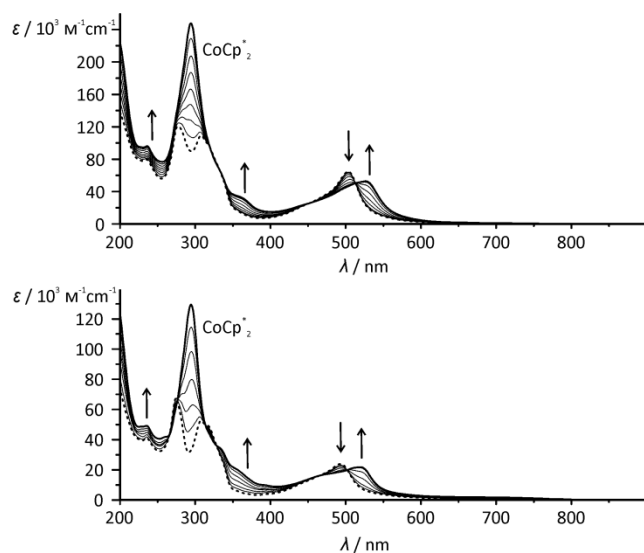


**Figure S14.** UV/Vis absorption spectra of  $\mathbf{3}^{4+}$  and  $\mathbf{4}^{2+}$  in dry  $\text{CH}_3\text{CN}$  upon titration with a solution of  $\text{CoCp}^*_2$  in  $\text{CH}_3\text{CN}$  (0 eq.  $\rightarrow$  4 eq. for  $\mathbf{3}^{4+}$ , 0 eq.  $\rightarrow$  2 eq. for  $\mathbf{4}^{2+}$ ). Arrows indicate spectral changes. Dashed lines indicate spectra of  $\mathbf{3}^{4+}$  and  $\mathbf{4}^{2+}$ , bold lines show deprotonated species  $\mathbf{3-H}^{3+}$  and  $\mathbf{4-H}^+$ .

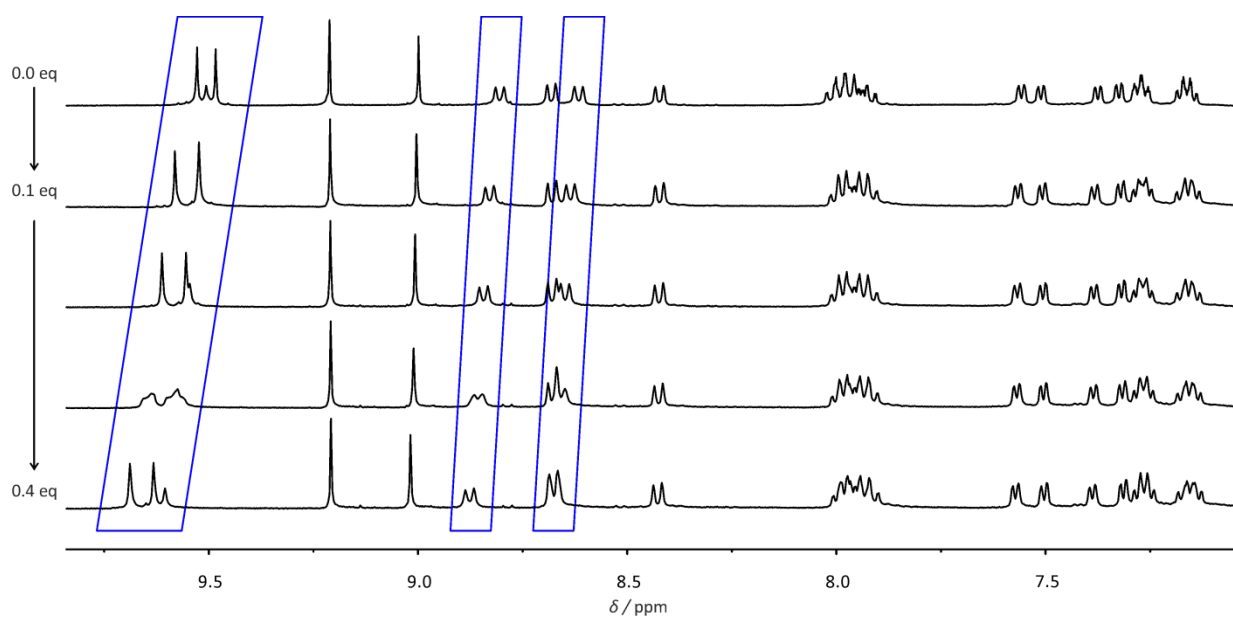


**Figure S15.**  $^1\text{H}$  NMR spectra of  $\mathbf{3}^{4+}$  in  $\text{CD}_3\text{CN}$  upon deprotonation to  $\mathbf{3-H}^{3+}$  with substoichiometric amounts of  $\text{CoCp}^*_2$ . Blue frames highlight most significant spectral changes.

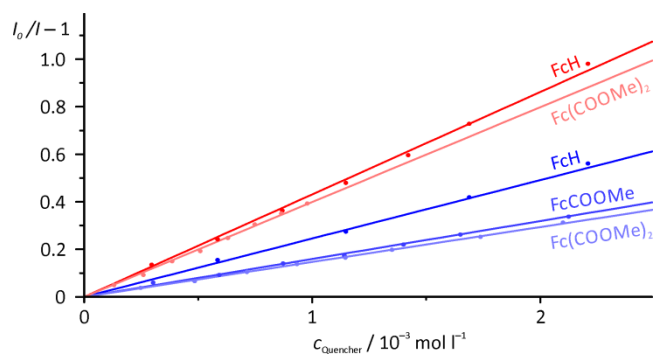


**Figure S16.** Stern-Volmer plots of the mono- and dinuclear complexes  $4^{2+}$  (blue) and  $3^{4+}$  (red) employing ferrocene derivatives as quenchers. Plots were obtained using complex concentrations of  $c = 2 \times 10^{-5} \text{ mol l}^{-1}$ .

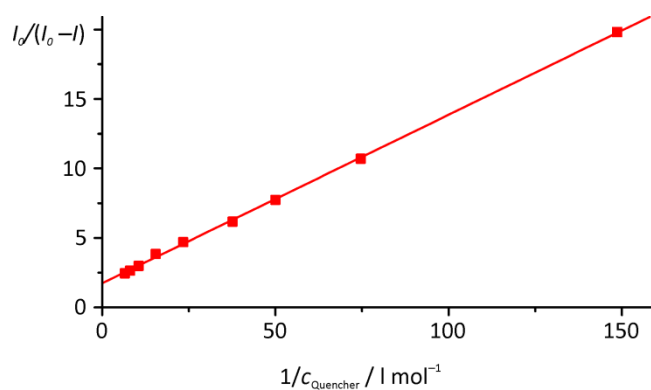


**Figure S17.** Linearized Stern-Volmer plot  $I_0/(I_0 - I)$  of the dinuclear complex  $3^{4+}$  employing *N,N*-dimethylaniline as quencher. Plot was obtained using a complex concentration of  $c = 2 \times 10^{-5} \text{ mol l}^{-1}$ .



### 6.3 SUPPORTING INFORMATION TO 3.2: UNDERSTANDING THE EXCITED STATE BEHAVIOR OF CYCLOMETALATED BIS(TRIDENTATE)RUTHENIUM(II) COMPLEXES: A COMBINED EXPERIMENTAL AND THEORETICAL STUDY

**Synthesis of ethyl 3,5-di-(pyridin-2-yl)benzoate L3:** Ethyl 3,5-dibromobenzoate **LD** (1.21 g, 3.93 mmol, 1 eq.) was dissolved under argon in abs. toluene (50 ml) and tri-*n*-butyl-(pyridin-2-yl)stannane<sup>1</sup> (4.94 g, 13.4 mmol, 3.4 eq), Pd(PPh<sub>3</sub>)<sub>4</sub> (0.17 g, 0.15 mmol, 4 mol%) and lithium chloride (1.39 g, 8.3 eq) were added. The reaction mixture was heated to reflux for 23 h. After cooling to room temperature the reaction was quenched with aqueous sodium hydroxide solution (1 M, 50 ml). The mixture was extracted with ethyl acetate (3×100 ml) and the combined organic phases were dried over magnesium sulfate before evaporation of the solvent under reduced pressure. The crude product was purified by column chromatography on silica gel (diethyl ether/hexanes 1:2, after elution of organotin impurities: diethyl ether/hexanes 2:1). Ethyl 3,5-di-(pyridin-2-yl)benzoate was obtained as colorless solid. Yield: 767 mg (2.52 mmol, 64 %). Anal. Calc. C<sub>19</sub>H<sub>16</sub>N<sub>2</sub>O<sub>2</sub> (304.34): C, 74.98; H, 5.30; N, 9.20. Found: C, 74.66; H, 5.64; N, 9.12. MS(FD<sup>+</sup>): *m/z* (%) = 304.2 (100) [M]<sup>+</sup>. <sup>1</sup>H NMR (CD<sub>2</sub>Cl<sub>2</sub>): δ [ppm] = 8.96 (s, 1H, H<sup>9</sup>), 8.74 (d, <sup>3</sup>J<sub>HH</sub> = 4 Hz, 2H, H<sup>8</sup>), 8.70 (s, 2H, H<sup>2</sup>), 7.93 (d, <sup>3</sup>J<sub>HH</sub> = 8 Hz, 2H, H<sup>5</sup>), 7.83 (dd, <sup>3</sup>J<sub>HH</sub> = 4 Hz, <sup>3</sup>J<sub>HH</sub> = 11 Hz, 2H, H<sup>6</sup>), 7.31 (m, 2H, H<sup>7</sup>), 4.44 (q, <sup>3</sup>J<sub>HH</sub> = 7 Hz, 2H, H<sup>11</sup>), 1.45 (t, <sup>3</sup>J<sub>HH</sub> = 7 Hz, 3H, H<sup>12</sup>). <sup>13</sup>C{<sup>1</sup>H} NMR (CD<sub>3</sub>CN): δ [ppm] = 166.8 (s, C<sup>10</sup>), 156.5 (s, C<sup>4</sup>), 150.4 (s, C<sup>8</sup>), 140.8 (s, C<sup>3</sup>), 137.4 (s, C<sup>6</sup>), 132.3 (s, C<sup>1</sup>), 130.0 (s, C<sup>9</sup>), 128.6 (s, C<sup>2</sup>), 123.3 (s, C<sup>7</sup>), 121.1 (s, C<sup>5</sup>), 61.8 (s, C<sup>11</sup>), 14.8 (s, C<sup>12</sup>).

#### Characterization of [Ru(dpb-COOEt)(tpy-NH<sub>2</sub>)](PF<sub>6</sub>)<sub>3</sub>(PF<sub>6</sub>)

Anal. Calc. for C<sub>34</sub>H<sub>27</sub>F<sub>6</sub>N<sub>6</sub>O<sub>2</sub>PRu (797.7): C, 51.20; H, 3.41; N, 10.54. Found: C, 51.49; H, 3.48; N, 10.22. MS(ESI<sup>+</sup>): *m/z* (%) = 653.1 (100) [M-PF<sub>6</sub>]<sup>+</sup>. HR-MS(ESI<sup>+</sup>, *m/z*): Calcd. for C<sub>34</sub>H<sub>27</sub>N<sub>6</sub>O<sub>2</sub>Ru [M-PF<sub>6</sub>]<sup>+</sup>: 647.1271; Found: 647.1273. <sup>1</sup>H NMR (CD<sub>3</sub>CN): δ [ppm] = 8.81 (s, 2H, H<sup>2B</sup>), 8.25 (d, <sup>3</sup>J<sub>HH</sub> = 8 Hz, 2H, H<sup>5B</sup>), 8.19 (d, <sup>3</sup>J<sub>HH</sub> = 8 Hz, 2H, H<sup>5A</sup>), 8.06 (s, 2H, H<sup>2A</sup>), 7.69 – 7.55 (m, 4H, H<sup>6A</sup>, H<sup>6B</sup>), 7.34 (d, <sup>3</sup>J<sub>HH</sub> = 5 Hz, 2H, H<sup>8B</sup>), 6.90 (d, <sup>3</sup>J<sub>HH</sub> = 5 Hz, 2H, H<sup>8A</sup>), 6.83 – 6.72 (m, 4H, H<sup>7A</sup>, H<sup>7B</sup>), 5.92 (s, 2H, NH<sub>2</sub>), 4.50 (q, <sup>3</sup>J<sub>HH</sub> = 7 Hz, 2H, H<sup>11</sup>), 1.51 (t, <sup>3</sup>J<sub>HH</sub> = 7 Hz, 3H, H<sup>12</sup>). <sup>13</sup>C{<sup>1</sup>H} NMR (CD<sub>3</sub>CN): δ [ppm] = 235.6 (s, C<sup>9B</sup>), 169.2 (s, C<sup>4B</sup>), 168.8 (s, C<sup>10</sup>), 160.3 (s, C<sup>4A</sup>), 155.7 (s, C<sup>8A</sup>), 155.3 (s, C<sup>1A</sup>), 153.4 (s, C<sup>3A</sup>), 152.6 (s, C<sup>8B</sup>), 143.9 (s, C<sup>3B</sup>), 136.2 (s, C<sup>6B</sup>), 136.1 (s, C<sup>6A</sup>), 126.9 (s, C<sup>7A</sup>), 124.3 (s, C<sup>2B</sup>), 124.0 (s, C<sup>5A</sup>), 122.9 (s, C<sup>7B</sup>), 121.8 (s, C<sup>1B</sup>), 120.6 (s, C<sup>5B</sup>), 108.3 (s, C<sup>2A</sup>), 61.4 (s, C<sup>11</sup>), 15.0 (s, C<sup>12</sup>).

<sup>1</sup> Bolm, C.; Ewald, M.; Felder, M.; Schlingloff, G. *Chem. Ber.* **1992**, *125*, 1169–1190.

## Ligand syntheses

The synthesis of ethyl dipyridylbenzoate **L3** was carried out adopting the literature-known synthesis of the analogous methyl ester.<sup>2,3</sup>

For the synthesis of the amino acid derivatives **1**<sup>+</sup> and **2**<sup>+</sup> synthetic procedures to the amino-substituted ligands **L1** and **L2** needed to be developed. In order to minimize the amount of undesired side reactions during the complexation we decided to protect the rather reactive amino functions by acetyl groups. The introduction of acetamide via palladium-catalyzed cross-coupling reactions has only been shown to occur with rather elaborate catalyst/ligand systems<sup>4,5,6</sup> and is highly dependent on the type of leaving group and the electronics of the aromatic system.<sup>7</sup> Screening experiments with one of Buchwald's amidation precatalysts (**[Pd]<sub>2</sub>**)<sup>8</sup> showed reasonable reactivity in the reaction of 1-bromo-3,5-dipyrid-2-ylbenzene and acetamide in refluxing toluene. With XantPhos as chelating ligand and sodium *tert*-butoxide as supporting base *N*-acetyl-3,5-di-(pyridin-2-yl)aniline **L1** was isolated in 78 % yield. Remarkably, under nearly the same conditions 4'-chloroterpyridine could be successfully reacted with acetamide in xylenes. Slightly higher reaction temperatures (130 °C instead of 110 °C) and longer reaction times (20 h instead of 8 h) gave *N*-acetyl-4'-amino-2,2':6',2''-terpyridine **L2** in essentially identical yields (76 %). Repeatedly, 4'-amino-2,2':6',2''-terpyridine was isolated as major byproduct in this reaction because the terpyridine fragment substantially increases the nucleophilicity of the carbonyl carbon and facilitates hydrolysis under the basic reaction conditions. The byproduct could eventually be transformed to the desired product by treatment with acetylchloride in refluxing dichloromethane (see Procedure b). Both *N*-acetylated ligands **L1** and **L2** were fully characterized by FD mass spectra (Figure S1) and NMR spectroscopy (Figures S4-S7) and their purity was confirmed by elemental analysis (see Experimental Section).

<sup>2</sup> Chen, L. S.; Chen, G. J.; Tamborski, C. J. *Organomet. Chem.* **1981**, *215*, 281–291.

<sup>3</sup> Williams, J. A. G.; Beeby, A.; Davies, E. S.; Weinstein, J. A.; Wilson, C. *Inorg. Chem.* **2003**, *42*, 8609–8611.

<sup>4</sup> Yin, J.; Buchwald, S. L. *J. Am. Chem. Soc.* **2002**, *124*, 6043–6048.

<sup>5</sup> Fors, B. P.; Dooleweerd, K.; Zeng, Q.; Buchwald, S. L. *Tetrahedron* **2009**, *65*, 6576–6583

<sup>6</sup> Crawford, S. M.; Lavery, C. B.; Stradiotto, M. *Chem. Eur. J.* **2013**, *19*, 16760–16771.

<sup>7</sup> Surry, D. S.; Buchwald, S. L. *Chem. Sci.* **2010**, *2*, 27–50.

<sup>8</sup> Bruno, N. C.; Tudge, M. T.; Buchwald, S. L. *Chem. Sci.* **2013**, *4*, 916–920.

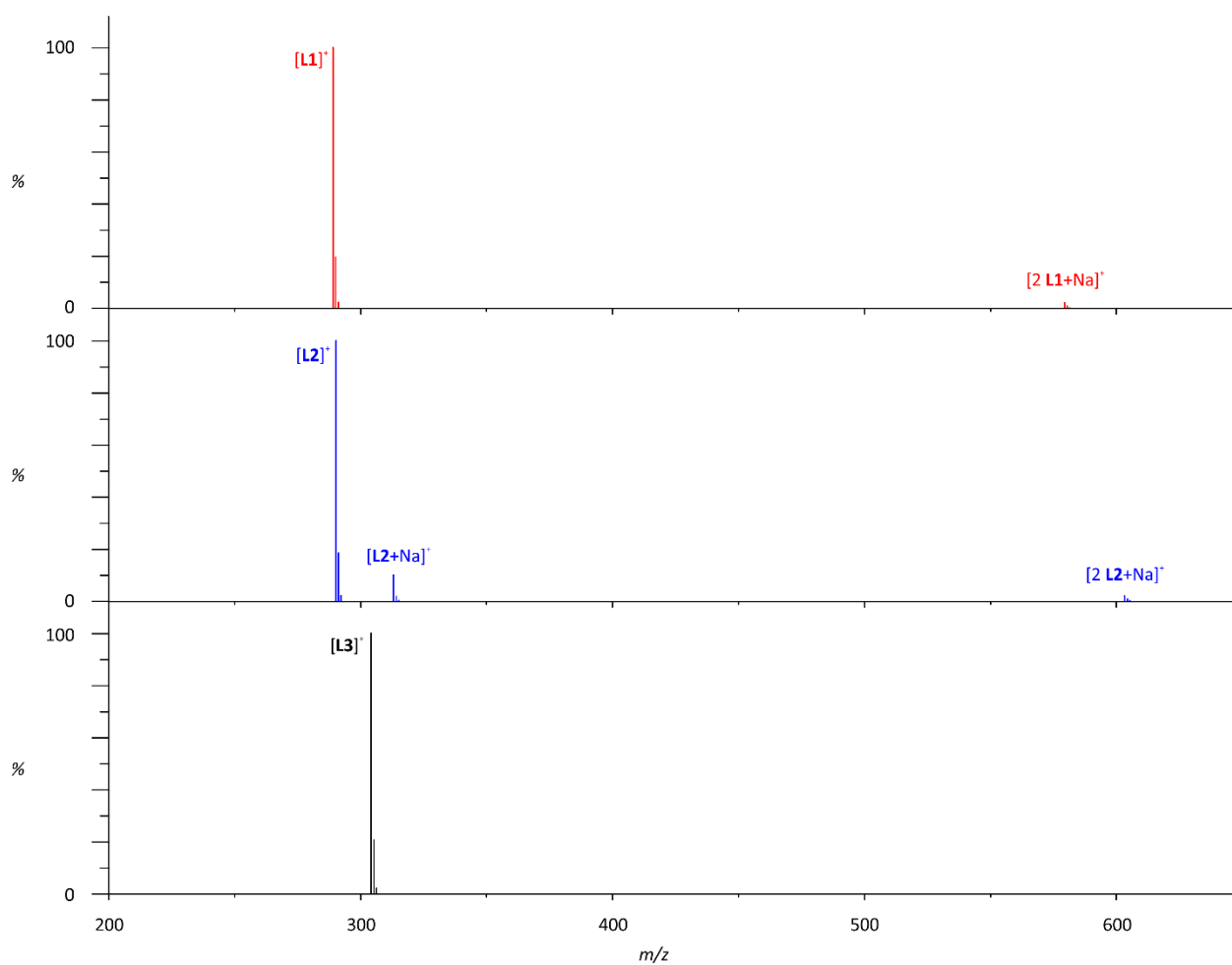


Figure S1 FD mass spectra of L1, L2 and L3 in  $\text{CH}_2\text{Cl}_2$ .

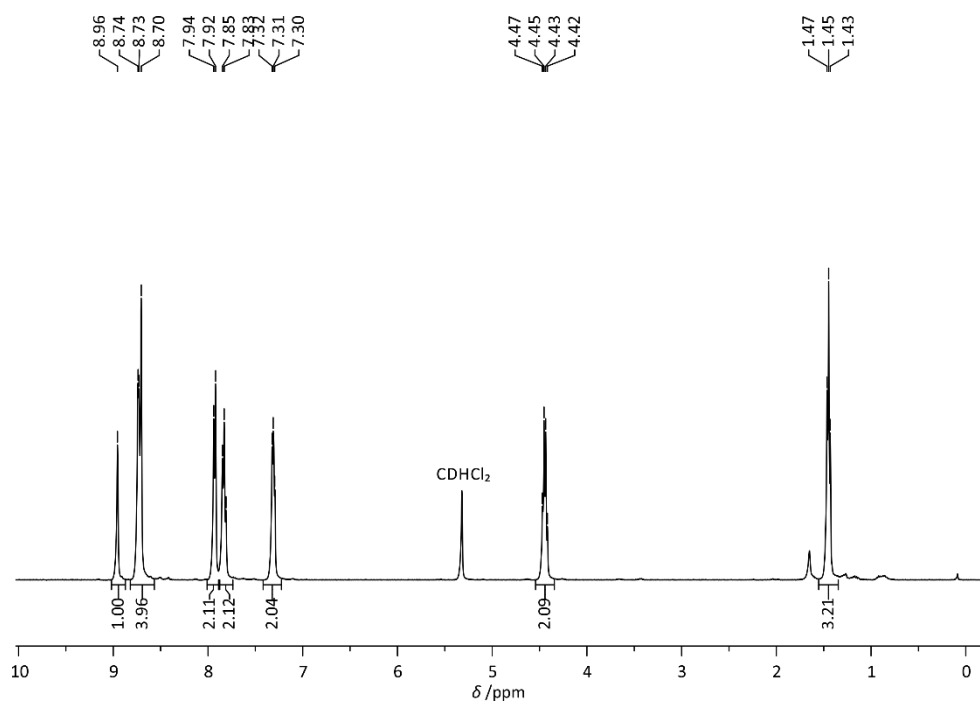


Figure S2  $^1\text{H}$  NMR spectrum (400 MHz,  $\text{CD}_2\text{Cl}_2$ ) of L3.

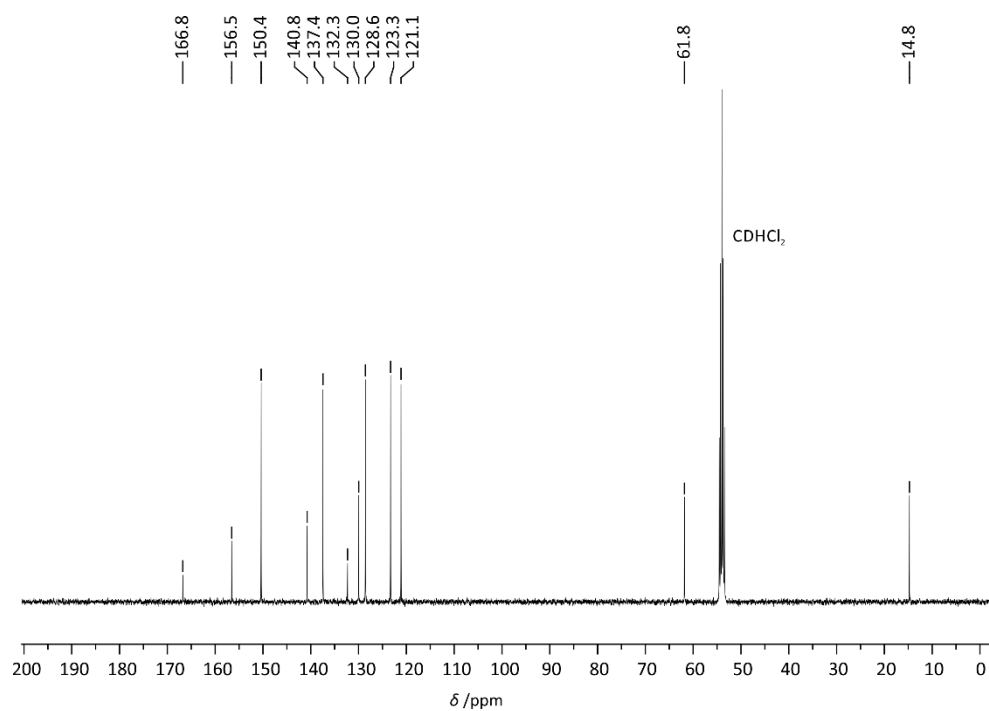


Figure S3  $^{13}\text{C}$  NMR spectrum (100 MHz,  $\text{CD}_2\text{Cl}_2$ ) of L3.

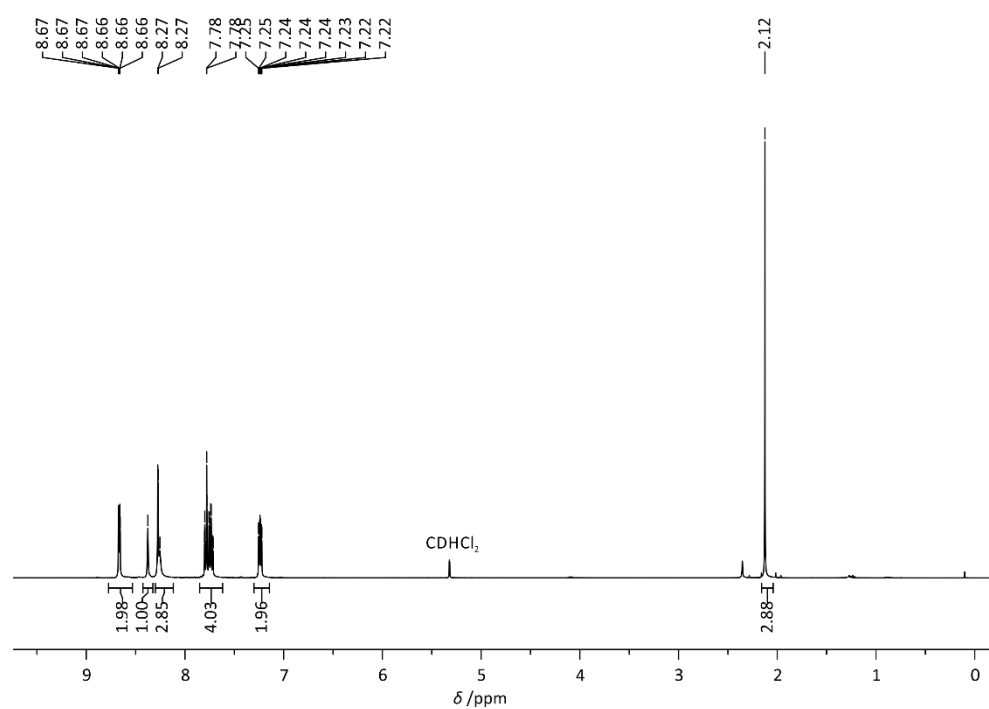


Figure S4  $^1\text{H}$  NMR spectrum (400 MHz,  $\text{CD}_2\text{Cl}_2$ ) of L1.

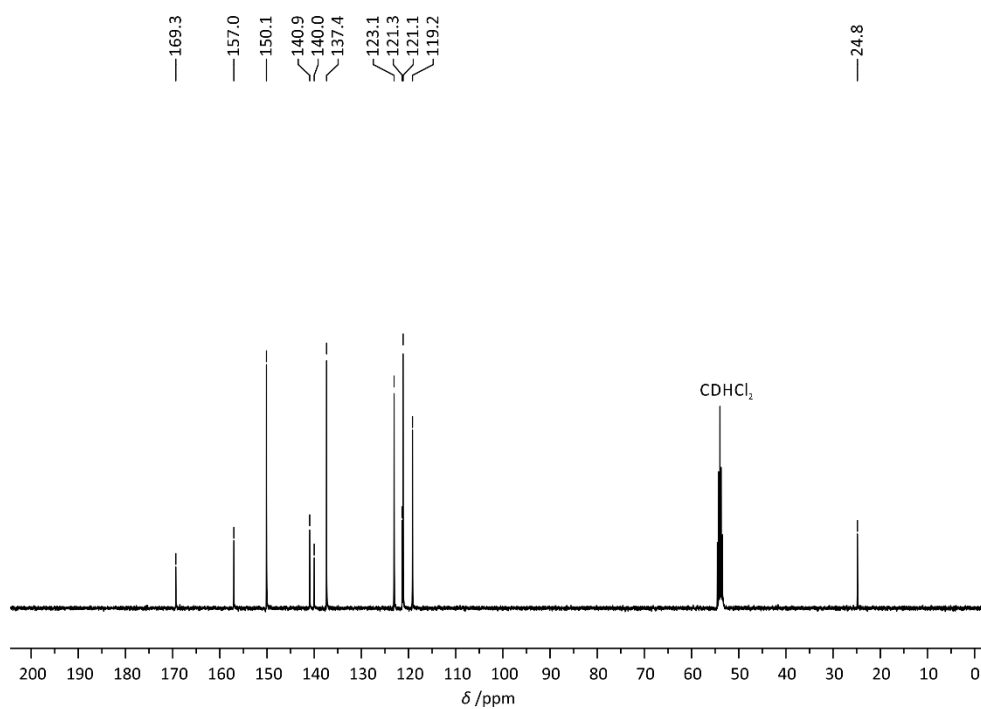


Figure S5 <sup>13</sup>C NMR spectrum (100 MHz, CD<sub>2</sub>Cl<sub>2</sub>) of L1.

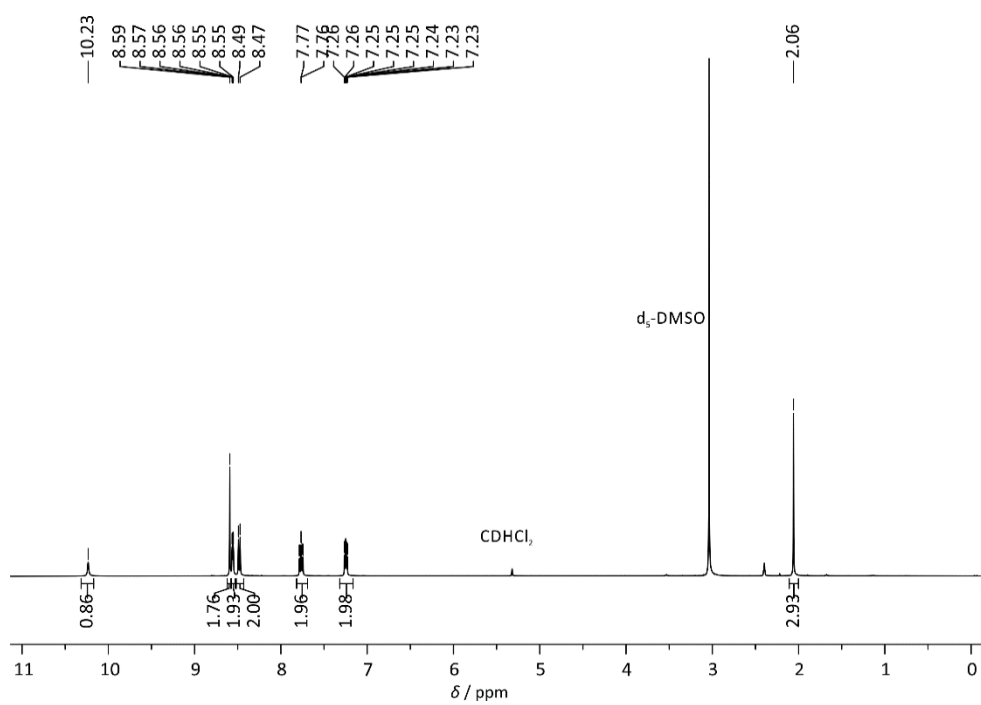
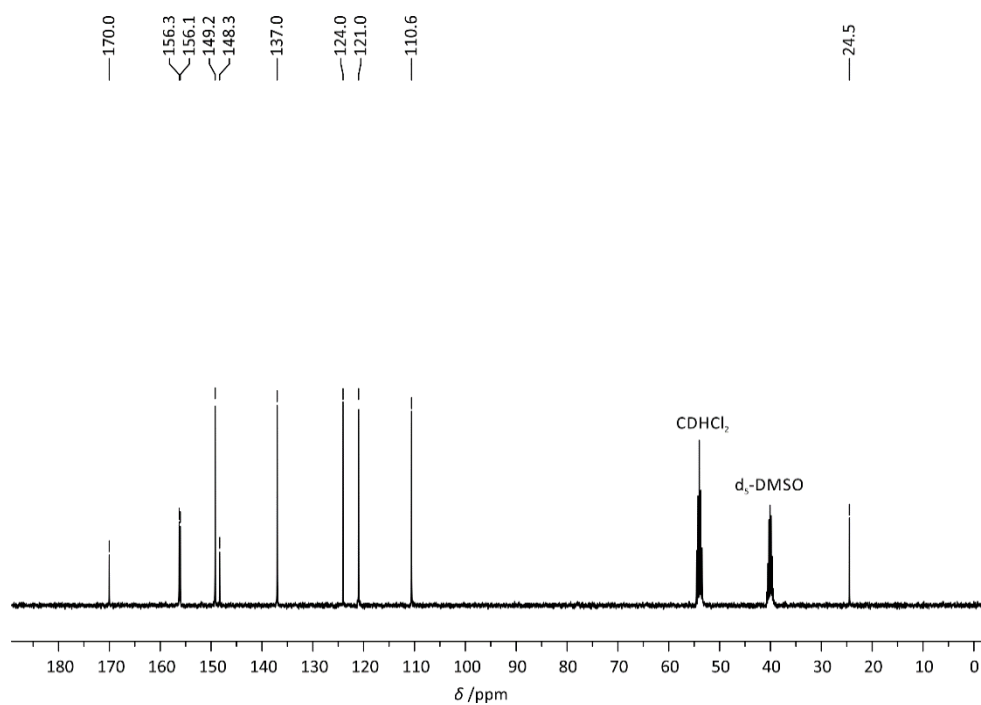
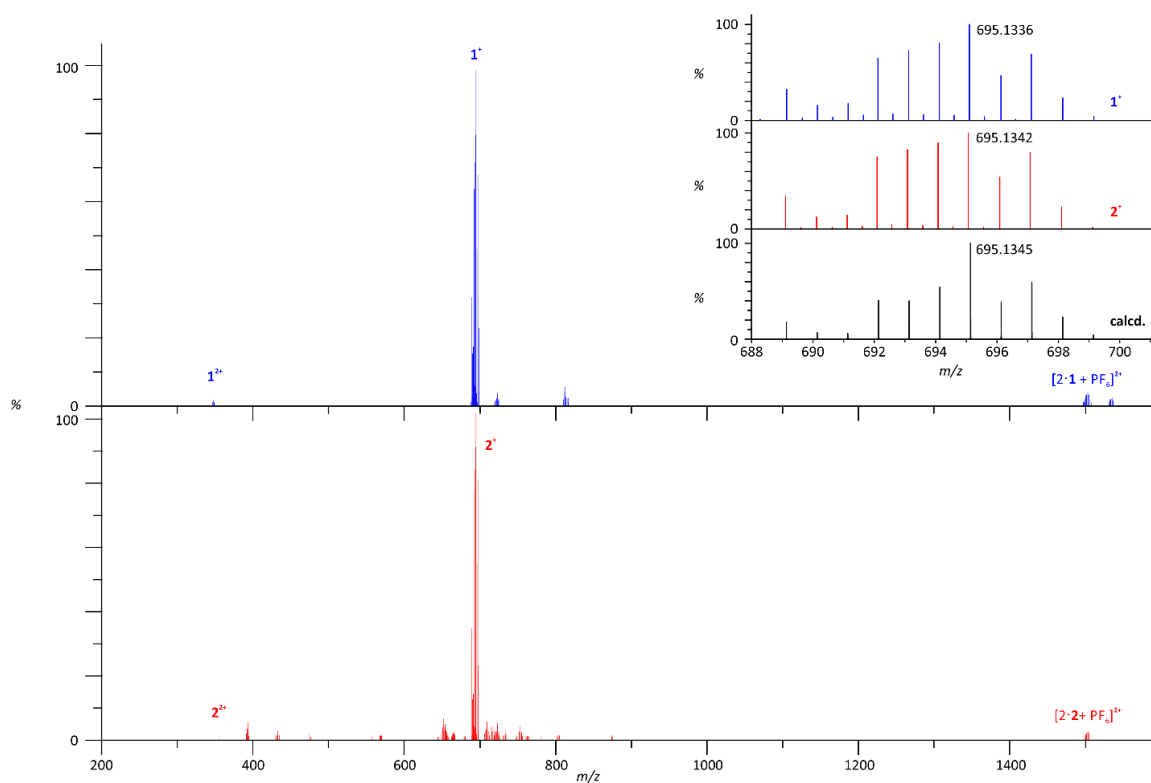


Figure S6 <sup>1</sup>H NMR spectrum (400 MHz, 0.5 ml CD<sub>2</sub>Cl<sub>2</sub> + 0.1 ml d<sub>6</sub>-DMSO) of L2.



**Figure S7**  $^{13}\text{C}$  NMR spectrum (100 MHz, 0.5 ml  $\text{CD}_2\text{Cl}_2$  + 0.1 ml  $\text{d}_6\text{-DMSO}$ ) of **L2**.



**Figure S8** ESI mass spectra of **1**( $\text{PF}_6$ ) (top, blue) and **2**( $\text{PF}_6$ ) (bottom, red). Inset shows isotope pattern of the most intense peak  $[\text{M}-\text{PF}_6]^+$  including calculated mass distribution for  $\text{C}_{36}\text{H}_{29}\text{N}_6\text{O}_3\text{Ru}$ .



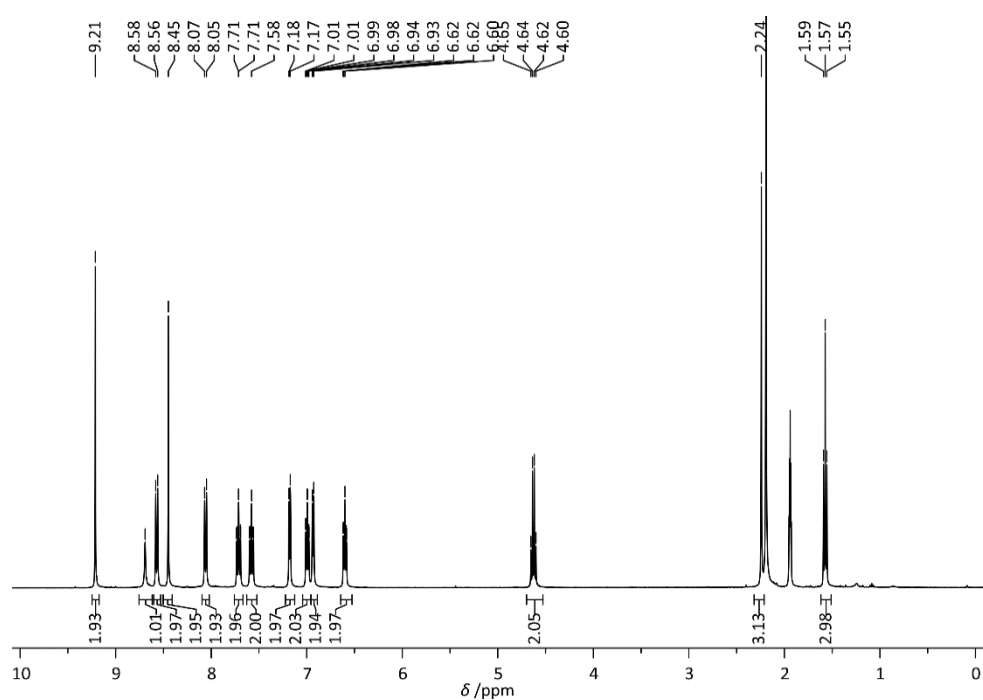


Figure S9  $^1\text{H}$  NMR spectrum (400 MHz,  $\text{CD}_3\text{CN}$ ) of **1**( $\text{PF}_6$ ).

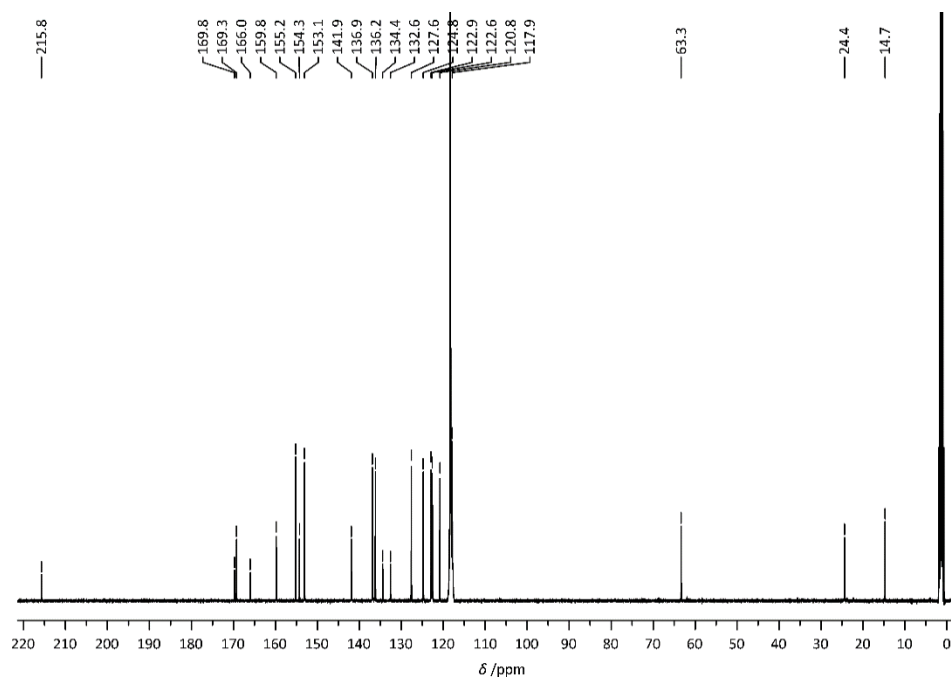
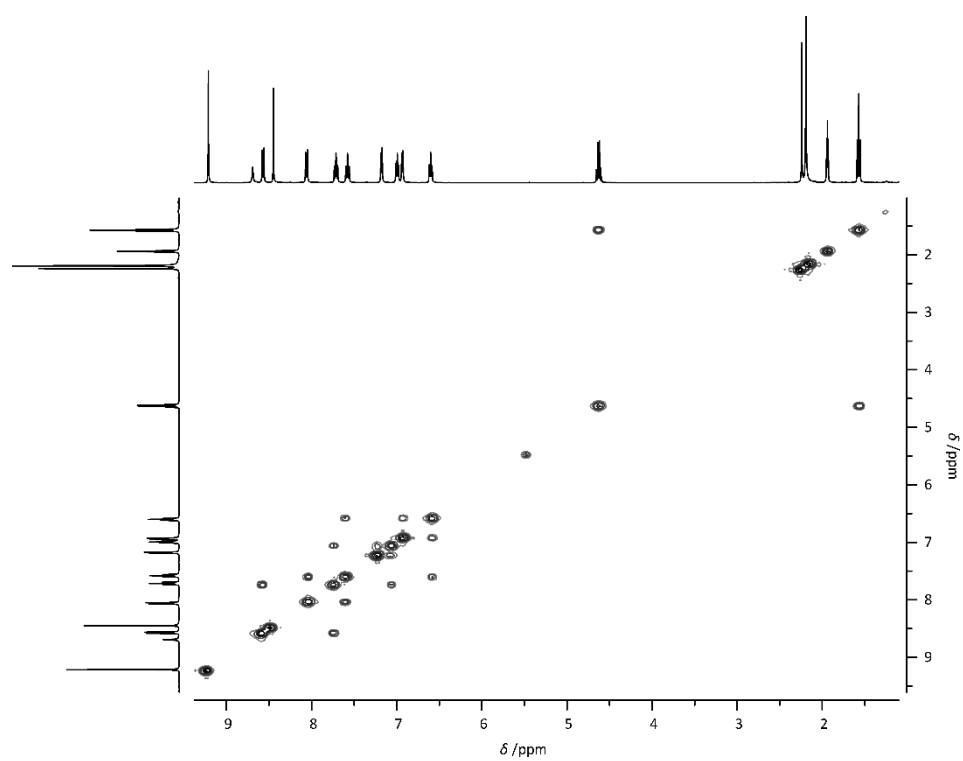
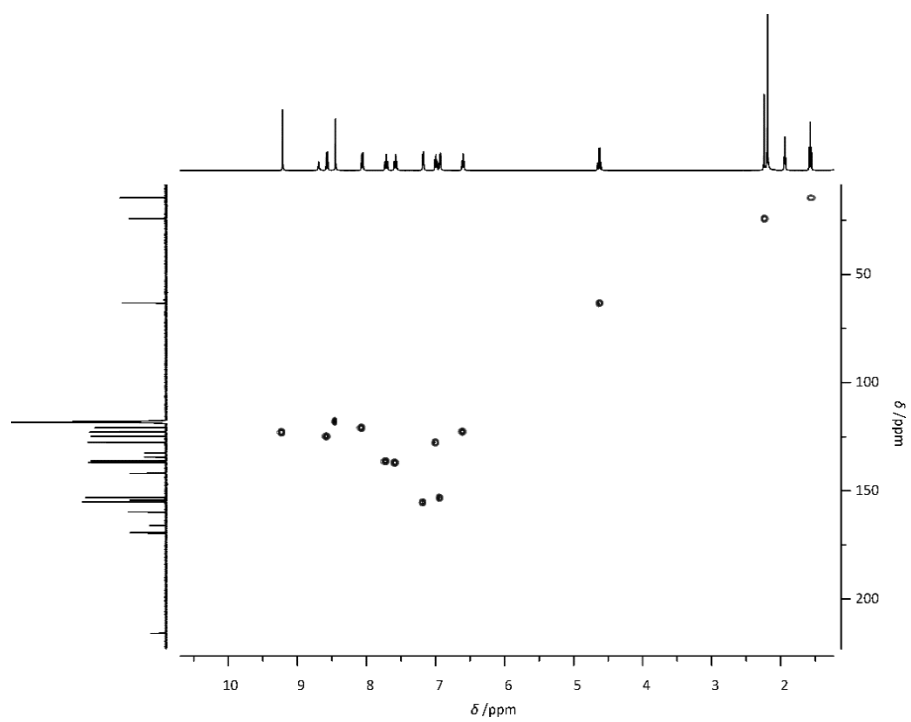


Figure S10  $^{13}\text{C}$  NMR spectrum (100 MHz,  $\text{CD}_3\text{CN}$ ) of **1**( $\text{PF}_6$ ).



**Figure S11**  $^1\text{H}$  COSY spectrum (400 MHz,  $\text{CD}_3\text{CN}$ ) of **1**( $\text{PF}_6$ ).



**Figure S12**  $^1\text{H}$ - $^{13}\text{C}$  HSQC spectrum ( $\text{CD}_3\text{CN}$ ) of **1**( $\text{PF}_6$ ).

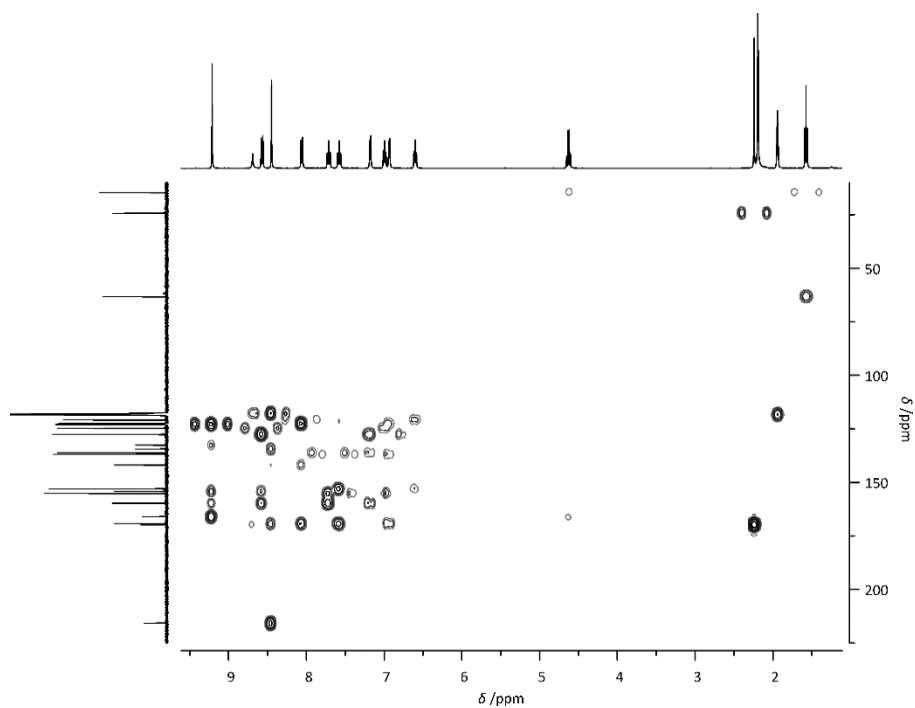


Figure S13  $^1\text{H}$ - $^{13}\text{C}$  HMBC spectrum ( $\text{CD}_3\text{CN}$ ) of **1**( $\text{PF}_6$ ).

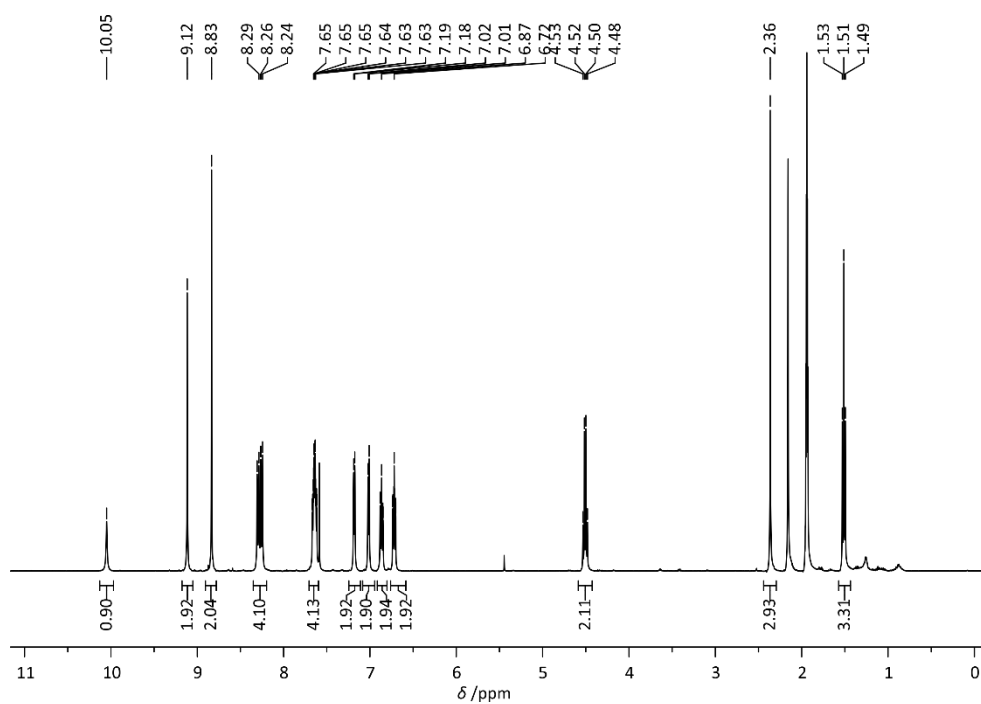


Figure S14  $^1\text{H}$  NMR spectrum (400 MHz,  $\text{CD}_3\text{CN}$ ) of **2**( $\text{PF}_6$ ).

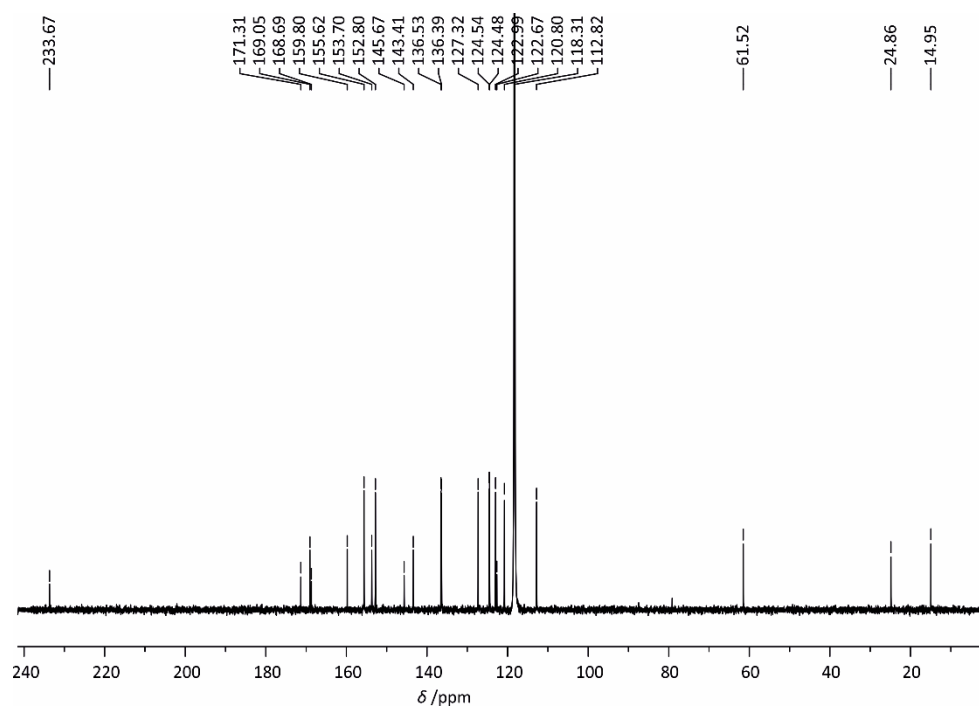


Figure S15  $^{13}\text{C}$  NMR spectrum (100 MHz,  $\text{CD}_3\text{CN}$ ) of **2**( $\text{PF}_6$ ).

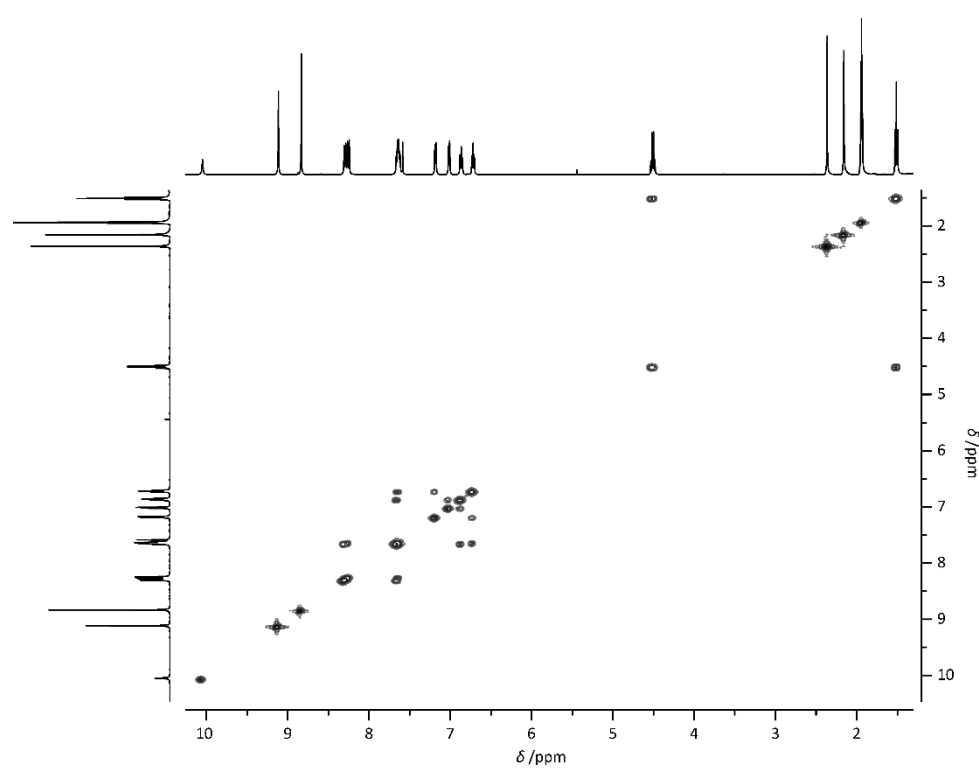


Figure S16  $^1\text{H}$  COSY spectrum (400 MHz,  $\text{CD}_3\text{CN}$ ) of **2**( $\text{PF}_6$ ).

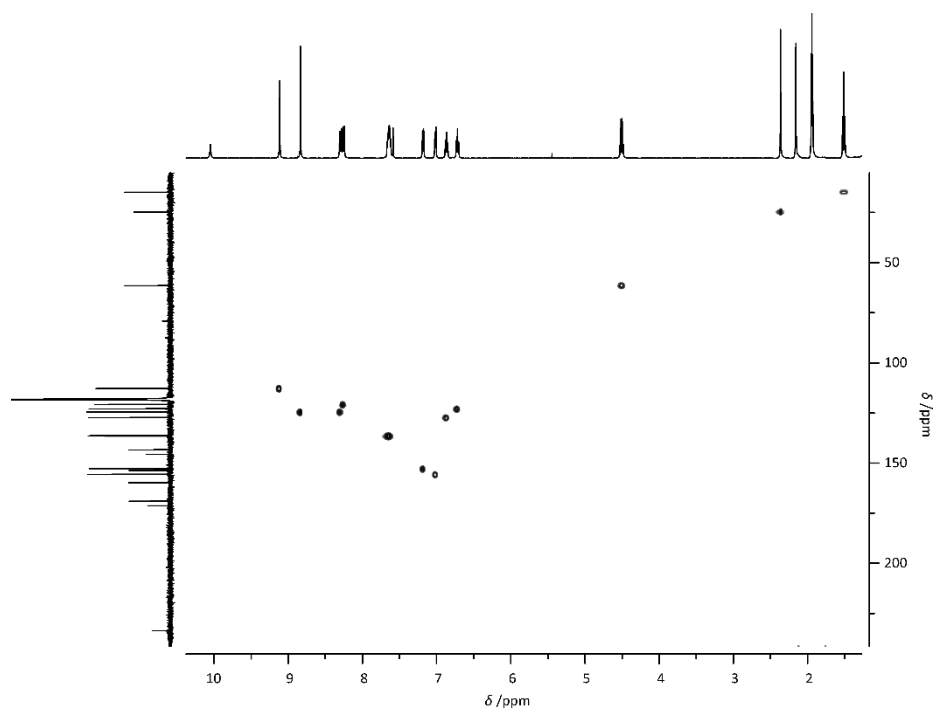


Figure S17  $^1\text{H}$ - $^{13}\text{C}$  HSQC spectrum ( $\text{CD}_3\text{CN}$ ) of **2**( $\text{PF}_6$ ).

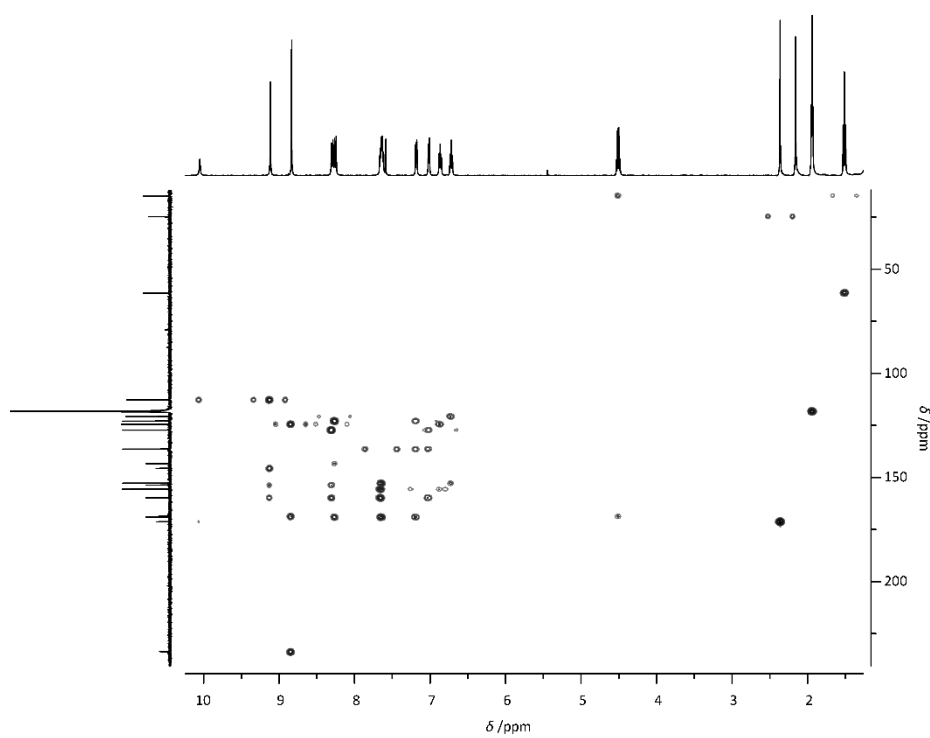


Figure S18  $^1\text{H}$ - $^{13}\text{C}$  HMBC spectrum ( $\text{CD}_3\text{CN}$ ) of **2**( $\text{PF}_6$ ).

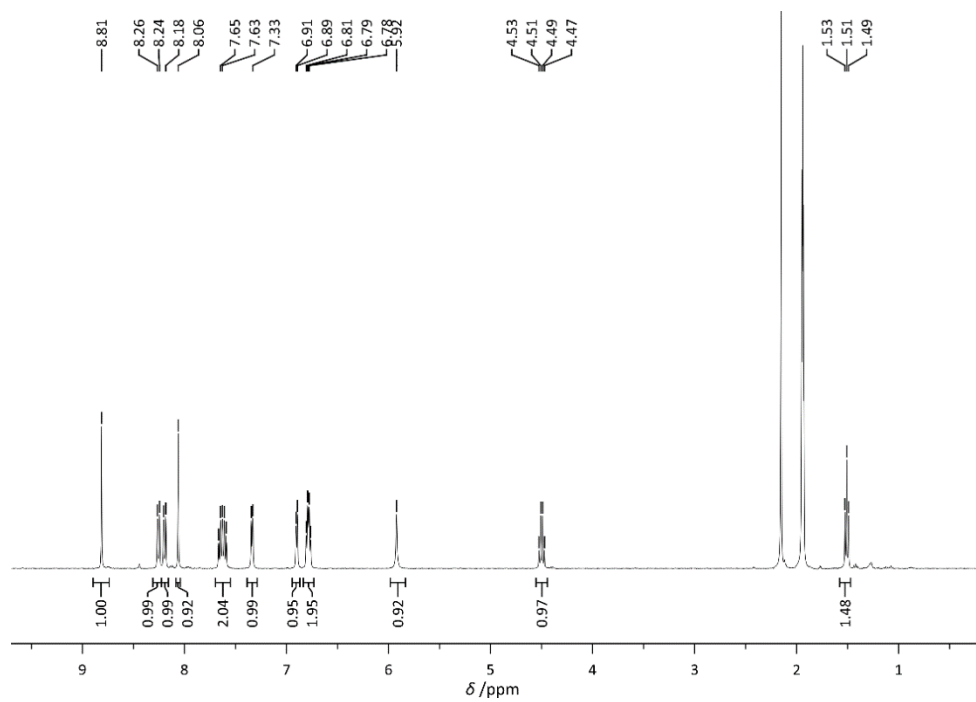


Figure S19  $^1\text{H}$  NMR spectrum (400 MHz,  $\text{CD}_3\text{CN}$ ) of **3**( $\text{PF}_6$ ).

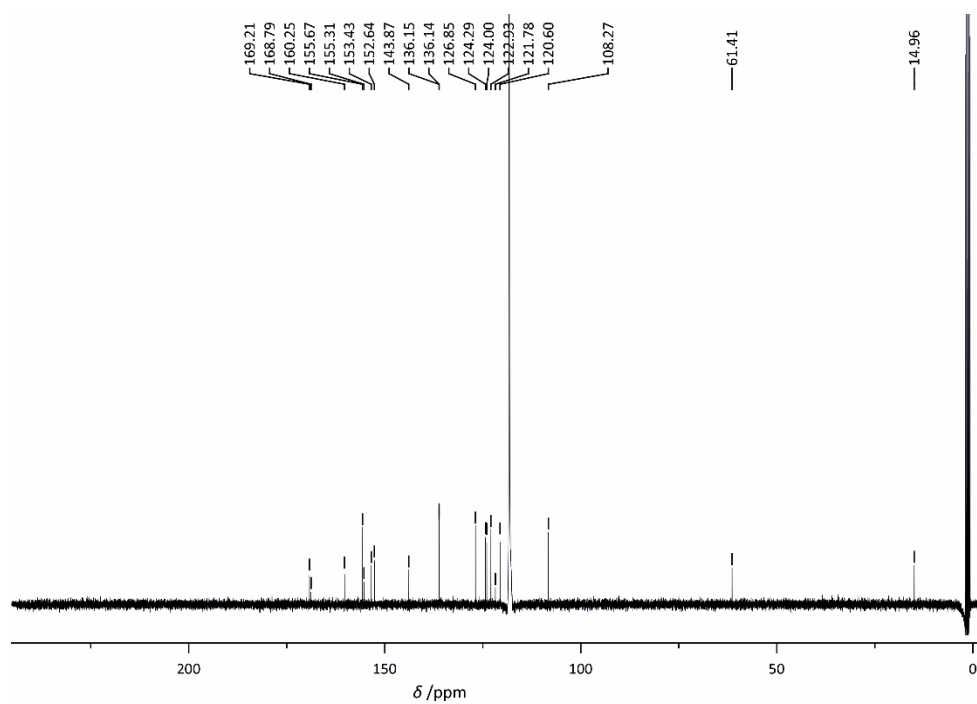


Figure S20  $^{13}\text{C}$  NMR spectrum (100 MHz,  $\text{CD}_3\text{CN}$ ) of **3**( $\text{PF}_6$ ).



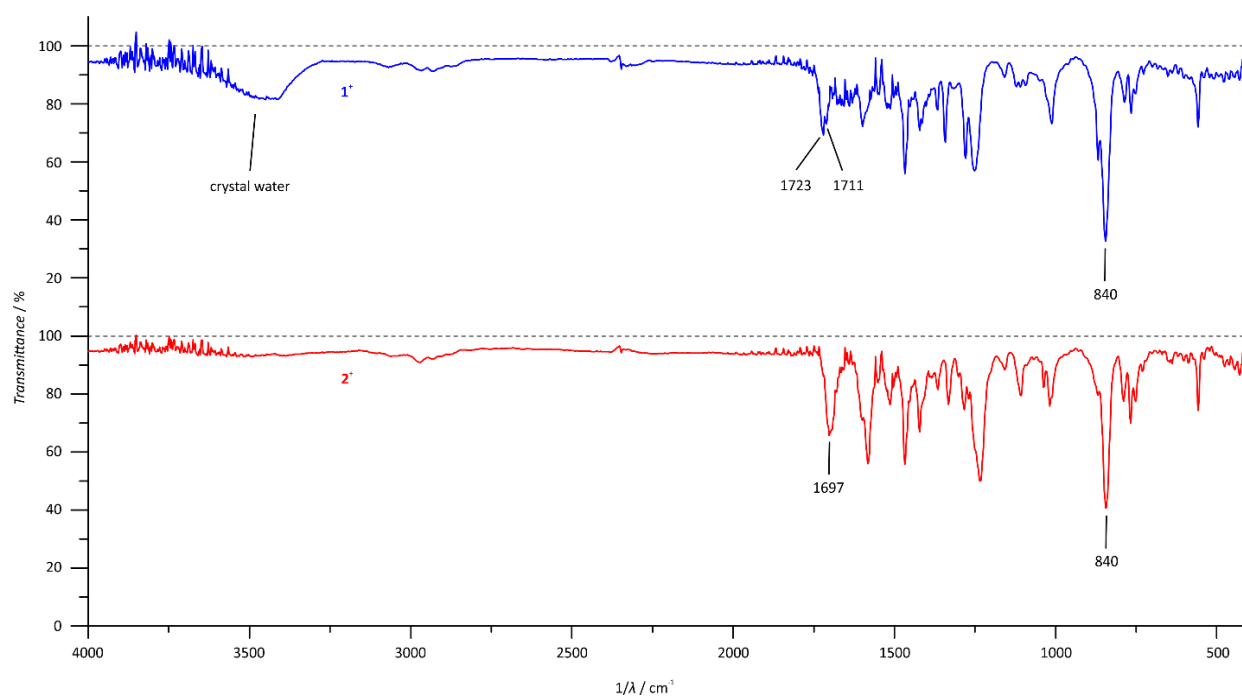
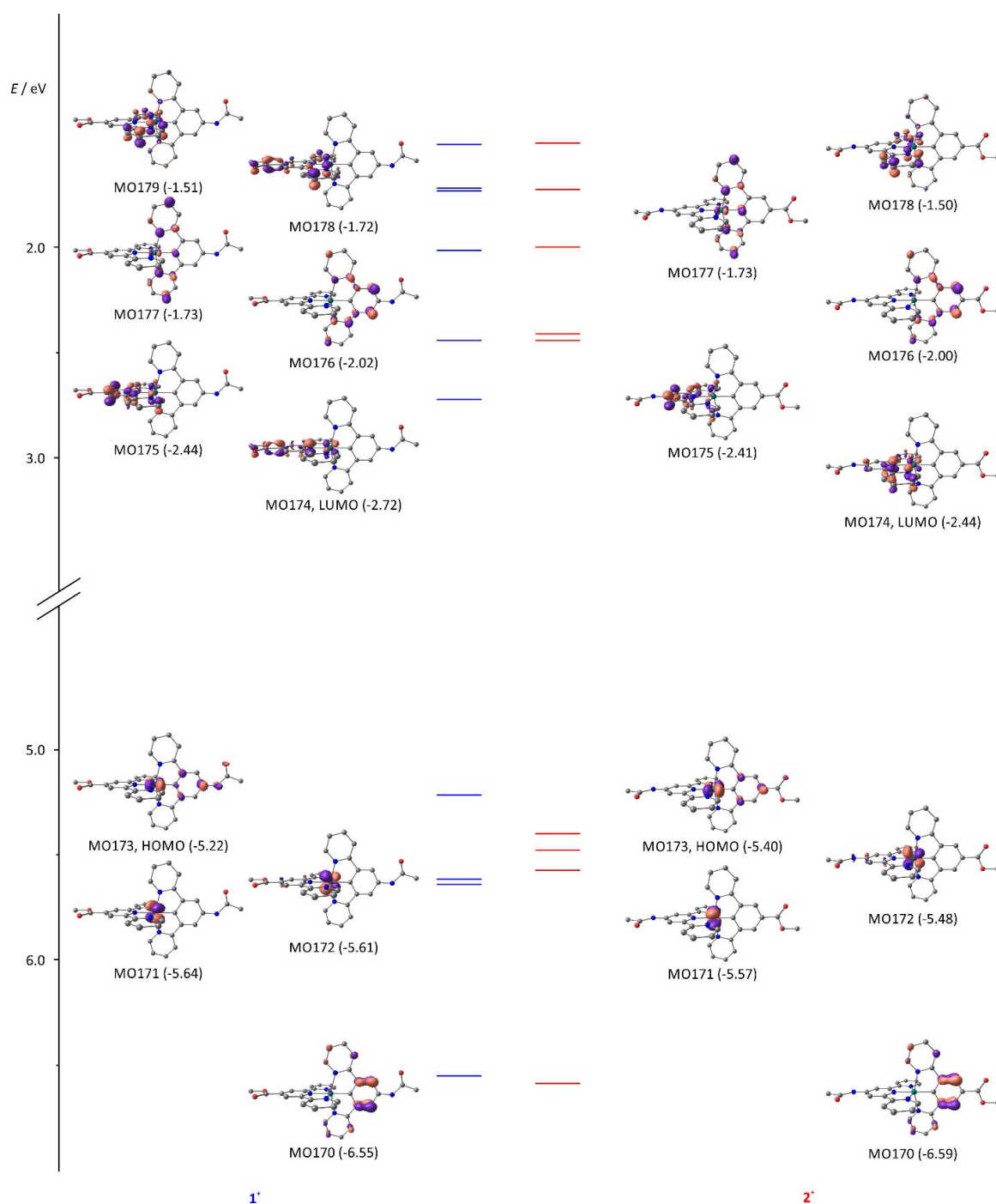
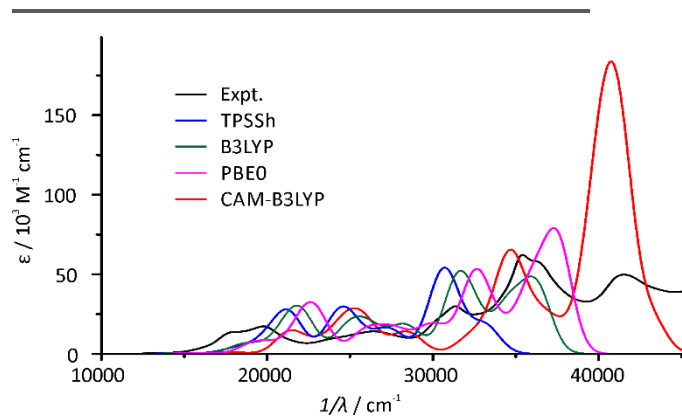


Figure S21 IR spectra of **1**(PF<sub>6</sub>) and **2**(PF<sub>6</sub>) in the solid state (KBr disk).



**Figure S22** MO diagram of  $1^+$  and  $2^+$  generated at the B3LYP, def2-TZVP, DKH, COSMO(acetonitrile) level of theory. Orbitals are plotted at a contour value of 0.07. Hydrogen atoms are omitted for clarity.



**Figure S23** Comparison of experimental (RT, acetonitrile solution) and calculated absorption spectra of  $1^+$  using different functionals.

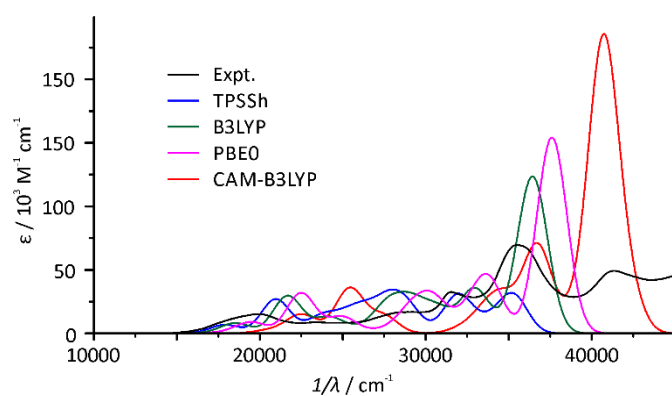
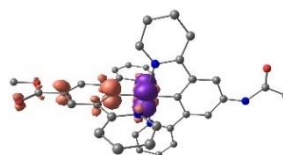
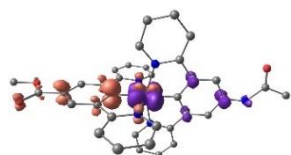


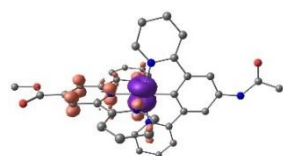
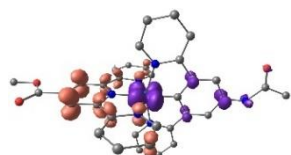
**Figure S24** Comparison of experimental (RT, acetonitrile solution) and calculated absorption spectra of  $2^+$  using different functionals.

**Table S1** First ten TD-DFT excitations of  $\mathbf{1}^+$  and all further with oscillator strengths  $f > 0.01$  (B3LYP, def2-TZVP, DKH, COSMO(acetonitrile)) and corresponding electronic difference densities  $\psi_{ES} - \psi_{GS}$  at a contour value of 0.005 (purple lobes indicate loss, orange lobes show increase of electron density upon excitation). Hydrogen atoms are omitted for clarity.

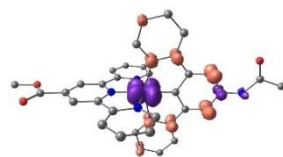
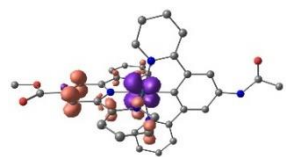
State 1:  $E = 12104 \text{ cm}^{-1}$ ,  $\lambda = 826 \text{ nm}$ ,  $f = 1.1 \times 10^{-5}$       State 2:  $E = 15095 \text{ cm}^{-1}$ ,  $\lambda = 663 \text{ nm}$ ,  $f = 5.5 \times 10^{-3}$



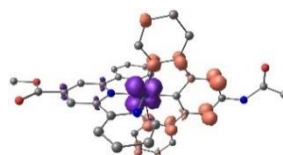
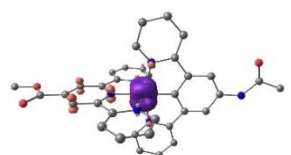
State 3:  $E = 15151 \text{ cm}^{-1}$ ,  $\lambda = 660 \text{ nm}$ ,  $f = 6.8 \times 10^{-4}$       State 4:  $E = 18194 \text{ cm}^{-1}$ ,  $\lambda = 550 \text{ nm}$ ,  $f = 0.030$



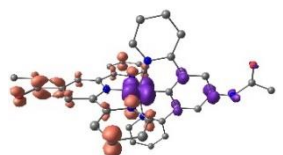
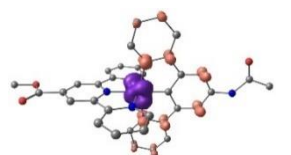
State 5:  $E = 19150 \text{ cm}^{-1}$ ,  $\lambda = 522 \text{ nm}$ ,  $f = 0.040$       State 6:  $E = 20914 \text{ cm}^{-1}$ ,  $\lambda = 478 \text{ nm}$ ,  $f = 0.091$



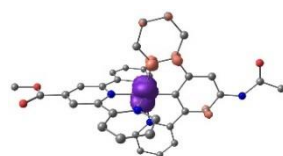
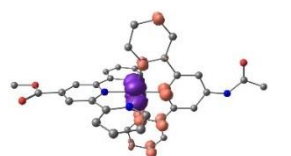
State 7:  $E = 21962 \text{ cm}^{-1}$ ,  $\lambda = 455 \text{ nm}$ ,  $f = 0.213$       State 8:  $E = 21843 \text{ cm}^{-1}$ ,  $\lambda = 457 \text{ nm}$ ,  $f = 2.6 \times 10^{-3}$



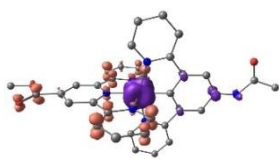
State 9:  $E = 22623 \text{ cm}^{-1}$ ,  $\lambda = 442 \text{ nm}$ ,  $f = 0.022$       State 10:  $E = 21505 \text{ cm}^{-1}$ ,  $\lambda = 465 \text{ nm}$ ,  $f = 1.3 \times 10^{-4}$



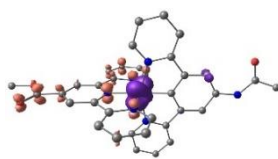
State 13:  $E = 24838 \text{ cm}^{-1}$ ,  $\lambda = 403 \text{ nm}$ ,  $f = 0.112$       State 14:  $E = 25216 \text{ cm}^{-1}$ ,  $\lambda = 397 \text{ nm}$ ,  $f = 0.010$



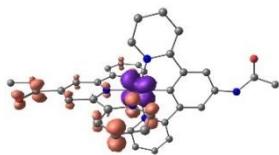
State 17:  $E = 25476 \text{ cm}^{-1}$ ,  $\lambda = 393 \text{ nm}$ ,  $f = 0.016$



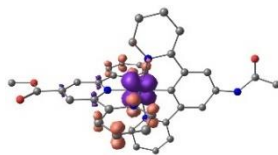
State 18:  $E = 25689 \text{ cm}^{-1}$ ,  $\lambda = 389 \text{ nm}$ ,  $f = 0.034$



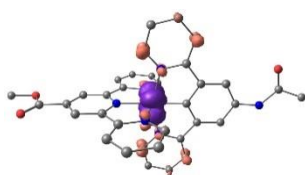
State 19:  $E = 26158 \text{ cm}^{-1}$ ,  $\lambda = 382 \text{ nm}$ ,  $f = 0.089$



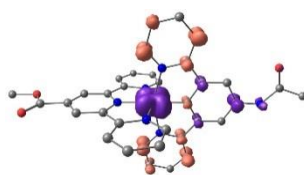
State 21:  $E = 27068 \text{ cm}^{-1}$ ,  $\lambda = 369 \text{ nm}$ ,  $f = 0.034$



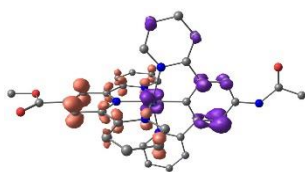
State 22:  $E = 28129 \text{ cm}^{-1}$ ,  $\lambda = 356 \text{ nm}$ ,  $f = 0.063$



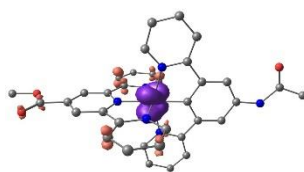
State 23:  $E = 28520 \text{ cm}^{-1}$ ,  $\lambda = 351 \text{ nm}$ ,  $f = 0.034$



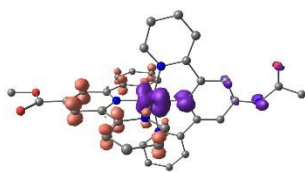
State 24:  $E = 27202 \text{ cm}^{-1}$ ,  $\lambda = 368 \text{ nm}$ ,  $f = 0.011$



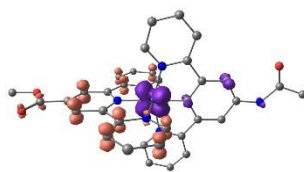
State 26:  $E = 29117 \text{ cm}^{-1}$ ,  $\lambda = 343 \text{ nm}$ ,  $f = 0.030$



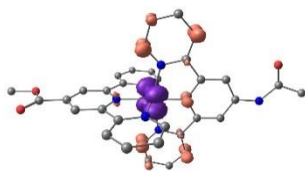
State 28:  $E = 28269 \text{ cm}^{-1}$ ,  $\lambda = 354 \text{ nm}$ ,  $f = 0.010$



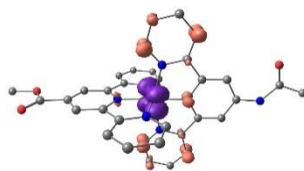
State 29:  $E = 28688 \text{ cm}^{-1}$ ,  $\lambda = 349 \text{ nm}$ ,  $f = 0.037$



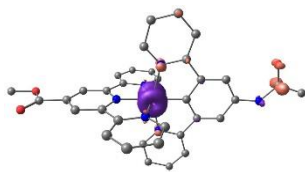
State 33:  $E = 31513 \text{ cm}^{-1}$ ,  $\lambda = 317 \text{ nm}$ ,  $f = 0.313$



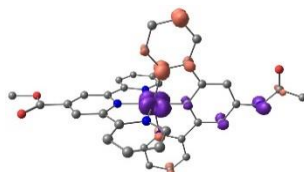
State 34:  $E = 31238 \text{ cm}^{-1}$ ,  $\lambda = 320 \text{ nm}$ ,  $f = 0.077$



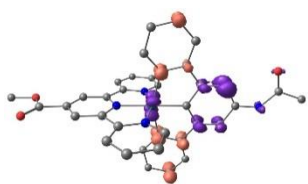
State 36:  $E = 32539 \text{ cm}^{-1}$ ,  $\lambda = 307 \text{ nm}$ ,  $f = 0.142$



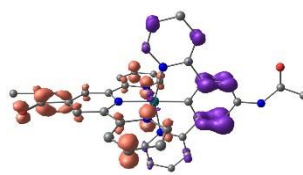
State 40:  $E = 29117 \text{ cm}^{-1}$ ,  $\lambda = 291 \text{ nm}$ ,  $f = 0.027$



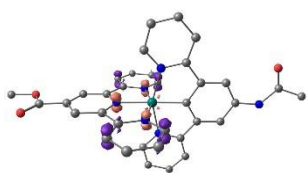
State 42:  $E = 34484 \text{ cm}^{-1}$ ,  $\lambda = 290 \text{ nm}$ ,  $f = 0.215$



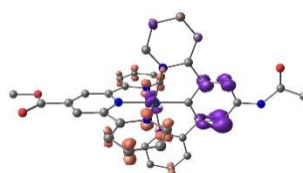
State 43:  $E = 32391 \text{ cm}^{-1}$ ,  $\lambda = 309 \text{ nm}$ ,  $f = 0.011$



State 46:  $E = 35609 \text{ cm}^{-1}$ ,  $\lambda = 281 \text{ nm}$ ,  $f = 0.054$



State 48:  $E = 35420 \text{ cm}^{-1}$ ,  $\lambda = 282 \text{ nm}$ ,  $f = 0.058$



State 49:  $E = 36342 \text{ cm}^{-1}$ ,  $\lambda = 275 \text{ nm}$ ,  $f = 0.326$

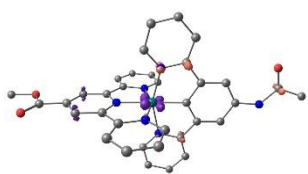
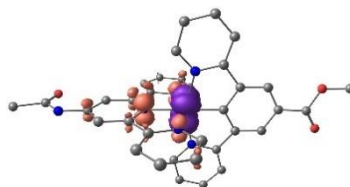
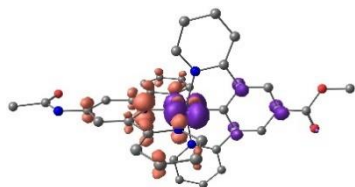


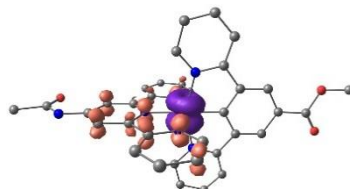
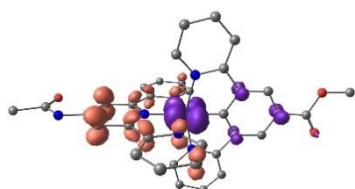


**Table S2** First ten TD-DFT excitations of  $\mathbf{2}^+$  and all further with oscillator strengths  $f > 0.01$  (B3LYP, def2-TZVP, DKH, COSMO(acetonitrile)) and corresponding electronic difference densities  $\psi_{ex} - \psi_{GS}$  at a contour value of 0.005 (purple lobes indicate loss, orange lobes show increase of electron density upon excitation). Hydrogen atoms are omitted for clarity.

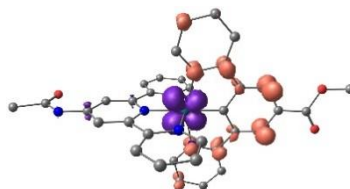
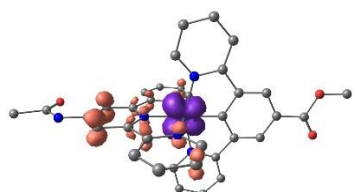
State 1:  $E = 15955 \text{ cm}^{-1}$ ,  $\lambda = 627 \text{ nm}$ ,  $f = 7.1 \times 10^{-5}$       State 2:  $E = 17378 \text{ cm}^{-1}$ ,  $\lambda = 575 \text{ nm}$ ,  $f = 5.0 \times 10^{-3}$



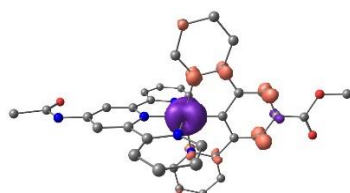
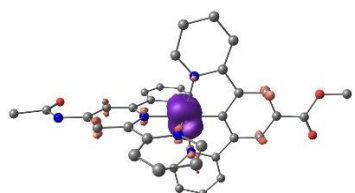
State 3:  $E = 16776 \text{ cm}^{-1}$ ,  $\lambda = 596 \text{ nm}$ ,  $f = 8.4 \times 10^{-4}$       State 4:  $E = 18332 \text{ cm}^{-1}$ ,  $\lambda = 546 \text{ nm}$ ,  $f = 0.014$



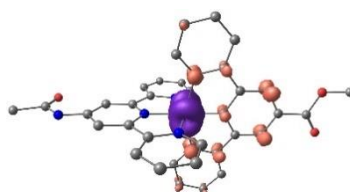
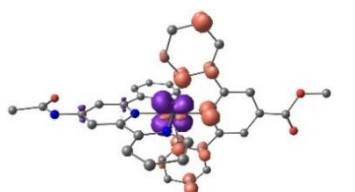
State 5:  $E = 18593 \text{ cm}^{-1}$ ,  $\lambda = 538 \text{ nm}$ ,  $f = 0.060$       State 6:  $E = 20657 \text{ cm}^{-1}$ ,  $\lambda = 484 \text{ nm}$ ,  $f = 5.1 \times 10^{-3}$



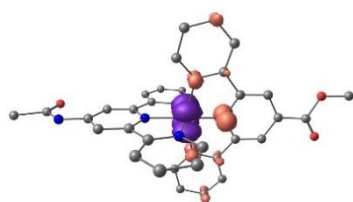
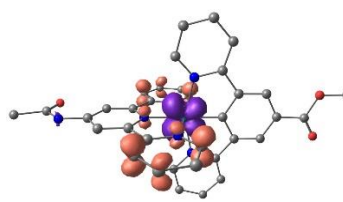
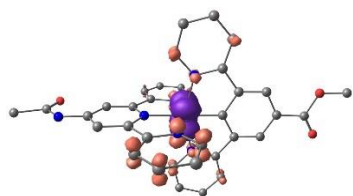
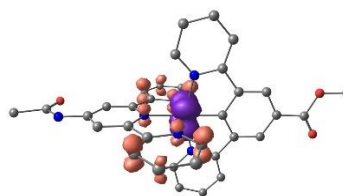
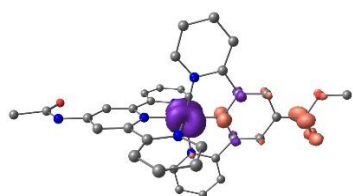
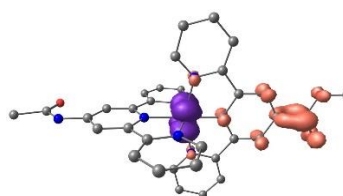
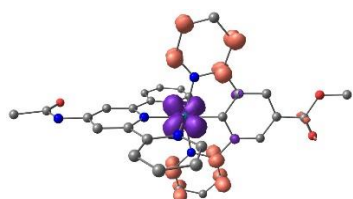
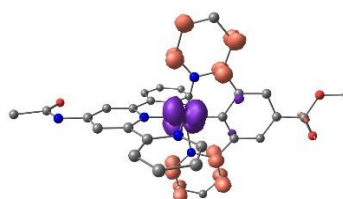
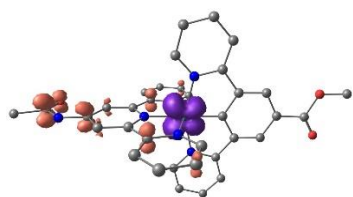
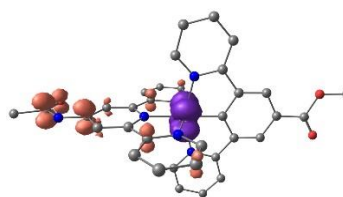
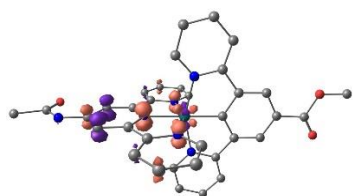
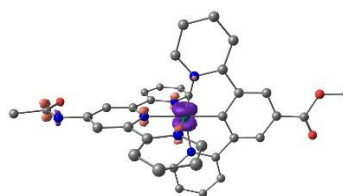
State 7:  $E = 21675 \text{ cm}^{-1}$ ,  $\lambda = 461 \text{ nm}$ ,  $f = 0.170$       State 8:  $E = 21681 \text{ cm}^{-1}$ ,  $\lambda = 461 \text{ nm}$ ,  $f = 0.096$

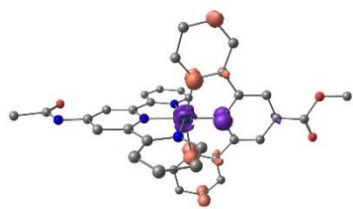
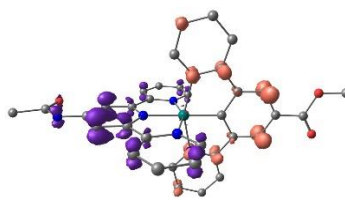
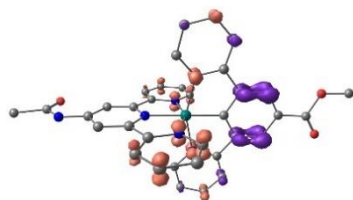
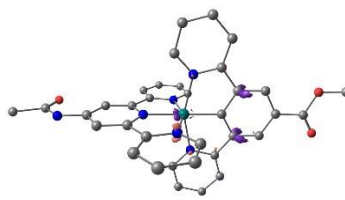
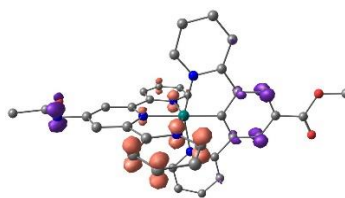
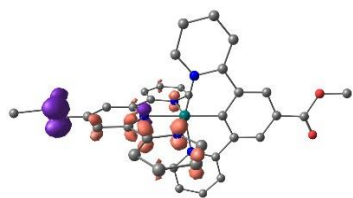


State 9:  $E = 22130 \text{ cm}^{-1}$ ,  $\lambda = 452 \text{ nm}$ ,  $f = 5.1 \times 10^{-5}$       State 10:  $E = 22631 \text{ cm}^{-1}$ ,  $\lambda = 442 \text{ nm}$ ,  $f = 6.4 \times 10^{-3}$



State 11:  $E = 24120 \text{ cm}^{-1}$ ,  $\lambda = 415 \text{ nm}$ ,  $f = 0.111$       State 16:  $E = 26366 \text{ cm}^{-1}$ ,  $\lambda = 379 \text{ nm}$ ,  $f = 0.026$

State 17:  $E = 27656 \text{ cm}^{-1}$ ,  $\lambda = 362 \text{ nm}$ ,  $f = 0.100$ State 18:  $E = 27600 \text{ cm}^{-1}$ ,  $\lambda = 362 \text{ nm}$ ,  $f = 0.049$ State 24:  $E = 29114 \text{ cm}^{-1}$ ,  $\lambda = 344 \text{ nm}$ ,  $f = 0.191$ State 25:  $E = 28016 \text{ cm}^{-1}$ ,  $\lambda = 357 \text{ nm}$ ,  $f = 0.039$ State 27:  $E = 29771 \text{ cm}^{-1}$ ,  $\lambda = 336 \text{ nm}$ ,  $f = 0.014$ State 28:  $E = 29764 \text{ cm}^{-1}$ ,  $\lambda = 336 \text{ nm}$ ,  $f = 0.012$ State 32:  $E = 30746 \text{ cm}^{-1}$ ,  $\lambda = 325 \text{ nm}$ ,  $f = 0.138$ State 36:  $E = 30849 \text{ cm}^{-1}$ ,  $\lambda = 324 \text{ nm}$ ,  $f = 0.018$ State 38:  $E = 32940 \text{ cm}^{-1}$ ,  $\lambda = 304 \text{ nm}$ ,  $f = 0.318$ State 43:  $E = 35975 \text{ cm}^{-1}$ ,  $\lambda = 278 \text{ nm}$ ,  $f = 0.082$ State 44:  $E = 36195 \text{ cm}^{-1}$ ,  $\lambda = 276 \text{ nm}$ ,  $f = 0.420$ State 45:  $E = 34743 \text{ cm}^{-1}$ ,  $\lambda = 288 \text{ nm}$ ,  $f = 0.030$

State 46:  $E = 36077 \text{ cm}^{-1}$ ,  $\lambda = 277 \text{ nm}$ ,  $f = 0.020$ State 47:  $E = 36739 \text{ cm}^{-1}$ ,  $\lambda = 272 \text{ nm}$ ,  $f = 0.445$ State 48:  $E = 36125 \text{ cm}^{-1}$ ,  $\lambda = 277 \text{ nm}$ ,  $f = 0.079$ State 50:  $E = 36720 \text{ cm}^{-1}$ ,  $\lambda = 272 \text{ nm}$ ,  $f = 0.158$ 

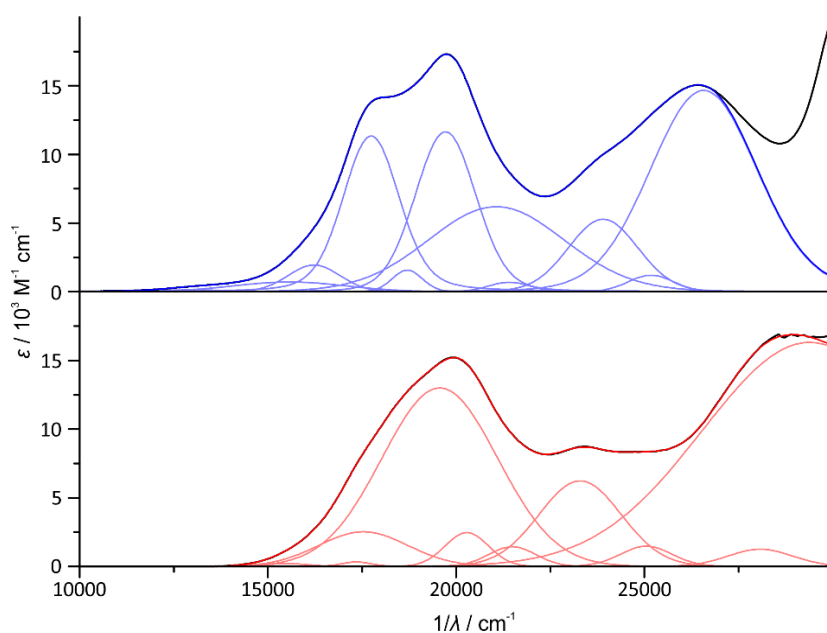


**Figure S25** Spectral decomposition of the absorption spectra of **1**(PF<sub>6</sub>) (top, black) and **2**(PF<sub>6</sub>) (bottom, black) in acetonitrile solution between 10000 and 30000 cm<sup>-1</sup> into separate absorption bands (light blue for **1**(PF<sub>6</sub>) and light red for **2**(PF<sub>6</sub>)). Sum of the individual contributions is shown as blue and red curve, respectively. Fit parameters are given in Tables 1 and 2, respectively.

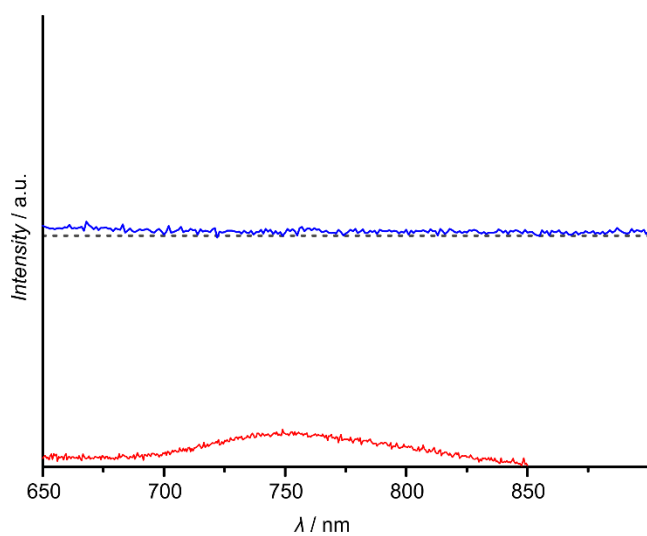


**Figure S26** Emission spectra of **1**(PF<sub>6</sub>) (top, blue) and **2**(PF<sub>6</sub>) (bottom, red) in deaerated acetonitrile at room temperature.

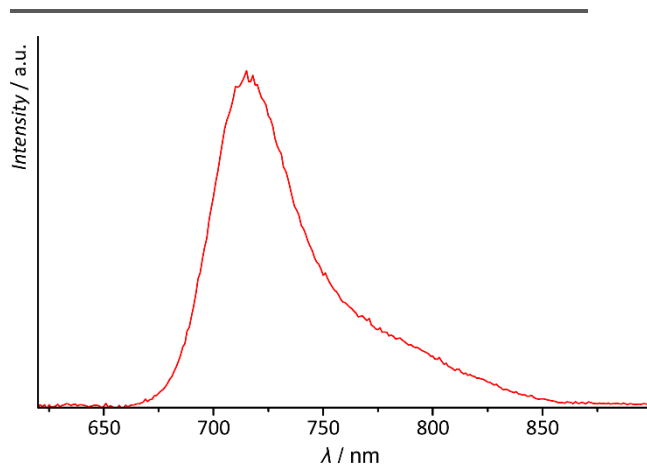


**Figure S27** Emission spectrum of **2**(PF<sub>6</sub>) at 77 K in a frozen butyronitrile glass.

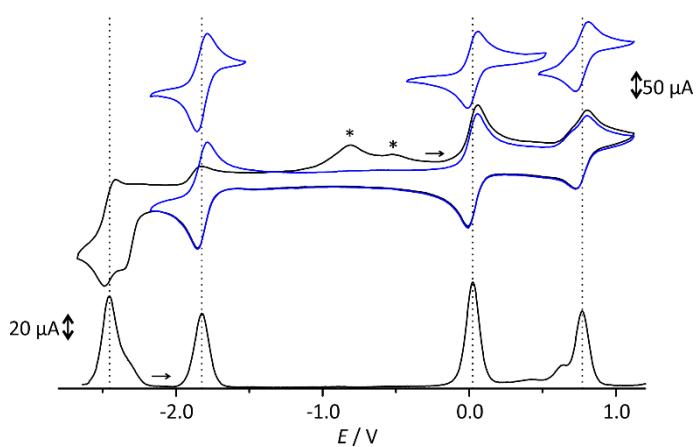


**Figure S28** Cyclic and square-wave voltammograms of **1**(PF<sub>6</sub>) ( $c = 1 \text{ mM}$ ) in acetonitrile with  $0.1 \text{ M}$  [NBu<sub>4</sub>][PF<sub>6</sub>] as supporting electrolyte. All potentials are referenced against the FcH/FcH<sup>+</sup> couple. Blue insets show the individual redox waves. Asterisks indicate reoxidation waves of follow-up products after three subsequent reduction steps.

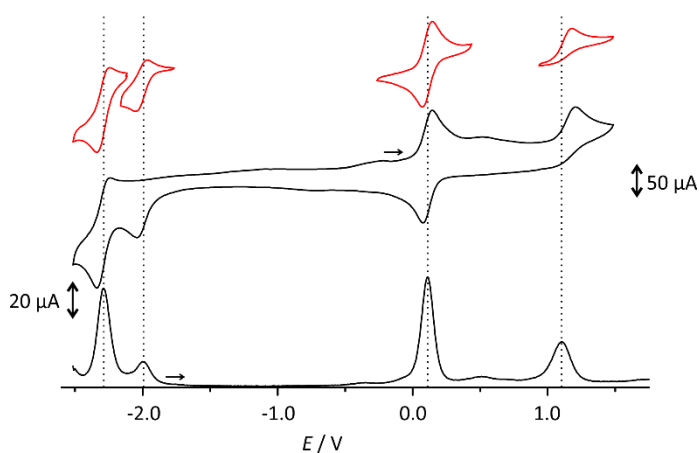


**Figure S29** Cyclic and square-wave voltammograms of **2**(PF<sub>6</sub>) ( $c = 1 \text{ mM}$ ) in acetonitrile with  $0.1 \text{ M}$  [NBu<sub>4</sub>][PF<sub>6</sub>] as supporting electrolyte. All potentials are referenced against the FcH/FcH<sup>+</sup> couple. Red insets show the individual redox waves.

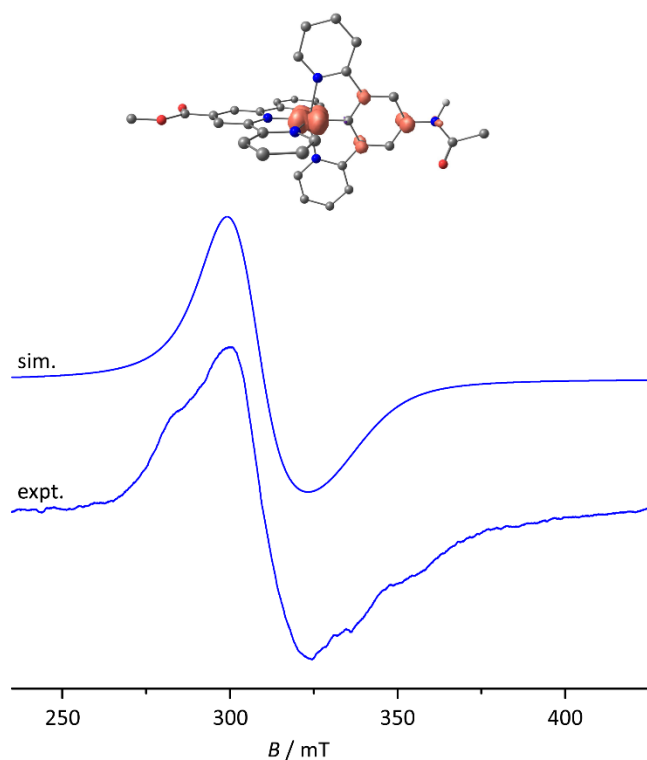


**Figure S30** DFT calculated spin density (B3LYP/def2-TZVP/DKH/COSMO(acetonitrile), contour value: 0.01) of  $\mathbf{1}^{2+}$  and experimental X-band EPR spectra ( $\nu \approx 9.4$  GHz) obtained from frozen acetonitrile solutions of  $\mathbf{1}^{2+}$  ( $c = 5$  mM) in situ generated with  $[\text{N}(\text{C}_6\text{H}_4\text{-4-Br})_3][\text{SbCl}_6]$ . CH hydrogen atoms are omitted for clarity.

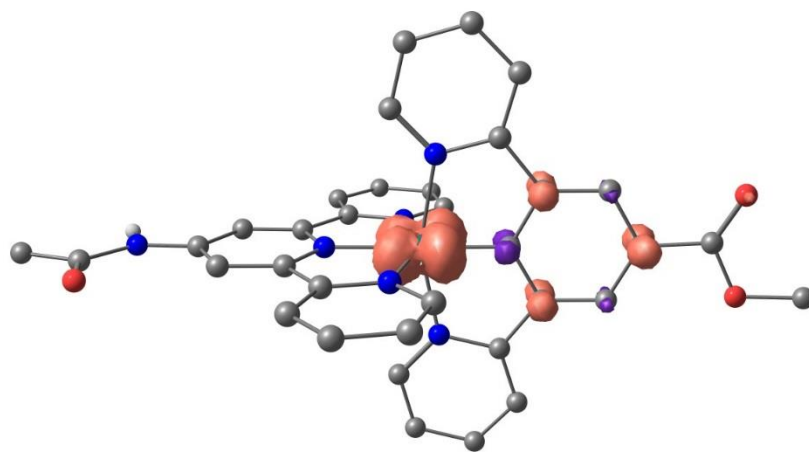


**Figure S31** DFT calculated spin density (B3LYP/def2-TZVP/DKH/COSMO(acetonitrile), contour value: 0.01) of  $\mathbf{2}^{2+}$ . CH hydrogen atoms are omitted for clarity.



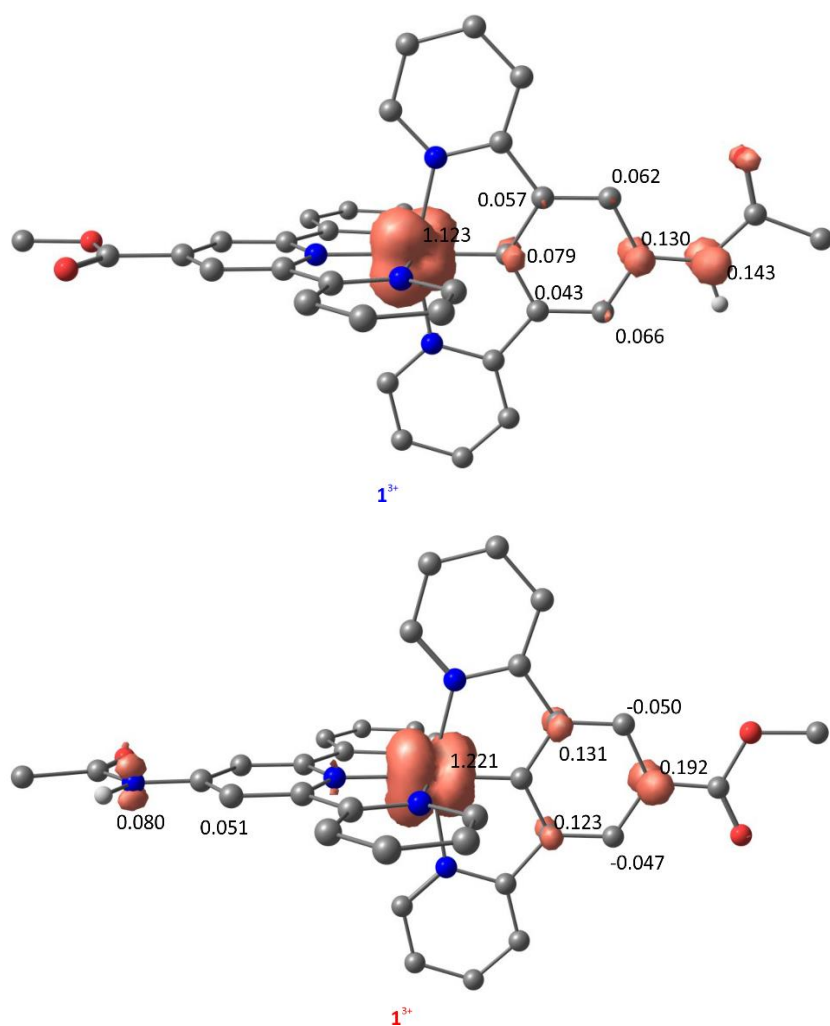


**Figure S32** DFT calculated spin densities (B3LYP/def2-SVP/DKH/COSMO(acetonitrile), contour value: 0.01) of  $1^{3+}$  (top) and  $2^{3+}$  (bottom). Significant Mulliken spin density populations ( $> 0.04$ ) are given at the respective atoms. CH hydrogen atoms are omitted for clarity.

## 6.4 SUPPORTING INFORMATION TO 3.3: THE PHOTOCHEMISTRY OF MONO- AND DINUCLEAR CYCLOMETALATED BIS(TRIDENTATE)RUTHENIUM(II) COMPLEXES: DUAL EXCITED STATE DEACTIVATION AND DUAL EMISSION

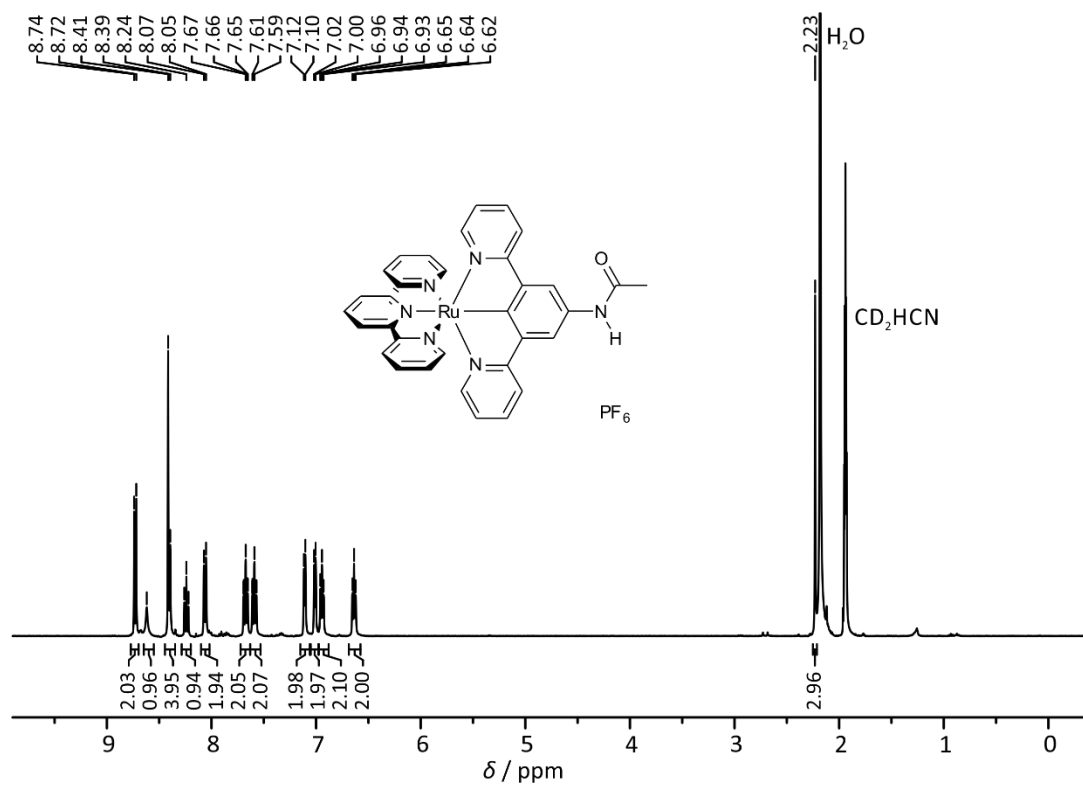


**Figure S1**  $^1\text{H}$  NMR spectrum (400 MHz) of **1**(PF<sub>6</sub>) in CD<sub>3</sub>CN.

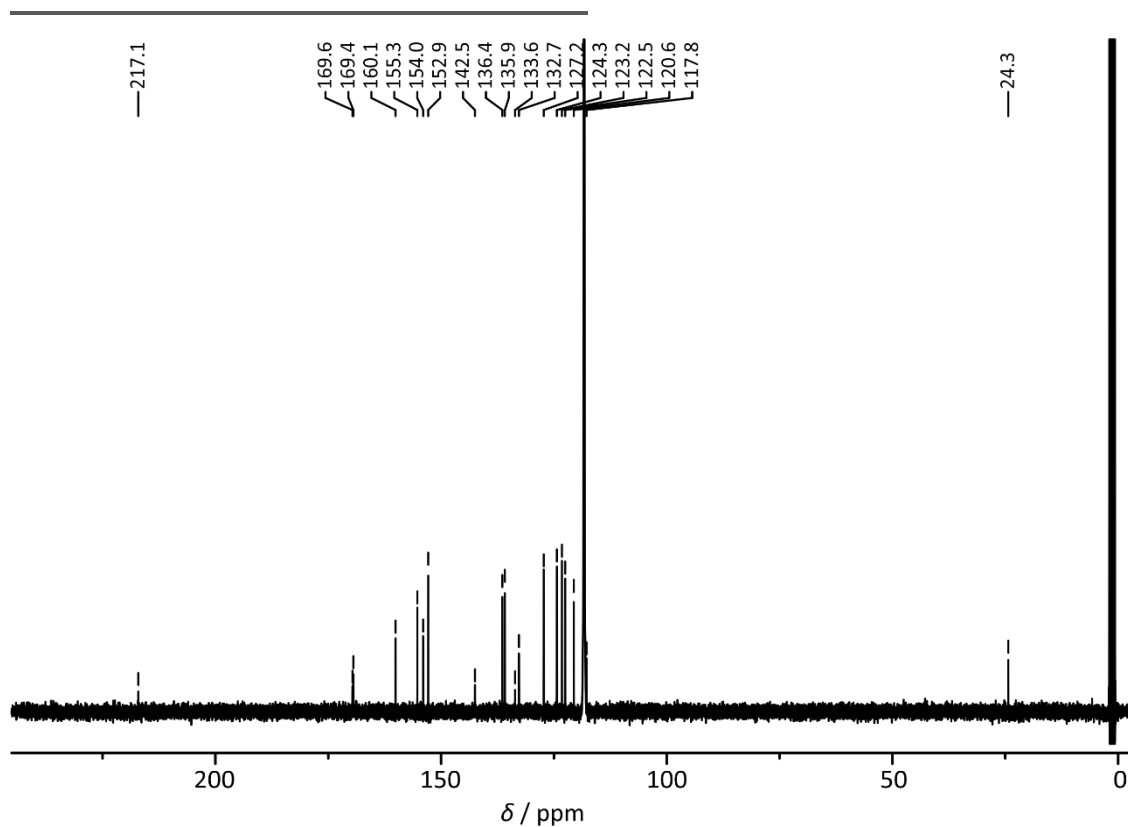


Figure S2  $^{13}\text{C}$  NMR spectrum (100 MHz) of **1**(PF<sub>6</sub>) in CD<sub>3</sub>CN.

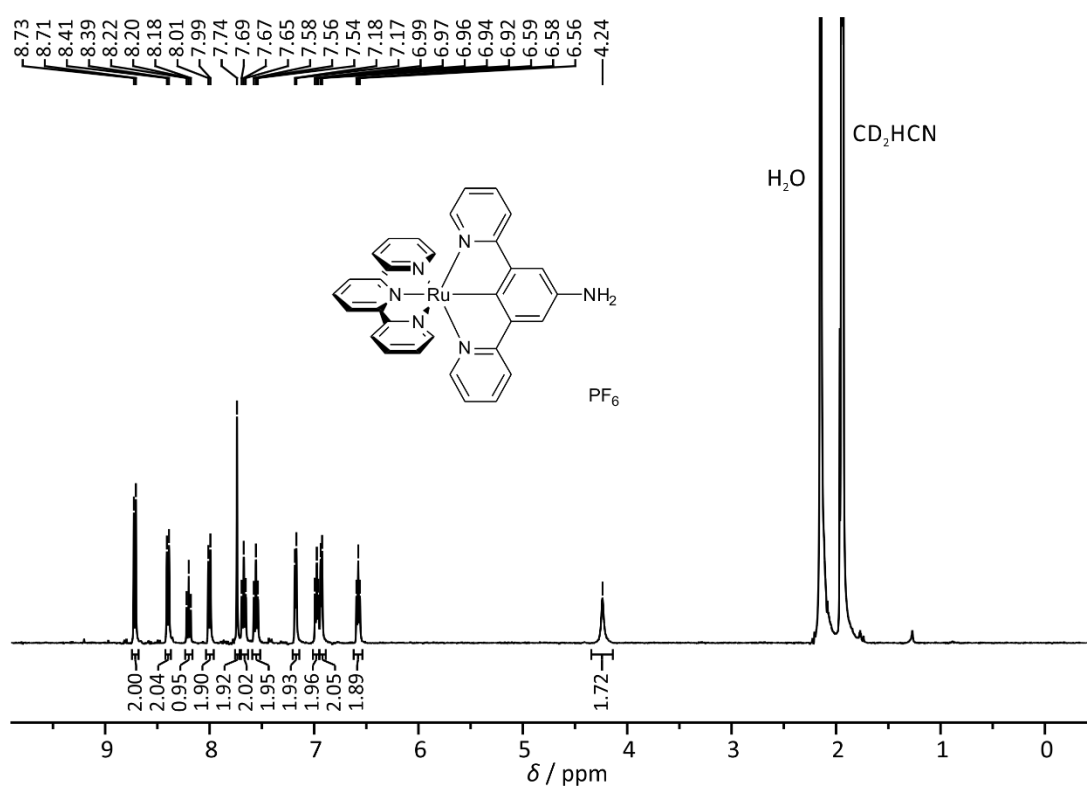


Figure S3  $^1\text{H}$  NMR spectrum (400 MHz) of **2**(PF<sub>6</sub>) in CD<sub>3</sub>CN.

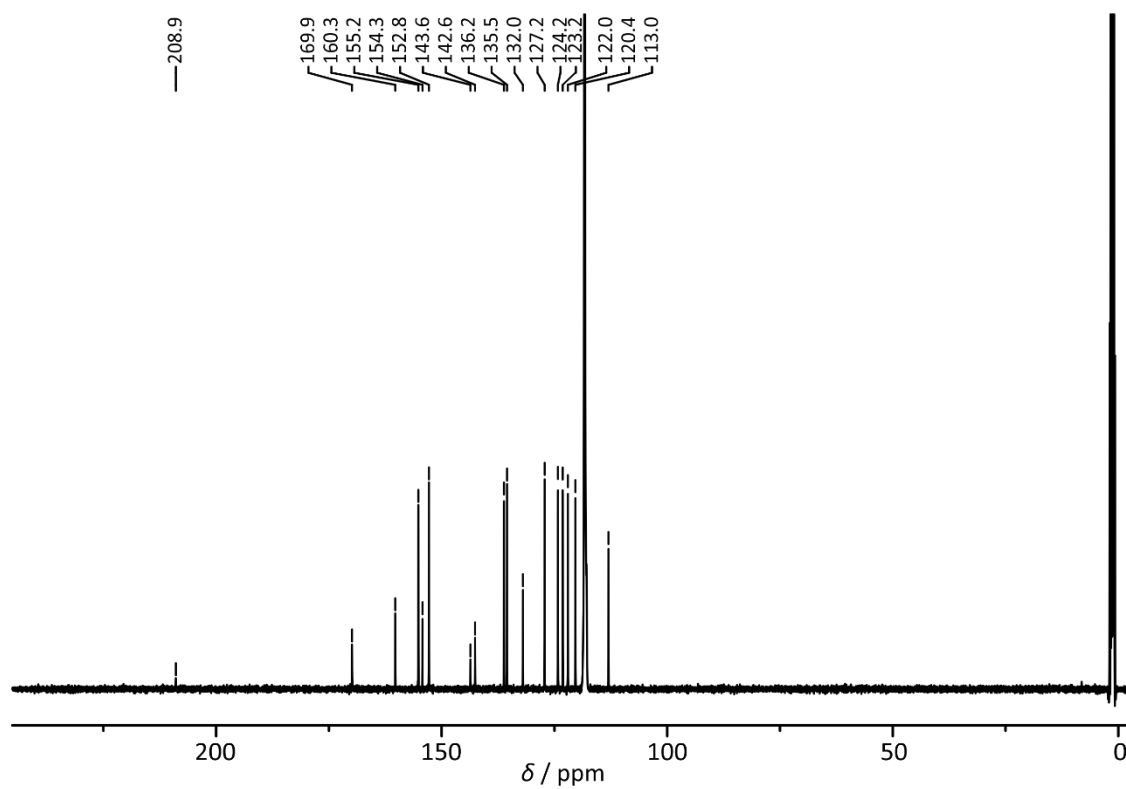


Figure S4  $^{13}\text{C}$  NMR spectrum (100 MHz) of **2**(PF<sub>6</sub>) in CD<sub>3</sub>CN.

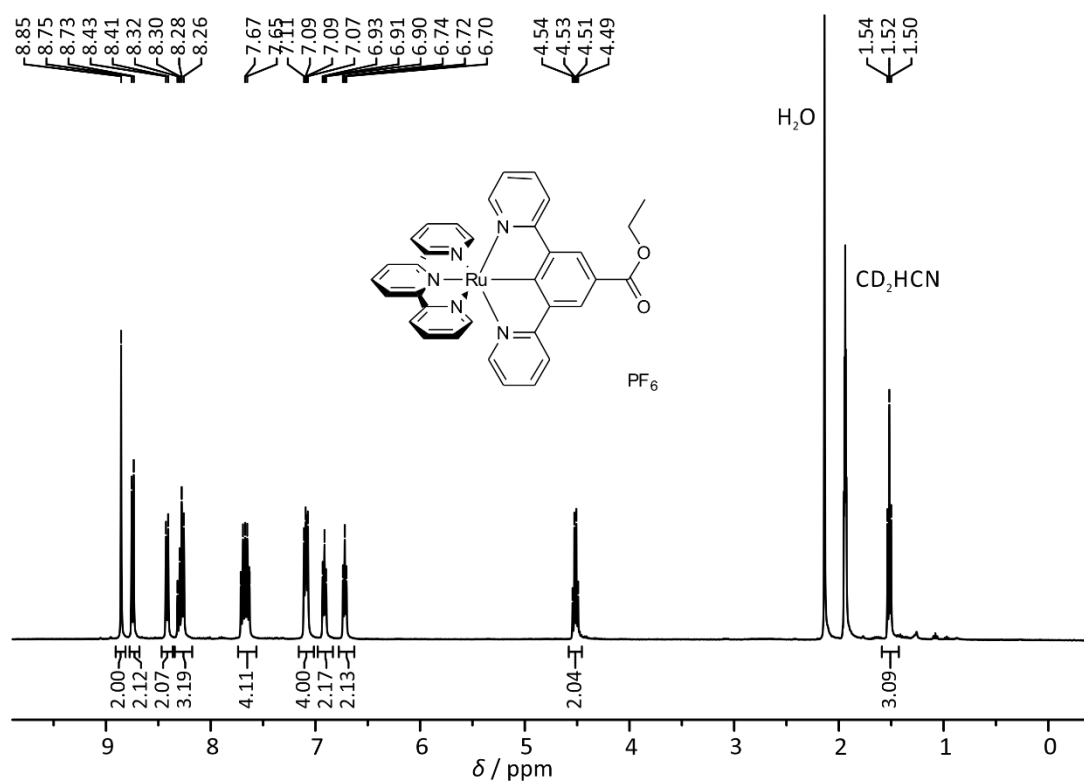


Figure S5  $^1\text{H}$  NMR spectrum (400 MHz) of **3**(PF<sub>6</sub>) in CD<sub>3</sub>CN.

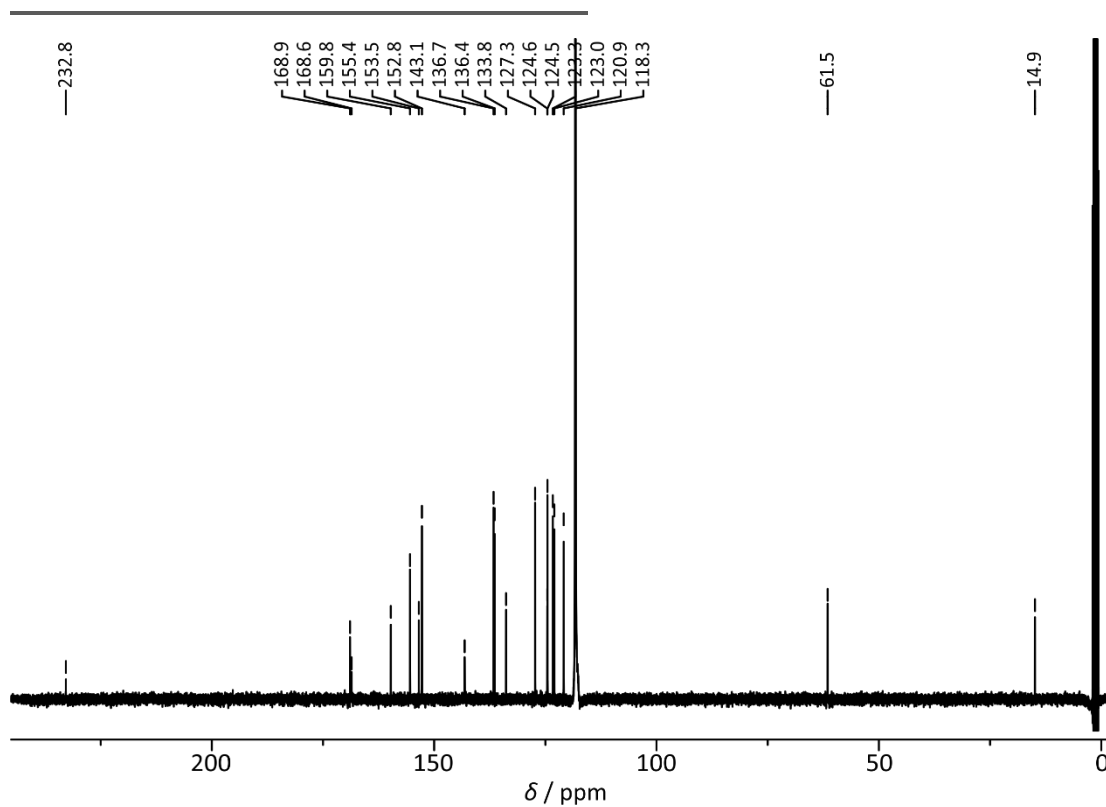


Figure S6  $^{13}\text{C}$  NMR spectrum (100 MHz) of **3**(PF<sub>6</sub>) in CD<sub>3</sub>CN.

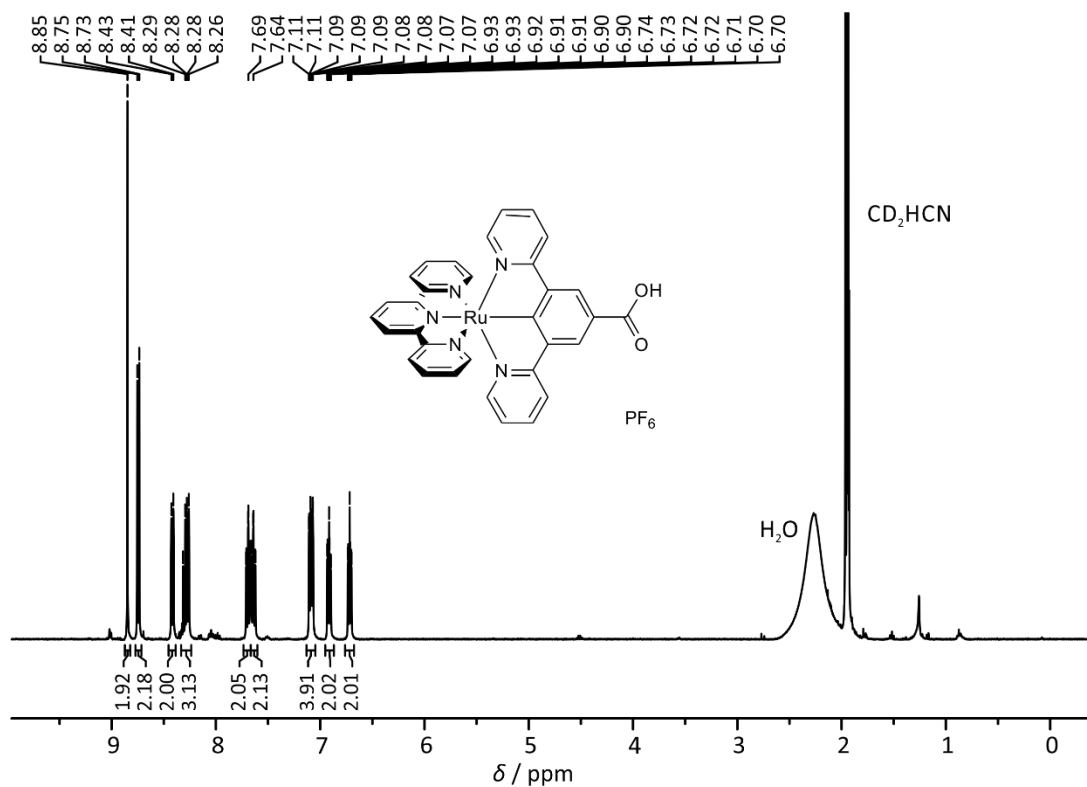


Figure S7  $^1\text{H}$  NMR spectrum (400 MHz) of **4**(PF<sub>6</sub>) in CD<sub>3</sub>CN.

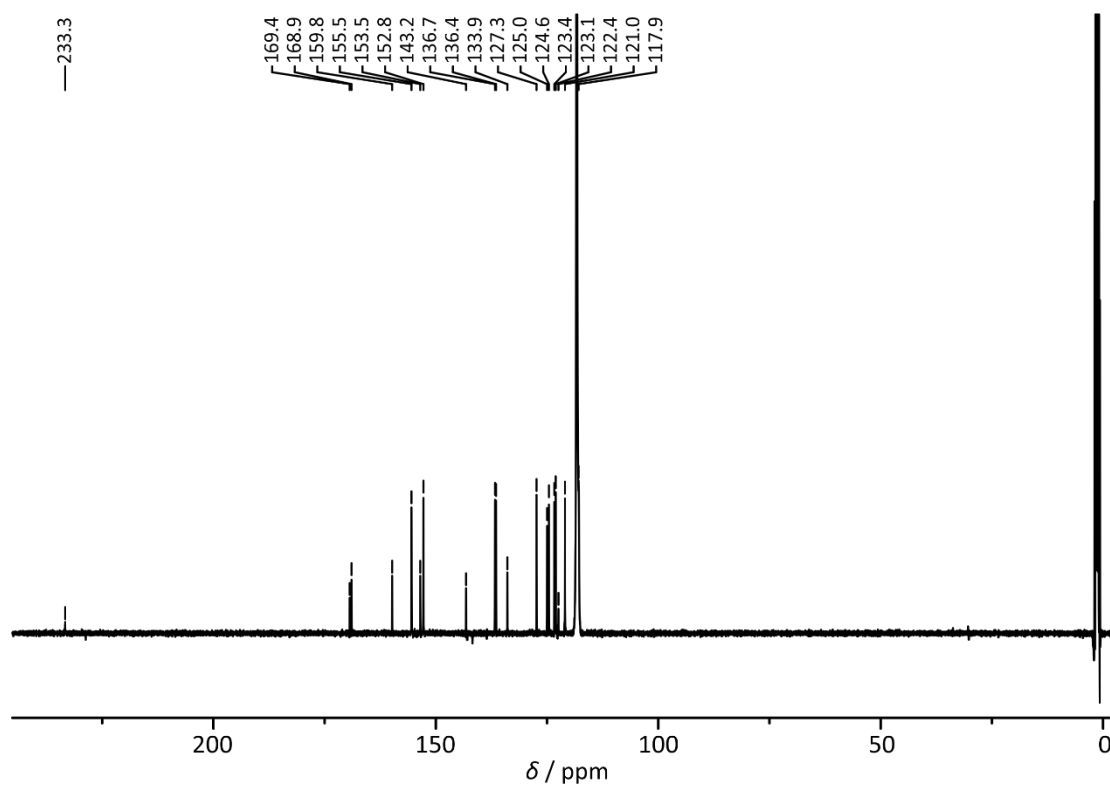


Figure S8  $^{13}\text{C}$  NMR spectrum (100 MHz) of **4**(PF<sub>6</sub>) in CD<sub>3</sub>CN.

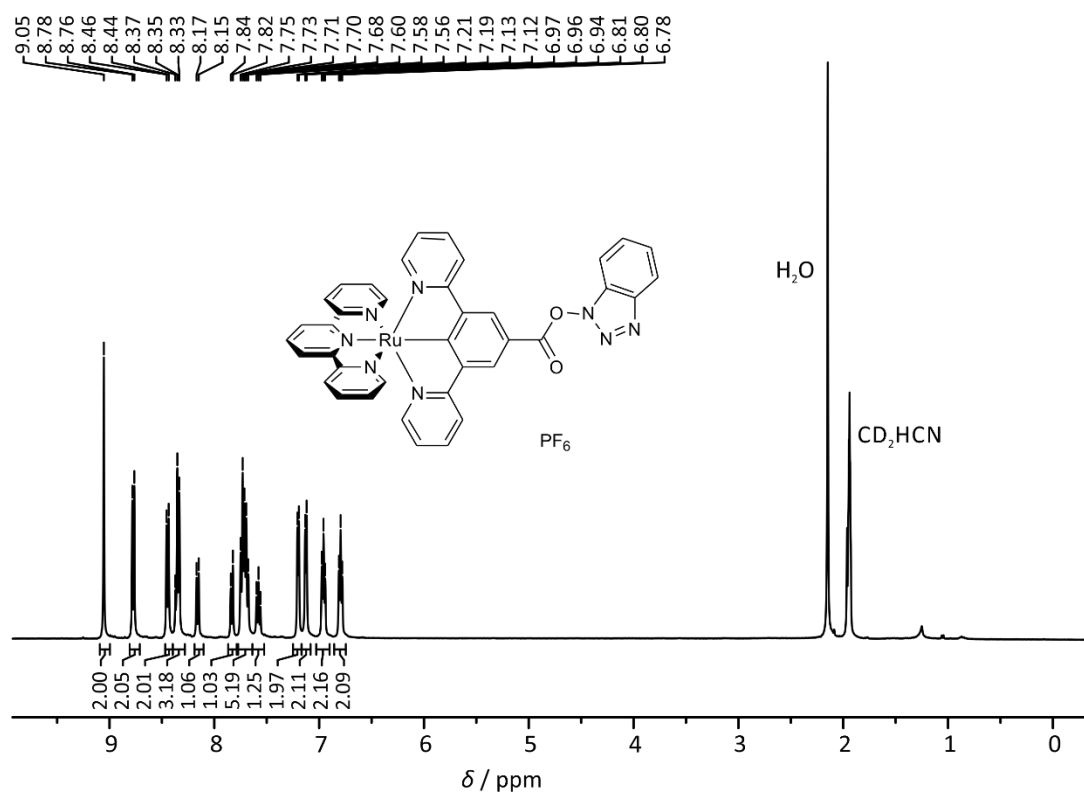


Figure S9  $^1\text{H}$  NMR spectrum (400 MHz) of **5**(PF<sub>6</sub>) in CD<sub>3</sub>CN.



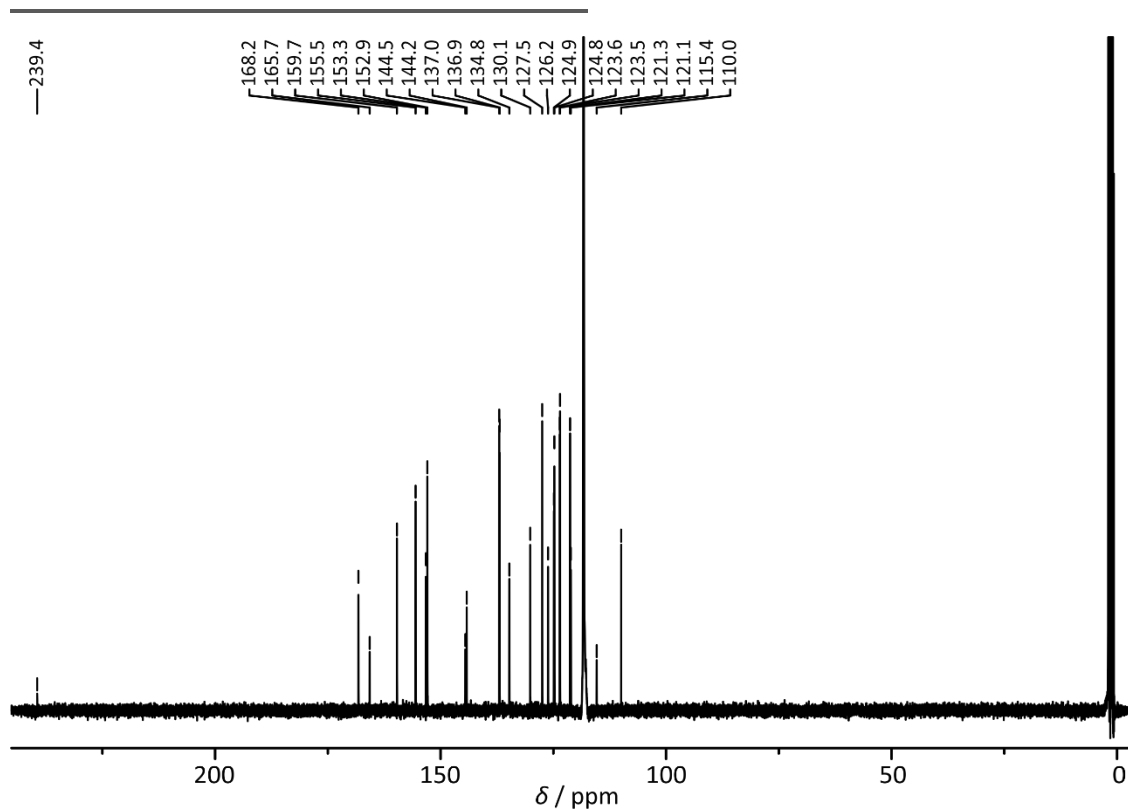


Figure S10  $^{13}\text{C}$  NMR spectrum (100 MHz) of **5**(PF<sub>6</sub>) in CD<sub>3</sub>CN.

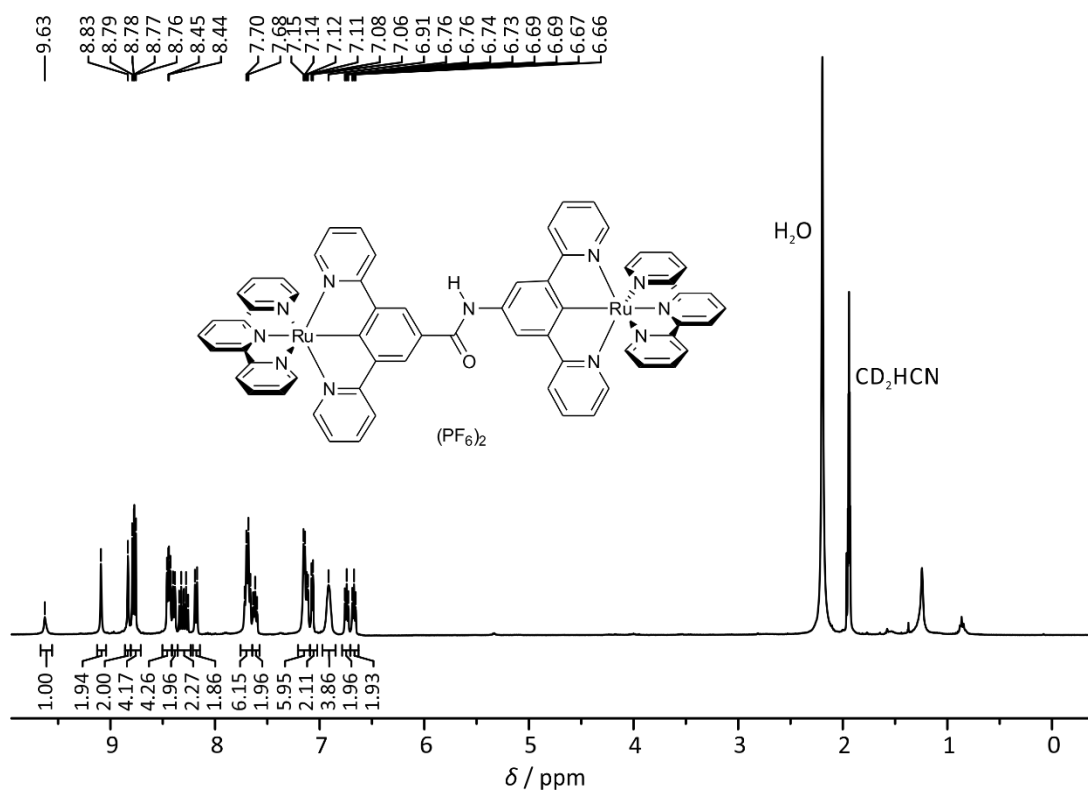


Figure S11  $^1\text{H}$  NMR spectrum (400 MHz) of **6**(PF<sub>6</sub>) in CD<sub>3</sub>CN.

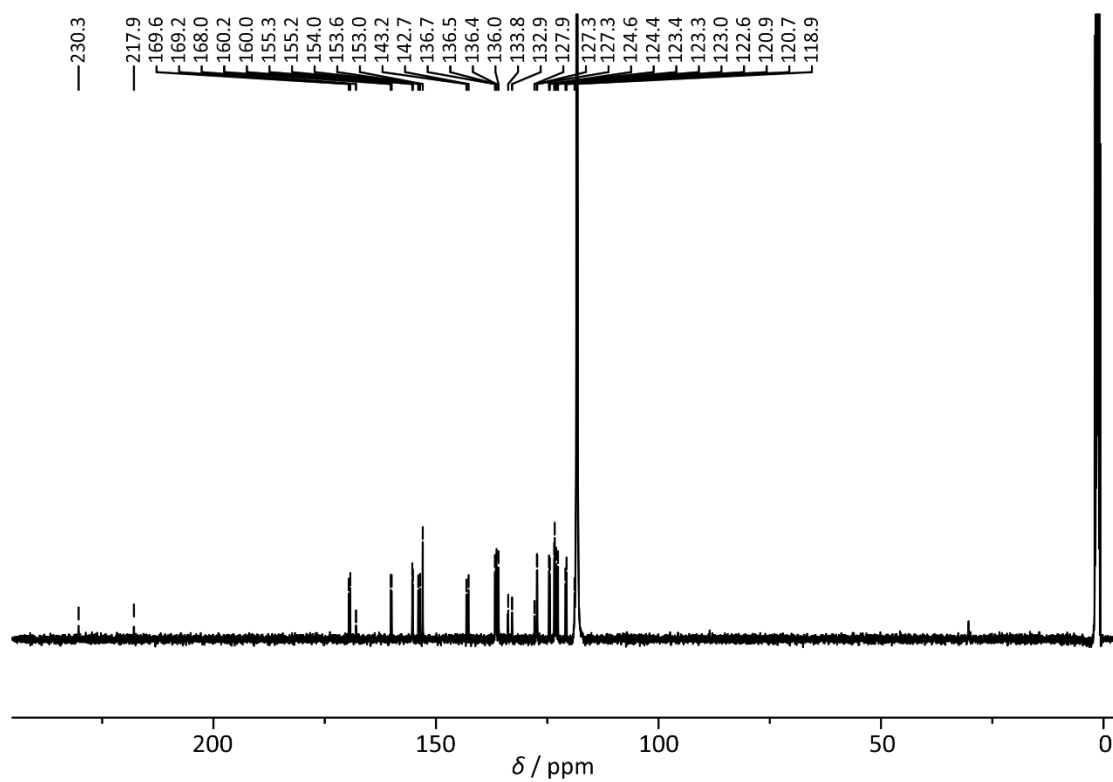


Figure S12  $^{13}\text{C}$  NMR spectrum (100 MHz) of **6**(PF<sub>6</sub>) in CD<sub>3</sub>CN.

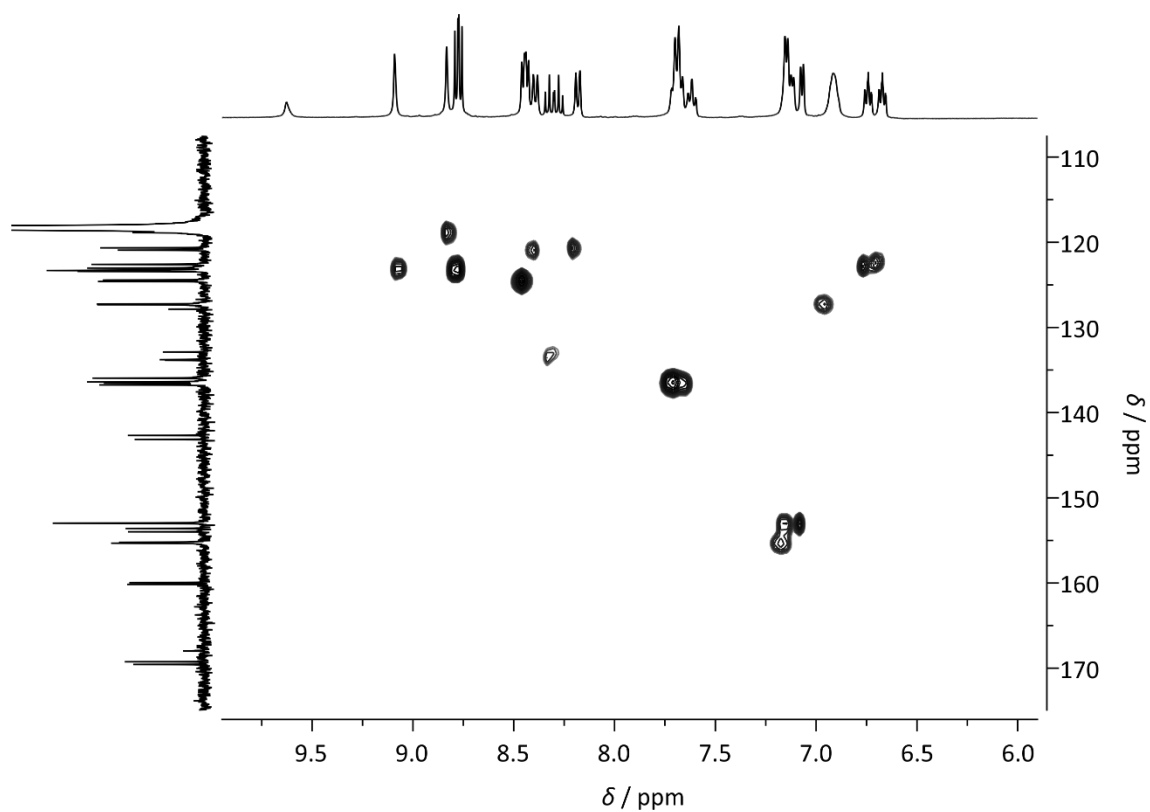
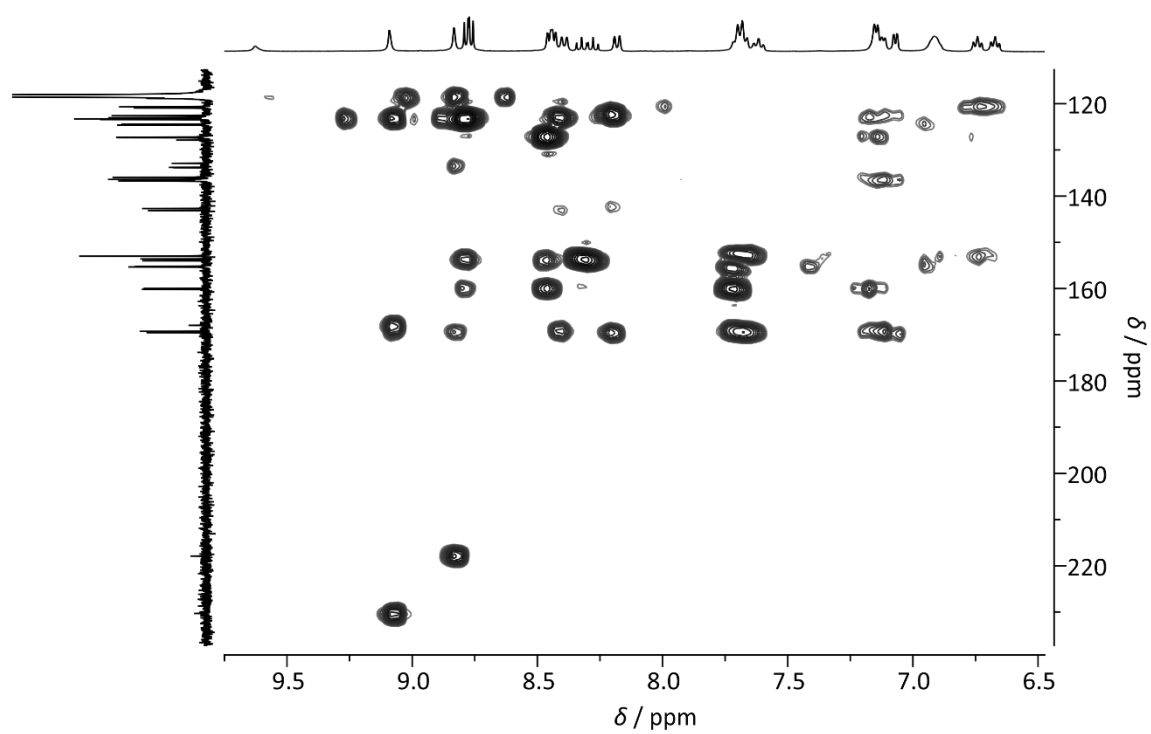
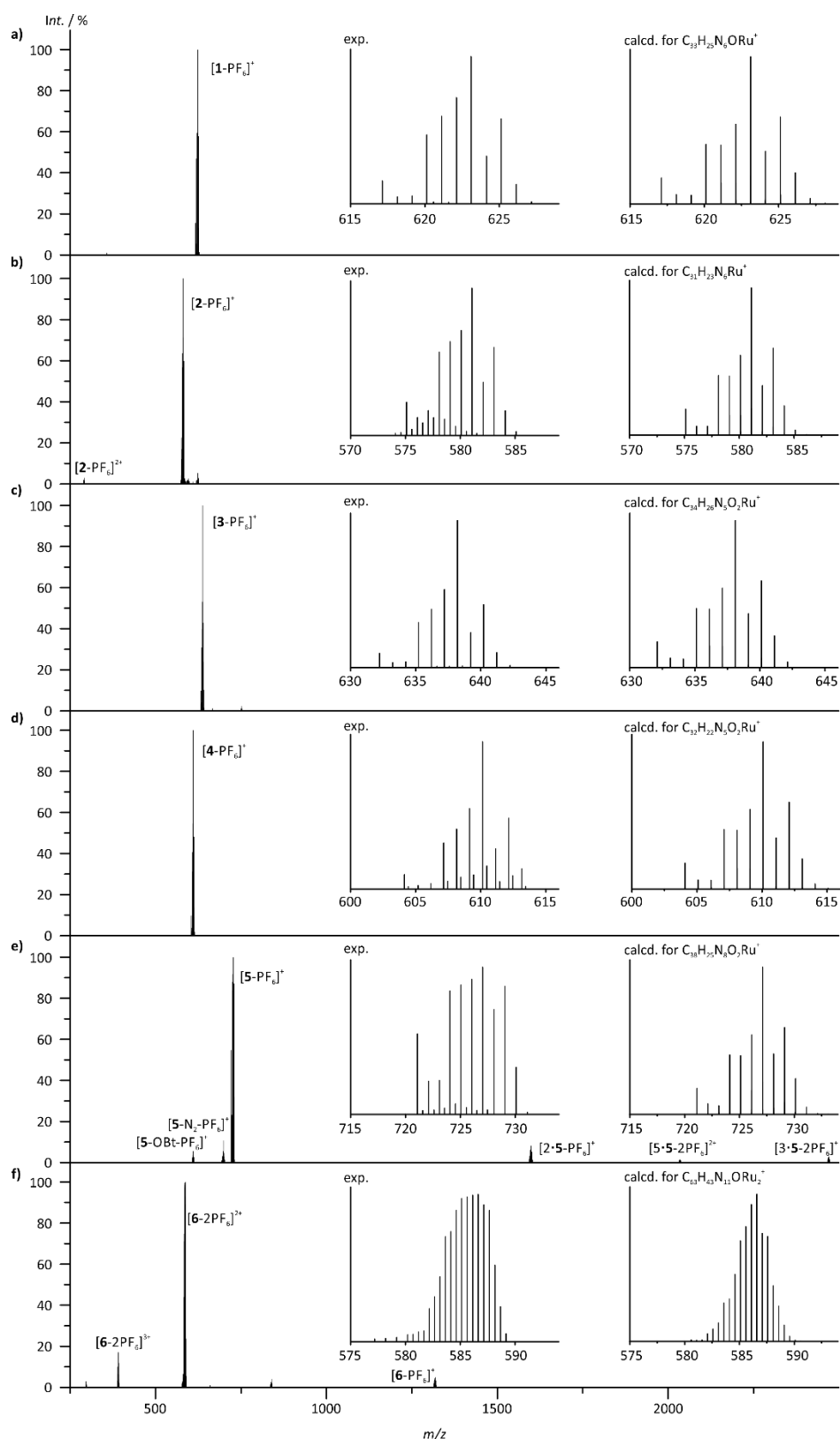


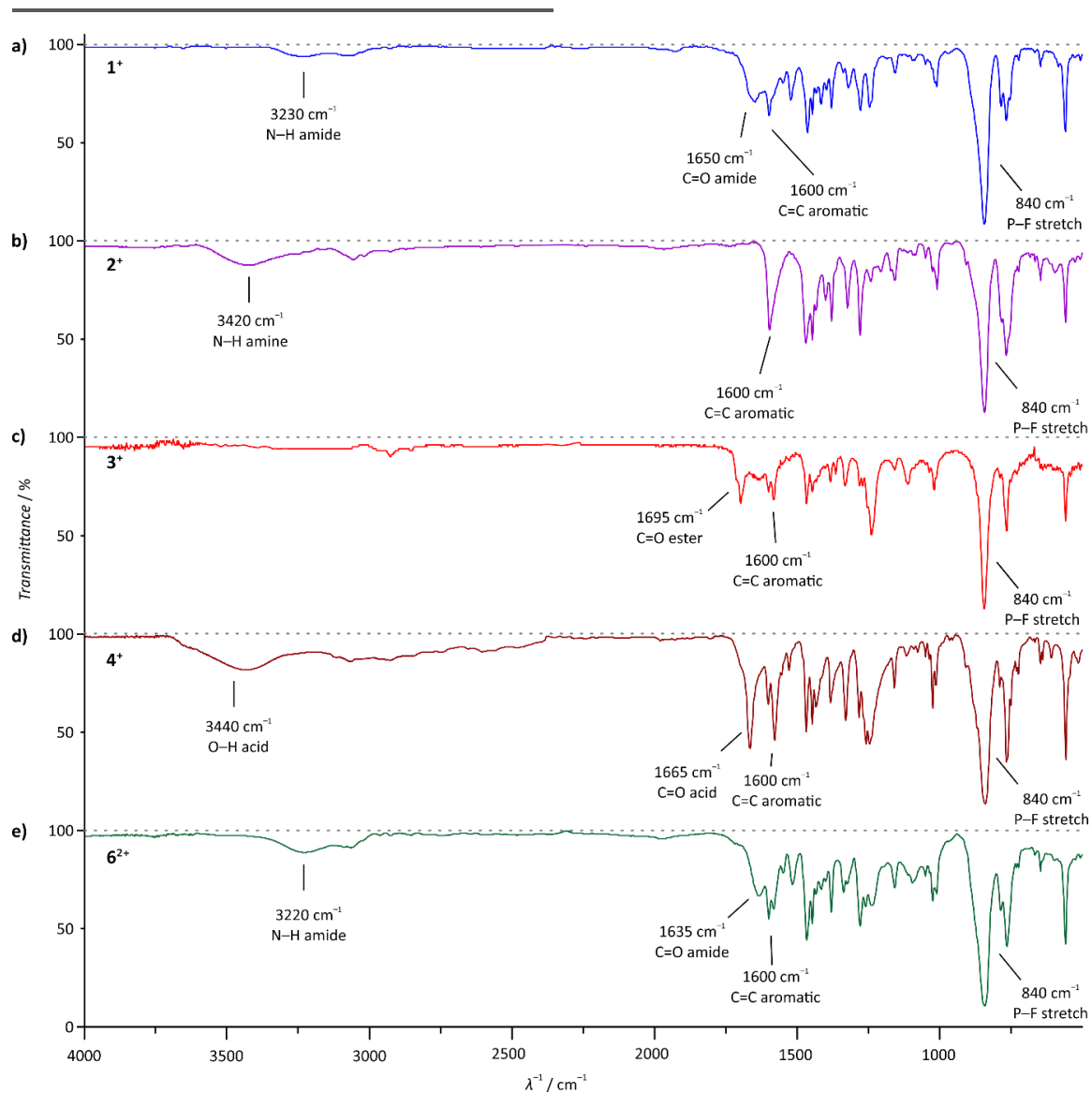
Figure S13 Aromatic region of the  $^1\text{H}$ - $^{13}\text{C}$  HSQC NMR spectrum of **6**(PF<sub>6</sub>) in CD<sub>3</sub>CN.



**Figure S14** Aromatic region of the  $^1\text{H}$ - $^{13}\text{C}$  HMBC NMR spectrum of **6**(PF<sub>6</sub>) in CD<sub>3</sub>CN.

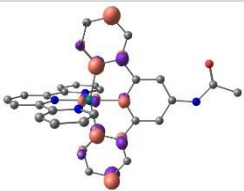
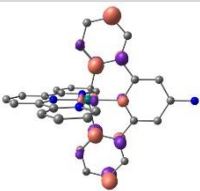
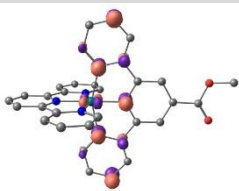
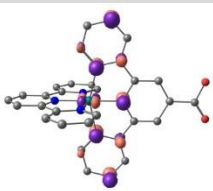
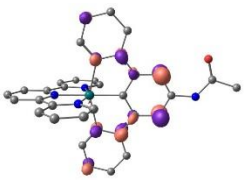
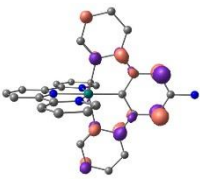
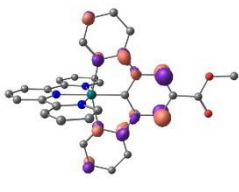
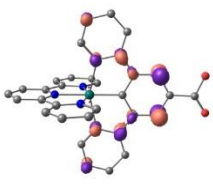
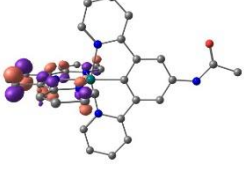
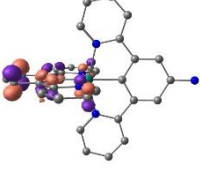
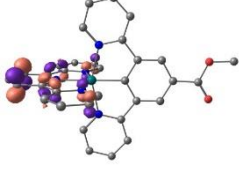
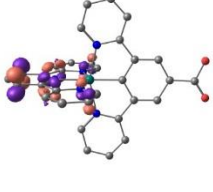
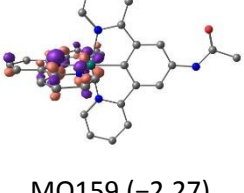
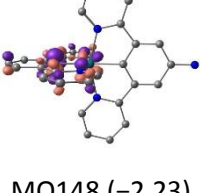
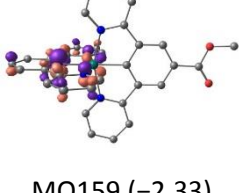
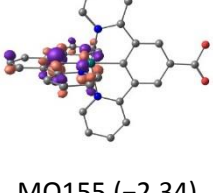
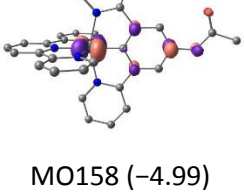
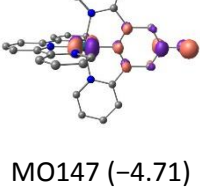
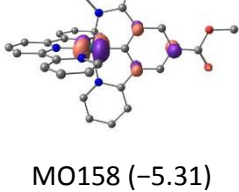
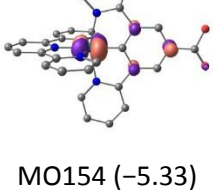
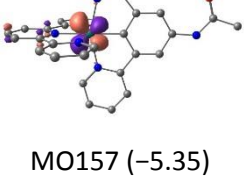
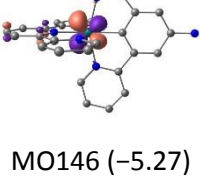
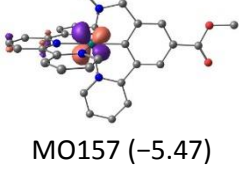
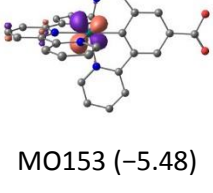


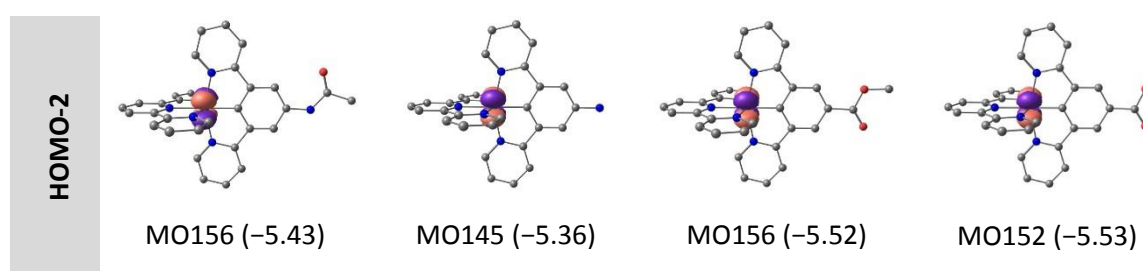
**Figure S15** ESI mass spectra of **a) 1**(PF<sub>6</sub>), **b) 2**(PF<sub>6</sub>), **c) 3**(PF<sub>6</sub>), **d) 4**(PF<sub>6</sub>), **e) 5**(PF<sub>6</sub>), and **f) 6**(PF<sub>6</sub>) in CH<sub>3</sub>CN. Insets show experimental and calculated isotopic pattern of the most intense peak.



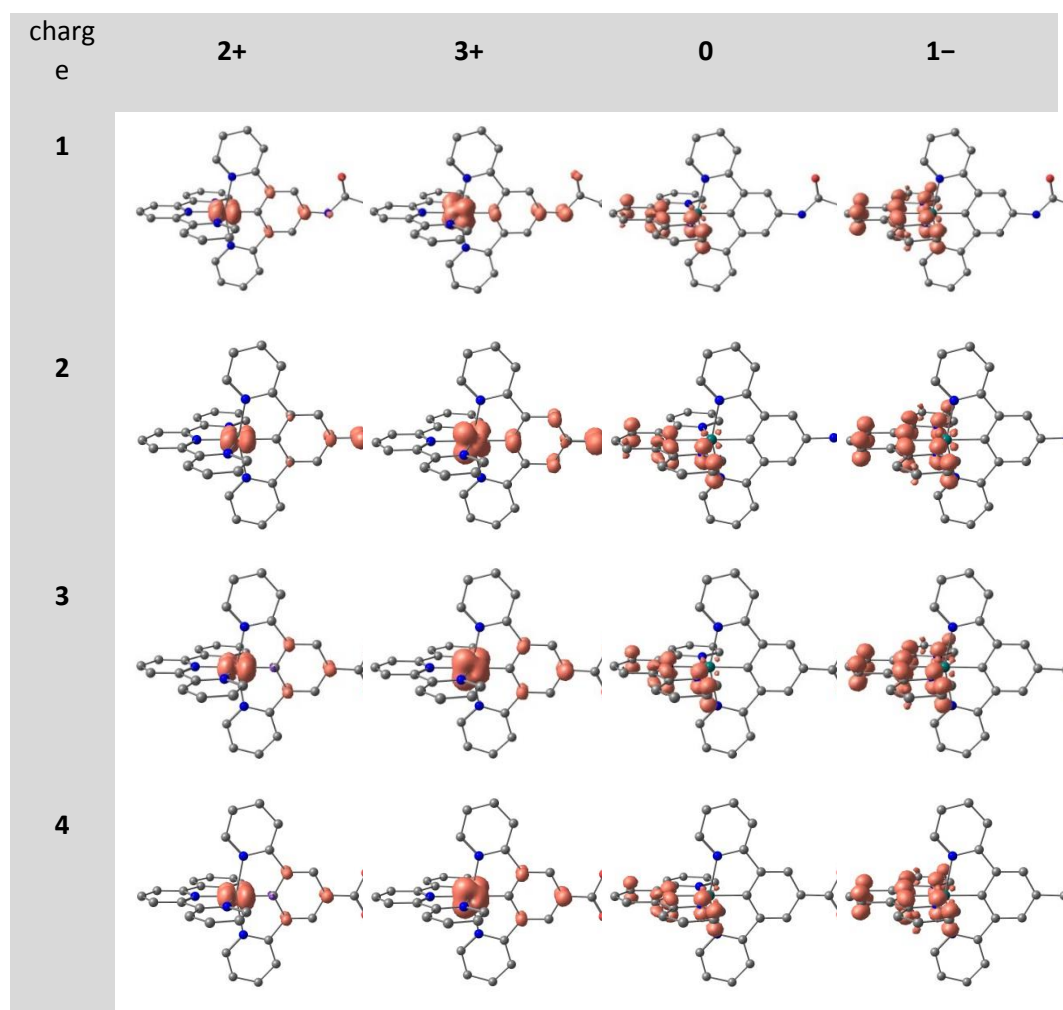
**Figure S16** IR spectra of complexes **a) 1**(PF<sub>6</sub>), **b) 2**(PF<sub>6</sub>), **c) 3**(PF<sub>6</sub>), **d) 4**(PF<sub>6</sub>) and **e) 6**(PF<sub>6</sub>)<sub>2</sub> in the solid state (KBr disk).

**Table S1** Selected molecular orbitals of  $1^+$ ,  $2^+$ ,  $3^+$ , and  $4^+$  (B3LYP, def2-SV(P), ZORA, COSMO(acetonitrile)) including orbital number (energy E in eV) (contour value 0.07). Hydrogen atoms are omitted for clarity.

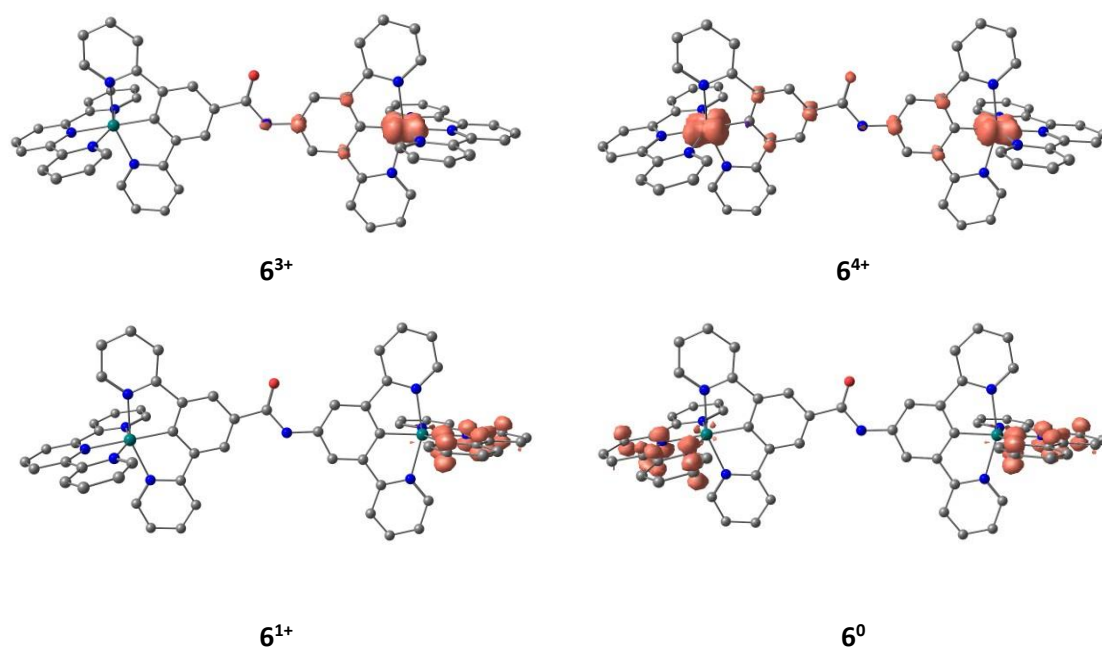
	$1^+$	$2^+$	$3^+$	$4^+$
LUMO+3	 MO162 (-1.50)	 MO151 (-1.45)	 MO162 (-1.57)	 MO158 (-1.58)
LUMO+2	 MO161 (-1.82)	 MO150 (-1.74)	 MO161 (-1.86)	 MO157 (-1.87)
LUMO+1	 MO160 (-2.23)	 MO149 (-2.20)	 MO160 (-2.27)	 MO156 (-2.28)
LUMO	 MO159 (-2.27)	 MO148 (-2.23)	 MO159 (-2.33)	 MO155 (-2.34)
HOMO	 MO158 (-4.99)	 MO147 (-4.71)	 MO158 (-5.31)	 MO154 (-5.33)
HOMO-1	 MO157 (-5.35)	 MO146 (-5.27)	 MO157 (-5.47)	 MO153 (-5.48)



**Table S2** DFT calculated spin densities of complexes  $1^+ - 4^+$  after single and double oxidation as well as single and double reduction (B3LYP, def2-SV(P), ZORA, COSMO(acetonitrile); contour value: 0.01).

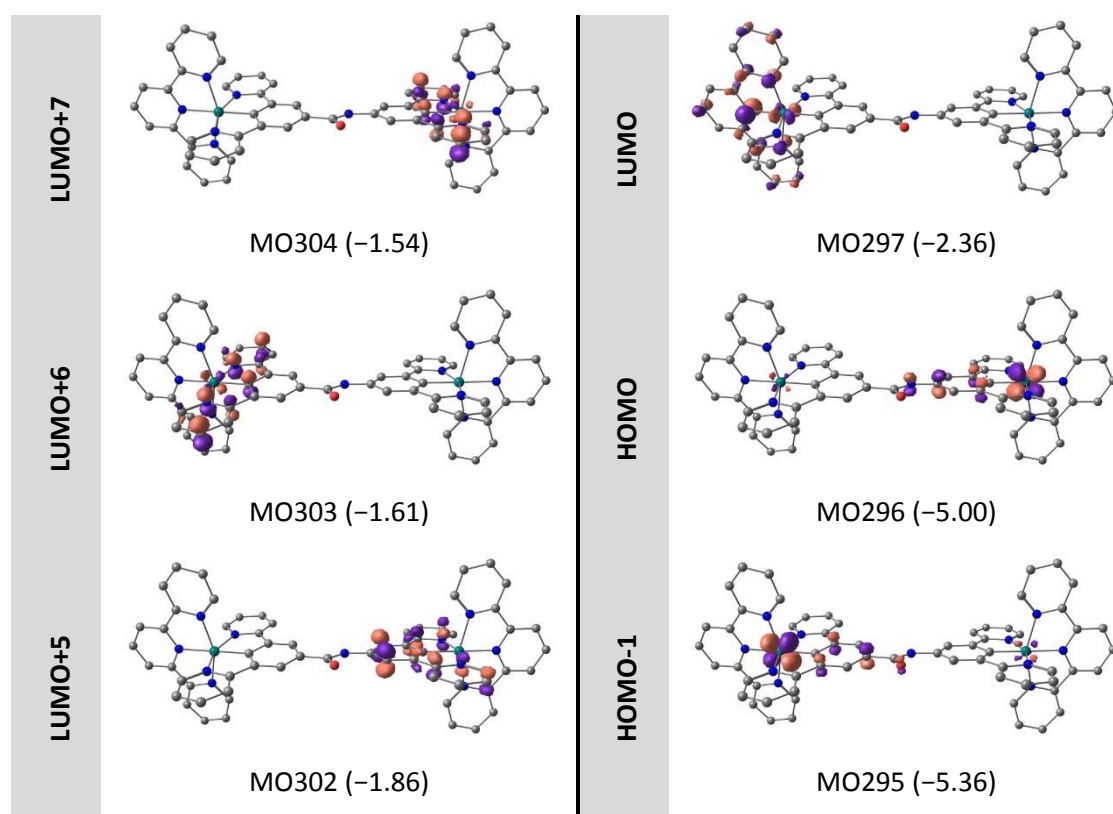


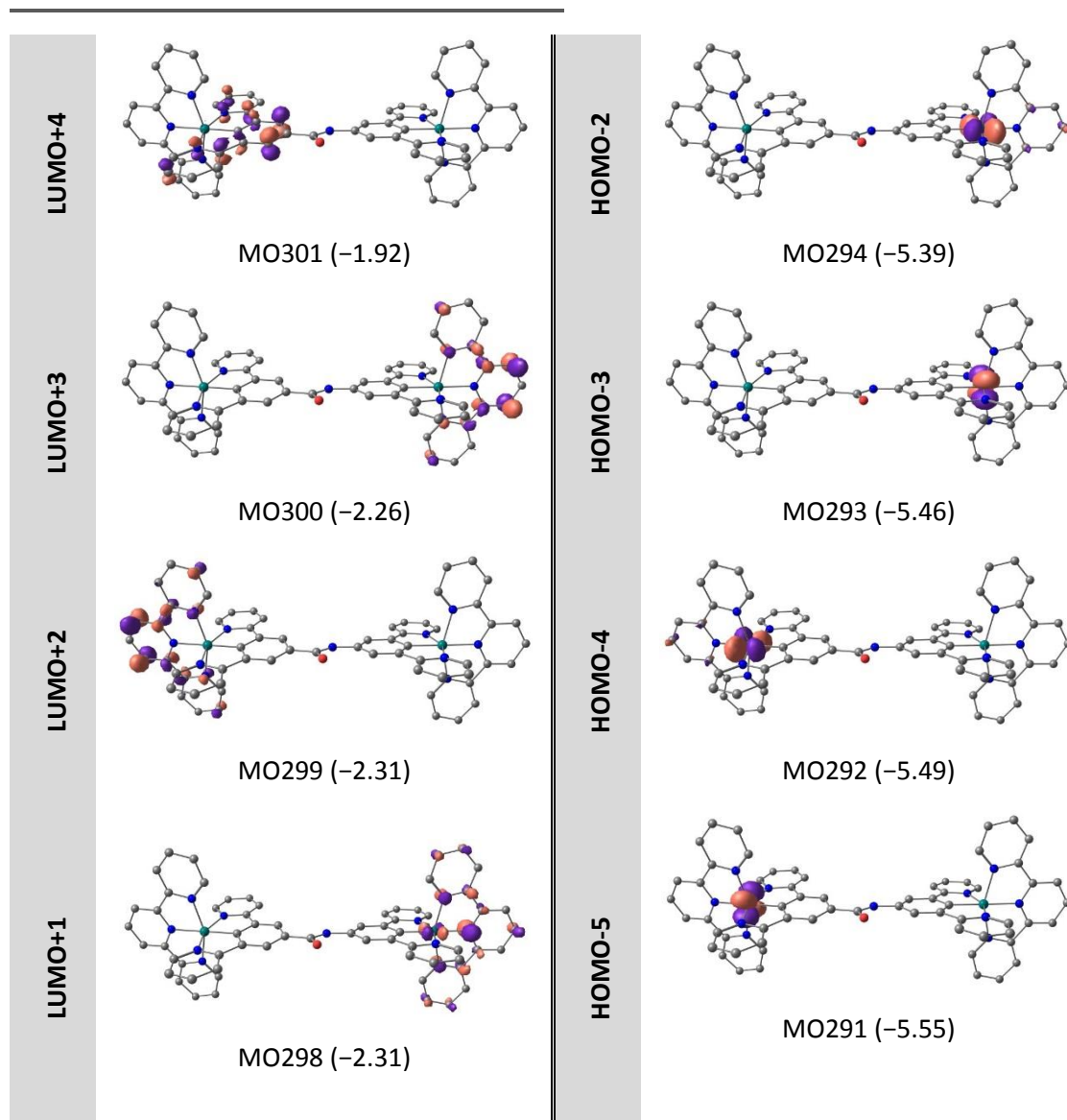




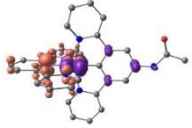
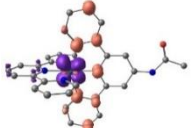
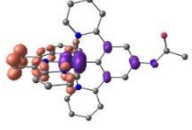
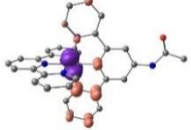
**Figure S17** DFT calculated spin densities of the singly and doubly oxidized complexes  $6^{3+}$  and  $6^{4+}$  as well as the singly and doubly reduced complexes  $6^+$  and  $6^0$  (B3LYP, def2-SV(P), ZORA, COSMO(acetonitrile); contour value: 0.01).

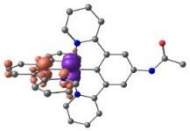
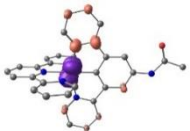
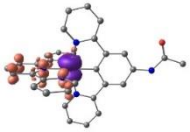
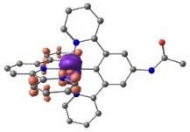
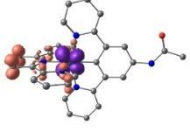
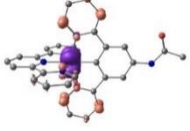
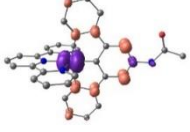
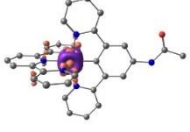
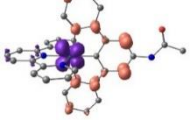
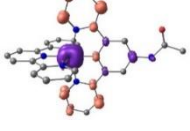
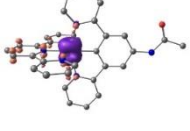
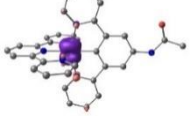
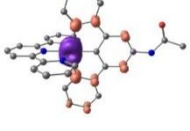
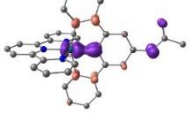
**Table S3** Selected molecular orbitals of  $6^{2+}$  (B3LYP, def2-SV(P), ZORA, COSMO(acetonitrile)) including orbital number (energy E in eV) (contour value 0.07). Hydrogen atoms are omitted for clarity.



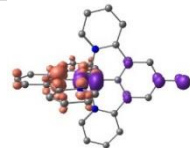
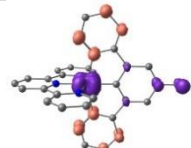
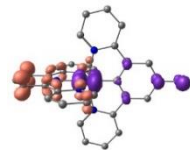
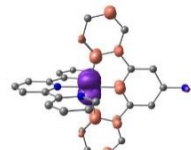


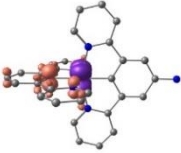
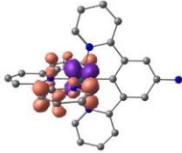
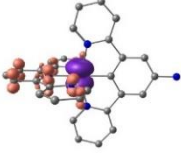
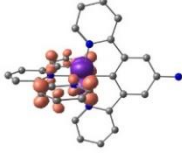
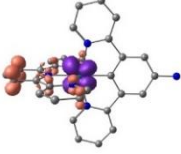
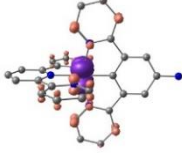
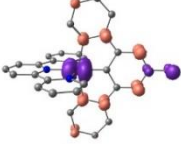
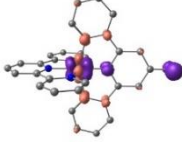
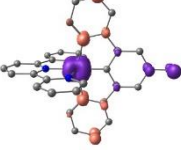
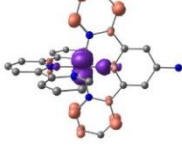
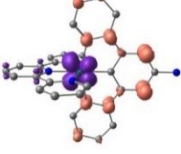
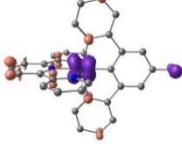
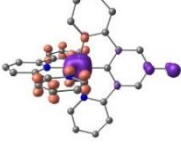
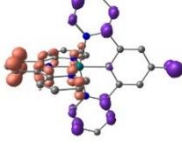
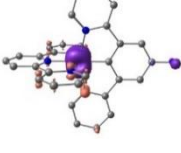
**Table S4** Selected vertical TD-DFT transitions of  $1^+$  (B3LYP, def2-SV(P), ZORA, COSMO(acetonitrile)) sorted by their energy including difference density plots  $|\psi_{ES}|^2 - |\psi_{GS}|^2$  (contour value 0.005, purple: depletion, orange: gain in electron density). Hydrogen atoms are omitted for clarity.

	$\tilde{\nu} / \text{cm}^{-1}$	$\lambda / \text{nm}$	$f_{osc}$	$ \psi_{ES} ^2 -  \psi_{GS} ^2$		$\tilde{\nu} / \text{cm}^{-1}$	$\lambda / \text{nm}$	$f_{osc}$	$ \psi_{ES} ^2 -  \psi_{GS} ^2$
1	13967	716	$4.30 \cdot 10^{-8}$		10	22891	437	0.00001	
2	14972	668	0.00066		13	24853	402	0.09267	

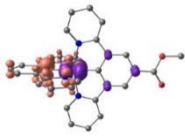
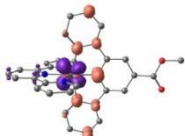
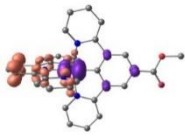
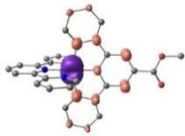
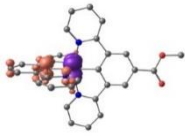
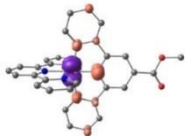
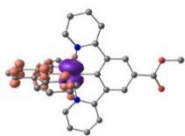
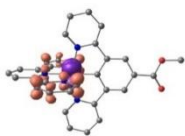
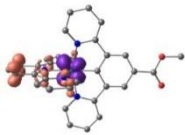
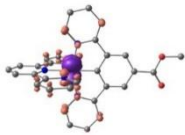
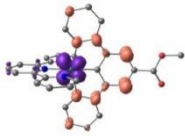
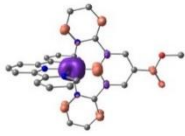
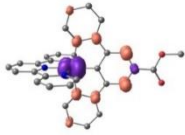
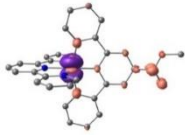
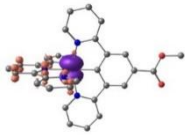
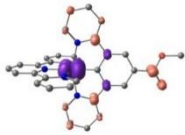
<b>3</b>	17170	582	0.00723		<b>14</b>	25051	399	0.03568	
<b>4</b>	18458	542	0.00512		<b>19</b>	28073	356	0.03405	
<b>5</b>	18728	534	0.05845		<b>20</b>	28080	356	0.03646	
<b>6</b>	20594	486	0.09011		<b>21</b>	28236	354	0.03297	
<b>7</b>	21029	476	0.00695		<b>23</b>	28339	353	0.04613	
<b>8</b>	21890	457	0.14519		<b>33</b>	32361	309	0.01697	
<b>9</b>	22432	446	0.01191		<b>34</b>	32565	307	0.02433	

**Table S5** Selected vertical TD-DFT transitions of  $2^+$  (B3LYP, def2-SV(P), ZORA, COSMO(acetonitrile)) sorted by their energy including difference density plots  $|\psi_{ES}|^2 - |\psi_{GS}|^2$  (contour value 0.005, purple: depletion, orange: gain in electron density). Hydrogen atoms are omitted for clarity.

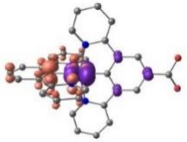
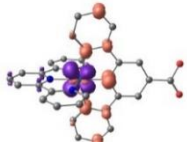
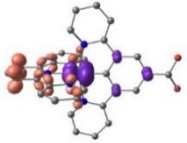
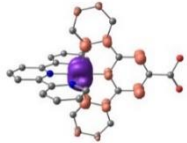
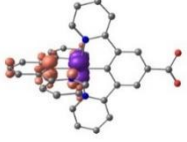
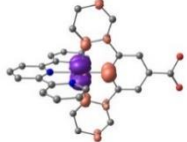
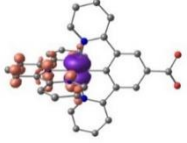
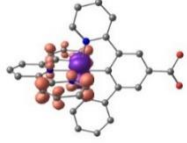
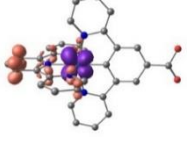
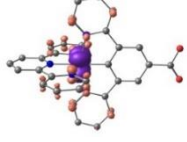
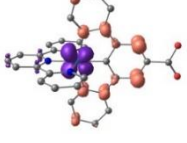
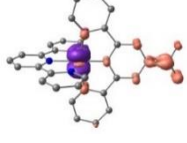
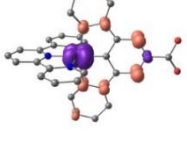
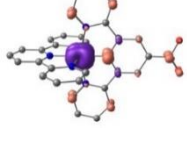
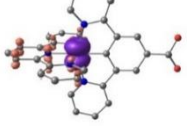
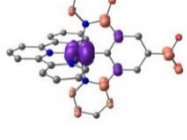
	$\tilde{\nu} / \text{cm}^{-1}$	$\lambda / \text{nm}$	$f_{\text{osc}}$	$ \psi_{ES} ^2 -  \psi_{GS} ^2$		$\tilde{\nu} / \text{cm}^{-1}$	$\lambda / \text{nm}$	$f_{\text{osc}}$	$ \psi_{ES} ^2 -  \psi_{GS} ^2$
<b>1</b>	12179	821	$4.57 \cdot 10^{-7}$		<b>15</b>	24593	407	0.02282	
<b>2</b>	12929	773	0.00062		<b>14</b>	24780	404	0.10567	

<b>3</b>	16901	592	0.00626		<b>18</b>	26283	381	0.01072	
<b>4</b>	18183	550	0.00412		<b>23</b>	27516	363	0.07089	
<b>5</b>	18431	543	0.06130		<b>24</b>	28019	357	0.06192	
<b>6</b>	19735	507	0.11450		<b>29</b>	30082	332	0.01847	
<b>7</b>	20703	483	0.05125		<b>32</b>	31177	321	0.01062	
<b>8</b>	20931	478	0.00062		<b>36</b>	32993	303	0.03505	
<b>9</b>	21795	459	0.03127		<b>46</b>	33168	302	0.02112	
<b>10</b>	22232	450	0.06565						

**Table S6** Selected vertical TD-DFT transitions of **3<sup>+</sup>** (B3LYP, def2-SV(P), ZORA, COSMO(acetonitrile)) sorted by their energy including difference density plots  $|\Psi_{ES}|^2 - |\Psi_{GS}|^2$  (contour value 0.005, purple: depletion, orange: gain in electron density). Hydrogen atoms are omitted for clarity.

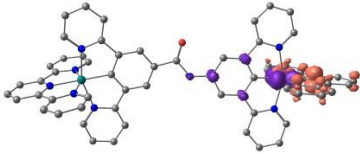
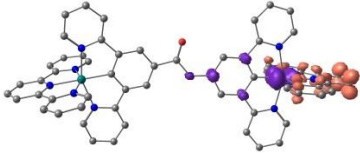
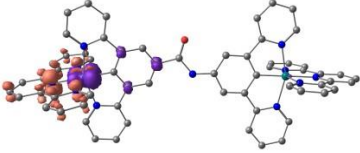
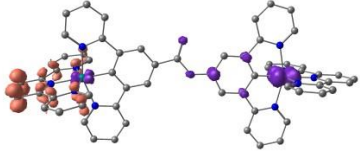
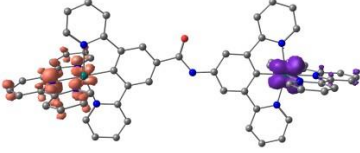
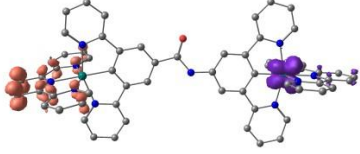
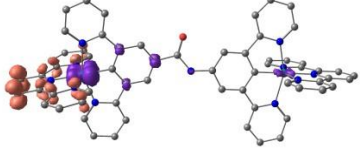
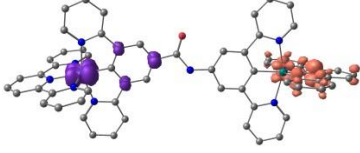
	$\tilde{\nu} / \text{cm}^{-1}$	$\lambda / \text{nm}$	$f_{\text{osc}}$	$ \Psi_{ES} ^2 -  \Psi_{GS} ^2$		$\tilde{\nu} / \text{cm}^{-1}$	$\lambda / \text{nm}$	$f_{\text{osc}}$	$ \Psi_{ES} ^2 -  \Psi_{GS} ^2$
<b>1</b>	15881	630	$1.75 \cdot 10^{-6}$		<b>10</b>	23117	433	$2.95 \cdot 10^{-7}$	
<b>3</b>	17096	585	0.00062		<b>9</b>	23166	432	0.00512	
<b>2</b>	17563	569	0.00902		<b>11</b>	24728	404	0.10876	
<b>4</b>	18873	530	0.00626		<b>18</b>	28165	355	0.05247	
<b>5</b>	19215	520	0.05380		<b>19</b>	28534	351	0.08369	
<b>8</b>	21496	465	0.00058		<b>24</b>	29891	335	0.11957	
<b>6</b>	21914	456	0.06001		<b>26</b>	30040	333	0.03531	
<b>7</b>	22283	449	0.17235		<b>28</b>	30815	325	0.05395	

**Table S7** Selected vertical TD-DFT transitions of  $4^+$  (B3LYP, def2-SV(P), ZORA, COSMO(acetonitrile)) sorted by their energy including difference density plots  $|\psi_{ES}|^2 - |\psi_{GS}|^2$  (contour value 0.005, purple: depletion, orange: gain in electron density). Hydrogen atoms are omitted for clarity.

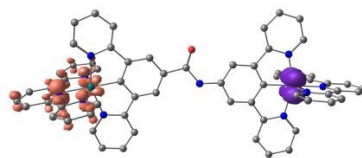
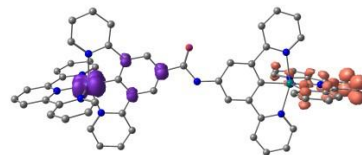
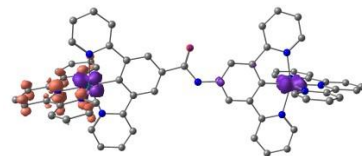
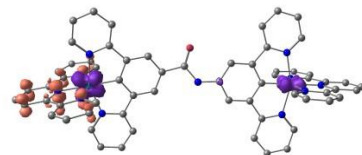
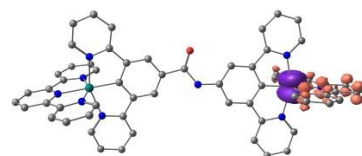
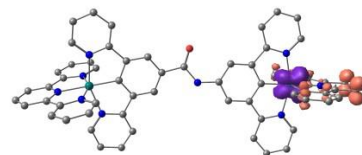
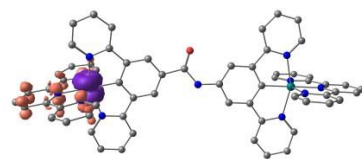
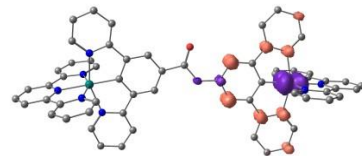
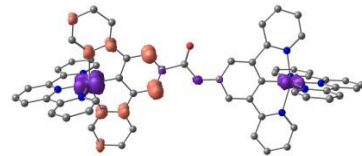
	$\tilde{\nu}$ / $\text{cm}^{-1}$	$\lambda$ / nm	$f_{\text{osc}}$	$ \psi_{ES} ^2 -  \psi_{GS} ^2$		$\tilde{\nu}$ / $\text{cm}^{-1}$	$\lambda$ / nm	$f_{\text{osc}}$	$ \psi_{ES} ^2 -  \psi_{GS} ^2$
<b>1</b>	15985	626	$3.06 \cdot 10^{-6}$		<b>10</b>	23117	433	$1.66 \cdot 10^{-6}$	
<b>3</b>	17210	581	0.00063		<b>9</b>	23179	431	0.00662	
<b>2</b>	17603	568	0.00919		<b>11</b>	24694	405	0.10794	
<b>4</b>	18916	529	0.00616		<b>18</b>	28199	355	0.05170	
<b>5</b>	19264	519	0.05350		<b>19</b>	28564	350	0.08182	
<b>8</b>	21518	465	0.00191		<b>26</b>	29633	338	0.04010	
<b>6</b>	21948	456	0.05880		<b>24</b>	29888	335	0.12162	
<b>7</b>	22325	448	0.16638		<b>28</b>	30892	324	0.03754	



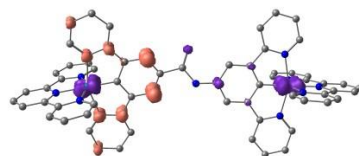
**Table S8** Selected vertical TD-DFT transitions of  $6^{2+}$  (B3LYP, def2-SV(P), ZORA, COSMO(acetonitrile)) sorted by their energy including difference density plots  $|\psi_{ES}|^2 - |\psi_{GS}|^2$  (contour value 0.005, purple: depletion, orange: gain in electron density). Hydrogen atoms are omitted for clarity.

	$\tilde{\nu} / \text{cm}^{-1}$	$\lambda / \text{nm}$	$f_{osc}$	$ \psi_{ES} ^2 -  \psi_{GS} ^2$
<b>1</b>	13941	717	$2.65 \cdot 10^{-6}$	
<b>3</b>	14926	670	0.00063	
<b>2</b>	15509	645	$5.04 \cdot 10^{-6}$	
<b>12</b>	15932	628	0.00149	
<b>21</b>	16101	621	$4.49 \cdot 10^{-6}$	
<b>25</b>	16358	611	$1.44 \cdot 10^{-6}$	
<b>6</b>	16487	607	0.00070	
<b>19</b>	16676	600	$2.95 \cdot 10^{-6}$	

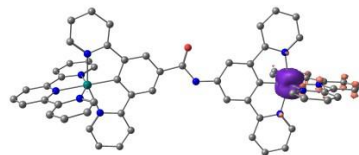


**26** 16800 595  $3.25 \cdot 10^{-7}$ **23** 16842 594 0.00013**11** 17953 557 0.02374**10** 18348 545 0.02801**7** 18491 541 0.00986**9** 18780 533 0.05506**8** 18854 530 0.01090**13** 20498 488 0.07937**14** 20813 481 0.05640

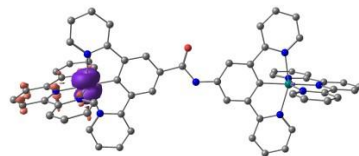
**22** 21003 476 0.00912



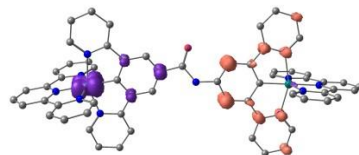
**15** 21806 459 0.34875



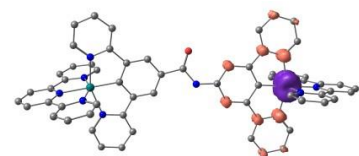
**18** 22284 449 0.13827



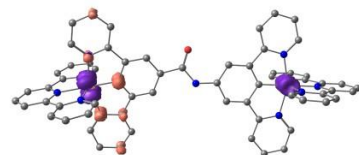
**41** 22291 449 0.01702



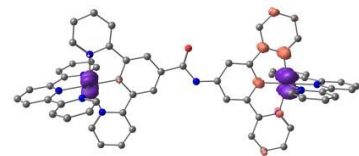
**20** 22393 447 0.00896



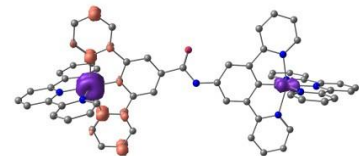
**36** 24755 404 0.04056



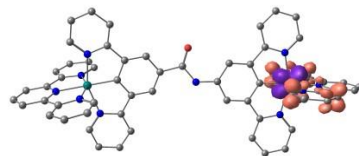
**38** 24977 400 0.16626

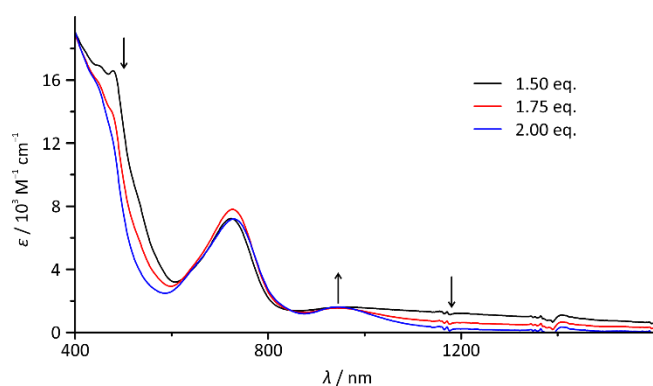


**44** 25891 386 0.03412



**50** 26642 375 0.01756

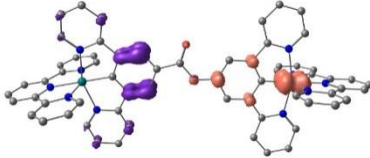
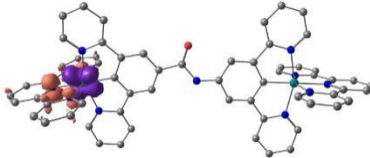
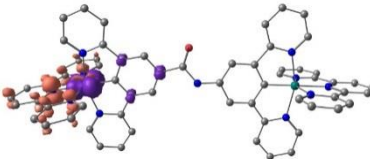
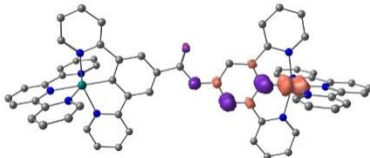
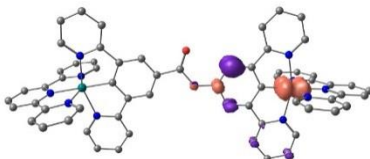
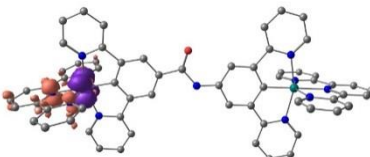
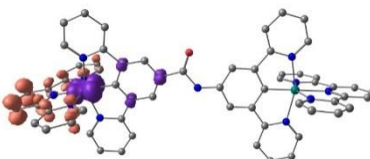
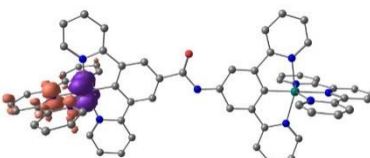
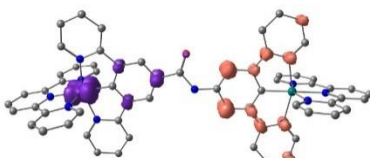




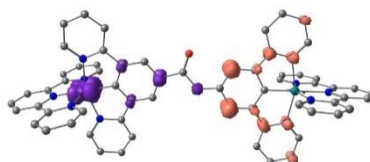
**Figure S18** Absorption spectra of  $6^{2+}$  after addition of 1.50, 1.75 and 2.00 equivalents of  $(\text{NH}_4)_2[\text{Ce}(\text{NO}_3)_6]$  as oxidant ( $6^{3+} \rightarrow 6^{4+}$ ).

**Table S9** Selected vertical TD-DFT transitions of  $6^{3+}$  (B3LYP, def2-SV(P), ZORA, COSMO(acetonitrile)) sorted by their energy including difference density plots  $|\psi_{\text{ES}}|^2 - |\psi_{\text{GS}}|^2$  (contour value 0.005, purple: depletion, orange: gain in electron density). Hydrogen atoms are omitted for clarity.

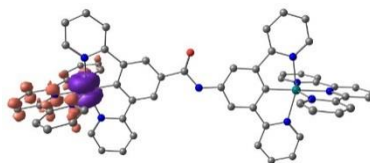
	$\tilde{\nu} / \text{cm}^{-1}$	$\lambda / \text{nm}$	$f_{\text{osc}}$	$ \psi_{\text{ES}} ^2 -  \psi_{\text{GS}} ^2$
1	4255	2350	$4.63 \cdot 10^{-7}$	
2	4495	2225	0.00026	
3	7172	1394	0.06523	
4	8319	1202	$2.50 \cdot 10^{-6}$	
5	8674	1153	0.00050	

<b>11</b>	13059	766	0.00423	
<b>6</b>	14873	672	0.00036	
<b>9</b>	15530	644	$8.00 \cdot 10^{-8}$	
<b>7</b>	15758	635	0.19415	
<b>8</b>	15988	626	0.04104	
<b>10</b>	16361	611	$5.85 \cdot 10^{-6}$	
<b>19</b>	17520	571	0.00070	
<b>13</b>	17850	560	0.00943	
<b>44</b>	17998	556	0.01475	

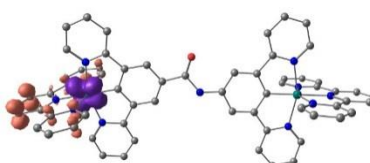
37 18303 546 0.01029



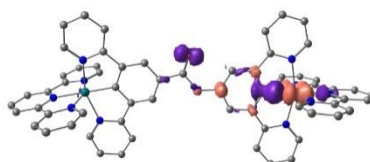
21 19180 521 0.01038



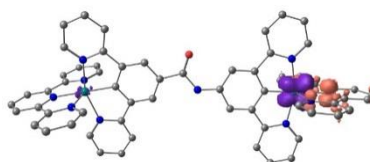
24 19526 512 0.05026



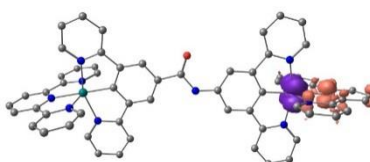
25 19889 503 0.00272



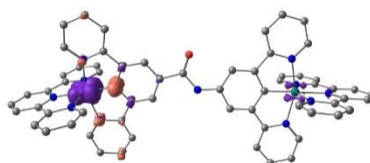
30 20522 487 0.00723



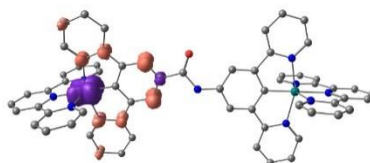
35 20717 483 0.00345



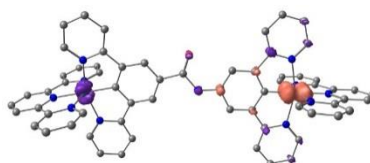
31 20725 483 0.00114



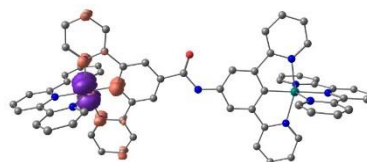
42 21775 459 0.05831



43 22161 451 0.20749



49 22512 444 0.01892



48 22618 442 0.07026

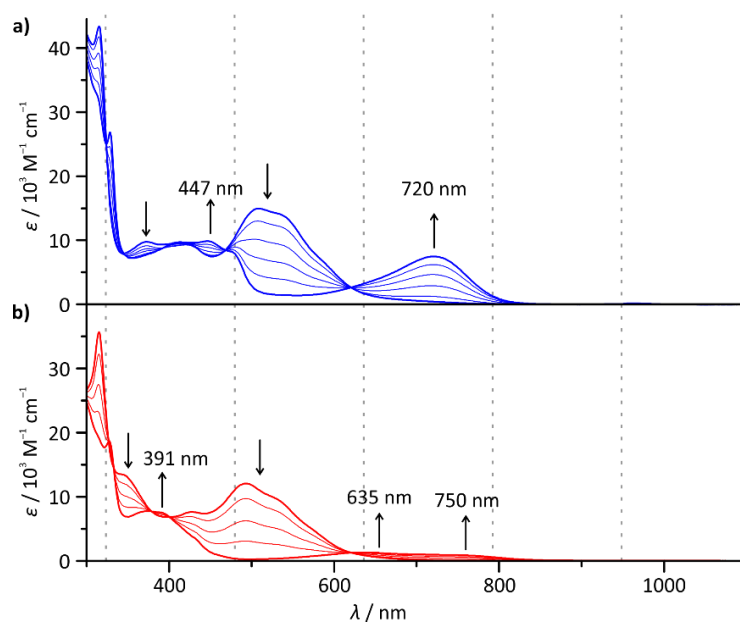
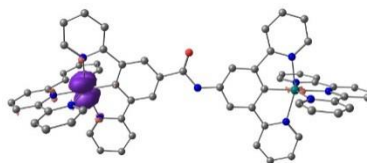


**Figure S19** UV-Vis absorption spectra of **1**<sup>+</sup> (top, blue) and **3**<sup>+</sup> (bottom, red) in dry acetonitrile upon addition of 0→1 equivalents of  $(\text{NH}_4)_2[\text{Ce}(\text{NO}_3)_6]$  as oxidant.

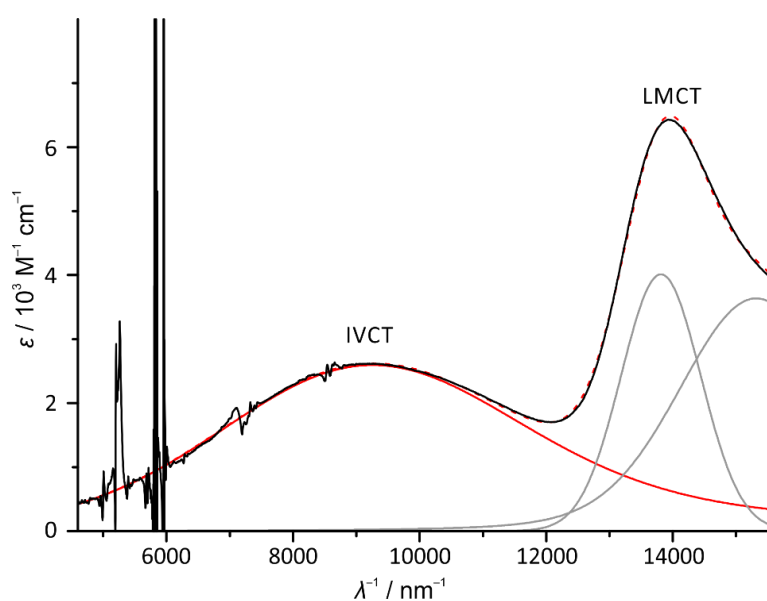


**Figure S20** Fit of the IVCT band of  $6^{3+}$  (generated in situ by oxidation of  $6^{2+}$  with one equivalent of  $(\text{NH}_4)_2[\text{Ce}(\text{NO}_3)_6]$  in acetonitrile). The figure shows the experimental spectrum (black), the fit of the spectral range between 3500 and 16000  $\text{cm}^{-1}$  (red, dashed), the band fits of the LMCT bands (grey) and the fit of the IVCT band (red).

Fit parameters:

**IVCT:**

$$\tilde{\nu}_{\text{max}} = 8585 \text{ cm}^{-1}$$

$$\epsilon_{\text{max}} = 2600 \text{ M}^{-1} \text{ cm}^{-1}$$

$$\tilde{\nu}_{1/2} = 6020 \text{ cm}^{-1}$$

**LMCT 1:**

$$\tilde{\nu}_{\text{max}} = 13780 \text{ cm}^{-1}$$

$$\epsilon_{\text{max}} = 4010 \text{ M}^{-1} \text{ cm}^{-1}$$

$$\tilde{\nu}_{1/2} = 1480 \text{ cm}^{-1}$$

**LMCT 2:**

$$\tilde{\nu}_{\text{max}} = 15225 \text{ cm}^{-1}$$

$$\epsilon_{\text{max}} = 3640 \text{ M}^{-1} \text{ cm}^{-1}$$

$$\tilde{\nu}_{1/2} = 2900 \text{ cm}^{-1}$$



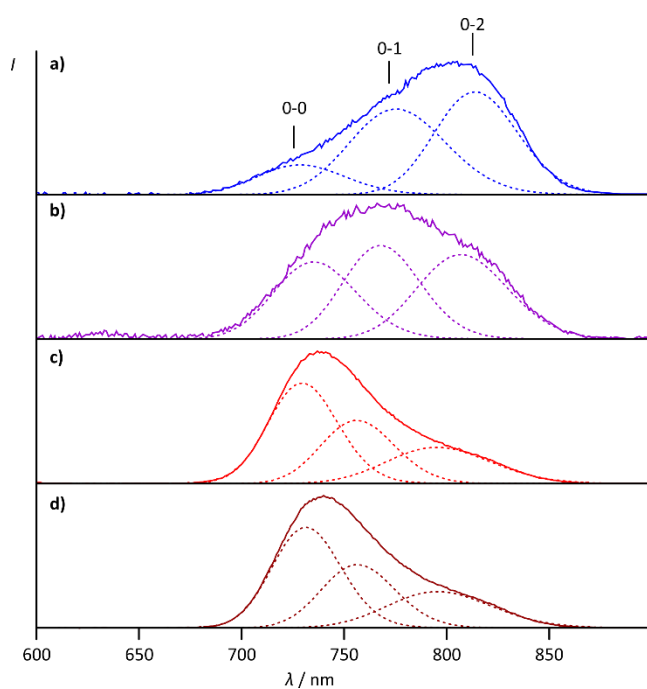


**Figure S21** Spectral decomposition of the emission spectra of **a) 1<sup>+</sup>** **b) 2<sup>+</sup>** **c) 3<sup>+</sup>** and **d) 4<sup>+</sup>** (recorded at 155 K in butyronitrile solution) into individual gaussians. Vibrational progression energies are  $740\text{ cm}^{-1}$  (**1<sup>+</sup>**),  $710\text{ cm}^{-1}$  (**2<sup>+</sup>**) and  $670\text{ cm}^{-1}$  (**3<sup>+</sup>** and **4<sup>+</sup>**).<sup>1,2</sup>

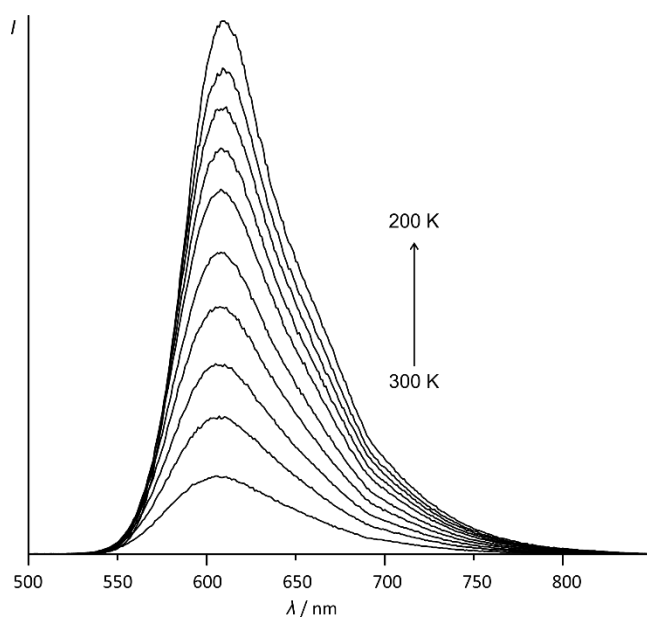


**Figure S22** Emission spectra of  $[\text{Ru}(\text{bpy})_3](\text{PF}_6)_2$  in butyronitrile in the temperature range between 300 K and 200 K.

<sup>1</sup> Z. Murtaza, D. K. Graff, A. P. Zipp, L. A. Worl, Jones, Wayne E. Jr., W. D. Bates and T. J. Meyer, *J. Phys. Chem.*, 1994, **98**, 10504–10513.

<sup>2</sup> K. Heinze, K. Hempel and M. Beckmann, *Eur. J. Inorg. Chem.*, 2006, **2006**, 2040–2050.

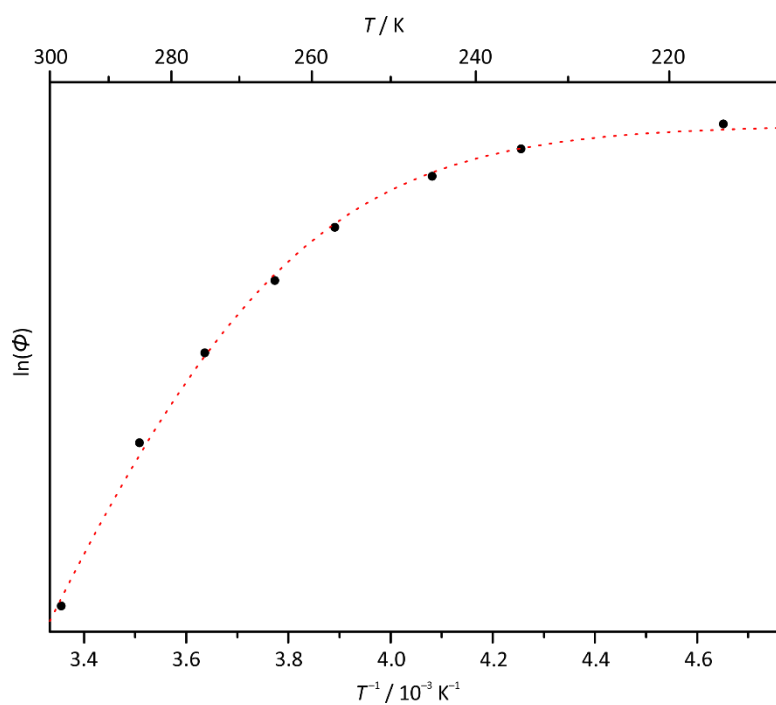


**Figure S23** Variable-temperature emission plot  $\ln(\phi)$  vs.  $T^{-1}$  of  $[\text{Ru}(\text{bpy})_3](\text{PF}_6)_2$  in air-equilibrated butyronitrile in the temperature range between 300 K and 200 K. Activation barrier  $\Delta E$  of  $36.0 \text{ kJ mol}^{-1}$  has been determined from the fit using Meyer's equation (literature value of  $\Delta E = 42.6 \text{ kJ mol}^{-1}$  for degassed butyronitrile).<sup>3</sup>

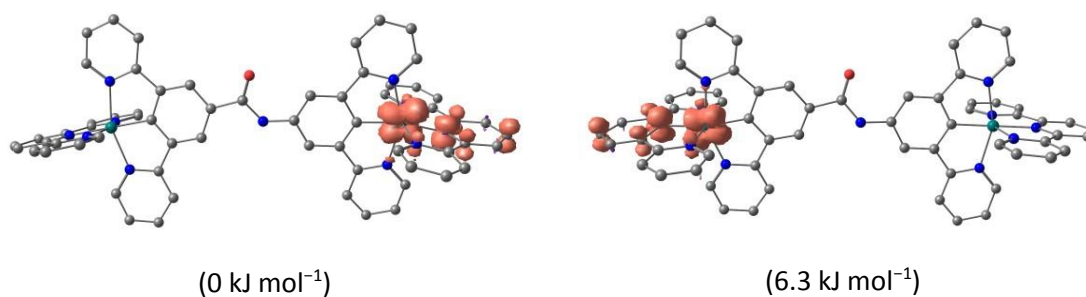


**Figure S24** DFT calculated spin densities of the  $^3\text{MLCT}$  states of  $6^{2+}$  (B3LYP, def2-SV(P), ZORA, COSMO(acetonitrile); contour value: 0.01). The relative electronic energies are given in parentheses.

<sup>3</sup> B. Durham, J. V. Caspar, J. K. Nagle and T. J. Meyer, *J. Am. Chem. Soc.*, 1982, **104**, 4803–4810.

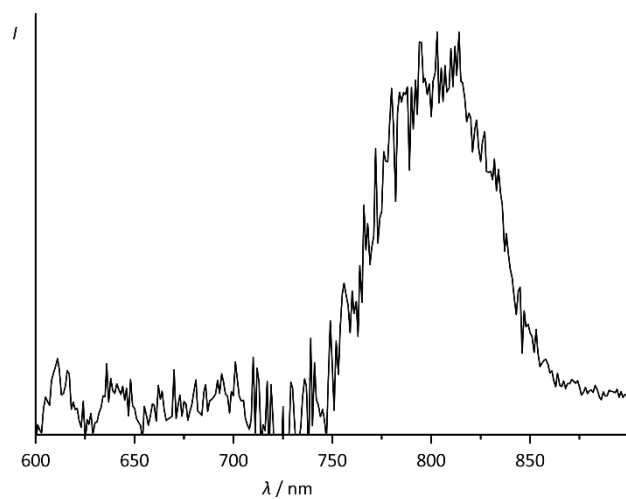
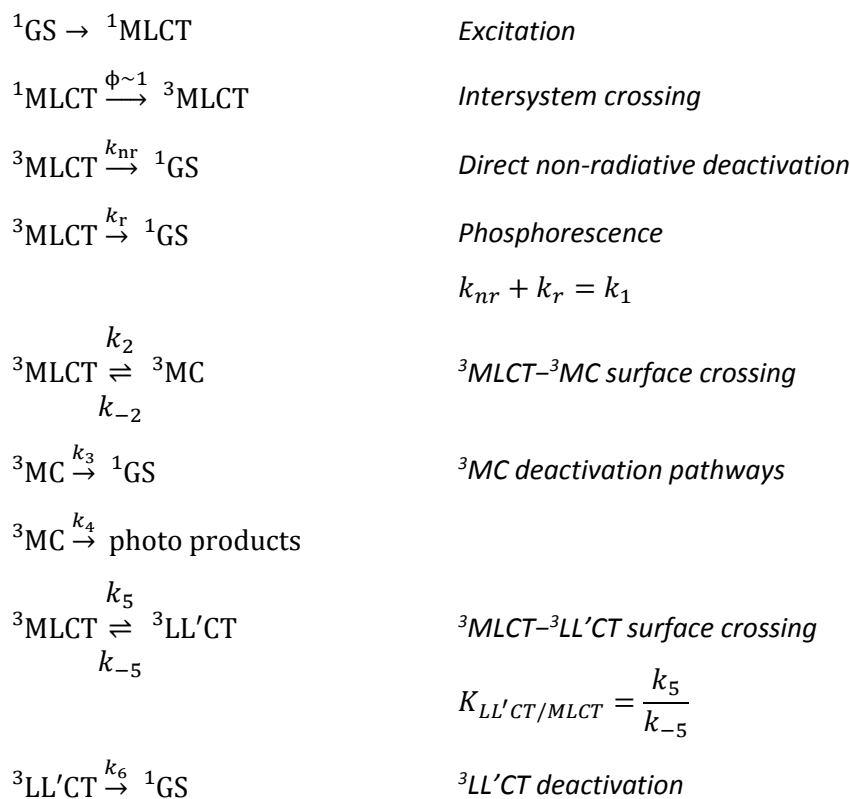


**Figure S25** Difference of the emission spectra of  $6^{2+}$  at 155 K in butyronitrile solution upon excitation at 560 nm and 480 nm.

### Derivation of the equation used to fit the $\ln(\phi)$ vs. $T^{-1}$ plots

Excited state reaction pathways:



We assume that the  $^3\text{LL}'\text{CT}$  state is chemically stable.

Based on the above reactions, the lifetime  $\tau_0$  of the  $^3\text{MLCT}$  state can be expressed as follows:

$$\frac{1}{\tau_0} = k_1 + k_2 \left( \frac{k_3 + k_4}{k_{-2} + k_3 + k_4} \right) + k_5 \left( \frac{k_6}{k_{-5} + k_6} \right) \quad (1)$$

In principle, all rate constants have to be considered as temperature-dependent. However, Meyer<sup>[4]</sup> argued, that the rate constants  $k_1$  and  $k_3$  for intersystem crossing describe processes at the respective Franck-Condon point and therefore are independent from the temperature. For the same reason,  $k_6$  can be considered temperature-independent.

Following Meyer's argumentation, the back reaction from the  $^3\text{MC}$  state to the  $^3\text{MLCT}$  state is slow compared to the  $^3\text{MC}$  state deactivation ( $k_{-2} \ll k_3 + k_4$ ). Therefore, the first fraction  $\left( \frac{k_3 + k_4}{k_{-2} + k_3 + k_4} \right)$  of equation (1) equals 1:

$$\frac{1}{\tau_0(T)} = k_1 + k_2(T) + k_5 \left( \frac{k_6}{k_{-5} + k_6} \right) \quad (2)$$

<sup>4</sup> B. Durham, J. V. Caspar, J. K. Nagle and T. J. Meyer, *J. Am. Chem. Soc.*, 1982, **104**, 4803–4810.

According to Meyer,  $k_2(T)$  is composed of a rate constant at infinite temperature ( $k_2^0$ ) and an Arrhenius-like activation barrier term, taking the  $^3\text{MLCT}$ - $^3\text{MC}$  activation barrier  $\Delta G_1^\ddagger$  into account.

$$k_2(T) = k_2^0 \exp\left(-\frac{\Delta G_1^\ddagger}{RT}\right) \quad (3)$$

For the second fraction  $k_5 \left(\frac{k_6}{k_{-5} + k_6}\right)$ , a differentiation into two limiting cases is necessary:

- a) When  $k_{-5}$  is small compared to  $k_6$ , the surface crossing to the  $^3\text{LL}'\text{CT}$  state is irreversible and for the lifetime of the  $^3\text{MLCT}$  state follows:

$$\frac{1}{\tau_0(T)} = k_1 + k_2(T) + k_5(T) \quad (4)$$

In this case, just as above for  $k_2(T)$ ,  $k_5(T)$  is composed of a rate constant at infinite temperature and an Arrhenius term, associated with the  $^3\text{MLCT}$ - $^3\text{LL}'\text{CT}$  activation barrier  $\Delta G_2^\ddagger$ .

$$k_5(T) = k_5^0 \exp\left(-\frac{\Delta G_2^\ddagger}{RT}\right) \quad (5)$$

- b) When the back reaction from the  $^3\text{LL}'\text{CT}$  to the  $^3\text{MLCT}$  state is faster than the depopulation of the  $^3\text{LL}'\text{CT}$  state into the ground state ( $k_{-5} < k_6$ ), the  $^3\text{LL}'\text{CT}$  and  $^3\text{MLCT}$  states are in thermal equilibrium:

$$\frac{1}{\tau_0(T)} = k_1 + k_2(T) + K_{\text{LL}'\text{CT}/\text{MLCT}} \cdot k_6 \quad (6)$$

An exponential term is required to describe the temperature dependence of the last component of the equation in this case as well, but it contains the difference between the Gibbs free enthalpies of the  $^3\text{LL}'\text{CT}$  and  $^3\text{MLCT}$  states.

$$K_{\text{LL}'\text{CT}/\text{MLCT}} \cdot k_6 = k_6 \exp\left(-\frac{\Delta G^0}{RT}\right) \text{ with } \Delta G^0 = G_{\text{LL}'\text{CT}}^0 - G_{\text{MLCT}}^0 \quad (7)$$

Thus, the mathematical description with a sum over two exponential terms, which was used to fit the  $\ln(\phi)$  vs.  $T^{-1}$  plots, is identical for both limiting cases, although the physical implications differ substantially:

$$\text{a) } \frac{1}{\tau_0(T)} = k_1 + k_2^0 \exp\left(-\frac{\Delta G_1^\ddagger}{RT}\right) + k_5^0 \exp\left(-\frac{\Delta G_2^\ddagger}{RT}\right) \quad (8\text{a})$$

$$\text{b) } \frac{1}{\tau_0(T)} = k_1 + k_2^0 \exp\left(-\frac{\Delta G_1^\ddagger}{RT}\right) + k_6 \exp\left(-\frac{\Delta G^0}{RT}\right) \quad (8\text{b})$$

A decision between the two cases a) or b) can only be made based on experimental data. When  $\Delta G^0$ , the difference between the Gibbs free enthalpies of the  $^3\text{LL}'\text{CT}$  and  $^3\text{MLCT}$  states, is negative, a decrease of the  $^3\text{MLCT}$  lifetime  $\tau_0(T)$  with decreasing temperature is expected for case b), while for case a) the lifetime should increase. In this study, the quantum yield  $\phi(T)$  instead of the  $^3\text{MLCT}$  lifetime  $\tau_0(T)$  is measured. This, however, does not affect the obtained data neither qualitatively nor quantitatively, because  $\phi$  and  $\tau_0(T)$  are linearly related when  $k_r$  is independent from the temperature:  $\phi(T) = k_r \cdot \tau_0(T)$ . This temperature-independence has been observed in all studies on luminescent polypyridine ruthenium(II) complexes.

## 6.5 SUPPORTING INFORMATION TO 3.4: STRONGLY COUPLED CYCLOMETALATED RUTHENIUM TRIARYLAMINE CHROMOPHORES AS SENSITIZERS FOR DSSCs

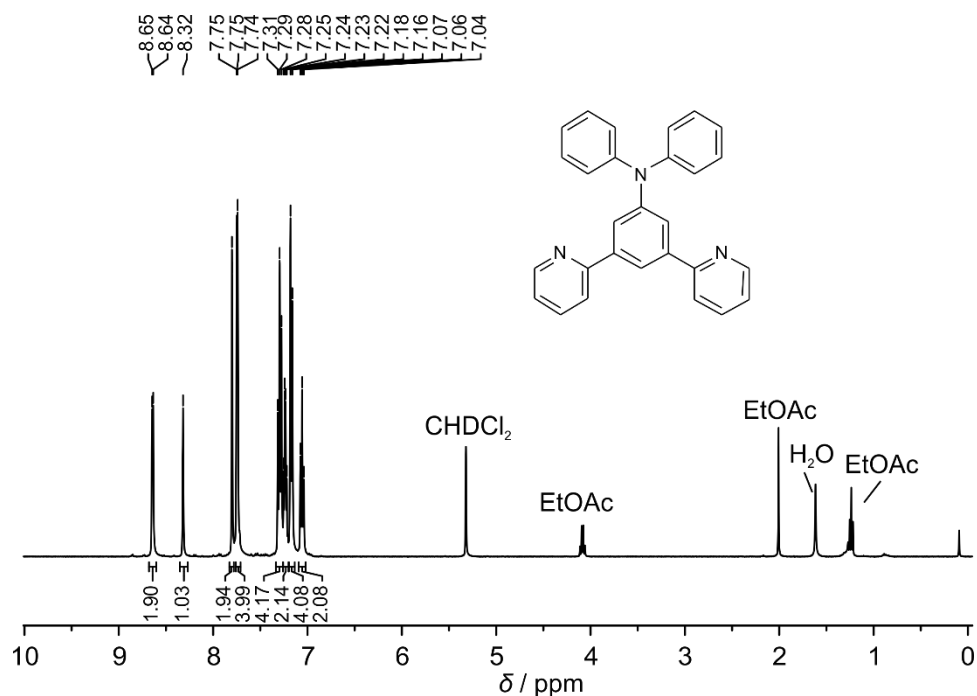


Figure S1 <sup>1</sup>H NMR spectrum (400 MHz) of ligand **L<sup>b</sup>** in CD<sub>2</sub>Cl<sub>2</sub>.

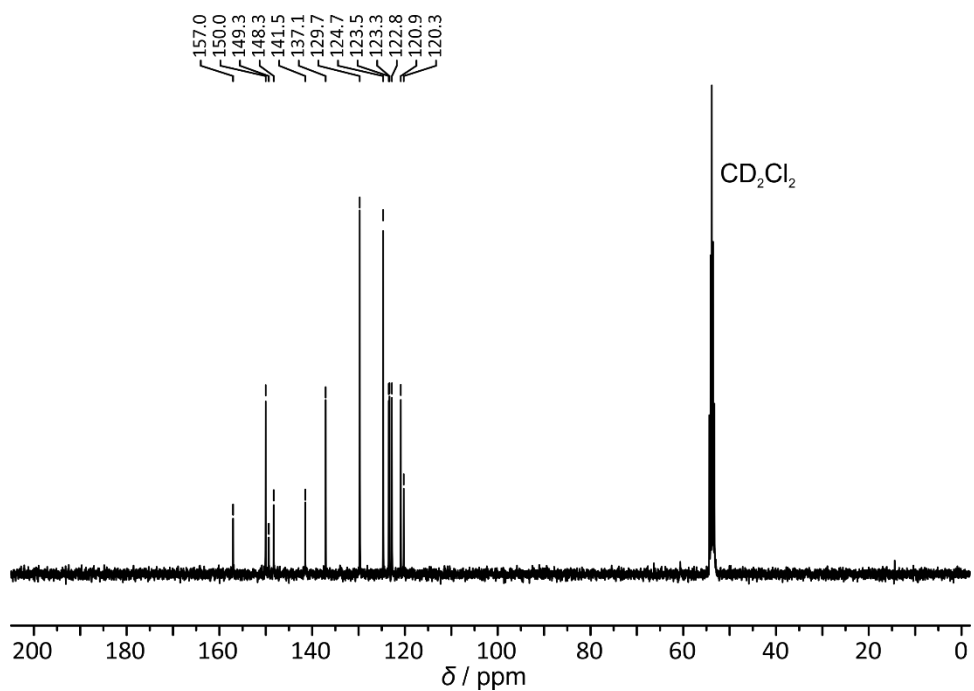


Figure S2 <sup>13</sup>C NMR spectrum (100 MHz) of ligand **L<sup>b</sup>** in CD<sub>2</sub>Cl<sub>2</sub>.

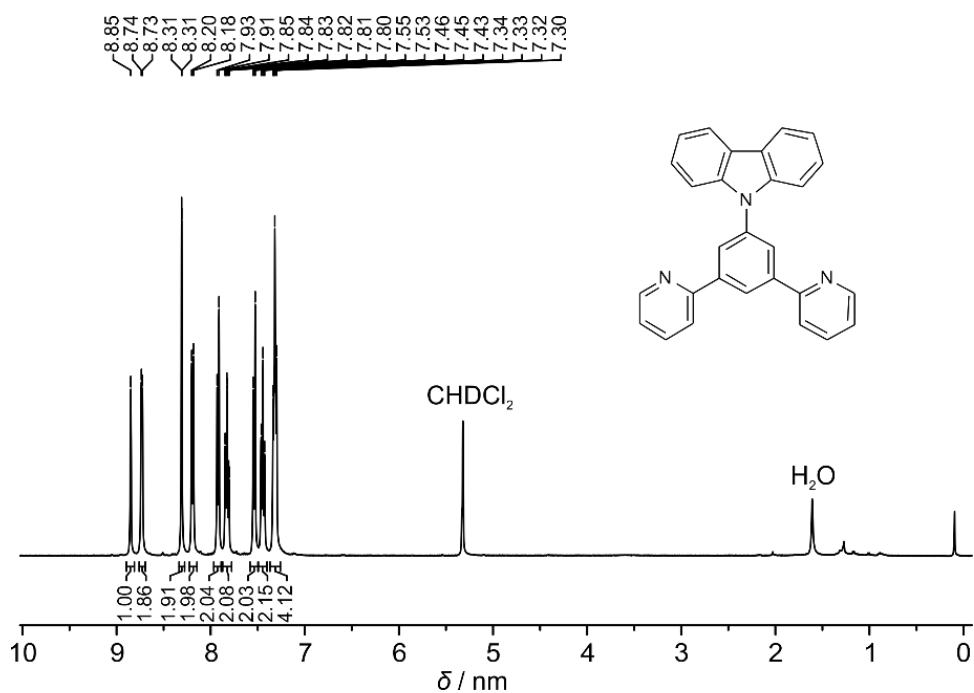


Figure S3  $^1H$  NMR spectrum (400 MHz) of ligand  $L^c$  in  $CD_2Cl_2$ .

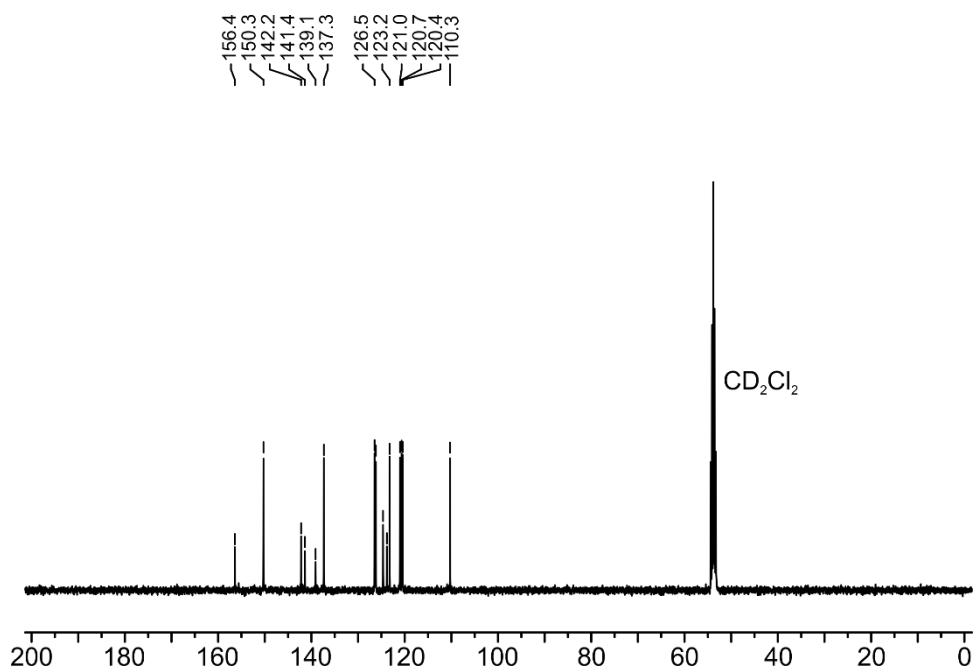
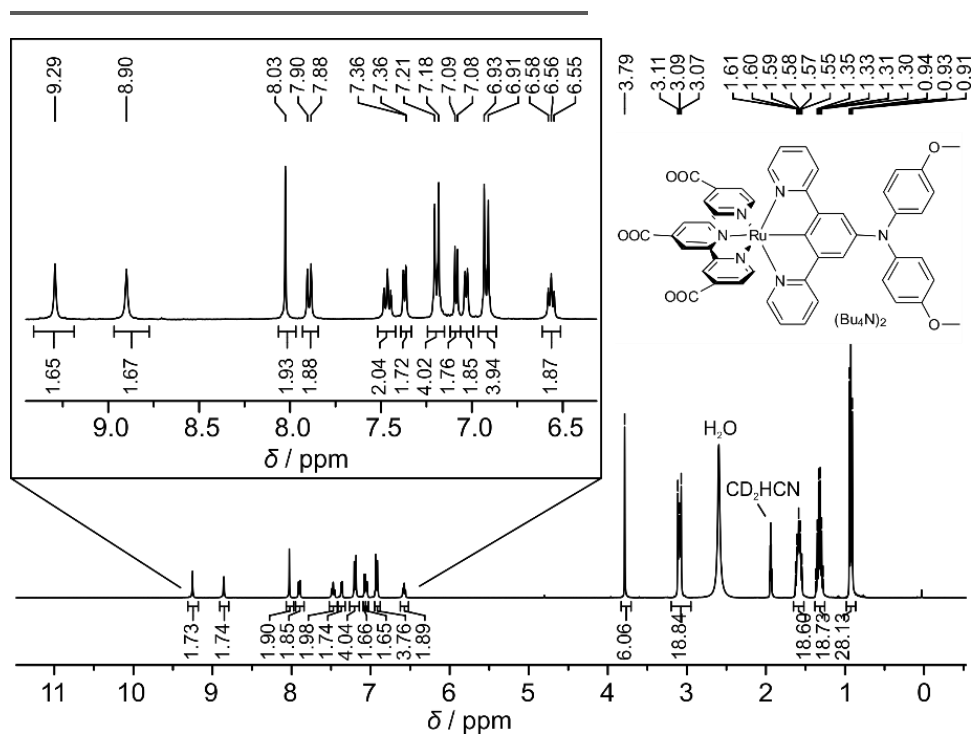
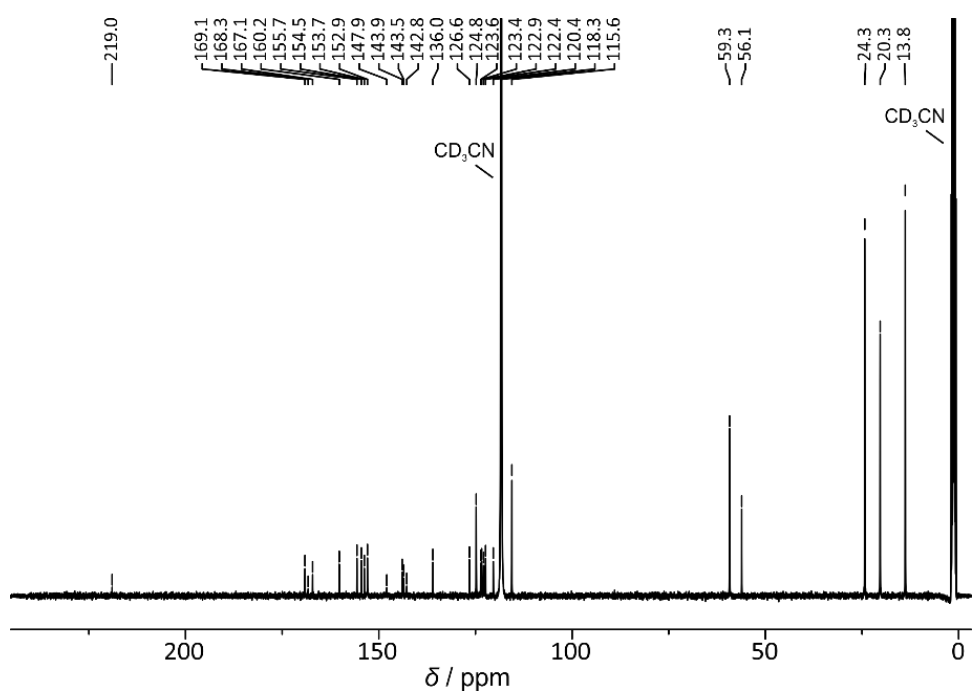


Figure S4  $^{13}C$  NMR spectrum (100 MHz) of ligand  $L^c$  in  $CD_2Cl_2$ .





**Figure S5**  $^1\text{H}$  NMR spectrum (400 MHz) of dye  $[\text{tBu}_4\text{N}]_2[\mathbf{2a}]$  in  $\text{CD}_3\text{CN}$ .



**Figure S6**  $^{13}\text{C}$  NMR spectrum (100 MHz) of dye  $[\text{tBu}_4\text{N}]_2[\mathbf{2a}]$  in  $\text{CD}_3\text{CN}$ .

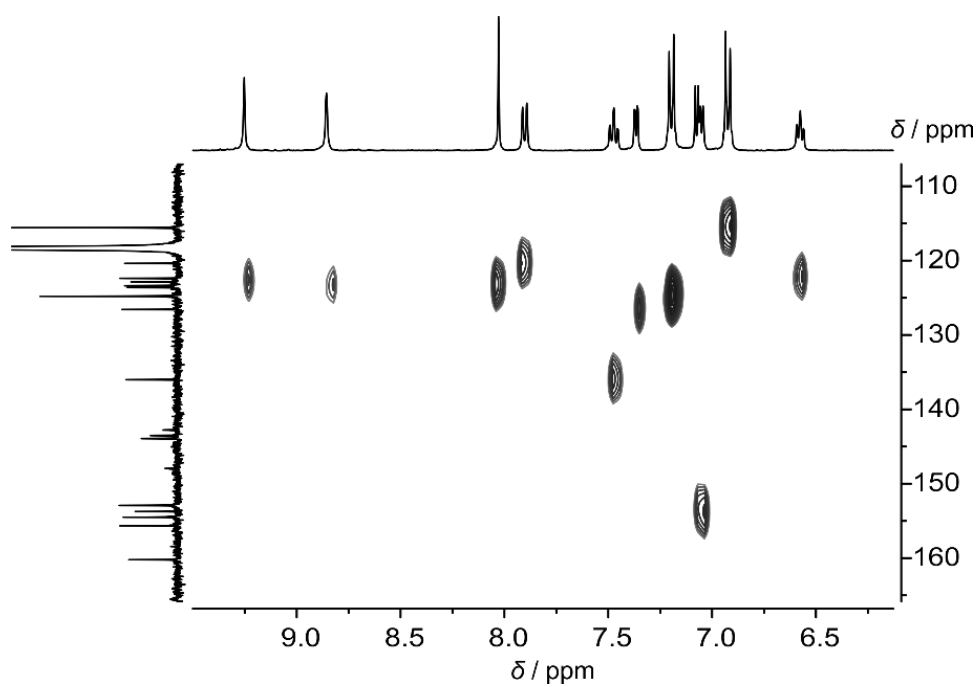


Figure S7  $^1\text{H}$ - $^{13}\text{C}$  HSQC NMR spectrum of the aromatic region of dye  $[\text{nBu}_4\text{N}]_2[\mathbf{2a}]$  in  $\text{CD}_3\text{CN}$ .

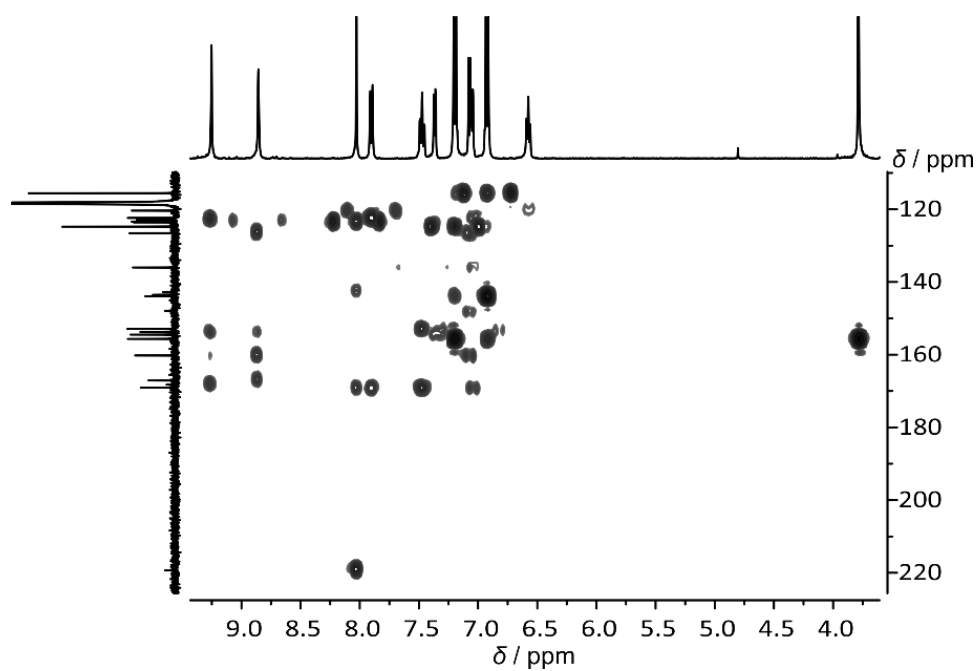


Figure S8  $^1\text{H}$ - $^{13}\text{C}$  HMBC NMR spectrum of the aromatic region of dye  $[\text{nBu}_4\text{N}]_2[\mathbf{2a}]$  in  $\text{CD}_3\text{CN}$ .

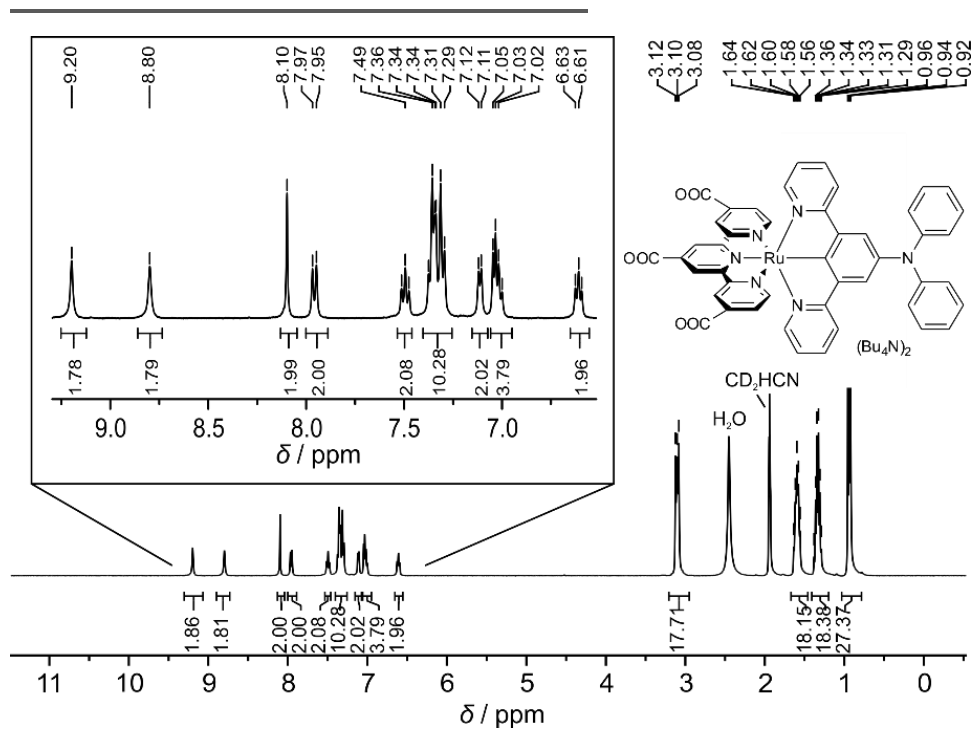


Figure S9  $^1\text{H}$  NMR spectrum (400 MHz) of dye  $[\text{nBu}_4\text{N}]_2[\mathbf{2b}]$  in  $\text{CD}_3\text{CN}$ .

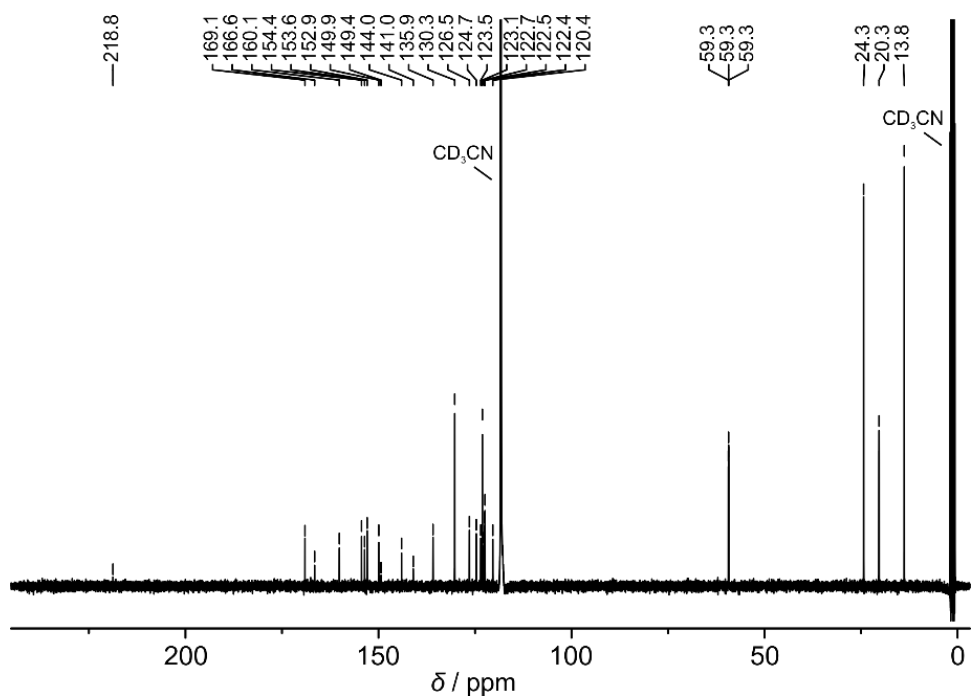


Figure S10  $^{13}\text{C}$  NMR spectrum (100 MHz) of dye  $[\text{nBu}_4\text{N}]_2[\mathbf{2b}]$  in  $\text{CD}_3\text{CN}$ .

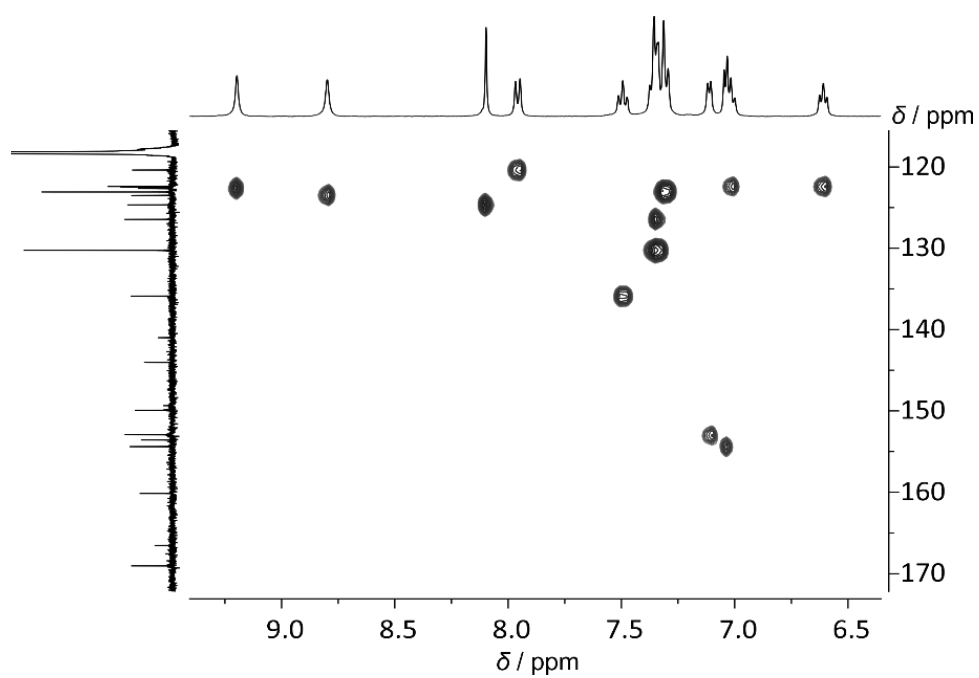


Figure S11  $^1\text{H}$ - $^{13}\text{C}$  HSQC NMR spectrum of the aromatic region of dye [ $n\text{Bu}_4\text{N}$ ] $_2$ [**2b**] in  $\text{CD}_3\text{CN}$ .

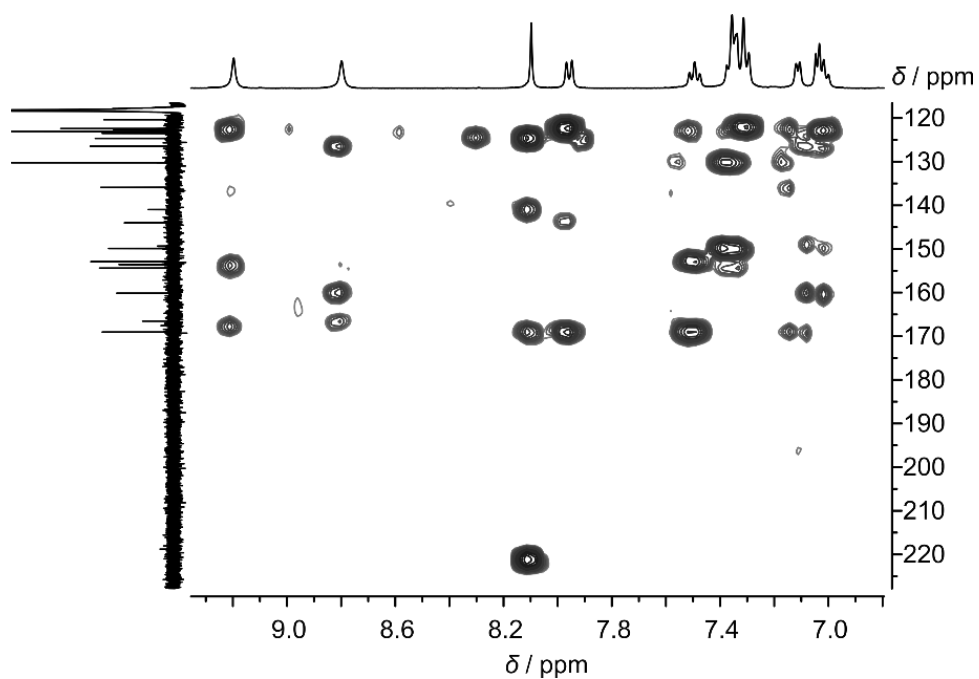
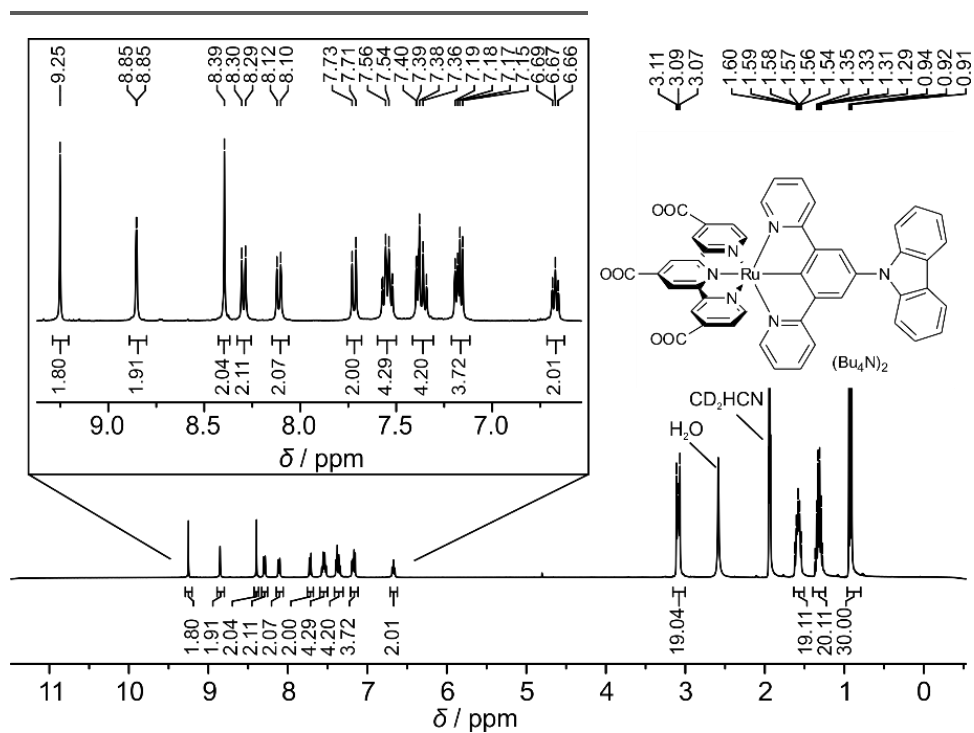
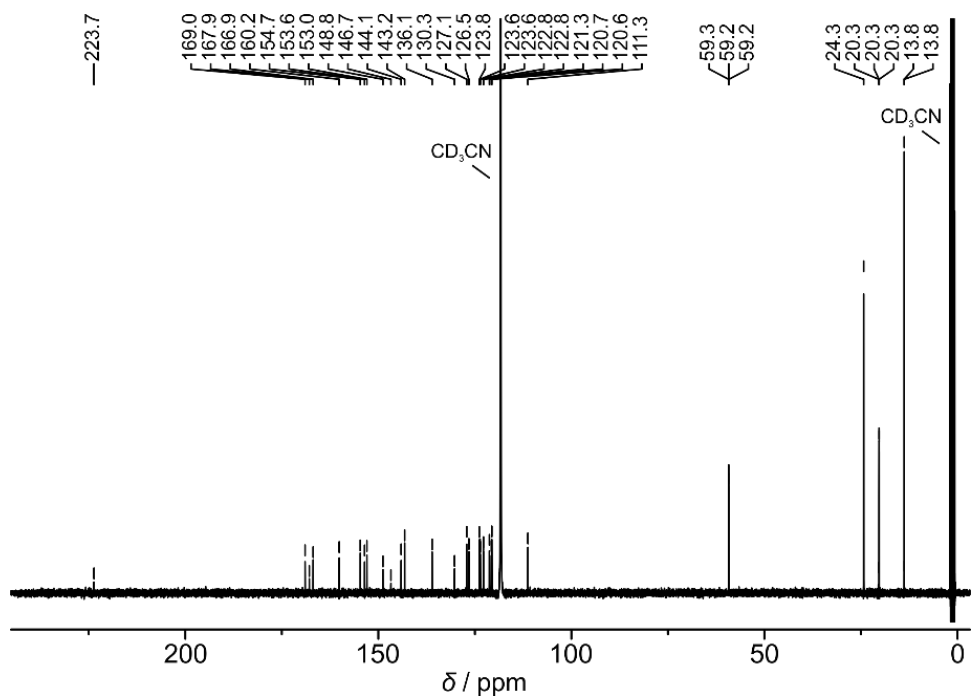


Figure S12  $^1\text{H}$ - $^{13}\text{C}$  HMBC NMR spectrum of the aromatic region of dye [ $n\text{Bu}_4\text{N}$ ] $_2$ [**2b**] in  $\text{CD}_3\text{CN}$ .



**Figure S13**  $^1\text{H}$  NMR spectrum (400 MHz) of dye  $[\text{nBu}_4\text{N}]_2[\mathbf{2c}]$  in  $\text{CD}_3\text{CN}$ .



**Figure S14**  $^{13}\text{C}$  NMR spectrum (100 MHz) of dye  $[\text{nBu}_4\text{N}]_2[\mathbf{2c}]$  in  $\text{CD}_3\text{CN}$ .

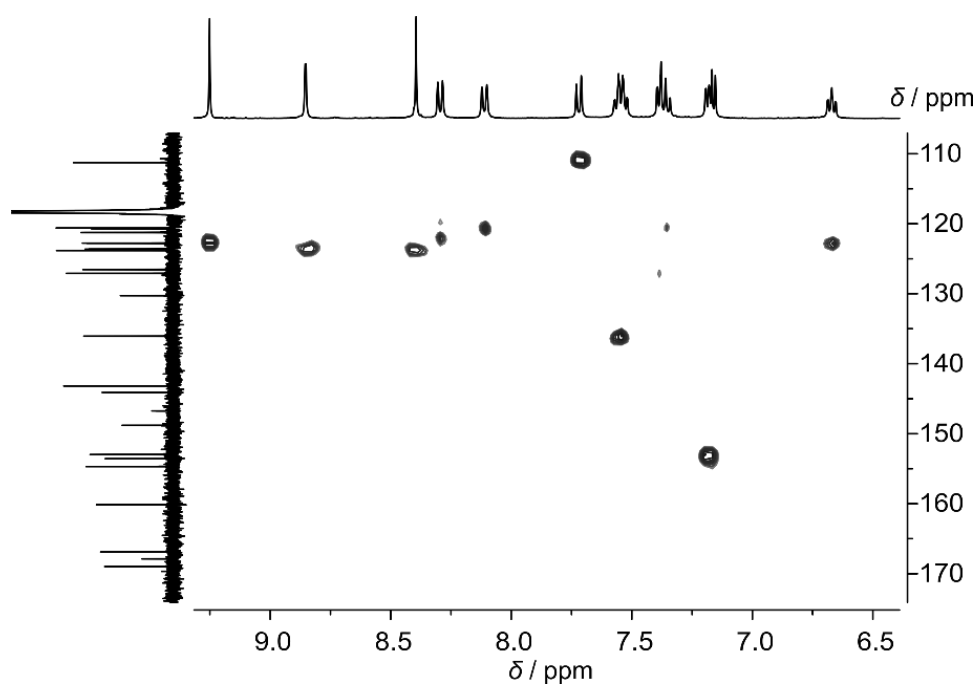


Figure S15  $^1\text{H}$ - $^{13}\text{C}$  HSQC NMR spectrum of the aromatic region of dye  $[\text{nBu}_4\text{N}]_2[\mathbf{2c}]$  in  $\text{CD}_3\text{CN}$ .

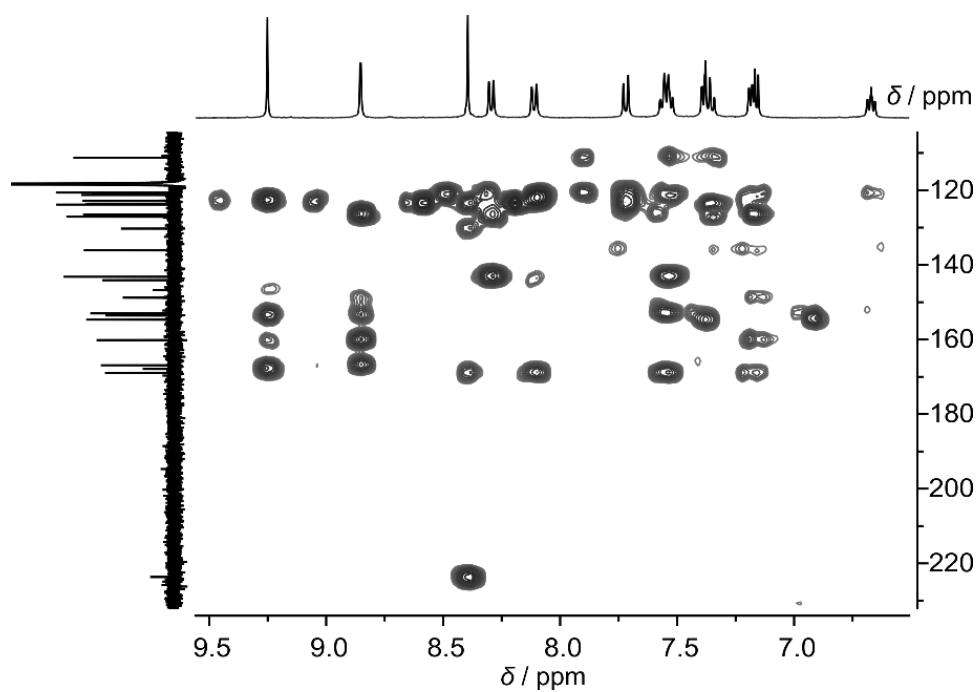
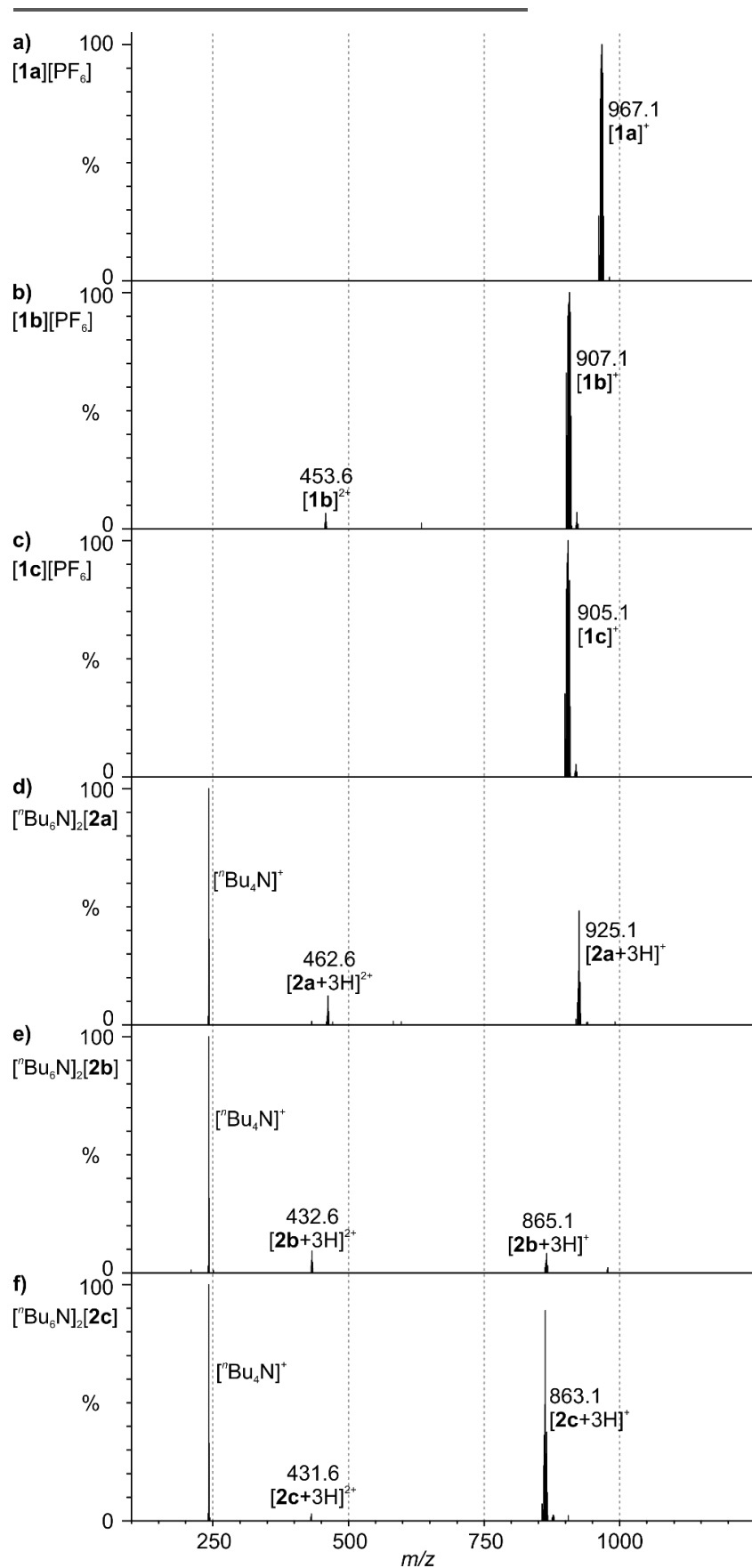
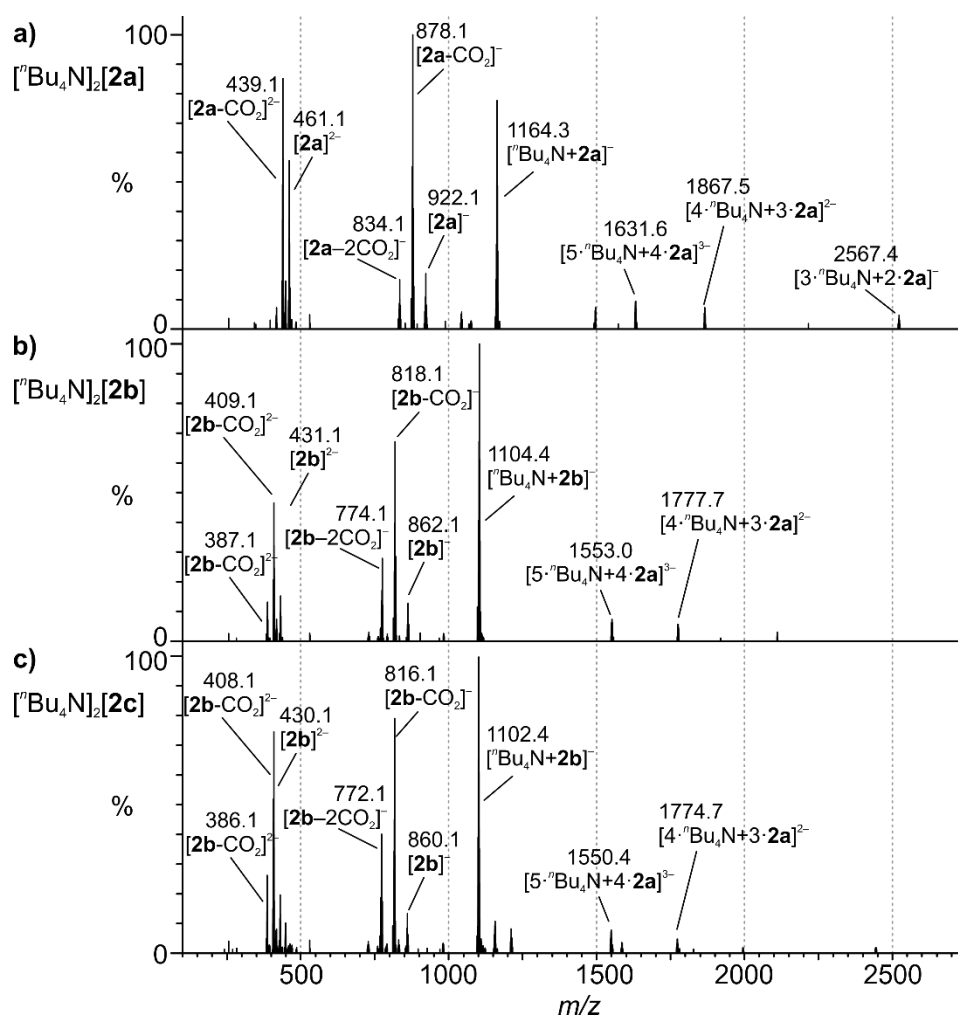


Figure S16  $^1\text{H}$ - $^{13}\text{C}$  HMBC NMR spectrum of the aromatic region of dye  $[\text{nBu}_4\text{N}]_2[\mathbf{2c}]$  in  $\text{CD}_3\text{CN}$ .



**Figure S17** ESI<sup>+</sup> mass spectra of dyes **a) [1a][PF<sub>6</sub>]**, **b) [1b][PF<sub>6</sub>]**, **c) [1c][PF<sub>6</sub>]**, **d) [Bu<sub>4</sub>N]<sub>2</sub>[2a]**, **e) [Bu<sub>4</sub>N]<sub>2</sub>[2b]** and **f) [Bu<sub>4</sub>N]<sub>2</sub>[2c]** from CH<sub>3</sub>CN solution.





**Figure S18** ESI+ mass spectra of dyes **a**)  $[n\text{Bu}_4\text{N}]_2[2\mathbf{a}]$ , **b**)  $[n\text{Bu}_4\text{N}]_2[2\mathbf{b}]$  and **c**)  $[n\text{Bu}_4\text{N}]_2[2\mathbf{c}]$  from  $\text{CH}_3\text{CN}$  solution.

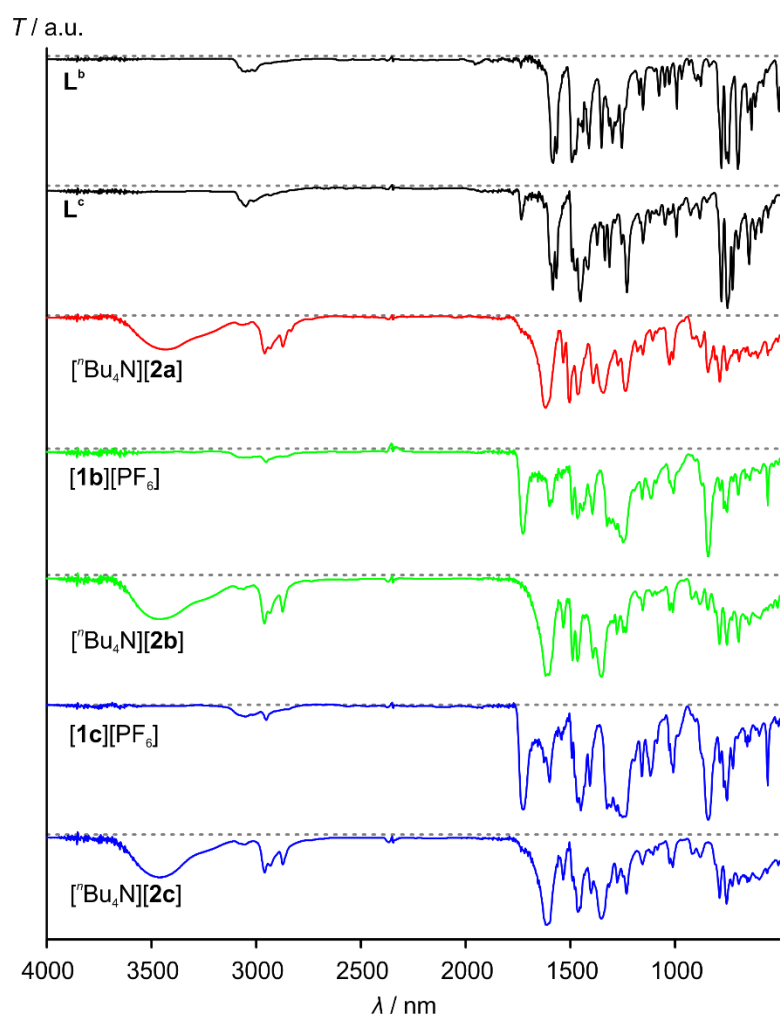


**Figure S19** Solid state IR spectra (KBr disk) of ligands  $L^b$  and  $L^c$  and dyes  $[\text{nBu}_4\text{N}][\mathbf{2a}]$ ,  $[\mathbf{1b}][\text{PF}_6]$ ,  $[\text{nBu}_4\text{N}][\mathbf{2b}]$ ,  $[\mathbf{1c}][\text{PF}_6]$  and  $[\text{nBu}_4\text{N}][\mathbf{2c}]$ .

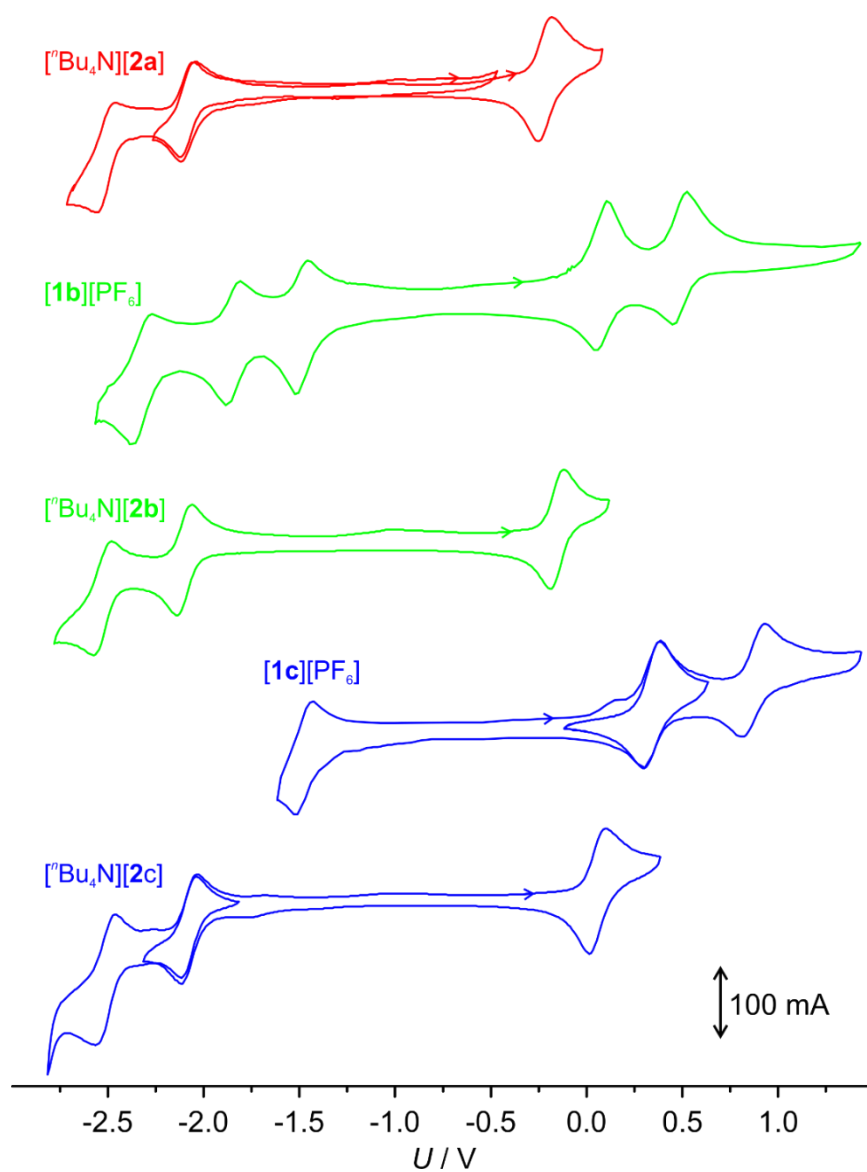


**Figure S20** Cyclic voltammograms of dyes [<sup>n</sup>Bu<sub>4</sub>N]<sub>2</sub>[**2a**], [**1b**][PF<sub>6</sub>], [<sup>n</sup>Bu<sub>4</sub>N]<sub>2</sub>[**2b**], [**1c**][PF<sub>6</sub>] and [<sup>n</sup>Bu<sub>4</sub>N]<sub>2</sub>[**2c**] in CH<sub>3</sub>CN ( $c = 0.1 \text{ mol l}^{-1}$ ; supporting electrolyte: [<sup>n</sup>Bu<sub>4</sub>N][PF<sub>6</sub>],  $c = 10^{-3} \text{ mol l}^{-1}$ ).

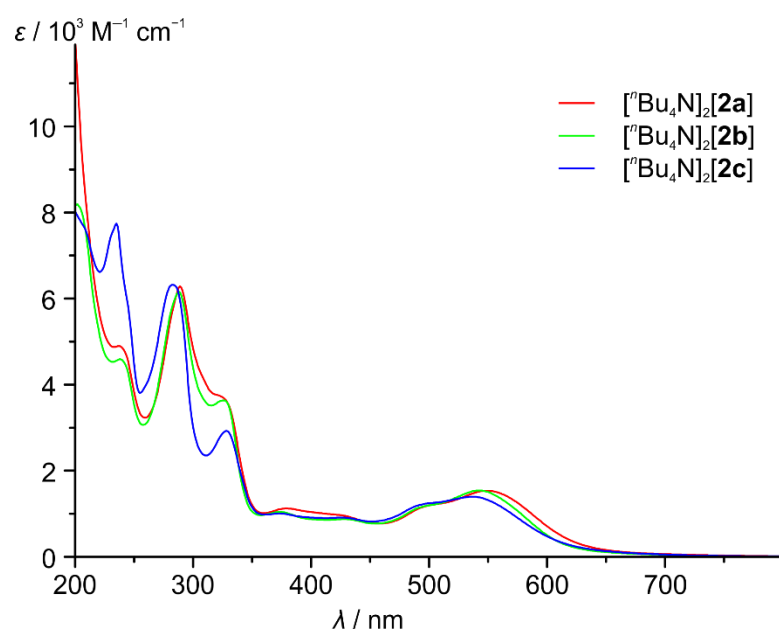


**Figure S21** UV-Vis spectra (200-800 nm) of dyes  $[n\text{Bu}_4\text{N}]_2[2\mathbf{a}]$ ,  $[n\text{Bu}_4\text{N}]_2[2\mathbf{b}]$  and  $[n\text{Bu}_4\text{N}]_2[2\mathbf{c}]$  in  $\text{CH}_3\text{CN}$  solution.

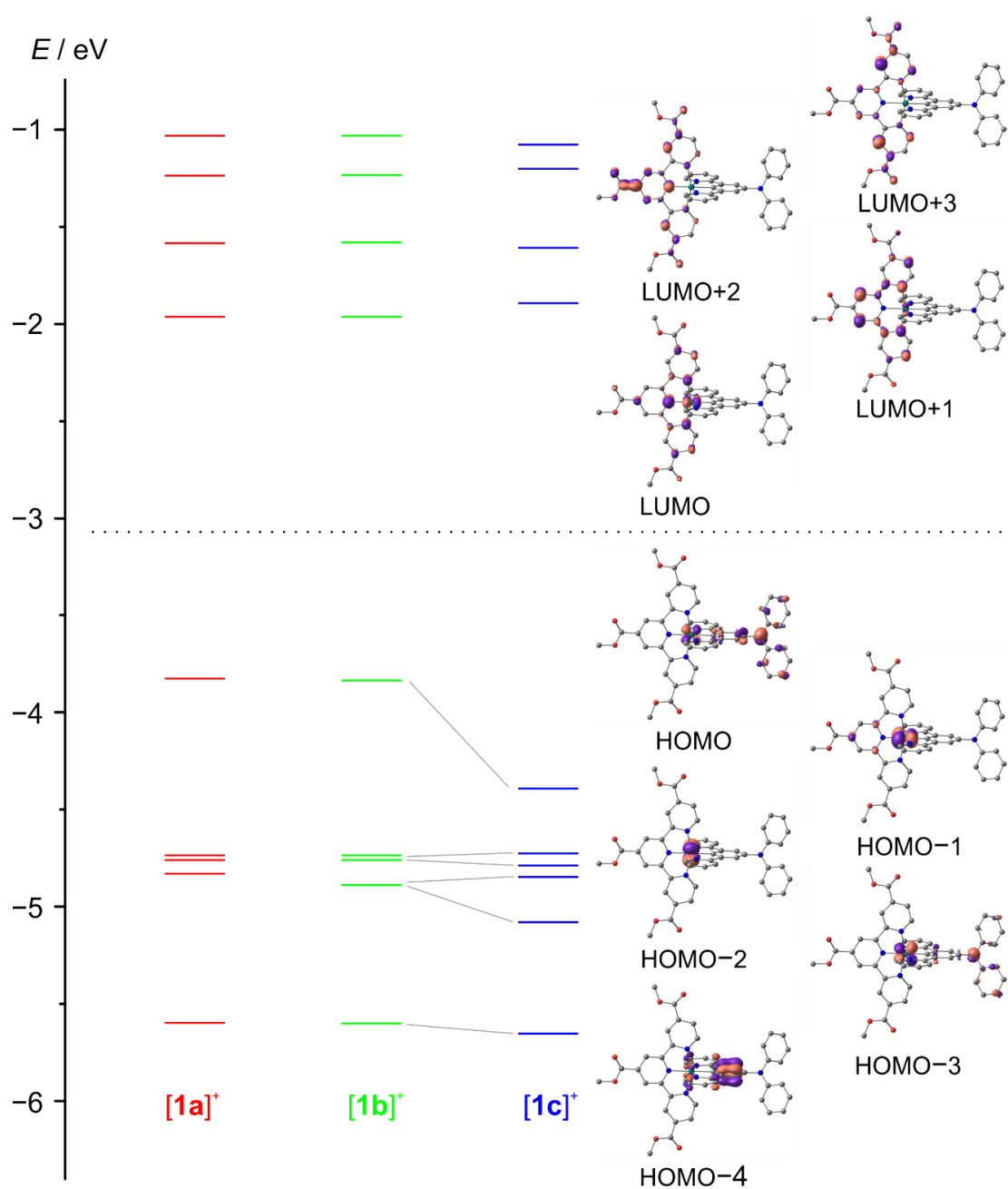


**Figure S22** DFT calculated MO diagram of ester complexes  $[1a]^+$ ,  $[1b]^+$  and  $[1c]^+$  and frontier orbitals of  $[1b]^+$  (contour value: 0.06).

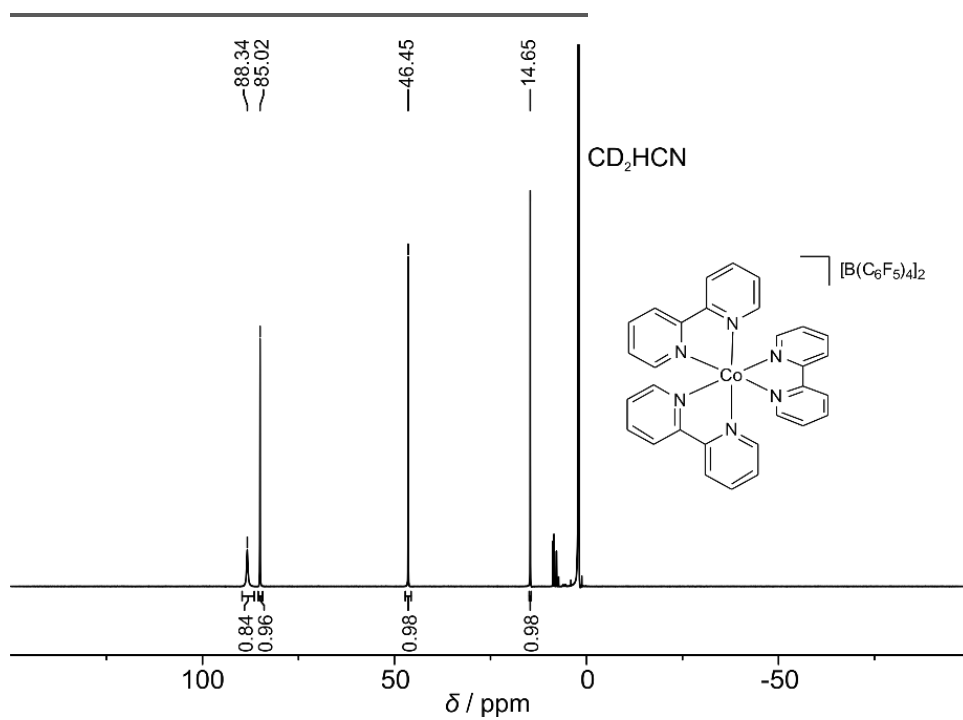


**Figure S23** Paramagnetic  $^1\text{H}$  NMR spectrum (400 MHz) of electrolyte  $[\mathbf{3}][\text{B}(\text{C}_6\text{F}_5)_4]_2$  in  $\text{CD}_3\text{CN}$ .

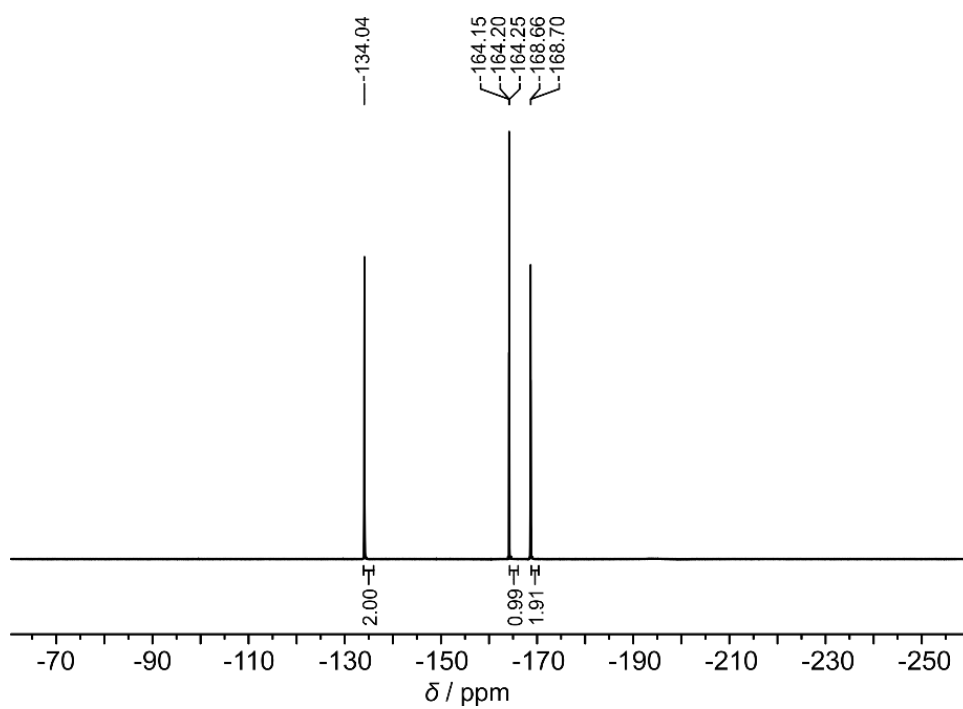


**Figure S24**  $^{19}\text{F}$  NMR spectrum (377 MHz) of electrolyte  $[\mathbf{3}][\text{B}(\text{C}_6\text{F}_5)_4]_2$  in  $\text{CD}_3\text{CN}$ .

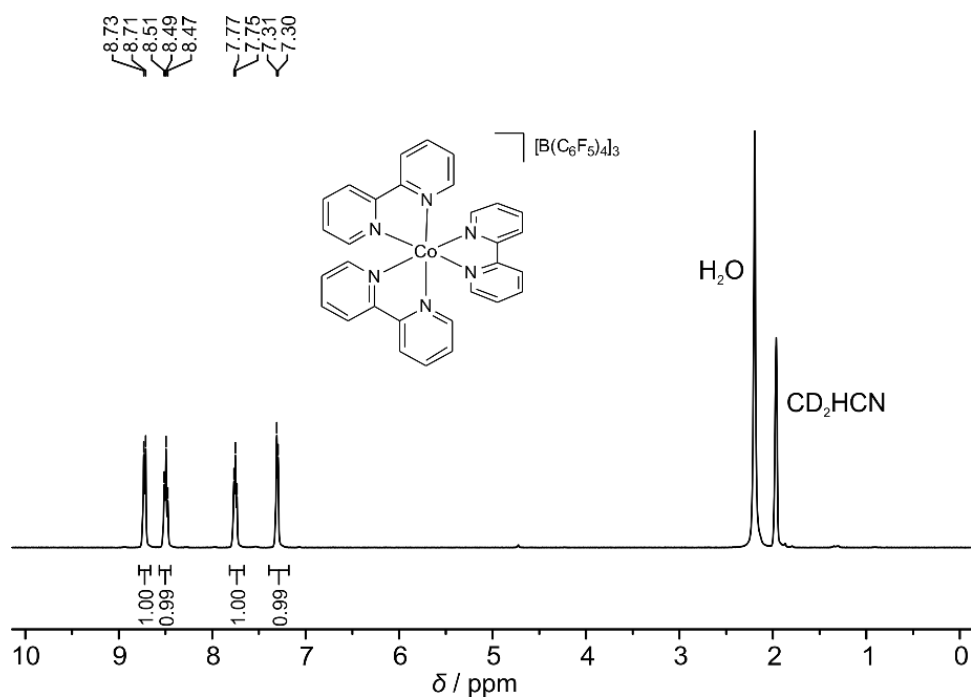


**Figure S25**  $^1\text{H}$  NMR spectrum (400 MHz) of electrolyte  $[3][\text{B}(\text{C}_6\text{F}_5)_4]_3$  in  $\text{CD}_3\text{CN}$ .

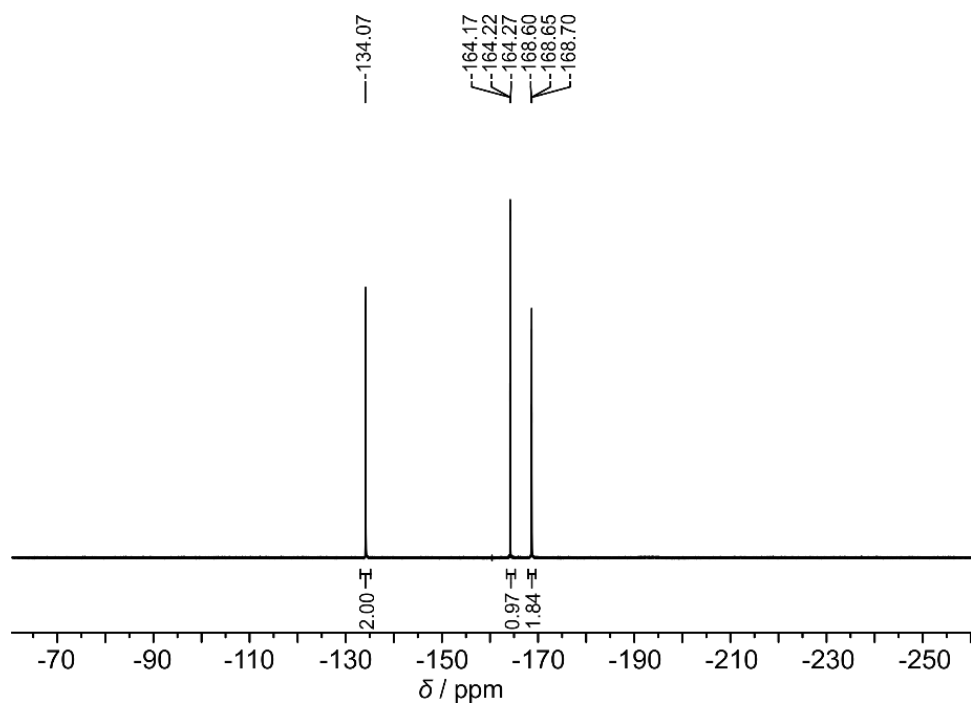


**Figure S26**  $^{19}\text{F}$  NMR spectrum (377 MHz) of electrolyte  $[3][\text{B}(\text{C}_6\text{F}_5)_4]_3$  in  $\text{CD}_3\text{CN}$ .



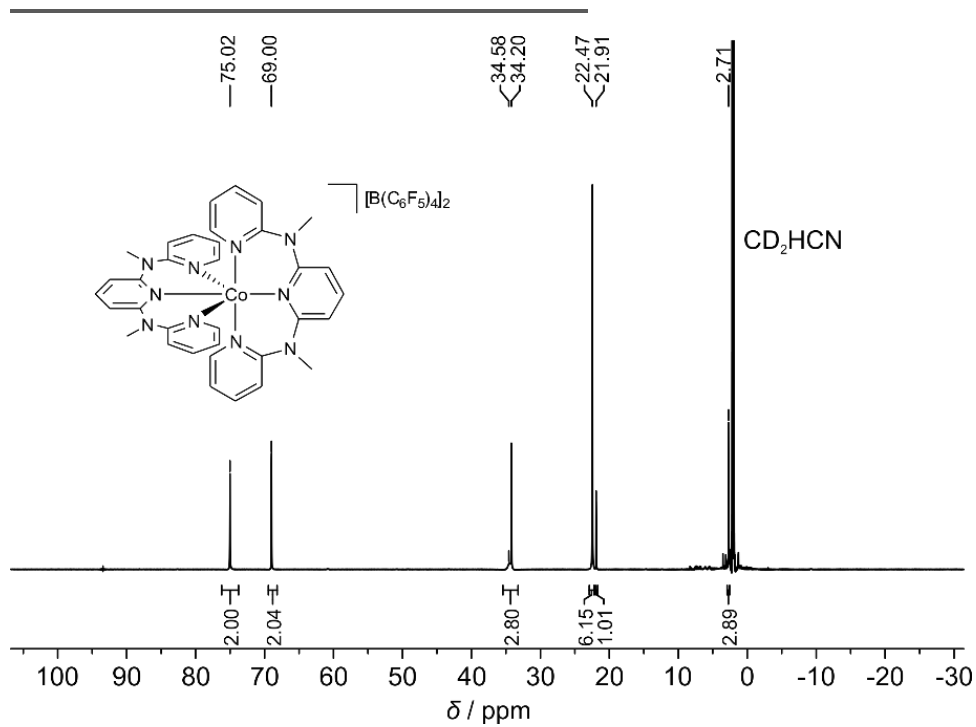


**Figure S27** Paramagnetic  $^1H$  NMR spectrum (400 MHz) of electrolyte  $[4][B(C_6F_5)_4]_2$  in  $CD_3CN$ .

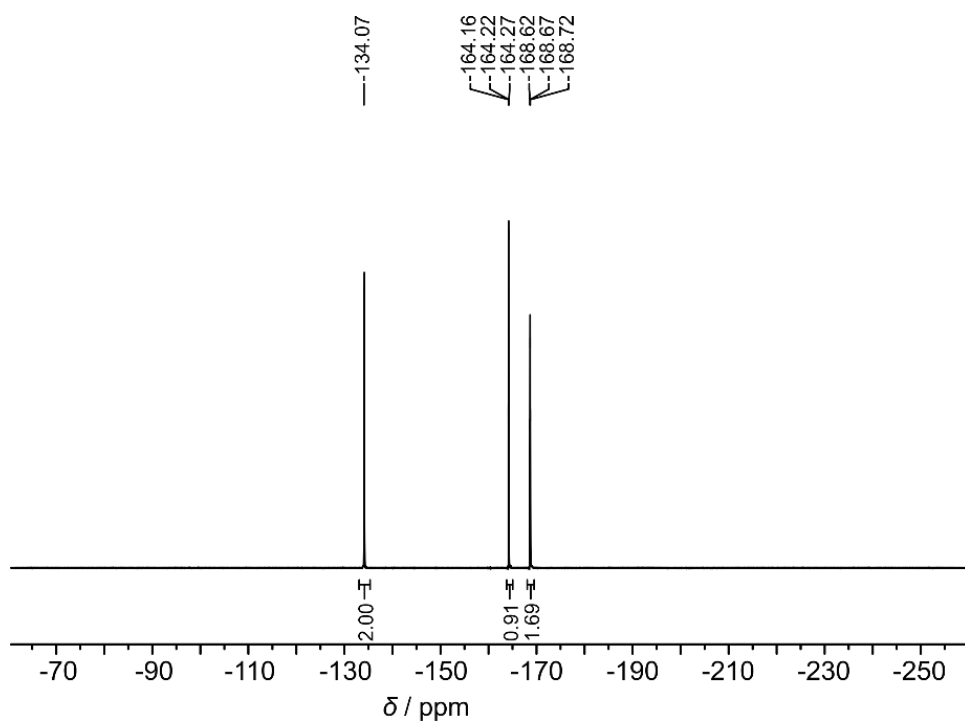


**Figure S28**  $^{19}F$  NMR spectrum (377 MHz) of electrolyte  $[4][B(C_6F_5)_4]_2$  in  $CD_3CN$ .

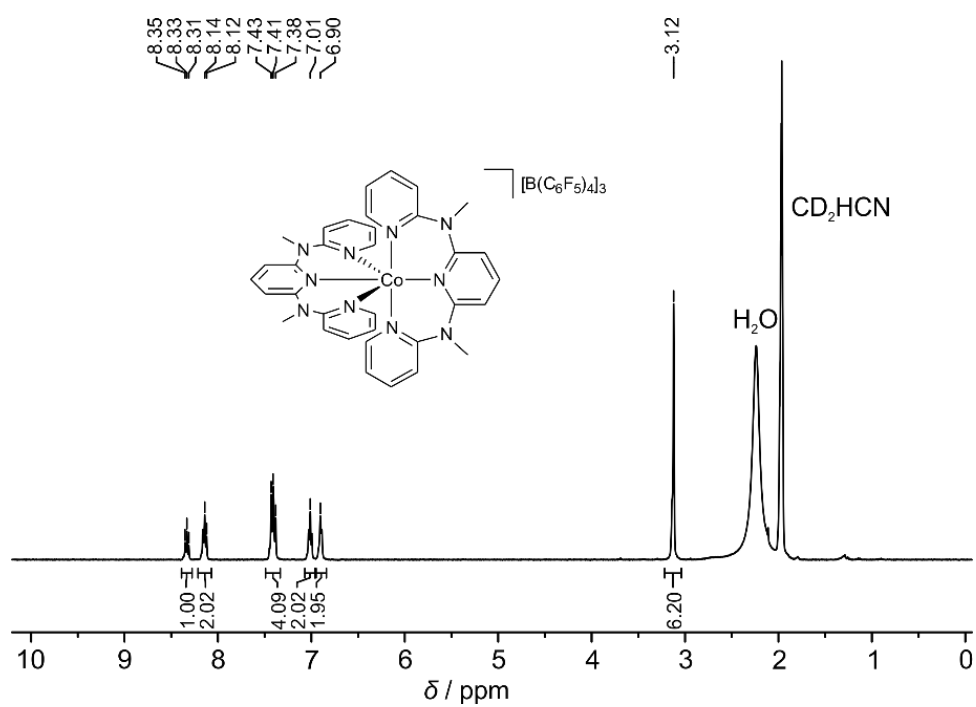


**Figure S29**  $^1\text{H}$  NMR spectrum (400 MHz) of electrolyte **[4]** $[\text{B}(\text{C}_6\text{F}_5)_4]_3$  in  $\text{CD}_3\text{CN}$ .

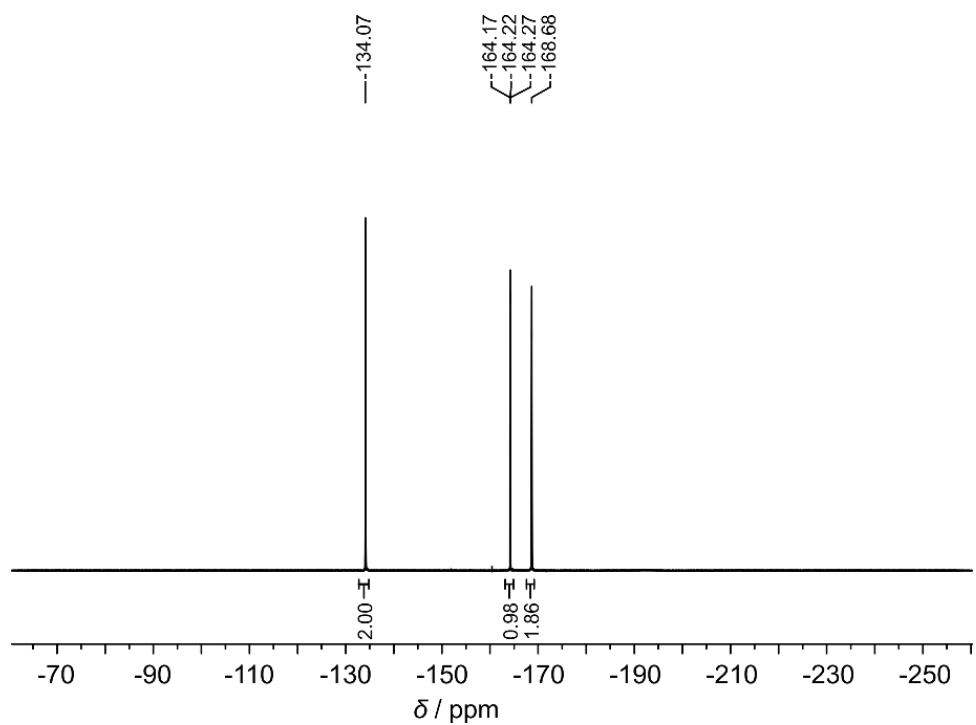


**Figure S30**  $^{19}\text{F}$  NMR spectrum (377 MHz) of electrolyte **[4]** $[\text{B}(\text{C}_6\text{F}_5)_4]_3$  in  $\text{CD}_3\text{CN}$ .

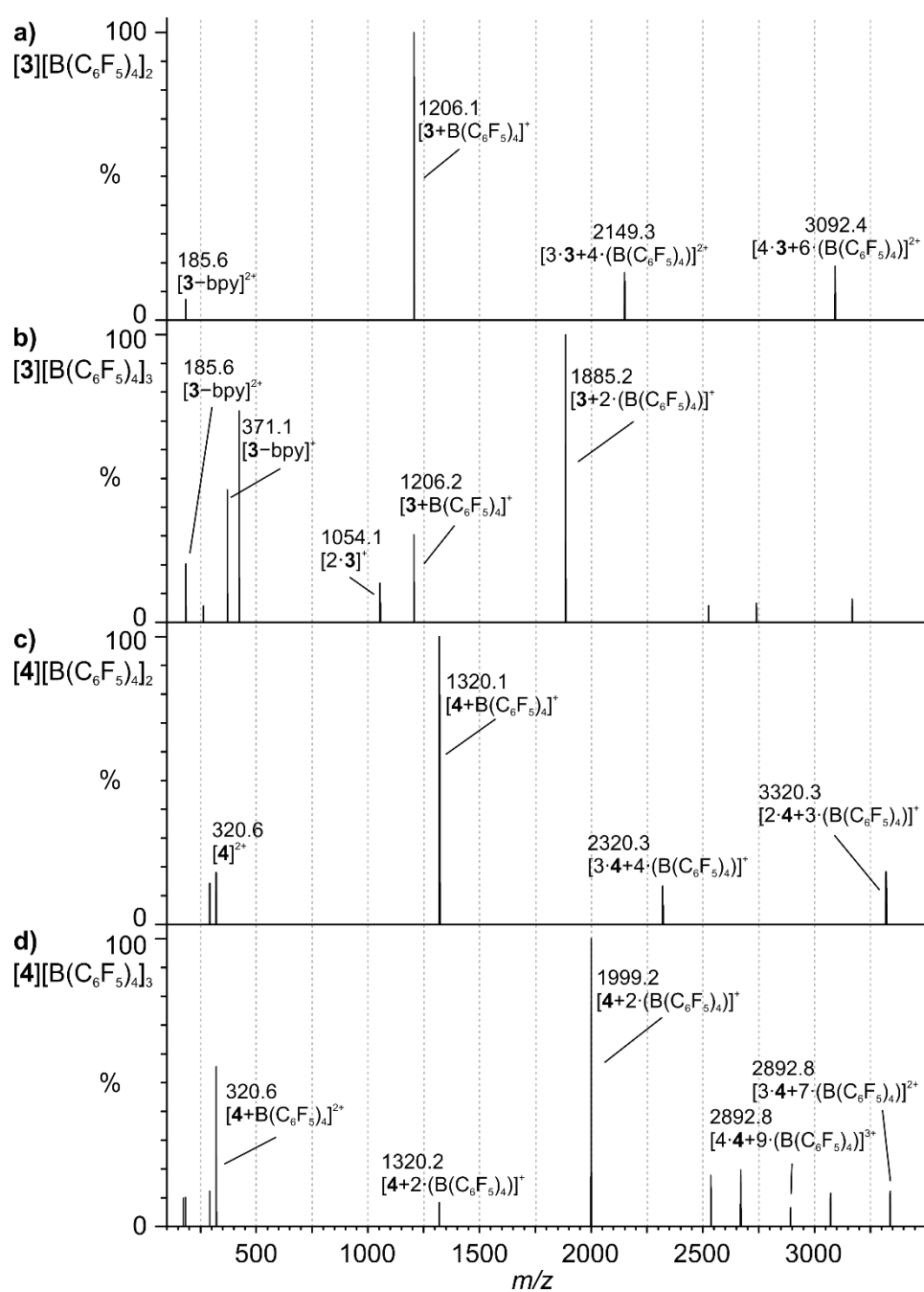


**Figure S31** ESI<sup>+</sup> mass spectra of electrolytes **a) [3][B(C<sub>6</sub>F<sub>5</sub>)<sub>4</sub>]<sub>2</sub>, b) [3][B(C<sub>6</sub>F<sub>5</sub>)<sub>4</sub>]<sub>3</sub>, c) [4][B(C<sub>6</sub>F<sub>5</sub>)<sub>4</sub>]<sub>2</sub> and d) [4][B(C<sub>6</sub>F<sub>5</sub>)<sub>4</sub>]<sub>3</sub> from CH<sub>3</sub>CN solution.**

## 6.6 SUPPORTING INFORMATION TO 3.5: EXCITED STATE DECAY OF CYCLOMETALATED POLYPYRIDINE RUTHENIUM COMPLEXES: INSIGHT FROM THEORY AND EXPERIMENT

DFT optimized Cartesian coordinates of the  $^1\text{GS}$  of  $[\text{Ru}(\text{bpy})_2(\text{ppy})]^+$

Ru	-0.02190206217445	0.02482014297240	-0.04958866603494
C	-0.10260797878980	-0.00097278653297	1.99617280883337
C	1.16113920144658	-0.15226189203276	2.64364539250481
C	-1.23041515264235	0.10784665775614	2.84095041203804
C	1.27259945119644	-0.18355793104483	4.04916281068880
C	-1.12183902913617	0.07575156227903	4.23709126001905
H	-2.22434743689963	0.22483267747609	2.40366863700977
C	0.13417172808340	-0.07036146115855	4.84896123325055
H	2.24568448406269	-0.29750595230729	4.52865888631826
H	-2.01875255553463	0.16425528639324	4.85424426028089
H	0.22205322599048	-0.09508671920532	5.93597064932104
N	2.01910435642795	-0.22665535415604	0.41429033688720
C	2.32131315340800	-0.26412076151074	1.74806006044785
C	3.01105158519582	-0.32394593262768	-0.49207481221912
C	3.65892494204589	-0.40389829502693	2.16241189620959
C	4.35092919660698	-0.46576416277989	-0.14107475611643
H	2.71329727409568	-0.29011114550564	-1.53800669127460
C	4.67965174907348	-0.50534098675499	1.21991675412589
H	3.89644088676804	-0.43171739488212	3.22359742028317
H	5.11022536027170	-0.54180848473995	-0.91770957257283
H	5.71559133881184	-0.61385899735353	1.54090244194931
N	-0.50646607849372	-1.98679396862291	-0.07776645898051
C	0.36535169941325	-3.00560862564891	0.06962691777329
C	-1.82899977927372	-2.27659271927598	-0.25216783835754
C	-0.02300009282522	-4.34264364373979	0.04547074362070
H	1.40734258119760	-2.73028388573022	0.21097473759375
C	-2.28413132000890	-3.60307140194975	-0.28340426748911
C	-1.37660916263980	-4.65047965163888	-0.13399979014487
H	0.72696814097076	-5.12228634823042	0.16861578477495
H	-3.34100639826499	-3.81697224981407	-0.42244085238233
H	-1.71921651967936	-5.68418714698018	-0.15583041851668
N	0.26208469983924	0.28051551340496	-2.19439158229186
C	0.18654858723719	-0.68804051299028	-3.12345932500422
C	0.48998677452576	1.55958971979255	-2.59018132089517
C	0.33308767128236	-0.44195521446586	-4.48798847565623
H	0.00440218654620	-1.69727934601571	-2.75681213172899
C	0.64664903859725	1.88085684567562	-3.94779854013224
C	0.56781162281716	0.8718555522741	-4.90768584875744
H	0.26264435688411	-1.26389884441838	-5.19861635487084
H	0.82502411810682	2.90715811467083	-4.25829037209472
H	0.68603334823092	1.10921285021622	-5.96434051020693
N	-2.07440801556631	0.10186799643092	-0.32709943756473
C	-2.70679038943560	-1.10463032801178	-0.40335257903076
C	-2.80936334048413	1.22591940052618	-0.45066239485484
C	-4.09181904879649	-1.18766358252074	-0.61035902462464
C	-4.18623125249344	1.21138634273544	-0.65725888254241
H	-2.26927637511847	2.16656200445894	-0.37790266183219
C	-4.84412392369910	-0.02139018200199	-0.74031584776151

H	-4.57993865216700	-2.15722392223119	-0.66995625703049
H	-4.72552229989484	2.15263182820108	-0.74963072016661
H	-5.92014288206236	-0.07387172192168	-0.90128568954490
N	0.33168656868028	2.08466991947955	-0.24145053574220
C	0.37413861672408	2.95110447022406	0.79166969400839
C	0.55524565175926	2.55887515786798	-1.50183661224162
C	0.63300265165631	4.31077425329070	0.63244725966143
H	0.18920928846883	2.52763405866212	1.77551524774962
C	0.82257664707099	3.91755870983914	-1.72753858969592
C	0.86332325785208	4.80667296374059	-0.65450100258574
H	0.65205096422032	4.95991709508930	1.50635896195243
H	0.99959201607371	4.28168675054615	-2.73626040900053
H	1.07045132444103	5.86291267687124	-0.82167137735545

DFT optimized Cartesian coordinates of the  $^3\text{MLCT}$  state of  $[\text{Ru}(\text{bpy})_2(\text{ppy})]^+$

Ru	-0.00582391831081	0.02594705213624	0.00487677542443
C	-0.10202330324492	-0.03969146739102	2.03124169889945
C	1.15659134281037	-0.17837325186830	2.68619803888731
C	-1.25770683013009	0.03806604541994	2.83378338676050
C	1.23568772265027	-0.23137468601398	4.09075133824811
C	-1.17318613225537	-0.00145643624829	4.23076308969006
H	-2.23778168038295	0.13762756517188	2.36706334451717
C	0.07409961339392	-0.13932749668553	4.86077834399596
H	2.19716069286433	-0.34304902849711	4.59169553423964
H	-2.08091036314520	0.06878879798131	4.83227586007964
H	0.13891063428178	-0.17666115510330	5.94864840481599
N	2.04528648956580	-0.18737990648968	0.47330776932281
C	2.33060113314030	-0.26143965512106	1.80646654424385
C	3.04236587646479	-0.22610491024292	-0.42993897189471
C	3.66279727703305	-0.39587976687114	2.23383418993475
C	4.37950369757505	-0.35698689615406	-0.06596321029442
H	2.75332426617555	-0.15984971686612	-1.47703026209407
C	4.69225580202768	-0.44566658923048	1.29641875269381
H	3.88966694614924	-0.45885135996021	3.29560110649707
H	5.14989423447918	-0.38992017125593	-0.83423343136147
H	5.72633778877892	-0.55095697273243	1.62348164248203
N	-0.45622813175899	-1.98043710781621	-0.06530525349620
C	0.40762618711169	-3.00460186339516	0.12954378072723
C	-1.81226893225132	-2.25066239979692	-0.28716973364106
C	0.03283691843167	-4.33364041399523	0.08630684495762
H	1.44280141254435	-2.72581410724968	0.31787347778438
C	-2.24110112209771	-3.61203557393101	-0.33444836715334
C	-1.34078354025446	-4.63827506806540	-0.15652007859108
H	0.77468219591658	-5.11540308981447	0.23659475659152
H	-3.29192753624521	-3.83488081687903	-0.50868714413035
H	-1.67689189797397	-5.67461966814571	-0.19390605275837
N	0.20105967964042	0.27435735113347	-2.19764928687935
C	0.06181212514665	-0.70126462470621	-3.10683245478162
C	0.41007184875120	1.54969444029494	-2.60351711718399
C	0.12888405868561	-0.46043772001204	-4.47964711378695
H	-0.10589453393870	-1.70520896756133	-2.71956519204026
C	0.48339948723078	1.86673483906580	-3.96795490708361
C	0.34199707524101	0.85073293581749	-4.91469858490092
H	0.01220858687737	-1.28327375781662	-5.18262493707074

---

H	0.64615411532060	2.88994193067142	-4.29558426191443
H	0.39605589427788	1.08368885774694	-5.97748842360238
N	-2.04843567650735	0.12636240198787	-0.32775817085132
C	-2.66238266648466	-1.12003218707435	-0.43815891787566
C	-2.78413187394331	1.24780958671937	-0.47249498190253
C	-4.06707525257734	-1.17759414330527	-0.69128360950276
C	-4.14729058356568	1.23986101295940	-0.71960775286486
H	-2.24702810060867	2.19028089052149	-0.37572718474738
C	-4.80112193252053	-0.01984812468570	-0.83026801293197
H	-4.55656029901912	-2.14569712265762	-0.77587983356487
H	-4.68852256117734	2.17833883144470	-0.82195870690058
H	-5.87292935572475	-0.07002437187492	-1.02320201057537
N	0.40853307570580	2.09826614943241	-0.24844966293506
C	0.54695967873187	2.95695848478663	0.77934570880299
C	0.55306241821879	2.55425529798644	-1.52367241072608
C	0.82337537291786	4.31054429912261	0.59667107241334
H	0.42385912716453	2.54204170855464	1.77678412718717
C	0.83170348126075	3.90534593210521	-1.77251664641185
C	0.96678912530747	4.79432859216638	-0.70605119213873
H	0.92136374040117	4.96153672850165	1.46332967579251
H	0.94626953303180	4.26481336927161	-2.79148640281630
H	1.18249756881237	5.84542449451461	-0.89268098358470

#### DFT optimized Cartesian coordinates of the $^3MC$ state of $[Ru(bpy)_2(ppy)]^+$

Ru	-0.35189428368518	-0.11080288179678	-0.05974649397658
C	-0.34901844072056	-0.22258880017789	1.99369582165052
C	0.89558155394524	-0.26743906776530	2.69007269353272
C	-1.52556485870115	-0.25923407240878	2.77366297101283
C	0.92209728827479	-0.35205513418613	4.09892713468511
C	-1.49169902122391	-0.32714410492679	4.17211493068486
H	-2.50073637639817	-0.23183896256260	2.28106509053827
C	-0.26003793749430	-0.37965945131319	4.84126225889500
H	1.87254922396188	-0.41287800302189	4.62955784078633
H	-2.42433864986063	-0.34858925730853	4.73967478739579
H	-0.22172660258688	-0.44766266934687	5.92932836042573
N	2.02625502479739	-0.39943294359546	0.56370376400592
C	2.15109374194929	-0.22022539164127	1.90122110697632
C	3.10680457439803	-0.35748076028195	-0.22544652865885
C	3.42405481668825	0.01524491410816	2.46134641538907
C	4.39624249863895	-0.13747039177008	0.25958399534136
H	2.93458116740599	-0.51448904167909	-1.29238526576665
C	4.54934908537201	0.05504959968866	1.63853452757487
H	3.53422430752092	0.18072199396642	3.53078646633095
H	5.24688116259279	-0.11686791362497	-0.42038569773421
H	5.53413507027030	0.24065668248636	2.06801115019476
N	-0.79665043593874	-2.22408161948253	-0.06229150271323
C	0.17155843926770	-3.13412859131363	0.15685603000235
C	-2.05863071668810	-2.65880791637264	-0.32342497706353
C	-0.05346373671636	-4.50854300043366	0.11593242836546
H	1.15915732251452	-2.73303277477334	0.37412269903248
C	-2.35183406775500	-4.03063470990228	-0.39023293166980
C	-1.34369332111656	-4.96761327617780	-0.16903411300847
H	0.76902735847453	-5.19647480012259	0.30453373329281
H	-3.35928956034204	-4.36371004125669	-0.62733660020379
H	-1.56136689084997	-6.03388789394416	-0.22113978798046

N	0.13188411024017	0.16535467431698	-2.19200353389406
C	0.16471858763154	-0.79880819002213	-3.12678499298309
C	0.46839187232406	1.43686755756237	-2.52882449938327
C	0.53693295671145	-0.55569623059909	-4.44759372609184
H	-0.12031350197792	-1.79861587869172	-2.80189007330876
C	0.85437226054378	1.75397570244116	-3.84195053984326
C	0.88969562418421	0.74983008675972	-4.80877896048399
H	0.54790971411256	-1.37037161548553	-5.16970636994875
H	1.12672549789420	2.77110290948964	-4.11153660303338
H	1.18840662684080	0.98424387272893	-5.82986410794510
N	-2.62162250760602	-0.36788623937064	-0.75025382734202
C	-3.08978503863820	-1.61472784671164	-0.53123195583218
C	-3.48225002066925	0.63872997602241	-0.95085193685515
C	-4.47020431808744	-1.87647864628565	-0.49740051447223
C	-4.86618683851640	0.45984884612459	-0.94190639886141
H	-3.04622172241065	1.62275708733736	-1.12996411285820
C	-5.36647018735682	-0.82695865619953	-0.70628772333563
H	-4.84486764272740	-2.87741007430948	-0.29590907913036
H	-5.52966493044018	1.30539296830052	-1.11728487290905
H	-6.44027237816649	-1.01055386004129	-0.67965040701961
N	0.03243893364515	1.95055143465520	-0.21074547417542
C	-0.08028677839855	2.81890450310220	0.81688566618201
C	0.38659927309255	2.43173227845597	-1.43987562136782
C	0.14822658434747	4.18599311058372	0.68336297429577
H	-0.36138605967395	2.38966768302938	1.77545910717867
C	0.63657766168796	3.79859177971044	-1.63557457063955
C	0.51846732599325	4.68792001377219	-0.56872215373812
H	0.03949610985895	4.83663906638382	1.54955195187367
H	0.91702401911271	4.17019749136812	-2.61770487027826
H	0.70856416945341	5.75055490850930	-0.71434653013758

DFT optimized Cartesian coordinates of the  $^3\text{MLCT}-^3\text{MC}$  transition state of  $[\text{Ru}(\text{bpy})_2(\text{ppy})]^+$

Ru	0.10059725744503	0.03829869157653	-0.09700174905223
C	-0.15352728395743	-1.82459573913717	-0.92130778095472
C	-1.21808973912787	-2.65625211459010	-0.46392696206675
C	0.67965137748452	-2.33933453814504	-1.93802670376463
C	-1.40839828605785	-3.93950702936710	-1.02099484663494
C	0.47692233212446	-3.60842147318772	-2.49450688877076
H	1.51072217738310	-1.73617115519426	-2.31255764516431
C	-0.57123359104014	-4.41733582736774	-2.03078342862540
H	-2.20866795065657	-4.58514670112045	-0.65872228549305
H	1.14021402617894	-3.97020667859999	-3.28291922743888
H	-0.73022577903239	-5.41233289216810	-2.44790383277715
N	-1.70582458997020	-1.00398423129891	1.22226071899370
C	-2.11243222793549	-2.13722418352761	0.59924456744569
C	-2.45790552598107	-0.45768007291293	2.18524321433237
C	-3.33385810824475	-2.73905964464111	0.96647635059209
C	-3.67333399417409	-1.00020687927066	2.60279544835145
H	-2.06706287998340	0.45002628791350	2.64903046688954
C	-4.11542227151162	-2.16978162244131	1.97160819967498
H	-3.67937104043125	-3.63824739540112	0.46159589150274
H	-4.24939094148002	-0.52209742907689	3.39387802499092
H	-5.06198264097320	-2.63048199723850	2.25484541639260
N	1.69142858346631	-0.81271934139596	1.07696945430955
C	1.43817925461553	-1.59190042044933	2.14604941832058



---

C	2.98559951320335	-0.54156376081456	0.75476522538997
C	2.44145398035724	-2.13013855242927	2.94884220487235
H	0.38804490390033	-1.78587911587348	2.35356517664839
C	4.04465355695325	-1.04450115074892	1.52799380433923
C	3.77538564011639	-1.84685034603079	2.63546977849461
H	2.17507597715224	-2.75687819313285	3.79834408011491
H	5.07248476627246	-0.79736126261098	1.27331219243783
H	4.58991584817286	-2.23915123230388	3.24313902973132
N	-0.19539341657397	1.95067027707156	0.97702028304368
C	0.43364226083295	2.33665758859259	2.09870425206889
C	-1.15168651123689	2.74683980076651	0.43562903425056
C	0.14413735291649	3.53436495810224	2.75021425909436
H	1.19650562361062	1.66092513171241	2.48368952467310
C	-1.49341194944431	3.96960872206092	1.03741245628436
C	-0.84165782353244	4.36526282787629	2.20496723245500
H	0.67961460323228	3.80454760193168	3.65862182595187
H	-2.26098791747188	4.60713185177708	0.60657992263524
H	-1.10032000483803	5.30984472406176	2.68189697179019
N	2.11523638429280	0.97142626600519	-0.88521946278472
C	3.20311757979836	0.30336948723742	-0.44050694117762
C	2.21972880588658	1.76526972751847	-1.96117346492508
C	4.44181998730280	0.41540796572223	-1.09458240102588
C	3.41575518226549	1.93813000261030	-2.65676332814452
H	1.31241870988765	2.28611117820700	-2.27047669634397
C	4.54903172357435	1.24328308374834	-2.21289576011697
H	5.30780917032027	-0.14467754093894	-0.74917970698148
H	3.45674323430642	2.60153104672019	-3.51952249089448
H	5.50084753596859	1.33924813366251	-2.73434295787464
N	-1.37655326329130	1.01064323437773	-1.22794462823011
C	-1.90523557409249	0.51230193682800	-2.36588985637480
C	-1.77943035675092	2.24601249149476	-0.80475388424883
C	-2.84180466056843	1.20050163772230	-3.13254651682109
H	-1.55872631450012	-0.47505837429523	-2.66098291072190
C	-2.72327369124507	2.98648866537061	-1.53268693749894
C	-3.26282831020308	2.46461517381446	-2.70726262544314
H	-3.23002948778144	0.74549608963249	-4.04220498222241
H	-3.03229400862902	3.96998144651246	-1.18887554438983
H	-3.99380820830492	3.03553286508338	-3.27852897910883

#### DFT optimized Cartesian coordinates of the $^3\text{MC}^{-1}\text{GS}$ MECP of $[\text{Ru}(\text{bpy})_2(\text{ppy})]^+$

Ru	-0.59266234665190	-0.11908882786205	0.12845431123761
C	-0.16082339088075	-0.19633714902559	2.12895221891764
C	1.16262849239242	-0.24693419190606	2.65104922928732
C	-1.22726677951433	-0.19957793271765	3.05663239383905
C	1.36985873432140	-0.30773490170160	4.04672227856993
C	-1.01191308956290	-0.25288588902361	4.43921649900127
H	-2.25949415523287	-0.16038268571262	2.69687150710392
C	0.29698389922326	-0.31110048101609	4.93964182089557
H	2.38159433414344	-0.37412928058268	4.44745813645221
H	-1.86260297868274	-0.25617154496532	5.12378963452572
H	0.47875086449473	-0.36557681411539	6.01378391485999
N	2.03424302586296	-0.52441359686505	0.41997417634422
C	2.31178464335867	-0.23989042349256	1.71190487451598
C	3.01935313760749	-0.54853900404469	-0.48232229094358
C	3.63528700565228	0.05040931741136	2.10622482044833

C	4.35490826085719	-0.28574930910277	-0.16886071378847
H	2.73214911472861	-0.79377922737322	-1.50698198842960
C	4.66071486218842	0.02594444409950	1.16112103832845
H	3.86090862012508	0.30936856746712	3.13836631473969
H	5.12264270392067	-0.32112509193795	-0.94091837091665
H	5.68499339199535	0.25270679507225	1.45876256776160
N	-1.02425503032493	-2.20210820187459	0.13889815440617
C	-0.11952357863853	-3.09876943348954	0.58098315451189
C	-2.22782076219924	-2.65489811441466	-0.31146191352042
C	-0.35607488960351	-4.47130891053913	0.60081532287165
H	0.82608036079971	-2.68565261678103	0.92146480768856
C	-2.52562647883391	-4.02668602802610	-0.32425585731023
C	-1.58640850506816	-4.94752660325657	0.13757877524202
H	0.41422573041153	-5.14542630869619	0.97150730397946
H	-3.48291376085525	-4.37615944686626	-0.70184046959022
H	-1.81028829757984	-6.01363963997818	0.13037232922920
N	0.09090040118975	0.18354333338031	-1.99923440180989
C	0.21219452056460	-0.76493062013385	-2.93854963407635
C	0.42818193560241	1.46326894564688	-2.28283220985838
C	0.68134588324105	-0.49427022184952	-4.22362105325207
H	-0.07774359436890	-1.77483060805172	-2.64932556890763
C	0.90887238118108	1.81122754261691	-3.55737246387819
C	1.03685817151589	0.82369218357879	-4.53385484423740
H	0.76433838277969	-1.29545713113300	-4.95602906508599
H	1.18149152756798	2.83714575853037	-3.79097610040257
H	1.40982030609515	1.08106440077055	-5.52456563306996
N	-2.70118669302528	-0.37695630629877	-0.90820156439993
C	-3.18893751390749	-1.63009881833555	-0.78719054305308
C	-3.49832218896968	0.61068497024689	-1.33406618953817
C	-4.52972581626980	-1.91510656059439	-1.09584885094059
C	-4.83851967378742	0.40675948766016	-1.66595937067190
H	-3.04613551150879	1.59993685756225	-1.41630340881023
C	-5.36088286128265	-0.88542891033660	-1.54026187482425
H	-4.92912862978528	-2.91992840972347	-0.98377591655978
H	-5.45039416564827	1.23795048746778	-2.01250968934636
H	-6.40344653676139	-1.09029555711416	-1.78099929241512
N	-0.21887835707593	1.93486261701095	0.00024114918388
C	-0.44110964418517	2.79369264542459	1.01930154728025
C	0.24147299520419	2.43739778576858	-1.18539201365929
C	-0.21696368796179	4.16418464847209	0.92297565771131
H	-0.80522574554315	2.35249931440115	1.94376025498898
C	0.49528805193757	3.80895075644994	-1.34028169995831
C	0.26840476566444	4.68564975310141	-0.28084934652842
H	-0.41747053803874	4.80255827286308	1.78188167855160
H	0.86409602105339	4.19424559665492	-2.28722187976773
H	0.46191767606818	5.75139931728034	-0.39565765292269

DFT optimized Cartesian coordinates of the <sup>1</sup>GS of [Ru(dpb)(tpy)]<sup>+</sup>

C	12.70986134899085	1.98220383100623	3.71162115152764
C	12.38739122164992	0.73236027679925	3.16650298798295
C	13.21034724882957	0.20338594067972	2.16426246650927
C	14.33194571368258	0.91593461096831	1.72139318351112
C	14.60988425973646	2.16114775521095	2.30051821563134
N	13.79985449005086	2.64921569505625	3.26758731284669
H	11.51672264423244	0.17657163685905	3.50756238536650

---

H	14.96902557531010	0.50235430663386	0.94264602309717
C	11.86970819091090	4.64415544049135	6.08305472728813
C	10.71473505847850	4.20060876325122	6.72594460304821
C	10.17656552171168	2.96041785332860	6.36741902760661
C	10.81608875965492	2.21389532091951	5.37748635325243
C	11.97441360344888	2.71130146773052	4.76661263447539
N	12.49494219348044	3.93084550491562	5.12718804289036
H	9.27610109914716	2.58004474374099	6.84788515291804
H	12.31895487713878	5.60256086189951	6.33425691988814
H	10.25323217881131	4.82185660073879	7.49181775936554
H	10.41799928087446	1.24640533383714	5.07981435113701
C	15.73687564630091	3.06276226496691	1.97976443884069
C	16.70839126852085	2.76405686636038	1.01559095158435
C	17.75001784228006	3.66095381591704	0.77649870535925
C	17.79564337773860	4.84855838813408	1.51417316547163
C	16.79819370526775	5.09391431842504	2.45678085539192
N	15.78832953179915	4.23507152484043	2.69426787745731
H	18.51009891166827	3.43502306991568	0.02961217146751
H	16.65033738504896	1.83245151093874	0.45695395114841
H	18.58792604455079	5.58075239114786	1.36680215760469
H	16.79748443231684	6.00725063649152	3.04776582515725
C	14.10936767167928	7.40821571552064	4.26929500563293
C	14.41863914896342	8.66583848027731	4.81742481760086
C	15.25893614232609	8.74571330506218	5.94135137075609
C	15.79712901666393	7.58845236436631	6.53001485326376
C	15.49145860831185	6.32728034660117	5.98784397415586
H	14.02049727018489	9.58646716214816	4.38688095565026
H	16.44682670427978	7.68975444161002	7.40135557302214
C	12.39824561343533	5.40391605561244	1.74947915998820
C	11.70676252003390	6.31050550056326	0.94911968327575
C	11.80404811533112	7.67562152226252	1.24877631644268
C	12.58572381055274	8.07351771148857	2.33181311764658
C	13.26176454352422	7.11592189924528	3.10628164373781
N	13.15494451035803	5.77703405297390	2.79808402061305
H	11.27763870099253	8.41656752343506	0.64741881935551
H	12.34620272290756	4.33507635520533	1.54762401431819
H	11.10891443078957	5.94903201712825	0.11404674232119
H	12.67632111549822	9.12810200244582	2.58640984809851
C	15.95288782145127	5.01195548841332	6.45014507648960
C	16.79533721184075	4.78723544776261	7.55177552952038
C	17.17243315816100	3.49013720528868	7.89413921563184
C	16.69675361110377	2.42092447790364	7.12384924083098
C	15.86183601182768	2.69989098029918	6.04400208672058
N	15.49161574475104	3.94866735433826	5.70452936505871
H	17.82676630612323	3.31383491218595	8.74774124974577
H	17.15074501549084	5.63518557396702	8.13452943144196
H	16.96300359763747	1.38970795060190	7.34983349047346
H	15.47206570056079	1.89503915462450	5.42265807992537
Ru	14.23265442144270	4.47814384567735	4.08266421595330
C	14.64818125651387	6.23987032925084	4.85600174946847
H	12.97739854986061	-0.76631175809354	1.72737255314975
H	15.49755253577058	9.72218785062950	6.36351140188492

DFT optimized Cartesian coordinates of the  $^3\text{MLCT}$  state of  $[\text{Ru}(\text{dpb})(\text{tpy})]^+$

C	15.36665615195286	-0.89853322002545	4.68994605991724
---	-------------------	-------------------	------------------

C	14.88457240480534	-1.81309109686364	5.64374845494015
C	15.79167157945354	-2.54416010106605	6.42476756375261
C	17.17611091056390	-2.37554990144005	6.26854974720763
C	17.66347084431477	-1.46168910853326	5.31717862139610
C	16.75848870202374	-0.72662409681138	4.53157288272409
H	13.81351352133364	-1.96356481920765	5.78568863719652
H	17.85717732825504	-2.95812966656071	6.89002505116377
C	14.73031116148055	1.55992268368591	2.08335062691179
C	13.34530662691568	1.64489480017839	1.96952516531245
C	12.55400248247823	0.84360635482172	2.80261107501053
C	13.17399550712772	-0.00897606321773	3.71466785764950
C	14.57397545636277	-0.05642425772373	3.78880221356516
N	15.33005932305306	0.73670806259900	2.96367134825601
H	11.46675095087376	0.88365605110639	2.74131102743718
H	15.38225859787418	2.16494747006657	1.45513307276697
H	12.90503428020984	2.32517377705668	1.24291722001465
H	12.57990227441996	-0.64074939090569	4.37210125678823
C	19.06675157842557	-1.15401702773983	5.01682428295496
C	20.18027688928500	-1.73274440144371	5.64484778266370
C	21.46660737309161	-1.35058290291154	5.26726273719149
C	21.62124621694255	-0.38965285104760	4.26127739786702
C	20.47854862884783	0.14939415223024	3.67356146084525
N	19.23685307248518	-0.21640123795757	4.03417669985906
H	22.33599958177971	-1.79553836558249	5.75061524356128
H	20.03204647423579	-2.47755198655414	6.42455840777223
H	22.60471908319295	-0.05896393448418	3.93217738966370
H	20.55179017186756	0.89810429230936	2.88772111747233
C	18.67143779523406	1.32231300372970	0.60741890092396
C	19.19067922955207	2.20066017498465	-0.34196994437363
C	19.46230076140825	3.53317142777739	0.03092105946836
C	19.16969185764628	3.98945439605053	1.33277559329724
C	18.65136890106161	3.09308980601764	2.26574406314528
H	19.36709873236083	1.87791281484083	-1.36631396576656
H	19.32985407528335	5.03497337239241	1.58908308053532
C	17.20037142756006	-1.94767952498993	1.34629176520592
C	17.38207897452566	-2.69557639155800	0.18916371374320
C	18.03488290285438	-2.09402810796930	-0.90468123091905
C	18.47060061291586	-0.78017463369439	-0.79127189688418
C	18.26008988010880	-0.06398148656781	0.40430878716368
N	17.62152060446778	-0.67370189457712	1.47176985074281
H	16.70114064270322	-2.37303021368228	2.21508680541945
H	17.02333093890095	-3.72216398664305	0.14661813784394
H	18.98102423630040	-0.29871638845301	-1.62318077912754
C	18.22230723617704	3.38098771419146	3.63157181960776
C	18.41510534790169	4.62206643023500	4.27109955773080
C	17.96684257921330	4.81499809205838	5.57137365431691
C	17.31888302467993	3.75543414376194	6.23616467044822
C	17.15368028629182	2.55125762507436	5.56229271403035
N	17.58718202783463	2.34860677508943	4.30251893467043
H	18.92244489242124	5.42610762583708	3.74139454942572
H	16.95122305353820	3.86007495325570	7.25509160255380
H	16.65881341752837	1.70660702500387	6.03841518970751
Ru	17.40942670195578	0.58443327014827	3.15436814542743
N	18.47449829597344	1.77734826799580	1.89397143613881
H	18.19959080025723	-2.64861153873635	-1.82798367364019
H	19.86573211719298	4.22674798177651	-0.70496969040556
H	18.11816987924663	5.77346716251991	6.06690325553282

---

H 15.41632983825181 -3.25255585584749 7.16306075017540

**DFT optimized Cartesian coordinates of the <sup>3</sup>MC state of [Ru(dpb)(tpy)]<sup>+</sup>**

C	4.43137034484600	4.22899941565427	-1.13779472312929
C	4.18731407035750	2.92929435415081	-0.66983521566719
C	5.18077692790083	2.27350091205141	0.05941969588672
C	6.39301476017192	2.92304164610276	0.29767846825431
C	6.57735864305469	4.22347407802599	-0.19524244667518
N	5.60288128006359	4.85604423026593	-0.88692586214195
H	3.24723308363562	2.42665883365681	-0.88313660014390
H	7.18563861745090	2.41520427819620	0.84163892597410
C	3.15383310338480	6.85112718324117	-3.32136596654016
C	1.82526802210954	6.51243137258190	-3.57993851244884
C	1.30058018817933	5.36570377270782	-2.97120378992425
C	2.12624929133062	4.59778770445542	-2.14899745620421
C	3.45932374854661	4.99567028958229	-1.95234695992346
N	3.94566575816885	6.11971835779045	-2.52485729921983
H	0.26386781354066	5.07269659258513	-3.13410279776255
H	3.60276850221639	7.74043887154761	-3.76492425608636
H	1.22110977683629	7.13386352029228	-4.23946005469714
H	1.73305959518829	3.70621331708748	-1.66586867114274
C	7.83817359424459	4.98387977237753	-0.02819330118053
C	8.86717301843402	4.59639706028682	0.84637742360268
C	10.03673739848677	5.35589716123102	0.90039483572207
C	10.15239057639080	6.48337048710147	0.07767224228022
C	9.07831230441005	6.81433447017137	-0.74922715110665
N	7.95020878441423	6.09173643099441	-0.79529999078295
H	10.84465911978192	5.07189397394056	1.57402917808771
H	8.75803574138186	3.72056472234539	1.48223961393751
H	11.05237153997474	7.09658515793941	0.07613816000042
H	9.11795652917271	7.69094809382159	-1.39679111144298
C	6.69364156572647	9.23207719273884	-3.32018036999425
C	6.86707946004530	10.59293105625108	-3.64024016352025
C	6.51662050743235	11.57376772336614	-2.70274313636216
C	5.99389236846280	11.22514677273860	-1.44307380662827
C	5.81587552773686	9.87247401189237	-1.11608510751040
C	6.16716965707022	8.87684159785335	-2.05833879492193
H	7.27154383177196	10.90072590974169	-4.60554246815011
H	5.73470663021082	12.01833883470414	-0.74058011016842
C	7.01064732712790	5.73276771078638	-4.25797564543846
C	7.53145225325543	5.72951684025948	-5.55036099565535
C	7.79695438733869	6.95998962794887	-6.16733506551159
C	7.53403116256976	8.13593422750823	-5.46746957564886
C	7.00979395135365	8.07374140038114	-4.16473377674761
N	6.75094186262210	6.86134995635885	-3.57605725817554
H	8.20279317611410	6.99988571843603	-7.17783559772158
H	6.78933769718370	4.79926309251595	-3.74224115773359
H	7.72141164981534	4.78477809054288	-6.05732246670769
H	7.73148726534015	9.10407228180995	-5.92440763376452
C	5.28142846004700	9.33903031154309	0.15529697162401
C	4.85960197821285	10.12086916114516	1.23919180946441
C	4.36821179160060	9.50659774534675	2.39370319062240
C	4.30543508916379	8.11092907448740	2.44854025948141
C	4.74022514568119	7.38625817914954	1.33794198778719
N	5.21354965322560	7.96955737584114	0.22590502629043

H	4.03931055164529	10.11194775425862	3.23816421239678
H	4.91504094353513	11.20604561022724	1.17850945047070
H	3.93049281616743	7.58782506514367	3.32649043269590
H	4.70992625784011	6.29783820163401	1.33714991465397
Ru	5.91638982221294	6.98334803518108	-1.57405642124779
H	5.01824994487403	1.26050873883475	0.42454050053655
H	6.65206276994232	12.62655976618829	-2.95161058394094

DFT optimized Cartesian coordinates of the <sup>3</sup>LL'CT state of [Ru(dpb)(tpy)]<sup>+</sup>

C	15.31816003118714	-0.86461821038032	4.66172210129033
C	14.80153839632097	-1.77189047912937	5.60281957774737
C	15.69367644262167	-2.51932818627397	6.39029033386642
C	17.09138285810335	-2.38650662284775	6.26845878628807
C	17.61400511506414	-1.48179268788625	5.33281658306258
C	16.71604889621880	-0.73418719569880	4.54371868535377
H	13.72826939865165	-1.91033380119154	5.73752223646208
H	17.73698008283872	-2.99030426522132	6.90689256353865
C	14.79092005361711	1.64021742518002	2.05938780902454
C	13.40644881795057	1.75747291727453	1.92691339203636
C	12.58679710371503	0.96659928334539	2.73795248907554
C	13.17858669067851	0.09043561813476	3.64987983278192
C	14.57451643581129	0.01538637222474	3.73995964177250
N	15.36569732470048	0.79992519587603	2.93335748434879
H	11.50148066302608	1.03010905286565	2.66356871660050
H	15.46549515985138	2.23708966907102	1.44811869709894
H	12.99059147313711	2.45548573261133	1.20242681455281
H	12.56236253600744	-0.53508314038299	4.29299914405880
C	19.03991130593370	-1.18801580481354	5.05529406835875
C	20.12076022159477	-1.78895600226085	5.70916897457336
C	21.42815148901933	-1.42681270645868	5.36999193842585
C	21.63178350369356	-0.46493592176749	4.37792698298560
C	20.51372076150788	0.09907030489894	3.75887532696968
N	19.25942915373436	-0.24576542833526	4.07960307210279
H	22.27336561026839	-1.89152539968246	5.87683780460535
H	19.93996745258168	-2.53517185310203	6.48063247215481
H	22.63095431165447	-0.15094857194969	4.08175674256303
H	20.62367976253702	0.85211241872546	2.98005401648782
C	18.58636691435896	1.36511788926079	0.57433519601395
C	19.19251134689961	2.18938435529465	-0.36816054211499
C	19.49948847112861	3.52272751979220	0.00908143140102
C	19.19896082319207	3.98177690381957	1.28689194636359
C	18.58480216133518	3.11119199251819	2.21711341292324
H	19.42673004309111	1.83285490110262	-1.36848391349806
H	19.43270621654200	5.00826317288793	1.56462741630169
C	17.16587798917905	-1.91265276806066	1.37169753909916
C	17.32772052184989	-2.66873816251429	0.21662212957660
C	17.94746532305503	-2.07880738460766	-0.89579153392850
C	18.37302030130879	-0.75614630997651	-0.80441505016311
C	18.18561665675324	-0.03795001497247	0.38570516064769
N	17.58730647283327	-0.63299391873071	1.47097537747489
H	16.68950042342210	-2.33538728245677	2.25319228418658
H	16.97239476710286	-3.69716954227278	0.19425967108860
H	18.85092696360376	-0.27314332521836	-1.65387145016767
C	18.19895633589941	3.39239069660753	3.56993821120698
C	18.39841017448824	4.63261760044709	4.23221664207184

---

C	17.96752247703751	4.81627656617437	5.53100170416272
C	17.31410965449109	3.74530888653804	6.20139489494394
C	17.14150793249257	2.55030853671808	5.52528345305090
N	17.56941611717202	2.34627341191526	4.25686577905629
H	18.897844444320352	5.44108470381455	3.70039701534052
H	16.94929792482478	3.84642260203043	7.22162021646012
H	16.64722962919427	1.70688595673842	6.00422661609176
Ru	17.44584940623572	0.53101299866710	3.23337622644892
N	18.30090921626586	1.82582209010985	1.81507642064533
H	18.09218918782569	-2.64091196202861	-1.81752995677433
H	19.97034566747865	4.19114089293389	-0.71064478453923
H	18.12450573740016	5.77078155590843	6.03287087699009
H	15.29276463830833	-3.22349666126575	7.11940183545242

DFT optimized Cartesian coordinates of the  ${}^3\text{MLCT}-{}^3\text{LL}'\text{CT}$  transition state of  $[\text{Ru}(\text{dpb})(\text{tpy})]^+$

C	-2.881571	-0.680049	-0.217668
C	-4.258789	-0.405259	-0.318463
C	-4.697161	0.926754	-0.281285
C	-3.791652	1.995890	-0.145681
C	-2.416707	1.728736	-0.054864
C	-1.975879	0.391153	-0.094804
H	-4.992938	-1.205699	-0.418957
H	-4.176199	3.015950	-0.112694
C	-0.137204	-3.070809	-0.008616
C	-0.727868	-4.330473	-0.078505
C	-2.118222	-4.411258	-0.223561
C	-2.864129	-3.234916	-0.285182
C	-2.219148	-1.991607	-0.205350
N	-0.851391	-1.933381	-0.077050
H	-2.614297	-5.379355	-0.285542
H	0.940946	-2.961120	0.094886
H	-0.106171	-5.222204	-0.025433
H	-3.946769	-3.272680	-0.390722
C	-1.316627	2.703243	0.078061
C	-1.466506	4.095453	0.107883
C	-0.341192	4.914674	0.221237
C	0.925277	4.327403	0.303704
C	1.014627	2.935776	0.275605
N	-0.065120	2.145779	0.166098
H	-0.453389	5.998401	0.245894
H	-2.460721	4.532533	0.040020
H	1.829376	4.926265	0.395815
H	1.978148	2.434106	0.346008
C	2.612035	-0.496663	1.281468
C	3.984230	-0.709253	1.355745
C	4.720582	-0.744661	0.142201
C	4.082630	-0.576508	-1.085721
C	2.688847	-0.359686	-1.123969
H	4.489328	-0.849275	2.308618
H	4.662055	-0.619008	-2.006554
C	-0.590158	-0.205688	3.039696
C	-0.279170	-0.367180	4.385601
C	1.060990	-0.569416	4.748623
C	2.030103	-0.607659	3.749770
C	1.661595	-0.442861	2.405630



N	0.343369	-0.234371	2.066524
H	-1.616571	-0.041569	2.718191
H	-1.072864	-0.331082	5.129785
H	3.075178	-0.768237	4.005536
C	1.847381	-0.180782	-2.280897
C	2.319239	-0.153452	-3.617926
C	1.441014	0.014413	-4.672657
C	0.053784	0.157105	-4.403814
C	-0.367509	0.123445	-3.084939
N	0.474783	-0.031420	-2.039067
H	3.385690	-0.265733	-3.807100
H	-0.673744	0.284105	-5.203276
H	-1.422419	0.223344	-2.834211
Ru	-0.032480	0.005427	0.002862
N	2.012682	-0.320370	0.076435
H	1.342910	-0.696356	5.793146
H	5.796490	-0.912102	0.172376
H	1.811629	0.034513	-5.697329
H	-5.763581	1.139508	-0.354488

DFT optimized Cartesian coordinates of the  $^3\text{MLCT-}^3\text{MC}$  transition state of  $[\text{Ru}(\text{dpb})(\text{tpy})]^+$

C	-2.36864489353110	0.87237850700313	0.64134773038059
C	-3.77175419604035	0.81029682913068	0.53419705634385
C	-4.35849977449903	-0.15210047293970	-0.29942069263167
C	-3.57351806188466	-1.06091338750200	-1.03370266436684
C	-2.17534465403174	-1.00777628763679	-0.93014264514859
C	-1.57986506629813	-0.03850095827932	-0.09206776953627
H	-4.41373486504454	1.49698434783136	1.08766474950324
H	-4.06977450301763	-1.79423415168201	-1.67077251572694
C	0.59475931865583	2.42340156815806	2.07716428397209
C	0.12751620339968	3.43118070287481	2.91982656463684
C	-1.25608417037032	3.62423410406554	3.02537194253272
C	-2.11158675780258	2.80575256911000	2.28940081590516
C	-1.57891638236871	1.80463872426504	1.45994032853066
N	-0.22242000313658	1.63096373253122	1.36636043087018
H	-1.66135007006418	4.40211061130326	3.67239287982139
H	1.66247592642519	2.23897737473531	1.96395299175217
H	0.83307832078664	4.04633435891516	3.47595181943287
H	-3.19039814222348	2.93622154773989	2.35511938058548
C	-1.20399424189514	-1.88538698058313	-1.61916005023477
C	-1.54253668297091	-2.92322472063148	-2.49655833818450
C	-0.53747431068967	-3.69469052559331	-3.08588101656628
C	0.79922605070807	-3.41517331044270	-2.78761937523357
C	1.07590309285950	-2.36728389597940	-1.90843548799212
N	0.11517182859326	-1.62259958732707	-1.33935738117067
H	-0.79763630197486	-4.50358250159505	-3.76840406654809
H	-2.58887054549005	-3.12609665716230	-2.71602024519577
H	1.61532126756384	-3.98970170388861	-3.22188141704935
H	2.10209563182703	-2.11306362971649	-1.64874844267586
C	3.26933157194439	0.77762578644604	-0.80618016507176
C	4.67061491188745	0.80261127170093	-0.79126984168853
C	5.35158662547154	0.02946933358082	0.15480068566400
C	4.62673877879601	-0.74886419320453	1.06309857831940
C	3.22648109875654	-0.73478833363951	1.00226175128286
H	5.22431330236420	1.42565055699280	-1.49027561489357

---

H	5.14582228729734	-1.34004790394485	1.81447389549954
C	0.26235618234000	2.35675239746061	-2.12088628784997
C	0.67148122174460	3.04129753453992	-3.26074082526546
C	2.01763877014468	2.95243622984876	-3.65403759060309
C	2.89677889340120	2.20248757729197	-2.87623775683675
C	2.42144634653038	1.55548876102032	-1.72261346093852
N	1.10461623079144	1.62070385229292	-1.36977549421033
H	-0.77447618039482	2.39204410965432	-1.78730152098667
H	-0.04705829997013	3.63398589634836	-3.82495161890087
H	3.94297227148681	2.11500085105806	-3.16301656014388
C	2.33518374300430	-1.47833423978259	1.90563163533736
C	2.76179734298391	-2.51067750272028	2.75869493871587
C	1.84314635126242	-3.12062896262539	3.60998568210153
C	0.50771423725767	-2.68327813811820	3.59188181670661
C	0.14757880726321	-1.67298797548783	2.70594433755566
N	1.02826452249471	-1.08600246327056	1.87223544529511
H	3.80061719902034	-2.83478403014716	2.75003276005315
H	-0.24003425207711	-3.11514659074657	4.25527797243395
H	-0.87911716023599	-1.31149664246892	2.65350666037516
Ru	0.39000721066647	0.01704629050968	0.02672952446421
N	2.58127612313474	0.01294059482083	0.07510899805288
H	2.37145740671836	3.45918757627996	-4.55114402273257
H	6.44005183114239	0.04574152680685	0.19405738163836
H	2.15813489904788	-3.92241261638068	4.27702064954704
H	-5.44464134176029	-0.19863699682019	-0.38112021492668

#### DFT optimized Cartesian coordinates of the $^3\text{MC}^{-1}\text{GS}$ MECP of $[\text{Ru}(\text{dpb})(\text{tpy})]^+$

C	4.38470679815292	4.17076500507583	-1.09998123054573
C	4.15570297011802	2.90751097353839	-0.53319727102153
C	5.14497926167141	2.33861579656771	0.26920459203631
C	6.33710689545686	3.03414197675186	0.47278222361019
C	6.50048171372369	4.29712191586051	-0.11806731599752
N	5.52686574441872	4.85206415282219	-0.86922470337152
H	3.23397424687978	2.36544654497053	-0.72864116218649
H	7.13364553691555	2.58862180359476	1.06350599441438
C	3.12626394549021	6.53774904566726	-3.56135332103208
C	1.82197992445969	6.13191633868455	-3.84866597497328
C	1.30520618820921	5.02611096980045	-3.16357198860359
C	2.11356621836272	4.36390753479239	-2.23776928574841
C	3.42174657761863	4.82653467976509	-2.01875768419102
N	3.89980062408706	5.90824987301357	-2.66734432975930
H	0.28753933828004	4.68278249409209	-3.34687385421043
H	3.56946875174746	7.39931426910931	-4.06267744404180
H	1.23111504308422	6.67073681294023	-4.58793848536903
H	1.72500407885772	3.50587284217991	-1.69407196063948
C	7.75944660801955	5.07732046201249	0.01007418509262
C	8.74380324865493	4.79578200276583	0.97359023776954
C	9.91576886126860	5.55480526570807	0.98473892910646
C	10.07381360966569	6.57245618644621	0.03690774736822
C	9.03510268811746	6.79872036368934	-0.86994098425172
N	7.91060437965419	6.07575558541433	-0.87877637269440
H	10.69150253977390	5.35538206433896	1.72378818364238
H	8.59901850845686	4.00815194953261	1.70997964385010
H	10.97583842607923	7.18192437386980	0.00220717394617
H	9.10546129200951	7.59466686979074	-1.61327721523492

C	6.75201604159672	9.31255158123966	-3.28856096686528
C	7.06883413972527	10.66477443819301	-3.52526259254639
C	6.84637653798825	11.61280268479290	-2.51814374229603
C	6.31485525986489	11.24027413147174	-1.26900383011694
C	5.99298126199607	9.89668986944868	-1.02629529714516
C	6.20673542131676	8.93711290351122	-2.04171149802541
H	7.49307302280703	10.98847833927682	-4.47665183206832
H	6.16188711605762	12.00777693596642	-0.50927408951358
C	6.75232936288312	5.85678030832646	-4.41229174562837
C	7.28803539199305	5.87354489217600	-5.69853715304554
C	7.66382327902605	7.10533024423442	-6.25189292458435
C	7.49576982103393	8.26361723576016	-5.49482009533608
C	6.95368505896774	8.18100517668822	-4.20135791963512
N	6.57875541821678	6.96906614595016	-3.67718806782415
H	8.08232540228768	7.16008432473178	-7.25647951089809
H	6.44150876835871	4.92272838582588	-3.94706009753480
H	7.40280744761232	4.94198415018393	-6.25056949629427
H	7.78363014508894	9.23230554846735	-5.89967117006893
C	5.42888547781248	9.34057673174020	0.22372915605402
C	5.08932452921728	10.09427976103457	1.35409050163174
C	4.54354284984739	9.46245393329997	2.47502655080767
C	4.34425829381511	8.07976417025305	2.44670188212162
C	4.70924805036117	7.38265468258685	1.29334322665000
N	5.23731711025868	7.98214331912406	0.21571440707853
H	4.27747094146672	10.04532228088540	3.35660178470147
H	5.24655061625848	11.17104103293965	1.35528090676358
H	3.92177638998087	7.54370838375779	3.29463225306805
H	4.57907177529512	6.30380172597418	1.23180405420115
Ru	5.74444966740833	7.04973776124694	-1.68290178493078
H	4.99772659829462	1.35513108381861	0.71325230335696
H	7.09407678392897	12.65844168429891	-2.70183253904138

DFT optimized Cartesian coordinates of the  ${}^3\text{MLCT}-{}^1\text{GS}$  MECP of  $[\text{Ru}(\text{dpb})(\text{tpy})]^+$

C	15.40484049240013	-0.88345726144979	4.67290211562383
C	14.94754647926214	-1.80500092938010	5.63322591973987
C	15.86735006528119	-2.52420595782918	6.40183923356242
C	17.24219374658701	-2.32987650540788	6.21944508723134
C	17.70861701688645	-1.41080383444737	5.26240030674557
C	16.79373759322178	-0.68206275263216	4.48267281298562
H	13.87957419464140	-1.96371072826052	5.78354054786139
H	17.94413827218692	-2.89929253547154	6.82856280321915
C	14.60367056497956	1.54813304150502	2.09915391747670
C	13.21533549491118	1.59380415067267	2.02896082321080
C	12.47404042959764	0.76923877985877	2.88625244894212
C	13.14349893839878	-0.06687880094169	3.77812484941638
C	14.54592823577888	-0.07435454747098	3.80805400998993
N	15.24461566620492	0.73814594136014	2.96277924583522
H	11.38492041166255	0.77935584760720	2.85834707333634
H	15.22176861306172	2.17122828682848	1.45253168244898
H	12.73345435534352	2.26157603897678	1.31775017373802
H	12.58589350980225	-0.71425315985898	4.45149640219587
C	19.12255532924218	-1.12334564026840	4.98527776079038
C	20.21646046876207	-1.71950408366729	5.63357009473006
C	21.51138957338004	-1.34856564534365	5.27032967626743
C	21.68726225760729	-0.39005175073395	4.26642450935622

C	20.55153654339953	0.15758389963834	3.66679411291781
N	19.31165738967484	-0.19796095276491	4.01536784084155
H	22.37055393716787	-1.80185399187783	5.76456223918181
H	20.05542613005032	-2.46313551633017	6.41163486392774
H	22.67854439649378	-0.06967383824452	3.95000439047635
H	20.62749612572942	0.90600903222417	2.87963933841034
C	18.78681451586253	1.26982533793107	0.65456728844805
C	19.30023402574685	2.15533155127804	-0.28580277170369
C	19.60407800472820	3.48256335794422	0.08505209491452
C	19.27933826967863	3.93569682979084	1.38140003530421
C	18.76683212733781	3.04862864723617	2.32084386103413
H	19.43031275158510	1.83918038296745	-1.31975835617745
H	19.39281529875844	4.98976726410595	1.63032688117575
C	17.04347640177903	-1.87351775344298	1.27713732176576
C	17.24585344640456	-2.63990436921467	0.13644740323133
C	18.00912505998313	-2.08985363822064	-0.91279528642626
C	18.53345259576657	-0.81243872856842	-0.77586230897963
C	18.29965720486892	-0.07689343090251	0.40679395401633
N	17.55162638513612	-0.63491207103361	1.42352948642596
H	16.45793954068919	-2.25347125347459	2.11268935761466
H	16.81973037811792	-3.63901219432983	0.07087418785775
H	19.13440769998231	-0.37588775237086	-1.57123027221005
C	18.26232220220065	3.37777925903336	3.64345443489264
C	18.47834312714679	4.60714132667052	4.30399350526601
C	17.94031590026054	4.82019397592822	5.56510524337559
C	17.18087217520412	3.80095892786556	6.17392556452204
C	16.99552597831762	2.61206017740364	5.48000733587735
N	17.51749650353924	2.39167157264199	4.25820588204822
H	19.07685287020168	5.37858363859300	3.82326163752581
H	16.74471758565209	3.92608761311111	7.16296506093197
H	16.41364801678941	1.79690845636811	5.90717965534584
Ru	17.30659631396221	0.68815508234196	3.04135337450720
N	18.66157963728374	1.68718557357099	1.99011971029106
H	18.19241723012228	-2.66153646890871	-1.82227445152951
H	20.00138664867259	4.17752601566264	-0.65224632647679
H	18.10998561793944	5.76595474792969	6.07918242163703
H	15.51403849956687	-3.23790341019833	7.14553705303492

#### DFT optimized Cartesian coordinates of the $^1\text{GS}$ of $[\text{Ru}(\text{tpy})(\text{pbpy})]^+$

C	12.74521562833022	1.95490289053854	3.76119933536019
C	12.45868542841642	0.68376668504466	3.25081750186654
C	13.29339122522544	0.13994414217331	2.26765659789958
C	14.39715473410017	0.86827698210373	1.80886616481376
C	14.64886090445029	2.13580298441614	2.34586889086865
N	13.82479841068104	2.64662475926470	3.30209044814486
H	11.59982651966680	0.12140975235201	3.61062787084164
H	15.04921511690488	0.44966441067639	1.04532772292855
C	11.85352524592396	4.65285729437298	6.05037937087397
C	10.70477003003662	4.21148083138506	6.70401207012244
C	10.18425839678606	2.95314113797450	6.37927176195252
C	10.83472037145227	2.18741111632069	5.41223822543540
C	11.98749182484208	2.68575303653428	4.78997578740968
N	12.48777453843325	3.92095627952269	5.11522778685950
H	9.28863119704088	2.57448561500970	6.87001167563632
H	12.28834314160832	5.62389344877784	6.27899039493245

H	10.23374011271928	4.84632861709586	7.45273622364213
H	10.45103107895906	1.20623850585168	5.14136834329680
C	15.75465771801265	3.04169856923670	1.99483358098373
C	16.73487580837206	2.74470264025971	1.03788514372457
C	17.75117497588445	3.66409569375002	0.77948647860197
C	17.76346481987185	4.87103600338486	1.48892647799367
C	16.75970875444248	5.11065949652407	2.42497479205648
N	15.77405987775666	4.22962419572461	2.67987668318202
H	18.51883963438869	3.44202503682480	0.03924374971418
H	16.70256833154536	1.79893329572430	0.50143867003726
H	18.53637756739475	5.62011527289818	1.32478283217553
H	16.73787318232410	6.03680896782337	2.99571163664174
C	14.11743304774658	7.38479875076768	4.27983650473617
C	14.41296225511687	8.64451392436043	4.81493800864275
C	15.24726638329367	8.71810780996924	5.93627159675053
C	15.76693048574328	7.54994739902167	6.49849461855912
C	15.44528407470801	6.30586540975312	5.93091654758392
H	14.00656130146252	9.55072146335351	4.37253126936735
H	16.41668451231850	7.60442269517592	7.36945604716985
C	12.34936712491264	5.51146141753226	1.69027799751470
C	11.68818883275178	6.47240555103074	0.92511452151309
C	11.82910147270612	7.81901263655948	1.27640272375149
C	12.62255881004128	8.15017190313750	2.37567615840372
C	13.25872758986386	7.13258069330615	3.10118581737121
N	13.11380968528862	5.82434638108386	2.74883377668281
H	11.32902547171545	8.60020016745984	0.70512839544242
H	12.26420403771407	4.45254139464700	1.44866697714437
H	11.07940374360197	6.16524031929787	0.07631896764249
H	12.74438084598587	9.19120522689144	2.66573082761323
C	15.89368883481598	4.97596717591248	6.37204534323800
C	16.73895848178298	4.78314217741729	7.48280524728292
C	17.13686003277949	3.49611203750343	7.85035864994381
C	16.68544906910564	2.39639372840521	7.10265968677629
C	15.84287698813811	2.58552363472172	5.99862099222482
C	15.41923828873027	3.86838661996780	5.59690272007006
H	17.79135866317775	3.34890152246904	8.71020385546479
H	17.09015731990586	5.63598712590451	8.06543195870517
H	16.99320683393514	1.38701396366127	7.38407031905902
H	15.51121660108683	1.70673522432742	5.44108596676036
Ru	14.20645585487862	4.43348288455966	4.04334006984424
N	14.63122689144188	6.26242596309963	4.83997060347489
H	13.08510716604031	-0.84811850056666	1.86097570306393
H	15.49099772363989	9.68741363770414	6.36967891020631

DFT optimized Cartesian coordinates of the <sup>3</sup>MLCT state of [Ru(tpy)(pbpy)]<sup>+</sup>

C	12.67660189415259	1.91482973878531	3.61413229680271
C	12.42637189112245	0.64744300646951	3.09555754029943
C	13.27462145110415	0.13055773303360	2.09521881065385
C	14.38890168372808	0.87015762765675	1.64820691251308
C	14.62579286357009	2.13588470103827	2.17605698974852
N	13.73650635197756	2.64703730552963	3.10685895981100
H	11.59487473715519	0.04946227021980	3.46346361464945
H	15.06229403181304	0.44150201147662	0.90845132899273
C	11.87219329906830	4.50100468392905	6.05946342518713
C	10.71819753927229	4.05669370543875	6.69537016950609

---

C	10.16443594246182	2.82385700152531	6.30063539443034
C	10.78425383264120	2.09815574206977	5.29107237841135
C	11.95075817443141	2.59725471817551	4.67848994391582
N	12.48097117706997	3.80879172296293	5.07838209954298
H	9.26196628065677	2.44155472993422	6.77629567441647
H	12.33488331372072	5.44599992118967	6.33931169180159
H	10.26611686174535	4.66036339021994	7.48023228908911
H	10.37116739593959	1.14473753978012	4.96784819679103
C	15.74696926531942	3.02203965463301	1.88345158052032
C	16.73131507839703	2.76281495152257	0.90919396137380
C	17.77035350488123	3.66441323229853	0.71279444667641
C	17.82115412035600	4.83203708172638	1.49852669895284
C	16.82254943632511	5.03969843795263	2.44327504790970
N	15.80812181671036	4.17678287970843	2.63987900305274
H	18.53283357999221	3.46659327273021	-0.03997469307286
H	16.67307100957535	1.85506734343309	0.31174991380135
H	18.61655228475724	5.56575545052230	1.38062563328048
H	16.82639549270988	5.92865480085416	3.07190681639383
C	14.16612539173117	7.32947066673166	4.29075394268052
C	14.47950630887131	8.58633485950216	4.81933373820394
C	15.31834176506314	8.65674163231982	5.93727428565609
C	15.82208096710873	7.48595195366940	6.50296659233320
C	15.48013773447466	6.24655957133265	5.93759582149975
H	14.08128715164628	9.49448395247068	4.37428992644514
H	16.47304111619703	7.53075017292230	7.37326325610846
C	12.34420071666518	5.48617096477300	1.72743839417577
C	11.69104373725377	6.45466342670496	0.96332585992551
C	11.85895495742060	7.79955533541796	1.30672344968737
C	12.66811288175587	8.12674024292332	2.39674032873860
C	13.29277784761941	7.10018921303927	3.11818907049088
N	13.12172678249681	5.80164129604649	2.77172053423177
H	11.36631781565324	8.58558814813179	0.73573419192373
H	12.24373674170179	4.42574158724832	1.49798882193539
H	11.06842039903441	6.15426246536548	0.12236399999221
H	12.80844568619657	9.16745608126187	2.67869934076175
C	15.90961559284557	4.91865398887904	6.38856842644080
C	16.74524188641425	4.69473666473318	7.49936277062373
C	17.10126522853694	3.39290386702486	7.85632166050833
C	16.61747636831403	2.31100415305526	7.10389766481483
C	15.78088415945359	2.52540542156106	5.99932195427156
C	15.41540719733644	3.82896183847970	5.61900226280487
H	17.74912275350825	3.21932543740001	8.71572347071845
H	17.11914010295562	5.53344670549776	8.08729888351095
H	16.89192682855390	1.29135662774279	7.37997178834502
H	15.41929536503553	1.66366756012848	5.43657105445727
Ru	14.23827460543424	4.31595126514310	4.03833961686097
N	14.66641456668263	6.20239196544968	4.84945558098664
H	13.08632682310878	-0.86068022308641	1.68676454204212
H	15.57540119727573	9.62508161331428	6.36466886937299

**DFT optimized Cartesian coordinates of the  $^3\text{MC}$  state of  $[\text{Ru}(\text{tpy})(\text{pbpy})]^+$** 

C	-2.76102499548434	1.12702377386616	0.28765099569250
C	-4.15808118418278	1.19140498309187	0.18398184481036
C	-4.85149381031882	0.12042195258441	-0.37959852187425
C	-4.13373016560589	-0.99157279154958	-0.81967530715916

---

C	-2.73777832829448	-1.00377864329344	-0.68865200962060
N	-2.06918849527796	0.04477611529524	-0.14735916616594
H	-4.69825530960821	2.07247598437968	0.52092502451219
H	-4.65419952136940	-1.83014520714206	-1.27531054565348
C	0.18068837184451	3.12032886664225	1.09101259665743
C	-0.29200213845034	4.22140238133657	1.80694181730009
C	-1.66605547086170	4.30472773838347	2.06444304784830
C	-2.50873605695000	3.29965752883088	1.58766520899194
C	-1.95478553574724	2.23064065706248	0.86161336279000
N	-0.62759759511806	2.15445482609416	0.63911350722326
H	-2.07652535483121	5.14040811122249	2.63059575656627
H	1.24275866932303	3.00840305222785	0.86764245156253
H	0.39913375988177	4.98939813714506	2.15083226730454
H	-3.57636983585324	3.34615410121787	1.78991465967890
C	-1.90836169800412	-2.14589833550791	-1.14091553393319
C	-2.43632136123881	-3.40959925535929	-1.45855694331224
C	-1.57406026609137	-4.41242266914456	-1.90408454507284
C	-0.20688923535313	-4.13274574744873	-2.02253319778427
C	0.23993169449312	-2.85834691433661	-1.67022270042102
N	-0.58672399899018	-1.89926747974854	-1.23726672907252
H	-1.96420385612774	-5.39897093792591	-2.15263679464414
H	-3.49857419969389	-3.61670233663012	-1.35060755652596
H	0.49862792149579	-4.88218147181379	-2.37801205233901
H	1.29616450813154	-2.59390034293569	-1.74015061969802
C	2.90822206585381	0.38642394473329	-0.88014516708982
C	4.31236793371106	0.32113140653227	-0.78157984483075
C	4.89494988374734	-0.20868574618442	0.36604170278995
C	4.08631129087374	-0.67135900063847	1.41821770396057
C	2.70036226188503	-0.58970919400853	1.28629324301975
N	2.14845663675068	-0.07292859483304	0.15594216357365
H	4.93618344070649	0.68187417104632	-1.59661131181770
H	4.54341537040503	-1.08286198725524	2.31449337348782
C	-0.10223802625385	1.35262430621099	-2.86425641920941
C	0.46531947634252	1.88762773719419	-4.02468593169533
C	1.86404758520133	1.93448806562996	-4.18073062312080
C	2.68417889990032	1.44571456858316	-3.16580843966906
C	2.11378916432691	0.90668244288069	-1.99176229419185
C	0.69082091068909	0.84315959126758	-1.81339358183238
H	2.30357036623667	2.35066755957031	-5.08804939318695
H	-1.19065373054366	1.33075834993555	-2.77423428818642
H	-0.17884792969117	2.27232888581874	-4.81838592538433
H	3.76776068170319	1.48596697598358	-3.28878305590183
C	1.72264714916337	-1.03311032435366	2.31726764746447
C	2.10831500768407	-1.57173347737862	3.55171996040048
C	1.12853949578574	-1.95989711677798	4.46935611624238
C	-0.21879584747297	-1.80261653321321	4.13481002901728
C	-0.53055190260299	-1.25907600514790	2.88676196574170
N	0.40587608282102	-0.88501983409767	2.00500715084026
H	1.41860140225541	-2.37859166583536	5.43234057951693
H	3.16018202089079	-1.68864924115065	3.80095380184794
H	-1.01514625974496	-2.09082017626086	4.81848043494780
H	-1.56714238823843	-1.11779467899539	2.58237948129498
Ru	0.13252028802661	0.01376489879761	-0.03092398559529
H	-5.93499637389381	0.15602092876591	-0.48371310386762
H	5.97945525376477	-0.26503269236338	0.45283417577188



DFT optimized Cartesian coordinates of the  $^3\text{MLCT}-^3\text{MC}$  transition state of  $[\text{Ru}(\text{tpy})(\text{pbpy})]^+$ 

C	-2.75354927205834	1.12758518422665	0.29199139926459
C	-4.14890455291455	1.19887895866046	0.17857089251439
C	-4.84222399792926	0.13008922160635	-0.39254658695705
C	-4.12780261280195	-0.98651773676722	-0.83037403549527
C	-2.73339165236175	-1.00567658550670	-0.68971892013974
N	-2.06727658242835	0.03948000838534	-0.13822289981865
H	-4.68659695438285	2.08283879879914	0.51319146575650
H	-4.64871248835143	-1.82255944733834	-1.29103803029254
C	0.21620401085835	3.09302898611763	1.04502309934211
C	-0.23169044543041	4.18054520188965	1.79410514570107
C	-1.59750138300368	4.26196856436891	2.10052526920488
C	-2.45715338891589	3.26814744021846	1.63278799870300
C	-1.93158681591202	2.21322046512345	0.86633330664698
N	-0.60808558671484	2.13427239918587	0.59987928613843
H	-1.98586524714157	5.08694321392209	2.69705111406689
H	1.27004003804592	2.98496993202617	0.78493731916276
H	0.47170326356084	4.94298436353355	2.12525413522650
H	-3.51795878917875	3.30859872224918	1.87082527559947
C	-1.89187056302891	-2.13712794341868	-1.13168073555929
C	-2.39629823933873	-3.41616180387722	-1.42515727531284
C	-1.52003994962333	-4.40673067382607	-1.86815015925306
C	-0.15908019311940	-4.09933600704339	-2.00732140589539
C	0.26760378853993	-2.81401623166349	-1.67594759058606
N	-0.57240186644720	-1.86265499726940	-1.24437444364842
H	-1.89189261968521	-5.40456719848801	-2.09877042768828
H	-3.45340952577055	-3.64047497396670	-1.29951487826535
H	0.55670778512377	-4.83748990544315	-2.36583644342333
H	1.31728945459858	-2.53036694305712	-1.76341697449292
C	2.89354379083846	0.39073350681475	-0.88051500500028
C	4.29746809569368	0.32965899233466	-0.77717647168420
C	4.87670325043192	-0.19669175099252	0.37385298802477
C	4.06599272318631	-0.66007316502573	1.42395078386271
C	2.68020834401003	-0.58251718914363	1.28667337355504
N	2.13274320039798	-0.06898031381324	0.15356628212668
H	4.92351926550284	0.69072979551232	-1.59027026376289
H	4.52125309946026	-1.06875969556847	2.32241811678225
C	-0.11339010198234	1.34580411484654	-2.87814871326597
C	0.45754358771864	1.88036611250692	-4.03744634726869
C	1.85646634380249	1.93061508579101	-4.18788640753580
C	2.67418844068793	1.44572130350688	-3.16906870074413
C	2.10088166021199	0.90735474706025	-1.99623467909088
C	0.67786185302632	0.84142897850853	-1.82475009592372
H	2.29841249466701	2.34640151709699	-5.09415523720539
H	-1.20192700511116	1.32090924817627	-2.79164161067231
H	-0.18456439123069	2.26190016731916	-4.83424151324845
H	3.75805081037573	1.48852279868006	-3.28797121490458
C	1.69887842753254	-1.02692775706340	2.31423192546475
C	2.08134616031624	-1.56303835174878	3.55061370812389
C	1.09902732410391	-1.95277525462822	4.46496780193879
C	-0.24734320141478	-1.79953893212514	4.12497021249209
C	-0.55588458858931	-1.25823069944859	2.87510865059128
N	0.38295323711400	-0.88259254339838	1.99672867462915
H	1.38647652982874	-2.36959035627777	5.42953064897016
H	3.13255506535007	-1.67690542466568	3.80397807650171
H	-1.04551132358399	-2.08924309503007	4.80587701864418

H	-1.59162798444991	-1.12009513353675	2.56634005418172
Ru	0.11493087974475	0.01555961731688	-0.04224186810891
H	-5.92457256379568	0.17179841707972	-0.50605620666362
H	5.96102796196758	-0.24973775273201	0.46482011869129

DFT optimized Cartesian coordinates of the 3MC-1GS MECP of [Ru(tpy)(pbpy)]<sup>+</sup>

C	-2.61493034534291	1.04366822521681	0.45781862424740
C	-4.00902873226880	1.19595118017195	0.52515865914716
C	-4.83393164864842	0.21435938553557	-0.02325654033724
C	-4.25040685884401	-0.89614634818210	-0.62866264218616
C	-2.85093570865961	-0.99199204634059	-0.66474760147989
N	-2.05812228724584	-0.03709095823884	-0.12915905286159
H	-4.45177383241122	2.07346038723464	0.98769594380962
H	-4.87546087534866	-1.67042481532353	-1.06517465633768
C	0.50603512357210	2.78932667479091	1.16352933181865
C	0.14953700495120	3.92633173595996	1.89435029646300
C	-1.20147231400113	4.11421350603726	2.19955537523526
C	-2.13246004894730	3.17587443195657	1.75121010070758
C	-1.68634188403353	2.06829295613102	1.00710577412434
N	-0.38294440461319	1.88825911560673	0.74047308504594
H	-1.52941910887059	4.97798299738384	2.77733058497422
H	1.54950315691442	2.60206065964940	0.91068858375602
H	0.91162382262634	4.63504536233777	2.21469312666611
H	-3.18494724162375	3.31044826427166	1.98701097017676
C	-2.14382101157311	-2.12974047644463	-1.28901517350702
C	-2.79317253786459	-3.21346341489474	-1.90324703205642
C	-2.03579390080484	-4.23558159918576	-2.47277904346079
C	-0.63884739526004	-4.14975811852020	-2.42145369651687
C	-0.06248672245600	-3.04394281052425	-1.80190261424575
N	-0.79369230571411	-2.06247518858956	-1.24171172291568
H	-2.52684979585084	-5.08203783430813	-2.95133217053059
H	-3.87865302539915	-3.26143820188229	-1.93940072985290
H	-0.00350394714571	-4.91867010009843	-2.85763235335441
H	1.02049148759010	-2.93142181080828	-1.75361681096138
C	2.86591558506496	0.70196830458019	-0.75554964132898
C	4.21023442231151	1.01551690840609	-0.49386959203120
C	4.75249608580065	0.72115180774536	0.75900584245974
C	3.96694218150152	0.10855376100458	1.74616294790564
C	2.63226816567514	-0.18468430622669	1.45327789326376
N	2.12036130939026	0.12811290797377	0.23438903635863
H	4.82642327620221	1.48028992922595	-1.26038318353723
H	4.39749251129751	-0.13473604065568	2.71414353852674
C	0.03531607067485	0.61877558429846	-3.19875712209368
C	0.59639540060129	1.24046270276736	-4.32250689460856
C	1.924444676030077	1.69890540540096	-4.29656539951659
C	2.68366989203777	1.53094087573898	-3.13659321853824
C	2.12000489392573	0.90856434629251	-2.00490256268650
C	0.76572136886746	0.42855283172671	-2.00746846169419
H	2.36008608657419	2.18139386981678	-5.17214003114659
H	-0.99936307288434	0.27312848631279	-3.25461844294640
H	-0.00204190244596	1.36932036789953	-5.22712611469691
H	3.71444603617835	1.88797604975387	-3.11832943178858
C	1.67699061892084	-0.84392449306159	2.37833901993527
C	2.00000770526967	-1.16928647929053	3.70261679221722
C	1.05000726398870	-1.80204504046085	4.50757864650347

---

C	-0.20423089295620	-2.09864709199312	3.96690260185440
C	-0.45782150429933	-1.74382754443286	2.64023542895543
N	0.44769723708164	-1.13172264547892	1.86340312121954
H	1.28811538695899	-2.05653272943761	5.53962698402379
H	2.98057500054063	-0.92880999351841	4.10637827803992
H	-0.97663582813041	-2.59224791800700	4.55434370624187
H	-1.42353420611855	-1.95594143524479	2.18287486764461
Ru	0.22663176006425	-0.43154395689027	-0.23322094483818
H	-5.91744273587323	0.31760227088872	0.01658582794517
H	5.79449746075236	0.95913710592292	0.96922289278892

**DFT optimized Cartesian coordinates of the  $^3\text{MLCT}^{-1}\text{GS}$  MECP of  $[\text{Ru}(\text{tpy})(\text{pbpy})]^+$** 

C	12.61358178681654	1.97126149828555	3.54868678378587
C	12.49352295068037	0.63615942223376	3.19029890132533
C	13.36289985175564	0.07715983749838	2.22824603939377
C	14.43823169408147	0.85277829001862	1.74170062947695
C	14.55672556297348	2.18701346027740	2.10267348828781
N	13.53842772336366	2.80237279794331	2.87094838689399
H	11.75839075249189	0.00408808150430	3.68672701857455
H	15.20420044501372	0.38788087804342	1.12236777609929
C	11.89263451810404	4.48616207616055	6.08343881124608
C	10.71612640178375	4.06962753157569	6.69738486490413
C	10.11517427454121	2.87835579931180	6.25132898702288
C	10.70419534542836	2.16331863346184	5.21578879840548
C	11.89652394957860	2.63561706358213	4.62893698080609
N	12.46963740038362	3.80063630819390	5.08166774579514
H	9.19158274603602	2.52089045740653	6.70589660516705
H	12.39933645539078	5.39614936962469	6.40063811188129
H	10.28439594476710	4.66094706026866	7.50258939228465
H	10.24462200516214	1.24946372389694	4.84473578528681
C	15.69243792413750	3.05283820273245	1.81404438252031
C	16.64997400736016	2.81984287895913	0.80483818327567
C	17.70665182243004	3.70698626667666	0.63864048191869
C	17.80407839667354	4.83066122155712	1.47974632907618
C	16.82949691060908	5.01143494363075	2.45550763841105
N	15.80353354042125	4.15927671566227	2.62241832743179
H	18.44750084973798	3.53428848626346	-0.14182454981401
H	16.54839089784376	1.95359610365765	0.15397561353576
H	18.61508750660947	5.54984019056508	1.38149060614923
H	16.86563497596011	5.86281386933985	3.13334496982937
C	14.15122130153326	7.30481056925188	4.30353217386350
C	14.44548827594954	8.55941398553222	4.84764308049253
C	15.27132215016172	8.63191827515839	5.97411703449319
C	15.78290519756611	7.46189370295850	6.53014360288512
C	15.45919429924853	6.22533524500600	5.94815137731063
H	14.04177872851538	9.46609834726248	4.40515462163460
H	16.42739114880366	7.50168575346438	7.40525653485800
C	12.38888801329946	5.49990531497811	1.68613515080719
C	11.74295203247803	6.47532326880566	0.92230320689088
C	11.89386406966817	7.81572109761726	1.28890606261785
C	12.67948185189074	8.13359812978422	2.39951976276460
C	13.29514614668341	7.09670514850593	3.11430205564634
N	13.13937707920070	5.80892043735605	2.74730510767862
H	11.40696551967098	8.60677187888171	0.71974692963491
H	12.31098246757531	4.43817688468965	1.45153785663076

---

H	11.13954070472020	6.18438614816110	0.06407603180235
H	12.80705945685031	9.17124977028875	2.69802798680928
C	15.91259150385345	4.90863548354901	6.39870136000802
C	16.74709340567725	4.68154030553692	7.50963879748664
C	17.12208630186260	3.37992656540976	7.84695933992996
C	16.66279099529401	2.30030625116827	7.07566319474583
C	15.82966380982320	2.51585640334509	5.96890557858786
C	15.44704900700391	3.82059218619813	5.61993574539542
H	17.76851834454947	3.20373756319255	8.70662956149355
H	17.10486457584656	5.51684895408664	8.11177428089967
H	16.95414442271228	1.28193711804760	7.33693250718034
H	15.48634509614720	1.65754283876209	5.38797602393103
Ru	14.25514072257642	4.22105532389564	4.04783517732174
N	14.65382424365441	6.17538343391092	4.85271395766795
H	13.27443726330260	-0.97183650483572	1.95253468184238
H	15.51255122374571	9.59928295169886	6.41264112771804

## 6.7 SUPPORTING INFORMATION TO 3.6: [Cr(DDPD)<sub>2</sub>]<sup>3+</sup>: A MOLECULAR, WATER-SOLUBLE, HIGHLY NIR-EMISSIVE RUBY ANALOGUE

### General procedures

CrCl<sub>2</sub> (95%, ABCR), deoxyguanosine monophosphate (dGMP) and (HOCH<sub>2</sub>)<sub>3</sub>CNH<sub>3</sub>Cl (Tris-HCl) (Sigma-Aldrich) and 2,2'-bipyridine (bpy) (Alpha Aesar) were purchased from commercial suppliers. The ligand ddpd was synthesized according to a literature procedure.<sup>1</sup> [Cr(bpy)<sub>3</sub>](PF<sub>6</sub>)<sub>2</sub> was prepared similar to a literature procedure.<sup>2</sup> Air- or moisture-sensitive reactions were performed in dried glassware under inert gas atmosphere (argon, quality 4.6). Acetonitrile was refluxed over CaH<sub>2</sub> and distilled under argon prior to use in these reactions. UV/Vis spectra were recorded on a Varian Cary 5000 spectrometer in 1 cm cuvettes. Emission spectra were recorded on a Varian Cary Eclipse spectrometer (single crystal **1**(BF<sub>4</sub>)<sub>3</sub>×3CH<sub>3</sub>CN and **1**(PF<sub>6</sub>)<sub>3</sub> in solution) or on an Edinburgh Instruments spectrometer (FSP 920). Luminescence decay curves in the μs-range were measured with an Edinburgh Instruments spectrometer (FSP 920) using a μs Xe-flashlamp and multi-channel scaling mode. Fluorescence decays in the ns-range were recorded using an Edinburgh Instruments lifetime spectrometer (FLS 920) equipped with a MCP-PMT (R3809U-50, Hamamatsu), and a TCSPC module (TCC 900). A supercontinuum laser (SC400-PP, Fianium) was used for excitation wavelengths > 400 nm, for excitation at 330 nm a ps-laserdiode (ELED, Edinburgh Instruments) was used. All luminescence measurements were performed using magic angle condition (polarization 0° in the excitation and 54.7° in the emission channel). Luminescence quantum yields were determined using an Ulbricht integrating sphere (Quantaaurus-QY C11347-11, Hamamatsu).<sup>3</sup> Relative uncertainty is estimated to be +/- 5 %. Oxygen was removed from the solvents by purging with argon and the oxygen concentration in the sample solutions was measured using an Neofox-GT (sensor Phosphor-R) optical detection system (OceanOptics). For the single crystal absorption and emission spectra a single crystal of **1**(BF<sub>4</sub>)<sub>3</sub>×3CH<sub>3</sub>CN of approximate 0.5 x 0.3 x 0.1 cm<sup>3</sup> dimension was placed a microcuvette, covered with heptane and analyzed by absorption and emission spectroscopy. ESI<sup>+</sup> mass spectra were recorded on a Micromass QToF Ultima API mass spectrometer with analyte solutions in acetonitrile. Elemental analyses were performed by the microanalytical laboratory of the chemical institutes of the University of Mainz. Electrochemical experiments were performed with a BioLogic SP-50 voltammetric analyser using platinum wire working and counter electrodes and a 0.01 M Ag/AgNO<sub>3</sub> reference electrode. Measurements were carried out at a scan rate of 100 mV s<sup>-1</sup> for

<sup>1</sup> A. Breivogel, C. Förster, K. Heinze, *Inorg. Chem.* **2010**, *49*, 7052-7056.

<sup>2</sup> B. R. Baker, B. D. Metha, *Inorg. Chem.* **1962**, *4*, 848-854.

<sup>3</sup> a) C. Würth, D. Geißler, T. Behnke, M. Kaiser, U. Resch-Genger, *Anal. Bioanal. Chem.* **2015**, 407, 59–78; b) C. Würth, M. G. González, R. Niessner, U. Panne, C. Haisch, U. Resch-Genger, *Talanta* **2012**, *90*, 30–37; c) C. Würth, J. Pauli, C. Lochmann, M. Spieles, U. Resch-Genger, *Anal. Chem.* **2012**, *84*, 1345–1352.

cyclic voltammetry experiments using 0.1 M [*n*Bu<sub>4</sub>N][PF<sub>6</sub>] as supporting electrolyte in acetonitrile. Potentials are given relative to the ferrocene/ferrocenium couple (0.40 V vs. SCE<sup>4</sup>,  $E_{1/2} = 0.90 \pm 5$  mV under the given conditions). EPR spectra were recorded on a Miniscope MS 300 X-band CW spectrometer (Magnettech GmbH, Germany). Values of *g* are referenced to Mn<sup>2+</sup> in ZnS as external standard ( $g = 2.118, 2.066, 2.027, 1.906, 1.986, 1.946$ ). Simulations were performed with the EasySpin program package.<sup>5</sup> Magnetic susceptibility measurements were carried out with a Quantum Design MPMS-XL7 SQUID magnetometer under an applied magnetic field of 1 T. Experimental susceptibility data were corrected by the underlying diamagnetism using Pascal's constants. The magnetic contribution of the holder was experimentally determined and subtracted from the measured susceptibility data.

**Density functional theoretical calculations** were carried out using the ORCA program package (version 3.0.2).<sup>6</sup> Tight convergence criteria were chosen for all calculations (Keywords TightSCF and TightOpt, convergence criteria for the SCF part: energy change  $1.0 \cdot 10^{-8}$  E<sub>h</sub>, 1-El. energy change  $1.0 \cdot 10^{-5}$  E<sub>h</sub>, orbital gradient  $1.0 \cdot 10^{-5}$ , orbital rotation angle  $1.0 \cdot 10^{-5}$ , DIIS Error  $5.0 \cdot 10^{-7}$ ; for geometry optimizations: energy change:  $1.0 \cdot 10^{-6}$  E<sub>h</sub>, max. gradient  $1.0 \cdot 10^{-4}$  E<sub>h</sub> bohr<sup>-1</sup>, RMS gradient  $3.0 \cdot 10^{-5}$  E<sub>h</sub> bohr<sup>-1</sup>, max. displacement  $1.0 \cdot 10^{-3}$  bohr, RMS displacement  $6.0 \cdot 10^{-4}$  bohr). All calculations make use of the resolution of identity (Split-RI-J) approach for the coulomb term in combination with the chain-of-spheres approximation for the exchange term (COSX).<sup>7</sup> Geometry optimizations were performed using the B3LYP functional<sup>8</sup> in combination with Ahlrichs' split-valence double- $\xi$  basis set def2-SV(P) for all atoms which comprises polarization functions for all non-hydrogen atoms.<sup>9</sup> The optimized geometries were confirmed to be local minima on the respective potential energy surface by subsequent numerical frequency analysis ( $N_{imag} = 0$ ). TD-DFT calculations were performed based on the B3LYP/def2-SV(P) optimized geometry. The ZORA relativistic approximation<sup>10</sup> was used to describe relativistic effects in all calculations. Fifty vertical transitions were calculated in TD-DFT calculations. Explicit counterions and/or solvent molecules were neglected.

<sup>4</sup> N. G. Connelly, W. E. Geiger, *Chem. Rev.* **1996**, *96*, 877–910.

<sup>5</sup> S. Stoll, A. Schweiger, *J. Magn. Reson.* **2006**, *178*, 42–55.

<sup>6</sup> F. Neese, *WIREs Comput Mol Sci* **2012**, *2*, 73–78.

<sup>7</sup> a) F. Neese, F. Wennmohs, A. Hansen, U. Becker, *Chem. Phys.* **2009**, *356*, 98–109; b) R. Izsák, F. Neese, *J. Chem. Phys.* **2011**, *135*, 144105.

<sup>8</sup> A. D. Becke, *J. Chem. Phys.* **1993**, *98*, 5648–5642.

<sup>9</sup> a) A. Schäfer, H. Horn, R. Ahlrichs, *J. Chem. Phys.* **1992**, *97*, 2571; b) A. Schäfer, C. Huber, R. Ahlrichs, *J. Chem. Phys.* **1994**, *100*, 5829.

<sup>10</sup> a) E. van Lenthe, E. J. Baerends, J. G. Snijders, *J. Chem. Phys.* **1993**, *99*, 4597; b) C. van Wüllen, *J. Chem. Phys.* **1998**, *109*, 392; c) D. A. Pantazis, X.-Y. Chen, C. R. Landis, F. Neese, *J. Chem. Theory Comput.* **2008**, *4*, 908–919.

**Crystal Structure Determinations.** Intensity data were collected with a Bruker AXS Smart 1000 CCD diffractometer with an APEX II detector and an Oxford cooling system and corrected for absorption and other effects using Mo  $K_{\alpha}$  radiation ( $\lambda = 0.71073 \text{ \AA}$ ) at 173(2) K. The diffraction frames were integrated using the SAINT package, and most were corrected for absorption with MULABS.<sup>11,12</sup> The structures were solved by direct methods and refined by the full-matrix method based on  $F^2$  using the SHELXTL software package.<sup>13,14</sup> All non-hydrogen atoms were refined anisotropically, while the positions of all hydrogen atoms were generated with appropriate geometric constraints and allowed to ride on their respective parent carbon atoms with fixed isotropic thermal parameters. See Table S2 for crystal and structure refinement data. **1(PF<sub>6</sub>)<sub>3</sub>×2CH<sub>3</sub>CN** crystallized as small plates resulting in weakly diffracting crystals and a low observed/unique data ratio. Furthermore, **1(PF<sub>6</sub>)<sub>3</sub>×2CH<sub>3</sub>CN** features two independent cations in the unit cell together with the corresponding (partially disordered) counter anions and solvent molecules. The disordered anions have been refined with split-models with the following occupancies for the disordered atoms: **1(PF<sub>6</sub>)<sub>3</sub>×2CH<sub>3</sub>CN** (anion P2, P4, P6: 0.5:0.5), **1(BF<sub>4</sub>)<sub>3</sub>×3CH<sub>3</sub>CN** (anion B2, B3: 0.896(4):0.104(4)). SAME and SADI geometric restraints have been used and the SIMU and DELU instructions in some cases to enable anisotropic refinement of the disordered anions. Crystallographic data (excluding structure factors) for the structure reported in this paper have been deposited with the Cambridge Crystallographic Data Centre as supplementary publication no CCDC-1059802 [**1(BF<sub>4</sub>)<sub>3</sub>×3CH<sub>3</sub>CN**] and CCDC-1059801 [**1(PF<sub>6</sub>)<sub>3</sub>×2CH<sub>3</sub>CN**]. Copies of the data can be obtained free of charge upon application to CCDC, 12 Union Road, Cambridge CB2 1EZ, U.K. [fax (0.44) 1223-336-033; e-mail deposit@ccdc.cam.ac.uk].

**Synthesis of [Cr(ddpd)<sub>2</sub>](BF<sub>4</sub>)<sub>3</sub> [1(BF<sub>4</sub>)<sub>3</sub>]:** Anhydrous chromium(II) chloride (220 mg, 1.95 mmol) and ddpd<sup>1</sup> (810 mg, 2.78 mmol) were dissolved in deaerated CH<sub>3</sub>CN/H<sub>2</sub>O (1:1, 45 ml). The deep green solution was stirred under argon for 12 h. Addition of a solution of ammonium tetrafluoroborate (5 ml, 1.06 M in H<sub>2</sub>O) yielded a green precipitate. The solid was removed by filtration and extracted once with diethyl ether. The solvents of the orange solution were removed under reduced pressure. The orange residue was dissolved in CH<sub>3</sub>CN. Addition of diethyl ether yielded orange crystals, which were dried under reduced pressure. Diffusion of diethyl ether into a concentrated CH<sub>3</sub>CN solution yielded large diffraction quality crystals. Yield: 970 mg (1.08 mmol, 78 %).

**Synthesis of [Cr(ddpd)<sub>2</sub>](PF<sub>6</sub>)<sub>3</sub> [1(PF<sub>6</sub>)<sub>3</sub>] (route I):** Anhydrous chromium(II) chloride (90 mg, 0.732 mmol) and ddpd<sup>1</sup> (304 mg, 1.04 mmol) were dissolved in deaerated water (50 ml). The deep green

<sup>11</sup> SMART Data Collection and SAINT-Plus Data Processing Software for the SMART System, various versions; Bruker Analytical X-ray Instruments, Inc.: Madison, WI, 2000.

<sup>12</sup> R. H. Blessing, *Acta Crystallogr.* **1995**, A51, 33–38.

<sup>13</sup> G. M. Sheldrick, *SHELXTL*, version 5.1; Bruker AXS: Madison, WI, 1998.

<sup>14</sup> G. M. Sheldrick, *SHELXL-97*; University of Göttingen: Göttingen, Germany, 1997.



solution was stirred under argon for 15 h. Addition of a solution of potassium hexafluorophosphate (10 ml, 0.17 M in H<sub>2</sub>O) yielded a green and orange colored precipitate. The solids were collected by filtration and washed once by diethyl ether. The orange residue was dissolved in CH<sub>3</sub>CN. Addition of diethyl ether yielded orange crystals, which were dried under reduced pressure. Diffusion of diethyl ether into a concentrated CH<sub>3</sub>CN solution yielded diffraction quality crystals. Yield: 200 mg (0.187 mmol, 36 %).

**Synthesis of [Cr(ddpd)<sub>2</sub>](PF<sub>6</sub>)<sub>3</sub> [1(PF<sub>6</sub>)<sub>3</sub>] (route II):** Potassium hexafluorophosphate (97 mg, 0.527 mmol) was added to a concentrated aqueous solution of [Cr(ddpd)<sub>2</sub>](BF<sub>4</sub>)<sub>3</sub> (98.6 mg, 0.110 mmol). The resulting orange precipitate was collected by filtration and dissolved in acetonitrile. Slowly adding diethyl ether resulted in precipitation of yellow crystals. Yield: 90.7 mg (0.085 mmol, 77 %).

**Synthesis of [Cr(bpy)<sub>3</sub>](ClO<sub>4</sub>)<sub>3</sub> <sup>2</sup>:** 2,2'-Bipyridine (750 mg, 4.80 mmol) was added to a solution of anhydrous chromium(II) chloride (99 mg, 0.806 mmol) in deaerated 0.1 M perchloric acid (40 ml). After stirring the resulting black-purple suspension for 15 minutes at room temperature air was bubbled through the reaction mixture for 5 hours. Yellow crystals precipitated from the yellow solution overnight. The crystals were collected by filtration, washed with ethanol and dried under reduced pressure. Yield: 560 mg (0.684 mmol, 84 %).

**Synthesis of [Cr(bpy)<sub>3</sub>](PF<sub>6</sub>)<sub>3</sub>:** Potassium hexafluorophosphate (480 mg, 2.61 mmol) was added to a concentrated aqueous solution of [Cr(bpy)<sub>3</sub>](ClO<sub>4</sub>)<sub>3</sub> (410 mg, 0.500 mmol). The resulting yellow precipitate was collected by filtration and dissolved in acetonitrile. Slowly adding diethyl ether resulted in precipitation of yellow crystals. Yield: 348 mg (0.364 mmol, 73 %).

**Stability tests:** Isoabsorptive solutions (at 430 nm) of **1(PF<sub>6</sub>)<sub>3</sub>** and [Cr(bpy)<sub>3</sub>](PF<sub>6</sub>)<sub>3</sub> in 0.1 M [*n*Bu<sub>4</sub>N]Cl H<sub>2</sub>O/MeCN (1:1) solution were irradiated with an LED torch at 430 nm under aerobic conditions. Isoabsorptive solutions (at 430 nm) of **1(PF<sub>6</sub>)<sub>3</sub>** and [Cr(bpy)<sub>3</sub>](PF<sub>6</sub>)<sub>3</sub> in 0.1 M [*n*Bu<sub>4</sub>N]Cl H<sub>2</sub>O/MeCN (1:1) solution with pH = 11.4 adjusted with [*n*Bu<sub>4</sub>N](OH) were irradiated under the same conditions. The reaction progress was monitored at the respective emission maximum (777 and 727 nm) over a time of 5 hours.

**Quenching with dGMP:** 3.3 × 10<sup>-5</sup> M solutions of **1(PF<sub>6</sub>)<sub>3</sub>** and [Cr(bpy)<sub>3</sub>](PF<sub>6</sub>)<sub>3</sub> in 50 mM aqueous Tris-HCl buffer were titrated with a 6.45 mM solution of deoxyguanosine monophosphate (dGMP) dissolved in the same buffer. Emission quenching was monitored at the respective emission maximum (777 and 727 nm) up to a dGMP concentration of 3.14 × 10<sup>-4</sup> M.

Table S1. Analytical data of **1(BF<sub>4</sub>)<sub>3</sub>** and **1(PF<sub>6</sub>)<sub>3</sub>**.



	<b>1(BF<sub>4</sub>)<sub>3</sub></b>	<b>1(PF<sub>6</sub>)<sub>3</sub></b>
molecular formula	C <sub>34</sub> H <sub>34</sub> B <sub>3</sub> CrF <sub>12</sub> N <sub>10</sub>	C <sub>34</sub> H <sub>34</sub> CrF <sub>18</sub> N <sub>10</sub> P <sub>3</sub>
molecular mass	895.11 g mol <sup>-1</sup>	1069.59 g mol <sup>-1</sup>
solubility in CH <sub>3</sub> CN	122 g l <sup>-1</sup> (0.136 mol l <sup>-1</sup> )	222 g l <sup>-1</sup> (0.208 mol l <sup>-1</sup> )
solubility in H <sub>2</sub> O	42.9 g l <sup>-1</sup> (0.048 mol l <sup>-1</sup> )	1.73 g l <sup>-1</sup> (0.0016 mol l <sup>-1</sup> )
MS (ESI): <i>m/z</i> =	171.5 (13) [M-3BF <sub>4</sub> ] <sup>3+</sup> , 292.1 (47) [ddpd+H] <sup>+</sup> , 362.1 (23) [M-2BF <sub>4</sub> ] <sup>2+</sup> , 808.2 (100) [M-BF <sub>4</sub> ] <sup>+</sup> , 1703.4 (15) [2M-BF <sub>4</sub> ] <sup>+</sup>	171.5 (7) [M-3PF <sub>6</sub> ] <sup>3+</sup> , 291.1 (12) [ddpd] <sup>+</sup> , 389.6 (4) [M-2PF <sub>6</sub> ] <sup>2+</sup> , 924.1 (100) [M-PF <sub>6</sub> ] <sup>+</sup> , 1994.2 (22) [2M-PF <sub>6</sub> ] <sup>+</sup>
IR (KBr): $\tilde{\nu}$ =	1606 (vs), 1585 (s), 1568 (m), 1497 (vs), 1455 (s), 1435 (vs), 1365 (w), 1343 (s), 1237 (m), 1141 (s), 1095-1035 (vs br, BF) cm <sup>-1</sup>	1609 (vs), 1585 (s), 1570 (m), 1499 (vs), 1455 (s), 1437 (vs), 1369 (w), 1346 (s), 1240 (m), 1178 (w), 1141 (s), 838 (vs, PF) cm <sup>-1</sup>
Magnetism (300 K): $\chi T$ =	-	1.833 cm <sup>3</sup> K mol <sup>-1</sup>
EPR (77 K) in CH <sub>3</sub> CN $g_{av}$ =	-	1.990 (broad)
UV/Vis (CH <sub>3</sub> CN): $\lambda_{max}$ ( $\epsilon/M^{-1}$ cm <sup>-1</sup> ) =	436 (3770, LMCT+MC), 315 (sh, 25500, LMCT+MC), 302 (28100, LMCT), 220 (sh, 53600, $\pi\pi^*$ ) nm	436 (4095, LMCT+MC), 315 (sh, 25700, LMCT+MC), 301 (28700, LMCT), 218 (56000, $\pi\pi^*$ ) nm
UV/Vis (H <sub>2</sub> O): $\lambda_{max}$ ( $\epsilon/M^{-1}$ cm <sup>-1</sup> ) =	435 (3980, LMCT+MC), 315 (sh, 24700, LMCT+MC), 301 (27600, LMCT), 217 (sh, 53400, $\pi\pi^*$ ) nm	436 (3530, LMCT+MC), 315 (sh, 21840, LMCT+MC), 301 (24500, LMCT), 219 (48000, $\pi\pi^*$ ) nm
UV/Vis (single crystal): $\lambda_{max}$ ( $\epsilon/M^{-1}$ cm <sup>-1</sup> ) =	776 (<1), 736 (<1), 697 (<1) nm	-
Emission (CH <sub>3</sub> CN, $\lambda_{exc}$ = 435): $\lambda_{max}$ (rel. intensity) =	776 (1.0), 739 (0.20), 500 (very weak) nm	776 (1.0), 738 (0.2), 500 (very weak) nm
Emission (H <sub>2</sub> O, $\lambda_{exc}$ = 435): $\lambda_{max}$ (rel. intensity) =	777 (1.0), 739 (0.20), 500 (very weak) nm	-
Emission (single crystal, $\lambda_{exc}$ = 435): $\lambda_{max}$ (rel. intensity) =	778 (1.0), 740 (0.2), 594 (0.2) nm	-
Emission (single crystal, $\lambda_{exc}$ = 435): $\tau$ =	443 $\mu$ s	-
CV ([ <i>n</i> Bu <sub>4</sub> N][PF <sub>6</sub> ]/CH <sub>3</sub> CN, vs. Fc): $E_{1/2}$ =	-	-1.11 V (Cr <sup>III</sup> /Cr <sup>II</sup> )
Elemental analysis found / calcd.	C 44.98 (45.22) H 4.17 (3.83) N 15.04 (15.65)	C 37.90 (38.18) H 2.95 (3.20) N 12.98 (13.10)
Photographs of crystals		

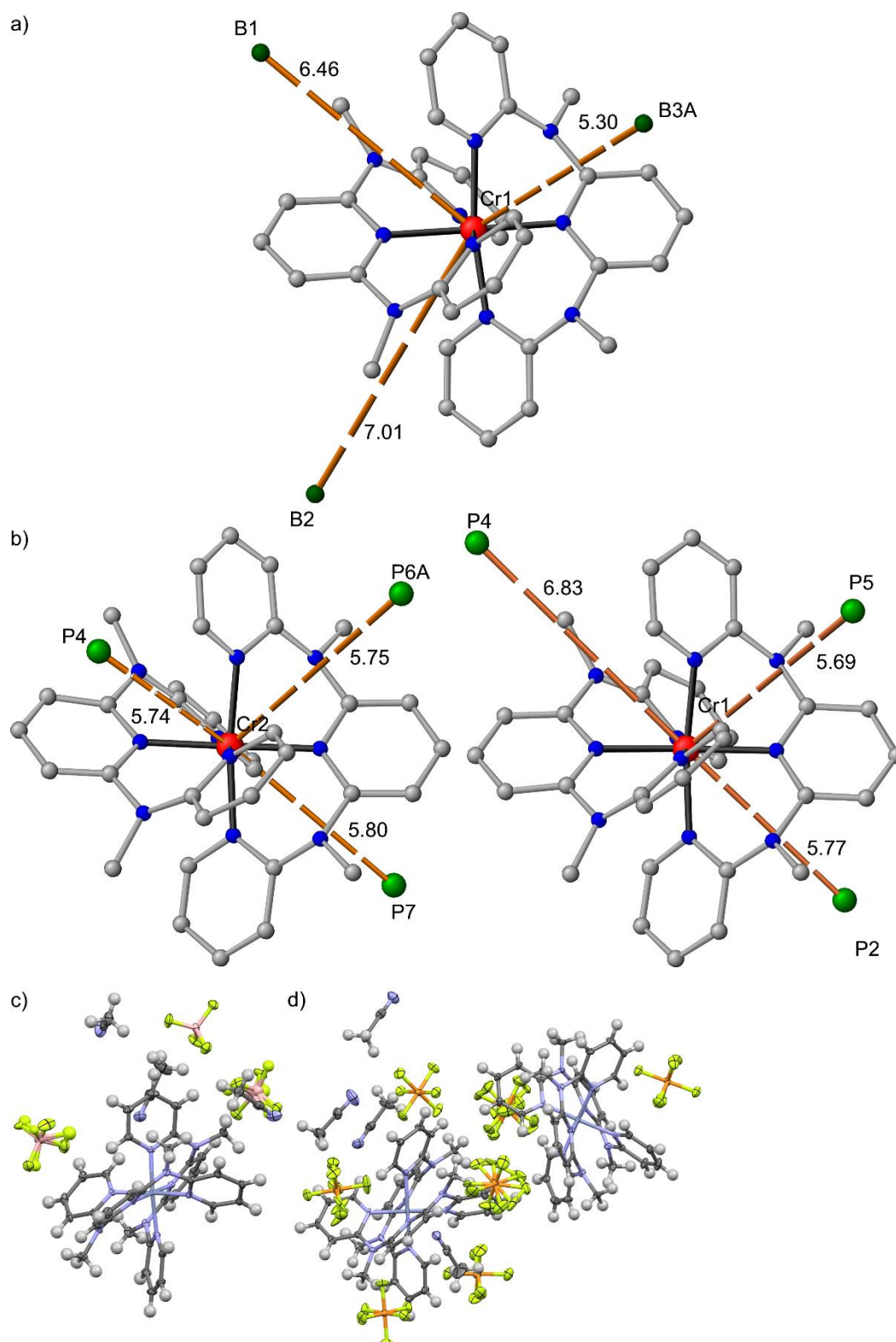
Table S2. Summary of X-ray data of **1(BF<sub>4</sub>)<sub>3</sub>·3CH<sub>3</sub>CN** and **1(PF<sub>4</sub>)<sub>3</sub>·2CH<sub>3</sub>CN**.

	<b>1(BF<sub>4</sub>)<sub>3</sub>·3CH<sub>3</sub>CN</b>	<b>1(PF<sub>4</sub>)<sub>3</sub>·2CH<sub>3</sub>CN</b>
Empirical formula	C <sub>40</sub> H <sub>43</sub> B <sub>3</sub> CrF <sub>12</sub> N <sub>13</sub>	C <sub>38</sub> H <sub>40</sub> CrF <sub>18</sub> N <sub>11</sub> P <sub>3</sub>
Formula weight	1018.30	1151.73
Crystal color, habit	red block	orange plate
Crystal dimensions / mm	0.74 x 0.50 x 0.34	0.32 x 0.09 x 0.07
Crystal system	monoclinic	monoclinic
Space group	<i>Pn</i>	<i>P2<sub>1</sub>/c</i>
<i>a</i> / Å	11.5125(8)	28.2212(12)
<i>b</i> / Å	16.5554(11)	11.7062(5)
<i>c</i> / Å	12.9721(9)	34.0629(13)
$\alpha$ / °	90	90
$\beta$ / °	111.890(2)	124.479(3)
$\gamma$ / °	90	90
<i>V</i> / Å <sup>3</sup>	2294.2(3)	9312.7(7)
<i>Z</i>	2	8
<i>F</i> (000)	1042	4664
Density (calcd) / g cm <sup>-3</sup>	1.474	1.643
Absorption coefficient $\mu$ / mm <sup>-1</sup>	0.345 (MULABS)	0.467 (MULABS)
Theta range / °	2.02 – 27.90	1.20 – 28.04
Index ranges	-14 ≤ <i>h</i> ≤ 15 -21 ≤ <i>k</i> ≤ 21 -17 ≤ <i>l</i> ≤ 17	-37 ≤ <i>h</i> ≤ 36 -13 ≤ <i>k</i> ≤ 15 -44 ≤ <i>l</i> ≤ 44
Reflections collected	27213	90048
Independent reflections	9828 ( <i>R</i> <sub>int</sub> = 0.0504)	22407 ( <i>R</i> <sub>int</sub> = 0.1510)
Observed reflections	9828	22407
Parameters, restraints	666, 22	1439, 688
Max. / min. transmission	0.784 / 0.892	0.9681 / 0.8650
Goodness-of-fit on <i>F</i> <sup>2</sup>	1.041	1.042
Largest difference peak and hole / e Å <sup>-3</sup>	0.315 / -0.347	1.647 / -1.018
<i>R</i> <sub>1</sub> ( <i>I</i> > 2σ( <i>I</i> ))	0.0409	0.1087
<i>R</i> <sub>1</sub> (all data)	0.0439	0.2304
<i>wR</i> <sub>2</sub> ( <i>I</i> > 2σ( <i>I</i> ))	0.1105	0.3165
<i>wR</i> <sub>2</sub> (all data)	0.1127	0.3529
absolute structure parameter	-0.005(12)	-

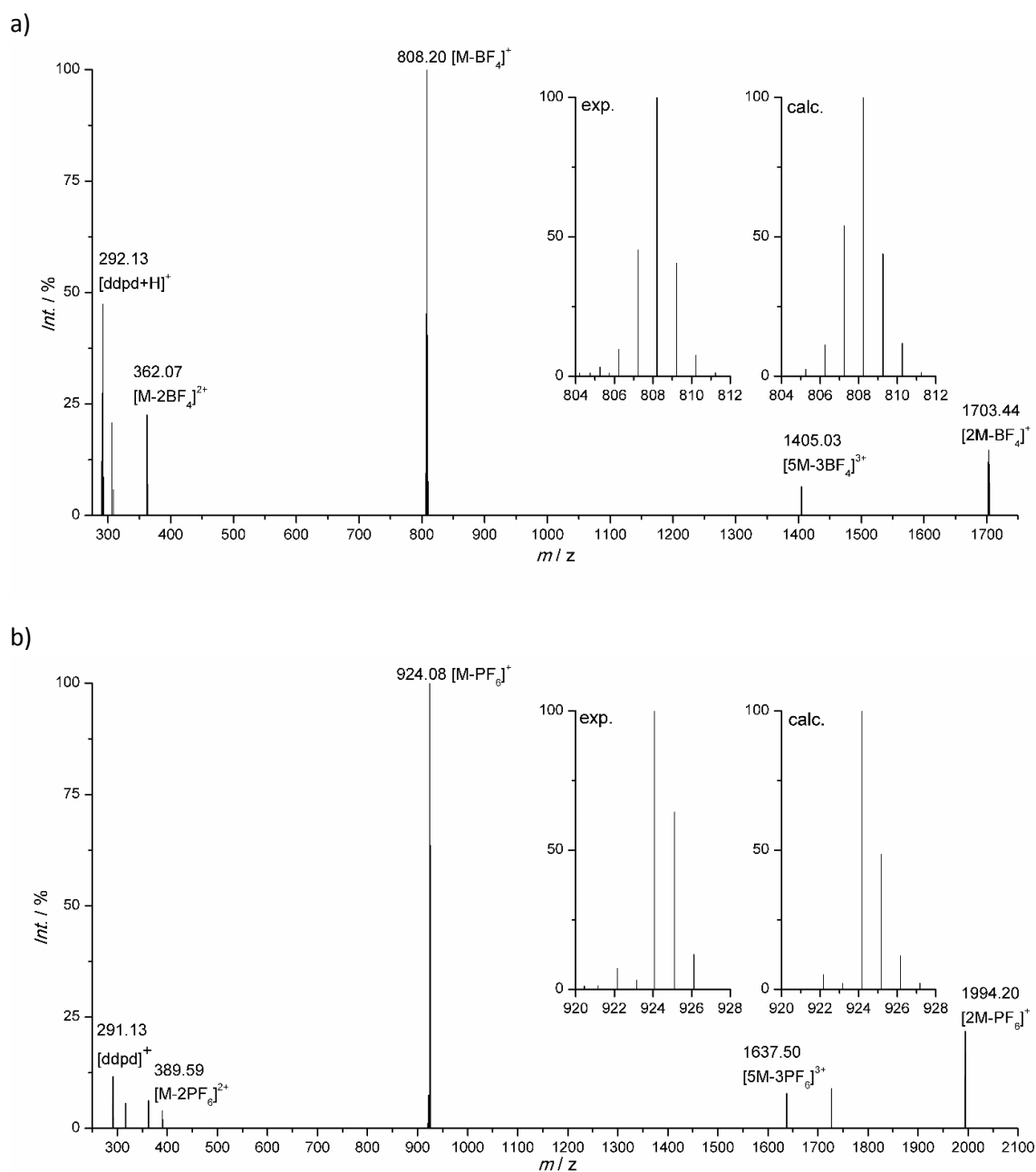
Table S3. Selected distances [Å] and angles [deg] of **1(BF<sub>4</sub>)<sub>2</sub>x3CH<sub>3</sub>CN** and **1(PF<sub>4</sub>)<sub>3</sub>x2CH<sub>3</sub>CN**.

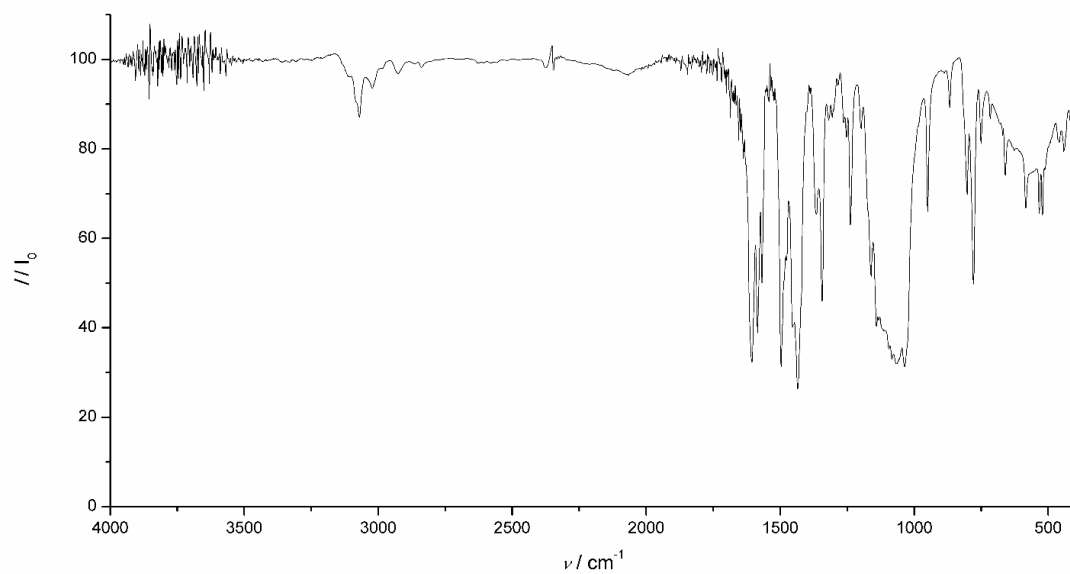
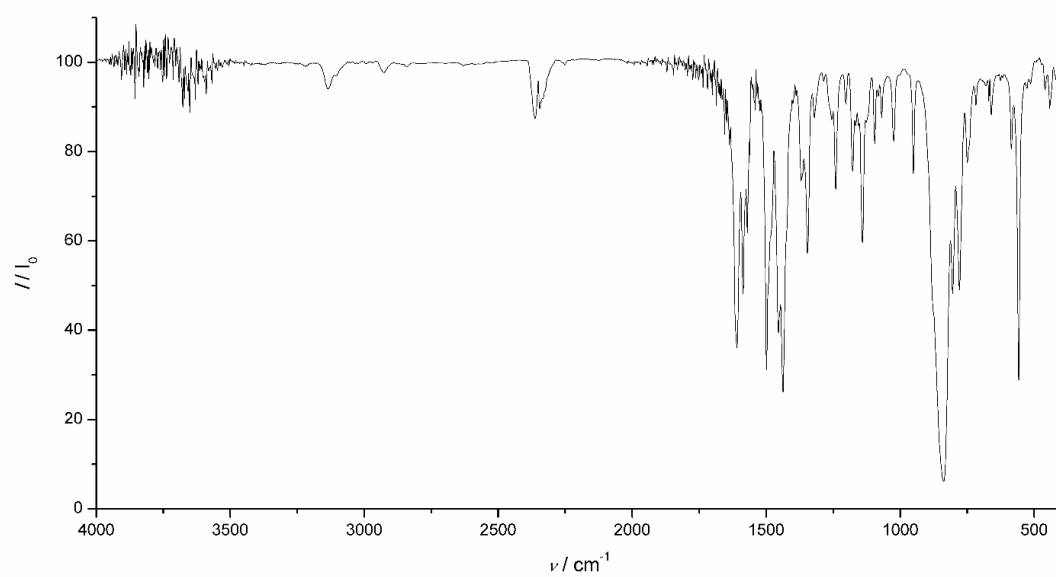
	<b>1(BF<sub>4</sub>)<sub>2</sub>x3CH<sub>3</sub>CN</b>	<b>1(PF<sub>4</sub>)<sub>3</sub>x2CH<sub>3</sub>CN (molecule A)</b>	<b>1(PF<sub>4</sub>)<sub>3</sub>x2CH<sub>3</sub>CN (molecule B)</b>
Cr1-N1	2.0485 (0.0018)	2.0410 (0.0058)	2.0395 (0.0069)
Cr1-N3	2.0393 (0.0018)	2.0535 (0.0065)	2.0296 (0.0068)
Cr1-N5	2.0394 (0.0019)	2.0280 (0.0062)	2.0327 (0.0068)
Cr1-N6	2.0446 (0.0017)	2.0398 (0.0067)	2.0400 (0.0061)
Cr1-N8	2.0444 (0.0018)	2.0538 (0.0071)	2.0465 (0.0066)
Cr1-N10	2.0485 (0.0018)	2.0476 (0.0068)	2.0302 (0.0059)
N1-Cr1-N3	85.13 (0.08)	85.74 (0.25)	86.78 (0.28)
N1-Cr1-N5	170.86 (0.08)	172.27 (0.25)	172.57 (0.27)
N1-Cr1-N6	91.06 (0.07)	89.98 (0.25)	90.45 (0.27)
N1-Cr1-N8	95.23 (0.08)	95.47 (0.25)	93.71 (0.27)
N1-Cr1-N10	89.49 (0.07)	90.37 (0.26)	89.23 (0.27)
N3-Cr1-N5	85.74 (0.07)	86.71 (0.26)	86.03 (0.27)
N3-Cr1-N6	95.10 (0.07)	93.89 (0.27)	95.33 (0.26)
N3-Cr1-N8	178.94 (0.08)	178.61 (0.28)	179.01 (0.29)
N3-Cr1-N10	94.02 (0.07)	95.13 (0.27)	91.60 (0.26)
N5-Cr1-N6	89.68 (0.07)	92.20 (0.27)	88.38 (0.27)
N5-Cr1-N8	89.68 (0.07)	92.10 (0.26)	93.51 (0.27)
N5-Cr1-N10	91.22 (0.07)	88.64 (0.27)	92.82 (0.27)
N6-Cr1-N8	85.89 (0.07)	85.42 (0.27)	85.54 (0.25)
N6-Cr1-N10	170.88 (0.07)	170.97 (0.27)	173.03 (0.27)
N8-Cr1-N10	84.99 (0.07)	85.56 (0.27)	87.54 (0.26)

**Figure S1** Short anion-cation contacts (Å) in crystals of a)  $1(\text{BF}_4)_2 \times 3\text{CH}_3\text{CN}$  and b)  $1(\text{PF}_4)_3 \times 2\text{CH}_3\text{CN}$  (F and H atoms omitted) and structure of c)  $1(\text{BF}_4)_2 \times 3\text{CH}_3\text{CN}$  and d)  $1(\text{PF}_4)_3 \times 2\text{CH}_3\text{CN}$  with thermal ellipsoids at 30 % probability.

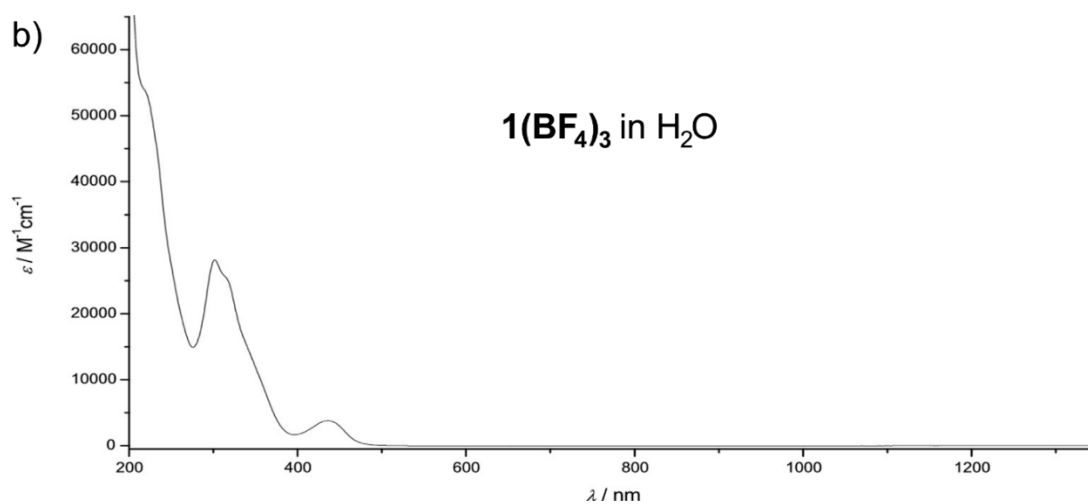
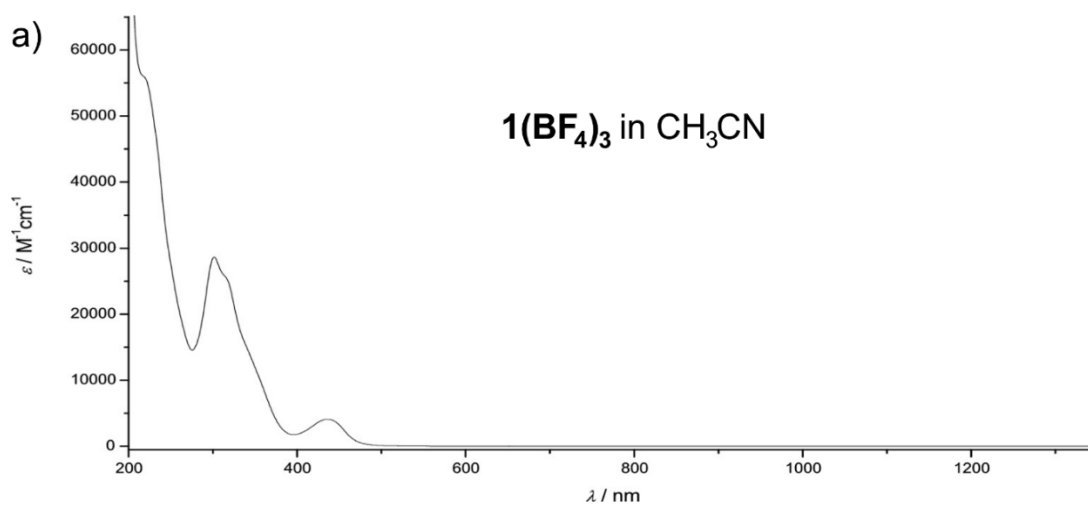


**Figure S2** a) ESI mass spectrum of **1**(BF<sub>4</sub>)<sub>3</sub> including experimental and calculated isotopic pattern of [M-BF<sub>4</sub>]<sup>+</sup> and b) ESI mass spectrum of **1**(PF<sub>6</sub>)<sub>3</sub> including experimental and calculated isotopic pattern of [M-PF<sub>6</sub>]<sup>+</sup>.

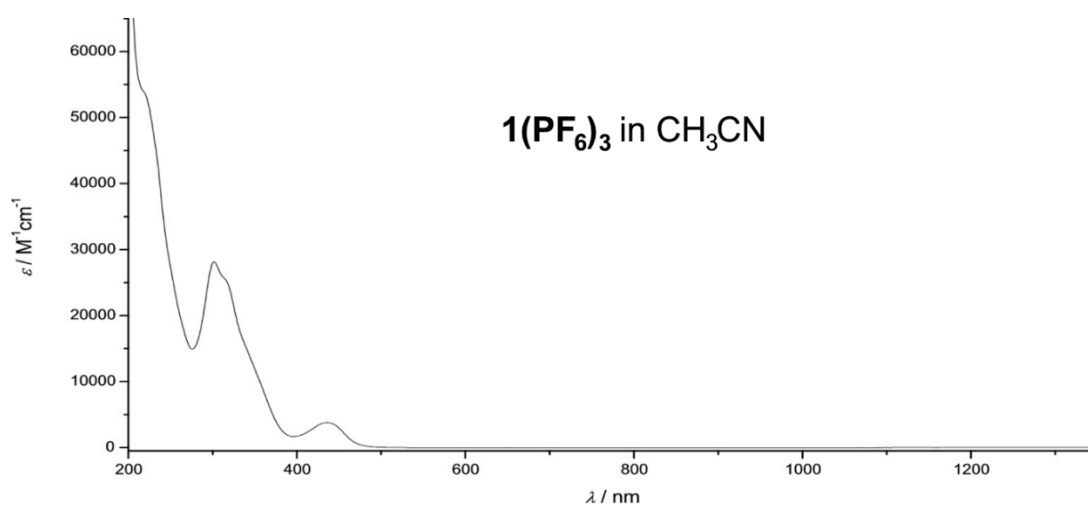


**Figure S3** IR spectrum of **1(BF<sub>4</sub>)<sub>3</sub>** as KBr disk.**Figure S4** IR spectrum of **1(PF<sub>6</sub>)<sub>3</sub>** as KBr disk.

**Figure S5** UV/Vis spectra of **1(BF<sub>4</sub>)<sub>3</sub>** a) in CH<sub>3</sub>CN and b) in H<sub>2</sub>O.

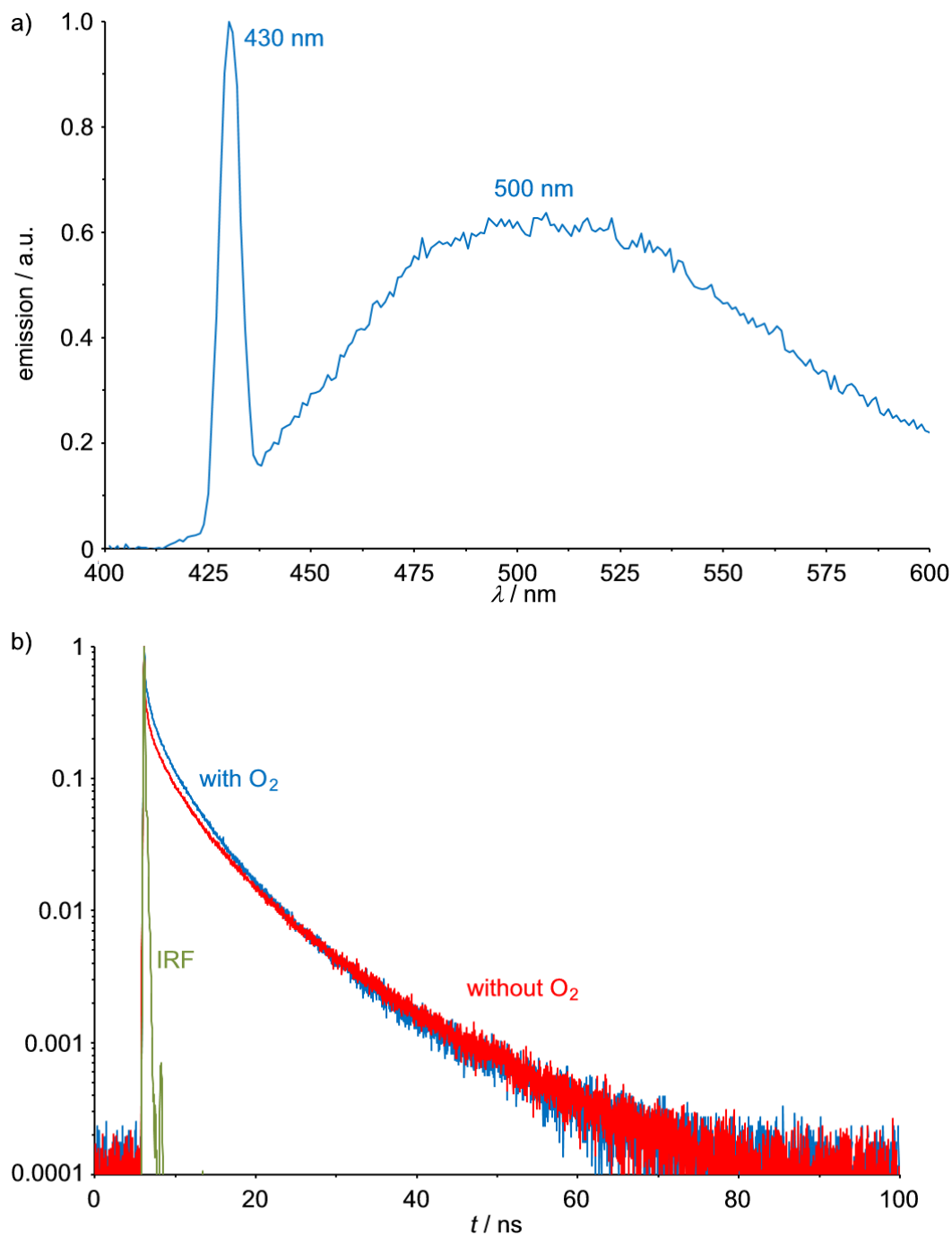


**Figure S6** UV/Vis spectrum of **1(PF<sub>6</sub>)<sub>3</sub>** in CH<sub>3</sub>CN.

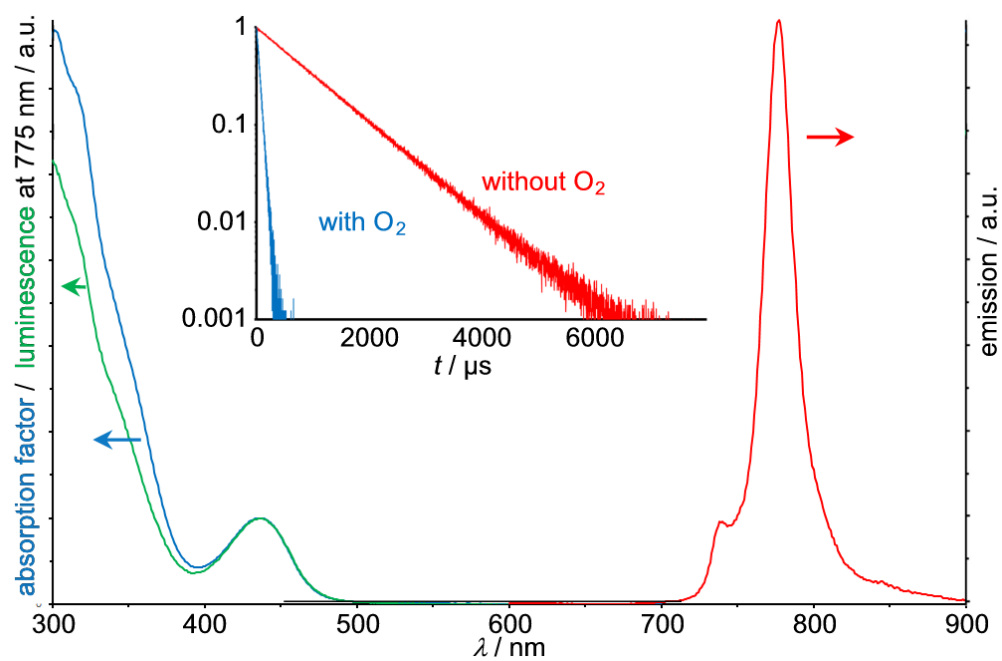


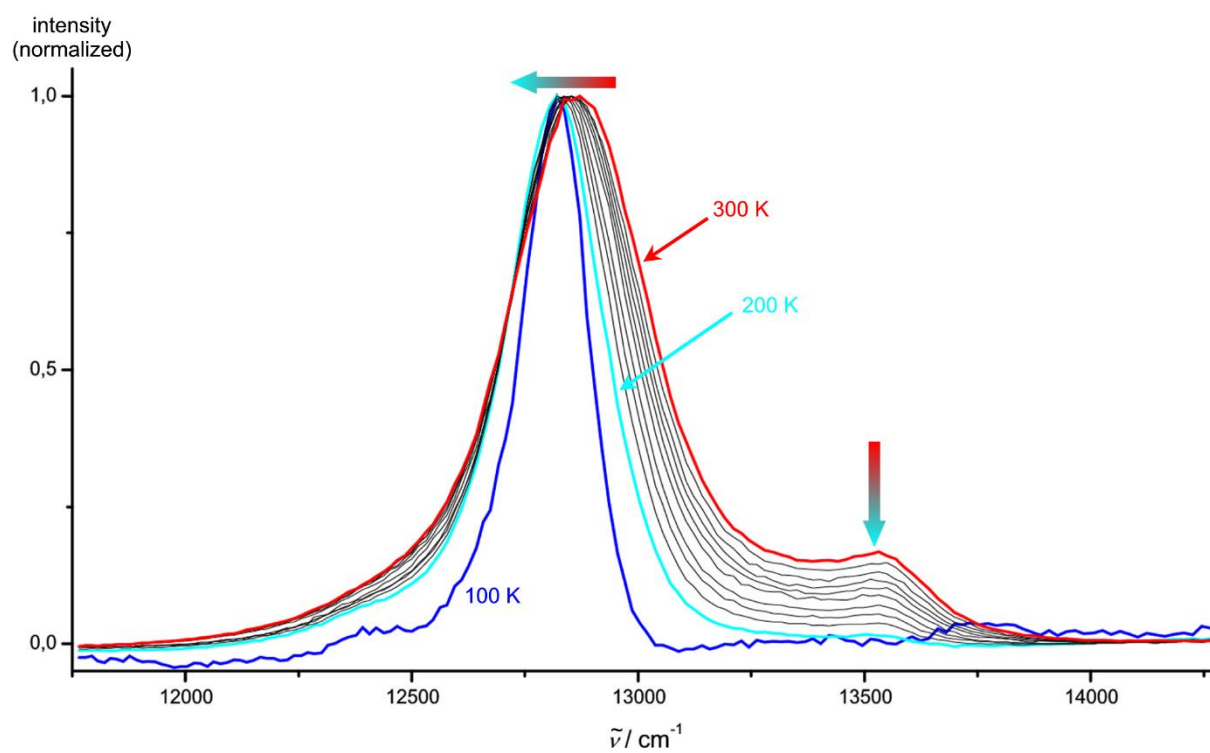


**Figure S7** a) Emission spectrum of **1(BF<sub>4</sub>)<sub>3</sub>** in air-saturated CH<sub>3</sub>CN in the region 400 – 600 nm ( $\lambda_{\text{exc}} = 430$  nm) and b) decay curves of the broad band luminescence at 500 nm in air-saturated and oxygen-free acetonitrile ( $\lambda_{\text{exc}} = 450$  nm,  $\lambda_{\text{obs}} = 500$  nm). The fast initial decay resembling the pulse profile of the excitation light pulse (IRF) is caused by Raman and Rayleigh scattered excitation light.

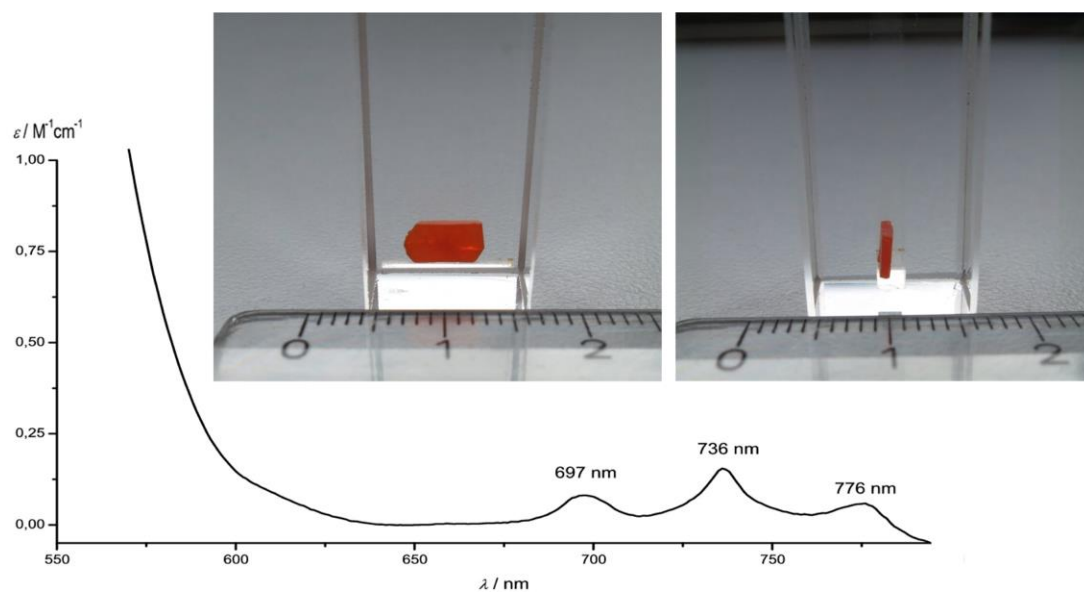


**Figure S8** Absorption factor, excitation ( $\lambda_{\text{obs}} = 775 \text{ nm}$ ) and emission spectrum ( $\lambda_{\text{exc}} = 435 \text{ nm}$ ) of **1(BF<sub>4</sub>)<sub>3</sub>** in CH<sub>3</sub>CN (inset shows decay curve in the presence and absence of O<sub>2</sub>,  $\lambda_{\text{exc}} = 435 \text{ nm}$ ,  $\lambda_{\text{obs}} = 775 \text{ nm}$ ).

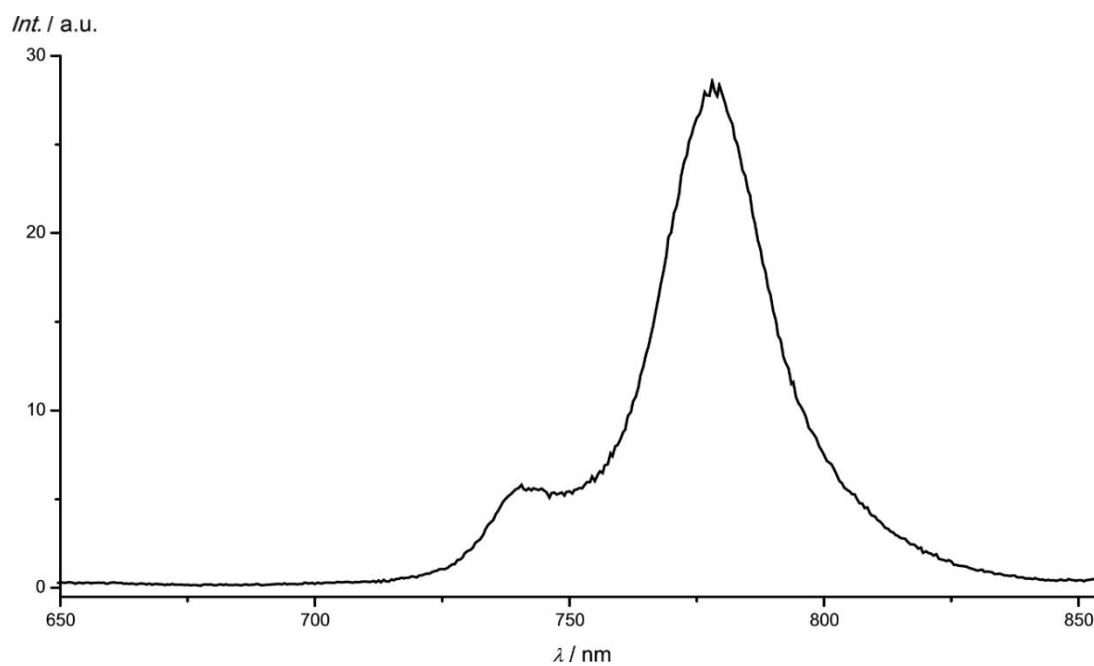


**Figure S9** Temperature dependent emission spectra of **1(BF<sub>4</sub>)<sub>3</sub>** in butyronitrile (100 K – 300 K).

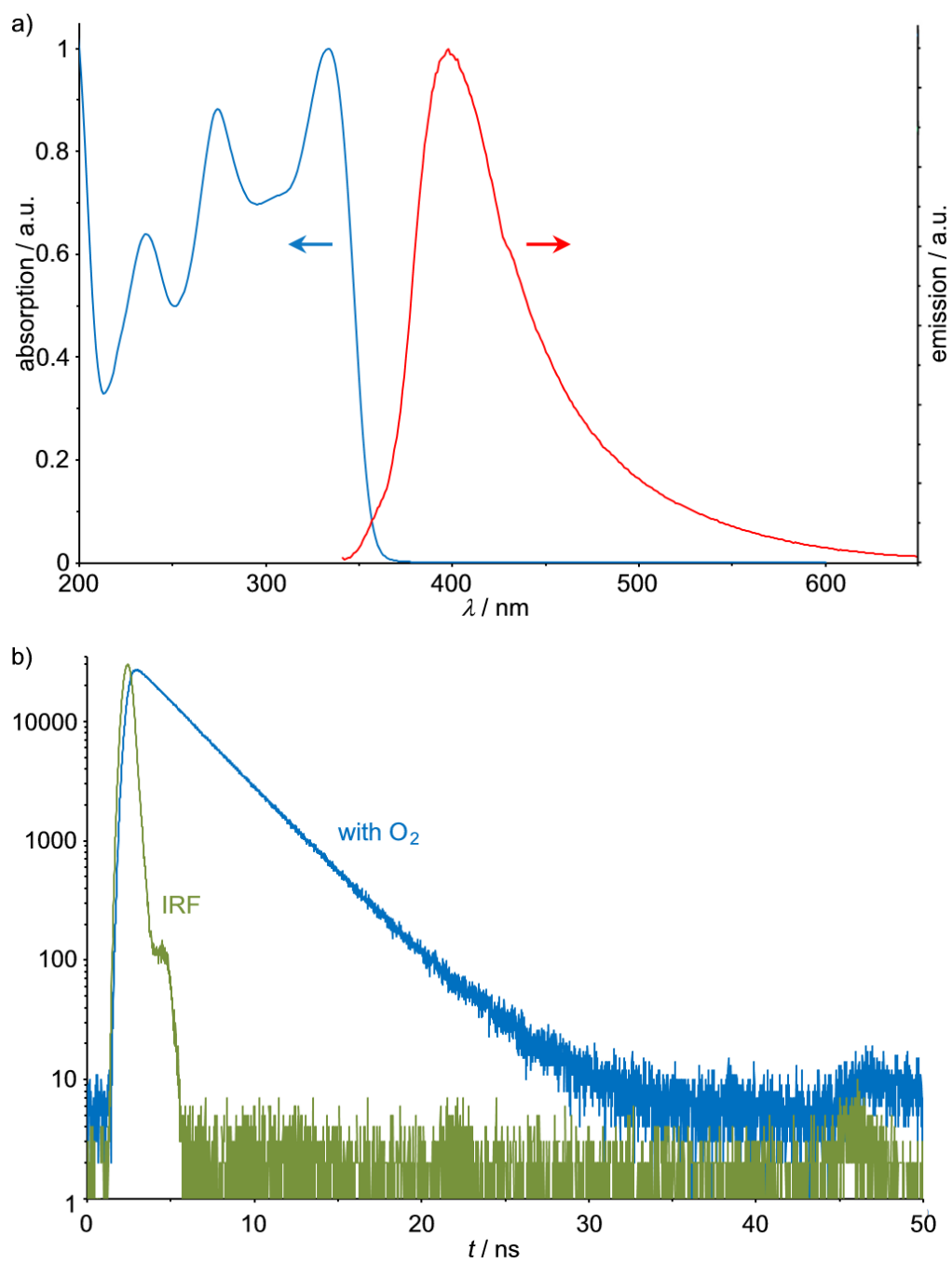
**Figure S10** Absorption spectrum of a single crystal of  $1(\text{BF}_4)_3 \times 3\text{CH}_3\text{CN}$  and photographs of the measured single crystal of  $1(\text{BF}_4)_3 \times 3\text{CH}_3\text{CN}$ .



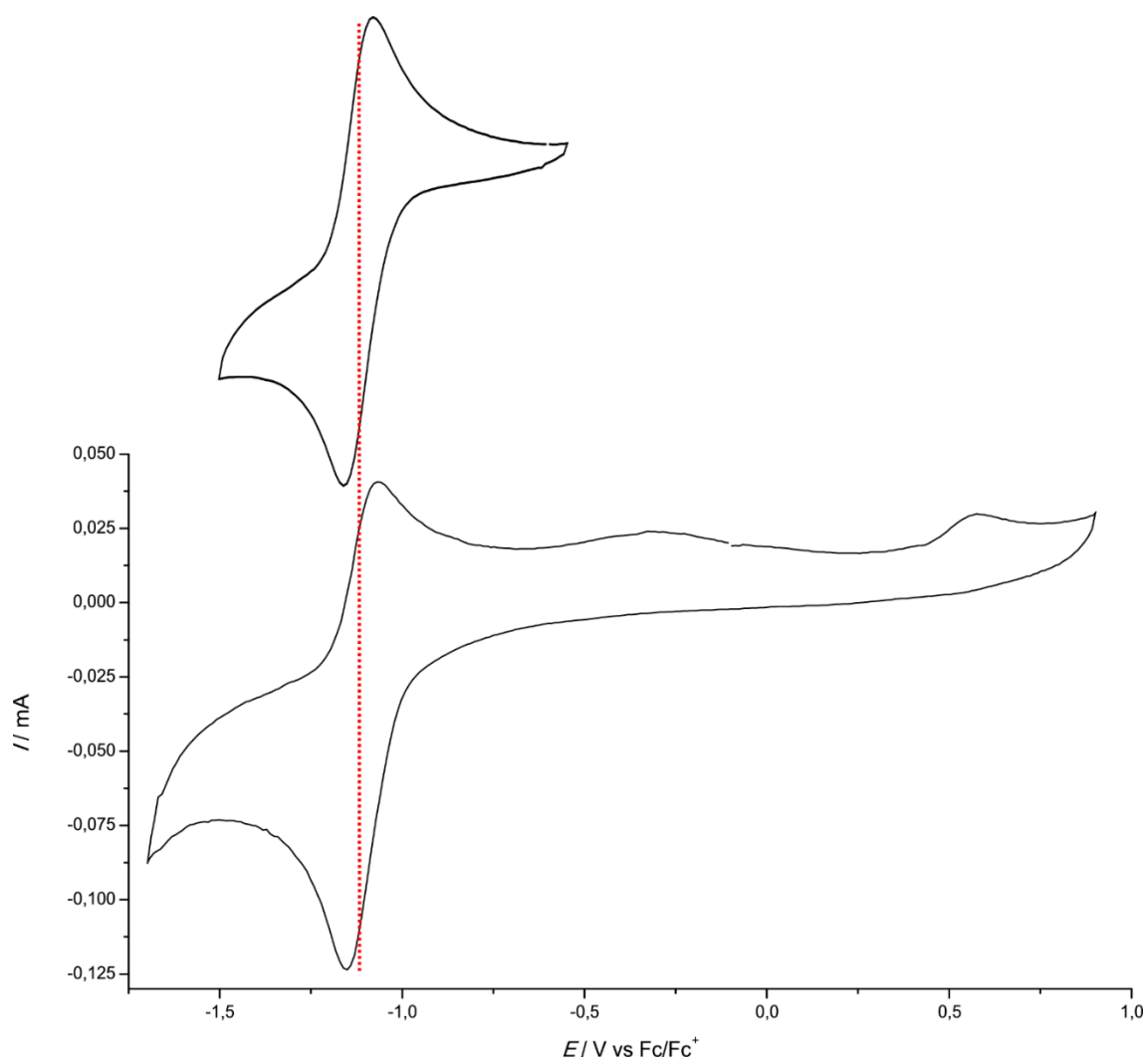
**Figure S11** Emission spectrum of a single crystal of  $1(\text{BF}_4)_3 \times 3\text{CH}_3\text{CN}$ .

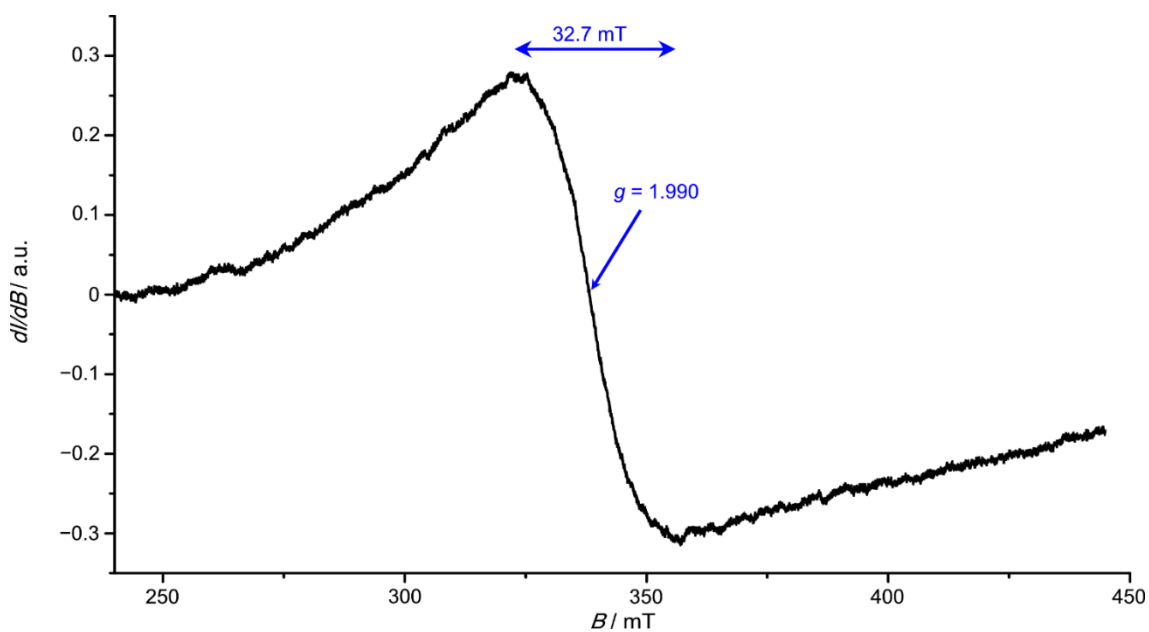
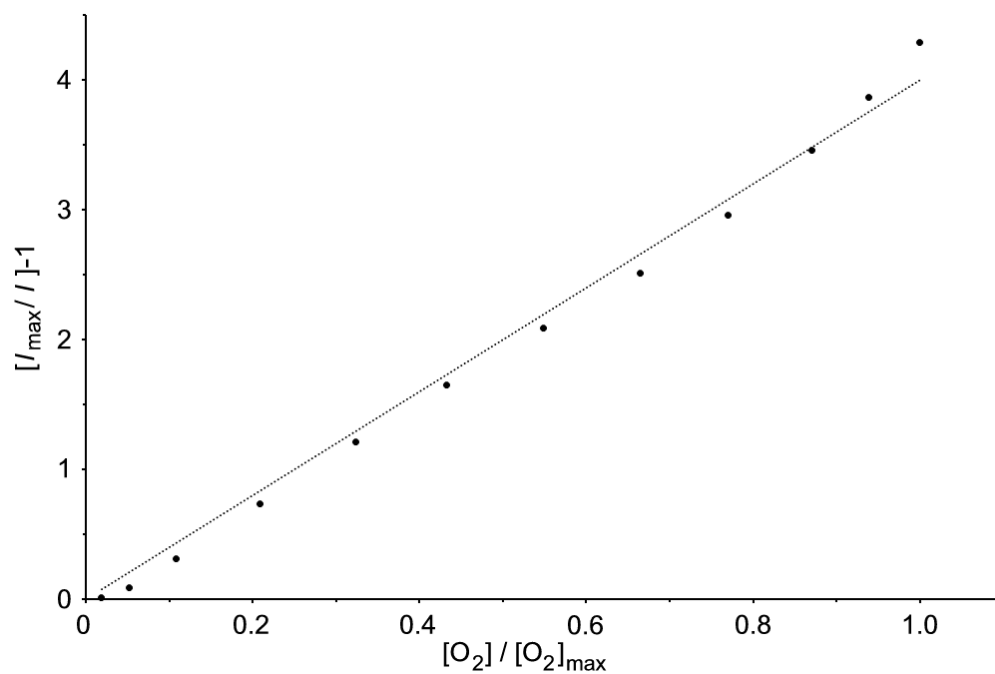


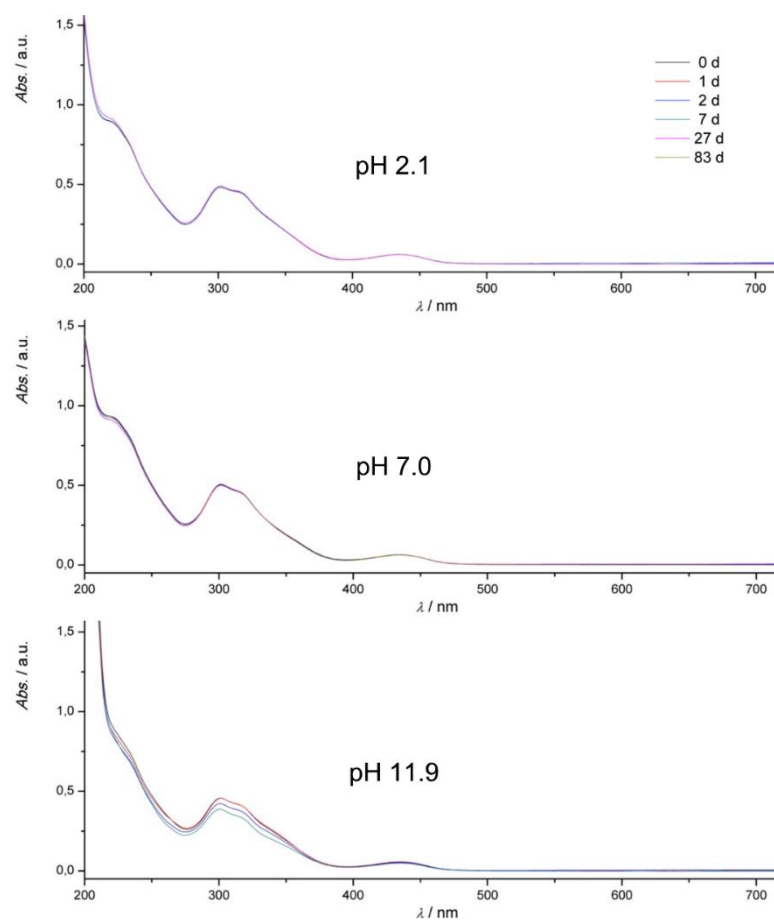
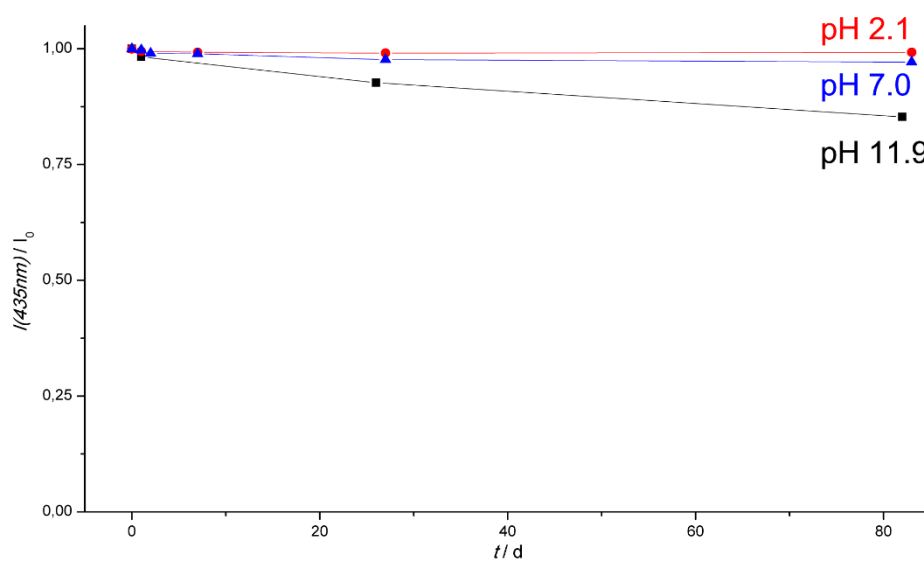
**Figure S12** a) Absorption and emission spectra ( $\lambda_{\text{exc}} = 330$  nm) of ddpd in  $\text{CH}_3\text{CN}$  and b) fluorescence decay curve ( $\lambda_{\text{exc}} = 330$  nm,  $\lambda_{\text{obs}} = 398$  nm).



**Figure S13** Cyclic voltammogram of **1**(PF<sub>6</sub>)<sub>3</sub> in 0.1 M [*n*Bu<sub>4</sub>N][PF<sub>6</sub>]/CH<sub>3</sub>CN, Pt electrodes, referenced against ferrocene.

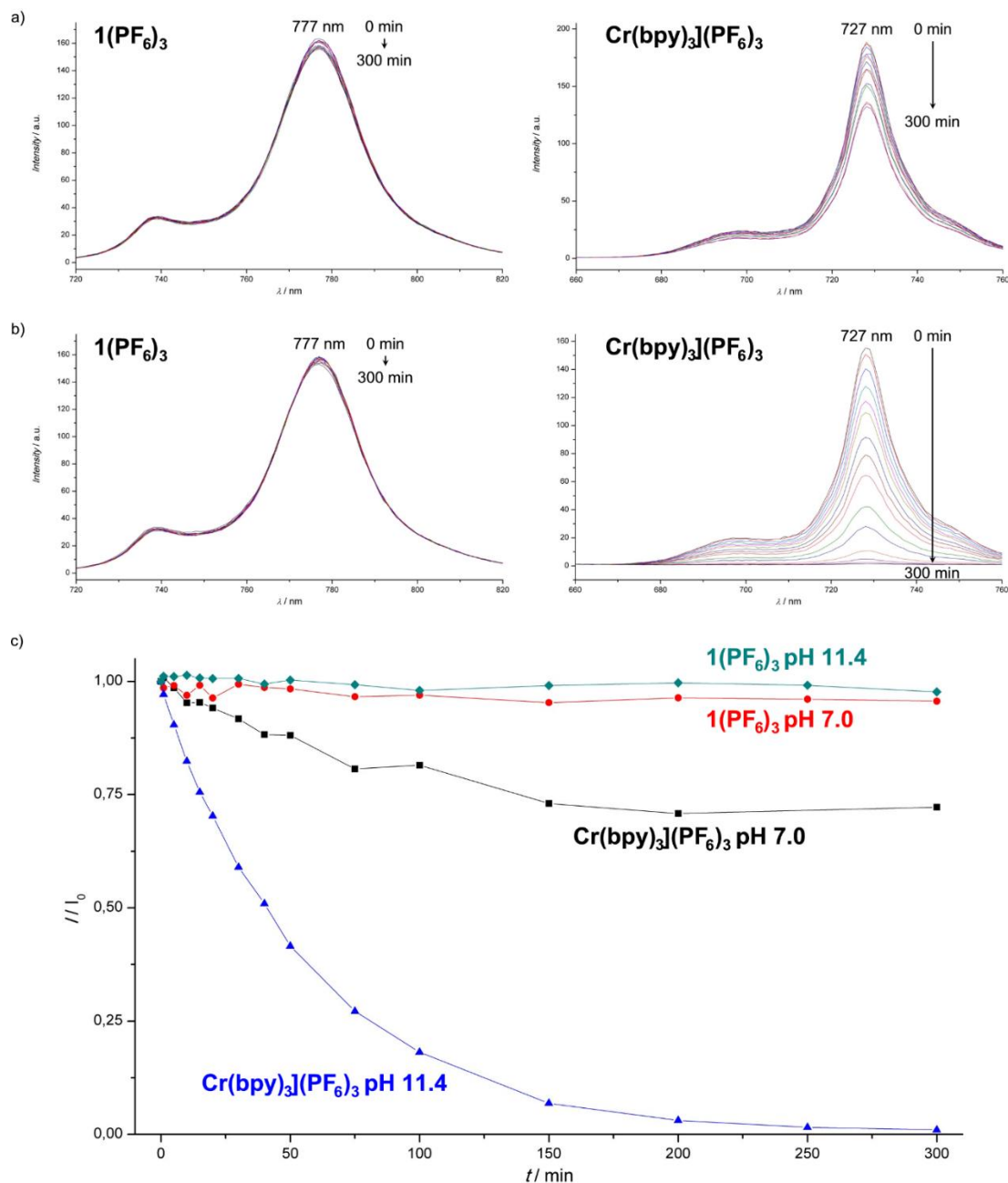


**Figure S14** EPR spectrum of **1**(PF<sub>6</sub>)<sub>3</sub> at 77 K in CH<sub>3</sub>CN, frequency 9.410 GHz.**Figure S15** Stern-Volmer plot of **1**(BF<sub>4</sub>)<sub>3</sub> in H<sub>2</sub>O by quenching with O<sub>2</sub> ( $\lambda_{\text{exc}} = 435$  nm,  $\lambda_{\text{obs}} = 775$  nm). Dotted line is a linear regression of the data.

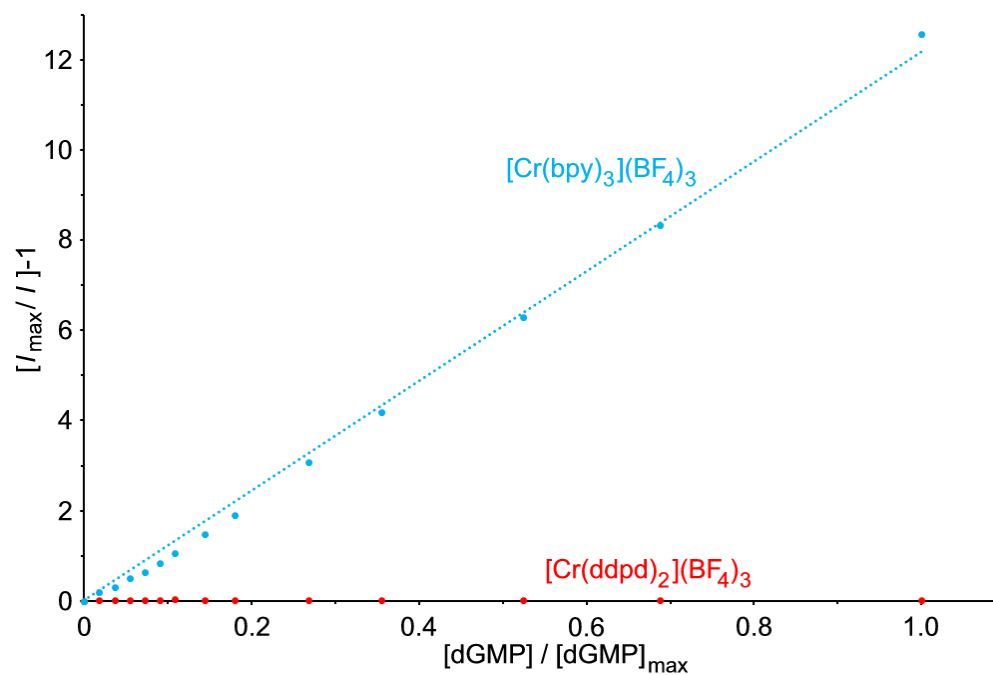
**Figure S16** UV/Vis absorption spectra of  $1(\text{BF}_4)_3$  under air in  $\text{H}_2\text{O}$  at different pH over time.**Figure S17** Traces of the intensity of the absorption band at 435 nm of  $1(\text{BF}_4)_3$  under air in  $\text{H}_2\text{O}$  at different pH over time.



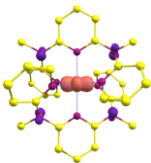
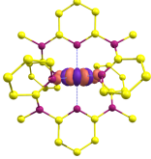
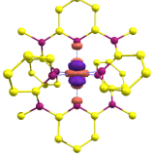
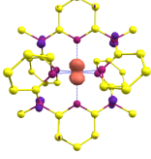
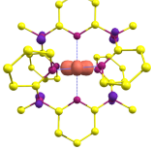
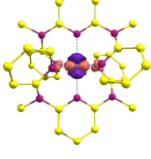
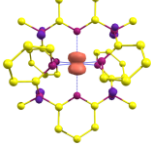
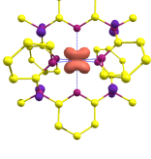
**Figure S18** a) Emission spectra of isoabsorptive solutions of **1**(BF<sub>4</sub>)<sub>3</sub> and [Cr(bpy)<sub>3</sub>](PF<sub>6</sub>)<sub>2</sub> in 0.1 mM [nBu<sub>4</sub>N]Cl H<sub>2</sub>O/MeCN (1:1) solution under aerobic conditions with 430 nm irradiation over time, b) emission spectra of isoabsorptive solutions of **1**(BF<sub>4</sub>)<sub>3</sub> and [Cr(bpy)<sub>3</sub>](PF<sub>6</sub>)<sub>2</sub> in H<sub>2</sub>O/MeCN (1:1) solution with pH = 11.4 adjusted with [nBu<sub>4</sub>N](OH) under aerobic conditions with 430 nm irradiation over time and c) traces of the emission intensity over time.



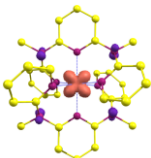
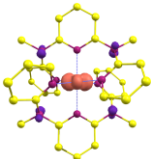
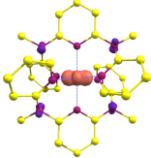
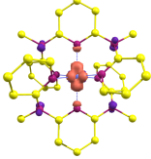
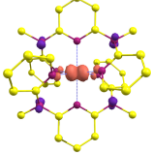
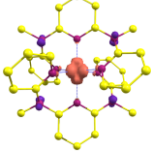
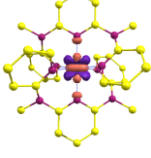
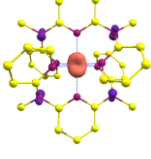
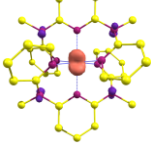
**Figure S19** Stern-Volmer plots of **1**(PF<sub>4</sub>)<sub>3</sub> ( $\lambda_{\text{obs}} = 777$  nm, red) and [Cr(bpy)<sub>3</sub>](PF<sub>6</sub>)<sub>3</sub> ( $\lambda_{\text{obs}} = 727$  nm, blue) by quenching with dGMP in H<sub>2</sub>O ( $\lambda_{\text{exc}} = 435$  nm). Dotted line is a linear regression of the data.

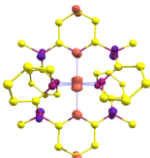
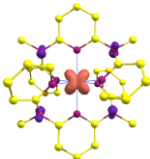
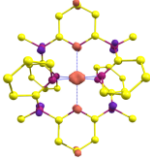
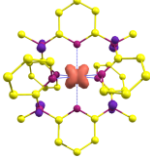
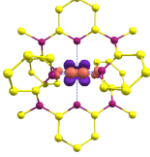
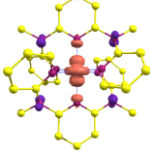
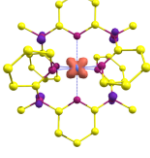
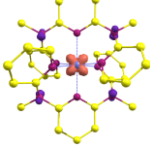
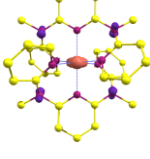


**Figure S20** TD-DFT calculated transitions of  $1^{3+}$  (B3LYP, RIJCOSX, Def2-SVP/J, Def2-SVP, ZORA), assignments and corresponding difference electron densities  $\psi_{ES} - \psi_{GS}$  at a contour value of 0.005 (purple lobes indicate loss, orange lobes show increase of electron density upon excitation, hydrogen atoms omitted for clarity).

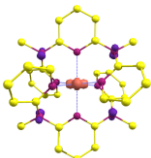
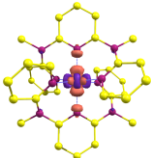
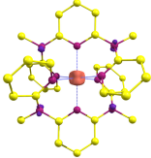
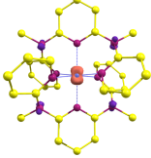
#	$\lambda$ / nm	character	from	to	difference electron density
1	441.7	LMCT	p (amine-N)	$t_{2g} (d_{xy})$	
2	439.0	MC	$t_{2g} (d_{xy})$	$e_g (d_{x^2-y^2})$	
3	436.9	MC	$t_{2g} (d_{xz})$	$e_g (d_{z^2})$	
4	431.8	LMCT	p (amine-N)	$t_{2g} (d_{xz})$	
5	428.3	LMCT	p (amine-N)	$t_{2g} (d_{xy})$	
6	427.7	MC	$t_{2g} (d_{xz})$	$e_g (d_{x^2-y^2})$	
7	422.2	LMCT	p (amine-N)	$t_{2g} (d_{xz})$	
8	409.8	LMCT	p (amine-N)	$t_{2g} (d_{yz})$	

---

9	399.5	LMCT	p (amine-N)	$t_{2g} (d_{yz})$	
10	375.7	LMCT	p (amine-N)	$t_{2g} (d_{xy})$	
11	373.4	LMCT	p (amine-N)	$t_{2g} (d_{xy})$	
12	369.5	LMCT	p (amine-N)	$e_g (d_{z^2})$	
13	367.6	LMCT	p (amine-N)	$e_g (d_{x^2-y^2})$	
14	363.6	LMCT	p (amine-N)	$e_g (d_{x^2-y^2} + d_{z^2})$	
15	358.4	MC	$t_{2g} (d_{yz})$	$e_g (d_{z^2})$	
16	357.3	LMCT	p (amine-N)	$t_{2g} (d_{xz})$	
17	356.0	LMCT	p (amine-N)	$t_{2g} (d_{xz})$	

18	352.3	LMCT	p (amine-N)	$t_{2g} (d_{xz})$	
19	350.8	LMCT	p (amine-N)	$t_{2g} (d_{yz})$	
20	348.9	LMCT + ππ*	p (amine-N)	$e_g (d_{x^2-y^2})$	
21	348.0	LMCT	p (amine-N)	$t_{2g} (d_{yz})$	
22	347.7	MC	$t_{2g} (d_{xy})$	$e_g (d_{x^2-y^2})$	
23	339.2	LMCT	p (amine-N)	$e_g (d_{z^2})$	
24	338.8	LMCT	p (amine-N)	$t_{2g} (d_{yz})$	
25	336.4	LMCT	p (amine-N)	$t_{2g} (d_{yz})$	
26	333.0	LMCT	p (amine-N)	$t_{2g} (d_{xy})$	

---

27	329.2	LMCT	p (amine-N)	$t_{2g} (d_{xy})$	
28	327.1	MC	$t_{2g} (d_{xy})$	$e_g (d_{z^2})$	
29	323.5	LMCT	p (amine-N)	$t_{2g} (d_{xy} + d_{xz} + d_{yz})$	
30	322.7	LMCT	p (amine-N)	$t_{2g} (d_{xz})$	

**Figure S21** DFT calculated spin density of  $1^{3+}$  ( $^4A_2$  ground state) (B3LYP, RIJCOSX, Def2-SVP/J, Def2-SVP, ZORA); isosurface value 0.01 a.u.; hydrogen atoms omitted for clarity; distances in Å.

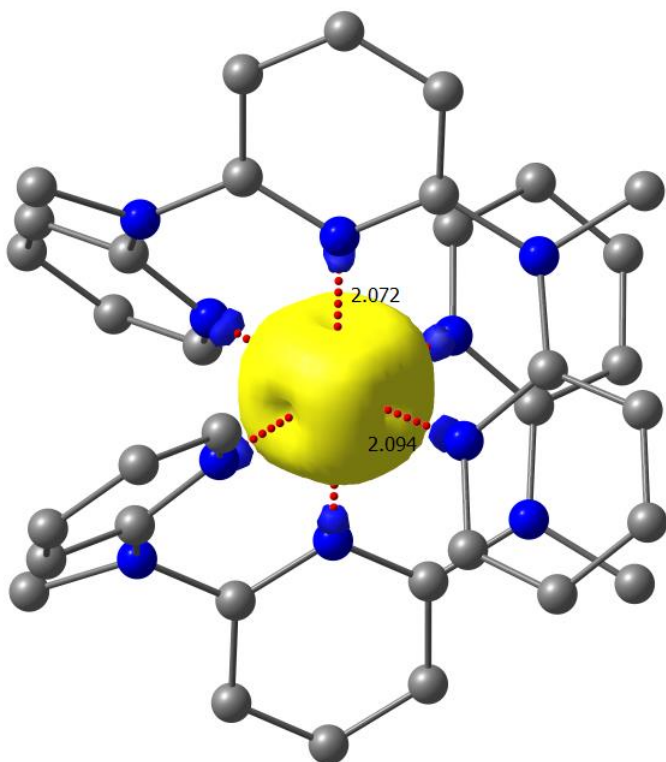


**Figure S22** DFT calculated spin density of  $1^{3+}$  ( $^2E$  state) (B3LYP, RIJCOSX, Def2-SVP/J, Def2-SVP, ZORA); isosurface value 0.01 a.u.; hydrogen atoms omitted for clarity; distances in Å.

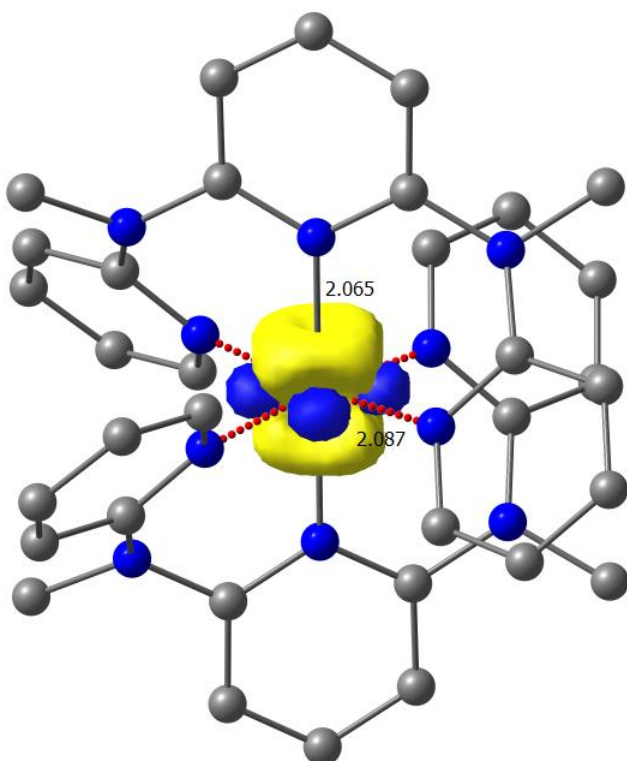


**Figure S23** DFT calculated spin density of  $1^{3+}$  ( ${}^2T_2$  state) (B3LYP, RIJCOSX, Def2-SVP/J, Def2-SVP, ZORA); isosurface value 0.01 a.u. (hydrogen atoms omitted for clarity).

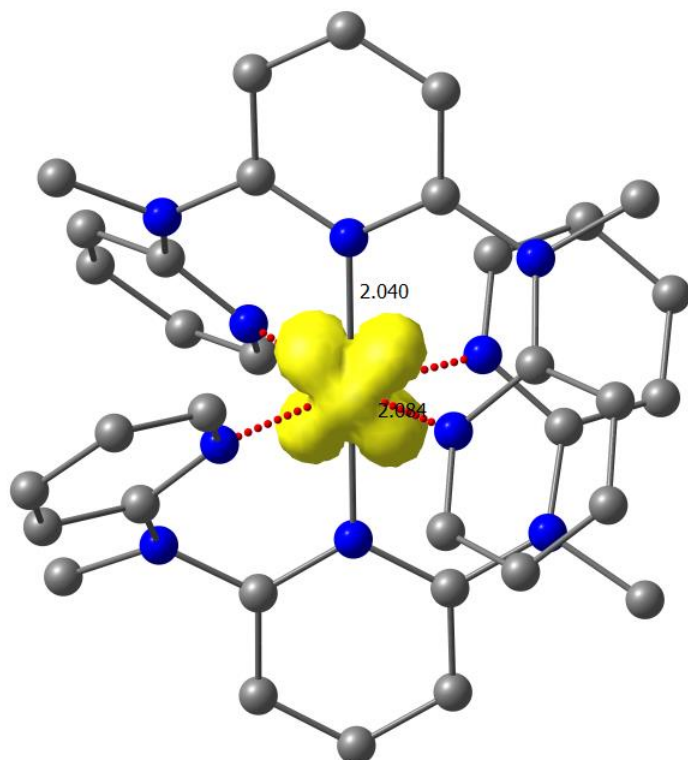


**Figure S24** DFT calculated spin density of  $1^{3+}$  ( ${}^4T_2$  state) (B3LYP, RIJCOSX, Def2-SVP/J, Def2-SVP, ZORA); isosurface value 0.01 a.u. (hydrogen atoms omitted for clarity).

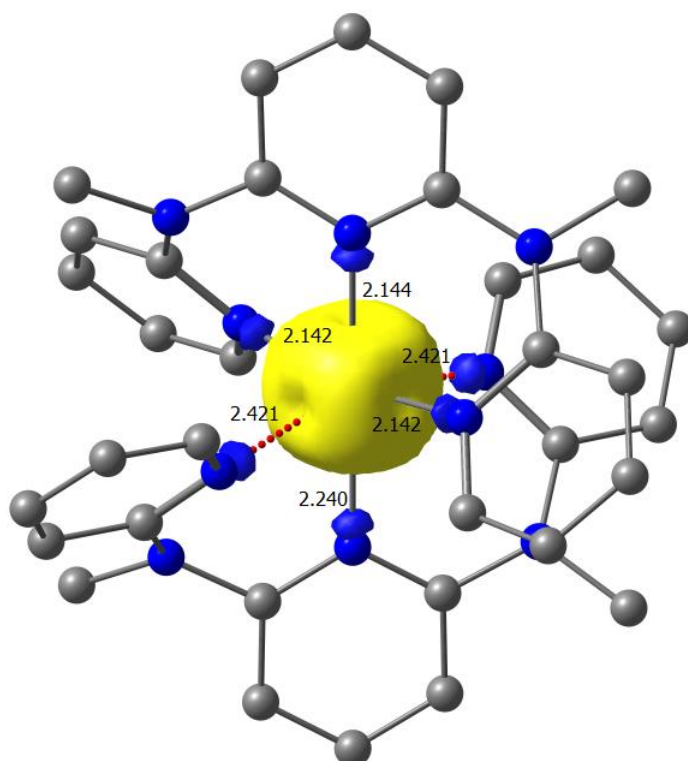




**Figure S25** DFT calculated spin density of  $1^{2+}$  ( $^5E$  state) (B3LYP, RIJCOSX, Def2-SVP/J, Def2-SVP, ZORA); isosurface value 0.01 a.u. (hydrogen atoms omitted for clarity).

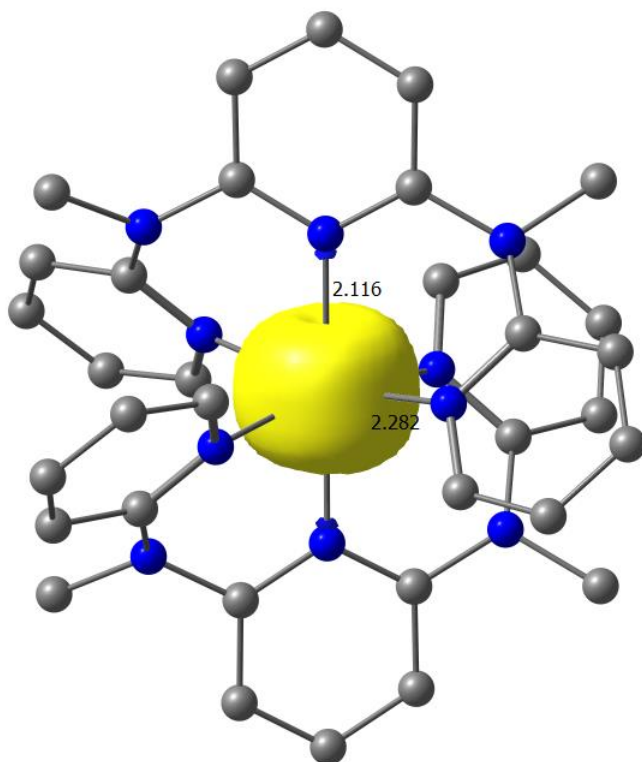


**Figure S26** DFT calculated spin density of  $1^{2+}$  ( $^3T_1$  state) (B3LYP, RIJCOSX, Def2-SVP/J, Def2-SVP, ZORA); isosurface value 0.01 a.u. (hydrogen atoms omitted for clarity).

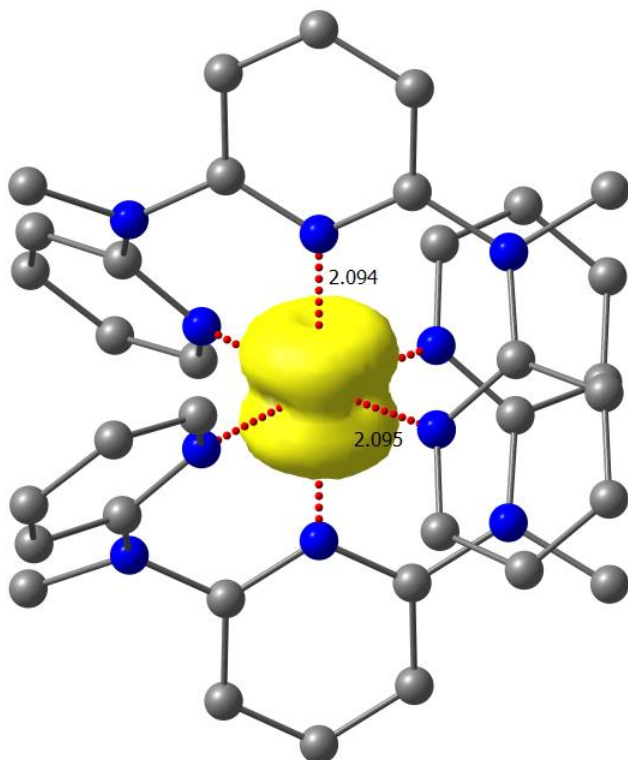


**Table S4** Selected distances [Å] and angles [deg] of DFT optimized geometries (B3LYP, RIJCOSX, Def2-SVP/J, Def2-SVP, ZORA).

	<b>1<sup>3+</sup></b>				<b>1<sup>2+</sup></b>	
	<sup>4</sup> A <sub>2</sub>	<sup>2</sup> E	<sup>2</sup> T <sub>2</sub>	<sup>4</sup> T <sub>2</sub>	<sup>5</sup> E	<sup>3</sup> T <sub>1</sub>
Cr1-N1 / Å	2.094	2.087	2.084	2.421	2.282	2.095
Cr1-N3 / Å	2.072	2.065	2.040	2.240	2.116	2.094
Cr1-N5 / Å	2.094	2.087	2.084	2.421	2.282	2.095
Cr1-N6 / Å	2.094	2.087	2.084	2.142	2.282	2.095
Cr1-N8 / Å	2.072	2.065	2.040	2.144	2.116	2.094
Cr1-N10 / Å	2.094	2.087	2.084	2.142	2.282	2.095
N1-Cr1-N3 / °	86.61	86.71	85.89	78.43	83.32	86.41
N1-Cr1-N5 / °	173.23	173.41	171.77	156.86	166.64	172.81
N1-Cr1-N6 / °	92.29	92.60	91.43	92.48	95.88	92.21
N1-Cr1-N8 / °	93.39	93.30	94.11	101.58	96.69	93.59
N1-Cr1-N10 / °	88.11	87.78	89.16	90.00	85.68	88.24
N3-Cr1-N5 / °	86.61	86.70	85.89	78.43	83.32	86.41
N3-Cr1-N6 / °	93.39	93.30	94.11	96.23	96.68	93.59
N3-Cr1-N8 / °	180.00	180.00	180.00	179.99	179.99	180.00
N3-Cr1-N10 / °	93.39	93.30	94.12	96.22	96.67	93.60
N5-Cr1-N6 / °	88.11	87.78	89.16	90.00	85.67	88.24
N5-Cr1-N8 / °	93.39	93.30	94.12	101.56	96.68	93.60
N5-Cr1-N10 / °	92.29	92.60	91.43	95.51	95.89	92.21
N6-Cr1-N8 / °	86.61	86.71	85.89	83.78	83.32	86.41
N6-Cr1-N10 / °	173.23	173.41	171.77	167.55	166.65	172.81
N8-Cr1-N10 / °	86.61	86.70	85.89	83.78	83.32	86.41



## 7 ACKNOWLEDGMENTS

[REDACTED]

[REDACTED]

[REDACTED]

[REDACTED]

[REDACTED] 🙏

[REDACTED]

[REDACTED]

[REDACTED]

[REDACTED]

[REDACTED]



## 8 CURRICULUM VITAE

### Christoph Kreitner

*Date of Birth:* 21.09.1988  
*Place of Birth:* Wiesbaden, Germany  
*Nationality:* German



#### EDUCATION

*Johannes Gutenberg-University Mainz, Germany*

**Doctorate** (Chemistry) **01/2013 – 06/2016**

*„Synthesis and Characterization of new Ruthenium complexes:  
 Functional chromophores and electron transfer relays”*

Advisor: [REDACTED]

*Johannes Gutenberg-University Mainz, Germany*

**Diploma** (Chemistry, *very good*, 1.0) **10/2007 – 09/2012**

Main: Inorganic chemistry; Elective: Theoretical chemistry

**Diploma thesis** (*very good*, 1.0) **01/2012 – 09/2012**

*„Synthesis, experimental and theoretical characterization  
 of new mixed-valent ruthenium complexes”*

Advisor: [REDACTED]

**Teaching Assistant**, inorganic and physical chemistry **10/2008 – 08/2011**

*University of Toronto, Toronto, Canada*

**Research internship** **09/2010 – 03/2011**

*“Reactivity of Frustrated Lewis Pairs with Lactones and Lactide”*

Advisor: [REDACTED]

*Gymnasium Theresianum Mainz, Germany*

**Abitur** (*very good*, 1.1) **08/1999 – 03/2007**

**Research paper** (chemistry, *very good*, 1.0) **02/2006**

*“The basics of coordination chemistry on the basis of  
 the synthesis of tetraamminecopper(II)-sulfate”*

**BEGYS** (school intern talent training) **09/2001 – 07/2004**

*International Language School, Cannes, France*

**French language course**, 2 weeks **08/2005**

*Pinkerton Academy, Derry (NH), USA*

**Student exchange**, 4 weeks **09/2004**

### AWARDS AND SCHOLARSHIPS

<b>Gutenberg Academy</b> , Johannes-Gutenberg University Mainz <b>Junior Membership</b> Awarded to the 25 best PhD students of the University	since <b>03/2014</b>
<b>Materials Science in Mainz (MAINZ)</b> , Graduate School of Excellence <b>Graduate Student Scholarship</b>	since <b>05/2013</b>
<b>Poster Prize of the International Union of Pure and Applied Chemistry (IUPAC)</b> at the GDCh Wissenschaftsforum 2013, Darmstadt, Germany	<b>09/2013</b>
<b>Adolf Todt Award 2013</b> of the Johannes Gutenberg-University Mainz for an excellent diploma thesis	<b>04/2013</b>
<b>Travel stipend</b> of the Graduate School <b>Materials Science in Mainz</b>	<b>09/2010 – 02/2011</b>
<b>Award</b> of the GdCh for " <i>the best Abitur in Chemistry</i> "	<b>03/2007</b>
<b>Award</b> of the "Förderverein Theresianum e.V." " <i>for exemplary behavior within the school community, for outstanding scholastic achievements and for the longtime engagement in the instrumental ensembles of the school</i> "	<b>03/2007</b>

### LANGUAGE SKILLS

<b>German</b>	native language
<b>English</b>	business fluent
<b>French</b>	very good (CEFR level C1)
<b>Latin</b>	Latin proficiency certificate

### SUMMER SCHOOLS AND WORKSHOPS

<i>Max-Planck-Institute for Chemical Energy Conversion, Mülheim, Germany</i> <b>Summer School</b> <i>"Methods in Molecular Energy Research: Theory and Spectroscopy"</i>	<b>09/2014</b>
<i>University of Manchester, UK</i> <b>Summer School</b> <i>"Introductory workshop on the Theory and Practice of EPR spectroscopy"</i>	<b>05/2013</b>
<i>Johannes Gutenberg-University Mainz, Germany</i> <b>Workshops</b> Poster Design and Communication	<b>10/2013</b>
Presenting in English	<b>02/2014</b>
Intercultural Communication	<b>09/2014</b>
Introductory Workshop on High Performance Computing	<b>11/2014</b>

Mainz, 1<sup>st</sup> of June, 2016

## 8.1 LIST OF PUBLICATIONS

- C. Kreitner**, S. J. Geier, L. J. E. Stanlake, C. B. Caputo, D. W. Stephan, Ring openings of lactone and ring contractions of lactide by frustrated Lewis pairs. *Dalton Trans.* **2011**, 40, 6771–6777.
- C. B. Caputo, S. J. Geier, E. Y. Ouyang, **C. Kreitner**, D. W. Stephan, Chloro- and phenoxy-phosphines in frustrated Lewis pair additions to alkynes. *Dalton Trans.* **2012**, 41, 237–242.
- A. Breivogel, **C. Kreitner**, K. Heinze, Redox and Photochemistry of Bis(terpyridine)ruthenium(II) Amino Acids and Their Amide Conjugates - from Understanding to Applications. *Eur. J. Inorg. Chem.* **2014**, 2014, 5468–5490. – **Highlighted Cover Article**
- C. Kreitner**, M. Grabolle, U. Resch-Genger, K. Heinze, Dual Emission and Excited-State Mixed-Valence in a Quasi-Symmetric Dinuclear Ru–Ru Complex. *Inorg. Chem.* **2014**, 53, 12947–12961.
- C. Kreitner**, E. Erdmann, W. W. Seidel, K. Heinze, Understanding the Excited State Behavior of Cyclometalated Bis(tridentate)ruthenium(II) Complexes: A Combined Experimental and Theoretical Study. *Inorg. Chem.* **2015**, 54, 11088–11104. – **Highlighted Cover Article**
- S. Otto, M. Grabolle, C. Förster, **C. Kreitner**, U. Resch-Genger, K. Heinze, [Cr(ddpd)<sub>2</sub>]<sup>3+</sup>: ein molekulares, wasserlösliches, hoch NIR-lumineszentes Rubin-Analogon. *Angew. Chem.* **2015**, 127, 11735–11739. [Cr(ddpd)<sub>2</sub>]<sup>3+</sup>: A Molecular, Water-Soluble, Highly NIR-Emissive Ruby Analogue. *Angew. Chem. Int. Ed.* **2015**, 54, 11572–11576. **Highlighted as Hot Paper**
- C. Kreitner**, K. Heinze, The photochemistry of mono- and dinuclear cyclometalated bis(tridentate)ruthenium(II) complexes: Dual excited state deactivation and dual emission. *Dalton Trans.* **2016**, 45, 5640–5658.
- C. Kreitner**, A. K. Mengel, T. K. Lee, W. Cho, K. Char, Y. S. Kang, K. Heinze, Strongly Coupled Cyclometalated Ruthenium Triarylamine Chromophores as Sensitizers for DSSCs. *Chem. Eur. J.* **2016**, published online 19 May 2016, DOI: 10.1002/chem.201601001.
- C. Kreitner**, K. Heinze, Excited State Decay of Cyclometalated Polypyridine Ruthenium Complexes: Insight from Theory and Experiment, **2016**, *submitted*.



## 8.2 CONFERENCE CONTRIBUTIONS

- 09/2013      **GDCh Wissenschaftsforum**, Darmstadt Germany  
Poster presentation
- 08/2014      **41<sup>st</sup> International Conference on Coordination Chemistry**, Singapore  
Poster presentation
- 09/2014      **Summer School** "*Methods in Molecular Energy Research: Theory and Spectroscopy*", Gelsenkirchen, Germany  
Poster presentation
- 09/2014      **Vortragstagung der Wöhlervereinigung**, Saarbrücken, Germany  
Poster presentation
- 03/2015      **Koordinationschemie-Tagung**, Paderborn, Germany  
Oral presentation